Gaute Linga

Fluid Flows with Complex Interfaces: Modelling and Simulation from Pore to Pipe

Thesis submitted to the PhD School of The Faculty of Science,
University of Copenhagen, for the degree of Doctor of Philosophy

ABSTRACT

In this thesis, aspects of fluid flow with disordered interfaces are investigated by numerical and theoretical means, and their relations to geophysically relevant systems are discussed. The research output consists of physical models, numerical methods and tools, and applications of the models and methods to problems ranging from the pore to the pipe scale.

A part of the work focuses on single-phase fluid flow. In order to address the universality class of the laminar–turbulent transition in pipe flow, particle-based models for the interaction between turbulent domains are introduced. To illuminate the joint effects of a disordered geometry and fluid inertia on macroscopic transport properties, transitional flow in rough fractures is investigated by direct numerical simulations. In the limit of creeping flow, the coupling between flow and stress in dissolving porous rock is studied.

The remainder of the work concerns flows where the effects of a second phase, chemical transport, and electric fields, are included. Models for such electrohydrodynamic and two-phase flows are analysed herein. Furthermore, efficient numerical methods are developed both for single- and two-phase electrohydrodynamic flow, and a simulation framework, based on a diffuse-interface model, is introduced to facilitate simulation of phenomena including wetting at the pore scale and microfluidic devices.

DANSK RESUMÉ

I denne afhandling undersøges aspekter af væskestrømning med uordnede grænseflader i numeriske og teoretiske termer. Forskningsresultaterne består af fysiske modeller, numeriske metoder og værktøjer samt anvendelser af modellerne og metoderne til problemer, der spænder fra pore- til rørskala.

En del af arbejdet fokuserer på enfasestrømning. For at undersøge universalitetsklassen for overgangen fra laminær til turbulent strømning i rør, introduceres partikelbaserede modeller for interaktionen mellem turbulente domæner. For at belyse den koblede virkning af en uordnet geometri og væskens inerti på de makroskopiske transportegenskaber, undersøges strømning ved den turbulente overgang i ru sprække ved hjælp af direkte numerisk simulering. I grensen af krybende strømning undersøges forbindelsen mellem strømning og spænding i porøse stenarter der undergår opløsning.

Resten af arbejdet beskæftiger sig med strømning, hvor virkningerne af en anden fase, kemisk transport og elektriske felter er inkluderet. Modeller af sådan elektrohydrodynamisk strømning og tofasestrømning analyseres. Yderligere udvikles effektive numeriske metoder til både en og to faser, og et simuleringsværktøj baseret på en diffus-grænsefladmodel, indført for at muliggøre simulering af fænomener som vædning på poreskala og mikrofluidiske indretninger.

ACKNOWLEDGEMENTS

I would like to thank my advisor, Joachim Mathiesen, for giving me the opportunity to take on this PhD project, and for both allowing me and (at times when I did not believe in them myself) encouraging me to pursue my own ideas. I would like to express my gratitide to my collaborators at the Niels Bohr Institute, including Asger Bolet, Anier Hernandez-Garcia, and Mads Madsen. I am sincerely grateful to François Renard and Luiza Angheluta at the University of Oslo for good collaboration and for always providing an open door at the Physics building. Thanks are due also to other collaborators, including Tore Flåtten and Halvor Lund, former colleagues at Sintef, and to Nigel Goldenfeld and Hong-Yan Shih, University of Illinois at Urbana-Champaign, for a fruitful autumn of 2017. Further, I thank my colleagues and friends at NBI and in NanoHeal network for making my PhD period a predominantly joyful experience.

I would also like to thank my friends in Copenhagen, Oslo, Trondheim, Bergen, and Paris, for providing supplementary perspectives on life to that of science. Sincere thanks are due to my family for keeping me warm and well fed during my formative years (which continue to this day), and for teaching me the value of the saying "perfect is the enemy of good."

Finally, I would like to express my gratitude to Linn Helmich Pedersen for displaying terrific patience and enduring support during the past three years, and for being an inexhaustible source of joy in my life.

Copenhagen, August 2018
Gaute Linga

The following papers were published during the course of the PhD period, but are not included in the thesis.

- Creep rupture of fiber bundles: A molecular dynamics investigation.
  Gaute Linga, Pietro Ballone, and Alex Hansen.
  Physical Review E **92**, 022405 (2015).

- Two-phase nozzle flow and the subcharacteristic condition.
  Gaute Linga, Peder Aursand, and Tore Flåtten.
  Journal of Mathematical Analysis and Applications **426**, 917–934 (2015).

- Thermodynamic modeling with equations of state: present challenges with established methods.
  Øivind Wilhelmsen, Ailo Aasen, Geir Skaugen, Peder Aursand, Anders Austegard, Eskil Aursand, Magnus Aa. Gjennestad, Halvor Lund, Gaute Linga, and Morten Hammer.
  Industrial & Engineering Chemistry Research **56** (13), 3503–3513 (2017).

CONTENTS

INTRODUCTION

1.1   A CONTEMPORARY SURVEY OF *FLUID* NATURAL RESOURCES

How do fluids flow through rocks? Answers to this blunt question are not simple and straightforward, but the advances made by humanity in addressing this question has had widespread consequences for the standard of living in the 21ˢᵗ century. From the moment you wake up in the morning and brew yourself a cup of coffee, you enjoy the fruits of fluid flow in porous media.

From a purely geophysical perspective, fluid circulation from the mantle to the atmosphere shapes the world around us. In porous rocks, fluid flow is an important factor for pattern formation and rock weathering [215], as it controls mineral transport and heat flow from the nanoscale to the field scale [359]. Deformation coupled to fluid flow is also tightly connected with the triggering of earthquakes [171,303,384,409]. Hence, understanding the intimate coupling between fluid flow, reaction and deformation of rocks is crucial for understanding how patterns form in nature and how sceneries are sculpted.

From a more industrial point of view, many of the Earth's most desired natural resources are found below the surface, in a liquid state of matter in porous rock formations. Freshwater stored in aquifers, i.e. underground water-bearing rock formations, is an essential natural resource. Groundwater accounts for roughly a third of the available freshwater resources in the world [407], and has served to keep the author, among others, hydrated during the last three years. Due to food production requirements for a rapidly growing global population, many groundwater resources are becoming depleted [114]. Unsustainable harvesting of groundwater may not only have dire consequences for drinking and irrigation purposes, but may also reduce the integrity of rock formations [12]. Simultaneously, human activity has led to unintended groundwater contamination [103].[1] In fact, the scarcity of drinkable water (being in surface or subsurface reservoirs) represents such a fundamental issue that it can trigger future wars.[2] In this respect, technological progress in *desalination*—roughly speaking, turning seawater into freshwater—could prevent future conflicts. The downside with many current methods is that they are highly energy consuming.

In this respect, petroleum (oil and natural gas)—another important fluid resource found in porous geological formations—has been a major contributor to covering the Earth's exploding energy consumption during the last century. At the time of writing, petroleum accounts for more than half of the total global energy usage [65]. Many renewable energy sources, such as wind and solar energy, cannot produce energy *on-demand*, as both wind and sun conditions fluctuate in time and space. The only completely renewable energy source that can be used to provide a base load in the global electrical grid is hydroelectricity. However, in many developed countries, the majority of available waterfalls are already exploited [469], at least to the point where they pose a threat to biological diversity in and around the affected drainage systems. It thus seems clear that hydroelectricity alone cannot compensate for the soaring demand for (green) energy in

[1] As anyone knows who has seen the movie *Erin Brockovich* (2000).

[2] Like it has in the past, see e.g. [348].

the world. An alternative candidate for providing a base load is nuclear energy, where the basic energy production process does not release CO_2. Despite large reserves, unfortunate accidents, most recently caused by earthquakes (Fukushima, 2011), have degraded public and political opinion on nuclear energy and stalled development[469].

Geothermics is another practically renewable energy resource, where water heated deep in the Earth's crust is pumped from reservoirs to either drive power plants or directly heat buildings.

In the advent of *sufficiently* large-scale renewable energy production, petroleum will therefore remain a major source of energy. If coal is the direct alternative (as with Germany's phase-out of nuclear plants), oil and (in particular) natural gas appear to be the lesser of evils. In this respect, basic knowledge of how fluid flows from the nanometer to the basin scale is essential. A contrasting *laissez-faire* attitude likely leads to unforeseen consequences such as, e.g., induced seismicity[173,434] (generation of earthquakes by human activity), and land lowering or groundwater contamination due to shale gas extraction[98].

The Paris Agreement from 2015 states that global warming should be limited to $1.5\,°C$ above pre-industrial levels—a goal which seems to be at odds with current trends in energy consumption. A possible remedy from the dire consequences of continued reliance on fossil fuels, is to reduce the net release of CO_2 by means of carbon capture, transport and storage (CCS)[204]. The idea behind CCS is to capture the CO_2 where it is released, typically at an industrial site; transport it to suitable storage sites, e.g. saline aquifers or depleted petroleum reservoirs; and inject it into the formation through injection wells[203,260,328]. Injected CO_2 should then bind to the rock[291], and by that and other trapping mechanisms[112,203] remain permanently stored in the geological formations. Although CCS is already being carried out in practice (e.g. in Norwegian deep saline aquifers since 1996), many fundamental processes are not fully understood[203]. Injection of CO_2 into petroleum reservoirs can be used to increase the amount of oil that can be harnessed—called *enhanced oil recovery*—closing the circle between CCS and petroleum production. Enhanced oil recovery is, however, usually carried out using other fluids and water of varying salinity, surfactants, or other chemicals[382].

Taken together, fluid natural resources are essential to our existence. Knowing how fluids flow in rocks, pipes, fractures, and other geophysical systems, can improve safety and efficiency of energy harnessing and transport and storage of CO_2.[3] While the applications differ, the underlying physical mechanisms, the resulting equations, and the methods used to investigate them, are largely similar. In these cases the results are not limited to, e.g., a given type of rock or fluid composition, but universal or general properties can be found which have consequences for a broad range of systems. Thus, it makes sense to address these topics in a unified way.

[3] And is, of course, interesting *in itself.*

1.2   scope and objectives

The survey in the previous section is not intended to be complete, but merely to motivate why fluid flow in disordered geometries—and in particular why the question asked at the beginning of the chapter—is relevant.

The present thesis does not mainly concern specific applications, but addresses instead the general physical concepts *behind* the applications, using theory and numerical simulations. A recurrent theme in this thesis is flow resistance, or conversely, *permeability*. In most applications, it is desirable to minimize the driving force needed to sustain a certain flow rate; that is, to maximize the permeability. This holds valid for flow across several scales; from the pore scale, through networks of pores and fractures, to the corrugated internal surface of a pipe. Complex interfaces, between either a solid and a fluid phase, or between two fluid phases, also have consequences for flow resistance on macroscopic scales, and are not fully understood. Physical processes such as ion migration and surface charges inducing an electric field, may influence flow properties
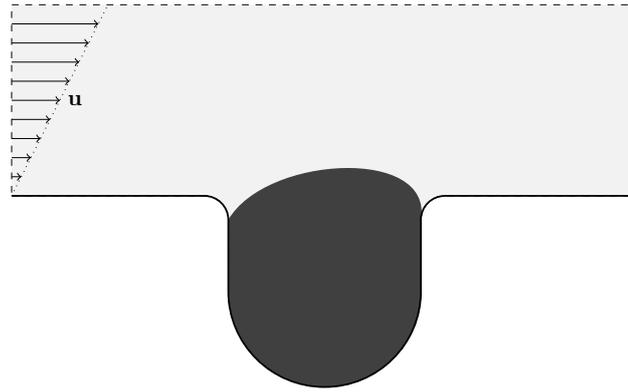
FIGURE 1.1: A conceptual dead-end pore filled with conceptual oil, while water is flowing above. A slight distortion of the oil surface is observed, but the oil remains stuck in the pore. (Figure courtesy of A. Bolet.)

even on large scales.

As an illustrative example, consider Fig. 1.1 where we show a schematic dead-end pore wherein an amount of "oil" is stuck. Above the pore, another phase a shear flow of "water" is imposed, and the two phases are taken to be immiscible. This is a basic example of a multiphase system with complex interfaces, where a solid phase provides a disordered confining geometry and the two liquid phases interact nonlinearly.

To both a petroleum engineer (seeking to harness the oil) and an environmental remediator (seeking to decontaminate the soil), it would be desirable to get the oil out of the pore. As the water flows above it, however, the droplet remains stuck in its dead-end pore. Two apparent suggestions on how to get the droplet out are the following:

- Increase the flow rate, i.e., the effect of *inertia*.

- Account for the effect of ions in the solution and the electric field due to surface charges on the pore walls, i.e., include electrohydrodynamics (EHD).

The scope of this thesis is rather broad, and it aims to address effects on flow typically present in geologically relevant systems—in particular, the roles of inertia, disordered interfaces, and the effect of surface charges and ionic solutions.

Using continuum-scale descriptions, these effects are investigated on scales from a single pore, through fractures and pore networks, to pipe flow. As these scales span roughly from sub-micrometer to the kilometer scale, it is clear that this thesis cannot cover all aspects of flow in this range. Hence, the objectives can (in some retrospect) be summarized as the following:

1. Develop and analyse physically consistent continuum-scale models for single- and two-phase flow in geophyisically relevant systems, including solute transport and electric fields.

2. Develop methods for simulating such models, predominantly using the finite element method.

3. Apply the developed models and methods to studying flows with complex interfaces.

In particular, both models and methods are developed, and studies are carried out.

Although the broad, overarching question was posed already in the first sentence of this chapter, the more specific *physical* research questions in this thesis include the following:

- How does a disordered geometry influence the macroscopic transport properties of geophysically relevant media?

- What is the combined effect of inertia and a disordered geometry?

- How do charged surfaces and ions in solution influence the wetting behaviour and macroscopic flow properties in disordered geometries?

Progress towards answering these questions is presented in this thesis. Moreover, numerical methods and software are developed that can help gaining even more insights into these questions in the future.

The results are primarily given in the papers that make up the thesis. Summaries of these and more specified research questions are given in chapter 5, along with some complementary information. In Table 1.1, the interested reader will find a simple overview of how the appended papers relate to each other.

TABLE 1.1: How the different papers comprising this thesis relate to each other. The overview indicates included physical effects and novelties in the appended papers. The papers are grouped according to the summary in chapter 5.

Paper	Phases		Scale			Including		Novelty		
	1	2	Pore	Fracture	Pipe	Inertia	EHD	Model	Method	Study
Turbulent fronts in pipe flow (section 5.1)										
1	✓				✓	✓		✓	✓	✓
Flow in fractured and porous media (section 5.2)										
2	✓		✓						✓	✓
3	✓			✓		✓				✓
Electrohydrodynamics (section 5.3)										
4	✓		✓	✓			✓		✓	✓
5	✓		✓	✓		✓	✓	✓	✓	
6		✓	✓	✓		✓	✓		✓	
7		✓	✓				✓	✓		✓
Homogenized models for two-phase flow (section 5.4)										
8		✓		✓	✓			✓		
9		✓		✓	✓			✓	✓	✓

1.3 APPLICATIONS TO OTHER FIELDS

Obviously, although the results presented in this thesis have in common that they are related to geophysics, the results are by no means limited to such systems. Below follows a brief and incomplete list of topics to which the results presented here may be of relevance.

- **Microfluidics:** The coupling of two-phase fluid flow and electrochemistry probably has even more applications within micro-[74,418] and nanofluidics[400] than in geophysics. Technological applications span from fabricating microelectromechanical devices[249,361,419], electronic displays[37,38,183,210], desalination devices[411], inkjet printing, and more.

- **Phase separation:** Two-phase systems with electric fields and chemical effects have applications to electrocoalescers, i.e., devices used to separate water and crude oils in emulsions[135,280].

- **Biology:** Unsteady, inertial flow in disordered geometries, e.g. rough pipes, has applications to how blood flows in our bodies. In particular, inertial effects are important in the larger arteries; in the aorta the Reynolds number (see next

chapter) is around 4000 [238], which is far beyond the point where turbulence arises in smooth pipes or tubes [23].

Moreover, electrohydrodynamic (or at least electrokinetic) effects control how fluid is transported in the brain [198], and how neural signals propagate [281,416]. As another unexpected link, the Barkley model [28–30] that describes the turbulent transition in pipe flow as an excitable medium, is inspired by models for nerve signals.

Multiphase porous flows and poroelasticity is also relevant in biological tissue, e.g. in the dynamics of cancerous invasions [461].

- **Nuclear engineering:** Many of the models for two-phase flow that are now extensively used for petroleum and CO_2 transport, have not only applications to, but actually their origin in, nuclear engineering [24,46]; where they describe the flow of the working fluid (heated in the nuclear reactors) used to drive the steam turbines that produce electricity.

- **Semiconductor physics:** The equations of electrohydrodynamics, in particular the Nernst–Planck equations, find wide use in semiconductor physics [91,268]. At least through the use and development of numerical methods, these fields could find common ground.

- **Food industry:** Foams, sauces (some of which are oil-in water emulsions), milk, etc., are all realizations of two-phase flow with chemical interactions, and thus relevant to the present work.

Finally, we return to the first paragraph of the chapter, and to the freshly brewed cup of coffee that you might enjoy in the morning. Consolidated, grinded coffee is perhaps the archetypical example of a porous medium. In the art of coffee making, a multitude of physical and chemical processes are at play and must be controlled. Influenced by gravity, one fluid (water) intrudes and displaces the other (air) within the porous medium, the porous medium deforms, chemical reactions and diffusion (extraction) occur, and heat flows through the system; but still you are likely left with a reproducible cup of coffee.[4] Adding the socio-economic aspects of cultivating coffee to the picture (e.g. freshwater requirements, global export), makes it clear that coffee brewing is a far too complicated task to take on in this project. We will therefore leave it to the baristas, for now.[5]

[4] For a popular-science based introduction to coffee brewing, see [185].

[5] Perhaps, some day, coffee brewing will be the subject of a Horizon 2020 Initial Training Network.

1.4   STRUCTURE OF THE THESIS

The structure of this thesis is as follows. Chapter 1, which you are now reading, is an attempt to put the topics of this thesis into a broader context, without diving into too specific details; and in a broad sense to motivate the work presented. Chapter 2 gives an overview of historical development, phenomenology, and the state of the art of the topics involved. Chapter 3 deals with the physical models employed in the present work. In chapter 4, an overview is given of the numerical methods, spatial and temporal discretization strategies, and numerical software employed and developed in this work. In chapter 5, brief summaries of the research articles that comprise the results of this thesis are given. Finally, chapter 6 concludes and points to future avenues of research. The research papers are collated in appendix A.

BACKGROUND

2.1 BRIEF HISTORICAL DEVELOPMENT AND PHENOMENOLOGY

The Navier–Stokes equations, which can be stated for an incompressible fluid evolving in space $\mathbf{x}$ and time t, as

$$\rho\left(\partial_t \mathbf{u} + \mathbf{u} \cdot \boldsymbol{\nabla}\mathbf{u}\right) - \mu \boldsymbol{\nabla}^2 \mathbf{u} = -\boldsymbol{\nabla}p, \tag{2.1a}$$

$$\boldsymbol{\nabla} \cdot \mathbf{u} = 0, \tag{2.1b}$$

are at the heart of this thesis. Equation (2.1) describes the velocity $\mathbf{u}(\mathbf{x}, t)$ and pressure $p(\mathbf{x}, t)$ of a fluid of constant density ρ and dynamic viscosity μ. The left hand side of eq. (2.1a) constitutes a balance between intertial forces, represented by the parenthesis term, and viscous forces, represented by the last term. Roughly speaking, the viscous term dampens out fluctuations, and when it dominates over the inertial term, the flow field tends to be smooth and predictable, i.e. *laminar*, much like the flow of syrup under calm breakfast conditions. Conversely, when the inertial term dominates, fluctuations may be enhanced rather than dampened, eventually leading to unsteady and irregular flow patterns—colloquially termed *turbulence*. Such flows can be observed (under the same breakfast conditions) by vigorously pouring milk into your coffee, leading to the formation of unsteady swirls, or turbulent *eddies*. This simple physical experiment is shown in fig. 2.1 (b). The eddies eventually decay, as the viscous term takes its toll, when you stop injecting energy.

FIGURE 2.1: Different flow regimes related to coffee. (a) Creeping flow (Re $\ll$ 1) through a consolidated porous medium during the brewing process. (b) Turbulent flow (Re $\gg$ 1) triggered by pouring of milk into a cup of coffee. Turbulent eddies can be observed. (Photos by Linn Helmich Pedersen.)

Building on work by, among others, Euler[138], Navier[330] with the improvements of Stokes[102,423] arrived at the equations (2.1) which bear their name. However, scientific investigations of fluid dynamics predate these, as will become apparent below. As an example, the first recorded sketch and description of turbulent eddies is due to da Vinci[202]. The following account is neither complete (reference is given to more elaborate

texts where appropriate) nor chronological, but gives a primer on the phenomenology and history of the themes encountered in this thesis.

In 1883, Reynolds[380] set out to investigate the "circumstances which determine whether the motion of water shall be direct or sinuous," or in modern terms, what conditions determine whether flow in pipes is laminar or turbulent. The investigation led to the identification of a dimensionless number, now called the *Reynolds number*,

$$\mathrm{Re} = \frac{\rho u d}{\mu}, \tag{2.2}$$

where u is the mean axial velocity and d is the pipe diameter. The number Re roughly measures the ratio of inertial to viscous forces. Reynolds indentified Re, as the sole parameter determining the flow regime: when Re was below a "critical" value $\mathrm{Re_c} \simeq 2000$, the flow was laminar, whereas above, it could become turbulent. In a transitional region around $\mathrm{Re_c}$, the turbulence would appear as intermittent flashes, being neither fully laminar nor turbulent. We will revisit this transitional region in section 2.1.2.

As we will see, the Reynolds number is an extremely useful quantity for all aspects of fluid flow, giving a simple criterion for which flow regimes are relevant, and which approximations can be made.

2.1.1   *Flow in disordered media*

Due to its ubiquity, flow in *porous media* has been a subject of scientific investigations since the days of Euler[111,139,140]. Two examples of porous media are shown in fig. 2.1 (a) and in fig. 2.2 (b). A porous medium can arise as an aggregation of solid particles and by chemical or biological processes. The resulting solid matrix contains pores that, if connected from inlet to outlet, can allow a macroscopic flow through the system. As a lowest-order description of its geometry, a porous medium can be characterised by its porosity ϕ. Due to the unfeasibility of analytically solving the equations of fluid motion within the pore, much of the theory of porous media flow has been focused on obtaining macroscopic equations for flow through representative elementary volumes. A basic question (in e.g. hydrogeology) has thus been how to relate the *flow rate* $\mathbf{q}$, i.e. volumetric discharge per unit area, through a porous medium, to the imposed pressure gradient $\boldsymbol{\nabla} p$. Following pioneering work by Woltmann[468], Delesse[117], and Fick[149], Darcy[106] came up with his celebrated law,

$$\mathbf{q} = -\frac{k}{\mu} \boldsymbol{\nabla} p, \tag{2.3}$$

where k is the *permeability* of the porous medium. This linear relationship has a direct link from the $\mathrm{Re} \ll 1$ limit of the Navier–Stokes eq. (2.1), where the inertial part can be neglected, leading to the Stokes equations,

$$\mu \boldsymbol{\nabla}^2 \mathbf{u} = \boldsymbol{\nabla} p, \quad \boldsymbol{\nabla} \cdot \mathbf{u} = 0. \tag{2.4}$$

This is often a good approximation in porous media, where the characteristic pore diameter d is exceedingly small. For a more complete historical account of the development of the theory for porous media, see e.g.[111]. Herein, of particular relevance to the present thesis might be the work of Biot concerning the mechanical behaviour of fluid-saturated solids, called *poroelasticity*[49–52,384,459].

Historically, much effort has been devoted to relating the permeability, k in eq. (2.3), to quantities such as the porosity ϕ[99,292]. The arguably most popular such relation is the Kozeny–Carman equation[84,85,237],

$$k \propto \frac{\phi^3 d^2}{(1-\phi)^2}. \tag{2.5}$$
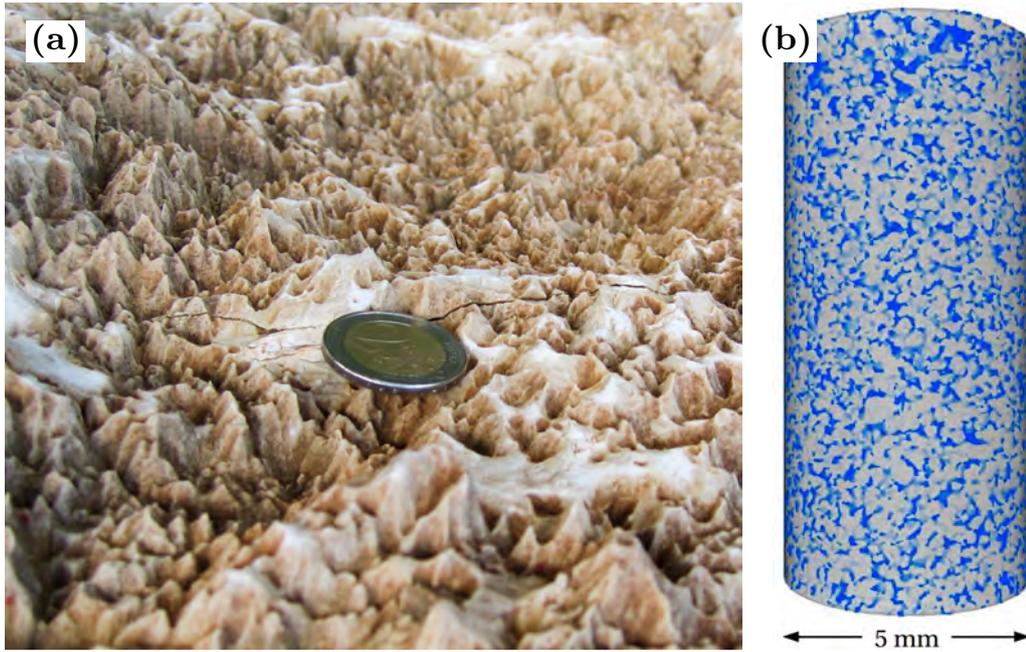
FIGURE 2.2: Examples of rough and porous systems in nature. (a) Rough stylolite surface. (b) Sample of a reservoir rock (Fontainebleu sandstone), imaged by X-ray microtomography. The blue color indicates porosity. (Courtesy of François Renard.)

where d is a characteristic pore diameter. The relation (2.5) is typically applicable to packed beds. Other common modelling choices is to use empirical power laws, $k \sim \phi^m$ (with high exponents m) suitable for soils[159], or exponential forms, cf.[131].

Darcy obtained eq. (2.3) (in a one-dimensional form) by empirically-based considerations, but both eq. (2.3) and improvements thereof have been found by systematic means. Homogenization techniques (e.g. volume averaging) can be used, as demonstrated by Whitaker[465], to derive from first principles a generalized version of eq. (2.3),

$$\mathbf{q} = -\frac{\mathbf{k}}{\mu}\boldsymbol{\nabla}p, \qquad (2.6)$$

where $\mathbf{k}$ is the permeability tensor, reflecting the fact that the discharge need not be directed parallel to the pressure gradient. For non-negligible inertia (moderate Re), empirical corrections eq. (2.3) are due to e.g. Forchheimer[156] and Ergun[134], who both on empirical grounds proposed to add a positive term $\propto \rho|\mathbf{q}|\mathbf{q}$ (where ρ is still the density), to the left hand side of eq. (2.3)[159,412]. A more general power-law description $\propto \rho|\mathbf{q}|^n\mathbf{q}$ (where n is an empirical exponent) is due to Izbash[209]. Correction terms can also be found by homogenization, see e.g.[466] for the Forcheimer term above, which is valid for strong inertia. For weaker inertia, Mei and Auriault[298] found a correction term $\propto |\mathbf{q}|^2\mathbf{q}$[412]. Early disputes concerned whether the departure from the linear Darcy law was due to turbulence, but careful analysis has shown that this is not a necessity (see section I in[243]).

In crustal rock, the permeability is often so low that the fluid transport is not controlled by the microscopic pore size distribution, but takes place mainly in fracture networks spanning large scales[36,297,390]. To estimate the macroscopic permeability of such rocks, a description of both the fracture network topology and of the single fractures is necessary. An intriguing property of fracture surfaces is that they display *scale-invariance*. In particular, they are *self-affine*[61], i.e. the fracture surface $z = h(x,y)$ is *statistically invariant* under the transformation

$$x \to \lambda x, \quad y \to \lambda y, \quad z \to \lambda^H z, \qquad (2.7)$$

When both the porous rock and the fracture network contribute to permeability, so-called *dual-porosity models* are often applied, where voids can correspond to either pores or fractures[120].

or $h(x,y) \sim \lambda^{-H}h(\lambda x, \lambda y)$ in a statistical sense[26,146]. Here, H is called the Hurst exponent, characterizing how correlated the surface is, and λ is a real number. The exponent $H = 0.8$ has been shown to hold for both synthetic and natural three-dimensional

fractures in a wide range of materials[61,62,282,398]. There are, however, notable exceptions, such as in sandstones ($H \simeq 0.6$)[364], and in glassy ceramics ($H \simeq 0.4$)[59,333].

Classically, a fracture geometry was approximated by two parallel plates separated by a constant separation d, which amounts to so-called plane Poiseuille flow where an analytical solution is available—often termed the parallel plate law. Improvements to the latter can be found when the flow is creeping ($\mathrm{Re} \ll 1$), and the in-plane length scale of the height variations is much larger than the *local* fracture aperture $d(x,y)$ (here, the local distance between the upper surface $z_{\max}$ and the lower surface $z_{\min}$). In particular, the *lubrication approximation* can be used. Defining the aperture-averaged flux by $\mathbf{Q} = \int_{z_{\min}(x,y)}^{z_{\max}(x,y)} \mathbf{u}(x,y,z)\,\mathrm{d}z$, a variant of the Darcy equation (cf. eq. (2.3)) arises[336],

$$\mathbf{Q} = -\frac{d^3(x,y)}{12\mu}\boldsymbol{\nabla}p. \tag{2.8}$$

Equation (2.8) is commonly termed the local cubic law (LCL)[40] due to the (local) presence of the d^3 term. The parallel plate law is given by eq. (2.8) with a constant d. Generalizations to eq. (2.8) for the case of non-neglible inertia in the lines of Forchheimer[156] are commonly applied[412]. By imposing conservation of mass, i.e. $\boldsymbol{\nabla} \cdot \mathbf{Q} = 0$, the velocity can be eliminated, which yields the Reynolds equation[381]

$$\boldsymbol{\nabla} \cdot \left(d^3(x,y)\boldsymbol{\nabla}p\right) = 0, \tag{2.9}$$

which has been of extensive use in the literature. However, once the roughness varies abruptly over small length scales, the lubrication approximation is inapplicable. Modelling approaches for flow in fractured rock were reviewed by Zimmerman and Yeo[484], and on somewhat larger scales by Berre et al.[42].

In general, increasing inertia, and decreasing permeability, is associated with increased energy dissipation or equivalently pressure loss (or hydraulic head loss). Since this is often unsought in industrial settings, flow in fractures is scientifically closely connected to flow in pipes, with smooth or rough internal surfaces. All industrial pipes are rough on some microscopic scale[9], and in many cases (such as in geothermics) transport supersaturated aqueous solutions that lead to precipitation patterns on the pipe walls; a phenomenon known as *scaling*[174]. Scaling increases flow resistance and can lead to clogging.[6]

Efforts to estimate the friction loss, or conversely, the permeability, in pipes and channels date back at least to measurements by French hydrologists Chézy and Prony in the early 18th century (see[71]). Poiseuille[360] and Hagen[177] independently empirically found the relation between flow rate, pressure gradient, and tube dimensioms for laminar flow in smooth tubes (now known as Hagen–Poiseille flow, see[429] for a more complete historical account), which can be summarized as

$$u = \frac{d^2}{32\mu}|\boldsymbol{\nabla}p|, \tag{2.10}$$

where u is the mean velocity and R is the tube radius. Weisbach[464] collected results from several experiments and proposed to write the relation in the following form, known as the Darcy–Weisbach equation,

$$|\boldsymbol{\nabla}p| = f_{\mathrm{D}}\frac{\frac{1}{2}\rho u^2}{d} \tag{2.11}$$

where the dimensionless quantity f_{D} is called the Darcy friction factor (due to improved experiments by Darcy[107]). The Fanning[144] friction factor f_{F}, which is also often used,

---

[6] Similar to the effect that can lead to atherosclerosis in arteries.

(a) (b) (c) (d)
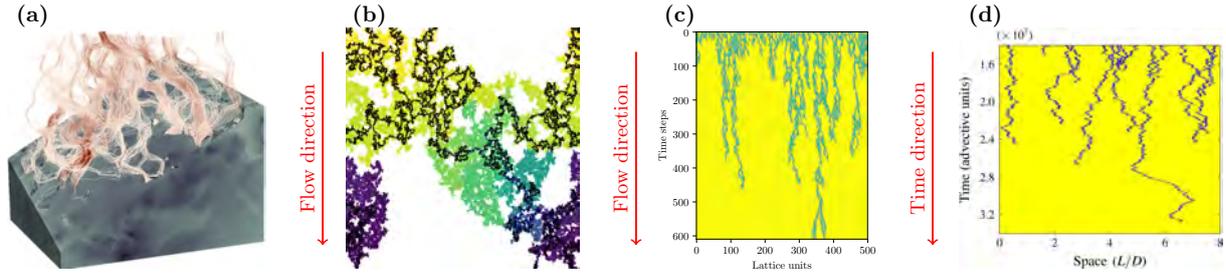
FIGURE 2.3: Variations over percolation. (a) Numerically resolved flow through a porous rock sample, from[261]. (b) Bond percolation on a hexagonal lattice, slightly above the percolation threshold. The percolating cluster was extracted, Darcy's law was assumed to hold for each bond, and a pressure drop was imposed from top to bottom. The pressure is shown in the background color coding (lighter is higher). The collection of squiggly dark lines is the conducting part of the cluster, i.e. the percolation backbone. (c) Directed percolation model, below the critical point (blue are active sites). (d) Spatio-temporal dynamics of puffs (blue), slightly below criticality, in the experiments by Mukund and Hof[327]. (Reprinted from[327].)

is simply $f_\mathrm{F} = f_\mathrm{D}/4$. For turbulent flow in smooth pipes, Blasius, a student of Prandtl, found the scaling $f \sim \mathrm{Re}^{-1/4}$ for large Re. Rough pipes turned out to be more elusive. Nikuradse[339], another student of Prandtl, carried out an impressive range of experiments, where the interior of pipes were coated with sand of a characteristic particle size, i.e. roughness size, r. From his data, spanning many decades in Re and several roughness sizes, it could be seen that the friction factor f_D stabilized at a certain value for hight Re. This asymptotic value displays the Strickler scaling $f_\mathrm{D} \sim (r/d)^{1/3}$[164,424]. In the years following, e.g., Colebrook and White[96] provided experiments with less uniform roughness. With the introduction and resultant popularity of the Moody diagram[316] (which plots f_D as a function of Re), the Darcy–Weisbach equation (2.11) and the Darcy friction factor f_D became the accepted way of expressing friction in pipe flow[71]. The data from Nikuradse's experiments are plotted in a Moody diagram in fig. 2.4 (e), showing the friction factor f_D as a function of Re for varying roughness. Much research has been directed into attempts to connect the empirical laws to *fully developed* turbulence; in particular recently due to the evident connection to dynamical critical phenomena from statistical physics[164,165]. The fully-developed limit will not be a focus of this thesis; rather we will be focused in coming sections on the *transition region* from laminar flow to turbulence. This region is indicated as the crossover region between laminar and Blasius scaling in fig. 2.4 (e).

Having taken a detour into high-velocity flows with disordered boundaries, we now return to the pore network scale. The perhaps most obvious contribution from the statistical physics community to flow in porous and fractured media has been to draw attention towards spatial (or temporal) fluctuations, e.g. in porosity and velocity, instead of the average quantities. In this respect, *percolation* is a conceptually important class of models. These models were originally devised by Flory[155] and Stockmayer[422] to describe polymers. The application to porous flows was pioneered by Broadbent and Hammersley[70], who coined the name due to its resemblance to the phenomena taking place in a coffee percolator[390]. The basic variant of percolation considers a lattice with sites (site percolation) or bonds (bond percolation) that all can be open with a probability s. The analogy to a porous medium is striking, both on the level of pores and single fractures in a fracture network—s being analogous to porosity. A comparison between flow in porous rock and a percolation cluster is shown in fig. 2.3 (a) and (b). At a certain value $s = s_\mathrm{c}$, there appears a connected path through the system from one end to the other, and the system is permeable. Continuing the analogy to porous media flow, it is clear (from conservation of mass) that the same flux of fluid must pass through any cross-section, implying that in sych systems, close to s_c, the local velocities will vary by orders of magnitude. This is illustrated in fig. 2.3 (b). Considering s as a control parameter, and the percolation probability $P(s)$ as the order parameter, the system exchibits a continuous phase transition at s_c, with associated critical exponents. A thorough introduction to percolation can be found in the book by Stauffer and Aharony[420] and their many applications and implications for flow in rocks have been reviewed by Sahimi[390,391].

Several versions of percolation models beyond the basic ones apply to porous media, such as invasion percolation (one phase displacing another), or gradient percolation (in the presence of an external field). In this work, we shall mainly be acquainted with directed percolation (DP), which is a variant of bond percolation where the bonds are *directed.* Typically, one considers a $45°$ tilted square lattice, where the "fluid" is only allowed to flow downwards. A realisation of directed percolation is shown in fig. 2.3 (c), and is seen to yield a different pattern than regular percolation, cf. fig. 2.3 (c). Percolation models have in general had important consequences for understanding fluctuations in two-phase flow (e.g. related to imbibition and drainage) in porous media, but we will not consider that here. For overviews of such studies, the reader is referred to the recent thesis of Moura[322] and references therein, or the review of pore network models by Joekar-Niasar and Hassanizadeh[225].

2.1.2 *Pipe flow phenomenology*

FIGURE 2.4: From laminar to turbulent flow in pipes. Figures (a)–(d) show the four flow regimes of single phase pipe flow, for increasing Reynolds number Re. Figure (e) shows the data from the seminal experiments by Nikuradse[339] replotted in a Moody diagram. Here, the Darcy friction factor f_D is plotted against Re, k is a roughness amplitude and R is the pipe radius. The laminar scaling $f_D \sim \mathrm{Re}^{-1}$, corresponding to (a), and the Blasius scaling $f_D \sim \mathrm{Re}^{-1/4}$ corresponding to (d) are indicated as dashed lines. Additionally, the region of transitional flow, where (b) and (c) belong, is indicated, along with the critical point $\mathrm{Re}_\times$, measured by Avila et al.[23], where solitary puffs are equally likely to split as to decay.

(a) Laminar flow, Re $= 1900$

(b) Metastable puff, Re $= 1950$

(c) Weak slug, Re $= 2600$

(d) Turbulence, Re $= 4000$
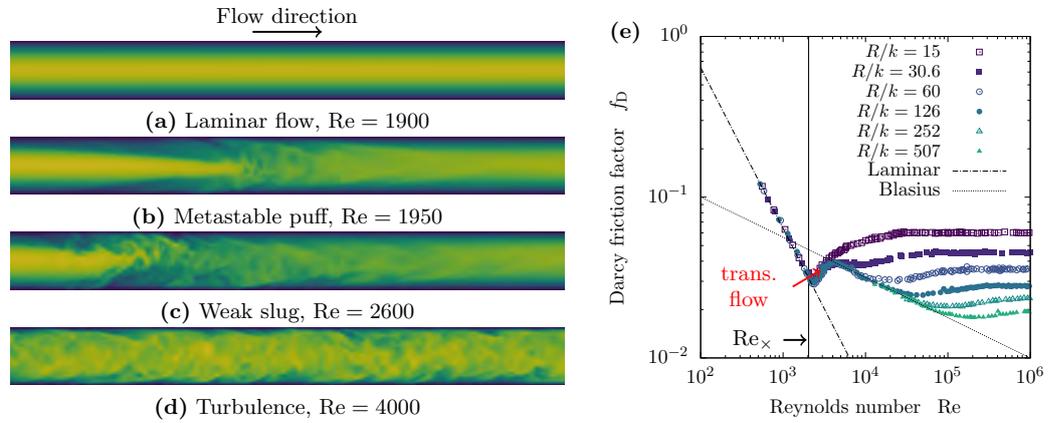
We now return to Reynolds' experiments on transitional flow in smooth pipes. Although his investigations led to the estimate of a critical Re, the picture of the transition between laminar flow and turbulence was not complete—and remains incomplete to this day[29,327]. Nevertheless, he noted that depending on how carefully the inlet conditions were prepared, laminar flow (see fig. 2.4 (a)) could be sustained up to $\mathrm{Re} \simeq 13000$. That, along with the identification of a critical Re below which turbulence would ultimately decay, pointed to the fact that he already *then* identified the transition to turbulence as *subcritical*: *finite* perturbations are required to trigger turbulence, and nonlinearity drives the instability that ultimately leads to turbulence. It is now generally believed that the laminar Hagen–Poiseuille solution (see fig. 2.4 (a)) to the Navier–Stokes equation is linearly stable for all Re—as demonstrated in simulations up to $\mathrm{Re} \simeq 10^7$ [300,392], and underpinned by experiments[105,470]. This supports the view of the transition as a subcritical one, and also helps explain why approaches to account for this transition using hydrodynamic stability theory (Orr–Sommerfeldt method) have been fruitless[129]. Other shear flows, such as that in a Taylor–Couette cell (shear flow between counter-moving cylinders), *does* exhibit a linear instability at finite Re, and for such systems, the global 'period doubling' route to turbulence by chaos theorists proved successful (see e.g.[430]). Here, we will consider only the transition to turbulence in pipe flow. For fully developed turbulence, consider standard textbooks on the topic (e.g.[313,440]), and for the transition in shear flows in general, consider the reviews by Manneville[283,284].

Reynolds noted that around the critical point, turbulence did not rise uniformly, but occurred as intermittent "flashes," which are now usually termed turbulent *puffs* and *slugs.* These structures are shown, respectively, in fig. 2.4 (b) and (c). This underpins the notion that transitional flow does not consist of a diffuse mix of laminar flow and turbulence,

but rather as a spatial and temporal distribution of relatively sharply separated domains of *either* turbulence or laminar flow. *Puffs* are arrowhead-shaped patches of localized turbulence that travel downstream at approximately the mean velocity of the flow. A turbulent puff is separated upstream from laminar flow by a sharp interface, leading to early analogies to gas–liquid phase transitions[29,97,470]. At the downstream front the flow more gradually relaminarises, eventually reaching the Hagen–Poiseuille profile (unless a trailing puff comes along). The puffs may either *split* or *decay* spontaneously. During puff splitting, a daughter puff is created at the downstream end of a mother puff[23,29,471], leading to two coexisting puffs, and accordingly a higher fraction of the pipe being in a turbulent state. At low Re, puffs are more likely to decay than to split, whereas for higher Re, they are more likely to split than to decay. Evidently, for (spatially localized) puffs, the upstream front travels at the same net speed as the downstream one. At a certain *second* critical Re, the downstream puff starts to move faster than the upstream front, and single puffs start to expand. These expanding puffs are known as *slugs*. When the downstream front is characterized by gradual relaminarization, the slugs are termed *weak slugs*, whereas when the Re is sufficiently high for the downstream edge to invade the laminar flow as aggressively as the upstream front, the slugs are termed *strong slugs*. At the Reynolds where slugs are present, the entire system will be filled with turbulence; see fig. 2.4 (d). A clear description of the transition of turbulence in pipe flow is given by Barkley[29], and, in particular, the Barkley model[28–30] has given a near complete understanding—at least qualitatively—of the dynamics that gives rise to turbulence in a smooth pipe.

2.1.3 *Two-phase flow*

Two-phase flow in pipes and tubes, typically of two immiscible fluids (e.g. gas and liquid), displays a significantly more complex phase diagram than what does single-phase flow in the same geometries. These flows can, for example, be classified into the following categories[6,104,197], which are also shown schematically in fig. 2.5:

- **Stratified flow:** The lighter phase (e.g. gas) floats on top of the liquid, and there is a clear interface separating the phases. Such flows occur when gravity is important and the pipe is horizontal or inclined from vertical.

- **Dispersed flow:** One of the phases is dispersed in the other, as small bubbles, drops or droplets.[7]

- **Annular flow:** The lighter phase flows through the center of the pipe, while the other phase flows along the walls.

- **Slug flow:** Alternating, unsteady, intermittent flow of extended bubbles of one fluid, intersped by the other phase.

In addition to the fact that turbulence can occur in both phases, the phenomena are further complicated by the existence of surface forces on the fluid-fluid interface. Nevertheless, accurate phenomenological descriptions of the thermophysical properties of two-phase mixtures transported in tubes is of critical importance for an impressively wide range of applications, including nuclear reactors[46], heat exchangers, petroleum production[1] and CO_2 transport[328]. As a first-principles simulation of the complex interface is generally unachievable for large systems, experimentally based correlations are usually employed in simulations[266]. These correlations are algebraic expressions that relate the macroscopic heat transfer, friction, etc., to dimensionless parameters describing the flow. In two-phase flow, there can be several other dimensionless parameters than the Reynolds number Re which control the flow. Some of these are:

(a) Stratified flow

(b) Dispersed flow

(c) Annular flow

(d) Slug flow

FIGURE 2.5: The author's impression of the four flow regimes listed in the text.

[7] *Droplet* means 'small *drop*' and typically refers to a drop less than $500\,\mu\mathrm{m}$ in size.
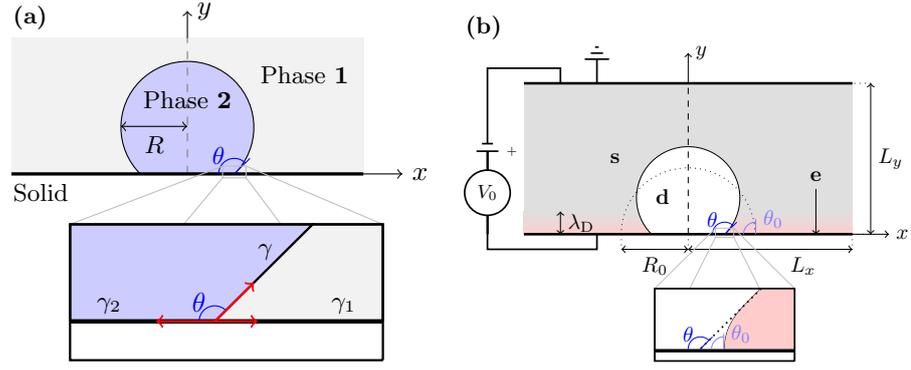
- The Weber number, We: inertia to surface forces,

- The Capillary number, Ca: viscous to surface forces,

- The Bond number Bo or Eötvös number Eo: buoyant to surface forces.

At smaller scales, such as in porous media (where two-phase flow was briefly in-
troduced in section 2.1.1) or when modelling individual droplets, the Reynolds number
will often be small, and a more important control parameter will then be the capillary
number Ca. As mentioned above, it measures the ratio of viscous to surface forces, and
it is defined by

$$\mathrm{Ca} = \frac{u\mu}{\gamma}, \tag{2.12}$$

where u is a characteristic velocity, and γ is the fluid–fluid interface tension. For flow
near solid boundaries, an essential concept is *wetting*, which is the ability of a liquid phase
to adhere to the surface. The wetting properties of two-phase flows are of importance in
a wealth of applications (see e.g. [60]), including in geophysics, as they are a controlling
factor e.g. oil recovery [44]. Observations of wetting and capillarity date, at least, back
to da Vinci, and the foundations of its theoretical understanding were laid by, among
others, Hauksbee [180], Young [478], Laplace [242], Plateau [357], and Gibbs [162] (see [251]).

For a static droplet (or drop) immersed in another liquid, the Young–Laplace law
states

$$\Delta p = \gamma \kappa, \tag{2.13}$$

where Δp is the pressure difference between the inside and the outside of the droplet,
and κ is the curvature, which for a spherical droplet with radius R (in 3D) is given by
$\kappa = 2/R$. The *wettability* is often quantified through the *spreading parameter* S:

$$S = \gamma_1 - (\gamma + \gamma_2), \tag{2.14}$$

where γ_1 is the surface tension between the solid and the surrounding phase and γ_2
is that between the solid and the droplet. If $S > 0$, it is energetically favoured for the
droplet to wet the entire solid; in practice a thin (nanometer-sized) film will remain.
If $S < 0$, the droplet is partially wetting. Then, in equilibrium, the contact angle θ_{eq},
which quantifies partial wettability, is given by the energy balance—or alternatively force
balance—at the three-phase contact line. This balance gives Young's law,

$$\cos\theta_{\mathrm{eq}} = \frac{\gamma_1 - \gamma_2}{\gamma}. \tag{2.15}$$

A droplet wetting a solid substrate is shown in fig. 2.6 (a), along with the force balance,
and the contact angle, at the contact line.

Out of equilibrium, e.g. when a glass plate is slowly lifted out of a water bath, the contact line may be forced to move along the solid substrate. Huh and Scriven[201] demonstrated that blindly assuming that there is no hydrodynamic slip (which is common, and usually valid, for the single phase case) leads to a logarithmically diverging energy dissipation near the contact line. Thus, in their words, "not even Herakles could a sink a solid"[60,201]. The no-slip Navier–Stokes equations are therefore not directly compatible with a moving contact line (MCL). Near the moving contact line, a more precise *microscopic* description is needed to supplement the purely hydrodynamic model. One way is to abandon the no-slip condition and regularize the microscopic length scale that leads to the divergence, with a slip length; referred to as a Navier slip boundary condition. This is compatible with the Voinov–Tanner–Cox law for Ca $\ll 1$[81,101,435,455],

$$\theta \sim \mathrm{Ca}^{1/3}, \qquad R(t) \sim t^{1/10}. \tag{2.16}$$

Here, R is the radius of a droplet spreading on a substrate in time t, and θ is an *apparent* contact angle, valid on scales beyong the moving contact line. Equation (2.16) also has experimental support for a range of systems[60]. Other models for the moving contact line include molecular kinetic theory[54], and evaporation and condensation at the fronts, which is particularly relevant for a moving liquid droplet surrounded by its vapour[60]. Another complicating factor is that surfaces usually have a micro- to macroscopic roughness or chemical inhomogeneities, which means that in the static case there are several metastable states that locally minimize the energy, imparting hysteresis effects[374]. For a broader introduction to the field of wetting, consider the seminal reviews by de Gennes[113], Leger and Joanny[251], and Bonn et al.[60], as well as that by Snoeijer and Andreotti[415] for modelling contact line motion.

2.1.4   *Electrohydrodynamics*

Loosely speaking, *electrohydrodynamics* constitutes the joint effects of fluid flow and solute transport in the presence of electric fields. Such effects are important within geophysics[207], because charged surfaces appear naturally as rocks are exposed to water. Electrohydrodynamic effects can be harnessed for detecting seismic events or earthquakes[35,310,442], and have been suggested as a source of increased dissipation during seismic activity[366]. Moreover, electrohydrodynamics is of relevance e.g. for geothermics[379] and environmental remediation of soils or aquifers[163]. In addition to being important for the permeability of reservoirs, electrokinetic effects may be of importance for two-phase flow, as surface charges and electric fields are known to change the wetting properties of fluids[145,382]. Electrohydrodynamic effects could thus be instrumental in the explanation of why and how oil recovery can be enhanced by injecting water of a particular salinity[179,192].

The possibly first report of electric fields generating fluid motion was given by Reuss[378], who observed that clay particles moved relative to the fluid when subjected to an electric field; an effect now known as *electrophoresis*. The *streaming potential*, i.e. the build-up of an electric potential due to the flow of an electrolyte solution through a charged channel, was first observed by Quincke[375]. von Helmholtz[457,458] provided early theoretical results explaining the 'double layer' at the electrolyte-solid interface, and its role as a capacitor. Separate from this, Nernst[331,332] and Planck[355,356] worked, albeit not together (see the review[281]), on the problem of electrodiffusion. Not long after, Smoluchowski modelled electrophoresis and streaming potential[413,414]. Gouy[167,168], and later Chapman[90], derived the Poisson–Boltzmann equation, which gave an expression for the extent of the electrical double layer. The latter is termed the *Debye length* λ_D, named after Debye, who rederived it in his work with Hückel[115,116]. These theoretical

descriptions formed the basis for refinements by Stern[421], Grahame[169], and others. A more complete historical review can be found e.g., in[34], and introductions to the broader field of electrochemistry can be found in several books, see for example[27,233,367].

Observations of electrohydrodynamics in two-phase fluid systems date back to the seminal experiments by Lippmann[267] in 1875, where he pioneered the field of *electro-capillarity*, or, the study of the relationship between capillarity and electric fields[325].[8] Lippmann observed that the contact angle of mercury in contact with an electrolytic solution in a capillary could be modified by applying a potential difference V_0 between the mercury and the electrolyte. In particular, he found the quadratic relation

$$\cos\theta = \cos\theta_{\text{eq}} + \frac{1}{2}BV_0^2, \tag{2.17}$$

[8] Lippmann later went on to win the Nobel prize for inventing color photography.

where θ is the observed (apparent) contact angle, θ_{eq} is the equilibrium contact angle without any applied field, typically given by eq. (2.15), and B is a phenomenological parameter. A similar setup (on an electrode instead of in a capillary), demonstrating the effect of imposing an electric field on the wetting properties of a single droplet, is sketched in fig. 2.6 (b). Eq. (2.17) can also be inferred from Gibbs' adsorption isotherm[257,314]. This discovery not only led to the first electrocardiograph by Waller in 1887[45,462], but also laid the foundation for the field of electrowetting. Further studies were carried out by Pellat[350,351]. Frumkin et al.[160] studied wetting of an oil droplet sitting on a mercury electrode. More recently, electrowetting-on-dielectric (EWOD) was pioneered by Berge[39,450] and this technology has since found wide use in e.g. electronic displays[37,38,183,210]. For a more complete overview of the state-of-the-art of electrowetting, the reader is referred to the reviews by Mugele and coworkers[324–326].

Around 1905, it was discovered that applying electric fields to water-in-oil emulsions (i.e. dispersed flows, cf. the start of section 2.1.3) could help speed up the deemulsification process[135] needed for the oil to become usable as fuel. This led to the invention of the electrocoalescer by Cottrell and Speed[100] (see[135] for a brief history of the latter invention). Recent reviews of electrocoalescence are available in the literature[280,302].

In 1913, Millikan[304] published the findings from his and Fletcher's elegant oil drop experiment. Oil droplets were charged and sprayed into a chamber, and by measuring the terminal velocity with and without an electric field, they could find the charge of a droplet. This charge turned out always to be an integer multiplum of the elementary charge, q_e, which they could measure with (overly) high precision. This led to Millikan receiving the Nobel prize in 1923.

The controversy regarding the share of labour between Millikan and Fletcher is not entered here; it suffices to state that Fletcher's own recollection[154] is an interesting read.

Much of the early theoretical work on two-phase electrohydrodynamics was, if not directly motivated by electrocoalescers, at least applicable to such configurations, as it was concerned with the physics of single droplets of one liquid suspended in another. The early models assumed that the two phases were either perfectly dielectric (non-conductive) or perfectly conductive materials. Both these models predict a prolate deformation of the droplet in the direction normal to the applied electric field[8,345]. Careful experiments by Allan and Mason[8], on the other hand, showed that the deformation could be either prolate or oblate depending on the conductivities in the two phases. The conundrum was partly resolved by Taylor[436]. In his "leaky-dielectric" model, the phases were assumed to be weakly conducting, thus allowing a net current through the system including droplets. This, in turn, could drive a circulation in the droplet and gives rise to interfacial stresses that enables the oblate shape, which was shown analytically for small displacements. The main approximation behind Taylor's model is (1) that the electric field is strong, and (2) that the electric double layer is vanishingly thin compared to the droplet; hence the conductivity is taken to be constant and net charges are confined to the interface, i.e., diffusion of charges is neglected. When either of these assumptions are not satisfied, the

model cannot be expected to hold quantitatively. This concerns in particular situations with mobile charge carriers, where there can be regions of net charge, and where the conductivity is not uniform[43,88]. Phenomena such as concentration polarization cannot be captured by such models.[9] As an improvement over Taylor's analytical solution to the leaky-dielectric model, Zholkovskij et al.[483] developed analytical expressions for droplets with arbitrarily thick Debye layers in one of the phases (but still for small perturbations). The latter could interpolate between the asymptotic solutions for a perfectly dielectric and a leaky-dielectric model. Saville[396] outlined how the leaky-dielectric model can be derived from the basic electrokinetic equations, illuminating the assumptions made in the process. Schnitzer and Yariv[399] showed rigorously, building on the work by Baygents and Saville[32], how the leaky-dielectric model can be seen as a limit of the full model.

[9] That being said, neither could Millikan's experiment, since in Taylor's model, no droplet can have a net charge.

2.2 STATE OF THE ART

2.2.1 *Direct simulation of flow in disordered geophysical media*

Pore scale simulations

The search for macroscopic transport properties such as porosity, permeability and turtuosity from a pore-scale description has recently become possible to address numerically, through the development of numerical methods and improved computational facilities. The development of the field of *digital rock physics* imparts calculation of flow properties, as well as mechanical properties, from 3D images of porous samples obtained using X-ray microtomography or other imaging techniques[14,20,56,76,488]. Methods for numerically simulating such flow, reviewed by Meakin and Tartakovsky[294], has enabled simulation of solute transport[47,48,226,307], multiphase flow[308], and time-dependent evolution of the microstructure e.g. through dissolution and precipitation kinetics[341] Simulations have revealed that the macroscopic behaviour is controlled by local heterogeneities[41]. Computed elastic properties depend on the initial microstructure and change during rock transformation processes[467], and the preferred dissolution patterns impact the mechanical properties and seismic wave velocities[21].

Pore-scale simulations have revealed that there exists large (several orders of magnitude) variations in local flow velocities in porous networks[48,110,247] and in fracture joints[72]. Much of the information that is contained in the Eulerian velocity field can be captured by the probability distribution function (PDF) sampled uniformly over the pore space. Recent simulations of ensembles of synthetically generated porous media have suggested that the velocity PDFs can be captured by either a stretched exponential[95,199,410] or a 'power-exponential' distribution[293]

$$P(u) = \begin{cases} a \left(\frac{u}{u_s}\right)^{\eta-1} \exp\left[-\left(\frac{u}{u_s}\right)^{\eta}\right] & \text{(stretched exponential)}, \\ a \exp\left[-\left(\frac{u-u_0}{u_s}\right)^{\eta}\right] & \text{(power-exponential)}. \end{cases} \tag{2.18}$$

Here u_0 (peak), u_s (spread) and η (exponent) are fitted parameters that depend on the geometry, a is a normalizaton factor, and $u \geq 0$ can refer to both the (absolute) transveral and longitudinal component of the velocity field $\mathbf{u}$, as well as to its absolute value. Note that the two distributions have the same asymptotic behaviour for $u \gg u_s$, i.e. $P(u) \sim \exp[-(u/u_s)^{\eta}]$. In particular, Matyka et al.[293] found the exponent η in the power-exponential distributions for the longitudinal component and the absolute value to be an increasing function of the porosity which interpolates between a broad distribution ($\eta < 1/2$) at (relatively) low porosity, through exponential ($\eta \simeq 1$) and a Gaussian distribution ($\eta \simeq 2$) at high porosity. Here, the considered porosities were

in the range $\phi > 0.4$, as compared to $0.2 < \phi < 0.6$ in the study of Siena et al.[410], who suggested a stretched exponential distribution. The latter study also encompassed a different porous medium generation protocol. A stretched exponential distribution can be theoretically inferred by heuristically assuming the medium to be a collection of cylindrical pores with exponentially distributed radii, wherein the flow is given by the Hagen–Poiseuille solution, as demonstrated by[199]. Other studies have suggested both exponential and Gaussian distributions for different porous systems[48,108,223,248,285]. Close to the percolation threshold, the velocity PDF obeys a power-law distribution over several orders of magnitude, as shown in Navier–Stokes simulations in the backbone of a site percolation network[15]. These observations together suggest that (i) the velocity distributions are not a simple function of porosity alone, but that (ii) a general trend is that a broad (power-law) distribution at low porosity (the percolation threshold) is gradually turned into a more narrow stretched exponential, exponential, and finally Gaussian distribution as the porosity is increased. However, these observations apply only for porous media when flow and deformation are decoupled.

Mechanical coupling

Voronov et al.[460] considered the viscous stress associated with the flow field in a highly porous medium, and proposed a gamma distribution to describe the PDF of the largest eigenvalue of the rate of strain tensor for the bulk. Pham et al.[354] performed a similar study on packed beds and Berea sandstone, and found a lognormal distribution of stress. For assessing the impact of fluid stress on the state of stress in the solid, the pore-wall stress would be more relevant. In deformable porous media, numerical simulations have suggested that the relationship between the imposed pressure gradient and velocity flux becomes non-linear and saturates for large pressure gradients[189], and can impart hysteresis effects[176]. Saenger et al.[389] studied the effect of fluid viscosity on the effective elastic parameters of rocks. Nonetheless, rocks can usually only deform very slightly (less than 1%) before they are irreversibly damaged. Opening of microfractures and collapse of pores lead to a non-linear evolution of porosity and permeability with the pore pressure gradient[109]. Jasinski et al.[219] considered the evolution of elastic parameters and permeability of a Bentheim sandstone under small deformations, through experiments and simulations. Lan et al.[239] found normal (within grains) and bimodal (at grain boundaries) distributions of principal stress in 2D discrete simulations of compressing granite rock. Laubie et al.[244] studied the stress distributions in 2D artificial "swiss cheese" porous media. The probability density functions were found to decay as stretched exponentials for high stresses, and the distributions broadened with the degree of disorder. They also observed the formation of stress chains analogously to what are known for granular packings. Other researchers have considered transient coupling between the fluid flow and solid matrix through precipitation[222], dissolution[352] (thermodynamically driven morphology evolution), erosion and deposition[213,214].

Fracture flow

Most numerical studies of flow in rough fractures, up until about a decade ago, have been carried out in the regime of creeping flow, often using a lubrication approximation (i.e. the local cubic law, eq. (2.8))[40]. The main challenge is then to relate the permeability to the aperture field[358,432]. The default assumption is to use the distance between boundaries along the normal direction to the flow plane[40], but this is clearly unsuitable for situations e.g. where the surface varies sharply over short distances, or perfect fracture joints resulting from 'mode 1' fracture (no shear displacement). To compensate for this discrepancy, Mourzenko et al.[323] suggested the method of fitting the largest possible

spheres at each point in the fracture to calculate the effective aperture. Brown[72] solved the Reynolds equation (2.9) in a synthetic rough fracture and showed that wall roughness strongly affected the transport. Méheust and Schmittbuhl[295,296] showed experimentally and numerically (in the same lubrication paradigm) that the heterogeneity of the rough surfaces can lead to both enhanced and inhibited flow compared to parallel plates with the same mean separation, and is moreover dependent on the orientation of the pressure gradient. Further, long-range correlations in the aperture fields are transmitted to the flow fields, leading to flow channeling[297].

Gutfraind and Hansen[175] and Zhang et al.[482] simulated flow in 2D and 3D fractures, respectively, beyond the lubrication approximation, considering creeping flow in 2D self-affine channels. Drazer and Koplik[121] studied flow in self-affine fractures, and the analysis was extended to 3D and compared to effective medium theory[122]. Through direct 3D simulations, Brush and Thomson[73] evaluated the effect of roughness and Re on the validity of the lubrication approximation, giving explicit bounds (on Re and roughness) on the validity range of the latter. Previous such analyses were based on an order-of-magnitude analysis[346]. Lo and Koplik[269,270] considered both pure fluid and suspension flow in similar geometries. Jin et al.[224] investigated the role of roughness in 2D simulation, and found, following Talon et al.[433], three regimes for the permeability dependency on roughness. In particular, it has been found that the permeability is often dominated by the narrowest constriction, but this effect is more pronounced in 2D than in 3D[412,432].

Auradou et al.[22] investigated the effect of a shear displacement on fracture walls, comparing experiments to numerical simulations, and found that the permeability depended linearly on the variance in local aperture. This effect was previously estimated by geometric considerations[386], and may reduce permability by several orders of magnitude, as shown in laboratory experiments[125]. Flow in rough fractures imposes a significant stress on the solid walls, as numerically demonstrated by Lo and Koplik[270]. Boundary roughness also leads to increased solute dispersion[64]. Other lines of research concern the coupling of fluid flow to heat transfer in fractures[333–335], solute transport[64], and flow in propped fractures[218].

Inertial effects on the flow properties in porous media have been considered in 2D geometries[15,16,130,385] and in 3D spherical packings[157,190,191], suggesting that for moderate Re, steady eddies are responsible for the quadratic deviation from Darcy flow. Lo Jacono et al.[271] simulated weak inertial flow (first-order correction to Poiseuille flow) in a rough channel, verifying the initial cubic deviation. Gutfraind and Hansen[175] simulated flow in a channel with one self-affine wall. High-velocity flow in a 2D self-affine fracture joint was simulated by Skjetne et al.[412] up to $Re = 52$, who found that the relation between pressure gradient and velocity was well described by a weak inertial correction at low Re and a Forchheimer equation at higher Re. Cardenas et al.[80] simulated flow and solute transport in a 2D asymmetric fracture, paying particular attention to the role of eddies. A similar study for a larger range in Re, and for several values of the Hurst exponent H, was carried out by Briggs et al.[69], but display only a weak nonlinearity and an Izbash (power-law) equation provided a better fit than a Forchheimer equation. The Forchheimer equation also appears to be applicable to flow of non-Newtonian fluids in 2D fractures[474]. Zou et al.[486] studied unsteady flow in 2D fractures up to $Re = 1000$. The same authors studied steady flow in 3D fractures up to $Re = 400$[487] (see also[485]), while Wang et al.[463] studied steady flow in self-affine fractures for somewhat lower Reynolds numbers. On the experimental side, laboratory experiments[220,448] yield good agreement with the phenomenological Forchheimer equation. Experimental studies of flow in fractures indicate that turbulence sets in at lower Re for rougher fractures[369,370]. In general, a "critical" Reynolds number,

where either (i) laminar non-linear effects (steady eddies) become apparent, or (ii) the laminar flow field becomes linearly unstable, seems to be highly sample-dependent. Conceptually, this is understandable for 2D geometries, where the flow is limited by the narrowest passage along the path. In 3D, however, the flow will tend to pass around obstacles, yielding lesser impact[412]. The comparative investigation of (i) and (ii) above have been largely omitted in the literature, particularly in 3D, where most studiest have been carried out by solving the time-independent Navier–Stokes equations. On the other hand, the spatiotemporal dynamics of the transition to turbulence in rough channels was recently investigated numerically by Ishida et al.[206]. These simulations were concerned with homogeneous small-scale roughness that could be numerically incorporated as an effective body force near the domain walls[77], thus not enabling the possibility of eddies deattaching from the boundary and entering into the bulk flow. Nevertheless, their results showed spatially localized turbulent structures similar, and complementary, to the stripes and bands observed for transitional plane Poiseuille flows. Thus, they provide a first link between the studies of the transition to turbulence in shear flows and the field of fracture flow, briefly introduced above.

Electrohydrodynamics in disordered media

Due to the strong inherent nonlinearity that arises when coupling the Navier–Stokes equations to electrokinetic transport, computational studies of such phenomena have been largely limited to two-dimensional[150,151] or axisymmetric geometries[286,287]. Recently, a method to simulate steady-state electrohydrodynamic phenomena in nanopores was presented by Mitscha-Baude et al.[309]. As an alternative, Obliger et al.[344] studied the transport properties of a pore-network model of electrokinetic flow.

2.2.2 *Directed percolation and the transition to turbulence in pipe flow*

Since Reynolds performed his pipe experiment, much experimental effort has been invested into determining the precise value of the critical Reynolds number $\mathrm{Re_c}$ (see[327] for a concise historical overview). However, it was not until the work of Avila et al.[23] that an unambiguous value, (approximately) free of finite-size effects and other systematic errors, could be determined. This was done solely based on single-puff statistics. The 'life times' of uncorrelated single puffs are distributed exponentially, so the probability distribution can be expressed as $P_\mathrm{d}(t) \sim \exp(-t/\tau_\mathrm{d})$ where $\tau_\mathrm{d}(\mathrm{Re})$ is a function of Re. An equivalent distribution holds for the characteristic splitting times τ_s. By fitting to experimental data, precise values of τ_s and τ_d could be obtained for a wide range of Re. It turns out that both these characteristic times depend superexponentially on the Reynolds number, i.e. like $\tau_i \sim \exp(\exp(a_i\mathrm{Re} + b_i))$, where $i \in \{\mathrm{s}, \mathrm{d}\}$ and a_i, b_i are empirically determined numerical prefactors. The dependence of the lifetime τ_d on Re can be inferred from extreme value statistics[166]. When the two values are equal, i.e. when a single puff is equally likely to decay as to spread, a critical Reynolds number $\mathrm{Re}_\times$ can be defined. Avila et al.[23] found a value $\mathrm{Re}_\times \simeq 2040$, strikingly close to the value $\mathrm{Re} \simeq 2000$ estimated by Reynolds. The transition is, however, not fully quantified by simply locating a critical value of the control parameter.

Pomeau[362] first pointed out that the spreading of turbulent spots in pipe flow had a striking analogue to directed percolation (DP, described in section 2.1.1). In this picture, the downward ('flow propagation') direction in DP must be identified as the time axis, and the horizontal direction corresponds to the flow direction (in a co-moving reference frame). Here, an occupied site corresponds to a coarse-grained region of turbulence, i.e. a puff, while unoccupied sites corresponds to laminar regions. This analogy between the rise of turbulence in pipe flow and directed percolation is seen by comparing fig. 2.3 (c) and

(d). Like in DP, there is in transitional pipe flow a spatio-temporal competition between an *active* (turbulent) state and an absorbing *inactive* (laminar) state. The absorbing property of laminar flow is given by its linear stability: a laminar region must by contaminated by a nearby puff to become turbulent; it does not turn turbulent by itself.

As a universality class, DP models have proven to be robust with respect to the details of the microscopic interaction rules. Janssen and Grassberger[170,193,216] conjectured that models should belong to the DP universality class provided that they possess the following necessary ingredients:

1. The system exhibits a continuous phase transition from a fluctuating active state to a unique absorbing state,

2. the system is characterised by a positive one-component order parameter,

3. the system has no additional symmetries or quenched randomness,

4. there are only short-range interaction rules.

In this picture, the turbulent fraction F, i.e. the fraction of the pipe occupied by turbulence,[10] fulfils the condition for being the order parameter, and the other conditions seem also to be satisfied. Hence, Pomeau's conjecture—a view that since has been advocated by several others[283,284]—is that pipe flow belongs to the universality class of 1+1 DP (which refers to 1 spatial and 1 temporal dimension). If this conjecture holds true, the *instantaneous* turbulent fraction F_t, i.e., the fraction of the pipe that is occupied by turbulence at any time t, should display the dynamic power-law scaling

$$F_t \sim t^\alpha \tag{2.20}$$

at the critical Re. Close to criticality, the order parameter $F = \lim_{t\to\infty} F_t$ should obey the scaling

$$F \sim (\mathrm{Re} - \mathrm{Re_c})^\beta, \tag{2.21}$$

close to the critical point. Moreover, the distributions of laminar gaps in space (ℓ_x) and time (ℓ_t) should display the scalings

$$P(\ell_x) \sim \ell_x^{\nu_x} \quad \text{and} \quad P(\ell_t) \sim \ell_t^{\nu_t} \tag{2.22}$$

at the critical point. The critical exponents α, β, ν_x, and ν_t given here should be those of 1+1 DP, which are listed in table 2.1.

Finding experimental realizations of DP, even in other systems than pipe flow, has proven to be a delicate matter.[11] Lemoult et al.[252] provided strong evidence that Couette flow (countermoving plates, or actually countermoving cylinders with large radii and small gap size) belongs to the 1+1 DP universality class. Experiments by Sano and Tamai[393] indicated that plane Poiseuille flow (PPF) belongs to the universality class of 2+1 DP (two spatial dimensions). The latter experiments hinged on grid-generated turbulence at the inlet and were far from reaching a steady state[327] and reported a critical Re in disagreement with more elaborate studies[472]. Hence the quality of their observations is dubious. On the other hand, Chantry et al.[89] recently provided clear evidence that a reduced-order model of Navier–Stokes PPF, Waleffe flow, belongs to 2+1 DP. This type of flow, though less computationally requiring, contains the essential self-sustaining mechanisms of turbulence and provides strong hints to what should be expected in experiments.

With regard to pipe flow, Shih et al.[406] provided a conceptual link between transitional flow and predator-prey models, where *zonal flow* takes on the role as predator,

[10] In DNS or experiments, the square of the non-axial part of the velocity vector averaged over the cross section, *viz.*

$$q = \left\langle u_r^2 + u_\theta^2 \right\rangle_{r,\theta} \tag{2.19}$$

makes up a good indicator for whether a region is turbulent or not.

TABLE 2.1: Critical exponents in 1+1 directed percolation. Values taken from[221].

Exponent	Value
β	0.276 486(8)
ν_x	1.733 847(6)
ν_t	1.096 854(4)
$\alpha = \frac{\beta}{\nu_x}$	0.159 464(6)

[11] Despite the theoretical success, experimental observations of DP were lacking[194] until 2+1 DP scaling was displayed for electrohydrodynamic convection in nematic liquid crystals by Takeuchi et al.[431].

which could be shown to belong to DP by renormalization group methods. However, the numerical simulations on which their model was based were incomprehensive, and the significance of zonal flow is generally believed to be minor[29].[12] Using his model for pipe flow, Barkley[28,29] performed simulations which are consistent with 1+1 DP, whereas a validation using experiments or DNS is still lacking. Mukund and Hof[327] observed in $7800d$ long pipe experiments a discontinuous transition without signs of scale invariance. Instead, above criticality, the system was jammed in a 'crystalline' state, where puffs were approximately equidistantly spaced (at $\mathrm{Re} \simeq 2060$). Below, the system would always die out (at $\mathrm{Re} \simeq 2020$). This points to two possible explanations:

[12] The predator-prey oscillations they observe are not unlikely to be the result of the feedback between friction factor and mean flow, which is a pronounced finite size effect that is ubiquitous for periodic pipes with short lengths—see the discussion near the end of this section.

- The DP scaling range in Re is extremely narrow, i.e. smaller than $2020 \lesssim \mathrm{Re} \lesssim 2060$ (within 2 %); or

- the transition to turbulence in pipe flow is not in the DP universality class.

The latter position was advocated by Pomeau[363], against his own conjecture[362], 30 years after he posed it. A reason for the transition not being in the DP universality class, could be the asymmetric *interaction* observed between puffs. As noted already by Hof et al.[195] and Barkley[29], the interaction between two puffs manifests itself in the properties of the downstream puff, while the upstream puff remains unaffected[327]. As the downstream puff is fed less energetic flow, i.e. a more flattened profile than that of Hagen–Poiseuille flow, the closer to the upstream puff it is, it will be more likely to decay and less likely to split. Additionally, it will travel at a faster speed downstream, moving away from the upstream puff. Furthermore, in the crystalline puff state, dowstream waves, originating from colliding puffs, were observed, representing an emergent property of puff–puff interactions.

A final point in this section concerns the friction factor for transitional flow. At the same Re, pipe flow completely contaminated by turbulence will exhibit a higher friction than what will a compeletely laminar flow. This is connected to the transitional region in the Moody diagram, where the friction factor f_{D} crosses over from the laminar branch, where $f_{\mathrm{D}}^{(\mathrm{lam})} \sim \mathrm{Re}^{-1}$, to the turbulent branch, where $f_{\mathrm{D}}^{(\mathrm{turb})} \sim \mathrm{Re}^{-1/4}$. For flow in finite tubes driven by a constant body force (or pressure gradient), this gives rise to a negative feedback loop between friction and flow velocity; shown schematically:

$$\begin{array}{ccccc}
\text{Higher speed} & \rightarrow & \text{More turbulence} & \rightarrow & \text{Higher friction} \\
\uparrow & & & & \downarrow \\
\text{Lower friction} & \leftarrow & \text{Less turbulence} & \leftarrow & \text{Lower speed}
\end{array}$$
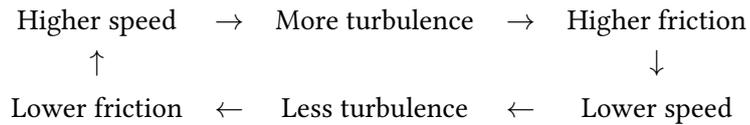
This leads to the instananeous Re being a fluctuating quantity. For sufficiently long pipes, i.e. in the termodynamic limit, these fluctuations should vanish and the Re number can be considered as the prescribed control parameter. For DNS, this effect must however be accounted for.

Recent experimental work by Cerbus et al.[87] has shown that the friction factor in transitional flow can be written as the linear combination

$$f_{\mathrm{D}}(\mathrm{Re}) = F_t f_{\mathrm{D}}^{(\mathrm{turb})}(\mathrm{Re}) + (1 - F_t) f_{\mathrm{D}}^{(\mathrm{lam})}(\mathrm{Re}), \tag{2.23}$$

where $F_t \in [0, 1]$ is (still) the instantaneous turbulent fraction, which they could measure directly from experiments. Thus, the transtional region in the Moody diagram in reality appars directly from the spatial mixture of turbulent and laminar patches. In the steady state, in particular close to the critical point, the behaviour of F is expected to be described by the universal exponents (table 2.1). This illustrates also a practical need for a first-principles description and understanding of the dynamics, and in particular, knowledge of whether the transition belongs to the DP universality class.

2.2.3 *Models and methods for two-phase flow*

Overview of methods

Methods for modelling the flow of two immiscible fluids (components or phases) where the detailed interface is resolved, can be classified into two groups: interface-*tracking* and interface-*capturing* methods. In general, these methods adopt a "one-fluid" formulation, such that the governing equations are written in terms of one continuous field[368]. Some of the most popular methods are the following:

- The *volume-of-fluid* (VOF) method[397], an improvement of the now obsolete marker-in-cell method by Harlow and Welch[178], is perhaps the most widely used method for the computation of multiphase flows. Here, a marker function (the volume fraction of one of the phases) which takes the value zero or one, is advected in a conservative manner. The surface is then reconstructed typically using piecewise linear interface calculation. Surface forces typically depend on the curvature (which is found from the reconstructed surface), and are often implemented using the continuous surface force (CSF) approach, which means that the singular ('delta function') force on an interface is replaced by a surface force that is smeared over a finite "interface thickness"[66]. VOF conserves mass locally very well, but provides inaccurate curvature calculation[427].

- The *front-tracking* method for multiphase flow belongs to the class of interface-tracking methods. Pioneered by Unverdi and Tryggvason[449], the methods consists of representing the interface as a collection of connected Lagrangian markers, i.e. a mesh of codimension 1, which is advected with the flow[368]. This method is closely linked to the immersed boundary method, which was originally developed for fluid-structure interaction in the heart (see[353]). Hence, such methods may be particularly suitable for elastic interfaces[137], and can simulate, for example, very low capillary number flows[4]. The method can be highly accurate, but topological changes, such as bubble splitting and collapse, are not easily handled. This is particularly true in 3D, where the required remeshing can be cumbersome and deteriorate the solution. The method is also prone to numerical instabilities.

- The *level-set* (LS) method[347,428] (see also the review[401]) describes the interface as the zero-level of a level-set function which is defined in the whole domain. This method handles topological changes automatically, provided that the level-set function is well-behaved. In order to do this, it must be reinitialized every few time steps (which is based on heuristics and tends to degrade the solution)[368]. Further, robust curvature calculations can be challenging[136,253]. Interface forces can be included either using the ghost-fluid method (sharp inclusion of forces) or by using the continuous surface force approach. A weakness of the level-set method is that it does not properly conserve mass, although mitigation strategies have been proposed.

- *Lattice Boltzmann* methods (LBM)[425], founded on statistical mechanics and developed as a refinement of lattice-gas automata, represent a completely different class of methods. Rather than approximating the Navier–Stokes equations, fluid dynamics is simulated by collisions of particle distributions which obey Boltzmann statistics (with a discrete set of velocities). Several methods are available that extend the lattice Boltzmann method to multiple phases. One advantage of the lattice Boltzmann method is that it is trivially parallelizable as all interactions are local; another is that it easily handles complex boundaries. Hence, it has been applied to,

for example, porous media flows, and constitutes thus another important contribution from the statistical physics community to flow in porous media. However, time step limitations are more restricted than in other methods, as the method is (at least in principle) fully explicit. In industrial settings unstructured meshes are often used, and the unstructured lattice Boltzmann method (ULBM) for both single and multiphase flow has been a research topic in the group of the author (see[186,288–290,307,308]). However, some of the intuitiveness and efficiency contained in the (structured) lattice Boltzmann method is lost through this generalization.

- The *phase-field* (or diffuse-interface) method (see[13] for an early review, and[232] for a more recent one) represents the interface implicitly by the phase field ϕ which interpolates the fluid parameters smoothly between the phases, and includes the interface forces through a phase field chemical potential derived from a free energy. This method has been used in the present thesis, and is discussed in more depth below.

In addition, less established methods such as smoothed particle hydrodynamics (see e.g. the review[312]), and stochastic rotation dynamics[205], are available, but these are not discussed here. Moreover, there exist methods that attempt to exploit the strengths and eliminate the shortcomings of the different methods, such as the combined level-set/volume-of-fluid (CLSVOF) method[427]. More extensive overviews than presented here are found in e.g. several books[368,447] and reviews[306,365,397,426].

Phase-field models

Phase-field models can typically be derived as a gradient flow of a free energy functional describing the system, imparting that interface forces can be included directly in a thermodynamically consistent way. Typically, the order parameter, or phase field, ϕ, equals 1 in one phase, and -1 in the other. At the interface, the phase field interpolates between the two values. The gradient flow can be taken in L^2 or H^{-1}, which leads to a non-conserved and conserved order parameter, respectively. We will in this work consider the latter, which, coupled to hydrodynamics, typically results in variations over the Cahn–Hilliard–Navier–Stokes system.

In phase-field models, topological changes are handled automatically without reinitialization. Provided that all relevant physical terms are included in the free energy functional, the topological changes should also be physically sound. In practical simulations, however, the interface width must be chosen to be much higher than the *physical* interface width (which is typically a few molecules wide), and it is not clear whether the thermodynamic consistency represents an advantage over other methods when the interface is unrealistically thick. On the other hand, it has become standard for many of the sharp-interface methods to incorparate the interface forces in a continuous way over a smoothed interface (cf. the continuous surface force approach in volume-of-fluid or level-set methods). Sharp jumps in physical quantities such as density and viscosity also represent a numerical challenge, and smoothing is often done in other methods (e.g. smoothed Heaviside function). Thus the conceptual difference is not all different.

The phase-field model generally conserves mass globally well, but the phase field is allowed to move by diffusion in addition to advection, and thus larger droplets will grow at the expense of smaller ones (Ostwald ripening)[479]. However, this can be mitigated by using a phase-field mobility that makes this time scale much longer than the simulation time. On the other hand, standard phase-field models may give equilibrium solutions where $|\phi| > 1$ in the pure phases, which can be catastrophic if the density ratio is large[306,479]. Mitigations exist, but however they mean that the model is no longer a gradient flow.

Other advantages of phase-field methods is that they are relatively easy to implement in any finite element framework, and that it is possible to rigorously prove stability and convergence of numerical schemes.

In general, it is probably not possible to find a method that is entirely satisfactory, and it is hard to find completely fair comparisons between methods in the literature. An important advantage of phase-field methods over other methods, however, is the way complex boundaries are handled. The phase-field model can be easily implemented in finite-element methods, and can thus operature on unstructured meshes representing complex geometries. Moreover, implementation of moving contact line models does not require any additional ad-hoc modelling, in contrast to most other methods. The contact line moves by diffusion, but contact line dissipation can be introduced in different ways, which reproduces experimental results both in the nanoscale[371,373] and at the continuum scale[83].

We now focus on the phase-field models directly applicable to the purposes of this thesis. Phase-field models have a long history in fluid mechanics, as the concept of a diffuse interface dates back to Lord Rayleigh[376] and van der Waals[454]. However, they have only relatively recently appeared as a serious tool for *quantitative* simulation, notably starting with the work by Jacqmin[211,212]. The basic phase-field model is the 'Model H' by Hohenberg and Halperin[196], which was introduced to describe phase separation of binary fluids near the critical point. This model consists of the coupled Cahn–Hilliard–Navier–Stokes equations and describes fluids with matched densities and viscosities. Lowengrub and Truskinovsky[276] derived a thermodynamically consistent generalization of Model H for fluids with different densities in the two phases, however with the numerical difficulty that the velocity field was not divergence free. In contrast, the model by Ding et al.[118] is a straightforward generalization of Model H, where a constant density is replaced by a phase dependent one, while the velocity field remains solenoidal. That model does not appear to be thermodynamically consistent, as it seems unfeasible to construct a free energy functional for the model that decays in time. To circumvent these issues, Shen and Yang[403] heuristically added a term proportional to $\partial_t \rho + \nabla \cdot (\rho \mathbf{u})$ (which vanishes in the bulk but contributes at the interface) to the momentum equation; and found an associated energy dissipation law. From a more fundamental starting point, Abels et al.[2] developed a thermodynamically consistent, frame invariant model for two-phase flow with density contrast. In contrast to the model by Lowengrub and Truskinovsky[276], the velocity field in the latter three models[2,118,403] is divergence free, allowing for the use of efficient numerical methods.

Electrohydrodynamic simulations

Most simulations of electrohydrodynamics have been concerned with the leaky-dielectric model or perfect dielectrics. In this respect, Fernández et al.[147] extended the front-tracking method by Unverdi and Tryggvason[449] to include electric forces at the fluid-fluid interface. Zhang and Kwok[481] developed a lattice Boltzmann method with the same capabilities. Tomar et al.[443] developed a combined level-set/volume-of-fluid (CLSVOF) method to simulate the aforementioned mentioned models. López-Herrera et al.[274] developed a charge-conservative CLSVOF as an enhancement to the model by Tomar et al.[443]. As a refinement to the model by López-Herrera et al.[274], Berry et al.[43] developed a CLSVOF method that resolves the full electrokinetic problem, where ions were allowed to dissolved in only one of the phases. Bjørklund[53], Teigen and Munkejord[437,438] developed a LS method for a leaky-dielectric model including surfactants. The possibly first phase-field model for such phenomena was introduced by[277], but their model was limited to Hele–Shaw cells, using a Darcy equation to

describe the hydrodynamics, and the electric effects were only effectively modelled. Eck et al.[128] presented a charge conservative phase-field model of the dielectric type with the purpose of studying electrowetting, and Nochetto et al.[340] followed thereafter with a similar model which included a generalized Navier boundary condition and density contrast. Lin et al.[258] presented a leaky-dielectric phase-field model which is a straightforward simplification of the model by Eck et al.[128]. A thermodynamically consistent phase-field model which fully accounts for electrokinetic effects, based on the model by Abels et al.[2], was derived by Campillo-Funollet et al.[79]. This model is of central importance to the electrohydrodynamic simulations in this thesis, as its single-phase limit is consistent with standard electrokinetic description. Numerical resolution of these models is addressed in chapter 4.

Homogenized models

We now move to several orders of magnitude larger scales. A whole different class of methods for two-phase flows are those that deal with transport of compressible fluids over large scales, where the interface and the flow patterns are so complex that it is impossible to resolve the full interface in practical situations. As indicated previously, this is typically the case for flows in industrial pipelines. Although early models were purely empirical, it has been recognized that physical modelling strategies are needed e.g. to better predict operating conditions.

In order to obtain models that are tractable, and that simultaneously contain the essential physics, homogenization techniques (much like those that can be employed to derive Darcy's law in a porous medium[465]) are employed; see Drew and Passman[124]. Thus, by averaging either over a representative elementary volume, over time[208], over ensembles, or simply over cross sections, one ends up with a set of equations that describes each phase without any notion of an interface. The resulting *two-fluid models* are derived from such considerations, and are distinguished from one-fluid models in that both fluids are governed by a separate set of quantities, including velocity, occupying the same space[123].[13] Additionally, a separately governed volume fraction (which summed over phases must add up to 1) of each phase is added to the description. The detailed description of the interaction between the two phases is replaced by (more or less empirical) source terms, typically driving the phases towards thermodynamic equilibrium, and effectively introducing dissipation due to friction between the phases or between the fluid and the pipe wall. Since diffusive processes are slow, second order differential terms are typically omitted (with coarse grids, they will often be dominated by numerical diffusion anyway), and we are left with models that can be written as first-order hyperbolic systems with source terms[279,317].

One such averaged model is the Baer–Nunziato model[24], originally developed to model the detonation-to-deflagration transition in solid-gas systems. This model was revived and stated in a more practical form for the purpose of modelling compressible multiphase flow by Saurel and Abgrall[394], and has since found wide use. The Baer–Nunziato model describes two phases which are not in equilibrium with each other, in the sense that all thermodynamic quantities are governed separately in each phase. However, for many practical purposes, it is both physically and numerically sound to simplify by imposing *partial* equilibrium between the two phases, e.g. in temperature, pressure, chemical potential, or velocity.[14] Combination of zero or more of these partial equilibrium conditions leads to a possible hierarchy of models, one model for each combination. The assumption of equilibrium in velocity leads to the branch of the hierarchy denoted as *homogeneous flow models*, which was studied by Flåtten and Lund[153], Lund[278]. For an overview of models studied by other authors, see the introduction of Paper 8[259].

---

[13] Separate velocities allows, for example, a coarse-grained dispersed phase to move in the opposite direction of the other phase within the same computational cell.

[14] That is, imposing equal phase velocities, which can be valid e.g. for well-mixed flows.

Accurate prediction of the fluid-mechanical speed of sound (in practice, the velocity of information propagation) is important for many purposes—from preventing running ductile fracture of pipelines[317] to constructing efficient numerical schemes. It has long been folklore knowledge in the community that equilibrium constraints tend to decrease the speed of sound in the resulting models. In the terminology of hyperbolic relaxation systems (see the review by Natalini[329]), this corresponds to the *subcharacteristic condition*, which is closely linked to the stability of such systems. By building on results from the literature, Flåtten and Lund[153], Lund[278] showed that this condition was satisfied for the entire homogeneous flow branch of the hierarchy. Other authors[148,318] have shown this condition to hold also for two-fluid models. The reader is referred to recent theses[279,317] or to the appended article[259] (Paper 8), for a broader overview of the topic. A continuation of this discussion is found in section 5.4.

3

3.1 SINGLE-PHASE FLOW

In reality, fluids are composed of discrete atoms and molecules that attract and repel each other. In practice, however, the basic assumption underpinning most of fluid mechanics, and the work presented in this thesis, is *the continuum assumption*, i.e., that all matter can, beyond a certain scale, be assumed to be continuous. On the one hand, the success of continuum mechanics in describing physical phenomena and enabling industrial applications is a testimony of the validity of this assumption. On the other hand, the macroscopic equations of fluid flow can be formally derived from kinetic theory (see for example,[425] Chapter 5). For our purposes, not much is gained from the latter procedure compared to the macroscopic approach, which we will adopt in the following.

We assume for now that the fluid we consider is a pure phase and that in the region it occupies, it is completely space-filling, described by a continuous velocity field $\mathbf{u}$, density ρ, dynamic viscosity μ, etc. For macroscopic derivations of the equations of fluid flow, e.g. using the Reynolds transport theorem, consider standard textbooks on the topic, e.g.[245].

3.1.1 *Fundamental principles*

Now, we consider a fixed domain Ω, with a boundary $\partial\Omega$, which does not vary in time. For a closed system, the following fundamental physical principles should be satisfied:

- Conservation of mass,

- conservation of momentum (in the absence of friction),

- conservation of (total) energy,

- the second law of thermodynamics, i.e. that the global entropy should be non-decreasing.

We next present the fundamental compressible flow model and show that the above points are satisfied.

The equation of state

Generally, fluids, and in particular gases, are compressible. We assume the fluid to be in *local thermodynamic equilibrium*, such that the thermodynamic quantities, e.g. pressure p, temperature T, and chemical potential μ, are state functions. In particular they are related by an *equation of state*. Thus all thermodynamic quantites can be found as differentials of a thermodynamic Helmholtz free energy a. Given that we are by definition in a pure stable phase (not on the spinodal), any thermodynamic quantity can then be found by knowledge of exactly two others.[15]

15 This is not strictly necessary, but will suffice for the arguments made here.

For real fluids, their 'real' equations of state must be approximated by algebraic expressions with complexity and parameter values that depend on the physical parameter ranges of interest. Examples of equations of state often employed in simulations, ordered by increasing complexity, are (i) the ideal gas, (ii) the stiffened gas, (iii) van der Waals[453] and other cubic equations of state, and (iv) the Span–Wagner equation of state for CO_2[417]. The latter expression contains a total of 51 terms, including exponentials and logarithms, and uses accurate critical exponents[16] for the behaviour near the gas-liquid critical point. It can therefore be computationally costly to use in numerical simulations.

[16] Which illustrates the importance of universality classes in practical settings.

The following variables are of central to the thermodynamic description of a compressible single-phase fluid:

ρ — density $[\mathrm{kg\,m^{-3}}]$,

p — pressure $[\mathrm{Pa}]$,

e — specific internal energy $[\mathrm{J\,kg^{-1}}]$,

T — temperature $[\mathrm{K}]$,

s — specific entropy $[\mathrm{J\,K^{-1}\,kg^{-1}}]$,

g — specific chemical potential $[\mathrm{J\,kg^{-1}}]$.

Compressible flow

The archetypal model of compressible fluid flow can be stated as the following set of equations:

$$\partial_t \rho + \boldsymbol{\nabla} \cdot (\rho \mathbf{u}) = 0, \tag{3.1a}$$

$$\partial_t(\rho \mathbf{u}) + \boldsymbol{\nabla} \cdot (\rho \mathbf{u} \otimes \mathbf{u}) + \boldsymbol{\nabla} p - \boldsymbol{\nabla} \cdot \boldsymbol{\sigma}_{\mathrm{visc}} = \mathbf{0}, \tag{3.1b}$$

$$\partial_t E + \boldsymbol{\nabla} \cdot ((E + p)\mathbf{u}) - \boldsymbol{\nabla} \cdot (\mathbf{h} + \boldsymbol{\sigma}_{\mathrm{visc}}\mathbf{u}) = 0. \tag{3.1c}$$

Here, $\boldsymbol{\sigma}_{\mathrm{visc}}$ is the (objective and symmetric) viscous stress tensor. For a Newtonian fluid, where the stress is linear in the velocity field $\mathbf{u}$, the following stress–strain rate relationship holds:

$$\boldsymbol{\sigma}_{\mathrm{visc}} = 2\mu \mathbf{Du} + \lambda \mathbf{I}\boldsymbol{\nabla} \cdot \mathbf{u}, \tag{3.2}$$

where the symmetric rate-of-strain tensor is given by $\mathbf{Du} = (\boldsymbol{\nabla}\mathbf{u} + \boldsymbol{\nabla}\mathbf{u}^\top)/2$, and $\mu, \lambda > 0$ are viscosity parameters. Further, the total energy per volume is defined by

$$E = \frac{1}{2}\rho \mathbf{u}^2 + \rho e. \tag{3.3}$$

The heat flux, $\mathbf{h}$, is proportional to the temperature gradient, and given by

$$\mathbf{h} = K_T \boldsymbol{\nabla} T \tag{3.4}$$

where $K_T > 0$ is the thermal diffusivity. As noted above, the internal specific energy e is assumed to be a thermodynamic state variable. Thus it is specified by any two other thermodynamic variables, such as the pair (ρ, T). Note that in the absence of any viscous dissipation and heat transfer, $\boldsymbol{\sigma}_{\mathrm{visc}}, \mathbf{h} \to \mathbf{0}$, and we arrive at the classical Euler equations.

Boundary conditions

In addition to bulk equations, boundary conditions for $\mathbf{x} \in \partial\Omega$ must be specified. The no-slip boundary condition $\mathbf{u} = \mathbf{0}$ is usually applied. The latter is valid down to the

nanometer scale, but for certain materials it be replaced by the more general Navier slip condition (see e.g. [31]),

$$\mathbf{u} \cdot \hat{\mathbf{n}} = 0, \quad [\boldsymbol{\sigma}_{\text{visc}} \hat{\mathbf{n}} + l\mathbf{u}] \times \hat{\mathbf{n}} = \mathbf{0}, \tag{3.5}$$

where l is a slip coefficient. In the limit $l \to 0$, a shear-free boundary condition is achieved, while the no-slip condition is recovered in the limit $l \to \infty$.

Conservation laws

Local mass conservation is given by eq. (3.1a). The total mass $\mathcal{M} = \int_\Omega \rho$ is conserved:

$$\frac{\mathrm{d}\mathcal{M}}{\mathrm{d}t} = \int_\Omega \partial_t \rho = -\int_\Omega \boldsymbol{\nabla} \cdot (\rho\mathbf{u}) = -\int_{\partial\Omega} \rho\hat{\mathbf{n}} \cdot \mathbf{u} = 0, \tag{3.6}$$

where $\hat{\mathbf{n}}$ is the outward directed normal of the domain, and we have used that the velocity flux vanishes at the boundary. For a thermally insulated system, $\hat{\mathbf{n}} \cdot \mathbf{h} = 0$ can be set on the boundary; otherwise Dirichlet boundary conditions on T can be imposed.

The evolution of momentum is governed by eq. (3.1b). Note that due to the presence of viscous dissipation, the global momentum $\mathcal{P} = \int_\Omega \rho\mathbf{u}$ is *not* generally conserved.

Energy balance can in general be written as eq. (3.1c). The global energy $\mathcal{E} = \int_\Omega E$ is conserved:

$$\frac{\mathrm{d}\mathcal{E}}{\mathrm{d}t} = \int_\Omega \partial_t E = 0, \tag{3.7}$$

given that either the shear stress or the tangential velocity vanishes at the boundary, and that the heat flux across the boundary, $\hat{\mathbf{n}} \cdot \mathbf{h} = 0$.

Entropy production

The global entropy is given by $\mathcal{S} = \int_\Omega \rho s$. Now, the second law of thermodynamics states that the entropy should be non-decreasing. The fundamental thermodynamic differential can be written as

$$\mathrm{d}e = T\mathrm{d}s + \frac{p}{\rho^2}\mathrm{d}\rho. \tag{3.8}$$

Using eqs. (3.1a) to (3.1c) and (3.8), we find, with some calculation, that the time derivative of the global entropy can be written as

$$\frac{\mathrm{d}\mathcal{S}}{\mathrm{d}t} = \int_\Omega \frac{2\mu|\mathbf{Du}|^2}{T}\mathrm{d}\Omega + \int_\Omega \frac{\lambda|\boldsymbol{\nabla} \cdot \mathbf{u}|^2}{T}\mathrm{d}\Omega + \int_\Omega K_T|\boldsymbol{\nabla}\ln T|^2\,\mathrm{d}\Omega, \tag{3.9}$$

which, given that $\mu, \lambda, T > 0$ on physical grounds, must be non-negative. Hence, the second law of thermodynamics is satisfied. It is worth noting that when no diffusive processes (viscous damping and heat transfer) are present in the system, the entropy is conserved.

3.1.2 Approximations

Isothermal flow

In many physical applications, the temperature can be taken to be constant. This amounts to assuming that the heat generated externally or internally, i.e. by viscous dissipation, is negligible, or that temperature equilibrium with the surroundings is enforced instantaneously. The energy equation eq. (3.1c) can then be replaced directly by the condition

$T = T_0$, where T_0 is a specified temperature. In this case, the thermodynamic pressure, density, internal energy, and so forth, becomes dependent on a single variable.

It is clear that in the case of thermal equilibrium with the surroundings, the energy conservation principle will not be satisfied. The laws of thermodynamics require that [373]

$$\frac{\mathrm{d}\mathcal{F}}{\mathrm{d}t} = -T\frac{\mathrm{d}\mathcal{S}}{\mathrm{d}t} + \frac{\mathrm{d}\mathcal{W}}{\mathrm{d}t}, \tag{3.10}$$

where $\mathcal{W}$ denotes work and $\mathcal{F}$ is a free energy. In the absence of external work, it can be seen that the equivalent to entropy increase, in the case of isothermal flow, is a decrease in the free energy. This is a relevant quantity to inspect for many of the models presented in this work.

Incompressible flow

In many cases, in particular those considered herein, the flow can be considered to be incompressible, i.e., the density is constant:

$$\rho = \text{constant.} \tag{3.11}$$

This is a good approximation for most liquids. A more general condition can be found based on the Mach number $\mathrm{Ma} = u/c$, i.e. the ratio of the fluid speed u to the speed of sound c. The incompressibility assumption is physically justified when $\mathrm{Ma}^2 \ll 1$ (see [446], sec. 5.8).

Using eq. (3.11), we find from eq. (3.1a):

$$\boldsymbol{\nabla} \cdot \mathbf{u} = 0, \tag{3.12}$$

i.e., the velocity field is *solenoidal*, or divergence free. In particular, the condition eq. (3.12) imparts that information propagates infinitely fast, i.e. all points in the domain affect each other instantly. This is because the pressure wave associated with eq. (3.1a) travels with the speed $c \to \infty$ in an incompressible (infinitely stiff) medium.[17]

Now, the momentum eq. (3.1b) can be written as

$$\rho \left(\partial_t \mathbf{u} + \mathbf{u} \cdot \boldsymbol{\nabla}\mathbf{u} \right) + \boldsymbol{\nabla}p - \boldsymbol{\nabla} \cdot \left(2\mu\mathbf{D}\mathbf{u} \right) = \mathbf{0} \tag{3.13}$$

and the energy eq. (3.1c) becomes decoupled from the mass and momentum equations, and is thus superfluous to the flow description. The only thermodynamic *variable* left now is the pressure, which can be seen as a Lagrange multiplier that makes the velocity field solenoidal. All other thermodynamic quantities, although uncoupled from the flow, are given by p alone.

Taking now the viscosity μ to be constant, which is valid approximation unless temperature or pressure variations are too large, we obtain the classical incompressible Navier–Stokes equations,

$$\rho \left(\partial_t \mathbf{u} + \mathbf{u} \cdot \boldsymbol{\nabla}\mathbf{u} \right) + \boldsymbol{\nabla}p - \mu\boldsymbol{\nabla}^2\mathbf{u} = \mathbf{0}, \tag{3.14a}$$

$$\boldsymbol{\nabla} \cdot \mathbf{u} = 0. \tag{3.14b}$$

Laminar and creeping flow

As introduced in the previous chapter, an important dimensionless quantity that arises in the study of fluid flow is the Reynolds number Re, defined as the ratio of intertial to viscous forces in eq. (3.14),

$$\mathrm{Re} = \frac{\rho u d}{\mu} \simeq \frac{\rho|\mathbf{u} \cdot \boldsymbol{\nabla}\mathbf{u}|}{\mu|\boldsymbol{\nabla}^2\mathbf{u}|}, \tag{3.15}$$

[17] From a numerical standpoint, the velocity field being divergence free can be both advantageous and disadvantageous. On the one hand, it is a simplification, as one does not have to resolve the fast pressure wave. On the other hand, the infinitely fast information propagation means that no interactions are local, yielding possible issues with parallel scalability. Further, incompressible flow is prone to numerical instabilities; see the Babuska–Brezzi criterion in section 4.3.

where d is a typical length scale, and u is a characteristic velocity.

Laminar flow is a regime associated with low Re, where the fluid travels in a smooth and predictable way, and there is essentially no transfer of energy across scales. Since perturbations have a tendency to decay in such flows, such flows can often be taken to be time-independent. Still assuming incompressibility, the flow can then be described by the time-independent Navier–Stokes equations, obtained by imposing steady-state flow, $\partial_t \mathbf{u} = 0$, in eqs. (3.14a) and (3.14b):

$$\rho \mathbf{u} \cdot \boldsymbol{\nabla} \mathbf{u} + \boldsymbol{\nabla} p - \mu \boldsymbol{\nabla}^2 \mathbf{u} = \mathbf{0}, \quad \boldsymbol{\nabla} \cdot \mathbf{u} = 0. \tag{3.16}$$

With the presence of the advective term $\mathbf{u} \cdot \boldsymbol{\nabla} \mathbf{u}$, the time-symmetry is broken, and standing vortices may be present e.g. behind obstacles.

When the characteristic velocity and the length scale is so small that $\mathrm{Re} \ll 1$, the flow is not only laminar, but *creeping*.[18] That is, the viscous forces completely dominate over the inertial forces and eqs. (3.14a) and (3.14b) simplifies to

$$\mu \boldsymbol{\nabla}^2 \mathbf{u} = \boldsymbol{\nabla} p, \quad \boldsymbol{\nabla} \cdot \mathbf{u} = 0 \tag{3.17}$$

which are known as the Stokes equations. As can be seen from eq. (3.17), the equation is linear and the solution is completely specified by the boundary conditions.[19] In fact, the flow field becomes—up ta a scaling with the value of the forcing—a purely geometric property. To see this, consider a domain Ω with the no-slip condition $\mathbf{u} = \mathbf{0}$ imposed on the boundary $\partial\Omega$, except at an inlet $\partial\Omega_{\mathrm{in}}$, where an inlet pressure p_{in} is specified, and an outlet $\partial\Omega_{\mathrm{out}}$, where an outlet pressure p_{out} is specified. We can then introduce the dimensionless variables $\tilde{\mathbf{u}}, \tilde{p}, \tilde{\mathbf{x}}$, defined by:

$$\tilde{\mathbf{u}} = \frac{\mu}{L(p_{\mathrm{in}} - p_{\mathrm{out}})} \mathbf{u}, \quad \tilde{p} = \frac{p - \frac{1}{2}(p_{\mathrm{in}} + p_{\mathrm{out}})}{p_{\mathrm{in}} - p_{\mathrm{out}}}, \quad \tilde{\mathbf{x}} = \frac{\mathbf{x}}{L}. \tag{3.18}$$

The scaled problem (3.17) then becomes

$$\tilde{\boldsymbol{\nabla}}^2 \tilde{\mathbf{u}} = \tilde{\boldsymbol{\nabla}} \tilde{p}, \quad \text{with} \quad \tilde{p} = \begin{cases} \frac{1}{2} & \text{for} \quad \tilde{\mathbf{x}} \in \partial\tilde{\Omega}_{\mathrm{in}} \quad \text{and} \\ -\frac{1}{2} & \text{for} \quad \tilde{\mathbf{x}} \in \partial\tilde{\Omega}_{\mathrm{out}}, \end{cases} \tag{3.19}$$

where $\partial\tilde{\Omega}$ is the boundary of the scaled domain. Clearly, the solution $(\tilde{\mathbf{u}}, \tilde{p})$ is *independent* of the inlet/outlet pressures $p_{\mathrm{in}}, p_{\mathrm{out}}$, the viscosity μ and the scale L of the system. Thus, the flow field inherently only depends on the shape of the domain, including the location of the inlet and outlet. The flux Q is proportional to the magnitude of the physical flow field, and hence we can write down the relation

$$Q = kA \frac{p_{\mathrm{in}} - p_{\mathrm{out}}}{L\mu}, \tag{3.20}$$

where the permeability k is a function of the shape of the domain, and A is a cross-sectional area. Heuristically taking the continuum limit, i.e. letting $(p_{\mathrm{in}} - p_{\mathrm{out}})/L \to |\boldsymbol{\nabla} p|$ and $Q \to A|\mathbf{q}|$, we find that this is consistent with Darcy's law,

$$\mathbf{q} = -\frac{k}{\mu} \boldsymbol{\nabla} p, \tag{3.21}$$

where $\mathbf{q}$ is the discharge per area. This invariance is heavily exploited in Paper 2[261], which will be summarized in section 5.2.

[18] This can be shown by nondimensionalization of eq. (3.16), and matching the 'Lagrange multiplier' p to the dominating term.

[19] Since the equation is invariant under the transformation $(\mathbf{u}, p) \to (-\mathbf{u}, -p)$, the flow field is reversible. The implications of this can be observed in captivating experiments on 'reversible mixing' of tracer dyes in a Taylor–Couette cell. See e.g. https://www.youtube.com/watch?v=p08_KlTKP50.

FIGURE 3.1: Two phase flow modelling. (a) The sharp-interface description. (b) A diffuse-interface model meant to represent (a). The red line corresponds to (c). (c) Profile of the phase field ϕ across the interface.
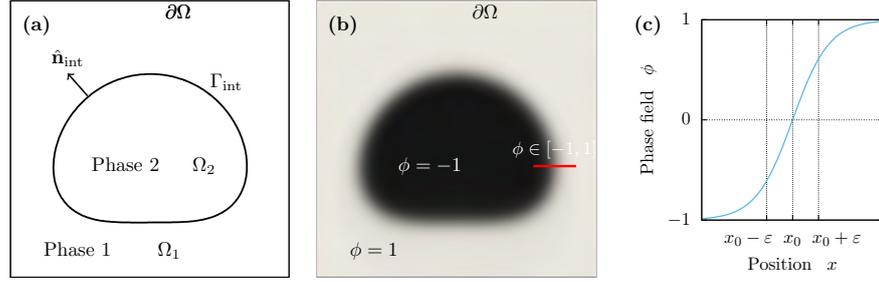
3.2 TWO-PHASE FLOW

Having established the fundamental equations for the continuum description of single-phase flow, we proceed now to describing the concurrent flow of two fluid phases. Equations (3.1a) to (3.1c) describe a single phase, and these equations are expected to hold in the *bulk* of the two phases; but the sets of parameters in the two phases will be separate. Therefore, we can replace ρ by ρ_i, and correspondingly for the other quantities, where $i = 1, 2$ denotes either of the two phases. However, the bulk phases are separated by an interface which requires an explicit description. For simplicity, we will consider, in the bulk of this section, isothermal and incompressible flow. Under the same conditions as with single-phase flow, this is usually a good approximation at scales where the interface is explicitly modelled. We briefly return to compressible two-phase flow in section 3.2.3.

3.2.1 *Interface conditions*

As mentioned briefly already, the two-phase interface is not sharp on the molecular scale, but rather a diffuse one. However, this thickness is usually only a few molecular layers thick[475] (i.e. $\sim 10^{-9}$ m),[20] and thus already below the micrometer scale ($\sim 10^{-6}$ m) it is perfectly valid to view it as an infinitely thin region where the physical properties change sharply and local interface forces are acting. A sharp-interface two-phase domain is sketched in fig. 3.1 (a).

[20] At least far from the gas–liquid critical point, where the interface thickness diverges.

We denote the jump in a physical quantity χ_i across the interface by $[\chi_i]_-^+$. That is, assuming that the interface is located at $x = 0$, and that phase 1 is in the subdomain $x < 0$ and phase 2 in the subdomain $x > 0$:

$$[\chi_i]_-^+ = \chi_2|_{x\to0^+} - \chi_1|_{x\to0^-}.$$ (3.22)

Further, we take $\hat{\mathbf{n}}_{\text{int}}$ to be the unit vector normal to the interface.

Due to the incompressibility condition (3.14b), the continuity condition holds for the velocity field:

$$[\mathbf{u}]_-^+ = 0.$$ (3.23)

Further, the interface stress condition is given by

$$[p]_-^+ \, \hat{\mathbf{n}}_{\text{int}} - [2\mu_i \mathbf{Du}]_-^+ \cdot \hat{\mathbf{n}}_{\text{int}} = \gamma\kappa\hat{\mathbf{n}}_{\text{int}},$$ (3.24)

where κ is the curvature. In equilibrium, shear stresses vanish, and this condition trivially reduces to the Young–Laplace law (2.13), which in the new notation reads $[p]_-^+ = \gamma\kappa$.

Boundary conditions

At the solid–fluid interface, i.e. the boundary of the domain $\partial\Omega$, the no-slip condition is still expected to hold in the bulk of each phase. However, as mentioned in section 2.1.3,

the hydrodynamic theory with a no-slip condition predicts a non-integrable stress singularity at the MCL (the Huh–Scriven paradox[201]). By some physical means, this must be regularized; and as listed by Bonn et al.[60] several mechanisms have been proposed and are relevant in different settings. In particular, hydrodynamic *slip* at the contact line was proposed by Huh and Scriven[201] (see also[126]) as a mitigation strategy, and it has since been shown in molecular dynamics simulations that this slip is physically justified, and moreover extends a significant distance from the contact line[371,372,377,426]. Ren and E[377] proposed a boundary condition for the sharp-interface contact line motion, which amounts to imposing the Navier slip condition, cf. eq. (3.5),

$$l_i u_x = \mu_i \partial_y u_x \qquad \text{away from the contact line, and} \qquad (3.25a)$$
$$l_{\mathrm{CL}} u_{x,\mathrm{CL}} = \gamma \left(\cos \theta_{\mathrm{eq}} - \cos \theta \right), \qquad \text{at the contact line.} \qquad (3.25b)$$

Here, the surface is oriented along x, and the surface normal is in the y direction, θ_{eq} is the equilibrium contact angle given by Young's law (2.15), θ is the instantaneous *dynamic* contact angle, and l_i, l_{CL} are the slip coefficients in the bulk phases and at the contact line, respectively. It is, however, not straightforward to implement such a boundary condition numerically.

3.2.2 Phase-field modelling

Phase-field modelling is a way to avoid the numerical difficulties associated with satisfying the jump conditions at the fluid–fluid interface (eqs. (3.23) and (3.24)), and is on sound physical grounds, as the interface on the microscopic scale *is* diffuse. Early phase-field models included compressibility and and an energy equation, and were reviewed by Anderson et al.[13], but as noted by Kim[232], much progress has taken place since then.[21]

Here we focus on the fully incompressible formulation by Abels et al.[2], and compare it to other formulations. A phase-field model is characterized by the order parameter field, i.e. the phase field, ϕ, which typically takes the value 1 in one phase, and -1 in the other.[22] At the interface, $\phi \in (-1, 1)$. In the forthcoming, the value $\phi = 1$ corresponds to phase $i = 1$ (with the associated phasic quantitites), while $\phi = -1$ corresponds to phase $i = 2$.

The thermodynamically consistent and frame indifferent model by Abels et al.[2] is given by

$$\rho(\phi)\partial_t(\mathbf{u}) + (\mathbf{m} \cdot \boldsymbol{\nabla})\mathbf{u} - \boldsymbol{\nabla} \cdot [2\mu(\phi)\mathbf{Du}] + \boldsymbol{\nabla}p = -\phi\boldsymbol{\nabla}g_\phi, \qquad (3.26a)$$
$$\boldsymbol{\nabla} \cdot \mathbf{u} = 0, \qquad (3.26b)$$
$$\partial_t \phi + \mathbf{u} \cdot \boldsymbol{\nabla}\phi = \boldsymbol{\nabla} \cdot (M(\phi)\boldsymbol{\nabla}g_\phi), \qquad (3.26c)$$
$$g_\phi = \chi\gamma \left[\varepsilon^{-1}W'(\phi) - \varepsilon\boldsymbol{\nabla}^2\phi \right]. \qquad (3.26d)$$

Here, eqs. (3.26a) and (3.26b) are the Navier–Stokes equations, but augmented by a body force and a few new factors, which are explained below. Equations (3.26c) and (3.26d) govern the conservative evolution of the phase field, and represent the Cahn–Hilliard equation coupled to an advective field. Thus the system (3.26) is called the (augmented) Navier–Stokes–Cahn–Hilliard system.

The following new quantities have been introduced:

$\rho(\phi)$ — the phase-dependent density, which interpolates between the phasic values such that $\rho(1) = \rho_1$ and $\rho(-1) = \rho_2$. Here, we use the arithmetic average:

$$\rho(\phi) = \frac{1 + \phi}{2}\rho_1 + \frac{1 - \phi}{2}\rho_2, \qquad (3.27)$$

[21] Much progress has occurred also since the latter review[232], as briefly surveyed in section 2.1.3.

[22] It is also commonplace to let it denote a local phase fraction, so that $\phi \in [0, 1]$ but the difference is trivial.

which is the only average that ensures global mass conservation; as realized by integrating over the domain and using that the flux of the phase field vanishes at the boundary.

$\mu(\phi)$ — the phase-dependent dynamic viscosity. It interpolates between the phasic values, corresponding to $\rho(\phi)$ above; an arithmetic average is usually used, but again a harmonic or geometric average may be more suitable if the viscosity contrast is large.

g_ϕ — the phase-field chemical potential $[\mathrm{N\,m^{-2}}]$. It contains $W(\phi)$, a double well-potential, which has minima at $\phi = \pm 1$. Here, we use the Ginzburg–Landau potential

$$W(\phi) = \frac{1}{4}(1 - \phi^2)^2. \tag{3.28}$$

Moreover, χ is a numerical prefactor to ensure the correct surface energy [211] given by $\chi = 3/\sqrt{8} \simeq 1.06$.

ε — the interface thickness [m].

$\mathbf{m}$ — the advecting momentum, given by:

$$\mathbf{m} = \rho(\phi)\mathbf{u} - \rho'(\phi)M(\phi)\boldsymbol{\nabla}g_\phi, \tag{3.29}$$

which only differs from the canonical momentum $\rho\mathbf{u}$ at the interface, since g_ϕ is constant in the bulk.

$M(\phi)$ — The phase-field mobility function $[\mathrm{m^3\,s\,kg^{-1}}]$. Two common alternatives are given by:

$$M(\phi) = \varepsilon M_0, \tag{3.30a}$$

$$M(\phi) = M_0(1 - \phi^2)_+, \tag{3.30b}$$

where M_0 is a constant parameter, and $(\cdot)_+ = \max(\cdot, 0)$. An aim of these mobility functions is to reduce the diffusive mass currents that lead to unphysical (numerical) Ostwald ripening effects. To the author's knowledge, there have been few comparative studies of the effect of various mobility functions.

Abels et al. [2] showed through a matched asymptotic expansion that the model (3.26) reduces to the correct sharp-interface description (see previous section) in the limit where the interface thickness $\varepsilon \to 0$, provided that the phase-field mobility is modelled as in eq. (3.26). In particular, the correct fluid–fluid interface conditions are contained in the model, provided that the interface is sufficently thin. The model by Ding et al. [118] is simply (3.26) with $\mathbf{m} = \rho(\phi)\mathbf{u}$ instead of eq. (3.29). This formulation is not thermodynamically consistent (see below), but reduces to the correct interface description. The model by Shen and Yang [403] is similar to the model by Ding et al. [118] in that $\mathbf{m} = \rho(\phi)\mathbf{u}$, but additionally a term

$$\frac{\mathbf{u}}{2}\left(\partial_t\rho + \boldsymbol{\nabla}\cdot(\rho\mathbf{u})\right) \tag{3.31}$$

is added to the left hand side of eq. (3.26a). This admits an energy dissipation law (thermodynamic consistency), but the model does not appear to be frame invariant. It is not known (at least to the author) whether this model reduces to the correct sharp-interface limit.

Note that the weighted arithmetic average (WAA), e.g. as in eq. (3.27), is not the only interpolation function that can be used for phasic quantities across the interface. Two

common alternatives are the weighted harmonic (WHA) and the weighted geometric average (WGA). For a general quantity A, these three averages are defined by

$$A_j(\phi) = \begin{cases} A_{j,1}\frac{1+\phi}{2} + A_{j,2}\frac{1-\phi}{2} & \text{(WAA)}, \\ \left[A_{j,1}^{-1}\frac{1+\phi}{2} + A_{j,2}^{-1}\frac{1-\phi}{2}\right]^{-1} & \text{(WHA)}, \\ A_{j,1}^{\frac{1+\phi}{2}} \cdot A_{j,2}^{\frac{1-\phi}{2}} & \text{(WGA)}. \end{cases} \qquad (3.32)$$

and they are compared as a function of ϕ in fig. 3.2. A problem with the WAA, and to some extent the WHA, is that for values of $|\phi|$ numerically only slightly above 1 (which can occur in phase-field simulations), is that the value of the interpolated quantity may become negative. This is also seen in fig. 3.2 and can lead to ill-posed problems. The WGA avoids this, but is more costly to compute. Some authors claim that using the WHA instead of the WAA for the density, yields more accurate computations[232,476,477], but this strictly imparts to violate mass conservation (however, the phase-field is conserved).

Boundary conditions

A boundary condition directly on the contact angle and contact line motion, as that specified in the sharp-interface limit, i.e. eq. (3.25), cannot be directly applied to a diffuse interface. The static contact angle θ_{eq} can be imposed through the condition

$$\chi\epsilon\hat{\mathbf{n}} \cdot \boldsymbol{\nabla}\phi = \cos(\theta_{\text{eq}})f_{\text{w}}'(\phi), \quad \hat{\mathbf{n}} \cdot \boldsymbol{\nabla}g_\phi = 0, \qquad (3.33)$$

where the wall energy function

$$f_{\text{w}}(\phi) = \frac{1}{4}\left(2 + 3\phi - \phi^3\right) \qquad (3.34)$$

interpolates smoothly between 0 (at $\phi = -1$) and 1 (at $\phi = 1$). Note that other forms of $f_{\text{w}}(\phi)$ that satisfy the criterion $f_{\text{w}}(1) - f_{\text{w}}(-1) = 1$ (and are smooth) are viable options, as discussed by Huang et al.[200]. However, the formulation (3.34) is the only one that is compatible with the equilibrium solution to eqs. (3.26c) and (3.26d), i.e. $g_\phi = $ constant.

Due to the presence of a diffuse interface, the contact line will move even when eq. (3.33) is coupled to a no-slip condition on the velocity, due to interface diffusion. This can be admissible when the dynamics are governed by processes away from the contact line, but is not satisfactory on the microscopic scale. A remedy is due to Qian et al.[371,373], who extracted phase-field parameters from carefully executed molecular dynamics simulations, and proposed a generalized Navier boundary condition (GNBC)[5] valid for $\mathbf{x} \in \partial\Omega$:

$$\mathbf{u} \cdot \hat{\mathbf{n}} = 0, \quad [\boldsymbol{\sigma}_{\text{visc}}\hat{\mathbf{n}} + l(\phi)\mathbf{u} - L[\phi]\boldsymbol{\nabla}\phi] \times \hat{\mathbf{n}} = \mathbf{0}, \quad \text{on the velocity field}, \qquad (3.35a)$$

$$\partial_t\phi + \mathbf{u} \cdot \boldsymbol{\nabla}\phi = -\Gamma L[\phi], \quad \hat{\mathbf{n}} \cdot \boldsymbol{\nabla}g_\phi = 0, \quad \text{on the phase field}, \qquad (3.35b)$$

where

$$L[\phi] = \gamma\left[\chi\epsilon\hat{\mathbf{n}} \cdot \boldsymbol{\nabla}\phi + \cos(\theta_{\text{eq}})f_{\text{w}}'(\phi)\right], \qquad (3.35c)$$

$$l(\phi) = l_1\frac{1+\phi}{2} + l_2\frac{1-\phi}{2}. \qquad (3.35d)$$

Here, $l(\phi)$ can be interpreted as an inverse slip length, interpolating between the values in the two phases, and Γ is a phenomenological parameter. It should be noted that the simulations supporting the GNBC were carried out in a slow wetting regime[82], and the
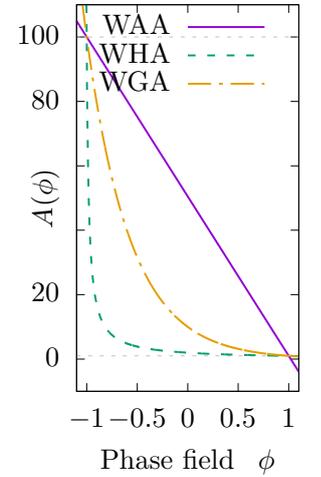

FIGURE 3.2: A comparison of three ways to interpolate a phasic quantity across the phase-field interface: Weighted arithmetic average (WAA), weighted harmonic average (WHA), and weighted geometric average (WGA).

interface width was matched to the actual, molecular one. It is less clear how well the GNBC works outside this domain.

An important limit to the GNBC is that of short slip length, which is obtained by letting $l_1, l_2 \to \infty$ in eq. (3.35). Then the no-slip boundary condition $\mathbf{u} = \mathbf{0}$ is recovered, along with the phase-field boundary condition

$$\Gamma^{-1}\partial_t\phi = \gamma\left[-\chi\epsilon\hat{\mathbf{n}}\cdot\boldsymbol{\nabla}\phi + \cos(\theta_e)f'_{\mathrm{w}}(\phi)\right],\qquad(3.36)$$

which was obtained by Carlson et al.[82] on phenomenological grounds, and previously proposed by Jacqmin[211]. Here, $\tau_{\mathrm{w}} = \epsilon/(\Gamma\gamma)$ can be interpreted as a characteristic relaxation time. It was shown e.g. in Refs.[82,83] that the condition (3.36) is fully capable of modelling rapid non-equilibrium wetting at the millimeter scale. In the limit $\tau_{\mathrm{w}} \to 0$ ($\Gamma \to \infty$), the static condition eq. (3.33) is recovered.

Free energy

Fundamental to most phase-field models is that they can be derived as the gradient flow of some energy functional. The system eq. (3.26) is associated with the energy functional

$$\mathscr{F} = \mathscr{F}_\phi + \mathscr{F}_{\mathrm{w}} + \mathscr{F}_{\mathbf{u}},\qquad(3.37)$$

where the Cahn–Hilliard free energy[78] is given by:

$$\mathscr{F}_\phi = \int_\Omega \chi\gamma\left[\epsilon^{-1}W(\phi) + \tfrac{1}{2}\epsilon|\boldsymbol{\nabla}\phi|^2\right].\qquad(3.38)$$

The fluid-solid interface energy is given by:

$$\mathscr{F}_{\mathrm{w}} = \int_{\partial\Omega}\left[\gamma_2 + (\gamma_1 - \gamma_2)f_{\mathrm{w}}(\phi)\right],\qquad(3.39)$$

where Young's law eq. (2.15) gives $\gamma_1 - \gamma_2 = \gamma\cos\theta_{\mathrm{eq}}$. The kinetic energy is given by

$$\mathscr{F}_{\mathbf{u}} = \int_\Omega \tfrac{1}{2}\rho(\phi)|\mathbf{u}|^2.\qquad(3.40)$$

The time evolution of $\mathscr{F}$ is given by using eqs. (3.26a) to (3.26c), along with the GNBC (3.35), and yields

$$\frac{\mathrm{d}\mathscr{F}}{\mathrm{d}t} = -\int_\Omega\left[M(\phi)|\boldsymbol{\nabla}g_\phi|^2 + 2\mu(\phi)|\mathbf{Du}|^2\right] - \int_{\partial\Omega}\left[l(\phi)|\mathbf{u}|^2 + \Gamma|L[\phi]|^2\right].\qquad(3.41)$$

In particular, all terms within brackets are squares with positive coefficients, i.e. the conditions $M, \mu, l, \Gamma \geq 0$ ensure that the model is dissipative.

3.2.3 *Homogenized models*

We now return to two-phase flow in pipes. In typical phenomena of interest to these flows, such as rapid decompression, running ductile fracture[317], the phenomena of interest occur at $\mathrm{Ma} \sim 1$; i.e. incompressibility cannot be justified. Thus, fully compressible models must be employed. Instead of resolving the interface, the Baer–Nunziato model[24] is based on averaged equations where the interaction between the phases across the interface is modelled effectively. The model is widely used in practice and extensively studied in the literature[480]. These effective interaction processes, that should drive the phases towards equilibrium (i) with each other, and (ii) with the surroundings, can be modelled as relaxation source terms.

The following processes can be physically motivated to take place:

    p — **Volume transfer**: Relaxation towards mechanical equilibrium due to pressure differences between the phases, i.e. expansion or compression.

    T — **Heat transfer**: Relaxation towards thermal equilibrium, due to temperature differences between the phases.

    g — **Mass transfer**: Relaxation towards chemical equilibrium due to differences between the phases in chemical potential.

    $\mathbf{u}$ — **Momentum transfer**: Relaxation towards equal velocities, which occurs through momentum transfer due to interface friction when the phasic velocities are different.

Additionally, heat and momentum transfer can occur due to interaction with the surroundings, e.g. the confining pipe.

With all possible relaxation terms, the Baer–Nunziato model [24], formulated in the lines of Saurel and Abgrall [394], can be stated compactly as

$$\partial_t \alpha_k + \mathbf{u}_{\text{int}} \cdot \boldsymbol{\nabla} \alpha_k = I_k, \tag{3.42a}$$

$$\partial_t (\alpha_k \rho_k) + \boldsymbol{\nabla} \cdot (\alpha_k \rho_k \mathbf{u}_k) = K_k, \tag{3.42b}$$

$$\partial_t (\alpha_k \rho_k \mathbf{u}_k) + \boldsymbol{\nabla} \cdot (\alpha_k \rho_k \mathbf{u}_k \otimes \mathbf{u}_k + \alpha_k p_k \mathbf{I}) - p_{\text{int}} \boldsymbol{\nabla} \alpha_k = \mathbf{u}_{\text{int}} K_k + \mathbf{M}_k \\ + \mathbf{M}_{k,\text{ext}}, \tag{3.42c}$$

$$\partial_t E_k + \boldsymbol{\nabla} \cdot (E_k \mathbf{u}_k + \alpha_k p_k \mathbf{u}_k) - p_{\text{int}} \mathbf{u}_{\text{int}} \cdot \boldsymbol{\nabla} \alpha_k = -p_{\text{int}} I_k + \mathbf{u}_{\text{int}} \cdot \mathbf{M}_k \\ + \left(g_{\text{int}} + \tfrac{1}{2} \mathbf{u}_{\text{int}}^2 \right) K_k \\ + H_k + H_{k,\text{ext}}, \tag{3.42d}$$

for each phase $k \in \{\mathrm{g}, \ell\}$, where g denotes gas and ℓ denotes liquid. Here, p_{int}, g_{int}, $\mathbf{u}_{\text{int}}$ are interface quantities that result from the homogenization procedure and must be explicitly modelled in a physically consistent way. Moreover, α_k denotes the volume fraction of the phase k, such that the condition $\alpha_{\mathrm{g}} + \alpha_{\ell} = 1$ makes eq. (3.42a) for one of the phases superfluous. Thus, we are left with 7 independently governed partial differential equations (where two are vectorial).

In the model (3.42), the relaxation source terms I_k, K_k, H_k and M_k, are modelled as the following:

- $I_{\mathrm{g}} = -I_{\ell} = \mathcal{J}(p_{\mathrm{g}} - p_{\ell})$ drives the phases towards equal pressure through volume transfer,

- $K_{\mathrm{g}} = -K_{\ell} = \mathcal{K}(g_{\ell} - g_{\mathrm{g}})$ drives the phases towards equal chemical potential through mass transfer,

- $H_{\mathrm{g}} = -H_{\ell} = \mathcal{H}(T_{\ell} - T_{\mathrm{g}})$ drives the phases towards equal temperature through heat transfer,

- $\mathbf{M}_{\mathrm{g}} = -\mathbf{M}_{\ell} = \mathcal{M}(\mathbf{u}_{\ell} - \mathbf{u}_{\mathrm{g}})$ drives the phases towards equal velocities through momentum transfer.

- $\mathbf{M}_{k,\text{ext}} = \alpha_k \rho_k \mathbf{a}_{\text{grav}} - f_{k,\mathrm{D}} \mathbf{u}$ represents momentum transfer due to external sources; here $\mathbf{a}_{\text{grav}}$ represents the graviational acceleration, and $f_{k,\mathrm{D}}$ represents friction with the pipe wall (proportional to a Darcy friction factor for phase k).

- $H_{k,\text{ext}}$ represents the heat transfer from surroundings.

The quantities $\mathcal{J}, \mathcal{K}, \mathcal{H}, \mathcal{M}$ can be interpreted as coefficients that can depend on thermophysical properties of the flow, e.g. flow regime or temperature. On physical grounds, they must all be non-negative; see e.g.[153,259,278].

It should be noted that the model (3.42) in practice is comprised of the Euler equations for each of the phases, supplemented by interface interaction terms and source terms. In the absence of external source terms, the model (3.42) conserves

- total mass, $\mathcal{M} = \int_{\Omega}(\alpha_{\mathrm{g}}\rho_{\mathrm{g}} + \alpha_{\ell}\rho_{\ell})$, which is realized by summing eq. (3.42b) over the phases k;

- total momentum, $\mathcal{P} = \int_{\Omega}(\alpha_{\mathrm{g}}\rho_{\mathrm{g}}\mathbf{u}_{\mathrm{g}} + \alpha_{\ell}\rho_{\ell}\mathbf{u}_{\ell})$, as seen by summing (3.42c) over k; and

- total energy, $\mathcal{E} = \int_{\Omega}(E_{\mathrm{g}} + E_{\ell})$, as seen by summing eq. (3.42d) over k.

Moreover, a second law analysis similar to that shown in section 3.1.1, but by combining the two phases, can be used to determine the interface parameters such that the model is thermodynamically consistent[259].

Writing out the differentials and for simplicity assuming a one-dimensional description along x (which is currently of most practical importance), eq. (3.42) can be written in the quasilinear form

$$\partial_t \mathbf{U} + \mathbf{A}(\mathbf{U})\partial_x \mathbf{U} = \sum_i \frac{1}{\tau_i}\mathbf{Q}_i(\mathbf{U}), \qquad (3.43)$$

Here, $\mathbf{U}$ is the (seven-dimensional) vector of unknowns, the matrix $\mathbf{A}$ is denotes the Jacobian of the system, and $\mathbf{Q}_i$ contains the relaxation terms for each relaxation process i, with the associated characteristic timescale τ_i (explicit expressions are omitted here). The eigenvalues of $\mathbf{A}$ are independent of the choice of $\mathbf{U}$ and determine the propagation velocities, i.e. the fluid-mechanical sound velocities, of the system.

Partial equilibrium

When one or more of the timescales τ_i are much faster than other time scales involved in the problem, it may be physically valid and practically advantageous to *directly* enforce equilibrium in one or more of the aforementioned processes. For example, pressure equilibrium imparts that

$$p_k \equiv p, \quad \text{which corresponds to} \quad \mathcal{J} \to \infty, \qquad (3.44)$$

and similarly for the other processes. Enforcing eq. (3.44) effecively removes one unknown from the problem, so that one of the 7 equations in eq. (3.42) becomes superfluous. Typically, eq. (3.42a) is removed for such p-relaxation. Evidently, all the combinations of equilibrium conditions lead to different models, as mentioned in section 2.2.3. When all equilibrium are enforced, the *homogeneous equilibrium model* arises, which is basically the Euler equations supplied with a two-phase equation of state.

Zein et al.[480] discuss the physical mechanisms of the involved relaxation processes, arguing that pressure relaxation is much faster than temperature relaxation, which again is faster than chemical potential relaxation; i.e.

$$\tau_p \ll \tau_T \ll \tau_g, \qquad (3.45)$$

which are also common assumptions in the literature. The velocity relaxation time $\tau_{\mathbf{u}}$ is expected to depend strongly on the flow regime. For stratified flow, the phase velocities

can be very different, while for dispersed flow it is reasonable to assume that the velocity relaxation is fast[279]. On the other hand, for these processes, full equilibrium in pressure will not be achieved. This is due to (i) gravity, which in stratified flow gives a pressure difference between the upper and lower phase, and (ii) surface tension, which through the Young–Laplace law (2.13) gives a higher pressure inside droplets in dispersed flow.

It is evident that replacing a PDE in eq. (3.42) by a functional relationship, such as eq. (3.44), changes the eigenstructure of the problem. Thereby, the propagation velocities, i.e. the fluid-mechanical speeds of sound, of the system change. In particular, it can be shown in the limit of equal phase velocities, that any equilibrium assumption reduces the fluid-mechanical speed of sound of such models[153,259,278]. This supports the folklore knowledge in the compressible multiphase flow community that the *equilibrium* speed of sound is always lower than the *frozen* speed of sound.

3.3 SINGLE-PHASE ELECTROHYDRODYNAMICS

The previous section concerned how to extend the modelling of single-phase flow to including a second phase. In this and the next section, we discuss the extension to modelling electrohydrodynamics, i.e. how to include the joint effects of dissolved ions and applied electric fields. The present section considers single-phase electrohydrodynamics, while in section 3.4 electrohydrodynamics in two phases is described.

The archetypical model for electrohydrodynamic flow, with N chemical species, is given by the following set of equations. The flow is assumed to be incompressible, isothermal and the electric currents are (safely) assumed to be to suffiently small for magnetic forces to be neglected.

$$\rho \left(\partial_t \mathbf{u} + \mathbf{u} \cdot \boldsymbol{\nabla} \mathbf{u} \right) + \boldsymbol{\nabla} p - \mu \boldsymbol{\nabla}^2 \mathbf{u} = - \sum_{j=1}^{N} c_j \boldsymbol{\nabla} g_{c_j}, \tag{3.46a}$$

$$\boldsymbol{\nabla} \cdot \mathbf{u} = 0, \tag{3.46b}$$

$$\partial_t c_j + \mathbf{u} \cdot \boldsymbol{\nabla} c_j = \boldsymbol{\nabla} \cdot \left(\frac{D_j c_j}{k_{\mathrm{B}} T} \boldsymbol{\nabla} g_{c_j} \right), \tag{3.46c}$$

$$g_{c_j} = k_{\mathrm{B}} T \ln \left(\frac{c_j}{c_j^{\mathrm{ref}}} \right) + q_e z_j V, \tag{3.46d}$$

$$\epsilon_0 \epsilon_{\mathrm{r}} \boldsymbol{\nabla}^2 V = -\rho_e. \tag{3.46e}$$

Herein, the following physical quantities are introduced:

c_j — number density, i.e. concentration, of species $j \in \{1, \ldots, N\}$ [m^{-3}].

g_{c_j} — chemical potential of species j [J].

k_{B} — The Boltzmann constant [J K^{-1}].

D_j — diffusivity of species j [m^2 s^{-1}].

c_j^{ref} — reference concentration for species c_j [m^{-3}].

q_e — the elementary charge [C],

V — electric potential [V]. The electric field is given by $\mathbf{E} = -\boldsymbol{\nabla} V$.

z_j — valency of ionic species j [−],

ϵ_0 — the vacuum permittivity [C V^{-1} m^{-1}],

ϵ_{r} — the relative permittivity [−],

In the literature, the terms *electrohydrodynamics* (EHD), *electrokinetics* (EK) and (to some extent) *electro-fluid-dynamics* are often used interchangably. Bazant[33] uses electrokinetics to refer to models which explicitly take into account ion transport, while electrohydrodynamics refers to modelling weakly conducting liquids with charged interfaces. The reason for the separate terminology is, in part, that the two fields have evolved separately and only recently are starting to become unified. Bruus[74, pp. 141] uses electrohydrodynamics in a broad sense, *including* electrokinetic effects. We have in this work opted for the latter definition; in particular electrokinetics refers to the part of electrohydrodynamics where diffusion of ions is important.

ρ_e — the charge density field $[\mathrm{C\,m^{-3}}]$. It is given by:

$$\rho_e = q_e \sum_{j=1}^{N} z_j c_j. \tag{3.47}$$

Above, eqs. (3.46a) and (3.46b) are the Navier–Stokes equations (3.14), where the momentum equation (3.46a) is augmented, on the right hand side, by an 'electrochemical' body force.

The form of the body force is somewhat unconventional. In most studies, the term on the right hand side of eq. (3.46a) is taken to be $\mathbf{f} = -\rho_e \boldsymbol{\nabla} V$. This formulation is related to the form stated in eq. (3.46a) by a redefinition of the pressure to include an osmotic contribution, i.e. the thermodynamical pressure (in the conventional form) $p_{\mathrm{therm}} = p + k_{\mathrm{B}} T \sum_{j=1} c_j$ (where p is the same as in eq. (3.46a)). The adopted form has advantages over the conventional one, e.g. as it avoids pressure build-up in the electrical double layers[337]. In this redefinition, care must primarily be taken in applying pressure conditions at boundaries with different concentrations, but not otherwise, since the role of the pressure in incompressible flow is to keep the velocity divergence free.

Equation (3.46c), with (3.46d) inserted, is the Nernst–Planck equation. The two terms in eq. (3.46d) represent the contribution to the flux from, in written order, diffusion and migration. Equation (3.46e) is the Poisson equation for electrostatic equilibrium (Gauss' law).

In Paper 5 (ref.[265]), a generalized version of the model (3.46) is presented, where fluid parameters such as density, viscosity and permittivity, are allowed to depend on the local concentrations. Additionally, a source term in the concentration equation, allowing for chemical reactions to occur, term is included. This is discussed in more depth in section 5.3.

Boundary conditions

The same boundary conditions as for single-phase flow are expected to apply to the velocity field as before. Here, we assume the standard Navier slip boundary condition (3.5).

For the concentration fields, the constant concentrations can be set at inlet and outlet parts of the domain $\partial\Omega$, alternatively a no-flux condition is set by imposing $\hat{\mathbf{n}} \cdot \boldsymbol{\nabla} g_{c_j} = 0$. The electric potential can e.g. be set to a fixed value V_0 on a part of the boundary. In the presence of a surface charge, the boundary condition

$$\hat{\mathbf{n}} \cdot \boldsymbol{\nabla} V = \frac{\sigma_e}{\epsilon_0 \epsilon_{\mathrm{r}}}, \tag{3.48}$$

where σ_e is the surface charge $[\mathrm{C\,m^{-2}}]$.

Free energy

The free energy functional associated with eq. (3.46) is given by

$$\mathscr{F} = \mathscr{F}_{\mathbf{u}} + \sum_{j=1}^{N} \mathscr{F}_{c_j} + \mathscr{F}_V, \tag{3.49}$$

where the kinetic energy $\mathscr{F}_{\mathbf{u}}$ is given by eq. (3.40), the chemical energy is given by

$$\mathscr{F}_{c_j} = \int_\Omega k_{\mathrm{B}} T c_j \left(\ln\left(\frac{c_j}{c_j^{\mathrm{ref}}}\right) - 1 \right), \tag{3.50}$$

and the electric field energy is given by

$$\mathscr{F}_V = \int_\Omega \tfrac{1}{2}\epsilon_0\epsilon_{\mathrm{r}}|\boldsymbol{\nabla}V|^2. \tag{3.51}$$

Assuming no-flux boundary conditions and a Navier slip condition, the time derivative becomes:

$$\frac{\mathrm{d}\mathscr{F}}{\mathrm{d}t} = -\int_\Omega \left[2\mu|\mathbf{Du}|^2 + \sum_{j=1}^{N} \frac{D_j c_j}{k_{\mathrm{B}}T}|\boldsymbol{\nabla}g_{c_j}|^2 \right] - \int_{\partial\Omega} l|\mathbf{u}|^2. \tag{3.52}$$

Hence, the model is dissipative, and thus thermodynamically consistent.

Creeping flow and steady-state

For microscale flows, the assumption $\mathrm{Re} \ll 1$ is usually justified. In this case, the inertial term of eq. (3.46a) can be neglected. Further, we are often interested in the *steady-state* transport through microchannels, and hence all time derivatives vanish. The steady-state equations for creeping flow can be summarized as:

$$\boldsymbol{\nabla}p - \mu\boldsymbol{\nabla}^2\mathbf{u} = -\sum_{j=1}^{N} c_j\boldsymbol{\nabla}g_{c_j}, \tag{3.53a}$$

$$\boldsymbol{\nabla}\cdot\mathbf{u} = 0, \tag{3.53b}$$

$$\boldsymbol{\nabla}\cdot(c_j\mathbf{u}) = D_j\boldsymbol{\nabla}^2 c_j + \boldsymbol{\nabla}\cdot\left(\frac{D_j q_e z_j c_j}{k_{\mathrm{B}}T}\boldsymbol{\nabla}V\right), \tag{3.53c}$$

$$\epsilon_0\epsilon_r\boldsymbol{\nabla}^2 V = -\rho_e. \tag{3.53d}$$

Despite the simplification, this is a strongly coupled non-linear system, which can only be solved analytically in particular limits and simple geometries.

Equilibrium

In equilibrium, all fluxes should vanish, including the one that is proportional to $\boldsymbol{\nabla}g_{c_i}$. Thus, the chemical potential defined in eq. (3.46d) must be constant:

$$g_{c_i} = k_{\mathrm{B}}T\ln\left(\frac{c_j}{c_j^{\mathrm{ref}}}\right) + q_e z_i V = k_{\mathrm{B}}T\ln\left(\frac{c_j^0}{c_j^{\mathrm{ref}}}\right), \tag{3.54}$$

where we have implicitly defined a reference concentration c_i^0 at a grounded part of the boundary. Solving this for c_i yields

$$c_i = c_i^0 e^{-\frac{q_e z_i V}{k_{\mathrm{B}}T}}, \tag{3.55}$$

i.e., the concentrations follow the Boltzmann distribution. We can now insert the distributions eq. (3.55) into eq. (3.53d):

$$\boldsymbol{\nabla}^2 V = -\frac{q_e}{\epsilon_0\epsilon_r}\sum_{i=1}^{N} z_i c_i^0 e^{-\frac{q_e z_i V}{k_{\mathrm{B}}T}}, \tag{3.56}$$

which is a non-linear equation to be solved for the single variable V. The latter becomes particularly appealing when considering a binary symmetric electrolyte, i.e., $i \in \{\pm\}$

and $z_\pm = \pm z$, which is taken to be neutral at the reference point, such that $c_\pm^0 = c^0$. Then, we obtain the classical nonlinear Poisson–Boltzmann equation

$$\boldsymbol{\nabla}^2 V = \frac{2q_e z c^0}{\epsilon_0 \epsilon_r} \sinh\left(\frac{q_e z V}{k_B T}\right). \tag{3.57}$$

Here, we can identify the *thermal voltage* V_T and the Debye length λ_D, respectively defined by

$$V_T = \frac{k_B T}{q_e z}, \quad \text{and} \quad \lambda_D = \sqrt{\frac{k_B T \epsilon_0 \epsilon_r}{2z^2 q_e^2 c^0}}. \tag{3.58}$$

Equations (3.57) and (3.58) yield an equation for the scaled electric potential $\varphi = V/V_T$:

$$\boldsymbol{\nabla}^2 \varphi = \frac{1}{\lambda_D^2} \sinh \varphi. \tag{3.59}$$

The concentrations can subsequently be found from eq. (3.55) as $c_\pm = c^0 e^{\mp\varphi}$. Equation (3.59) can be solved exactly in the one-dimensional case, considering a semi-infinite domain. The so-called Gouy–Chapman solution, given in the domain $\Omega = \{x \in [0, \infty)\}$, with the potential $\varphi = \varphi_0$ prescribed at $x = 0$, is given by[74]

$$\varphi = 4 \tanh^{-1}\left[\tanh\left(\frac{\varphi_0}{4}\right) e^{-x/\lambda_D}\right]. \tag{3.60}$$

Clearly, the magnitude of $|\varphi_0|$ determines the 'nonlinearity' of the potential distribution. In many practical settings, the magnitude of the scaled surface potential φ_0 is so small that eq. (3.59) (and (3.60)) can be linearized. In this limit, the so-called Debye–Hückel approximation, $|\varphi| \ll 1$ ($|V| \ll V_T$), yields the *linearized* Poisson–Boltzmann equation,

$$\boldsymbol{\nabla}^2 \varphi = \frac{1}{\lambda_D^2} \varphi, \tag{3.61}$$

where the corresponding solution to (3.60) is $\varphi = \varphi_0 e^{-x/\lambda_D}$. Thus, it is clearly seen that the Debye length λ_D is a characteristic length of the diffusive layer, i.e. it measures the extent of the electric double layer (EDL).

In many applications, a surface charge is prescribed instead of a surface potential. In the general nonlinear case, these are related through eq. (3.60). By using the surface-charge boundary condition $\sigma_e = -\hat{\mathbf{n}} \cdot \mathbf{E}$ at the surface, we can obtain the Grahame equation,

$$\sigma_e = \frac{2\epsilon_0 \epsilon_r V_T}{\lambda_D} \sinh\left(\frac{\zeta}{2V_T}\right) = \sqrt{8k_B T \epsilon_0 \epsilon_r c^0} \sinh\left(\frac{\zeta}{2V_T}\right), \tag{3.62}$$

which relates the surface charge to the *surface potential* $\zeta = \varphi_0 V_T$, often referred to as the *zeta potential*.

Streaming potential and the electroviscous effect

We now have a basic understanding of the electrokinetic effects present in the absence of fluid flow. A qualitative impression of the effect of coupling to fluid flow becomes apparent by inspecting fig. 3.3. Here, we consider a capillary of finite length, where a surface charge is applied to the capillary walls. In fig. 3.3 (a), there is no pressure difference between inlet and outlet, and hence, in equilibrium, the surface charge is screened by counterions. In fig. 3.3 (c) a pressure difference is applied across the system. In the steady state, the ion distributions are continuously advected by the velocity field,
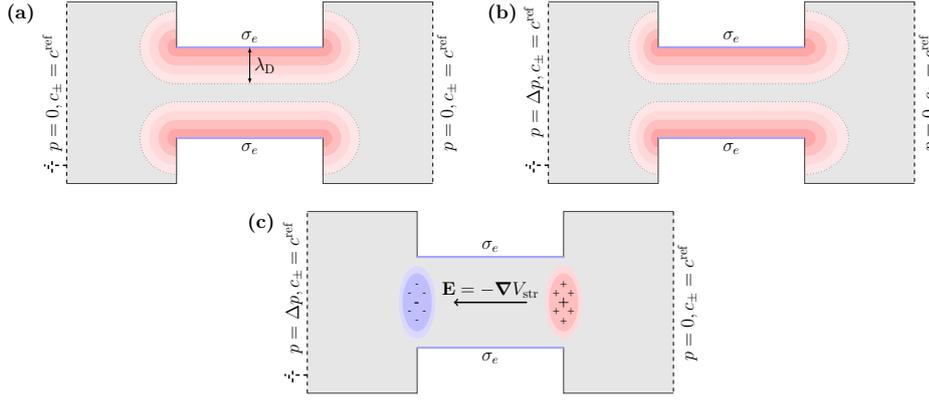
FIGURE 3.3: Streaming potential, electric double layer, and the electroviscous effect. Red indicates positive net charge, and blue indicates negative net charge. (a) The charge distribution in a model capillary with surface charges on the wall, where the pressure is the same at inlet and outlet. (b) Same as (a), but a pressure difference is imposed across the system, skewing the electric double layer. (c) The streaming potential effectively resulting from the skewed electrical double layers in (b). A net negative charge builds up to the left, and a net positive charge builds up to the right, which sets up an electric field counteracting fluid motion. (Courtesy of Asger Bolet.)

which means that the electrical double layer is distorted and ions are moved away from the inlet side and spill out on the outlet side. This, as shown in fig. 3.3 (c) effectively induces a dipole moment and sets up an electric field $\mathbf{E}$ due to the difference in net charge at each end. This electric field can be attributed to a streaming potential V_{str}, i.e. $\mathbf{E} = -\boldsymbol{\nabla} V_{\text{str}}$. The associated electric field will act on the fluid, which has a net charge, effectively inhibiting the flow.

This effect can be quantified through the Helmholtz–Smoluchowski relation. For flow in an infinite cylindrical pore (oriented along z, with radius R), it may heuristically be derived by considering symmetric binary electrolyte. Then, the total charge flux can be written using eqs. (3.46c), (3.46d) and (3.47):

$$\mathbf{J}_e = \rho_e \mathbf{u} - D\boldsymbol{\nabla}\rho_e + K\mathbf{E}, \tag{3.63}$$

such that $\partial_t \rho_e = \boldsymbol{\nabla}\cdot\mathbf{J}_e$. Here, we have identified the conductivity $K = Dz^2 q_e^2(c_+ + c_-)/(k_{\text{B}}T)$. Further, we assume the flux to be given by the Hagen–Poiseuille solution:

$$\mathbf{u} = u_z(r)\hat{\mathbf{z}} = \frac{f_z}{4\mu}(R^2 - r^2)\hat{\mathbf{z}}, \tag{3.64}$$

where $f_z = -\partial p/\partial z + f_e$ is the total average driving force on the fluid, composed by the constant average pressure gradient, $\partial p/\partial z$, and the induced electric force, f_e. In the steady state, the cross sectional integral of $\mathbf{J}_e$ must vanish, and so must the integral of the diffusive term; i.e. the second term on the right of eq. (3.63). By taking the cross-sectional integrals of eq. (3.63), we find

$$I_{\text{str}} + I_{\text{cond}} = 0, \tag{3.65}$$

where we have identified the streaming current I_{str} and the conducting current I_{cond} respectively as

$$I_{\text{str}} = 2\pi \int_0^R \rho_e(r)u_z(r)r\,\mathrm{d}r \quad \text{and} \quad I_{\text{cond}} = 2\pi \int_0^R KE_z r\,\mathrm{d}r \tag{3.66}$$

Within the realm of the linearized Poisson–Boltzmann equation (3.61), we may approximate $c_+ + c_- \simeq 2c^0$ and thus K can be taken constant. Further, in the expression for I_{str}, we may introduce the new coordinate $\xi = R - r$, linearize the resulting expression in ξ (assuming $\lambda_{\text{D}} \ll R$), insert eq. (3.46e) and integrate by parts. We thus obtain

$$I_{\text{str}} = -\frac{f_z \epsilon_0 \epsilon_{\text{r}} \zeta}{\mu} \quad \text{and} \quad I_{\text{cond}} = KE_z = \frac{2Dz^2 q_e^2 c^0}{k_{\text{B}}T}E_z. \tag{3.67}$$

Using eqs. (3.58) and (3.65) we find

$$E_z = -\frac{\lambda_{\text{D}}^2 \zeta}{D\mu}f_z. \tag{3.68}$$

Using the fact that $|f_e| \ll |f_z|$, and the relation $E_z = \partial V_{\mathrm{str}}/\partial z$, we find the Helmholtz–Smoluchowski relation:

$$\frac{\partial V_{\mathrm{str}}/\partial z}{\partial p/\partial z} = -\frac{\lambda_{\mathrm{D}}^2 \zeta}{\mu D}. \tag{3.69}$$

We are, however, interested in an approximation of the flow resistance in the capillary. Thus we retain eq. (3.68) and seek an approximation of f_e, i.e. we take the cross-sectional average over $\mathbf{f}_e = -\rho_e \mathbf{E}$:

$$f_e \simeq \frac{2}{R^2} \int_0^R \rho_e(r) E_z r \, \mathrm{d}r \simeq 2E_z \frac{\epsilon_0 \epsilon_{\mathrm{r}} \zeta}{R \lambda_{\mathrm{D}}} = -\frac{2\epsilon_0 \epsilon_{\mathrm{r}} \zeta^2}{D\mu} \frac{\lambda_{\mathrm{D}}}{R} f_z, \tag{3.70}$$

where we have integrated by parts using eq. (3.46e), used the linearized Grahame eq. (3.62), and finally inserted eq. (3.68) in the last equality. Solving for f_z, we obtain

$$f_z = \frac{-\partial p/\partial z}{1 + \Xi}, \quad \text{where} \quad \Xi = \frac{2\epsilon_0 \epsilon_{\mathrm{r}} \zeta^2}{D\mu} \frac{\lambda_{\mathrm{D}}}{R}. \tag{3.71}$$

Clearly, the actual driving force that acts on the fluid in the capillary is *less* than the average pressure gradient, $-\partial p/\partial z$, since $\Xi \geq 0$ on physical grounds. Now, interpreting this expresion in terms of an effective *electric viscosity* μ_e as a proportionality factor between flow rate and imposed pressure (see e.g. eq. (2.10)), gives the following relation:

$$\mu_e = (1 + \Xi)\mu, \tag{3.72}$$

which is larger than the viscosity in the absence of electrokinetic effects, μ. While the derivation of eq. (3.72) was heuristic, it suffices to illustrate the *electroviscous effect*, which in practice quantifies the increased flow resistance due to surface charges and ions in solution. A more general version of eq. (3.72), using a more elaborate derivation with less restrictive assumptions, was presented by Rice and Whitehead[383] and later by Mansouri et al.[286,287]. Here, e.g. the distortion of the velocity profile due to the electric force near the boundary is taken into account.

In Paper 4[58] (see also[57]), corresponding expressions to those in Refs.[286,287] are found for plane Poiseuille flow. These expressions are mainly used for the purpose of validating a numerical code. Clearly, the assumption of infinitely long capillaries is highly idealized, and the results are expected to differ for finite and less ideal geometries. The main purpose of Paper 4[58] is to investigate electroviscous effects beyond those present in the simplest geometries—we will revisit these in section 5.3.

Much is known about electrical double layers at solid-fluid interfaces. However, at fluid-fluid interfaces double layers have been less studied, although an overview for oil–water interfaces can be found in[456]. Depending on the concentration, the Debye length λ_{D} can generally stretch from (roughly) 10^{-10}–10^{-6} m, meaning that the clear separation of scales which is usually the case in the study of droplets/two-phase flow is less clear here, since the EDL and the physical interface thickness *can* have comparable size.

3.4   TWO-PHASE ELECTROHYDRODYNAMICS

We now consider electrohydrodynamics in two phases. In this respect, we will first present the sharp-interface relations that we expect to hold when the interface thickness becomes vanishingly thin, and thereafter present the related phase-field modelling approach. We assume the single-phase description (3.46) to hold within the bulk of each fluid. At the interface, however, new conditions must be supplied.

3.4.1   *Sharp-interface conditions*

The same continuity in the velocity field should hold as without any electric fields, namely $[\mathbf{u}]_-^+ = 0$. The stress balance at the interface changes from eq. (3.73), in that the electric stresses must be included:

$$[p]_-^+ \, \hat{\mathbf{n}}_{\mathrm{int}} - [2\mu_i \mathbf{D}\mathbf{u}]_-^+ \cdot \hat{\mathbf{n}}_{\mathrm{int}} - \left[\epsilon_0 \epsilon_{\mathrm{r},i} \mathbf{E} \otimes \mathbf{E} - \tfrac{1}{2}\epsilon_0 \epsilon_{\mathrm{r},i} |\mathbf{E}|^2 \mathbf{I} \right]_-^+ \cdot \hat{\mathbf{n}}_{\mathrm{int}} = \gamma\kappa\hat{\mathbf{n}}_{\mathrm{int}}, \tag{3.73}$$

where $\mathbf{E} = -\boldsymbol{\nabla} V$ is (still) the electric field. The Maxwell stress tensor,

$$\boldsymbol{\sigma}_{\mathrm{M}} = \epsilon_0 \epsilon_{\mathrm{r},i} \mathbf{E} \otimes \mathbf{E} - \tfrac{1}{2} \epsilon_0 \epsilon_{\mathrm{r},i} |\mathbf{E}|^2 \mathbf{I} \tag{3.74}$$

is included in the above expression, and should balance the viscous and pressure forces at the interface. Here, $\epsilon_{\mathrm{r},i}$ denotes the relative permittivity of phase i. Note that an osmotic contribution (see section 3.3) has been integrated in the definition of the pressure p above.

In general, the same ionic species j can be present in both phases, such that it can cross the interface. However, the ionic species will have a different solubility and diffusivity in the two phases. Similar to what is done with other phasic quantities, such as density and viscosity, the latter can be included by generalizing (i) the reference concentration c_j^{ref} to $c_{j,i}^{\mathrm{ref}}$, denoting reference concentration of species j in phase i; and (ii) the diffusivity D_j to $D_{j,i}$, denoting the diffusivity of species j in phase i.

Now, the missing pieces is the continuity of the electric potential V across the interface (in the absence of any accumulated charges) and the continuity of the normal component of the displacement field:

$$[V]_-^+ = 0, \quad \text{and} \quad \hat{\mathbf{n}}_{\mathrm{int}} \cdot [\epsilon_{\mathrm{r},i} \mathbf{E}]_-^+ = 0. \tag{3.75}$$

Finally, the chemical potential g_{c_j} must be continuous across the interface:

$$\left[g_{c_j} \right]_-^+ = 0. \tag{3.76}$$

Using eqs. (3.46d), (3.75) and (3.76), the following relation is shown to hold at the interface:

$$\frac{c_j|_{x \to 0^+}}{c_j|_{x \to 0^-}} = \frac{c_{j,2}^{\mathrm{ref}}}{c_{j,1}^{\mathrm{ref}}}, \tag{3.77}$$

which gives a direct interpretation of the quantities involved at the right hand side. Alternatively, the quantities c_j can be related via a Henry jump condition[2]:

$$\frac{c_{j,2}^{\mathrm{ref}}}{c_{j,1}^{\mathrm{ref}}} = \exp\left(-\frac{\beta_{j,2} - \beta_{j,1}}{k_{\mathrm{B}} T} \right), \tag{3.78}$$

where

$$\beta_{j,i} = -k_{\mathrm{B}} T \ln \left(\frac{c_{j,i}^{\mathrm{ref}}}{c^{\mathrm{ref}}} \right) \tag{3.79}$$

can be interpreted physically as an energy penalty for dissolving species j in phase i, i.e. a *solubility energy*. In eq. (3.79), c^{ref} is an arbitrary global reference concentration (to make the units consistent). With eq. (3.79) inserted, eq. (3.46d) becomes

$$g_{c_j} = k_{\mathrm{B}} T \ln \left(\frac{c_j}{c^{\mathrm{ref}}} \right) + \beta_{j,i} + q_e z_j V. \tag{3.80}$$

The energetic approach to the solubility of a species in a phase differs from the approach by Berry et al.[43], who, in their sharp-interface model, strictly assumed the ionic species to be confined to one of the phases. Nonetheless, such immiscibility can be captured efficiently with the energetic approach, as demonstrated e.g. in Refs.[263,264,301].

3.4.2 Phase-field modelling

Campillo-Funollet et al.[79] presented an extension of the two-phase flow model by Abels et al.[2] (which was presented in the previous section), by including electrokinetic transport. The model is given by the following set of equations:

$$\rho(\phi)\partial_t \mathbf{u} + \mathbf{m} \cdot \boldsymbol{\nabla}\mathbf{u} + \boldsymbol{\nabla}p - \boldsymbol{\nabla} \cdot (2\mu(\phi)\mathbf{D}\mathbf{u}) = -\phi\boldsymbol{\nabla}g_\phi - \sum_{j=1}^{N} c_j\boldsymbol{\nabla}g_{c_j}, \qquad (3.81a)$$

$$\boldsymbol{\nabla} \cdot \mathbf{u} = 0, \qquad (3.81b)$$

$$\partial_t \phi + \mathbf{u} \cdot \boldsymbol{\nabla}\phi = \boldsymbol{\nabla} \cdot (M(\phi)\boldsymbol{\nabla}g_\phi), \qquad (3.81c)$$

$$g_\phi = \chi\gamma \left[\varepsilon^{-1}W'(\phi) - \varepsilon\boldsymbol{\nabla}^2\phi\right]$$
$$+ \sum_{j=1}^{N} \beta'_j(\phi)c_j - \tfrac{1}{2}\epsilon_0\epsilon'_r(\phi)|\boldsymbol{\nabla}V|^2, \qquad (3.81d)$$

$$\partial_t c_j + \mathbf{u} \cdot \boldsymbol{\nabla}c_j = \boldsymbol{\nabla} \cdot \left(\frac{D_j(\phi)c_j}{k_B T}\boldsymbol{\nabla}g_{c_j}\right), \qquad (3.81e)$$

$$g_{c_j} = k_B T \ln\left(\frac{c_j}{c^{\text{ref}}}\right) + \beta_j(\phi) + q_e z_j V, \qquad (3.81f)$$

$$\boldsymbol{\nabla} \cdot (\epsilon_0\epsilon_r(\phi)\boldsymbol{\nabla}V) = -\rho_e. \qquad (3.81g)$$

Here, we have introduced interpolation functions for the diffusivities D_j, the solubility energies β_j, and the relative permittivities $\epsilon_r(\phi)$. For the diffusivity, both weighted arithmetic average (WAA) and the weighted geometric average (WGA) are viable options; see eq. (3.32) for their definitions. The advantage of using the latter, is that this prevents leakage of ions across the interface if the associated ionic diffusivity is much lower in one phase than in the other (see [263]). Further, it *strictly* does not allow negative values of the interpolated function (if $|\phi| > 1$ numerically), which would lead to ill-posedness of the discretized problem. For the solubility energy β_j and the relative permittivity ϵ_r, we use the WAA:

$$\beta_j(\phi) = \beta_{j,1}\frac{1+\phi}{2} + \beta_{j,2}\frac{1-\phi}{2}, \qquad (3.82a)$$

$$\epsilon_r(\phi) = \epsilon_{r,1}\frac{1+\phi}{2} + \epsilon_{r,2}\frac{1-\phi}{2}. \qquad (3.82b)$$

By considering the averaging eq. (3.82a) in terms of the reference concentration, c_j^{ref}, instead, using the definition (3.79) and eq. (3.82a), we find that

$$c_j^{\text{ref}}(\phi) = c^{\text{ref}}\exp\left(-\frac{\beta_j(\phi)}{k_B T}\right) = \left(c_{j,1}^{\text{ref}}\right)^{\frac{1+\phi}{2}} \cdot \left(c_{j,2}^{\text{ref}}\right)^{\frac{1-\phi}{2}}, \qquad (3.83)$$

which is exactly a WGA, ideal for preserving the physically required positivity of c_j^{ref}. Choosing the arithmetic averages also simplifies the numerical treatment of the equations above, as the derivatives with respect to their arguments, β'_j and ϵ'_r, simply become constants and do not require matrix assembly (in the finite element method, see section 4.1) at each time step.

Other choices for interpolating the permittivity have been reported in the literature. Tomar et al.[443] found, for their combined level-set/volume-of-fluid leaky-dielectric and perfect-dielectric models with smoothed interfacial properties, that a weighted harmonic average (WHA) gave more accurate computations of the electric field than what the

WAA did. However, for a model including free charges, López-Herrera et al.[274] found no evidence that WHA was superior.

The model stated in eq. (3.81) is a unification of the two-phase model eq. (3.26), and the single-phase electrohydrodynamics model eq. (3.46). The eqs. (3.81a) and (3.81b) are the incompressible Navier–Stokes equations with variable density, augmented by a body force that accounts for the interface forces *and* the chemical forces.[23] The eqs. (3.81c) and (3.81d) are the Cahn–Hilliard equations, where two new terms have been added in eq. (3.81d) due to the chemical transport, compared to the formulation without electrohydrodynamics, eq. (3.26d). These give, effectively, rise to new force contributions in the momentum eq. (3.81a). The third term in eq. (3.81d) gives an osmotic contribution, while the last term yields a Helmholtz force, which arises due to permittivity gradients. The eqs. (3.81e) to (3.81g) are the Poisson–Nernst–Planck system, where the permittivity and solubility now depends on the phase ϕ.

Campillo-Funollet et al.[79] showed that the model reduced to the correct sharp-interface description in the limit $\varepsilon \to 0$ by a matched asymptotic expansion. The same boundary conditions as for the pure two-phase problem, and the single-phase electrohydrodynamic problem, apply to this model.

Free energy

Associated with the model (3.81), we have the free energy functional

$$\mathscr{F} = \mathscr{F}_{\mathbf{u}} + \mathscr{F}_\phi + \mathscr{F}_{\mathrm{w}} + \sum_{j=1}^N \mathscr{F}_{c_j} + \mathscr{F}_V. \tag{3.84}$$

Here, $\mathscr{F}_{\mathbf{u}}$ is given by eq. (3.40), the phase-field energy $\mathscr{F}_\phi$ is given by eq. (3.38), and the fluid-solid interface energy is given by eq. (3.39). The chemical free energy (3.50) can be written in terms of the solubility energy $\beta_j(\phi)$ as

$$\mathscr{F}_{c_j} = k_{\mathrm{B}} T c_j \left[\ln\left(\frac{c_j}{c^{\mathrm{ref}}}\right) - 1 \right] + \beta_j(\phi) c_j, \tag{3.85}$$

while $\mathscr{F}_V$ is given by eq. (3.51).

With the general GNBC boundary condition, the time evolution of the free energy can be written as

$$\frac{\mathrm{d}\mathscr{F}}{\mathrm{d}t} = -\int_\Omega \left[2\mu(\phi)|\mathbf{D}\mathbf{u}|^2 + M(\phi)|\boldsymbol{\nabla} g_\phi|^2 + \sum_{j=1}^N \frac{D_j c_j}{k_{\mathrm{B}} T}|\boldsymbol{\nabla} g_{c_j}|^2 \right]$$
$$- \int_{\partial\Omega} \left[l(\phi)|\mathbf{u}|^2 + \Gamma|L[\phi]|^2 \right]. \tag{3.86}$$

Thus, the model is dissipative.

Comparison to other models

Several authors have noted the need to connect the electrokinetic description of two-phase flow to the leaky-dielectric description[396,399,445,483]. Taylor's original assumption[436] was to impose an instantaneous steady-state charge distribution in the system, neglecting the diffusive and convective contributions and the continuity of the displacement field. Through the solution of the Poisson eq. (3.81g), this gives rise to charge accumulation at the interface. Melcher and Taylor[299] reviewed the latter model, and included in their updated model the effect of convection of charges located at the interface.

Baygents and Saville[32] outlined the analysis of how electrokinetic effects could alter the leaky-dielectric results. Zholkovskij et al.[483] considered the electrokinetic description for two phases, and assumed that no solute could be adsorbed to the interface. They obtained an expression for infinitesimal droplet deformation under a weak field approximation, which was shown to reduce to the leaky-dielectric result[436] in the limit of vanishingly thin Debye layers, and to the perfect dielectric result[8,345] in the opposite limit. Schnitzer and Yariv[399] considered a binary electrolyte and included rates for the adsorption of charges at the interface, meaning that a net charge would generally accumulate there in a steady-state. They showed rigorously that the model using for electrokinetics for each phase, in the limit of strong fields and thin Debye layers, reduced to the original model of Taylor[436]. In particular, the convection of charge at the interface was found to be insignificant to the lowest order in their expansion.

In the model (3.81), ions are not allowed to be adsorbed *at* the interface, although they may accumulate in thin layers on either side. It is possible that a phase contrast in β_j could suffice to model these effects. On the other hand, using ideas from the related topic of surfactants—molecules that tend to stick to the interface and change the surface tension[135,438]—it may be possible to extend the model to incorporate this effect.

Several phase-field models for soluble surfactants have been proposed, see e.g.[3,4,7,133,161,439]. Engblom et al.[133] discuss well-posedness of such models derived from a variational principle, i.e. as a gradient flow. A surfactant species can be included in the model by endowing the surfactant concentration ψ with the free energy functional

$$\mathscr{F}_\psi = \int_\Omega \left\{ k_\mathrm{B}T \left[\psi \ln \left(\frac{\psi}{\psi_\mathrm{max}} \right) + (\psi_\mathrm{max} - \psi) \ln \left(1 - \frac{\psi}{\psi_\mathrm{max}} \right) \right] + \psi \beta_\psi(\phi) \right\} \quad (3.87)$$

where ψ_max is a maximum concentration such that $\psi \in [0, \psi_\mathrm{max}]$, and the solubility energy is given by

$$\beta_\psi(\phi) = -A_\psi \frac{(1 - \phi^2)^2}{4} + B_\psi \frac{\phi^2}{4}. \quad (3.88)$$

Here, the first term on the right hand side is a smooth approximation of a Dirac delta function centered at the interface, which makes it energetically favorable to dissolve surfactants there. Conversely, the last term penalises the presence of surfactant in either of the pure phases. The coefficients A_ψ, B_ψ are related to the adsorption rates. The resulting chemical potential (assuming non-ionic surfactants) is given by

$$g_\psi = k_\mathrm{B}T \ln \frac{\psi}{\psi_\mathrm{max} - \psi} + \beta_\psi(\phi), \quad (3.89)$$

The dynamics is analogous to how chemical transport occurs:

$$\partial_t \psi_j + \mathbf{u} \cdot \boldsymbol{\nabla} \psi_j = \boldsymbol{\nabla} \cdot (M_\psi \boldsymbol{\nabla} g_\psi), \quad (3.90)$$

except that the mobility is modelled as $M_\psi(\psi) = M_{\psi,0}\psi(1 - \psi)$. This was shown in[133] to yield the Langmuir adsorption isotherm. In precursor work of[133], Van der Sman and Van der Graaf[451] showed that the Langmuir equation of state for the *measured* surface tension γ',

$$\gamma' - \gamma \sim k_\mathrm{B}T \ln \left[1 - \frac{\psi}{\psi_\mathrm{max}} \right], \quad (3.91)$$

where γ is the equilibrium surface tension entering into the model, could be obtained with approprately chosen coefficients.

For discussions on alternative phase-field models with soluble and insoluble surfactants, see e.g.[3,4,7,161]. Note also that in a similar manner as above, increased interface

conductivity can be modeled by supplementing the interpolation function $D_j(\phi)$ with a similar delta function term at the interface as above.

In the review by Saville[396], chemical reactions are an integral part to how the author arrives at the macroscopic model for electrohydrodynamics. Chemical reactions can trivially be included in the model, as was done originally by Campillo-Funollet et al.[79]. In Paper 5[265], a single-phase model with reactions is considered. The formulation Saville[396] ends up with is of a leaky-dielectric type, except that net charge is described by a conservation law of the type

$$\partial_t \rho_e + \mathbf{u} \cdot \boldsymbol{\nabla} \rho_e = \boldsymbol{\nabla} \cdot (K(\phi) \boldsymbol{\nabla} V), \tag{3.92}$$

where K is the conductivity. A corresponding phase-field model was presented by Eck et al.[128], albeit a diffusive term was included for numerical purposes. As mentioned, such a model can be rigorously[399] derived from the full electrokinetic model (3.81) above, but the procedure is fairly cumbersome. Here, we do it instead heuristically by linearising the concentrations around c^{ref}, i.e.

$$c_j = c^{\text{ref}} + \delta c_j, \tag{3.93}$$

and truncating at the lowest order, assuming a weak electric field, which gives

$$\partial_t \delta c_j + \mathbf{u} \cdot \boldsymbol{\nabla} \delta c_j = \boldsymbol{\nabla} \cdot \left[D_j(\phi) \boldsymbol{\nabla} \delta c_j + \frac{D_j q_e z_j c^{\text{ref}}}{k_{\text{B}} T} \boldsymbol{\nabla} V \right]. \tag{3.94}$$

Assuming $D_j(\phi) = D(\phi)$ for all j, we multiply eq. (3.94) by $q_e z_j$, sum over j and obtain

$$\partial_t \rho_e + \mathbf{u} \cdot \boldsymbol{\nabla} \rho_e = \boldsymbol{\nabla} \cdot [D(\phi) \boldsymbol{\nabla} \rho_e + K(\phi) \boldsymbol{\nabla} V] \tag{3.95}$$

where we have identified the conductivity as $K(\phi) = D(\phi) q_e^2 c^{\text{ref}} (k_{\text{B}} T)^{-1} \sum_{j=1}^N z_j^2$ (cf. eq. (3.63) and the expression there for K). In this picture, ρ_e can be seen as a single chemical species associated with a modified free energy density $\propto \rho_e^2$. In the limit where we can neglect convection and diffusion, i.e. assume instantaneous steady-state, we obtain the following Laplace equation:

$$\boldsymbol{\nabla} \cdot [K(\phi) \boldsymbol{\nabla} V] = 0, \tag{3.96}$$

which yields V directly, and replaces all solute transport. This constitutes the leaky-dielectric approximation.

A phase-field model for leaky dielectrics was proposed by Lin et al.[258], constituted by the normal phase-field equations, supplied by force terms in the momentum equation, due to the permittivity and conductivity gradients in the two phases. The electric gradient terms were only included in the momentum equation, not in the chemical potential, and hence the model is further from being thermodynamically consistent than that of Eck et al.[128]. However, such terms in the phase-field chemical potential can lead to $O(\varepsilon)$ deviations from the pure phase values $\phi = \pm 1$ [133,311] (also curved interfaces may lead to this[479]). A possible mitigation strategy is to omit the additional terms in the phase-field equation, but include them in the momentum equation—a consequence being that the model loses its dissipative property. However, as mentioned earlier, it is not clear whether the thermodynamic consistency for unphysically large interface widths poses a significant advantage with regards to convergence to the correct sharp-interface description, apart from being advantagous when constructing numerical schemes[403,404].

3.4.3   *Electrokinetic scaling of the equations*

For both analytical and numerical purposes, it is useful to limit the problem to involving as few parameters as possible. Thus, we now nondimensionalize the equations, focusing in particular on the model (3.81) which also covers the special cases of single-phase electrohydrodynamics and pure two-phase flow. Dimensionless versions of physical variables are marked by a tilde, while reference values are marked with an asterisk (see also[263,264]). We let $\tilde{t} = t/t^*$, $\tilde{\rho} = \rho/\rho^*$, $\tilde{\mathbf{u}} = \mathbf{u}/u^*$, $\tilde{p} = p/p^*$, $\tilde{\mu} = \mu/\mu^*$, $\tilde{c}_j = c_j/c^*$, $\tilde{V} = V/V^*$, $\tilde{D}_\pm = D_\pm/D^*$, $\tilde{\epsilon} = \epsilon_{\rm r}/\epsilon^*$, and $\tilde{\gamma} = \gamma/\gamma^*$. The spatial dimensions are scaled by a reference linear size R^*, such that $\tilde{\mathbf{x}} = \mathbf{x}/R^*$. The electrostatic potential V is scaled by a thermal voltage (cf. eq. (3.58)),

$$V^* = V_T = \frac{k_{\rm B}T}{q_e},\qquad\qquad(3.97a)$$

while all other reference values are given by

$$t^* = \frac{R^*}{u^*},\quad \rho^* = \frac{q_e c^* V_T}{(u^*)^2},\quad D^* = u^* R^*,\quad p^* = q_e c^* V_T,\qquad(3.97b)$$

$$\mu^* = \frac{q_e c^* V_T R^*}{u^*},\quad \epsilon^* = \frac{q_e c^* (R^*)^2}{\epsilon_0 V_T},\quad \gamma^* = q_e c^* V_T R^*.\qquad(3.97c)$$

Altogether, this represents an invertible set of relations between the physical and dimensionless variables. Now, adopting the dimensionless variables and subsequently omitting the tildes, yields the model (3.81) with $q_e = k_B T = 1$ and $\epsilon_0 \epsilon_{\rm r} \to \epsilon$. This represents a simplification to the equations where the same physics is contained, which will be taken advantage of in the next section.

4

For all geometries but the very simplest ones, computational methods must be employed to solve the governing equations. In particular, the problems under scrutiny must be discretized both in space and time. This chapter gives an overview of the numerical methodology employed in this project. We will first introduce the finite element method, which is the main spatial discretization strategy used. Secondly, we consider temporal discretization strategies. In particular, we propose a general numerical scheme that is applicable to most of the systems in this thesis. Thereafter, we present methods for the simplified case of single-phase flow. Finally, we present an overview of the numerical software *employed* and *developed* in this work.

4.1   THE FINITE ELEMENT METHOD

The finite element method (FEM) is a popular and efficient method for solving partial differential equations (PDEs) in arbitrary geometries. The method relies on discretizing the domain by dividing it into simpler, finite elements. In contrast to finite difference and finite volume methods, that typically seek to find discrete approximations to the *equations* that are to be solved, the FEM consists in approximating the *solution* itself. This is achieved using calculus of variations, and by expressing an approximate solution as a linear combination of basis functions that are compactly supported on the elements. In the FEM, the original PDE is converted into a weak formulation, which, by using the Galerkin method, can be turned into a linear system of equations. The Galerkin method provides a solution that minimizes an error residual between the approximate solution, found by the finite basis, and the true solution. The finite element method works on linear PDEs, but by appropriate linearization and iterated solutions (Newton or Picard iteration) it can be straightforwardly adapted to solve nonlinear problems.

We shall illustrate the above concepts with an exemplary problem. For a more thorough and technical introduction into the theory of FEM, the reader is referred to standard textbooks on the topic (e.g. [67,132,172]).

A fairly general PDE relevant to many of the PDEs described in this thesis,[24] can be stated in the following form. Find $u \in \mathcal{U}$ such that

$$\mathscr{D}u \stackrel{\text{def}}{=} -\alpha u + \boldsymbol{\nabla} \cdot (\mathbf{w}(\mathbf{x})u + k(\mathbf{x})\boldsymbol{\nabla}u) = f(\mathbf{x}), \quad \text{for} \quad \mathbf{x} \in \Omega, \tag{4.1}$$

$$u = f_{\mathrm{D}}(\mathbf{x}), \quad \text{for} \quad \mathbf{x} \in \partial\Omega_{\mathrm{D}}, \tag{4.2}$$

$$\hat{\mathbf{n}} \cdot \boldsymbol{\nabla}u = f_{\mathrm{N}}(\mathbf{x}), \quad \text{for} \quad \mathbf{x} \in \partial\Omega_{\mathrm{N}}. \tag{4.3}$$

Here, $\mathcal{U}$ is the function space where the solution u lives, and the fields $\mathbf{w}(\mathbf{x}), k(\mathbf{x}), f(\mathbf{x})$ are taken only to depend on the spatial variable $\mathbf{x} \in \Omega \subset \mathbb{R}^d$, and not on u, while α is a constant. The subdomains $\partial\Omega_{\mathrm{D}}$ and $\partial\Omega_{\mathrm{N}}$ denote, respectively, the Dirichlet and Neumann parts of the boundary $\partial\Omega$ of the domain Ω. We also let $\hat{\mathbf{n}} \cdot \mathbf{w}(\mathbf{x}) = 0$ on $\partial\Omega$.

The inner product of two fields will be used recurrently in the forthcoming. It is denoted by $(\bullet, \bullet)$, and can be taken between a pair of scalars a, b; vectors $\mathbf{a}$, $\mathbf{b}$; or tensors

[24] For example, when $\alpha, \mathbf{w}$ vanish, eq. (4.1) reduces to the Poisson equation, which arises many places in this work (Gauss' law for electrostatics, Darcy flow, pressure correction). Then, k is analogous to a space dependent permittivity/permeability and f is a space-dependent source term. It is also easy to see how eq. (4.1) can be turned into a temporally discretized advection–diffusion–reaction equation.

A, **B**—related to the integral over the domain Ω respectively by

$$(a, b) = \int_\Omega ab, \quad (\mathbf{a}, \mathbf{b}) = \int_\Omega \mathbf{a} \cdot \mathbf{b}, \quad (\mathbf{A}, \mathbf{B}) = \int_\Omega \mathbf{A} : \mathbf{B}. \tag{4.4}$$

Now, we can find the variational form of eq. (4.1), by considering u as a *trial function* and multiplying eq. (4.1) by the *test function* v it and integrating over the domain,

$$(\mathscr{D}u, v) = -\alpha(u, v) - (\mathbf{w}u, \boldsymbol{\nabla}v) - (k\boldsymbol{\nabla}u, \boldsymbol{\nabla}v) + \int_{\partial\Omega_\mathrm{N}} k f_\mathrm{N} v = (f, v), \tag{4.5}$$

where we have integrated by parts and inserted eq. (4.3). Note that Equation (4.5) holds for any v.

The discretized domain Ω_h approximates the true domain Ω, and consists of a *tesselation* of N_el finite elements Ω_i, such that

$$\Omega_h = \bigcup_{i=1}^{N_\mathrm{el}} \Omega_i. \tag{4.6}$$

(a)

(b)
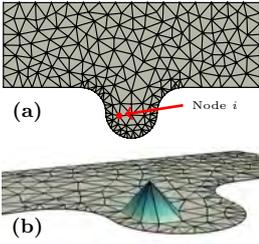
FIGURE 4.1: The finite element method in two dimensions. (a) Illustration of a discretized domain, i.e. a triangular mesh. (b) The P_1 'hat function' φ_i associated with node i indicated in (a). The maximum of $\phi_i(\mathbf{x})$ is $\phi_i(\mathbf{x}_i) = 1$, where $\mathbf{x}_i$ is the location of node i.

These elements can are typically simplicials; i.e. triangles (2D) and tetrahedra (3D); but other shapes, such as quadrilaterals (2D) and hexahedra (3D), are also common[132]. Here, we will primarily be concerned with simplicials. These unit cells share vertices, edges, and faces (in 3D) with their neighbouring elements. An exemplary discretized two-dimensional domain is shown in fig. 4.1 (a). The discretized domain is usually called a mesh, and is typically unstructured. In the following, we consider a mesh with N_vert vertices, N_edge edges, and N_el elements.

We shall now briefly discuss ways of constructing a set of basis functions φ_j from the discretized mesh, i.e. which discrete function spaces the solution should belong to. The most common elements belong to the P_k family (k times differentiable), e.g.:[25]

P_0 — Piecewise constant basis functions. (Note that these may be of limited use alone as their derivative is zero.)

P_1 — Piecewise linear basis functions.

P_2 — Piecewise quadratic basis functions.

Generally, P_{k-1} elements yield k^th order spatial convergence. Using a P_0 basis yields a set of N_el basis functions, while P_1 yields N_vert basis functions. P_2 elements have 'nodal' values also at the middle of each edge, such that a polynomial of order 2 can be uniquely fixed[132], and thus contain $N_\mathrm{vert} + N_\mathrm{edge}$ basis functions. In the P_k family, the basis functions are chosen such that $\varphi_j(\mathbf{x}_i) = \delta_{ij}$ where $\mathbf{x}_j$ are the positions of these nodes. An example of a single basis function from the common piecewise linear P_1 element, is shown in fig. 4.1 (b). Note that the set of such 'hat functions' for all nodes consitutes the P_1 basis for this domain. The generalization to three dimensions is straightforward, but harder to visualize.

[25] See also[19] or https://www.femtable.org for an overview of finite elements.

We shall here employ a set of basis functions φ_i, $i \in \{1, \ldots, n\}$, which in principle could represent all of the above elements. In the following, we use the Einstein convention, summing over repeated indices.

An approximation to the solution u of eq. (4.1) can be written as a linear combination of the basis functions:

$$u \simeq \hat{u} = U_i \varphi_i(\mathbf{x}), \tag{4.7}$$

where U_i are the hitherto unknown coefficients in this expansion. The Galerkin method now imparts letting the test functions belong to the same function space as $\hat{u}$. Thus,

$$v \simeq \hat{v} = V_i \varphi_i(\mathbf{x}). \tag{4.8}$$

Now, we can insert these into the terms in eq. (4.5) to obtain

$$(\hat{u}, \hat{v}) = (\phi_i, \phi_j) \, U_i V_j, \tag{4.9a}$$

$$(\mathbf{w}\hat{u}, \boldsymbol{\nabla}\hat{v}) = (\mathbf{w}\phi_i, \boldsymbol{\nabla}\phi_j) \, U_i V_j, \tag{4.9b}$$

$$(k\boldsymbol{\nabla}\hat{u}, \boldsymbol{\nabla}\hat{v}) = (k\boldsymbol{\nabla}\phi_i, \boldsymbol{\nabla}\phi_j) \, U_i V_j, \tag{4.9c}$$

$$\int_{\partial\Omega_{\mathrm{N}}} k f_{\mathrm{N}} v = \int_{\partial\Omega_{\mathrm{N}}} k f_{\mathrm{N}} \phi_j V_j, \tag{4.9d}$$

$$(f, v) = (f, \phi_j) \, V_j. \tag{4.9e}$$

Since eq. (4.5) should hold for any $\hat{v}$, the equations resulting from inserting eq. (4.9) should be independent of the choice of V_j. Thus, eq. (4.5) becomes

$$\alpha \, (\phi_i, \phi_j) \, U_i + (\mathbf{w}\phi_i, \boldsymbol{\nabla}\phi_j) \, U_i + (k\boldsymbol{\nabla}\phi_i, \boldsymbol{\nabla}\phi_j) \, U_i = \int_{\partial\Omega_{\mathrm{N}}} k f_{\mathrm{N}} \phi_j - (f, \phi_j), \tag{4.10}$$

We now define the matrix

$$\mathbf{A} = [A_{ij}], \quad \text{where} \quad A_{ij} = \alpha \, (\phi_i, \phi_j) + (\mathbf{w}\phi_i, \boldsymbol{\nabla}\phi_j) + (k\boldsymbol{\nabla}\phi_i, \boldsymbol{\nabla}\phi_j), \tag{4.11}$$

where the three contributing terms represent, respectively, the mass matrix, the advection matrix and the stiffness matrix. Further, the right hand side can be written as

$$\mathbf{b} = [b_j], \quad \text{where} \quad b_j = \int_{\partial\Omega_{\mathrm{N}}} k f_{\mathrm{N}} \phi_j - (f, \phi_j), \tag{4.12}$$

and the vector of unknowns can be written as $\mathbf{U} = [U_i]$. Thus, eq. (4.10) becomes

$$\mathbf{A}\mathbf{U} = \mathbf{b}, \tag{4.13}$$

which must be solved for $\mathbf{U}$. The numerical calculation of the elements of the matrix $\mathbf{M}$ and right hand side vector $\mathbf{b}$ in in eq. (4.13), is called to *assemble* the system. In terms of computationa, this process can often be comparatively costly to solving the matrix system[320].

Mixed elements

It should be noted that a to represent a PDE of order $2k$, one would expect that a discretized function space of (at least) order k is necessary, as this is the best balancing between trial and test functions that can be achieved by successive integration by parts. In the present work, this is particularly relevant for the fourth order phase-field equation, see eqs. (3.26c) and (3.26d). However, low-order elements can be used by introducing an auxiliary field, and employing *mixed* elements. For example, solving the equation

$$\boldsymbol{\nabla}^4 u = f, \tag{4.14}$$

for u (with appropriate boundary conditions), would intuitively correspond to the following variational problem: Find $u \in \mathcal{U}$ such that

$$\left(\boldsymbol{\nabla}^2 u, \boldsymbol{\nabla}^2 v\right) = (f, v), \tag{4.15}$$

for all $v \in \mathcal{U}$. Instead, one can introduce the auxiliary variable $g = \boldsymbol{\nabla}^2 w$, which turns eq. (4.14) into

$$\boldsymbol{\nabla}^2 u = g, \quad \boldsymbol{\nabla}^2 g = f. \tag{4.16}$$

The corresponding variational form becomes: Find $(u, g) \in \mathcal{U}' \times \mathcal{G}'$ such that

$$(\boldsymbol{\nabla}u, \boldsymbol{\nabla}v) = -\,(g, v), \quad (\boldsymbol{\nabla}g, \boldsymbol{\nabla}h) = -\,(f, h), \tag{4.17}$$

for all $(v, h) \in \mathcal{U}' \times \mathcal{G}'$. Here, the discrete approximations to the subspaces $\mathcal{U}'$ and $\mathcal{G}'$ can be of lower order than the approximation to the function space $\mathcal{U}$ in eq. (4.15). It is then a trivial task to turn eq. (4.17) into a matrix equation of the form eq. (4.13).

4.1.1 *Solvers and preconditioners*

Having assembled the system, as stated in the form (4.13), the task is now to isolate the vector $\mathbf{U}$ with as little computation—or as quickly—as possible. This is in general a task for numerical linear algebra routines. The most robust methods solve this *directly* (using lower–upper (LU) decomposition or Gaussian elimination). However, this is highly memory consuming for large systems and does not scale well with the number of unknowns. Better results are therefore achieved with methods that can exploit the structure of $\mathbf{A}$.

Since the basis functions have compact support, they are typically only nonzero in a small neighbourhood of a given node or element. Thus the involved inner products are predominantly zero, i.e., the resulting matrix $\mathbf{M}$ is very sparse. Moreover, the bulk of the nonzero entries are found close to the diagonal.

Such matrix structures are often suitable for use with *iterative* Krylov subspace methods. It is not within the scope of this thesis to enter into the technical theory on Krylov subspaces and sequences—the interested reader is referred to literature on the field, e.g.[387]. We will only briefly outline some of the most popular methods. For symmetric, positive definite systems, the conjugate gradient (CG) method[188] is typically the optimal method. For symmetric systems, the minimal residual (MinRes) method[349] is a viable option. For less restrictive requirements to the system matrices, the more robust generalized minimal residual (GMRES) method[388], or the biconjugate gradient stabilized (BiCGSTAB) method[452] can be used.

For these methods to converge, it is essential to use good *preconditioners*. This basically amounts to multplying both sides of eq. (4.13) by a matrix $\mathbf{P} \simeq \mathbf{A}^{-1}$ (the inverse of $\mathbf{A}$) to bring the system matrix closer to the identity matrix, or, generally make the system easier to solve. Common preconditioning techniques include Jacobi preconditioning, algebraic multigrid (AMG), incomplete LU factorization (ILU), and successive over-relaxation (SOR). The choice of an appropriate preconditioner also depends on the choice of linear solver, and for large-scale applications, it is fundamental to access parallel implementations of the preconditioner–solver pair. A thorough overview of preconditioners and linear solvers, with emphasis on fluid-mechanical problems, can be found in the book by Elman et al.[132].

4.1.2 *Comparison to other methods*

The main advantage of using the finite element method (FEM) is its versatility. The method is not restricted to a specific physical problem, and is intrinsically suited for a wide variety of physical models and problems. This includes elasticity and solid mechanics (where it originates from), advection and diffusion, fluid flow, and many more. Further, the method is not limited to specific mesh structures, but is formulated in terms of general discretized domains. This is in contrast to finite difference (FDM) and finite volume methods (FEM), which typically rely on structured meshes or grids. It is possible to extend FDM and FVM to unstructured grids, but it is not as intuitive as for the FEM[172]. In particular, FEM formulations on structured meshes often become equivalent to FDM or FVM stencils. Further, implicit or semi-implicit versions of all three problems typically reduce to solving a linear system of equations[241]. Gresho and Sani[172], sec. 1.7 provide an interesting discussion on the relation between FEM and FVM.

Another advantage of the FEM is that it straightforwardly allows to construct numerical schemes where certain stability properties can be shown. In particular, implicit and semi-implicit schemes can be constructed with easy by using finite differences in time. Moreover, enforcing Neumann (or even Robin) boundary conditions in a FEM is straightforward, as they enter directly in the weak formulation. This is, e.g., particularly

useful for imposing contact angle boundary conditions in phase-field simulations.

Progress in recent years indicate that for incompressible flow, the finite element method is fully competitive with FVM[320] in terms of computational performance. Compared to the lattice Boltzmann method (LBM), FEM solves the actual PDEs while the LBM approximates them using kinetic theory. If steady-state solutions are sought, implicit or semi-implicit schemes are preferred, as larger time steps are allowed. For turbulent flow, however, the time-step restrictions may be of lesser importance, and explicit methods such as the LBM (where all interactions are local) may be advantageous for parallel scalability. However, unbiased comparisons of the various methods for a representative spectrum of problems, is in general hard to find. In part, it is also a question of implicit versus explicit methods. Implicit methods are more stable, but also tend to smear out the solution more; i.e. they are more dissipative. For other applications, such as for compressible flow, the FVM is possibly still more mature than the FEM[395]. The unstructured lattice Boltzmann method (ULBM) represents an extension of LBM to unstructured meshes, opening the way for the same geometric flexibility as found with the FEM (or FVM). However, the velocities must typically be interpolated on the unstructured meshes by using FVM or FEM methods, and thus the method loses some of its advantages.

Finally, it should be mentioned that the choice of basis functions in the Galerkin method need not be limited to the compactly supported functions employed in the FEM. In simple geometries with a high degree of symmetry, such as periodic channels, pipes, and fully periodic geometries, spectral (and spectral Galerkin) methods yield superior accuracy and efficiency. For example, Lee and Moser[250] presented direct numerical simulations of plane channel flow at impressively high Reynolds number using a Fourier basis in the streamwise and spanwise directions and a B-spline collocation method in the wall-normal direction. Another option is the use a Chebyshev basis in the wall-normal direction, see e.g.[319]. However, these methods cannot be easily adapted to more complicated geometries. An alternative, conceptually halfway between these two approaches is the spectral element method (which is used e.g. in the CFD code NEK5000[152]) but that shall not be evaluated here.

For two-phase flow simulations, including front-tracking, level-set, volume-of-fluid and phase-field methods, it is also possible to combine different methods. The methods typically need some Navier–Stokes solver to advect the fluids, but are not dependent on which method is used for this purpose. For example, Campillo-Funollet et al.[79] used a FVM on a dual grid to solve the convective terms, while using FEM on the diffusive terms; thus taking advantage of the strengths of both methods.

Having discussed spatial discretization strategies, we now proceed to temporal discretization strategies, which are often independent of the spatial method. In particular, we consider finite-difference integration in time.

4.2   A NUMERICAL SCHEME FOR TRANSIENT FLOW

To apply the models considered herein to realistic time-dependent problems, reliable time-discretization schemes are needed. The models covered in this thesis concern, in a general sense, the incompressible Navier–Stokes equations, in many cases coupled to external fields. The latter fields are either an arbitrary number of concentration fields, or a single phase field.

We can state the models in the following compact form:

$$\rho \partial_t \mathbf{u} + \mathbf{m} \cdot \boldsymbol{\nabla} \mathbf{u} - \boldsymbol{\nabla} \cdot [2\mu \mathbf{D} \mathbf{u}] + \boldsymbol{\nabla} p = - \sum_{i=0}^{N} \psi_i \boldsymbol{\nabla} g_i, \tag{4.18}$$

$$\boldsymbol{\nabla} \cdot \mathbf{u} = 0, \tag{4.19}$$

$$\partial_t \psi_i + \mathbf{u} \cdot \boldsymbol{\nabla} \psi_i - \boldsymbol{\nabla} \cdot (K_i \boldsymbol{\nabla} g_i) = 0, \tag{4.20}$$

$$\boldsymbol{\nabla} \cdot (\varepsilon \boldsymbol{\nabla} V) = -\rho_e, \tag{4.21}$$

with appropriate boundary conditions, where ψ_i are the transported scalar fields, i.e. the collection of all phase and concentration fields,

$$\psi_i = \begin{cases} \phi & \text{for} \quad i = 0, \\ c_i & \text{for} \quad i \in \{1, \dots, N\}. \end{cases} \tag{4.22}$$

The associated chemical potentials can be written as the general functionals

$$g_i = g_i[\{\psi_j\}_{j=0}^N, V] = \begin{cases} g_\phi & \text{for} \quad i = 0, \\ g_{c_i} & \text{for} \quad i \in \{1, \dots, N\}. \end{cases} \tag{4.23}$$

and the generalized mobilities can be defined by

$$K_i = \begin{cases} M(\phi) & \text{for} \quad i = 0, \\ D_i(\phi)c_i & \text{for} \quad i \in \{1, \dots, N\}. \end{cases} \tag{4.24}$$

The advecting momentum $\mathbf{m}$ is, as before, given by eq. (3.29), such that the total density evolution can be written as

$$\partial_t \rho + \boldsymbol{\nabla} \cdot \mathbf{m} = 0. \tag{4.25}$$

The coupled problem of fluid flow, transport of scalar fields, and electrostatics, is in general a hard problem to solve numerically. It is thus beneficial to split the problem into multiple substeps. Here, we separate out the fluid flow problem from the scalar transport, while still being able to prove the same energy stability property that is associated with the continuous problem.

As unconditionally stable schemes of second or higher temporal order still seems lacking for two-phase flow with unmatched density, we will consider the following temporally first-order scheme. In particular, the splitting between velocity and pressure, as seen below, introduces an $O(\tau)$ error. The method is of arbitrary order in space, as it depends on the chosen finite element basis.

We will first present the step solving for the scalar fields, including the electric field, and subsequently the hydrodynamics step will be considered. We assume here for brevity that the dynamic boundary condition with no-slip (3.36), although the extension to a generalized Navier boundary condition (GNBC) (3.35) is straightforward (e.g. along the lines of[5]). To simplify the notation, we use the electrokinetic scaling of the model (3.81) outlined in section 3.4.3.

We consider schemes that use finite elements in space, and finite differences in time. Thus, we consider a discrete time step τ, and denote for conciseness the first-order discrete time derivative by

$$\partial_\tau^- \mathcal{A}^k \overset{\text{def}}{=} \frac{\mathcal{A}^k - \mathcal{A}^{k-1}}{\tau}. \tag{4.26}$$

Finally, we use the shorthand notation that when a general quantity $\mathcal{A}$ is evaluated at a timestep k, it is denoted by $\mathcal{A}^k$, e.g., $\mathcal{A}^k = \mathcal{A}(\phi^k)$.

For completeness, we define the following finite element subspaces:

$$\mathbf{U}_h = (U_h)^d \quad \text{where} \quad U_h = \{v \in H^1(\Omega)\} \quad \text{for velocity,} \tag{4.27a}$$
$$P_h = \{p \in L_0^2(\Omega)\} \qquad\qquad\quad \text{for pressure,} \tag{4.27b}$$
$$\Phi_h = \{\phi \in H^1(\Omega)\} \qquad\qquad \text{for scalar fields,} \tag{4.27c}$$
$$G_h = \{g \in H^1(\Omega)\} \qquad\qquad \text{for chemical potentials,} \tag{4.27d}$$
$$\mathcal{U}_h = \{V \in H^1(\Omega)\} \qquad\qquad \text{for the electrostatic potential.} \tag{4.27e}$$

4.2.1 Scalar transport step

The scalar transport step is given by the following discrete problem at each time step k. Assume that $\psi_0^{k-1}, \ldots, \psi_N^{k-1}, g_0^{k-1}, \ldots, g_N^{k-1}, V^{k-1}, \mathbf{u}^{k-1}, p^{k-1}$ are given. Then, using eqs. (4.22) and (4.23), solve:

$$\partial_\tau^- \psi_j^k + \boldsymbol{\nabla} \cdot (\mathbf{u}^* \psi_j^{k-1}) = \boldsymbol{\nabla} \cdot (K_j^{k-1} \boldsymbol{\nabla} g_j^k), \tag{4.28a}$$

$$g_\phi^k = \chi\gamma \left[\varepsilon^{-1} \overline{W'} - \varepsilon \boldsymbol{\nabla}^2 \phi^k \right] + \sum_j \frac{\partial \beta_j}{\partial \phi} \bar{c}_j - \frac{1}{2} \frac{\partial \epsilon}{\partial \phi} |\boldsymbol{\nabla} V^k|^2, \tag{4.28b}$$

$$g_{c_j}^k = \overline{\alpha'} + \overline{\beta}_j + z_j V^k, \tag{4.28c}$$

$$\boldsymbol{\nabla} \cdot (\varepsilon^k \boldsymbol{\nabla} V^k) = -\rho_e^k. \tag{4.28d}$$

Here,

$$\mathbf{u}^* = \mathbf{u}^{k-1} - \frac{\tau}{\rho^{k-1}} \sum_j \psi_j^{k-1} \boldsymbol{\nabla} g_j^k \tag{4.29}$$

is a forward-projected velocity, building on an idea by Minjeaud[305]. Moreover, we have introduced the following discretizations:

$\overline{W'}$ — A discrete approximation of the derivative of the Ginzburg–Landau double well potential, $W'(\phi)$, see eq. (3.28). Here, a convex-concave decomposition $W(\phi) = W_+(\phi) - W_-(\phi)$ is used (see e.g.[404]):

$$\overline{W'} = W'_+(\phi^k) - W'_-(\phi^{k-1}) \tag{4.30}$$

where $W_+(\phi) = (1 + \phi^4)/4$ and $W_-(\phi) = \phi^2/2$.

$\overline{f'_w}$ — A discrete approximation of the derivative of the wall energy interpolation function. Here, it is given by

$$\overline{f'_w} = \frac{1}{4}\left[3 - (\phi^k)^2 - \phi^k \phi^{k-1} - (\phi^{k-1})^2\right]. \tag{4.31}$$

$\bar{c}_j$ — interpolated concentration $\bar{c}_j = \omega c_j^k + (1 - \omega) c_j^{k-1}$, where $\omega \in [0, 1]$ is an arbitrary weighting coefficient.

$\overline{\beta}_j$ — interpolated solubility energy, $\overline{\beta}_j = (1 - \omega)\beta_j^k + \omega\beta_j^{k-1}$.

$\overline{\alpha'}$ — An approximation of the derivative of a generalized chemical energy $\alpha(c)$; we use

$$\overline{\alpha'} = \alpha'(c_j^k) = \ln c_j^k, \tag{4.32}$$

where the last equality holds for standard Nernst–Planck transport.

These discretizations have been made in this way to satisfy a discrete energy dissipation law, which we will show in the coming sections.

Weak form

For a finite-element implementation, a weak form of the above scheme must be found.
The following variational problem corresponds to the scheme (4.28).
Find $(\psi_0^k, \ldots, \psi_N^k, g_0^k, \ldots, g_N^k, V^k) \in \Phi_h^{N+1} \times G_h^{N+1} \times \mathcal{U}_h$ such that

$$\left(\partial_\tau^- \psi_j^k, \xi_j\right) - \left(\mathbf{u}^* \psi_j^{k-1}, \boldsymbol{\nabla}\xi_j\right) + \left(K_j^{k-1}\boldsymbol{\nabla} g_j^k, \boldsymbol{\nabla}\xi_j\right) = 0, \qquad (4.33\text{a})$$

$$\begin{aligned}
\left(g_\phi^k, h_0\right) &= \chi\gamma\varepsilon^{-1}\left(\overline{W'}, h_0\right) + \chi\gamma\varepsilon\left(\boldsymbol{\nabla}\phi^k, \boldsymbol{\nabla}h_0\right) \\
&\quad + \int_{\partial\Omega}\left[\gamma\cos(\theta_{\text{eq}})\overline{f_{\text{w}}'} + \Gamma^{-1}\partial_\tau^-\phi\right] h_0 \\
&\quad + \sum_j \left(\frac{\partial\beta_j}{\partial\phi}\bar{c}_j, h_0\right) - \left(\frac{1}{2}\frac{\partial\epsilon}{\partial\phi}|\boldsymbol{\nabla}V^k|^2, h_0\right),
\end{aligned} \qquad (4.33\text{b})$$

$$\left(g_{c_j}^k, h_j\right) = \left(\overline{\alpha'}, h_j\right) + \left(\overline{\beta}_j, h_j\right) + \left(z_j V^k, h_j\right), \qquad (4.33\text{c})$$

$$\left(\varepsilon^k\boldsymbol{\nabla}V^k, \boldsymbol{\nabla}U\right) = \left(\rho_e^k, U\right) + \int_{\partial\Omega}\sigma_e U, \qquad (4.33\text{d})$$

for all test functions $(\xi_0, \ldots, \xi_N, g_0, \ldots, g_N, U) \in \Phi_h^{N+1} \times G_h^{N+1} \times \mathcal{U}_h$.

4.2.2 *Fluid flow step*

To solve the Navier–Stokes equations with a non-constant density, many approaches
exist, specifically solving for velocity and pressure either in a coupled or in a decoupled
manner. The present method is based on a decoupled *fractional-step* method, which has
its roots back to the seminal works of Chorin[92,93]. The fluid flow step consists of three
substeps: *velocity prediction*, *pressure correction*, and *velocity correction*. They are given in
the following.

Assume that the scalar transport step (4.28) has been carried out, and thus

$$\psi_0^k, \ldots, \psi_N^k, g_0^k, \ldots, g_N^k, V^k, \mathbf{u}^{k-1}, p^{k-1}$$

are given. Then, carry out the following substeps.

1. **Tentative velocity step:** Solve the following problem for the tentative velocity
   step $\tilde{\mathbf{u}}^k$.

$$\begin{aligned}
\rho^{k-1}\frac{\tilde{\mathbf{u}}^k - \mathbf{u}^{k-1}}{\tau} + (\mathbf{m}^{k-1}\cdot\boldsymbol{\nabla})\tilde{\mathbf{u}}^k &- \boldsymbol{\nabla}\cdot\left(2\mu^k\mathbf{D}\tilde{\mathbf{u}}^k\right) + \boldsymbol{\nabla}p^{k-1} \\
&+ \frac{1}{2}\tilde{\mathbf{u}}^k\left[\partial_\tau^-\rho^k + \boldsymbol{\nabla}\cdot\mathbf{m}^{k-1}\right] = -\sum_i \psi_i^{k-1}\boldsymbol{\nabla}g_i^k, \quad (4.34\text{a})
\end{aligned}$$

   with the Dirichlet boundary condition $\tilde{\mathbf{u}}^k = \mathbf{0}$ on $\partial\Omega$. Here we have used

$$\mathbf{m}^k = \rho^k\mathbf{u}^k - \rho'(\phi)M^k\boldsymbol{\nabla}g_\phi^k. \qquad (4.34\text{b})$$

   Note also the presence of the last term in the right hand side of eq. (4.34a), which
   is an approximation of $\mathbf{0}$, cf. eq. (4.25). It is needed to satisfy a discrete energy law,
   as will be shown below.

2. **Pressure correction step:** Solve the following problem for the pressure p^k.

$$\frac{1}{\rho_0}\boldsymbol{\nabla}^2(p^k - p^{k-1}) = \frac{1}{\tau}\boldsymbol{\nabla}\cdot\tilde{\mathbf{u}}^k, \tag{4.34c}$$

where $\rho_0 = \min(\rho_1, \rho_2)$. Here the artificial Neumann condition $\mathbf{n}\cdot\boldsymbol{\nabla}(p^k - p^{k-1}) = 0$ should be enforced.

3. **Velocity correction step:** To obtain the corrected velocity $\mathbf{u}^k$, solve

$$\rho^k\frac{\mathbf{u}^k - \tilde{\mathbf{u}}^k}{\tau} = -\boldsymbol{\nabla}\left(p^k - p^{k-1}\right), \tag{4.34d}$$

with the Dirichlet boundary condition $\mathbf{u}^k = \mathbf{0}$ on $\partial\Omega$.

Weak form

The following variational problem corresponds to the scheme (4.34) above.

1. *Tentative velocity step:* Find $\tilde{\mathbf{u}}^k \in \mathbf{U}_h$ such that for all $\mathbf{v} \in \mathbf{U}_h$,

$$\left(\rho^{k-1}\frac{\tilde{\mathbf{u}}^k - \mathbf{u}^{k-1}}{\tau}, \mathbf{v}\right) + \left((\mathbf{m}^{k-1}\cdot\boldsymbol{\nabla})\tilde{\mathbf{u}}^k, \mathbf{v}\right) + \left(2\mu^k\mathbf{D}\tilde{\mathbf{u}}^k, \mathbf{Dv}\right)$$
$$- \left(p^{k-1}, \boldsymbol{\nabla}\cdot\mathbf{v}\right) + \frac{1}{2}\left(\tilde{\mathbf{u}}^k\partial_\tau^-\rho^k, \mathbf{v}\right) - \frac{1}{2}\left(\mathbf{m}^{k-1}, \boldsymbol{\nabla}(\tilde{\mathbf{u}}^k\cdot\mathbf{v})\right)$$
$$= -\sum_i\left(\psi_i^{k-1}\boldsymbol{\nabla}g_i^k, \mathbf{v}\right), \quad \text{(4.35a)}$$

with the Dirichlet boundary condition $\tilde{\mathbf{u}}^k = \mathbf{0}$ on $\partial\Omega$.

2. *Pressure correction step:* Find $p^k \in P_h$ such that for all $q \in P_h$, we have

$$\left(\frac{1}{\rho_0}\boldsymbol{\nabla}(p^k - p^{k-1}), \boldsymbol{\nabla}q\right) = -\frac{1}{\tau}\left(\boldsymbol{\nabla}\cdot\tilde{\mathbf{u}}^k, q\right). \tag{4.35b}$$

3. *Velocity correction step:* Find $\mathbf{u}^k \in \mathbf{U}_h$ such that for all $\mathbf{v} \in \mathbf{U}_h$,

$$\left(\rho^k\frac{\mathbf{u}^k - \tilde{\mathbf{u}}^k}{\tau}, \mathbf{v}\right) = \left(p^k - p^{k-1}, \boldsymbol{\nabla}\cdot\mathbf{v}\right), \tag{4.35c}$$

which we solve by explicitly imposing the Dirichlet boundary condition $\mathbf{u}^k = \mathbf{0}$ on $\partial\Omega$.

This completes the numerical time discretization scheme. Some remarks are in order:

- At each time step, the scalar transport equations (section 4.2.1) need to be solved *before* the hydrodynamic equations (section 4.2.2).

- The scalar transport equations (4.28) (or (4.33)) are *at least* weakly coupled through V^k and need to be solved simultaneously.

- Multiplying eq. (4.34d) by τ/ρ^k, taking the divergence, and using eq. (4.34c), yields:

$$\boldsymbol{\nabla}\cdot\mathbf{u}^k = \tau\boldsymbol{\nabla}\cdot\left[\left(\frac{1}{\rho_0} - \frac{1}{\rho^k}\right)\boldsymbol{\nabla}\left(p^k - p^{k-1}\right)\right], \tag{4.36}$$

i.e., the scheme admits a small $O(\tau^2)$ compressibility in the corrected velocity field. This might, however, stabilize the spatial method; see the discussion in section 4.3.

4.2.3 Energy stability

We now set out to show that there is a discrete energy law associated with the given scheme.

We start with the hydrodynamic part. First, we note that, using eq. (4.29), eq. (4.35a) can be written as

$$
\left(\rho^{k-1}\frac{\tilde{\mathbf{u}}^k - \mathbf{u}^*}{\tau}, \mathbf{v}\right) + \left((\mathbf{m}^{k-1}\cdot\boldsymbol{\nabla})\tilde{\mathbf{u}}^k, \mathbf{v}\right) + \left(2\mu^k\mathbf{D}\tilde{\mathbf{u}}^k, \mathbf{D}\mathbf{v}\right)
$$
$$
- \left(p^{k-1}, \boldsymbol{\nabla}\cdot\mathbf{v}\right) + \frac{1}{2}\left(\tilde{\mathbf{u}}^k\partial_\tau^-\rho^k, \mathbf{v}\right) - \frac{1}{2}\left(\mathbf{m}^{k-1}, \boldsymbol{\nabla}(\tilde{\mathbf{u}}^k\cdot\mathbf{v})\right) = 0. \quad (4.37)
$$

We let $\mathbf{v} = \tilde{\mathbf{u}}^k$ in eq. (4.37):

$$
\frac{1}{2\tau}\left[\left\|\sqrt{\rho^k}\tilde{\mathbf{u}}^k\right\|^2 - \left\|\sqrt{\rho^{k-1}}\mathbf{u}^*\right\|^2\right] + \left\|\sqrt{2\mu^k}\mathbf{D}\tilde{\mathbf{u}}^k\right\|^2 - \left(p^{k-1}, \boldsymbol{\nabla}\cdot\tilde{\mathbf{u}}^k\right)
$$
$$
= -\frac{1}{2\tau}\left\|\sqrt{\rho^{k-1}}(\tilde{\mathbf{u}}^k - \mathbf{u}^*)\right\|^2, \quad (4.38)
$$

and test eq. (4.29) with $\rho^{k-1}\mathbf{u}^*/\tau$:

$$
\frac{1}{2\tau}\left\|\sqrt{\rho^{k-1}}\mathbf{u}^*\right\|^2 - \frac{1}{2\tau}\left\|\sqrt{\rho^{k-1}}\mathbf{u}^{k-1}\right\|^2
$$
$$
= -\sum_j\left(\psi_j^{k-1}\boldsymbol{\nabla}g_j^k, \mathbf{u}^*\right) - \frac{1}{2\tau}\left\|\sqrt{\rho^{k-1}}(\mathbf{u}^* - \mathbf{u}^{k-1})\right\|^2. \quad (4.39)
$$

Further, we let $q = -\tau p^k$ in eq. (4.35b):

$$
\left(\boldsymbol{\nabla}\cdot\tilde{\mathbf{u}}^k, p^k\right) = -\frac{\tau}{2\rho_0}\left[\left\|\boldsymbol{\nabla}p^k\right\|^2 - \left\|\boldsymbol{\nabla}p^{k-1}\right\|^2 + \left\|\boldsymbol{\nabla}(p^k - p^{k-1})\right\|^2\right], \quad (4.40)
$$

and put $\mathbf{v} = \tilde{\mathbf{u}}^k$ in eq. (4.35c):

$$
\frac{1}{2\tau}\left\|\sqrt{\rho^k}\mathbf{u}^k\right\|^2 - \frac{1}{2\tau}\left\|\sqrt{\rho^k}\tilde{\mathbf{u}}^k\right\|^2 - \frac{1}{2\tau}\left\|\sqrt{\rho^k}(\mathbf{u}^k - \tilde{\mathbf{u}}^k)\right\|^2 = \left(p^k - p^{k-1}, \boldsymbol{\nabla}\cdot\tilde{\mathbf{u}}^k\right).
$$
$$
(4.41)
$$

From eq. (4.34d), we find

$$
\left\|\sqrt{\rho^k}(\mathbf{u}^k - \tilde{\mathbf{u}}^k)\right\|^2 = \tau^2\left\|\frac{1}{\sqrt{\rho^k}}\boldsymbol{\nabla}(p^k - p^{k-1})\right\|^2. \quad (4.42)
$$

Combining eqs. (4.38) to (4.42) we obtain:

$$
\partial_\tau^-\mathscr{F}_{\mathbf{u}}^k = -\left\|\sqrt{2\mu^k}\mathbf{D}\tilde{\mathbf{u}}^k\right\|^2 - \frac{1}{2\tau}\left\|\sqrt{\rho^{k-1}}(\tilde{\mathbf{u}}^k - \mathbf{u}^*)\right\|^2 - \frac{1}{2\tau}\left\|\sqrt{\rho^{k-1}}(\mathbf{u}^* - \mathbf{u}^{k-1})\right\|^2
$$
$$
- \frac{\tau}{2}\left\|\sqrt{\frac{1}{\rho_0} - \frac{1}{\rho^k}}\boldsymbol{\nabla}(p^k - p^{k-1})\right\|^2 - \sum_j\left(\psi_j^{k-1}\boldsymbol{\nabla}g_j^k, \mathbf{u}^*\right), \quad (4.43)
$$

where we have identified the *discrete* kinetic energy,

$$
\mathscr{F}_{\mathbf{u}}^k = \tfrac{1}{2}\left\|\sqrt{\rho^k}\mathbf{u}^k\right\|^2 + \frac{\tau^2}{2\rho_0}\left\|\boldsymbol{\nabla}p^k\right\|^2, \quad (4.44)
$$

which contains an additional $O(\tau^2)$ compressibility term compared to its continuous counterpart, eq. (3.40).

Now, we consider the evolution of the scalar fields. In the general case, eq. (4.33a) becomes, using $\xi_j = g_j^k$:

$$\left(\partial_\tau^- \psi_j^k, g_j^k\right) - \left(\mathbf{u}_j^* \psi_j^{k-1}, \boldsymbol{\nabla} g_j^k\right) = -\left\|\sqrt{K_j^{k-1}} \boldsymbol{\nabla} g_j^k\right\|^2. \tag{4.45}$$

For the phase field, we find, using $h_0 = \partial_\tau^- \phi^k$ in eq. (4.33b):

$$\begin{aligned}
\left(g_\phi^k, \partial_\tau^- \phi^k\right) &= \chi\gamma\varepsilon^{-1}\left(\overline{W'}, \partial_\tau^- \phi^k\right) + \chi\gamma\varepsilon\left(\boldsymbol{\nabla}\phi^k, \boldsymbol{\nabla}\partial_\tau^- \phi^k\right) + \partial_\tau^- \mathscr{F}_{\mathrm{w}}^k \\
&+ \int_{\partial\Omega} \left[\Gamma^{-1}|\partial_\tau^- \phi|^2\right] + \sum_j \left(\bar{c}_j, \partial_\tau^- \beta_j^k\right) - \left(\tfrac{1}{2}|\boldsymbol{\nabla}V^k|^2, \partial_\tau^- \epsilon^k\right).
\end{aligned} \tag{4.46}$$

Here we have used that

$$\overline{f_{\mathrm{w}}'}\partial_\tau^- \phi^k = \frac{1}{\tau}\left[f_{\mathrm{w}}(\phi^k) - f_{\mathrm{w}}(\phi^{k-1})\right], \tag{4.47}$$

and identified the discrete fluid-solid interface energy (cf. eq. (3.39)),

$$\mathscr{F}_{\mathrm{w}}^k = \int_{\partial\Omega}\left[\gamma_2 + \gamma\cos\theta_{\mathrm{eq}}f_{\mathrm{w}}(\phi^k)\right]. \tag{4.48}$$

Now, note that both $W_\pm(\phi)$ are convex functions, i.e. $W_\pm''(\phi) \geq 0$ for all ϕ. By Taylor expansion, we find, using the mean value theorem,

$$W_+(\phi^k) = W_+(\phi^{k-1}) + W_+(\phi^k)(\phi^k - \phi^{k-1}) - \tfrac{1}{2}(\phi^k - \phi^{k-1})^2 W_+''(\bar{\phi}_+), \tag{4.49a}$$
$$W_-(\phi^k) = W_-(\phi^{k-1}) + W_-(\phi^{k-1})(\phi^k - \phi^{k-1}) + \tfrac{1}{2}(\phi^k - \phi^{k-1})^2 W_-''(\bar{\phi}_-), \tag{4.49b}$$

for some $\bar{\phi}_\pm \in [\min(\phi^{k-1}, \phi^k), \max(\phi^{k-1}, \phi^k)]$. We thus find

$$\left(\overline{W'}, \partial_\tau^- \phi^k\right) = \left(W_+'(\phi^k) - W_-'(\phi^{k-1}), \phi^k - \phi^{k-1}\right) \tag{4.50}$$

$$= \int_\Omega\left[W(\phi^k) - W(\phi^{k-1})\right] + \Delta W, \tag{4.51}$$

where $\Delta W = \tfrac{1}{2}(\phi^k - \phi^{k-1})^2\left(W_+''(\bar{\phi}_+) + W_-''(\bar{\phi}_-)\right) \geq 0$. We also find that

$$\left(\boldsymbol{\nabla}\phi^k, \boldsymbol{\nabla}\partial_\tau^- \phi^k\right) = \frac{1}{2\tau}\left\|\boldsymbol{\nabla}\phi^k\right\|^2 - \frac{1}{2\tau}\left\|\boldsymbol{\nabla}\phi^{k-1}\right\|^2 + \frac{1}{2\tau}\left\|\boldsymbol{\nabla}(\phi^k - \phi^{k-1})\right\|^2. \tag{4.52}$$

For the chemical potential for the ions, we let $h_j = \partial_\tau^- c_j^k$ in eq. (4.33c):

$$\left(g_{c_j}^k, \partial_\tau^- c_j^k\right) = \left(\overline{\alpha'}, \partial_\tau^- c_j^k\right) + \left(\overline{\beta}_j, \partial_\tau^- c_j^k\right) + \left(z_j V^k, \partial_\tau^- c_j^k\right), \tag{4.53}$$

where we find that

$$\left(\overline{\alpha_j'}, \partial_\tau^- c_j^k\right) = \int_\Omega\left[\alpha_j(c_j^k) - \alpha_j(c_j^{k-1}) + \Delta\alpha_j\right] \tag{4.54}$$

where $\bar{c}_j \in [\min(c_j^{k-1}, c_j^k), \max(c_j^{k-1}, c_j^k)]$ and the last term, $\Delta\alpha_j = \tfrac{1}{2}\alpha_j''(\bar{c}_j)(c_j^k - c_j^{k-1})^2$ is non-negative since $\alpha_j''(c) \geq 0$ for all c.

From eq. (4.33d) we find

$$\left(\varepsilon^k \boldsymbol{\nabla} V^k, \boldsymbol{\nabla} V^k\right) = \left(\rho_e^k, V^k\right) + \int_{\partial\Omega} \sigma_e V^k, \tag{4.55}$$

$$\left(\varepsilon^{k-1} \boldsymbol{\nabla} V^{k-1}, \boldsymbol{\nabla} V^k\right) = \left(\rho_e^{k-1}, V^k\right) + \int_{\partial\Omega} \sigma_e V^k, \tag{4.56}$$

which gives

$$\left(\varepsilon^k \boldsymbol{\nabla} V^k - \varepsilon^{k-1} \boldsymbol{\nabla} V^{k-1}, \boldsymbol{\nabla} V^k\right) = \sum_j z_j \left(c_j^k - c_j^{k-1}, V^k\right). \tag{4.57}$$

Combining eqs. (4.45), (4.46), (4.51) to (4.54) and (4.57), and summing over j where appropriate, we obtain

$$\partial_\tau^- \left[\mathscr{F}_\phi^k + \mathscr{F}_{\mathrm{w}}^k + \sum_j \mathscr{F}_{c_j}^k + \mathscr{F}_V^k\right] = \sum_j \left(\mathbf{u}_j^* \psi_j^{k-1}, \boldsymbol{\nabla} g_j^k\right) - \sum_j \left\|\sqrt{K_j^{k-1}} \boldsymbol{\nabla} g_j^k\right\|^2$$

$$- \int_{\partial\Omega} \left[\Gamma^{-1} |\partial_\tau^- \phi|^2\right] - \int_\Omega \chi\gamma\varepsilon^{-1}\Delta W - \frac{\chi\gamma\varepsilon}{2\tau} \left\|\boldsymbol{\nabla}(\phi^k - \phi^{k-1})\right\|^2$$

$$- \frac{1}{2\tau} \left\|\sqrt{\epsilon^{k-1}}(\boldsymbol{\nabla} V^k - \boldsymbol{\nabla} V^{k-1})\right\|^2 - \sum_j \int_\Omega \Delta\alpha_j \tag{4.58}$$

where we have used

$$\left(\overline{c}_j, \partial_\tau^- \beta_j^k\right) + \left(\overline{\beta}_j, \partial_\tau^- c_j^k\right) = \frac{1}{\tau} \left[\beta_j^k c_j^k - \beta_j^{k-1} c_j^{k-1}\right], \tag{4.59}$$

and identified the following discrete free energy expressions:

$$\mathscr{F}_\phi^k = \chi\gamma \left[\int_\Omega \varepsilon^{-1} W(\phi^k) + \frac{\varepsilon}{2} \left\|\boldsymbol{\nabla}\phi^k\right\|^2\right] \tag{4.60}$$

$$\mathscr{F}_{c_j}^k = \int_\Omega \left[\alpha_j(c_j^k) + \beta_j^k c_j^k\right] \tag{4.61}$$

$$\mathscr{F}_V^k = \tfrac{1}{2} \left\|\sqrt{\epsilon^k} \boldsymbol{\nabla} V^k\right\|^2. \tag{4.62}$$

These are the discrete counterparts of eqs. (3.38), (3.50) and (3.51), respectively.

Now, we are in a position to combine the above results. Summing eqs. (4.43) and (4.58), we obtain

$$\partial_\tau^- \mathscr{F}^k = -\sum_j \left\|\sqrt{K_j^{k-1}} \boldsymbol{\nabla} g_j^k\right\|^2 - \left\|\sqrt{2\mu^k} \mathbf{D}\tilde{\mathbf{u}}^k\right\|^2 - \int_{\partial\Omega} \left[\Gamma^{-1} |\partial_\tau^- \phi|^2\right]$$

$$- \int_\Omega \chi\gamma\varepsilon^{-1}\Delta W - \frac{\chi\gamma\varepsilon}{2\tau} \left\|\boldsymbol{\nabla}(\phi^k - \phi^{k-1})\right\|^2 - \frac{1}{2\tau} \left\|\sqrt{\epsilon^{k-1}}(\boldsymbol{\nabla} V^k - \boldsymbol{\nabla} V^{k-1})\right\|^2$$

$$- \sum_j \int_\Omega \Delta\alpha_j - \frac{1}{2\tau} \left\|\sqrt{\rho^{k-1}}(\tilde{\mathbf{u}}^k - \mathbf{u}^*)\right\|^2$$

$$- \frac{1}{2\tau} \left\|\sqrt{\rho^{k-1}}(\mathbf{u}^* - \mathbf{u}^{k-1})\right\|^2 - \frac{\tau}{2} \left\|\sqrt{\frac{1}{\rho_0} - \frac{1}{\rho^k}} \boldsymbol{\nabla}(p^k - p^{k-1})\right\|^2 \tag{4.63}$$

where we have identified the total discrete energy,

$$\mathscr{F}^k = \mathscr{F}_{\mathbf{u}}^k + \mathscr{F}_\phi^k + \mathscr{F}_{\mathrm{w}}^k + \sum_j \mathscr{F}_{c_j}^k + \mathscr{F}_V^k. \tag{4.64}$$

We observe that all terms on the right hand side of eq. (4.63) are negative; hence $\partial_\tau^- \mathscr{F}^k \leq 0$, i.e. a discrete counterpart of eq. (3.86) is satisfied. Comparing eqs. (3.86) and (4.63), we also note that only the three first terms in eq. (4.63) are present in eq. (3.86); the rest of the terms in eq. (4.63) represent numerical dissipation and are at least of order $O(\tau)$.

4.2.4   Discussion

An advantage of using the above scheme is that it is highly *decoupled*: The hydrodynamic computation is decoupled from the scalar transport, and within the hydrodynamic subproblem, the computation of the velocity is decoupled from the pressure computation. This is achieved by a fractional step method, based on Chorin's method[92,93] and similar to that presented in[404] for pure two-phase flow. As noted, the method introduces a small numerical compressibility, see eq. (4.36), which also serves to stabilize the problem with regard to the Babuska–Brezzi criterion (see section 4.3 below). Furthermore, the discrete energy inequality, which is also an important property of the continuous version of the model, serves to limit the energy blowup that is often associated with the sharp gradients typically present in two-phase flow. The functional can possibly be used to prove convergence of the numerical scheme in the same way as done by Shen and Yang[404] for the case of pure two-phase flow, and more recently by Metzger[301] for a similar scheme to this.

A main disadvantage of this scheme is that all scalar fields must be solved simultaneously, and additionally, it requires using a nonlinear solver, for the discrete energy law to be satisfied. This may impart a FEM problem that is not necessarily easy to precondition and solve. Alternatively, a fully linear scheme where all nonlinear terms above are linearised around the variables at time step $k-1$ (and higher order terms are omitted) is presented in Paper 6[263]. Although free energy dissipation, as represented by eq. (4.63), can then not be guaranteed, the problem could be split between (i) computing the phase field, (ii) computing the chemical transport, and (iii) hydrodynamics. For the resulting subproblems (i) and (iii) there are efficient and robust solvers that can be used. For (ii) it has proven harder to solve the equations, in particular when the electric fields are so strong that we are well into the nonlinear electrokinetic regime ($V \gtrsim V_T$).

Another disadvantage, compared to solving *all* equations (including hydrodynamics) simultaneously—i.e. using a fully implicit scheme—is that the operator splitting imparts an explicit inclusion of the advective velocity. This introduces a restriction on how large time steps can be used for the scheme to remain stable, governed by the Courant–Friedrichs–Lewy (CFL) criterion. Again, however, it is not straightforward to find robust and efficient preconditioners and solvers for this problem, and fully implicit schemes are also affiliated with excessive numerical dissipation.

Finally, we propose here a way to provide efficient energy-stable simulations, i.e. solving for the scalar transport values simultaneously. Within the scalar transport subproblem, the following Picard iteration should be carried out at each time step k.

1. Let the tentative variables $\hat{\phi}_0^k = \phi^{k-1}$, $\hat{V}_0^k = V^{k-1}$, $\hat{c}_{j,0}^k = c_j^{k-1}$, and let $i = 1$.

2. Solve the phase field equations linearized around $\hat{\phi}_i^k$, and obtain the tentative value $\hat{\phi}_{i+1}^k$.

3. Solve the electrostatic problem with the newly obtained $\hat{\phi}_{i+1}^k$, and obtain $\hat{V}_{i+1}^k$.

4. Solve the chemical transport problem with the new $\hat{\phi}_{i+1}^k$, $\hat{V}_{i+1}^k$, and obtain $\hat{c}_{j,i+1}^k$.

5. Compute

$$\mathcal{E}_{i+1}^k = \sqrt{\left\| \hat{\phi}_{i+1}^k - \hat{\phi}_i^k \right\|^2 + \left\| \hat{V}_{i+1}^k - \hat{V}_i^k \right\|^2 + \sum_j \| \hat{c}_{j,i+1} - \hat{c}_{j,i} \|^2}. \qquad (4.65)$$

If $\mathcal{E}_{i+1}^k < \text{tol}$, where tol is some tolerance, assign $\phi^k = \hat{\phi}_{i+1}^k$, $V^k = \hat{V}_{i+1}^k$, $c_j^k = \hat{c}_{j,i+1}^k$, and proceed to the next time step $k+1$. Otherwise, increase $i \leftarrow i+1$ and go to step 2.

Steps 2–4 above are fairly standard procedures, as they require solving a sequence of decoupled linear equations. Nevertheless, when applicable, a Newton solver would converge in fewer iterations. However, with the iteration scheme above, effective reuse of matrices could be permitted in a finite element method, as outlined e.g. in [320] for a pure single-phase case, and in [119] for a two-phase model.

4.2.5 *Pure single-phase schemes*

Now we consider the flow of a *pure* single-phase fluid, i.e. the flow is not coupled to any additional scalar fields. The scheme above reduces to the classical Chorin scheme when applied to a single-phase case, where ρ, μ are taken to be constant. Then, the numerical problem reduces to sequentially solving

$$\rho\left(\frac{\tilde{\mathbf{u}}^k - \mathbf{u}^{k-1}}{\tau} + \mathbf{u}^{k-1}\cdot\boldsymbol{\nabla}\tilde{\mathbf{u}}^k\right) - \mu\boldsymbol{\nabla}^2\tilde{\mathbf{u}}^k + \boldsymbol{\nabla}p^{k-1} = \mathbf{0}, \tag{4.66a}$$

$$\boldsymbol{\nabla}^2(p^k - p^{k-1}) = \frac{\rho}{\tau}\boldsymbol{\nabla}\cdot\tilde{\mathbf{u}}^k, \tag{4.66b}$$

$$\rho\frac{\mathbf{u}^k - \tilde{\mathbf{u}}^k}{\tau} = -\boldsymbol{\nabla}(p^k - p^{k-1}). \tag{4.66c}$$

Here, the first and last equations should be solved with the no-slip boundary condition, $\tilde{\mathbf{u}}^k = \mathbf{0}$ and $\mathbf{u}^k = \mathbf{0}$, respectively. The pressure correction equation is typically solved with the artificial boundary condition $\hat{\mathbf{n}}\cdot\boldsymbol{\nabla}(p^k - p^{k-1}) = 0$. A temporally second-order version of Chorin's method can be found by a modification of the above equations (4.66) to arrive at the following fractional step scheme [320]:

$$\rho\left(\frac{\tilde{\mathbf{u}}^k - \mathbf{u}^{k-1}}{\tau} + \mathbf{u}_{\mathrm{AB}}^{k-1/2}\cdot\boldsymbol{\nabla}\tilde{\mathbf{u}}_{\mathrm{CN}}^{k-1/2}\right) - \mu\boldsymbol{\nabla}^2\tilde{\mathbf{u}}_{\mathrm{CN}}^{k-1/2} + \boldsymbol{\nabla}p^* = \mathbf{0}, \tag{4.67a}$$

$$\boldsymbol{\nabla}^2(p^{k-1/2} - p^*) = \frac{\rho}{\tau}\boldsymbol{\nabla}\cdot\tilde{\mathbf{u}}^k, \tag{4.67b}$$

$$\rho\frac{\mathbf{u}^k - \tilde{\mathbf{u}}^k}{\tau} = -\boldsymbol{\nabla}(p^{k-1/2} - p^*) \tag{4.67c}$$

Here, $\tilde{\mathbf{u}}_{\mathrm{CN}}^{k-1/2} = (\tilde{\mathbf{u}}^k + \mathbf{u}^{k-1})/2$ is the Crank–Nicolson interpolated velocity, and $\mathbf{u}_{\mathrm{AB}}^{k-1/2} = (3\mathbf{u}^{k-1} - \mathbf{u}^{k-2})/2$ is the Adams–Bashforth projected convecting velocity. Equations (4.67a) and (4.67b) are solved in an inner loop, where, before each iteration, $p^* \leftarrow p^{k-1/2}$.[26] Hence, this scheme is called an incremental pressure correcting scheme (IPCS). A convergence criterion based on $\left\|p^{k-1/2} - p^*\right\|$, or a desired maximum number of iterations, is typically set. See also the review by Langtangen et al. [241] for an overview of methods for incompressible single-phase flow.

> [26] The initial $p^{k-1/2}$ can be assigned by e.g. a projection $p^{k-1/2} \leftarrow 2p^{k-3/2} - p^{k-5/2}$.

Assuming the inner loop is solved with high accuracy, such that $p^* = p^{k-1/2}$, we obtain from eq. (4.67c) that $\tilde{\mathbf{u}}^k = \mathbf{u}^k$. Inserting these expressions into eq. (4.67a), testing with $\mathbf{u}_{\mathrm{CN}}^k = \tilde{\mathbf{u}}_{\mathrm{CN}}^k = (\mathbf{u}^k + \mathbf{u}^{k-1})/2$, and as usual using the no-slip condition, we obtain

$$\frac{1}{2\tau}\rho\left\|\mathbf{u}^k\right\|^2 - \frac{1}{2\tau}\rho\left\|\mathbf{u}^{k-1}\right\|^2 = -\left\|2\mu\mathbf{D}\mathbf{u}_{\mathrm{CN}}^{k-1/2}\right\|^2, \tag{4.68}$$

where we have also used that $\boldsymbol{\nabla}\cdot\mathbf{u}_{\mathrm{CN}}^k = 0$. Comparing to the first-order counterpart (4.43) (letting $\mathbf{u}^* = \mathbf{u}^{k-1}$ and $\rho^k = \rho$ and disregarding chemical potential terms) it is clear that the second-order scheme is less dissipative, while still retaining the sought energy stability. It is tempting to pursue such a direction for two-phase flow with density contrast, solute transport and electric fields, and it is trivial to construct schemes that are, at least, formally second order [403]. However, to the author's knowledge, even for two-phase flow with mass contrast it is an open question how to achieve energy stability, which again can allow for rigorous convergence results.

4.3 STEADY-STATE SCHEMES

For problems where a steady-state solution is sought, it is often undesirable to go through thousands of time steps to reach a steady state. Moreover, as seen from eq. (4.63), the steady state reached by a time-splitting scheme may contain spurious *numerical* dissipative terms of the order $O(\tau)$, and the artificial boundary condition on the pressure Poisson equation introduces an error $O(\tau)$ [241], sec. 5.1—which can be detrimental to the overall solution even when a higher-order method is used.

In this case, it might be worthwhile to solve for velocity and pressure in a coupled manner. For clarity, we consider the Stokes equation (3.17) for creeping flow, which we restate here,

$$-\mu \boldsymbol{\nabla}^2 \mathbf{u} + \boldsymbol{\nabla} p = \mathbf{f}, \tag{4.69}$$

$$\boldsymbol{\nabla} \cdot \mathbf{u} = 0. \tag{4.70}$$

Here, we have added the constant body force $\mathbf{f}$ to the right hand side of eq. (4.69). We impose the no-slip condition $\mathbf{u} = \mathbf{0}$ on the boundary $\partial\Omega$.

Equation (4.69) can be written as the following *linear* variational problem. Find $(\mathbf{u}, p) \in \mathbf{U}_h \times P_h$ such that

$$\mu \left(\boldsymbol{\nabla} \mathbf{u}, \boldsymbol{\nabla} \mathbf{v} \right) - (p, \boldsymbol{\nabla} \cdot \mathbf{v}) = (\mathbf{f}, \mathbf{v}) \tag{4.71a}$$

$$(\boldsymbol{\nabla} \cdot \mathbf{u}, q) = 0, \tag{4.71b}$$

for all test functions $(\mathbf{v}, q) \in \mathbf{U}_h \times P_h$. Solving and preconditioning this system remains an important area of research to this day. Particularly, this is relevant for cases where an accurate steady state is sought.

Finite element approximation

In the finite element method, as explained in section 4.1, we can expand the solution functions in a finite basis. For the velocity, we write the approximated solution as [241]

$$\mathbf{u} \simeq \hat{\mathbf{u}} = \sum_{j=1}^{n} \sum_{r=1}^{n_{\text{dim}}} U_{j,r} \mathbf{N}_j^r \tag{4.72}$$

where $\mathbf{N}_j^r = N_j \hat{\mathbf{e}}_r$ ($\hat{\mathbf{e}}_r$ are unit vectors), while the pressure can be approximated as

$$p \simeq \hat{p} = \sum_{j=1}^{m} P_j L_j. \tag{4.73}$$

Here, $U_{r,j}$, P_j are constant coefficients, while N_j, L_j are basis functions. Here, the velocity is represented by $n \cdot n_{\text{dim}}$ unknowns (n_{dim} is the number of spatial dimensions) and the pressure is represented by m unknowns. Using the Galerkin method, as demonstrated in section 4.1, we can express (4.71) in terms of the basis functions. We then obtain the following equation sets:

$$\sum_{j=1}^{n} \mu \left(\boldsymbol{\nabla} N_j, \boldsymbol{\nabla} N_i \right) U_{j,r} - \sum_{k=1}^{m} (L_k, \partial_r N_i) P_k = (f_r, N_i) ,$$

$$\text{for} \quad r \in \{1, \ldots, n_{\text{dim}}\}, \tag{4.74a}$$

$$\text{and} \quad i \in \{1, \ldots, n\},$$

$$\sum_{r=1}^{n_{\text{dim}}} \sum_{i=1}^{n} (L_k, \partial_r N_i) U_{i,r} = 0, \quad \text{for} \quad k \in \{1, \ldots, m\}. \tag{4.74b}$$

Evidently, we can identify the inner products as the matrices $\mathbf{A} = [A_{ij}]$ where $A_{ij} = \mu\left(\boldsymbol{\nabla} N_j, \boldsymbol{\nabla} N_i\right)$, and $\mathbf{B}_r = [B_{ik,r}]$ where $B_{ik,r} = -\left(\partial_r N_i, L_k\right)$; the source term vectors $\mathbf{Q}_r = [Q_{r,i}]$ where $Q_{r,i} = (f_r, N_i)$; and the vectors of unknowns $\mathbf{U}_r = [U_{i,r}]$, $\mathbf{P} = [P_i]$. Here $\mathbf{A}$ is an $n \times n$ matrix, $\mathbf{B}_r$ is a $n \times m$ matrix, $\mathbf{U}_r$ is an n-vector, and $\mathbf{P}$ is an m-vector. By defining $\mathbf{U} = [\mathbf{U}_1, \ldots, \mathbf{U}_{n_{\mathrm{dim}}}, \mathbf{P}]$ as the system vector of unknowns, $\mathbf{Q} = [\mathbf{Q}_1, \ldots, \mathbf{Q}_{n_{\mathrm{dim}}}, \mathbf{0}_m]$ ($\mathbf{0}_m$ is an m-dimensional zero vector) as the source term vector, and

$$\mathbf{M} = \begin{bmatrix} \mathbf{A} & & & \mathbf{B}_1 \\ & \ddots & & \vdots \\ & & \mathbf{A} & \mathbf{B}_{n_{\mathrm{dim}}} \\ \mathbf{B}_1^T & \ldots & \mathbf{B}_{n_{\mathrm{dim}}}^T & \end{bmatrix} \tag{4.75}$$

as the $(n \cdot n_{\mathrm{dim}} + m) \times (n \cdot n_{\mathrm{dim}} + m)$ system matrix, we can write the linear system as

$$\mathbf{MU} = \mathbf{Q}. \tag{4.76}$$

Now, the main quest is to solve eq. (4.76), i.e. choose basis functions N_j, L_k such that $\mathbf{M}$ is not singular. In this respect, the Babuska–Brezzi condition [67,68,241] is a central concept, which determines whether a finite element approximation is stable and leads to a uniquely defined solution vector $\mathbf{U}$. In practice, it imparts that a standard P_1–P_1 discretization (of $(\mathbf{u}, p)$), i.e. piecewise continuous basis functions on the discretized domain, cannot generally be used to solve the Stokes equations. The arguably most obvious choice is to use Taylor–Hood elements, which consists of P_2–P_1 elements; i.e. piecewise quadratic basis functions for the velocity and piecewise linear basis functions for the pressure. This, however, leads to a larger number of unknowns, and in general, a large linear system that is hard to solve. The criterion also enables several other mixed element formulations, such as P_{k+1}–P_k for $k > 1$, and more advanced elements such as the MINI element, the "bubble" elements, and Crouzeix–Raviart elements. We will not discuss such methods here, and the interested reader is referred elsewhere [132,172].

A more intuitive way of stabilizing the Stokes equations is to modify the governing equations, and include a mesh dependent parameter that ensures that convergence to the correct solution is obtained when the mesh is sufficiently refined, i.e. let the typical linear element size $h \to 0$. Such stabilization can enable the use of elements of the same order for both pressure and velocity, i.e. elements that would otherwise violate the Babuska–Brezzi criterion. When solving the Stokes equations numerically with elements that violate this criterion, the pressure field is usually found to be highly oscillatory. It is therefore consistent with physical intuition to add a term to the right hand side of eq. (4.70) that dampens out short-wavelength oscillations in the pressure field. Such a term can be expressed by

$$\boldsymbol{\nabla} \cdot \mathbf{u} = \delta h^2(\mathbf{x}) \boldsymbol{\nabla}^2 p, \tag{4.77}$$

where $h(\mathbf{x})$ is a local mesh size, and δ is parameter that is typically chosen heuristically. It is clear that the modification of the continuity equation, eq. (4.77), admits a compressibility proportional to δ, i.e. the velocity field is no longer divergence free. In particular, δ should be large enough to provide stable convergence, but small enough for the introduced compressibility to be unimportant for the final results.

The modification (4.77) leads to a resulting in a modification (from eq. (4.75)) of the system matrix $\mathbf{M}$ in eq. (4.76):

$$\mathbf{M}_{\mathrm{stab}} = \begin{bmatrix} \mathbf{A} & & & \mathbf{B}_1 \\ & \ddots & & \vdots \\ & & \mathbf{A} & \mathbf{B}_d \\ \mathbf{B}_1^T & \ldots & \mathbf{B}_d^T & -\delta\mathbf{C} \end{bmatrix}, \tag{4.78}$$

where the $m \times m$ matrix $\mathbf{C} = [C_{ij}]$ is defined by $C_{ij} = h^2 \left(\boldsymbol{\nabla} L_i, \boldsymbol{\nabla} L_j \right)$. For sufficiently large δ, the matrix $\mathbf{M}_{\text{stab}}$ becomes nonsingular even for P_1–P_1 elements.

The Babuska–Brezzi criterion is in general not only applicable to mixed elements and steady-state problems. It also applies to transient problems (the generalisation is straightforward), including those that inmpart splitting between velocity and pressure. However, for splitting methods, such as that presented in section 4.2, a weak numerical compressibility is introduced, $\boldsymbol{\nabla} \cdot \mathbf{u} \propto \tau^2 \partial_t p$, which can be seen from eq. (4.35b). This has a similar effect as the stabilization term (4.77) above, rendering simulations using P_1 elements for all fields possible. This can be a particularly viable alternative when the $O(\tau)$ splitting error dominates. Finally, mixed element formulations that actually violate the Babuska–Brezzi criterion may also work well in practice. For instance, the P_2–P_0 element has found wide use[241]. For more discussions on stabilization methods for single-phase fluid flow, see e.g.[172,241].

4.4 NUMERICAL SOFTWARE AND TOOLS

Computational tools are needed to numerically solve the discretized equations presented in the preceding sections. To consider the finite element method, the numerical tasks at hand include constructing meshes, computing basis functions, assembling system matrices (typically at each time step), preconditioning and solving the resulting sparse linear systems, and storing and analysing the data. Many of these steps are in themselves well-developed scientific topics, and hence it would be daunting task to implement everything from scratch. Luckily, there exist freely available numerical resources which allow to use highly optimized routines for all of these tasks. The obvious advantages of this approach is that one avoids 'reinventing the wheel' and the approach thus allows to obtain reliable results in a shorter amount of time—both in terms of implementation and simulation time. Obviously, this relies on the employed software to be trustworthy.

The importance of reproducibility in science was pointed out already by Boyle in the 17th century[402] pp. 82. Recently, an increased interest in reproducible research has emerged, particularly in computational science[75,135]. An essential component to reproducible science is transparency. For computational science, this imparts that the numerical codes should be available to the public, so that anyone can inspect and critically evaluate the validity of the tools with which results have been obtained. An important facilitator for development of such *open source* software has been the open version control system such as GIT[444] and MERCURIAL, combined with public code repositories such as GitHub and BitBucket.[27] In order to keep in line with this policy, we have opted both to *use* and *develop* open source codes.[28]

4.4.1 *FEniCS*

Most of the simulations presented in this thesis have been carried out within the finite element framework FEniCS[272]. FEniCS is an open-source computing platform for solving partial differential equations using the finite element method, which aims to automatize the discretization and assembly of the problems in question. The backend code is written in C++, while the features can be accessed using high-level PYTHON code. Since the bulk of the computation time in a finite element problem is spent on matrix assembly and linear solvers, the high-level PYTHON interface does not pose a significant cost in terms of efficiency[320]. Rather, it serves to cut time spent on code development, documentation, and maintenance. FEniCS consists as a collection of dedicated components that together make setting up finite element problems straightforward. DOLFIN[273] is the C++/PYTHON interface to the computational backend of FEniCS. The FEniCS Form Compiler FFC[235]

[27] Not only does this provide a powerful and transparent change-tracking environment, and allow users to quickly update their code (by "pulling" from the repository); it invites users to interact, point out errors or shortcomings (file "issues"), and provide fixes or new features themselves (submit "pull requests"), which in term can be incorporated into the main branch of the project by the code authors.

[28] Open science is also an important target for the Horizon 2020 programme of the European Commission[141], a funding agent for the present project.

translates variational forms into efficient c++ code for FEM assembly. The discretized variational forms can be specified by users via the Unified Form Language (UFL)[10]. The Finite element Automatic Tabulator (FIAT)[234] generates various types of finite elements (including P_k) elements. Dijitso[11] is a just-in-time compiler for c++ code generated by Python code.

Within a Python script, FEniCS users can specify a mesh, set up finite element spaces, specify a weak form of the governing equations, and impose boundary conditions. The numerical problem is then automatically converted to a linear matrix system by the c++ backend. The computational backend interfaces to highly optimized linear solver libraries, such as PETSc[25], Hypre[142], and Trilinos[187]. Which linear solvers and preconditioners to use can be specified by the user. In particular, all the solvers and preconditioners mentioned in section 4.1 can be accessed through FEniCS, and additional preconditioners are found e.g. in Fenapack[55]. In common with (and partly due to) its linear algebra backend, FEniCS is highly parallelized and developed with high-performance computing in mind. In particular, it uses the Message Parsing Interface (MPI) for parallel communication.

For a more thorough introduction to how FEniCS is used in practice, the reader is referred to the extensive tutorial by Langtangen and Logg[240]. In this project, FEniCS has been used as the underlying framework for solving the equations of elasticity, creeping flow, transient single-phase flow, and multiphase flow with electric fields and solutes, as we will se below.

4.4.2 *Oasis*

The Oasis (Optimized And Stripped Solver) software, developed by Mortensen and Valen-Sendstad[320], is a high-level, fast and flexible solver for the Navier–Stokes equations. Oasis is written entirely in Python, built on top of the FEniCS platform, and heavily exploits its PETSc backend. The runtime of the solver has been shown to be dominated by Krylov solver iterations, underpinning the fact that the high-level Python interface is insignificant to the overall performance. In particular, the solver was shown to yield similar efficiency as solvers written entirely in low level code, i.e. OpenFoam[217] and CDP[86] by comparative simulations on the Abel supercomputer at the University of Oslo, and weak scaling was demonstrated up to 256 cores.

Oasis is distributed as a Python package and is modular by design. Several solvers, i.e. numerical schemes, given as separate Python scripts, are implemented in the code. These include Chorin's method, i.e. eq. (4.66), and an optimized IPCS, i.e. eq. (4.67), and other methods. Problems, i.e. simulation cases, are implemented as separate Python scripts in a similar manner, and user specific problems can be easily defined, for example by modifying some of the default problems to fit the needs of the user. A customized version of Oasis[29] used in this project was developed by the author jointly with MSc student Mads H. A. Madsen, whom the author co-advised during the spring of 2016.

[29] The code can be found on the Git repository https://github.com/gautelinga/Oasis/tree/nbiOasis.

4.4.3 *Bernaise*

Bernaise (Binary Electrohydrodynamic Solver) is a flexible, high-level finite element solver of two-phase electrohydrodynamic flow problems in complex geometries, which has been developed in this project[263], in a joint venture with colleague Asger Bolet. Inspired by the famous sauce—and oil-in-water emulsion—Béarnaise[30], the solver aims at solving problems involving the smallest constituents of such phases, namely small droplets of one phase immersed in another phase, possibly subject to chemical transport and electric fields. The basic version of the solver targets solving the phase-field model (3.81) as proposed by Campillo-Funollet et al.[79], while other phase-field models can be

[30] The missing A in Bernaise compared to the sauce stands for Adaptivity, which is at the present not an implemented feature.

integrated with ease. Employing a phase-field model, the solver is better suited to handle topological changes and moving contact lines than comparable sharp-interface models; cf. [43]. Several numerical schemes are implemented, which include coupled velocity and pressure computation, fractional-step methods, energy stable schemes and fully linear schemes. This permits simulations both in two and in three dimensions. The 3D version of the solver is fully iterative and demonstrated strong scaling up to about 40 cores on an in-house computing cluster.

Bernaise is inspired by the Oasis solver, and is similar to the latter in both structure and implementation. This approach is chosen both in order to appeal to the same user base, and because it was the developers' opinion that the approach of Oasis is a sensible one. Many of the routine functions are similar, and problems and solvers can easily be implemented in a reminiscent[31] way by the user, i.e. by supplying single Python scripts. Nevertheless, it is our hope and opinion that most users—familiar with Oasis or not—should easily arrive at a decent level in Bernaise.

[31] As the two codes simulate related, but in many ways quite different physical problems, significant differences in the code structure are necessary.

In addition to the simulation environment, Bernaise comes with a set of utility tools. This includes post-processing tools for analysing data, producing figures, etc., a mesh generation utility, and a plotting utility.

The appended Paper 6[263] which documents the software, simulation method, and code validation, is described also section 5.3. Additionally, the code has been used for several of the other appended publications.

4.4.4 *Meshing tools*

Although meshing was mentioned only in passing in section 4.1, it represents a genuinely hard and important problem. Unstructured meshes have the initially persuasive feature that they allow to represent parts of the domain with finer elements and thus allowing to obtain locally higher accuracy. However, for complex domains in 3D, constructing quality meshes is a challenging task. In many settings, such as in simulation of incompressible flow, 'bad' elements can deteriorate the solution, and lead to instabilities in otherwise stable methods[241]. Moreover, splitting schemes for transient flow are subject to the CFL criterion and therefore strongly inhibited by the smallest grid size (or specifically, the highest local Courant number).

The CGAL library[441] is an extensive c++ library for meshing in 2D and 3D, but is difficult to master. TetGen[408] is another robust mesh generation tool with a more modest feature list. FEniCS' built-in meshing tool, the Python package Mshr[230] interfaces to both the above libraries. Another good Python package is MeshPy[236], which interfaces to Triangle[405] for 2D meshes and above-mentioned TetGen. Iso2Mesh[143] is a MatLab toolbox which both interfaces to CGAL and TetGen, and contains several other features.

In this work, Iso2Mesh was used to generate meshes from segmented X-ray microtomography data of a porous limestone (see section 5.2), using the interface to TetGen to produce the surface mesh and the CGAL interface to produce the interior tetrahedra.

Periodic domains constitute an additional difficulty, as nodal values must be mapped exactly to the opposing sides. This is particularly relevant for constructing meshes for rough channel or pipe geometries. To do this, a meshing tool was developed in Python,[32] that takes an arbitrary (rough) surface as input and creates a periodic mesh from it. Using a combination of manually written routines for the edges, Triangle (via MeshPy) for the flat (periodic) sides, and TetGen for the interior tetrahedra, reasonably high-quality meshes could be obtained that were also fully periodic. As will become obvious in the next chapter, these routines were taken advantage of in both electrohydrodynamic and transitional flows.

[32] Some of the meshing tools used in this project are available at the Git repository https://github.com/gautelinga/meshtools.

SUMMARY OF PAPERS

In this chapter, the research articles produced in this project are summarized. The papers are roughly organized into four overarching themes for which background material has been introduced in the previous chapters.

5.1 TURBULENT FRONTS IN PIPE FLOW

PAPER 1: Statistical mechanics of puff-splitting in the transition to pipe turbulence
Hong-Yan Shih, Gaute Linga, Grégoire Lemoult, Mukund, Vasudevan, Björn Hof, Joachim Mathiesen, and Nigel Goldenfeld
In preparation (2018)

Paper 1 concerns the spatio-temporal transition to turbulence in a smooth pipe, and starts off where the discussion in section 2.2.2 ended. As noted there, whether or not the transition belongs to the directed percolation universality class has been a long-standing puzzle in the community at the intersection between fluid mechanics and statistical physics. Recent experiments by Mukund and Hof[327] showed that even in (quasi-periodic) pipes of length $7800d$ (d is pipe diameter), a continuous transition to turbulence could *not* be observed. Rather, a *discontinuous* behaviour was observed, from the point where all turbulence died out at $\mathrm{Re} \simeq 2020$, shown in fig. 2.3 (d), to a point where turbulent puffs were 'jammed' in a crystalline state at $\mathrm{Re} \simeq 2060$, shown in fig. 5.1 (a). This relied on the standard view of considering the turbulent fraction F as the order parameter and Re as the control parameter[28,29]. Moreover, knowledge from studies on directed percolation suggests that the critical point, $\mathrm{Re_c}$, is somewhat higher than at the $\mathrm{Re_\times} \simeq 2040$ found by Avila et al.[23] based on single-puff statistics[23,29,193].[33] Here, we summarize and give some supplementary information to the appended preprint.

In this work, the main assumption is that the statistical properties of a puff depend (in average) only on the shear profile at its upstream front. In particular, the latter should depend only on the distance to the nearest neighbour upstream, and not on anything happening downstream of it. Thus, the dynamics are controlled only by *one-way* two-particle interactions. Moreover, the puffs can stochastically spontaneously split and decay with rates (or conversely, characteristic times) that depend only on Re and the distance ℓ to its upstream neighbour, and the speed u at which they travel downstream is also only dependent on ℓ and Re. Carefully executed experiments presented in this work show that, at fixed Re, both the decay times τ_d, splitting times τ_s, and downstream velocities u, can be described by the exponential[34] relations

$$\tau_\mathrm{d}(\ell) = \tau_{\mathrm{d},\infty} \left[1 - a_\mathrm{d} e^{-\ell/\lambda} \right], \quad \tau_\mathrm{s}(\ell) = \tau_{\mathrm{s},\infty} \left[1 + a_\mathrm{s} e^{-\ell/\lambda} \right], \tag{5.1}$$

$$u(\ell) = u_\infty \left[1 + b e^{-\ell/\lambda} \right], \tag{5.2}$$

where the parameters $\tau_{\mathrm{d},\infty}$, $\tau_{\mathrm{s},\infty}$, u_∞ are the single-puff properties. The first two, $\tau_{\mathrm{d},\infty}$ and $\tau_{\mathrm{s},\infty}$, depend superexponentially on Re and can be obtained from[23]. The last,

[33] However, as noted also by Avila et al.[23], the splitting and decay rates change so abruptly around $\mathrm{Re_\times}$ that $\mathrm{Re_c}$ is likely only be slightly larger.

[34] Which is perhaps not surprising given the exponential (in time) development of a Hagen–Poiseuille profile, see e.g.[321].
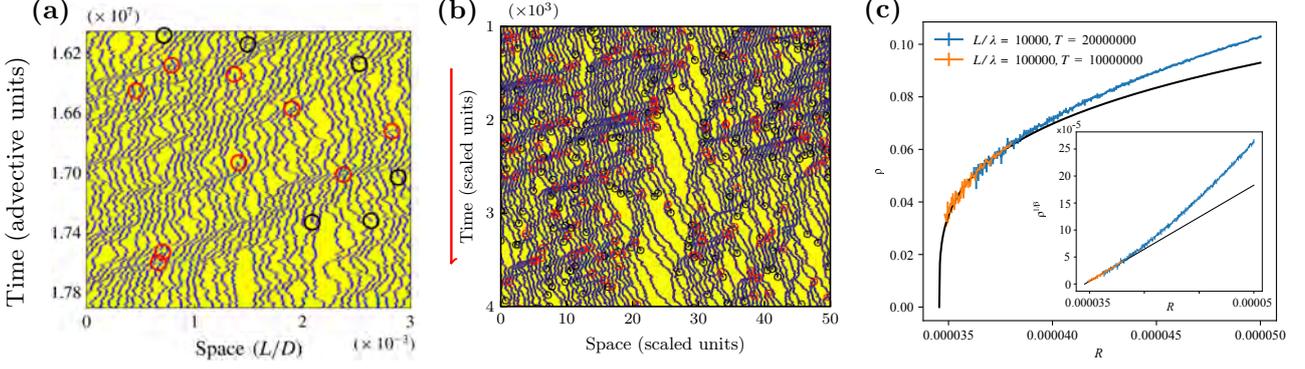
FIGURE 5.1: Puff-splitting in the transition to pipe turbulence. (a) The experiments by Mukund and Hof[327] above the critical point. (b) Simulations of the continuous model above the critical point. (c) Ensemble-averaged turbulent fraction in the steady-state.

u_∞, which has a weaker dependence on Re can be found from[30]. Finally, the amplification/reduction factors a_d, a_s, and b, and the interaction distance λ, are empirical parameters found from the experiment. Now, the motion of puff i can be described by the Langevin equation

$$\frac{\mathrm{d}x_i}{\mathrm{d}t} = u(x_i - x_{i-1}) + \sqrt{D}\xi_i(t), \tag{5.3}$$

where x_i is the puff position, and $i - 1$ is the upstream puff (to the left of i) such that $x_i > x_{i-1}$. The noise ξ_i is taken to be uncorrelated and Gaussian, i.e. $\langle \xi_i(t)\xi_j(t') \rangle = \delta_{ij}\delta(t - t')$. D is a heuristic diffusion coefficient that represents the stochastic motion of puffs observed experimentally, and can be determined from experiments or direct numerical simulations. We assume periodic boundary conditions in the axial direction in a pipe with length L, and puffs can be removed ('decay') and spawned at the downstream end of another ('split') with rates τ_d^{-1}, τ_s^{-1}, respectively.

For numerical implementation purposes, and to limit the number of parameters to a minimum, it is useful to nondimensionalize the equations. First, we move into a reference frame moving at the mean speed of newly spawned puffs, i.e. $\bar{U} = u_\infty(1 + b)$. Then, we introduce new space and time variables denoted by tildes, through $x_i = X\tilde{x}_i$ and $t = T\tilde{t}$, and correspondingly $D = \tilde{D}X^2/T$, $\tilde{\lambda} = X\lambda$, $L = X\tilde{L}$, $u = \tilde{u}X/T$, $\tau_i = T\tilde{\tau}_i$. Here, X and T are the spatial and temporal scales.

Equation (5.3) becomes

$$\frac{\mathrm{d}\tilde{x}_i}{\mathrm{d}\tilde{t}} = \tilde{u}(\tilde{x}_i - \tilde{x}_{i-1}) + \mathrm{sgn}(X)\sqrt{\tilde{D}}\xi_i(\tilde{t}), \tag{5.4}$$

where we have used $\xi_i(T\tilde{t}) = \xi_i(\tilde{t})/\sqrt{T}$, and

$$\tilde{u}(\tilde{\ell}) = \frac{Tu_\infty b}{X}\left[e^{-\tilde{\ell}/\tilde{\lambda}} - 1\right], \quad \tilde{\tau}_i(\tilde{\ell}) = \frac{\tau_{i,\infty}}{T}\left[1 - a_\mathrm{d}e^{-\tilde{\ell}/\tilde{\lambda}}\right]. \tag{5.5}$$

It is practical to choose the time scale $T = \tau_\times = \tau_{\mathrm{d},\infty}(\mathrm{Re}_\times) = \tau_{\mathrm{s},\infty}(\mathrm{Re}_\times)$ where $\mathrm{Re}_\times$ is the single-puff critical Reynolds number found by Avila et al.[23]. We also choose the spatial scale $X = \tau_\times u_\infty b(\mathrm{Re}_\times)$. For convenience, and compliance with the next model, we omit the tildes, flip the sign of the x-axis and invert the order over the puff indices, so that $x_{i+1} > x_i$. Further, we introduce the simplified control parameter $\varphi = \mathrm{Re} - \mathrm{Re}_\times$. We thus obtain eq. (5.4) with

$$u(\ell) = \alpha(\varphi)\left[e^{-\ell/\lambda} - 1\right], \qquad \alpha(\varphi) = \frac{u_\infty b(\mathrm{Re}_\times + \varphi)}{u_\infty b(\mathrm{Re}_\times)}, \tag{5.6a}$$

$$\tau_i(\ell) = \beta_i(\varphi)\left[1 - a_\mathrm{d}e^{-\ell/\lambda}\right], \qquad \beta_i(\varphi) = \frac{\tau_{i,\infty}(\mathrm{Re}_\times + \varphi)}{\tau_{i,\infty}(\mathrm{Re}_\times)}. \tag{5.6b}$$

Here, $\alpha(0) = \beta_i(0) = 1$, and can be linearized around $\varphi = 0$.[35] This model, which we call the *continuous model*, captures the dynamics of puff interaction well.

The equations can be numerically integrated explicitly using the Itô formalism. At time step k, we calculate

$$\Delta x^* = \Delta t\, u(x_{i+1}^k - x^k) + \sqrt{D\Delta t}N(0,1), \qquad (5.7)$$

where Δt is the discrete time step, and $N(0,1)$ is an uncorrelated random number drawn from a Gaussian distribution with mean 0 and variance 1. The position is then updated by

$$x_i^{k+1} = x_i^k + \max(0, \min(\Delta x_i^*, x_{i+1}^k - x_i^k)), \qquad (5.8)$$

to strictly avoid puffs passing each other. The integration is combined with an efficient double-linked list implementation in c++, where puffs are removed if $P_\mathrm{d} = 1 - e^{-\Delta t/\tau_\mathrm{d}} > R_\mathrm{d}$, where R_d is a random number drawn from a uniform distribution in the interval $(0,1)$.[35] Likewise, a puff is inserted into the list if $P_\mathrm{s} = 1 - e^{-\Delta t/\tau_\mathrm{s}}) > R_\mathrm{s}$, where R_s is another (uncorrelated) random number drawn from the same distribution as R_d. Since we are interested in ensemble properties, the optimal parallillization strategy is to run thousands of independent simulations simultaneously.

By coarse-graining the continuous model, a simplified lattice-based model can be obtained, which contains the basic phenomenology of puff interaction. The basic ingredients are splitting, decay, and propagation, which are all described by the rates ω_s, ω_d, p. In this picture, we are in a frame co-moving with the puffs going fastest downstream (as with the rescaled and shifted continuous model), and in this frame of reference, the puffs are propagating upstream.[37] If there are no puffs in front (i.e. upstream) of a given puff, the puff is free to move in that direction. If there is a puff in front of it, the puff cannot propagate, and a *queue* starts to form.

Readers who have experience with commuting to work by car, will probably recognize this dynamics from traffic congestion. Indeed, this lattice model is tightly connected to traffic models, namely those belonging to the class of asymmetric exclusion processes (ASEP)[94,184]. Such models have been well studied by statistical physicists[184]. In particular, the lattice model of puff dynamics is reminiscent of the totally asymmetric exclusion process (TASEP), in which only unidirectional motion is allowed. Puff dynamics displays, however, two notable differences from traffic applications: (i) "Cars" (or puffs) can spontaneously appear or disappear from the queue, and (ii) the boundary is periodic, i.e., the "cars" drive in circle. The lattice model is straighforward to implement, and the lattice sites can be set to be updated synchronizously. The processes *split*, *decay*, and *propagate* can be picked in a random order at each discrete time step.

The mean field equation for this process is given by

$$\partial_t \langle n_i \rangle = -p\langle n_i(1 - n_{i+1}) \rangle + p\langle n_{i-1}(1-n_i) \rangle - \omega_\mathrm{d}\langle n_i \rangle + \omega_\mathrm{s}\langle n_{i-1}(1-n_i)\rangle \quad (5.9)$$

where n_i is the occupation number of site i of the lattice. Here, the first two terms represent propagation, and the last two represent decay and splitting, respectively. If $p = 0$, the model contains the four ingredients of DP: diffusion, de-coagulation, coagulation and annihilation[193]. We can identify e.g. ω_s as a control parameter, such that the mean number of particles $\rho = \langle n_i \rangle \sim (\omega_{\mathrm{s},c} - \omega_\mathrm{c})^\beta$, where the exponent β is found in table 2.1.

By performing a Kramers–Moyal expansion to second order, a Fokker–Planck equation can be obtained, which again can be transformed to a Langevin equation representing the model. In this (further) coarse-grained continuum description, i.e. $i \rightarrow x$, the replacements

$$n_i \rightarrow \rho(x) \quad \text{and} \quad n_{i+1} \rightarrow \rho(x) + \partial_x\rho(x) + \tfrac{1}{2}\partial_x^2\rho(x), \qquad (5.10)$$

[35] The code is available at the Git repository https://github.com/gautelinga/puffdyn.

[36] Avila et al.[23] gave the functional form $\tau_i(\varphi) = \exp(\exp(a_i\varphi - b_i))$ for $i \in \{\mathrm{s}, \mathrm{d}\}$, including numerical values for the parameters a_i, b_i. Thus, τ_i are rapidly growing analytic functions. The linear range may however be very narrow, as seen by Taylor expansion of τ_i. Using the values from[23], we find that the contribution of the second order term is of the order 10% when $\varphi/\mathrm{Re}_\times \simeq 2\%$.

[37] This is also the correct way of looking at it, according to Barkley[29]; by viewing the puff motion as an interface propagation phenomenon.

must be made, leading to the equation

$$\partial_t \rho = -\omega_\mathrm{d}\rho + \tfrac{1}{2}(p + \omega_\mathrm{s})\partial_x^2\rho - (p + \omega_\mathrm{s})\partial_x\rho + \omega_\mathrm{s}\rho(1 - \rho)$$
$$+ (2p + \omega_\mathrm{s})\rho\partial_x\rho - \frac{\omega_\mathrm{s}}{2}\rho\partial_x^2\rho + \sqrt{\rho(1 - \rho)}\xi, \quad (5.11)$$

where $\xi(x, t)$ is a white noise, such that $\langle \xi(x,t)\xi(x',t')\rangle = \delta(x - x')\delta(t - t')$. Compared to the corresponding Langevin equation for DP, eq. (5.11) contains two terms proportional to $\sim \rho\partial_x^j\rho$ where $j = 1, 2$, which in TASEP models lead to shocks or 'traffic jams.' The question is now whether the presence of these terms change the universality class away from DP. By a renormalizaton group argument outlined in the appended preprint, it can be shown that these terms are indeed irrelevant at the DP fixed point.

To test this prediction, numerical simulations were carried out both for the continuous model and the lattice model. The experimental values provide a basis for the parameters in the continuous model, while in the lattice models the parameters are chosen more heuristically. Nevertheless, universal dynamics should not be *sensitively* dependent on the details of the implementation. Figure 5.1 (a) shows the puff dynamics in the experiment by Mukund and Hof[327], and in fig. 5.1 (b) we show corresponding simulations with the continuum model. The similarity between the two is striking, in particular with regard to how waves of puff repulsion propagate through the system. This behaviour is also captured in the discrete model, but in a more coarse-grained way. In this picture, the typical interaction distance λ in the continuous model, which presumably is proportional to a puff size, should correspond to a lattice unit. By carefully accounting for finite size effects, the DP scaling $\rho \sim \varphi^\beta$ could be reproduced with both models. For the continuous model a system size $L/\lambda = 10^5$ (and a simulation time $T/\tau_\times = 5 \cdot 10^4$) was required to obtain a reasonable scaling range, see fig. 5.1 (c).

In light of these insights, we can reinterpret the results of Mukund and Hof[327]. It is clear that with a puff interaction distance $\lambda \simeq 15d$ (estimated from experiments), the system size $L = 7800d$ corresponds to $L/\lambda \simeq 500$, which is nearly three orders of magnitude smaller than what we needed to obtain an acceptable range numerically. Knowing that asymptotically close to the critical point, the equilibration time diverges, it seems clear that an experimental measurement would be hard. A simple extrapolation from the continuous simulations carried out here, indicates that a system size of at least $L \sim 10^5d$ and a simulation time of $T \sim 10^{11}$ advective units would be necessary ($\tau_\times \sim 10^7$ advective units, from[23]). As a large ensemble is needed to obtain robust results, this might pose significant challenges to realize experimentally.

REMAINING WORK   The experimental work needs to be included in the manuscript. Furthermore, it would strengthen the paper to give a more quantitative prediction on how large systems and simulation times would be required to observe the DP scaling in an actual experiment.

CONTRIBUTIONS   For the first paper, the idea of probing the large-scale behaviour by using 'two-particle' puff statistics was conceived by Lemoult. The experiments were carried out by Mukund and Hof. Goldenfeld, Shih, Mathiesen and I developed an independent model and made through discussions the connection to the TASEP model. Lemoult, Mathiesen and I implemented different versions of the lattice model and carried out simulations. Lemoult and I developed independent versions of the continuous molecular dynamics model and carried out simulations. Goldenfeld and Shih derived the Langevin equation from the lattice model, and performed the renormalization group analysis. The manuscript in the appended state, was written mainly by Goldenfeld, with

input from the other authors, while the section on the continuous model was written by me.

5.2 FLOW IN FRACTURED AND POROUS MEDIA

PAPER 2: Self-similar distributions of fluid velocity and stress heterogeneity in a dissolving porous limestone
Gaute Linga, Joachim Mathiesen, and François Renard
Journal of Geophysical Research: Solid Earth **122**, 1726–1743 (2017)

PAPER 3: Transitional flow in self-affine rough fractures
Gaute Linga, Luiza Angheluta, and Joachim Mathiesen
In preparation (2018).

As mentioned in section 2.1.1, the disordered microstructure of porous rocks is known to cause a strong heterogeneity in local flow rates and solid stress. Accordingly, an evolving microstructure will have consequences on the distributions of fluid flow and stress in the solid. In Paper 2, we consider numerically the coupling between fluid flow and solid stress in a dissolving porous limestone sample. The aim of the study is to assess (i) how an imposed fluid flow through the pore space can affect the stress distribution in the solid, and (ii) how an evolving microstructure can affect the same distribution, and (iii) how dissolution in the rock can modify the flow heterogeneity. The simulation set-up is shown in fig. 5.2 (a).

The starting point for the investigation is the experiments by Noiriel et al.[342,343], where an acidic fluid was injected into a core sample of porous limestone in multiple rounds, leading to dissolution and porosity increase. The sample was imaged using X-ray microtomography at each stage of dissolution. Noiriel generously provided to the authors segmented three-dimensional images (consisting of fluid and solid voxels) at four stages of dissolution, with porosities ϕ ranging from 0.09 to 0.2. The segmented data was then post-processed, and unstructured meshes were generated of the sample at each dissolution stage (see section 4.4.4).

To model the coupling between the fluid flow and the state of stress in the solid, two main approximations are made. The first is to assume creeping flow, i.e. the Stokes equations (3.17) is assumed to hold. This assumption, which amounts to $\mathrm{Re} \ll 1$, can also be verified based on parameters from the actual experiment Noiriel et al.[342]. The second assumption is to consider *quasi-static* deformation; i.e., the time-scale of geometry change is considered to be slow, so that we can seek equilbrium solutions to the elastic problem. The assumption also imparts a *one-way coupling* from the fluid to solid: we assume that the effect of fluid flow and external forces is so small that the geometry does not deform enough for the velocity field to be affected. In particular, locally infinitesimal displacements of the solid matrix are assumed, and linear elasticity should be a valid description.

The assumptions imply that the Stokes equations need to be solved in a constant geometry, with the no-slip conditions at the pore wall, and with pressure boundary conditions at the inlet and outlet. As demonstrated in section 3.1.2, this is then a linear problem, and the velocity can be shown to be dependent solely on the *geometry* on the one hand, and (is proportional to) the pressure difference on the other hand. A similar linear relation holds for the pressure distribution, and accordingly for the fluid stress tensor. It is thus only necessary to perform *one* accurate steady-state solution in each mesh, and the solution for all pressure conditions can be found by a trivial rescaling. The boundary conditions entering the elasticity problem are given by the traction on the pore walls due to fluid flow and pressure.

Elastostatics is described by

$$\nabla \cdot \boldsymbol{\sigma}_{\mathrm{s}} = \mathbf{0}, \tag{5.12}$$
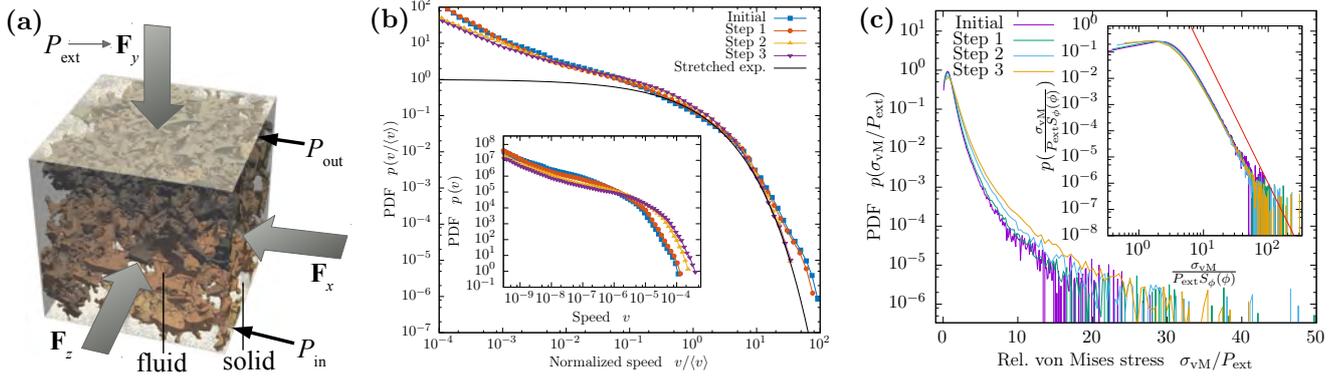
FIGURE 5.2: Flow and stress in a dissolving porous limestone, reprinted from [261]. (a) Schematic setup of the problem. (b) Probability density functions of the of the velocity sampled over the pore space, rescaled by mean velocity. A stretched exponential decay is plotted alongside the data. The inset shows the raw data. (c) Probability density functions of von Mises stress in the solid. The inset shows how the distributions collapse when rescaled by their means.

where the $\boldsymbol{\sigma}_s$ is the solid stress tensor, and external body forces have been neglected. Equation (5.12) is analogous to Stokes equations for creeping flow, except that it is not supplied by a divergence criterion. In linear elasticity, the stress tensor is given by

$$\boldsymbol{\sigma}_s[\mathbf{d}] = \frac{E}{1+\nu}\left[\mathbf{Dd} + \frac{\nu}{1-2\nu}\boldsymbol{\nabla}\cdot\mathbf{d}\right], \qquad (5.13)$$

where $\mathbf{d}(\mathbf{x})$ is the displacement vector, E is Young's modulus and ν is the Poisson ratio. The strain tensor is given by $\mathbf{Dd} = \mathrm{sym}(\boldsymbol{\nabla}\mathbf{d})$ (analogously to its fluid counterpart, the strain *rate* tensor $\mathbf{Du}$). In our set-up, eq. (5.12) is subjected to external loading on the outer boundary, along with internal stress from the fluid, in order to mimic experimental settings. Hence, we are left with solving a set of linear equations for a range of parameters.

With respect to the fluid phase, the results show that for the porosity range considered, the permeability k varies over more than an order of magnitude, and can be well described by a power law $k \sim \phi^\beta$ where $\beta \simeq 4$. This is consistent with observations in the literature (see section 2.1.1, but contrary to the Kozeny–Carman relation [84,85,237]. Secondly, we find that the probability density functions of velocity (sampled over volume) can be described by a stretched exponential function with exponent $1/2$ (see eq. (2.18) in section 2.2.1). The distributions are shown in fig. 5.2 (b). Moreover, even though the porosity varies by a factor two, and the permeability varies by a factor 10, the distributions can be collapsed onto the essentially same master curve by rescaling with the mean velocity. Whether these observations are a result of e.g. preferential dissolution in dominant channels, or of more generic nature, remains an open question.

By analyzing the pressure and viscous stress, we show that the contribution to the traction by pressure (normal stress) is dominant over that by viscous shear by an order of magnitude. Probability density functions of the *invariants* of the stress tensor (mechanical pressure and von Mises stress) also display a heavy tail, consistently with e.g. [244], and for all considered loading and flow conditions, they can be collapsed onto the same universal curve, cf. fig. 5.2 (c). With regard to the von Mises stress, which is often used as a fracture criterion, the heavy tail of the distribution implies that a small increase in dissolution and fluid flow rate can bring a large number of 'sites' in the rock across a critical threshold. Hence, if these results can be extrapolated to other rocks, they could provide an additonal explanation of the sensitivity of rocks to failure under slight changes of stress.

The stress that a flowing fluid exerts on the confining boundaries is directly related to the flow resistance, and thus the friction factor. In Paper 3, we disregard the state of stress in the solid, and abandon the paradigm of creeping flow. As documented in section 2.2.1, most numerical studies have considered steady-state flow, either creeping
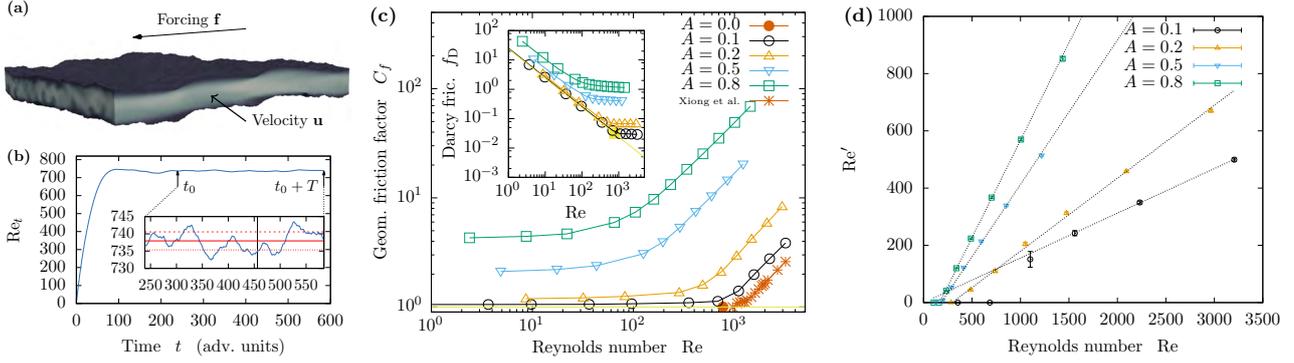
FIGURE 5.3: Transitional flow in self-affine rough channels, from[262]. (a) A snapshot from a simulation. (b) The instantaneous Reynolds number as a function of time. Inset: a close up of the sampling time in the steady state. (c) Geometric friction factor as a function of Reynolds number. Inset: Darcy friction factor. (d) The fluctuation-based Reynolds number, indicating the presence of turbulence, as a function of (fluxed-based) Reynolds number.

or laminar. Despite its apparent industrial relevance, unsteady, transitional flow in three dimensional fractures is largely unexplored. In this study, we consider a simple and generic fracture geometry that consists of a periodic self-affine surface (see eq. (2.7)) that has been shifted vertically by a distance d to form a rough model fracture joint. The main research questions underlying the investigations can be summarized as the following: (i) What is the impact of a generic roughness on the transport properties of a channel geometry? (ii) What is the effect of velocity fluctuations? (iii) How is the laminar–turbulent transition in such channels affected by including a boundary roughness?

To construct a mesh for the fracture joint, we generate a periodic self-affine surface h, parametrized in terms of $(x, y) \in [0, 10d] \times [0, 10d]$. This forms the lower boundary of the flow geometry. The same surface, shifted by a distance d along the z-axis, forms the upper boundary, and the flow is confined to the slab between these two boundaries. Since a self-affine surface does not have an intrinsic length scale, we define the roughness amplitude A as the root-mean-square height undulations of the surface $h(x, y)$. Here, we consider the four roughness amplitudes $A \in \{0.1d, 0.2d, 0.5d, 0.8d\}$ with the same self-affine realization.

Fluid flow in the spanwise and streamwise periodic domain is enforced using a fixed uniform body force $\mathbf{f} = f\hat{\mathbf{x}}$, and the Navier–Stokes equations (3.14) are integrated in time using an incremental pressure-correction scheme (see eq. (4.67) in section 4.2.5) in a modified OASIS solver (see section 4.4.2 and ref.[320]). Simulations are run until a steady state is reached, either in an absolute or in a statistical sense; the latter for unsteady flow. The instantaneous flow rate $u_x(t)$ can then be computed, and a flux-based Reynolds number can be measured by averaging it in time (indicated by an overline), i.e.

$$\mathrm{Re} = \frac{\rho \overline{u} d}{\mu}, \tag{5.14}$$

In fig. 5.3 (a) an instantaneous snapshot of a typical simulation is shown, and in fig. 5.3 (b) we display the development of the instantaneous Reynolds number Re_t (based on $u_x(t)$ instead of the time-averaged $\overline{u}_x$). In fig. 5.3 (c) we show the *geometric friction factor*, defined by

$$C_f = \frac{f d^2}{12 \mu \overline{u}} \tag{5.15}$$

as a function of Re, for all four considered roughness amplitudes A. This quantity has the property that it equals $C_f = 1$ in the double limit $\mathrm{Re}, A \to 0$, and can be seen as an inverse permeability relative to plane Poiseuille flow. The inset of the fig. 5.3 (c) shows the same data, but plots instead the Darcy friction factor $f_\mathrm{D} = 2fd/\rho u^2$ versus Re.

As discussed in section 2.2.1, the Forchheimer law is often used to describe relationships between friction loss and flow rates. In this work, we find that a generalized

Forchheimer equation, which takes into a finite crossover region between the scaling $C_f \sim$ constant for $\mathrm{Re} \ll \mathrm{Re_c}$, and $C_f \sim \mathrm{Re}$ for $\mathrm{Re} \gg \mathrm{Re_c}$, fits the data well. This leads us to identify a critical Reynolds number $\mathrm{Re_c}$, which quantifies the point where nonlinear flow sets in, and a purely geometric friction $C_{f,0}$. The latter two quantities depend on the roughness A, and lead to a reasonable data collapse for the data shown in fig. 5.3 (c). However, nonlinear friction is not synonymous with unsteadiness, and to assess the effect of transitional flow, we perform a Reynolds decomposition of the flow field,

$$\mathbf{u}'(\mathbf{x}, t) = \mathbf{u}(\mathbf{x}, t) - \overline{\mathbf{u}}(\mathbf{x}), \tag{5.16}$$

to obtain the velocity fluctuations $\mathbf{u}'(\mathbf{x}, t)$. Here, $\mathbf{u}(\mathbf{x}, t)$ is the transient flow field, and $\overline{\mathbf{u}}(\mathbf{x}) = \overline{\mathbf{u}(\mathbf{x}, t)}$ is the time-averaged flow field, sampled over a time period in the steady state as indicated in fig. 5.3 (b). Now, taking the time and space average of the squared velocity fluctuations, $q = \langle |\mathbf{u}'(\mathbf{x}, t)|^2 \rangle$, we obtain an indicator of the global turbulent intensity as the fluctuation-based Reynolds number $\mathrm{Re}' = \rho \sqrt{q} d / \mu$. In fig. 5.3 (d), we show the fluctuation-based Reynolds number Re' plotted against the flux-based Reynolds number Re for all roughness amplitudes A. We observe that the relation between the two quantities is linear beyond a certain *second* critical Reynolds number $\mathrm{Re_{c,q}}$. For sufficiently high roughness, this linear relation extends down to Re', indicating a supercritical transition to turbulence, while for low Re, the transition is subcritical. This suggests that at a certain roughness amplitude A, the transition changes character from subcritical to supercritical.

Further, given that $\mathrm{Re_{c,q}}$ and $\mathrm{Re_c}$ are of comparable magnitude, we conclude that transitional flow may play a significant role in fracture flow, and must be accounted for in simulations on larger scales when roughness and flow rates are sufficiently high.

REMAINING WORK   It would strengthen the results in Paper 3 to provide a more quantitative investigation of the suggested change of the transition from sub- to supercritical. Further, the robustness of the results to the particular realization of a self-affine surface, and secondly, to the streamwise and spanwise scale of the periodic domain, should be assessed. Numerical simulations investigating this are underway. Finally, it would be useful to estimate the quantitative contribution of the fluctuations to the friction factor.

CONTRIBUTIONS   For the first paper, I wrote most of the manuscript, carried out simulations and analysed data. Renard initiated the study and wrote significant parts of the introduction and discussion. Renard and Mathiesen contributed in discussions and interpretation of the results.

The second manuscript was written by me, and I carried out simulations and analysed data. Angheluta and Mathiesen participated in discussions and in interpretation of results.

5.3 ELECTROHYDRODYNAMICS

PAPER 4: Electrohydrodynamic channeling effects in narrow fractures and pores
Asger Bolet, Gaute Linga, and Joachim Mathiesen
Physical Review E **97**, 043114 (2018)

PAPER 5: Transient electrohydrodynamic flow with concentration-dependent fluid properties: modelling and energy-stable numerical schemes
Gaute Linga, Asger Bolet, and Joachim Mathiesen
Submitted to *Journal of Computational Physics* (2018)

PAPER 6: Bernaise: A flexible framework for simulating two-phase electrohydrodynamic flows in complex domains
Gaute Linga, Asger Bolet, and Joachim Mathiesen
Submitted (2018)

PAPER 7: Controlling wetting with electrolytic solutions: Phase-field simulations of a droplet-conductor system
Gaute Linga, Asger Bolet, and Joachim Mathiesen
Physical Review E **98**, 013101 (2018)

In Paper 4, we consider steady-state single-phase flow in a charged model microfracture. As mentioned briefly in section 2.1.1, the inherent nonlinearity of the governing equations has imparted that most numerical studies having been limited to geometries with a high degree of symmetry, such as 2D geometries[150,151] or axisymmetric cylindrical capillaries of finite length[286,287]. Here, we consider full three-dimensional simulations in a model fracture or narrow pore. Even simpler than the self-affine geometry in which we studied transitional flow (see section 5.2), we consider here a periodic channel where the bottom surface is sinusoidally undulated along the spanwise direction (see fig. 5.4).

We are here interested in electroviscous *flow channeling*, i.e. how fluid flow is directed to or from narrow parts of the channel, in the presence of a surface charge. This effect can have consequences for both transport on larger scales and surface growth in geological systems. We investigate the (i) impact of the Debye length λ_{D} (which characterises the extent of the electric double layer, see section 3.3), relative to the fracture aperture d, and (ii) the additional impact of the undulation amplitude on the flow channeling. The steady-state Stokes–Poisson–Nernst–Planck equations are solved using a hybrid algorithm similar to that proposed by Mitscha-Baude et al.[309]. The algorithm combines a Picard iteration scheme in an outer loop, splitting between the Stokes and the Poisson–Nernst–Planck subproblems. Here, the solver alternates between a linear solver for the linear Stokes problem, and a nonlinear solver for the Poisson–Nernst–Planck problem, which uses a Newton method in an inner loop. The method is detailed in the paper, and the problem is solved using FEniCS, with preconditioning using FENAPACK[55]. To quantify the flow channeling relative to the reference case of vanishing Debye length, we define the *relative asymmetry* (Eq. (29) in the paper). We find that compared to the case without surface charge, the flux can be reduced in the narrowest regions by up to 5%, and locally up to 10% velocity can be observed. Thus ridges may be more prone to precipitation than valleys, leading to even more pronounced channeling.

In Paper 5, we consider modelling of transient single-phase electrohydrodynamic flow. The model is derived by considering the single-phase electrohydrodynamic energy functional similar to that stated in eq. (3.49):


FIGURE 5.4: Sketch of the model microfracture or pore, wherein electrohydrody-namic channeling effects are studied. Reprinted from[58].

$$\mathscr{F} = \int_{\Omega} \left[\tfrac{1}{2}\rho|\mathbf{u}|^2 + \sum_{j=1}^{N} M_j + \tfrac{1}{2}\epsilon|\mathbf{E}|^2 - \rho\mathbf{x}\cdot\mathbf{a}_{\mathrm{grav}} \right]. \tag{5.17}$$

(a) $t = 3.0$, $\sigma_e = 0$

(b) $t = 3.0$, $\sigma_e = -10$

(c) $t = 6.0$, $\sigma_e = 0$

(d) $t = 6.0$, $\sigma_e = -10$

(e) $t = 9.0$, $\sigma_e = 0$

(f) $t = 9.0$, $\sigma_e = -10$
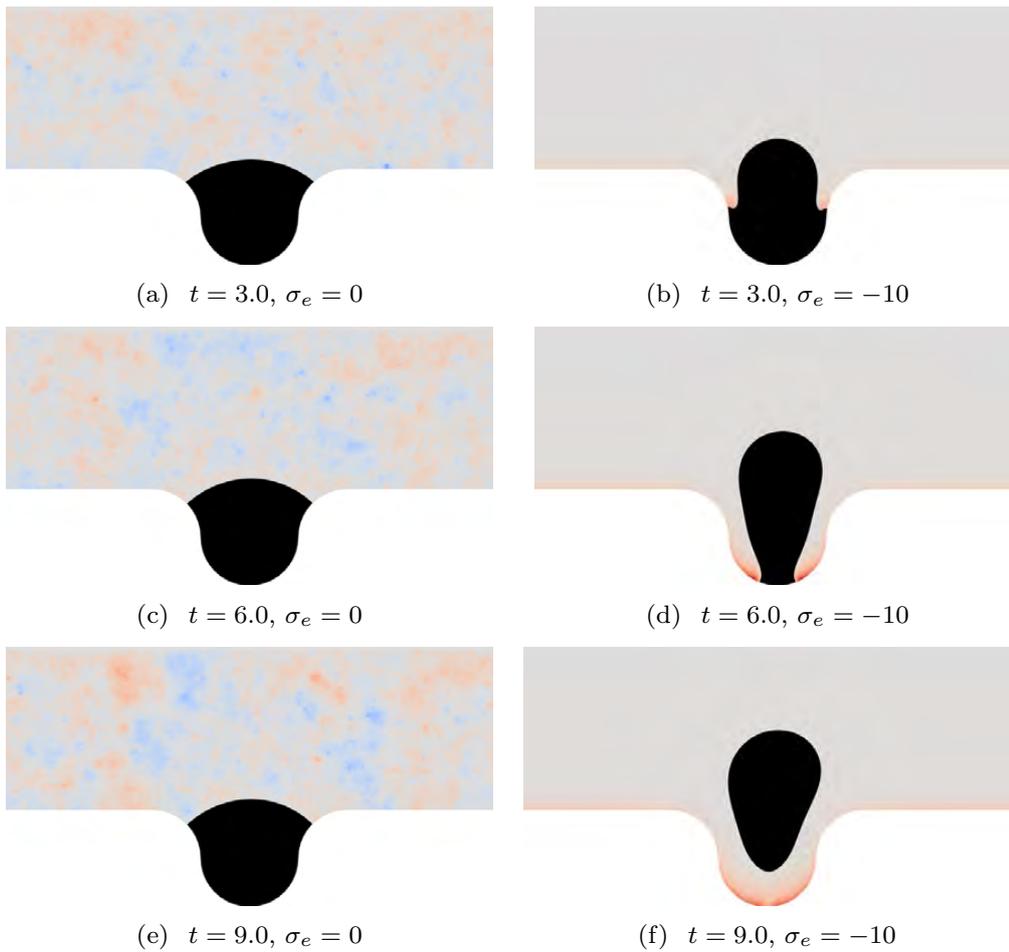
FIGURE 5.5: Snapshots of simulations of a dead-end pore under a shear flow. The black phase ("oil") does not contain solutes, and the other phase ("water") contains a symmetric monovalent electrolyte. The color indicates net charge, red is positive and blue is negative. The left column shows a simulation without surface charge (and hence only numerical noise can be seen of the charge field), while the right columns shows a simulation *with* surface charge. Reprinted from [263].

Here, the added last term represents gravitational energy, and M_j is a generalized chemical energy. In contrast to the modelling in section 3.3, fluid parameters such as density, permittivity, and viscosity, are allowed to depend on the concentration fields, and we allow for chemical reactions to occur. We determine the chemical fluxes and the induced body force by using the Onsager variational principle in a similar way as in Refs. [2,79]. For the resulting model, we propose a set of energy-stable numerical schemes, similar to the more general scheme presented in section 4.2. The numerical schemes are implemented in BERNAISE, and validated in the last part of the paper.

In Paper 6, we present BERNAISE, which was already described in section 4.4.3, a framework for simulating two-phase electrohydrodynamics in complex geometries. The literature and background for the modelling approach is introduced in the first part of the paper. The basic model [79] is then presented, whereupon we present two numerical schemes: (i) a fully implicit scheme, and (ii) an alternative linear, decoupled scheme which splits the problem into three subproblems, as outlined in section 4.2. The latter scheme is validated through numerical simulations. First, the convergence of the scheme towards the theoretical profile of the phase-field interface is verified in both space and time. While, to our knowledge, no analytical reference solutions are available for dynamical simulations of two-phase electrohydrodynamics with soluble species, phase-field models can (in contrast to sharp-interface models) provide such solutions if augmented by appropriate source terms. This is known as the *method of manufactured solution*, which constitutes a powerful tool for validating numerical implementations. To this end, we present an electrohydrodynamic Taylor–Green vortex to address the temporal and spatial convergence, and find satisfactory convergence results. Finally,

(a) $t = 0.0$ (b) $t = 0.25$ (c) $t = 0.5$ (d) $t = 0.75$ (e) $t = 1.0$ (f) $t = 1.25$ (g) $t = 1.5$

(h) $t = 1.75$ (i) $t = 2.0$ (j) $t = 2.25$ (k) $t = 2.5$ (l) $t = 2.75$ (m) $t = 3.0$ (n) $t = 4.0$
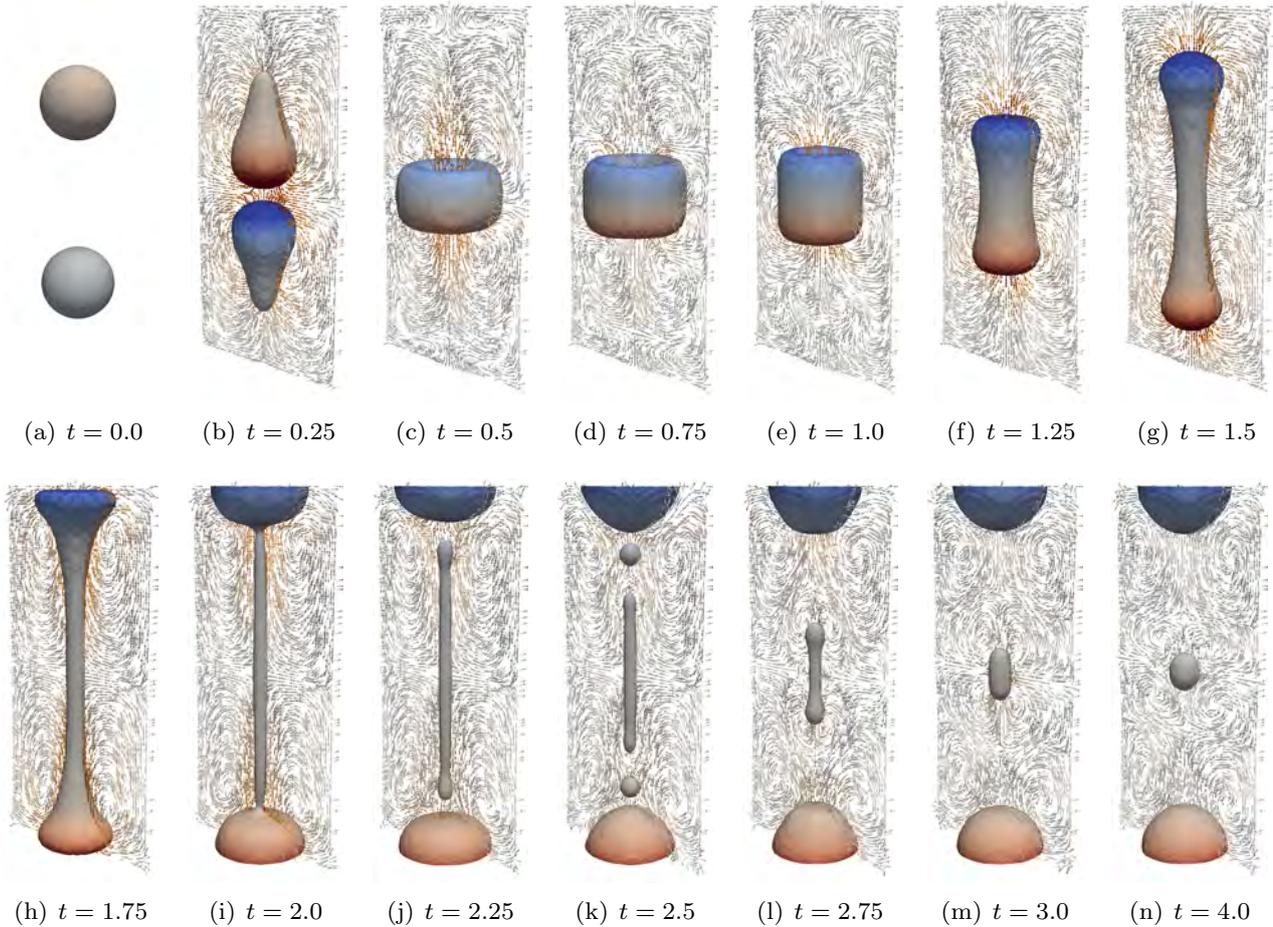
FIGURE 5.6: Coalescence and break-up of charged droplets, simulated using BERNAISE. Reprinted from [263].

convergence from the solution of the equations with finite interface thickness ε to the sharp-interface description in the limit $\varepsilon \to 0^+$ is verified by comparison to a high-resolotion reference solution. In a final part, we demonstrate two possible applications of the framework. First, we consider the expulsion of a droplet of one phase ("oil") which is placed in a dead-end pore, where another phase ("water") flows above. This should be a familiar set-up for readers who still remember section 1.2.

As shown in fig. 5.5, with shear flow and without any electrohydrodynamic effects, the droplet is stuck in the pore. By including electrohydrodynamic effects, a thin film of water is drawn into the pore and expels the oil droplet from the pore and releases it in the bulk flow. Although the parameter values used in the simulations are not real values, the results indicate that such a minimal model of electrochemical interactions at the pore scale can be a contributing factor to the enhanced oil recovery observed when injecting water of a particular salinity into porous rocks (see e.g. [145,179,192,382]). Secondly, we demonstrate that the code can be applied to studying droplet breakup and coalescence in full 3D, as shown in fig. 5.6.

In Paper 2, we quantitatively inspect the wetting properties of a single droplet of one phase sitting on an electrode, surrounded by a second phase. A potential drop is imposed across the system, and changes the wetting properties of the droplet, i.e. the contact angle. This set-up is fairly well-studied in terms of conducting liquids and relatively strong fields, in the context of electrowetting-on-dielectric (EWOD) devices. Here, we consider weak fields and a dissolved binary electrolyte in the surrounding fluid. We also consider an insulated electrode where no net current is allowed to pass through the system. Important theoretical progress in describing this system was achieved by Monroe

et al. [314,315], who used non-linear Poisson–Boltzmann theory to obtained an expression for the total Gibbs free energy of a so-called ITIES[38] system. They assumed that the Debye length was small enough to assume that one-dimensional back-to-back distributions could describe the chemical and potential distributions (and for the contact line region to be neglected), and by an energy minimization they obtained an expression for the dependence of the *apparent* contact angle (see section 2.1.3) on the applied potential and system parameters. In this work, we propose a heuristic generalization (or simplification) of the latter theory to concern a pure droplet phase. Dynamical simulations carried out using BERNAISE for a range of realistic parameters indicate that the theory well describes the apparent contact angle, and allows us to fit the only phenomenological dependence that appears in the theoretical description. From the simulations, we deduce an effective boundary condition that can be used in simulations on a larger scale, where the electric double layer is not fully resolved.

[38] Interface between TWO Immiscible Electrolyte solutions; where no ions can cross the fluid-fluid interface.

CONTRIBUTIONS   In the first paper, all authors took part in designing the study. The numerical program used to carry out most of the simulations was written by Bolet, with input from me. Bolet performed most of the simulations, and I constructed the meshes, performed complementary simulations and theory, and contributed in discussions.

The remaining papers were written mainly be me. The topics studied in the papers are results of discussions with Bolet, who also wrote some sections in the last paper, and performed some of the code validation. Both Bolet and Mathiesen contributed with discussions and feedback on the manuscripts.

FIGURE 5.7: Theory and application of homogenized two-phase flow models. (a) The hiererarchy of non-equilibrium two-phase flow models; reprinted from [259]. (b) Flow regimes in a CO_2 injection well during a blow-out scenario; reprinted from [260].
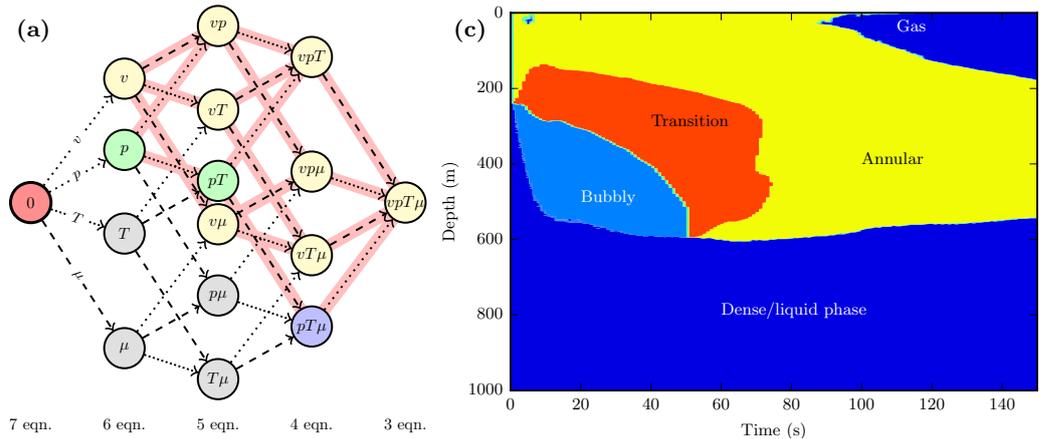
5.4 HOMOGENIZED MODELS FOR TWO-PHASE FLOW

PAPER 8: A hierarchy of non-equilibrium two-phase flow models
Gaute Linga and Tore Flåtten
Submitted to *ESAIM: Proceedings & Surveys* (2018).

PAPER 9: A two-fluid model for vertical flow applied to CO_2 injection wells
Gaute Linga and Halvor Lund
International Journal of Greenhouse Gas Control **51**, 71–80 (2016)

These two papers concern homogenized models for two-phase flow, which are typically applied to pipe flow. Flåtten presented paper 8 at the Workshop on Compressible Multiphase Flows: Derivation, closure laws, thermodynamics, Strasbourg, May 2018. Most of the work forming the basis of this section was carried out before starting the PhD project, but the papers were completed during the course the period.

In Paper 8, we start out with the Baer–Nunziato model[24], and consider the relaxation processes discussed in section 3.2.3. From this, we can derive a hierarchy of relaxation models for two-phase flow with equilibrium in one or more of the variables pressure, temperature, chemical potential, and velocity. We review the resulting hierarchy, derive the remaining models and provide expressions for the sound velocities of the models.[39] In the context of two-phase flow models, the subcharacteristic condition implies that the fluid-mechanical speed of sound is reduced by every equilibrium assumption. We show, using simple techniques, that this condition is everywhere respected in the hierarchy, in the analytically tractable limit of equal phase velocities. This analytical result is supported numerically by plots of the model speeds of sound for the entire hierarchy, using data from two industrially relevant two-phase mixtures.

[39] *That is, in the limit of instantaneously equal phase velocities, which makes the eigenstructure analytically tractable*

Paper 9 is of a more applied nature, and concerns modelling and simulation of two-phase flow in an injection well for CO_2. The model, which assumes equilibrium in pressure, temperature and chemical potential, incorporates correlations for interface friction, wall friction and heat condition based on flow regimes (see section 2.1.3), and employs the accurate industrial Span–Wagner equation of state for CO_2[417]. We apply the model to studying sudden blowout and shut-in cases, in a well configuration chosen to resemble the Sleipner CO_2 injection well. The model is simulated numerically using a finite volume method detailed in the paper.

CONTRIBUTIONS   The first paper was written by me, and I carried out the analysis. Flåtten contributed in designing the research, contributed in discussions, gave comments on the manuscript, and verified the analysis.

The second paper was written jointly with Lund. Both authors took part in development and implementation of the model and method, running simulations and writing of the paper.

CLOSING REMARKS

6

It is now time to revisit the blunt question asked in the opening lines of the introduction: How does fluid flow through rocks? Although it is apparent that this question touches upon many scientific disciplines, and poses neither a *single* nor a *simple* answer, the author is of the opinion that some insights have been provided through the work presented in this thesis. Perhaps more importantly, the results provided lay the foundations for ensuing research that could potentially continue in many directions.

The unifying theme has been numerically resolving fluid flows with disordered interfaces. In one aspect, fluid flows near complex solid boundaries, i.e. fluid-solid interfaces, have been considered, spanning from laminar flow in an evolving porous medium, through high-Reynolds number flows in rough model fractures, to electrohydrodynamic flow over charged surfaces. Another aspect concerns the propagation of turbulent–laminar interfaces, i.e. turbulent fronts. A third aspect is the concurrent motion of fluid–fluid interfaces, which has been investigated also in the presence of electrohydrodynamic effects. Although these interfacial flows are governed by inherently different mechanisms, where the role of inertia and the time scale of interface motion varies strongly, the theory describing them, and the tools used to explore them, bear many similarities.

In this work, the research output has been threefold: We have contributed with (i) physical modelling, (ii) development of numerical methods and tools, and (iii) applications of the developed models and methods.

In the part of the work concerning single-phase transitional flow, we have developed a model that could help resolve the conundrum regarding Pomeau's hypothesis on the universality class of the transition to turbulence in pipe flow. Also in fracture flow, the laminar–turbulent transition was investigated. Here, the friction factor was found to be sensitive to the roughness, leading to unsteady transitional flow accompanying the departure from linear friction. By numerically investigating the solid stress due to flow in a porous rock under dissolution, we observed a heavy-tailed distribution that could be useful to explaining how sensitive rocks are to slight increases in loading or fluid pressure.

In the part of the work concerning two-phase and electrohydrodynamic flows, multiple flow phenomena have been considered. This includes a numerical investigation of flow channeling in microfractures, wetting behaviour of droplets subject to electric fields, modelling of flow with concentration-dependent fluid properties, an analysis of a hierarchy of homogenized two-phase flow models, and modelling and simulation of a CO_2 injection well. Numerical methods that could provide efficient and robust simulations of electrohydrodynamic and interfacial flows have been developed.

Finally, and perhaps most prominently, the BERNAISE framework for simulating two-phase electrohydrodynamic flow has been developed and documented. It is our hope that this framework can be of use not only for studying geophysically relevant settings, but also to be a useful tool to the microfluidics community, where many researchers rely on using proprietary (and to some extent *black-box*) software.

6.1 OUTLOOK

Having experienced the ups and downs of a project with a broad focus, it has occurred to me that project management and planning skills might be underrated assets in (at least some parts of) academia. An optimum of scientific quality and productivity—relative to the workload—would, in the author's opinion, be obtained with a narrower focus and more rigid planning. On the other hand, perfect is the enemy of good. The broad scope (and the accompanying heavy workload) has, at least for the author, opened connections between topics that would otherwise seem less apparent.

It is my sincere hope that the work contained in this thesis will be helpful to others. In the following, I give some suggestions for avenues of future research, particularly with emphasis on the limitations of the present work.

TRULY EVOLVING MICROSTRUCTURE: With regard to the work presented in Papers 2 and 3, on single-phase flow in disordered geometries, it would be a natural step onwards to abondon the *one-way coupling* from the solid to fluid phase. The solid phase, and thus the accessible space for the fluid, would then deform due to fluid motion. This could occur due to dissolution or precipitation processes, either including a thermodynamic description, or along the lines of Hawkins et al.[181,182], where the solid grows proportionally to a concentration gradient. A part of the author's stay at the University of Oslo was dedicated to developing a phase-field model for interface evolution incorporating solid stress into the thermodynamic description. This essentially couples an Asaro–Tiller–Grinfeld instability (see e.g.[228,229]) to fluid flow. Evolving the microstructure by a sharp-interface method[17,18,338] would also be a possibility. However, precipitation kinetics becomes harder to model, since the precipitated solid need not inherit the state of stress from the solid it is precipitated onto; see e.g.[127] for a relevant discussion on crystal growth in confinement. A simpler approach is that taken by Jäger et al.[213,214] where interface evolution is driven by deposition and erosion depending on the tangential shear force.

FLOW AND STRESS DISTRIBUTIONS: A limitation of the work presented in Paper 2 is that it is unclear whether the results can be extrapolated to other rocks, and to other deformation mechanisms than dissolution. A different mechanism of deformation would be fracturing of a rock, and an investigation of flow and stress evolution is underway in collaboration with François Renard at the University of Oslo.

Another open question concerns the observed "universal" stretched-exponential or power-exponential distribution of velocity[293] in porous media, and how much information about the pore geometry is necessary to predict the velocity (and stress) distribution. It seems likely that the 'distance' (in porosity) from the percolation threshold might determine the range of power-law scaling. Moreover, the effects on the distributions of wall slip, which could be important at the nanoscale[31], and inertia, which could be important at larger scales, remain, to the author's knowledge, open questions.

PHASE-FIELD MODELLING: The phase-field modelling considered herein, and the related numerics, could be improved in many ways. Although fairly complicated (at least in terms of number of fields and equations), the model in the state presented in the current thesis, constitutes an idealised representation of electrohydrodynamics. Real systems are usually dirty. As such, many possibly important effects have been neglected in the present work, including electrochemical reactions at the fluid-solid interface, thermal gradients, surfactants or other large molecules at the fluid-fluid interface (which could imply elastic effects[137]), and boundary inhomogeneities, to name a few. It would therefore be important to properly benchmark the models against experiments and/or

ab initio simulations. (It was briefly outlined in section 3.4.2 how to include surfactants, but no proper testing of this has yet been done.)

Another avenue would be to extend the model, with and without electrohydrodynamics, to encompassing more than two fluid phases. It is possible that augmenting the three-phase model by Minjeaud[305] with electrohydrodynamics is not particularly challenging, but extending that formulation to more than three phases (even without electrohydrodynamics) is known to be a non-trivial task. It could also be useful for simulation of many relevant systems, to let the third phase be a solid phase, such that interface evolution with two fluid phases could be simulated. By evolving the solid interface, one should then be able model electrodeposition[338] in the single-phase limit; relevant phase-field modelling approaches can be found in Refs.[181,182,473].

NUMERICAL METHODS: The general scheme for two-phase electrohydrodynamics was presented and shown to be energy stable in section 4.2 and should thus provide robust solutions without energy blow-up. However, it is possible that these schemes introduce *too much* dissipation, i.e. that they require unecessarily fine mesh and small time steps to reproduce the continuum equations. Another point in question is whether phase-field models (with finite interface thickness) in themselves may be overly dissipative compared to the sharp-interface equations which they are meant to represent. In particular, a critical evaluation of (i) which weighted averages should be used for the fluid properties across the interface, and (ii) how to model the phase-field mobility, should be carried out.

A limitation of the schemes presented here is that they are only first-order in time. It would be desirable to obtain higher-order temporal accuracy, and as shown e.g. in[403], it is easy to construct schemes that are *formally* second-order using a backward differencing formula (BDF). However, it has not yet been possible to construct second-order schemes with the desired energy stability.

Finally, the solvers implemented in BERNAISE could be optimized heavily, especially in terms of reusing system matrices along the lines of ref.[320] and in particular ref.[119], possibly in combination with the Picard iteration scheme outlined in section 4.2.

HEAT AND SOLUTE TRANSPORT: In the spirit of e.g.[333–335], it would be interesting both from a fundamental and a geothermal engineering point of view to extend investigate heat transfer both in 3D and to higher Re flows, particularly in fractures. This would, as a first approximation, amount to a one-way coupling of incompressible fluid flow to a *passive* scalar temperature field (much like how a passive concentration field is described herein). The natural first investigative steps would then be to seek the dependence of the Nusselt number, Nu (which measures the ratio of convective to conductive heat transfer), on the Reynolds number Re.

Another topic, which has drawn much attention both by the author, collaborators and others, is that of passive tracer transport in disordered media. In contrast to the concentration *fields* described previously in this thesis, we are here concerned with ensembles of particles advected solely by the velocity field $\mathbf{u}$ (not by diffusion), similar to how tracer statistics is studied in turbulence. Early efforts on simplified models were reviewed by Bouchaud and Georges[63], while the recent access to high-fidelity simulation tools and high-resolution tomography data of natural rocks has revived the subject and complemented the early models with direct simulations in a variety of real and synthetic porous geometries. The displacement of particles has been observed to be superdiffusive (in the direction of forcing) and subdiffusive (in the direction normal to forcing), see e.g.[199,226,246,275]. This is closely connected to the wide distribution of velocities in such geometries, as manifested in the Eulerian velicity PDFs. In 2D (synthetic) and 3D (synthetic and natural) systems, continuous-time random walks have

provided a framework for describing such transport[158]. While homogeneous porous media is well understood[254–256,256], less is certain for dense and heterogeneous porous media, in particular close to the percolation point. However, as a numerical velocity field is only approximately divergence free, simulations in such geometries cause the problems that passive tracers can be spuriously 'adsorbed' to the boundary. This is particularly relevant for very narrow pore throats, and raises doubts about the validity of the results of e.g. Kang et al.[226]. As a first step, numerical solvers must be properly tested against pore network models, where quasi-analytical reference solutions can be found. Our prelimary results were reported in[186], but are omitted here.

Solute transport in fractures has also been studied[122], but many unanswered questions remain. In this respect, it would be interesting to study solute transport in 3D self-affine fractures at higher Re; in particular, can the results of Bouquain et al.[64] be generalized or extended to such geometries?

TURBULENT FRONTS IN ROUGH PIPES: As mentioned in section 2.1.2, flow in rough pipes has been extensively investigated in the fully turbulent regime, and transitional flows in smooth pipes have been studied for many years. However, little work has concerned the intersection of these two often separate areas—transitional flow in rough pipes—even though both roughness and transitional flows may appear in the context of blood flow in our bodies[238]. A reason for this being uncharted territory might be that it is extremely challenging to numerically resolve turbulent flow in large domains in the presence of complex boundaries, as spectral methods are not easily applicable to these settings (see section 4.1.2). Numerically, even lifetime statistics of puffs, at least close to criticality, may be out of reach for direct numerical simulations. It would therefore be a natural first step to investigate the speeds of turbulent fronts of single puffs and slugs in rough pipes, similar to the smooth-pipe study by Barkley et al.[30]. In this respect, the experiments by Cerbus et al.[87], who essentially measured the friction factor of single puffs and slugs, would be interesting to compare with.

SPATIO-TEMPORAL TRANSITION TO TURBULENCE: The Barkley model[28–30] has provided great qualitative insight into the transition to turbulence in pipe flow. Moreover, it can also *quantitatively* describe most features of the spatio-temporal dynamics near the transition. However, this relies on fitting a set of model parameters to resemble the observations from experiments or direct numerical simulations. As discussed by Barkley[29], a first-principles derivation of a macroscopic model (Barkley model or similar) for the transition is still lacking. The 'holy grail' is to predict, for example, front speeds from the Navier–Stokes equations. Another point to add, is the lack of an equivalent of the Barkley model for e.g. plane Poiseuille flow, which could help in understanding off-critical transitional flow in that system.

In this work, we studied transitional flow in fractures, but as demonstrated e.g. in Paper 1, the *really interesting* dynamics occurs in the study of collective motion of turbulent structures. By considering ensembles of large systems, thus, one might be able to investigate whether adding a 'quenched randomness' such as boundary roughness (possibly different from self-affine) may push shear flows out of the directed-percolation universality class.[40]

Investigations in this direction are already underway. Notably, the direct numerical simulation study by Ishida et al.[206] with transitional flow in the presence of several types of (effectively modelled) roughness displayed a richer phase diagram (in terms of flow regimes) than what has been observed for smooth-walled transitional flow. For large systems, however, computations are incredibly demanding. It is likely that the approach mainly taken in this project; involving unstructured meshes (explicitly representing

[40] Similar to how adding a quenched noise to the Kardar–Parisi–Zhang equation[227] changes its universality class[231].

the boundary) and using the finite element method, is *not* the way to proceed for large systems. Instead, spectral methods on structured grids which *effectively* incorporate the rough boundary as a body force (see [77,206]) would likely lead to significant computational speedup.

APPLICATIONS OF BERNAISE: The simulation framework developed in this project enables many possible applications, one of which being electrowetting, as shown in Paper [264] [264]. Another interesting application could be to study phase separation kinetics (spinodal decomposition) in the presence of an electric field; related to the original motivation of Hohenberg and Halperin [196] to introduce their 'Model H' phase-field model. Droplet motion, coalescence, break-up, and pinch-off, particularly in the presence of solid surfaces and electrokinetic effects, would all provide interesting studies. Such effects are now possible to simulate efficiently in full 3D, in contrast to earlier studies which have often been limited to axisymmetric geometries; cf. [43] and related publications. Finally, we hope that, in time (and with possibly more validation, testing, and incorporation of necessary additional features), the framework could be used by the microfluidics community for prototyping and optimizing lab-on-a-chip devices.

BIBLIOGRAPHY

[1] U. J. F. Aarsnes, T. Flåtten, and O. M. Aamo. Review of two-phase flow models for control and estimation. *Annu. Rev. Control*, 42:50–62, 2016. doi: 10.1016/j.arcontrol.2016.06.001.

[2] H. Abels, H. Garcke, and G. Grün. Thermodynamically consistent, frame indifferent diffuse interface models for incompressible two-phase flows with different densities. *Math. Models Methods Appl. Sci.*, 22(03):1150013, 2012. doi: 10.1142/S0218202511500138.

[3] H. Abels, H. Garcke, K. F. Lam, and J. Weber. Two-phase flow with surfactants: Diffuse interface models and their analysis. In *Transport Processes at Fluidic Interfaces*, pages 255–270. Springer, 2017.

[4] S. Aland. Phase field models for two-phase flow with surfactants and biomembranes. In *Transport Processes at Fluidic Interfaces*, pages 271–290. Springer, 2017.

[5] S. Aland and F. Chen. An efficient and energy stable scheme for a phase-field model for the moving contact line problem. *Int. J. Numer. Methods Fluids*, 81(11):657–671, 2016. doi: 10.1002/fld.4200.

[6] S. Aland, S. Boden, A. Hahn, F. Klingbeil, M. Weismann, and S. Weller. Quantitative comparison of Taylor flow simulations based on sharp-interface and diffuse-interface models. *Int. J. Numer. Methods Fluids*, 73(4):344–361, 2013. doi: 10.1002/fld.3802.

[7] S. Aland, A. Hahn, C. Kahle, and R. Nürnberg. Comparative simulations of Taylor flow with surfactants based on sharp-and diffuse-interface methods. In *Transport Processes at Fluidic Interfaces*, pages 639–661. Springer, 2017.

[8] R. Allan and S. Mason. Particle behaviour in shear and electric fields I. Deformation and burst of fluid drops. *Proc. Royal Soc. A*, 267(1328):45–61, 1962. doi: 10.1098/rspa.1962.0082.

[9] J. Allen, M. Shockling, G. Kunkel, and A. Smits. Turbulent flow in smooth and rough pipes. *Philos. Trans. R. Soc. A*, 365(1852):699–714, 2007. doi: 10.1098/rsta.2006.1939.

[10] M. S. Alnæs, A. Logg, K. B. Ølgaard, M. E. Rognes, and G. N. Wells. Unified form language: A domain-specific language for weak formulations of partial differential equations. *ACM Trans. Math. Softw.*, 40(2):9, 2014. doi: 10.1145/2566630.

[11] M. S. Alnæs, G. N. Wells, and J. Ring. Dijitso: Github repository. https://bitbucket.org/fenics-project/dijitso/, 2018.

[12] C. B. Amos, P. Audet, W. C. Hammond, R. Bürgmann, I. A. Johanson, and G. Blewitt. Uplift and seismicity driven by groundwater depletion in central California. *Nature*, 509(7501):483, 2014. doi: 10.1038/nature13275.

[13] D. M. Anderson, G. B. McFadden, and A. A. Wheeler. Diffuse-interface methods in fluid mechanics. *Annu. Rev. Fluid Mech.*, 30(1):139–165, 1998. doi: 10.1146/annurev.fluid.30.1.139.

[14] H. Andrä, N. Combaret, J. Dvorkin, E. Glatt, J. Han, M. Kabel, Y. Keehm, F. Krzikalla, M. Lee, C. Madonna, et al. Digital rock physics benchmarks – Part II: Computing effective properties. *Comput. Geosci.*, 50:33–43, 2013. doi: 10.1016/j.cageo.2012.09.008.

[15] J. Andrade Jr, M. Almeida, J. Mendes Filho, S. Havlin, B. Suki, and H. Stanley. Fluid flow through porous media: the role of stagnant zones. *Phys. Rev. Lett.*, 79(20):3901, 1997. doi: 10.1103/PhysRevLett.79.3901.

[16] J. Andrade Jr, U. Costa, M. Almeida, H. Makse, and H. Stanley. Inertial effects on fluid flow through disordered porous media. *Phys. Rev. Lett.*, 82(26):5249, 1999. doi: 10.1103/PhysRevLett.82.5249.

[17] L. Angheluta, E. Jettestuen, J. Mathiesen, F. Renard, and B. Jamtveit. Stress-driven phase transformation and the roughening of solid-solid interfaces. *Phys. Rev. Lett.*, 100(9):096105, 2008. doi: 10.1103/PhysRevLett.100.096105.

[18] L. Angheluta, E. Jettestuen, and J. Mathiesen. Thermodynamics and roughening of solid-solid interfaces. *Phys. Rev. E*, 79(3):031601, 2009. doi: 10.1103/PhysRevE.79.031601.

[19] D. N. Arnold and A. Logg. Periodic table of the finite elements. *SIAM News*, 47(9):212, 2014.

[20] C. H. Arns, M. A. Knackstedt, W. V. Pinczewski, and E. J. Garboczi. Computation of linear elastic properties from microtomographic images: Methodology and agreement between theory and experiment. *Geophysics*, 67(5):1396–1405, 2002. doi: 10.1190/1.1512785.

[21] C. Arson and T. Vanorio. Chemomechanical evolution of pore space in carbonate microstructures upon dissolution: Linking pore geometry to bulk elasticity. *J. Geophys. Res. Solid Earth*, 120(10): 6878–6894, 2015. doi: 10.1002/2015JB012087.

[22] H. Auradou, G. Drazer, J.-P. Hulin, and J. Koplik. Permeability anisotropy induced by the shear displacement of rough fracture walls. *Water Resour. Res.*, 41(9):W09423, 2005. doi: 10.1029/2005WR003938.

[23] K. Avila, D. Moxey, A. de Lozar, M. Avila, D. Barkley, and B. Hof. The onset of turbulence in pipe flow. *Science*, 333(6039):192–196, 2011. doi: 10.1126/science.1203223.

[24] M. Baer and J. Nunziato. A two-phase mixture theory for the deflagration-to-detonation transition (DDT) in reactive granular materials. *Int. J. Multiph. Flow*, 12(6):861–889, 1986. doi: 10.1016/0301-9322(86)90033-9.

[25] S. Balay, S. Abhyankar, M. F. Adams, J. Brown, P. Brune, K. Buschelman, L. Dalcin, V. Eijkhout, W. D. Gropp, D. Kaushik, M. G. Knepley, D. A. May, L. C. McInnes, K. Rupp, B. F. Smith, S. Zampini, H. Zhang, and H. Zhang. PETSc web page. http://www.mcs.anl.gov/petsc, 2017. URL http://www.mcs.anl.gov/petsc.

[26] A.-L. Barabási and H. E. Stanley. *Fractal concepts in surface growth.* Cambridge University Press, 1995.

[27] A. J. Bard and L. R. Faulkner. *Electrochemical methods: fundamentals and applications*, volume 2. Wiley, New York, 2 edition, 2001.

[28] D. Barkley. Simplifying the complexity of pipe flow. *Phys. Rev. E*, 84(1):016309, 2011. doi: 10.1103/PhysRevE.84.016309.

[29] D. Barkley. Theoretical perspective on the route to turbulence in a pipe. *J. Fluid Mech.*, 803:P1, 2016. doi: 10.1017/jfm.2016.465.

[30] D. Barkley, B. Song, V. Mukund, G. Lemoult, M. Avila, and B. Hof. The rise of fully turbulent flow. *Nature*, 526:550–553, 2015. doi: 10.1038/nature15701.

[31] J.-L. Barrat and L. Bocquet. Large slip effect at a nonwetting fluid-solid interface. *Phys. Rev. Lett.*, 82 (23):4671, 1999. doi: 10.1103/PhysRevLett.82.4671.

[32] J. Baygents and D. Saville. The circulation produced in a drop by an electric field: a high field strength electrokinetic model. In *AIP Conf. Proc.*, volume 197, pages 7–17. AIP, 1990.

[33] M. Z. Bazant. Electrokinetics meets electrohydrodynamics. *J. Fluid Mech.*, 782:1–4, 2015. doi: 10.1017/jfm.2015.416.

[34] M. Z. Bazant, K. Thornton, and A. Ajdari. Diffuse-charge dynamics in electrochemical systems. *Phys. Rev. E*, 70(2):021506, 2004. doi: 10.1103/PhysRevE.70.021506.

[35] D. Beamish and R. Peart. Electrokinetic geophysics: a review. *Terra Nova*, 10(1):48–55, 1998. doi: 10.1046/j.1365-3121.1998.00160.x.

[36] J. Bear, C.-F. Tsang, and G. De Marsily. *Flow and contaminant transport in fractured rock.* Academic Press, 1993.

[37] G. Beni and S. Hackwood. Electro-wetting displays. *Appl. Phys. Lett.*, 38(4):207–209, 1981. doi: 10.1063/1.92322.

[38] G. Beni and M. Tenan. Dynamics of electrowetting displays. *J. Appl. Phys.*, 52(10):6011–6015, 1981. doi: 10.1063/1.329822.

[39] B. Berge. Electrocapillarité et mouillage de films isolants par l'eau. *C. R. Acad. Sci. IIB*, 317(2):157–163, 1993.

[40] B. Berkowitz. Characterizing flow and transport in fractured geological media: A review. *Adv. Water Resour.*, 25(8-12):861–884, 2002. doi: 10.1016/S0309-1708(02)00042-8.

[41] Y. Bernabé and A. Revil. Pore-scale heterogeneity, energy dissipation and the transport properties of rocks. *Geophys. Res. Lett.*, 22(12):1529–1532, 1995. doi: 10.1029/95GL01418.

[42] I. Berre, F. Doster, and E. Keilegavlen. Flow in fractured porous media: A review of conceptual models and discretization approaches. arXiv:1805.05701, 2018.

[43] J. Berry, M. Davidson, and D. J. Harvie. A multiphase electrokinetic flow model for electrolytes with liquid/liquid interfaces. *J. Comput. Phys.*, 251:209–222, 2013. doi: 10.1016/j.jcp.2013.05.026.

[44] E. Bertrand, D. Bonn, D. Broseta, H. Dobbs, J. Indekeu, J. Meunier, K. Ragil, and N. Shahidzadeh. Wetting of alkanes on water. *J. Pet. Sci. Eng.*, 33(1-3):217–222, 2002. doi: 10.1016/S0920-4105(01)00191-7.

[45] E. Besterman and R. Creese. Waller–pioneer of electrocardiography. *Br. Heart J.*, 42(1):61, 1979.

[46] D. Bestion. The physical closure laws in the cathare code. *Nuclear Engineering and Design*, 124(3): 229–245, 1990. doi: 10.1016/0029-5493(90)90294-8.

[47] B. Bijeljic, A. H. Muggeridge, and M. J. Blunt. Pore-scale modeling of longitudinal dispersion. *Water Resour. Res.*, 40(11), 2004. doi: 10.1029/2004WR003567.

[48] B. Bijeljic, A. Raeini, P. Mostaghimi, and M. J. Blunt. Predictions of non-fickian solute transport in different classes of porous media using direct simulation on pore-scale images. *Phys. Rev. E*, 87(1): 013011, 2013. doi: 10.1103/PhysRevE.87.013011.

[49] M. A. Biot. General theory of three-dimensional consolidation. *J. Appl. Phys.*, 12(2):155–164, 1941. doi: 10.1063/1.1712886.

[50] M. A. Biot. Theory of elasticity and consolidation for a porous anisotropic solid. *J. Appl. Phys.*, 26(2): 182–185, 1955. doi: 10.1063/1.1721956.

[51] M. A. Biot. Theory of propagation of elastic waves in a fluid-saturated porous solid. I. Low frequency range. *J. Acoust. Soc. Am.*, 28(2):168–178, 1956. doi: 10.1121/1.1908239.

[52] M. A. Biot. Theory of propagation of elastic waves in a fluid-saturated porous solid. II. Higher frequency range. *J. Acoust. Soc. Am.*, 28(2):179–191, 1956. doi: 10.1121/1.1908241.

[53] E. Bjørklund. The level-set method applied to droplet dynamics in the presence of an electric field. *Comput. Fluids*, 38(2):358–369, 2009. doi: 10.1016/j.compfluid.2008.04.008.

[54] T. Blake and J. Haynes. Kinetics of liquid-liquid displacement. *J. Colloid Interface Sci.*, 30(3):421–423, 1969. doi: 10.1016/0021-9797(69)90411-1.

[55] J. Blechta and M. Řehoř. Fenapack. https://github.com/blechta/fenapack, 2018.

[56] M. J. Blunt, B. Bijeljic, H. Dong, O. Gharbi, S. Iglauer, P. Mostaghimi, A. Paluszny, and C. Pentland. Pore-scale imaging and modelling. *Adv. Water Resour.*, 51:197–216, 2013. doi: 10.1016/j.advwatres.2012.03.003.

[57] A. Bolet. *Electrohydrodynamics in one and two phases*. PhD thesis, Niels Bohr Institute, University of Copenhagen, 2018.

[58] A. Bolet, G. Linga, and J. Mathiesen. Electrohydrodynamic channeling effects in narrow fractures and pores. *Phys. Rev. E*, 97:043114, 2018. doi: 10.1103/PhysRevE.97.043114.

[59] D. Bonamy, L. Ponson, S. Prades, E. Bouchaud, and C. Guillot. Scaling exponents for fracture surfaces in homogeneous glass and glassy ceramics. *Phys. Rev. Lett.*, 97(13):135504, 2006. doi: 10.1103/PhysRevLett.97.135504.

[60] D. Bonn, J. Eggers, J. Indekeu, J. Meunier, and E. Rolley. Wetting and spreading. *Rev. Mod. Phys.*, 81 (2):739, 2009. doi: 10.1103/RevModPhys.81.739.

[61] E. Bouchaud. Scaling properties of cracks. *J. Phys. Condens. Matter*, 9(21):4319, 1997. doi: 10.1088/0953-8984/9/21/002.

[62] E. Bouchaud, G. Lapasset, and J. Planes. Fractal dimension of fractured surfaces: a universal value? *Europhys. Lett.*, 13(1):73, 1990. doi: 10.1209/0295-5075/13/1/013.

[63] J.-P. Bouchaud and A. Georges. Anomalous diffusion in disordered media: statistical mechanisms, models and physical applications. *Phys. Rep.*, 195(4-5):127–293, 1990. doi: 10.1016/0370-1573(90)90099-N.

[64] J. Bouquain, Y. Méheust, D. Bolster, and P. Davy. The impact of inertial effects on solute dispersion in a channel with periodically varying aperture. *Phys. Fluids*, 24(8):083602, 2012. doi: 10.1063/1.4747458.

[65] BP. BP Statistical Review of World Energy 2017, 2017.

[66] J. Brackbill, D. B. Kothe, and C. Zemach. A continuum method for modeling surface tension. *J. Comput. Phys.*, 100(2):335–354, 1992. doi: 10.1016/0021-9991(92)90240-Y.

[67] S. C. Brenner and L. R. Scott. *The Mathematical Theory of Finite Element Methods*. Springer Science & Business Media, 3 edition, 2008.

[68] F. Brezzi. On the existence, uniqueness and approximation of saddle-point problems arising from Lagrangian multipliers. *R.A.I.R.O. Analyse Numérique*, 8(R2):129–151, 1974. doi: 10.1051/m2an/197408R201291.

[69] S. Briggs, B. W. Karney, and B. E. Sleep. Numerical modeling of the effects of roughness on flow and eddy formation in fractures. *J. Rock Mech. Geotechnical Eng.*, 9(1):105–115, 2017. doi: 10.1016/j.jrmge.2016.08.004.

[70] S. R. Broadbent and J. M. Hammersley. Percolation processes: I. Crystals and mazes. In *Math. Proc. Camb. Philos. Soc.*, volume 53, pages 629–641. Cambridge University Press, 1957.

[71] G. O. Brown. The history of the Darcy–Weisbach equation for pipe flow resistance. In *Environmental and Water Resources History*, pages 34–43. American Society of Civil Engineers, 2003.

[72] S. R. Brown. Fluid flow through rock joints: the effect of surface roughness. *J. Geophys. Res. Solid Earth*, 92(B2):1337–1347, 1987. doi: 10.1029/JB092iB02p01337.

[73] D. J. Brush and N. R. Thomson. Fluid flow in synthetic rough-walled fractures: Navier–Stokes, Stokes, and local cubic law simulations. *Water Resour. Res.*, 39(4):SBH, 2003. doi: 10.1029/2002WR001346.

[74] H. Bruus. *Theoretical microfluidics*, volume 18. Oxford University Press, 2008.

[75] J. B. Buckheit and D. L. Donoho. Wavelab and reproducible research. In *Wavelets and statistics*, pages 55–81. Springer, 1995.

[76] T. Bultreys, W. De Boever, and V. Cnudde. Imaging and image-based fluid transport modeling at the pore scale in geological materials: A practical introduction to the current state-of-the-art. *Earth-Sci. Rev.*, 155:93–128, 2016. doi: 10.1016/j.earscirev.2016.02.001.

[77] A. Busse and N. D. Sandham. Parametric forcing approach to rough-wall turbulent channel flow. *J. Fluid Mech.*, 712:169–202, 2012. doi: 10.1017/jfm.2012.408.

[78] J. W. Cahn and J. E. Hilliard. Free energy of a nonuniform system. I. interfacial free energy. *J. Chem. Phys.*, 28(2):258–267, 1958. doi: 10.1063/1.1744102.

[79] E. Campillo-Funollet, G. Grün, and F. Klingbeil. On modeling and simulation of electrokinetic phenomena in two-phase flow with general mass densities. *SIAM J. Appl. Math.*, 72(6):1899–1925, 2012. doi: 10.1137/120861333.

[80] M. B. Cardenas, D. T. Slottke, R. A. Ketcham, and J. M. Sharp. Effects of inertia and directionality on flow and transport in a rough asymmetric fracture. *J. Geophys. Res. Solid Earth*, 114(B6), 2009. doi: 10.1029/2009JB006336.

[81] A. Carlson. *Capillarity and dynamic wetting.* PhD thesis, KTH Royal Institute of Technology, 2012.

[82] A. Carlson, M. Do-Quang, and G. Amberg. Modeling of dynamic wetting far from equilibrium. *Phys. Fluids*, 21(12):121701, 2009. doi: 10.1063/1.3275853.

[83] A. Carlson, G. Bellani, and G. Amberg. Universality in dynamic wetting dominated by contact-line friction. *Phys. Rev. E*, 85(4):045302, 2012. doi: 10.1103/PhysRevE.85.045302.

[84] P. C. Carman. Fluid flow through granular beds. *Trans. Inst. Chem. Eng.*, 15:150–166, 1937. doi: 10.1016/S0263-8762(97)80003-2.

[85] P. C. Carman. *Flow of gases through porous media.* Academic Press, 1956.

[86] CDP. CDP: the Unstructured LES Code. https://web.stanford.edu/group/cits/research/combustor/cdp. html, 2004.

[87] R. T. Cerbus, C.-c. Liu, G. Gioia, and P. Chakraborty. Laws of resistance in transitional pipe flows. *Phys. Rev. Lett.*, 120(5):054502, 2018. doi: 10.1103/PhysRevLett.120.054502.

[88] H.-C. Chang and L. Y. Yeo. *Electrokinetically driven microfluidics and nanofluidics.* Cambridge University Press, 2010.

[89] M. Chantry, L. S. Tuckerman, and D. Barkley. Universal continuous transition to turbulence in a planar shear flow. *J. Fluid Mech.*, 824:R1, 2017. doi: 10.1017/jfm.2017.405.

[90] D. L. Chapman. A contribution to the theory of electrocapillarity. *Philos. Mag.*, 25(148):475–481, 1913. doi: 10.1080/14786440408634187.

[91] R.-C. Chen and J.-L. Liu. An iterative method for adaptive finite element solutions of an energy transport model of semiconductor devices. *J. Comput. Phys.*, 189(2):579–606, 2003. doi: 10.1016/S0021-9991(03)00247-X.

[92] A. J. Chorin. A numerical method for solving incompressible viscous flow problems. *J. Comput. Phys.*, 2(1):12–26, 1967. doi: 10.1016/0021-9991(67)90037-X.

[93] A. J. Chorin. Numerical solution of the Navier–Stokes equations. *Math. Comp.*, 22(104):745–762, 1968. doi: 10.1090/S0025-5718-1968-0242392-2.

[94] T. Chou, K. Mallick, and R. Zia. Non-equilibrium statistical mechanics: from a paradigmatic model to biological transport. *Rep. Prog. Phys.*, 74(11):116601, 2011. doi: 10.1088/0034-4885/74/11/116601.

[95] A. Clauset, C. R. Shalizi, and M. E. Newman. Power-law distributions in empirical data. *SIAM Rev.*, 51 (4):661–703, 2009. doi: 10.1137/070710111.

[96] C. Colebrook and C. White. Experiments with fluid friction in roughened pipes. *Proc. Royal Soc. A*, 161(906):367–381, 1937. doi: 10.1098/rspa.1937.0150.

[97] D. Coles. Interfaces and intermittency in turbulent shear flow. *Mécanique de la Turbulence*, 108: 229–248, 1962.

[98] J. Cooper, L. Stamford, and A. Azapagic. Shale gas: a review of the economic, environmental, and social sustainability. *Energy Technology*, 4(7):772–792, 2016. doi: 10.1002/ente.201500464.

[99] A. Costa. Permeability-porosity relationship: A reexamination of the Kozeny–Carman equation based on a fractal pore-space geometry assumption. *Geophys. Res. Lett.*, 33(2):L02318, 2006. doi: 10.1029/2005GL025134.

[100] F. G. Cottrell and J. B. Speed. Separating and collecting particles of one liquid suspended in another liquid, 1911. US Patent 987, 115.

[101] R. Cox. The dynamics of the spreading of liquids on a solid surface. Part 1. Viscous flow. *J. Fluid Mech.*, 168:169–194, 1986. doi: 10.1017/S0022112086000332.

[102] A. D. Craik. George Gabriel Stokes on water wave theory. *Annu. Rev. Fluid Mech.*, 37:23–42, 2005. doi: 10.1146/annurev.fluid.37.061903.175836.

[103] E. Custodio. Trends in groundwater pollution: loss of groundwater quality and related services. Technical report, Groundwater Governance, 2013.

[104] T. J. Danielson. Transient multiphase flow: past, present, and future with flow assurance perspective. *Energy Fuels*, 26(7):4137–4144, 2012. doi: 10.1021/ef300300u.

[105] A. Darbyshire and T. Mullin. Transition to turbulence in constant-mass-flux pipe flow. *J. Fluid Mech.*, 289:83–114, 1995. doi: 10.1017/S0022112095001248.

[106] H. Darcy. *Les fontaines publiques de la ville de Dijon.* Victor Dalmont, Paris, 1856.

[107] H. Darcy. *Recherches expérimentales relatives au mouvement de l'eau dans les tuyaux*, volume 1. Mallet-Bachelier, 1857.

[108] S. S. Datta, H. Chiang, T. S. Ramakrishnan, and D. A. Weitz. Spatial fluctuations of fluid velocities in flow through a three-dimensional porous medium. *Phys. Rev. Lett.*, 111:064501, Aug 2013. doi: 10.1103/PhysRevLett.111.064501.

[109] C. David, T.-F. Wong, W. Zhu, and J. Zhang. Laboratory measurement of compaction-induced permeability change in porous rocks: Implications for the generation and maintenance of pore pressure excess in the crust. *Pure. Appl. Geophys.*, 143(1-3):425–456, 1994. doi: 10.1007/BF00874337.

[110] P. de Anna, T. Le Borgne, M. Dentz, A. M. Tartakovsky, D. Bolster, and P. Davy. Flow intermittency, dispersion, and correlated continuous time random walks in porous media. *Phys. Rev. Lett.*, 110(18): 184502, 2013. doi: 10.1103/PhysRevLett.110.184502.

[111] R. de Boer. Highlights in the historical development of the porous media theory: toward a consistent macroscopic theory. *Appl. Mech. Rev.*, 49(4):201–262, 1996. doi: 10.1115/1.3101926.

[112] J. A. de Chalendar, C. Garing, and S. M. Benson. Pore-scale modelling of Ostwald ripening. *J. Fluid Mech.*, 835:363–392, 2018. doi: 10.1017/jfm.2017.720.

[113] P.-G. de Gennes. Wetting: statics and dynamics. *Rev. Mod. Phys.*, 57(3):827, 1985. doi: 10.1103/RevModPhys.57.827.

[114] I. E. M. de Graaf. *Limits to global groundwater consumption: Effects on groundwater levels and river low flows.* PhD thesis, Utrecht University, 2016.

[115] P. Debye and E. Hückel. Zur theorie der elektrolyte. I. Gefrierpunktserniedrigung und verwandte erscheinungen. *Phyz. Z.*, 24(9):185–206, 1923.

[116] P. Debye and E. Hückel. Zur theorie der elektrolyte. II. Das grenzgesetz für die elektrische leitfähigkeit. *Phyz. Z.*, 24(9):185–206, 1923.

[117] A. Delesse. Procede mecanique pour determiner la composition des roches. *Ann. Min.*, 13:379–388, 1848.

[118] H. Ding, P. D. Spelt, and C. Shu. Diffuse interface model for incompressible two-phase flows with large density ratios. *J. Comput. Phys.*, 226(2):2078–2095, 2007. doi: 10.1016/j.jcp.2007.06.028.

[119] S. Dong and J. Shen. A time-stepping scheme involving constant coefficient matrices for phase-field simulations of two-phase incompressible flows with large density ratios. *J. Comput. Phys.*, 231(17): 5788–5804, 2012. doi: 10.1016/j.jcp.2012.04.041.

[120] J. Douglas Jr and T. Arbogast. Dual porosity models for flow in naturally fractured reservoirs. In *Dynamics of Fluids in Hierarchical Porous Media*, pages 177–221. Academic Press London, UK, 1990.

[121] G. Drazer and J. Koplik. Permeability of self-affine rough fractures. *Phys. Rev. E*, 62(6):8076, 2000. doi: 10.1103/PhysRevE.62.8076.

[122] G. Drazer and J. Koplik. Transport in rough self-affine fractures. *Phys. Rev. E*, 66(2):026303, 2002. doi: 10.1103/PhysRevE.66.026303.

[123] D. A. Drew. Mathematical modeling of two-phase flow. *Annu. Rev. Fluid Mech.*, 15(1):261–291, 1983. doi: 10.1146/annurev.fl.15.010183.001401.

[124] D. A. Drew and S. L. Passman. *Theory of multicomponent fluids*, volume 135. Springer, 2006.

[125] W. Durham and B. Bonner. Self-propping and fluid flow in slightly offset joints at high effective pressures. *J. Geophys. Res. Solid Earth*, 99(B5):9391–9399, 1994. doi: 10.1029/94JB00242.

[126] E. Dussan. On the spreading of liquids on solid surfaces: static and dynamic contact lines. *Annu. Rev. Fluid Mech.*, 11(1):371–400, 1979. doi: 10.1146/annurev.fl.11.010179.002103.

[127] D. K. Dysthe. Shaping the interface – interactions between confined water and the confining solid. In *Transport and Reactivity of Solutions in Confined Hydrosystems*, pages 199–212. Springer, 2014.

[128] C. Eck, M. Fontelos, G. Grün, F. Klingbeil, and O. Vantzos. On a phase-field model for electrowetting. *Interface Free Bound.*, 11(2):259–290, 2009. doi: 10.4171/IFB/211.

[129] M. Eckert. The troublesome birth of hydrodynamic stability theory: Sommerfeld and the turbulence problem. *Eur. Phys. J. H*, 35(1):29–51, 2010. doi: 10.1140/epjh/e2010-00003-3.

[130] D. Edwards, M. Shapiro, P. Bar-Yoseph, and M. Shapira. The influence of Reynolds number upon the apparent permeability of spatially periodic arrays of cylinders. *Phys. Fluids A*, 2(1):45–55, 1990. doi: 10.1063/1.857691.

[131] S. Ehrenberg, G. Eberli, M. Keramati, and S. Moallemi. Porosity-permeability relationships in inter-layered limestone-dolostone reservoirs. *AAPG Bulletin*, 90(1):91–114, 2006. doi: 10.1306/08100505087.

[132] H. C. Elman, D. J. Silvester, and A. J. Wathen. *Finite elements and fast iterative solvers: with applications in incompressible fluid dynamics.* Numerical Mathematics and Scientific Computation, 2014.

[133] S. Engblom, M. Do-Quang, G. Amberg, and A.-K. Tornberg. On diffuse interface modeling and simulation of surfactants in two-phase fluid flow. *Commun. Comput. Phys.*, 14(4):879–915, 2013. doi: 10.4208/cicp.120712.281212a.

[134] S. Ergun. Fluid flow through packed columns. *Chem. Eng. Prog.*, 48:89–94, 1952.

[135] Å. Ervik. *Multiscale modelling using molecular dynamics and interfacecapturing methods for two-phase flow simulation of droplets covered with surfactants or asphaltenes, and applications to electrocoalescence.* PhD thesis, NTNU, 2016.

[136] Å. Ervik, K. Y. Lervåg, and S. T. Munkejord. A robust method for calculating interface curvature and normal vectors using an extracted local level set. *J. Comput. Phys.*, 257:259–277, 2014. doi: 10.1016/j.jcp.2013.09.053.

[137] Å. Ervik, M. O. Lysgaard, C. Herdes, G. Jim'enez-Serratos, E. A. Müller, S. T. Munkejord, and B. Müller. A multiscale method for simulating fluid interfaces covered with large molecules such as asphaltenes. *J. Comput. Phys.*, 327:576 – 611, 2016. doi: 10.1016/j.jcp.2016.09.039.

[138] L. Euler. Principe generaux de l'etat d'equilibre des fluides. *Mémoires de l'Académie des Sciences de Berlin*, pages 217–273, 1757.

[139] L. Euler. Anleitung zur naturlehre. *Opera postuma mathematica et physica, Bd*, pages 1–2, 1762.

[140] L. Euler. *Lettres a une princesse d'Allemagne sur divers subject de physique et de philosophie.* St. Petersbourg: Imprimerie de l'Academie Imperiale des Sciences, 1768.

[141] European Commission. Horizon 2020, work programme 2017–2018, 2017.

[142] R. D. Falgout and U. M. Yang. hypre: A library of high performance preconditioners. In *International Conference on Computational Science*, pages 632–641. Springer, 2002.

[143] Q. Fang and D. A. Boas. Tetrahedral mesh generation from volumetric binary and grayscale images. In *Biomedical Imaging: From Nano to Macro, 2009. ISBI'09. IEEE International Symposium on*, pages 1142–1145. IEEE, 2009.

[144] J. T. Fanning. *A Practical Treatise on Water-supply Engineering: Relating to the Hydrology, Hydrodynamics, and Practical Construction of Water-works, in North America. With Numerous Tables and Illustrations.* D. Van Nostrand, 1877.

[145] S. J. Fathi, T. Austad, and S. Strand. "Smart water" as a wettability modifier in chalk: the effect of salinity and ionic composition. *Energy Fuels*, 24(4):2514–2519, 2010. doi: 10.1021/ef901304m.

[146] J. Feder. *Fractals.* Springer, 2013.

[147] A. Fernández, G. Tryggvason, J. Che, and S. L. Ceccio. The effects of electrostatic forces on the distribution of drops in a channel flow: Two-dimensional oblate drops. *Phys. Fluids*, 17(9):093302, 2005. doi: 10.1063/1.2043147.

[148] P. J. M. Ferrer, T. Flåtten, and S. T. Munkejord. On the effect of temperature and velocity relaxation in two-phase flow models. *ESAIM Math. Model. Numer. Anal.*, 46(2):411–442, 2012. doi: 10.1051/m2an/2011039.

[149] A. Fick. Ueber diffusion. *Ann. Phys.*, 170(1):59–86, 1855. doi: 10.1002/andp.18551700105.

[150] E.-A. Fiorentino, R. Toussaint, and L. Jouniaux. Lattice Boltzmann modelling of streaming potentials: variations with salinity in monophasic conditions. *Geophys. J. Int.*, 205(1):648–664, 2016. doi: 10.1093/gji/ggw041.

[151] E.-A. Fiorentino, R. Toussaint, and L. Jouniaux. Two-phase lattice Boltzmann modelling of streaming potentials: influence of the air-water interface on the electrokinetic coupling. *Geophys. J. Int.*, 208(2): 1139–1156, 2016. doi: 10.1093/gji/ggw417.

[152] P. Fischer, J. Kruse, J. Mullen, H. Tufo, J. Lottes, and S. Kerkemeier. Nek5000. https://nek5000.mcs.anl.gov/community/, 2018.

[153] T. Flåtten and H. Lund. Relaxation two-phase flow models and the subcharacteristic condition. *Math. Models Methods Appl. Sci.*, 21(12):2379–2407, 2011. doi: 10.1142/S0218202511005775.

[154] H. Fletcher. My work with Millikan on the oil-drop experiment. *Physics Today*, 35(6):43–47, 1982. doi: 10.1063/1.2915126.

[155] P. J. Flory. Molecular size distribution in three dimensional polymers. I. Gelation. *J. Am. Chem. Soc.*, 63(11):3083–3090, 1941. doi: 10.1021/ja01856a061.

[156] P. H. Forchheimer. Wasserbewegung durch boden. *Zeitz. Ver. Duetch Ing.*, 45:1782–1788, 1901.

[157] M. Fourar, G. Radilla, R. Lenormand, and C. Moyne. On the non-linear behavior of a laminar single-phase flow through two and three-dimensional porous media. *Adv. Water Resour.*, 27(6):669–677, 2004. doi: 10.1016/j.advwatres.2004.02.021.

[158] I. Fouxon and M. Holzner. Solvable continuous-time random walk model of the motion of tracer particles through porous media. *Phys. Rev. E*, 94(2):022132, 2016. doi: 10.1103/PhysRevE.94.022132.

[159] A. C. Fowler and A. C. Fowler. *Mathematical models in the applied sciences*, volume 17. Cambridge University Press, 1997.

[160] A. Frumkin, A. Gorodetskaya, B. Kabanov, and N. Nekrasov. Electrocapillary phenomena and the wetting of metals by electrolytic solutions, i. *I. Phys Z. Sowjetunion*, 1:255–339, 1932.

[161] H. Garcke, K. F. Lam, and B. Stinner. Diffuse interface modelling of soluble surfactants in two-phase flow. arXiv:1303.2559, 2013.

[162] J. W. Gibbs. A method of geometrical representation of the thermodynamic properties by means of surfaces. *Trans. Conn. Acad. Arts Sci.*, pages 382–404, 1873.

[163] R. Gill, M. J. Harbottle, J. Smith, and S. Thornton. Electrokinetic-enhanced bioremediation of organic contaminants: A review of processes and environmental applications. *Chemosphere*, 107:31–42, 2014. doi: 10.1016/j.chemosphere.2014.03.019.

[164] N. Goldenfeld. Roughness-induced critical phenomena in a turbulent flow. *Phys. Rev. Lett.*, 96(4): 044503, 2006. doi: 10.1103/PhysRevLett.96.044503.

[165] N. Goldenfeld and H.-Y. Shih. Turbulence as a problem in non-equilibrium statistical mechanics. *J. Stat. Phys.*, 167:575–594, 2017. doi: 10.1007/s10955-016-1682-x.

[166] N. Goldenfeld, N. Guttenberg, and G. Gioia. Extreme fluctuations and the finite lifetime of the turbulent state. *Phys. Rev. E*, 81(3):035304, 2010. doi: 10.1103/PhysRevE.81.035304.

[167] L. G. Gouy. Sur la constitution de la charge électrique à la surface d'un électrolyte. *C. R. Hebdo. Seances Acad. Sci.*, 149:354–357, 1909.

[168] L. G. Gouy. Sur la constitution de la charge électrique à la surface d'un électrolyte. *J. Phys. Theor. Appl.*, 9(1):457–468, 1910. doi: 10.1051/jphystap:019100090045700.

[169] D. C. Grahame. The electrical double layer and the theory of electrocapillarity. *Chem. Rev.*, 41(3): 441–501, 1947. doi: 10.1021/cr60130a002.

[170] P. Grassberger. On phase transitions in Schlögl's second model. *Z. Phys. B*, 47(4):365–374, 1982. doi: 10.1007/BF01313803.

[171] J.-P. Gratier, P. Favreau, and F. Renard. Modeling fluid transfer along California faults when integrating pressure solution crack sealing and compaction processes. *J. Geophys. Res. Solid Earth*, 108(B2):2104, 2003. doi: 10.1029/2001JB000380.

[172] P. M. Gresho and R. L. Sani. *Incompressible flow and the finite element method.* John Wiley & Sons, 1998.

[173] Y. Guglielmi, F. Cappa, J. P. Avouac, P. Henry, and D. Elsworth. Seismicity triggered by fluid injection-induced aseismic slip. *Science*, 348:1224–1226, 2015. doi: 10.1126/science.aab0476.

[174] I. Gunnarsson and S. Arnórsson. Impact of silica scaling on the efficiency of heat extraction from high-temperature geothermal fluids. *Geothermics*, 34(3):320–329, 2005. doi: 10.1016/j.geothermics.2005.02.002.

[175] R. Gutfraind and A. Hansen. Study of fracture permeability using lattice gas automata. *Transp. Porous Media*, 18(2):131–149, 1995. doi: 10.1007/BF01064675.

[176] R. A. Guyer and H. A. Kim. Theoretical model for fluid-solid coupling in porous materials. *Phys. Rev. E*, 91(4):042406, 2015. doi: 10.1103/PhysRevE.91.042406.

[177] G. Hagen. Ueber die bewegung des wassers in engen cylindrischen röhren. *Ann. Phys.*, 122(3):423–442, 1839.

[178] F. H. Harlow and J. E. Welch. Numerical calculation of time-dependent viscous incompressible flow of fluid with free surface. *Phys. Fluids*, 8(12):2182–2189, 1965. doi: 10.1063/1.1761178.

[179] T. Hassenkam, C. S. Pedersen, K. Dalby, T. Austad, and S. L. S. Stipp. Pore scale observation of low salinity effects on outcrop and oil reservoir sandstone. *Colloids Surf. A*, 390(1):179–188, 2011. doi: 10.1016/j.colsurfa.2011.09.025.

[180] F. Hauksbee. *Physico-mechanical Experiments on Various Subjects: Containing an Account of Several Surprizing Phaenomena Touching Light and Electricity, Producible on the Attrition of Bodies. With Many Other Remarkable Appearances, Not Before Observ'd. Together with the Explanations of All the Machines,(the Figures of which are Curiously Engrav'd on Copper) and Other Apparatus Us'd in Making the Experiments.* R. Brugis, 1709.

[181] C. Hawkins, L. Angheluta, Ø. Hammer, and B. Jamtveit. Precipitation dendrites in channel flow. *Europhys. Lett.*, 102(5):54001, 2013. doi: 10.1209/0295-5075/102/54001.

[182] C. Hawkins, L. Angheluta, and B. Jamtveit. Hydrodynamic shadowing effect during precipitation of dendrites in channel flow. *Phys. Rev. E*, 89(2):022402, 2014. doi: 10.1103/PhysRevE.89.022402.

[183] R. A. Hayes and B. J. Feenstra. Video-speed electronic paper based on electrowetting. *Nature*, 425 (6956):383, 2003. doi: 10.1038/nature01988.

[184] D. Helbing. Traffic and related self-driven many-particle systems. *Rev. Mod. Phys.*, 73(4):1067, 2001. doi: 10.1103/RevModPhys.73.1067.

[185] C. H. Hendon. Brewing a great cup of coffee depends on chemistry and physics. The Conversation. https://theconversation.com/brewing-a-great-cup-of-coffee-depends-on-chemistry-and-physics-84473, 2017.

[186] A. Hernandez-Garcia. *Numerical simulations and mathematical models of flows in complex geometries.* PhD thesis, Niels Bohr Institute, University of Copenhagen, 2016.

[187] M. A. Heroux, R. A. Bartlett, V. E. Howle, R. J. Hoekstra, J. J. Hu, T. G. Kolda, R. B. Lehoucq, K. R. Long, R. P. Pawlowski, E. T. Phipps, et al. An overview of the Trilinos project. *ACM Trans. Math. Softw.*, 31(3):397–423, 2005. doi: 10.1145/1089014.1089021.

[188] M. R. Hestenes and E. Stiefel. *Methods of conjugate gradients for solving linear systems*, volume 49. NBS Washington, DC, 1952.

[189] D. R. Hewitt, J. S. Nijjer, M. G. Worster, and J. A. Neufeld. Flow-induced compaction of a deformable porous medium. *Phys. Rev. E*, 93(2):023116, 2016. doi: 10.1103/PhysRevE.93.023116.

[190] R. J. Hill, D. L. Koch, and A. J. Ladd. The first effects of fluid inertia on flows in ordered and random arrays of spheres. *J. Fluid Mech.*, 448:213–241, 2001. doi: 10.1017/S0022112001005936.

[191] R. J. Hill, D. L. Koch, and A. J. Ladd. Moderate-Reynolds-number flows in ordered and random arrays of spheres. *J. Fluid Mech.*, 448:243–278, 2001. doi: 10.1017/S0022112001005936.

[192] E. Hilner, M. P. Andersson, T. Hassenkam, J. Matthiesen, P. Salino, and S. L. S. Stipp. The effect of ionic strength on oil adhesion in sandstone – the search for the low salinity mechanism. *Sci. Rep.*, 5: 9933, 2015. doi: 10.1038/srep09933.

[193] H. Hinrichsen. Non-equilibrium critical phenomena and phase transitions into absorbing states. *Adv. Phys.*, 49(7):815–958, 2000. doi: 10.1080/00018730050198152.

[194] H. Hinrichsen. On possible experimental realizations of directed percolation. *Braz. J. Phys.*, 30(1): 69–82, 2000. doi: 10.1590/S0103-97332000000100007.

[195] B. Hof, A. De Lozar, M. Avila, X. Tu, and T. M. Schneider. Eliminating turbulence in spatially intermittent flows. *Science*, 327(5972):1491–1494, 2010. doi: 10.1126/science.1186091.

[196] P. C. Hohenberg and B. I. Halperin. Theory of dynamic critical phenomena. *Rev. Mod. Phys.*, 49(3): 435, 1977. doi: 10.1103/RevModPhys.49.435.

[197] H. Holmås. *Numerical simulation of waves in two-phase pipe flow using 1D two-fluid models*. PhD thesis, Faculty of Mathematics and Natural Sciences, University of Oslo, 2008.

[198] K. E. Holter, B. Kehlet, A. Devor, T. J. Sejnowski, A. M. Dale, S. W. Omholt, O. P. Ottersen, E. A. Nagelhus, K.-A. Mardal, and K. H. Pettersen. Interstitial solute transport in 3D reconstructed neuropil occurs by diffusion rather than bulk flow. *Proc. Natl. Acad. Sci.*, 114(37):9894–9899, 2017. doi: 10.1073/pnas.1706942114.

[199] M. Holzner, V. L. Morales, M. Willmann, and M. Dentz. Intermittent Lagrangian velocities and accelerations in three-dimensional porous medium flow. *Phys. Rev. E*, 92(1):013015, 2015. doi: 10.1103/PhysRevE.92.013015.

[200] J.-J. Huang, H. Huang, and X. Wang. Wetting boundary conditions in numerical simulation of binary fluids by using phase-field method: some comparative studies and new development. *Int. J. Numer. Methods Fluids*, 77(3):123–158, 2015. doi: 10.1002/fld.3975.

[201] C. Huh and L. Scriven. Hydrodynamic model of steady movement of a solid/liquid/fluid contact line. *J. Colloid Interface Sci.*, 35(1):85–101, 1971. doi: 10.1016/0021-9797(71)90188-3.

[202] M. Hultmark, M. Vallikivi, S. Bailey, and A. Smits. Turbulent pipe flow at extreme Reynolds numbers. *Phys. Rev. Lett.*, 108(9):094501, 2012. doi: 10.1103/PhysRevLett.108.094501.

[203] H. E. Huppert and J. A. Neufeld. The fluid mechanics of carbon dioxide sequestration. *Annu. Rev. Fluid Mech.*, 46:255–272, 2014. doi: 10.1146/annurev-fluid-011212-140627.

[204] IEA. Energy technology perspectives 2014, 2014.

[205] T. Ihle and D. Kroll. Stochastic rotation dynamics: a Galilean-invariant mesoscopic model for fluid flow. *Phys. Rev. E*, 63(2):020201, 2001. doi: 10.1103/PhysRevE.63.020201.

[206] T. Ishida, G. Brethouwer, Y. Duguet, and T. Tsukahara. Laminar-turbulent patterns with rough walls. *Phys. Rev. Fluids*, 2(7):073901, 2017. doi: 10.1103/PhysRevFluids.2.073901.

[207] T. Ishido and H. Mizutani. Experimental and theoretical basis of electrokinetic phenomena in rock-water systems and its applications to geophysics. *J. Geophys. Res. Solid Earth*, 86(B3):1763–1775, 1981. doi: 10.1029/JB086iB03p01763.

[208] M. Ishii and T. Hibiki. *Thermo-fluid dynamics of two-phase flow*. Springer, 2010.

[209] S. Izbash. O filtracii v kropnozernstom materiale. Leningrad, USSR, 1931.

[210] J. Jackel, S. Hackwood, and G. Beni. Electrowetting optical switch. *Appl. Phys. Lett.*, 40(1):4–5, 1982. doi: 10.1063/1.92920.

[211] D. Jacqmin. Calculation of two-phase Navier–Stokes flows using phase-field modeling. *J. Comput. Phys.*, 155(1):96–127, 1999. doi: 10.1006/jcph.1999.6332.

[212] D. Jacqmin. Contact-line dynamics of a diffuse fluid interface. *J. Fluid Mech.*, 402:57–88, 2000. doi: 10.1017/S0022112099006874.

[213] R. Jäger, M. Mendoza, and H. J. Herrmann. Channelization in porous media driven by erosion and deposition. *Phys. Rev. E*, 95(1):013110, 2017. doi: 10.1103/PhysRevE.95.013110.

[214] R. Jäger, M. Mendoza, and H. J. Herrmann. Mechanism behind erosive bursts in porous media. *Phys. Rev. Lett.*, 119(12):124501, 2017. doi: 10.1103/PhysRevLett.119.124501.

[215] B. Jamtveit and Ø. Hammer. Sculpting of rocks by reactive fluids. *Geochem. Perspect.*, 1:341–477, 2012.

[216] H.-K. Janssen. On the nonequilibrium phase transition in reaction-diffusion systems with an absorbing stationary state. *Z. Phys. B*, 42(2):151–154, 1981. doi: 10.1007/BF01319549.

[217] H. Jasak, A. Jemcov, Z. Tukovic, et al. OpenFOAM: A C++ library for complex physics simulations. In *International workshop on coupled methods in numerical dynamics*, volume 1000, pages 1–20. IUC Dubrovnik, Croatia, 2007.

[218] L. Jasinski and M. Dabrowski. The effective transmissivity of a plane-walled fracture with circular cylindrical obstacles. *J. Geophys. Res. Solid Earth*, 123(1):242–263, 2018. doi: 10.1002/2017JB014509.

[219] L. Jasinski, D. Sangaré, P. Adler, V. Mourzenko, J.-F. Thovert, N. Gland, and S. Békri. Transport properties of a Bentheim sandstone under deformation. *Phys. Rev. E*, 91(1):013304, 2015. doi: 10.1103/PhysRevE.91.013304.

[220] M. Javadi, M. Sharifzadeh, K. Shahriar, and Y. Mitani. Critical Reynolds number for nonlinear flow through rough-walled fractures: The role of shear processes. *Water Resour. Res.*, 50(2):1789–1804, 2014. doi: 10.1002/2013WR014610.

[221] I. Jensen. Low-density series expansions for directed percolation: I. a new efficient algorithm with applications to the square lattice. *Journal of Physics A: Mathematical and General*, 32(28):5233, 1999. doi: 10.1088/0305-4470/32/28/304.

[222] F. Jiang and T. Tsuji. Changes in pore geometry and relative permeability caused by carbonate precipitation in porous media. *Phys. Rev. E*, 90(5):053306, 2014. doi: 10.1103/PhysRevE.90.053306.

[223] C. Jin, P. Langston, G. Pavlovskaya, M. Hall, and S. Rigby. Statistics of highly heterogeneous flow fields confined to three-dimensional random porous media. *Phys. Rev. E*, 93(1):013122, 2016. doi: 10.1103/PhysRevE.93.013122.

[224] Y. Jin, J. Dong, X. Zhang, X. Li, and Y. Wu. Scale and size effects on fluid flow through self-affine rough fractures. *Int. J. Heat Mass Transf.*, 105:443–451, 2017. doi: 10.1016/j.ijheatmasstransfer.2016.10.010.

[225] V. Joekar-Niasar and S. Hassanizadeh. Analysis of fundamentals of two-phase flow in porous media using dynamic pore-network models: A review. *Crit. Rev. Environ. Sci. Technol.*, 42(18):1895–1976, 2012. doi: 10.1080/10643389.2011.574101.

[226] P. K. Kang, P. Anna, J. P. Nunes, B. Bijeljic, M. J. Blunt, and R. Juanes. Pore-scale intermittent velocity structure underpinning anomalous transport through 3-D porous media. *Geophys. Res. Lett.*, 41(17): 6184–6190, 2014. doi: 10.1002/2014GL061475.

[227] M. Kardar, G. Parisi, and Y.-C. Zhang. Dynamic scaling of growing interfaces. *Phys. Rev. Lett.*, 56(9): 889, 1986. doi: 10.1103/PhysRevLett.56.889.

[228] K. Kassner and C. Misbah. A phase-field approach for stress-induced instabilities. *Europhys. Lett.*, 46 (2):217, 1999. doi: 10.1209/epl/i1999-00247-9.

[229] K. Kassner, C. Misbah, J. Müller, J. Kappey, and P. Kohlert. Phase-field modeling of stress-induced instabilities. *Phys. Rev. E*, 63(3):036117, 2001. doi: 10.1103/PhysRevE.63.036117.

[230] B. Kehlet. Mshr: Git repository. https://bitbucket.org/fenics-project/mshr, 2018.

[231] D. A. Kessler, H. Levine, and Y. Tu. Interface fluctuations in random media. *Phys. Rev. A*, 43(8):4551, 1991. doi: 10.1103/PhysRevA.43.4551.

[232] J. Kim. Phase-field models for multi-component fluid flows. *Commun. Comput. Phys.*, 12(3):613–661, 2012. doi: 10.4208/cicp.301110.040811a.

[233] B. J. Kirby. *Micro-and nanoscale fluid mechanics: transport in microfluidic devices.* Cambridge University Press, 2010.

[234] R. C. Kirby. Algorithm 839: Fiat, a new paradigm for computing finite element basis functions. *ACM Trans. Math. Softw.*, 30(4):502–516, 2004. doi: 10.1145/1039813.1039820.

[235] R. C. Kirby and A. Logg. A compiler for variational forms. *ACM Trans. Math. Softw.*, 32(3):417–444, 2006. doi: 10.1145/1163641.1163644.

[236] A. Klöckner. Meshpy. https://mathema.tician.de/software/meshpy/, 2018.

[237] J. Kozeny. Uber kapillare leitung der wasser in boden. *Royal Academy of Science, Vienna, Proc. Class I*, 136:271–306, 1927.

[238] D. N. Ku. Blood flow in arteries. *Annu. Rev. Fluid Mech.*, 29(1):399–434, 1997. doi: 10.1146/annurev.fluid.29.1.399.

[239] H. Lan, C. D. Martin, and B. Hu. Effect of heterogeneity of brittle rock on micromechanical extensile behavior during compression loading. *J. Geophys. Res. Solid Earth*, 115(B1):B01202, 2010. doi: 10.1029/2009JB006496.

[240] H. P. Langtangen and A. Logg. *Solving PDEs in Python.* Springer, 2017. ISBN 978-3-319-52461-0. doi: 10.1007/978-3-319-52462-7.

[241] H. P. Langtangen, K.-A. Mardal, and R. Winther. Numerical methods for incompressible viscous flow. *Adv. Water Resour.*, 25(8–12):1125–1146, 2002. doi: 10.1016/S0309-1708(02)00052-0.

[242] P. S. Laplace. *Traité de mécanique céleste. Supplément au dixième livre*, volume 4. Crapelet, 1805.

[243] D. Lasseux, A. A. Abbasian Arani, and A. Ahmadi. On the stationary macroscopic inertial effects for one phase flow in ordered and disordered porous media. *Phys. Fluids*, 23(7):073103, 2011. doi: 10.1063/1.3615514.

[244] H. Laubie, F. Radjai, R. Pellenq, and F.-J. Ulm. Stress transmission and failure in disordered porous media. *Phys. Rev. Lett.*, 119(7):075501, 2017. doi: 10.1103/PhysRevLett.119.075501.

[245] B. Lautrup. *Physics of continuous matter: exotic and everyday phenomena in the macroscopic world.* CRC Press, 2004.

[246] T. Le Borgne, M. Dentz, and J. Carrera. Lagrangian statistical model for transport in highly heterogeneous velocity fields. *Phys. Rev. Lett.*, 101(9):090601, 2008. doi: 10.1103/PhysRevLett.101.090601.

[247] T. Le Borgne, M. Dentz, and E. Villermaux. Stretching, coalescence, and mixing in porous media. *Phys. Rev. Lett.*, 110(20):204501, 2013. doi: 10.1103/PhysRevLett.110.204501.

[248] L. Lebon, L. Oger, J. Leblond, J. Hulin, N. Martys, and L. Schwartz. Pulsed gradient NMR measurements and numerical simulation of flow velocity distribution in sphere packings. *Phys. Fluids*, 8(2):293–301, 1996. doi: 10.1063/1.869307.

[249] J. Lee and C.-J. Kim. Surface-tension-driven microactuation based on continuous electrowetting. *J. Microelectromech. Syst.*, 9(2):171–180, 2000. doi: 10.1109/84.846697.

[250] M. Lee and R. D. Moser. Direct numerical simulation of turbulent channel flow up to $Re_\tau \approx 5200$. *J. Fluid Mech.*, 774:395–415, 2015. doi: 10.1017/jfm.2015.268.

[251] L. Leger and J. Joanny. Liquid spreading. *Rep. Prog. Phys.*, 55(4):431, 1992. doi: 10.1088/0034-4885/55/4/001.

[252] G. Lemoult, L. Shi, K. Avila, S. V. Jalikop, M. Avila, and B. Hof. Directed percolation phase transition to sustained turbulence in Couette flow. *Nat. Phys.*, 12(3):254–258, 2016. doi: 10.1038/nphys3675.

[253] K. Y. Lervåg. *Calculation of interface curvatures with the level-set method for two-phase flow simulations and a second-order diffuse-domain method for elliptic problems in complex geometries.* PhD thesis, Norges teknisk-naturvitenskapelige universitet, Fakultet for ingeniørvitenskap og teknologi, Institutt for energi-og prosessteknikk, 2013.

[254] D. Lester, G. Metcalfe, and M. Trefry. Anomalous transport and chaotic advection in homogeneous porous media. *Phys. Rev. E*, 90(6):063012, 2014. doi: 10.1103/PhysRevE.90.063012.

[255] D. R. Lester, G. Metcalfe, and M. G. Trefry. Is chaotic advection inherent to porous media flow? *Phys. Rev. Lett.*, 111:174101, Oct 2013. doi: 10.1103/PhysRevLett.111.174101.

[256] D. R. Lester, M. Dentz, and T. Le Borgne. Chaotic mixing in three-dimensional porous media. *J. Fluid Mech.*, 803:144–174, 2016. doi: 10.1017/jfm.2016.486.

[257] V. G. Levich. *Physicochemical hydrodynamics.* Prentice Hall, 1962.

[258] Y. Lin, P. Skjetne, and A. Carlson. A phase field model for multiphase electro-hydrodynamic flow. *Int. J. Multiph. Flow*, 45:1–11, 2012. doi: 10.1016/j.ijmultiphaseflow.2012.04.002.

[259] G. Linga and T. Flåtten. A hierarchy of non-equilibrium two-phase flow models. arXiv:1804.05241, 2018.

[260] G. Linga and H. Lund. A two-fluid model for vertical flow applied to CO_2 injection wells. *Int. J. Greenh. Gas Con.*, 51:71–80, 2016. doi: 10.1016/j.ijggc.2016.05.009.

[261] G. Linga, J. Mathiesen, and F. Renard. Self-similar distributions of fluid velocity and stress heterogeneity in a dissolving porous limestone. *J. Geophys. Res. Solid Earth*, 122(3):1726–1743, 2017. doi: 10.1002/2016JB013536.

[262] G. Linga, L. Angheluta, and J. Mathiesen. Transitional flow in self-affine rough channels. unpublished, 2018.

[263] G. Linga, A. Bolet, and J. Mathiesen. Bernaise: A flexible framework for two-phase electrohydrodynamic flow. submitted, 2018.

[264] G. Linga, A. Bolet, and J. Mathiesen. Controlling wetting with electrolytic solutions: Phase-field simulations of a droplet-conductor system. *Phys. Rev. E*, 98:013101, 2018. doi: 10.1103/PhysRevE.98.013101.

[265] G. Linga, A. Bolet, and J. Mathiesen. Transient electrohydrodynamic flow with concentration-dependent fluid properties: modelling and energy-stable numerical schemes. submitted, 2018.

[266] H. Linga. *Measurements of two-phase flow details: non-intrusive methods applied to slug and dispersed flows.* PhD thesis, Norges Tekniske Högskole, 1992.

[267] G. Lippmann. *Relations entre les phénomènes électriques et capillaires.* PhD thesis, Sorbonne, 1875.

[268] J.-L. Liu and B. Eisenberg. Numerical methods for a Poisson–Nernst–Planck–Fermi model of biological ion channels. *Phys. Rev. E*, 92(1):012711, 2015. doi: 10.1103/PhysRevE.92.012711.

[269] T. S. Lo and J. Koplik. Suspension flow and sedimentation in self-affine fractures. *Phys. Fluids*, 24(5):053303, 2012. doi: 10.1063/1.4717529.

[270] T. S. Lo and J. Koplik. Channeling and stress during fluid and suspension flow in self-affine fractures. *Phys. Rev. E*, 89(2):023010, 2014. doi: 10.1103/PhysRevE.89.023010.

[271] D. Lo Jacono, F. Plouraboué, and A. Bergeon. Weak-inertial flow between two rough surfaces. *Phys. Fluids*, 17(6):063602, 2005. doi: 10.1063/1.1923347.

[272] A. Logg, K.-A. Mardal, and G. Wells. *Automated solution of differential equations by the finite element method: The FEniCS book*, volume 84. Springer Science & Business Media, 2012.

[273] A. Logg, G. N. Wells, and J. Hake. DOLFIN: A C++/Python finite element library. In *Automated Solution of Differential Equations by the Finite Element Method*, pages 173–225. Springer, 2012.

[274] J. López-Herrera, S. Popinet, and M. Herrada. A charge-conservative approach for simulating electrohydrodynamic two-phase flows using volume-of-fluid. *J. Comput. Phys.*, 230(5):1939–1955, 2011. doi: 10.1016/j.jcp.2010.11.042.

[275] C. P. Lowe and D. Frenkel. Do hydrodynamic dispersion coefficients exist? *Phys. Rev. Lett.*, 77:4552–4555, Nov 1996. doi: 10.1103/PhysRevLett.77.4552.

[276] J. Lowengrub and L. Truskinovsky. Quasi-incompressible Cahn–Hilliard fluids and topological transitions. *Proc. Royal Soc. A*, 454(1978):2617–2654, 1998. doi: 10.1098/rspa.1998.0273.

[277] H.-W. Lu, K. Glasner, A. Bertozzi, and C.-J. Kim. A diffuse-interface model for electrowetting drops in a hele-shaw cell. *J. Fluid Mech.*, 590:411–435, 2007. doi: 10.1017/S0022112007008154.

[278] H. Lund. A hierarchy of relaxation models for two-phase flow. *SIAM J. Appl. Math.*, 72(6):1713–1741, 2012. doi: 10.1137/12086368X.

[279] H. Lund. *Relaxation models for two-phase flow with applications to CO_2 transport.* PhD thesis, Norges teknisk-naturvitenskapelige universitet, Fakultet for ingeniørvitenskap og teknologi, Institutt for energi-og prosessteknikk, 2013.

[280] L. Lundgaard, G. Berg, S. Ingebrigtsen, and P. Atten. Electrocoalescence for oil-water separation: Fundamental aspects. In J. Sjöblom, editor, *Emulsions and emulsion stability*, pages 549–592. Taylor & Francis, 2006.

[281] R. Maex. On the Nernst–Planck equation. *J. of Integr. Neurosci.*, 16(1):73–91, 2017. doi: 10.3233/JIN-170008.

[282] B. B. Mandelbrot, D. E. Passoja, and A. J. Paullay. Fractal character of fracture surfaces of metals. *Nature*, 308(5961):721, 1984. doi: 10.1038/308721a0.

[283] P. Manneville. On the transition to turbulence of wall-bounded flows in general, and plane Couette flow in particular. *Eur. J. Mech. B Fluids*, 49:345–362, 2015. doi: 10.1016/j.euromechflu.2014.03.017.

[284] P. Manneville. Transition to turbulence in wall-bounded flows: Where do we stand? *Mechanical Engineering Reviews*, 3(2):15–00684, 2016. doi: 10.1299/mer.15-00684.

[285] P. Mansfield and B. Issa. Fluid transport in porous rocks. I. EPI studies and a stochastic model of flow. *J. Magn. Reson., Ser A*, 122(2):137 – 148, 1996. ISSN 1064-1858. doi: 10.1006/jmra.1996.0189.

[286] A. Mansouri, C. Scheuerman, S. Bhattacharjee, D. Y. Kwok, and L. W. Kostiuk. Transient streaming potential in a finite length microchannel. *J. Colloid Interface Sci.*, 292(2):567–580, 2005. doi: 10.1016/j.jcis.2005.05.094.

[287] A. Mansouri, S. Bhattacharjee, and L. W. Kostiuk. Transient electrokinetic transport in a finite length microchannel:ccurrents, capacitance, and an electrical analogy. *J. Phys. Chem. B*, 111(44):12834–12843, 2007. doi: 10.1021/jp074386c.

[288] R. Matin. *From Pore Scale to Turbulent Flow with the Unstructured Lattice Boltzmann Method.* PhD thesis, Niels Bohr Institute, University of Copenhagen, 2016.

[289] R. Matin, M. K. Misztal, A. Hernández-García, and J. Mathiesen. Evaluation of the finite element lattice Boltzmann method for binary fluid flows. *Comput. Math. Appl.*, 74(2):281–291, 2017. doi: 10.1016/j.camwa.2017.04.027.

[290] R. Matin, M. K. Misztal, A. Hernández-García, and J. Mathiesen. Finite-element lattice Boltzmann simulations of contact line dynamics. *Phys. Rev. E*, 97(1):013307, 2018. doi: 10.1103/PhysRevE.97.013307.

[291] J. M. Matter, M. Stute, S. Ó. Snæbjörnsdottir, E. H. Oelkers, S. R. Gislason, E. S. Aradottir, B. Sigfusson, I. Gunnarsson, H. Sigurdardottir, E. Gunnlaugsson, et al. Rapid carbon mineralization for permanent disposal of anthropogenic carbon dioxide emissions. *Science*, 352(6291):1312–1314, 2016. doi: 10.1126/science.aad8132.

[292] M. Matyka, A. Khalili, and Z. Koza. Tortuosity-porosity relation in porous media flow. *Phys. Rev. E*, 78(2):026306, 2008. doi: 10.1103/PhysRevE.78.026306.

[293] M. Matyka, J. Gołembiewski, and Z. Koza. Power-exponential velocity distributions in disordered porous media. *Phys. Rev. E*, 93:013110, Jan 2016. doi: 10.1103/PhysRevE.93.013110.

[294] P. Meakin and A. M. Tartakovsky. Modeling and simulation of pore-scale multiphase fluid flow and reactive transport in fractured and porous media. *Rev. Geophys.*, 47(3):3002, 2009. doi: 10.1029/2008RG000263.

[295] Y. Méheust and J. Schmittbuhl. Flow enhancement of a rough fracture. *Geophys. Res. Lett.*, 27(18): 2989–2992, 2000. doi: 10.1029/1999GL008464.

[296] Y. Méheust and J. Schmittbuhl. Geometrical heterogeneities and permeability anisotropy of rough fractures. *J. Geophys. Res. Solid Earth*, 106(B2):2089–2102, 2001. doi: 10.1029/2000JB900306.

[297] Y. Méheust and J. Schmittbuhl. Scale effects related to flow in rough fractures. *Pure. Appl. Geophys.*, 160:1023–1050, 2003. doi: 10.1007/PL00012559.

[298] C. Mei and J.-L. Auriault. The effect of weak inertia on flow through a porous medium. *J. Fluid Mech.*, 222:647–663, 1991. doi: 10.1017/S0022112091001258.

[299] J. Melcher and G. Taylor. Electrohydrodynamics: a review of the role of interfacial shear stresses. *Annu. Rev. Fluid Mech.*, 1(1):111–146, 1969. doi: 10.1146/annurev.fl.01.010169.000551.

[300] A. Meseguer and L. N. Trefethen. Linearized pipe flow to Reynolds number 10^7. *J. Comput. Phys.*, 186(1):178–197, 2003. doi: 10.1016/S0021-9991(03)00029-9.

[301] S. Metzger. On stable, dissipation reducing splitting schemes for two-phase flow of electrolyte solutions. *Numer. Algorithms*, pages 1–30, 2018. doi: 10.1007/s11075-018-0530-2.

[302] S. Mhatre, V. Vivacqua, M. Ghadiri, A. Abdullah, M. Al-Marri, A. Hassanpour, B. Hewakandamby, B. Azzopardi, and B. Kermani. Electrostatic phase separation: A review. *Chem. Eng. Res. Des.*, 96: 177–195, 2015. doi: 10.1016/j.cherd.2015.02.012.

[303] S. A. Miller. Fluid-mediated influence of adjacent thrusting on the seismic cycle at parkfield. *Nature*, 382(6594):799, 1996. doi: 10.1038/382799a0.

[304] R. A. Millikan. On the elementary electrical charge and the avogadro constant. *Phys. Rev.*, 2(2):109, 1913. doi: 10.1103/PhysRev.2.109.

[305] S. Minjeaud. An unconditionally stable uncoupled scheme for a triphasic Cahn–Hilliard/Navier–Stokes model. *Numer. Methods Partial Differ. Equ.*, 29(2):584–618, 2013. doi: 10.1002/num.21721/full.

[306] S. Mirjalili, S. Jain, and M. Dodd. Interface-capturing methods for two-phase flows: An overview and recent developments. Annual research briefs, Center for Turbulence Research, 2017.

[307] M. K. Misztal, A. Hernandez-Garcia, R. Matin, D. Müter, D. Jha, H. O. Sørensen, and J. Mathiesen. Simulating anomalous dispersion in porous media using the unstructured lattice Boltzmann method. *Frontiers in Physics*, 3:50, 2015. doi: 10.3389/fphy.2015.00050.

[308] M. K. Misztal, A. Hernandez-Garcia, R. Matin, H. O. Sørensen, and J. Mathiesen. Detailed analysis of the lattice Boltzmann method on unstructured grids. *J. Comput. Phys.*, 297:316–339, 2015. doi: 10.1016/j.jcp.2015.05.019.

[309] G. Mitscha-Baude, A. Buttinger-Kreuzhuber, G. Tulzer, and C. Heitzinger. Adaptive and iterative methods for simulations of nanopores with the PNP–Stokes equations. *J. Comput. Phys.*, 338:452–476, 2017. doi: 10.1016/j.jcp.2017.02.072.

[310] H. Mizutani, T. Ishido, T. Yokokura, and S. Ohnishi. Electrokinetic phenomena associated with earthquakes. *Geophys. Res. Lett.*, 3(7):365–368, 1976. doi: 10.1029/GL003i007p00365.

[311] D. Mokbel, H. Abels, and S. Aland. A phase-field model for fluid-structure-interaction. *J. Comput. Phys.*, 372:823–840, 2018. doi: 10.1016/j.jcp.2018.06.063.

[312] J. Monaghan. Smoothed particle hydrodynamics and its diverse applications. *Annu. Rev. Fluid Mech.*, 44:323–346, 2012. doi: 10.1146/annurev-fluid-120710-101220.

[313] A. S. Monin and A. M. Yaglom. *Statistical fluid mechanics, volume II: mechanics of turbulence*, volume 2. Courier Corporation, 2013.

[314] C. W. Monroe, L. I. Daikhin, M. Urbakh, and A. A. Kornyshev. Electrowetting with electrolytes. *Phys. Rev. Lett.*, 97:136102, Sep 2006. doi: 10.1103/PhysRevLett.97.136102.

[315] C. W. Monroe, L. I. Daikhin, M. Urbakh, and A. A. Kornyshev. Principles of electrowetting with two immiscible electrolytic solutions. *J. Phys. Condens. Matter*, 18(10):2837, 2006. doi: 10.1088/0953-8984/18/10/009.

[316] L. F. Moody. Friction factors for pipe flow. *Trans. ASME*, 66:671–684, 1944.

[317] A. Morin. *Mathematical modelling and numerical simulation of two-phase multi-component flows of CO$_2$ mixtures in pipes*. PhD thesis, Norges teknisk-naturvitenskapelige universitet, Fakultet for ingeniørvitenskap og teknologi, Institutt for energi-og prosessteknikk, 2012.

[318] A. Morin and T. Flåtten. A two-fluid four-equation model with instantaneous thermodynamical equilibrium. *ESAIM Math. Model. Numer. Anal.*, 50(4):1167–1192, 2016. doi: 10.1051/m2an/2015074.

[319] M. Mortensen. A spectral-Galerkin turbulent channel flow solver for large-scale simulations. *arXiv:1701.03787*, 2017.

[320] M. Mortensen and K. Valen-Sendstad. Oasis: A high-level/high-performance open source Navier–Stokes solver. *Comput. Phys. Commun.*, 188:177–188, 2015. doi: 10.1016/j.cpc.2014.10.026.

[321] N. A. Mortensen and H. Bruus. Universal dynamics in the onset of a Hagen–Poiseuille flow. *Phys. Rev. E*, 74(1):017301, 2006. doi: 10.1103/PhysRevE.74.017301.

[322] M. Moura. *Burst dynamics in quasi-2D disordered systems: experiments on porous media two-phase flows*. PhD thesis, Department of Physics, University of Oslo, 2016.

[323] V. V. Mourzenko, J.-F. Thovert, and P. M. Adler. Permeability of a single fracture; validity of the Reynolds equation. *J. Phys. II*, 5(3):465–482, 1995. doi: 10.1051/jp2:1995133.

[324] F. Mugele. Fundamental challenges in electrowetting: from equilibrium shapes to contact angle saturation and drop dynamics. *Soft Matter*, 5(18):3377–3384, 2009. doi: 10.1039/B904493K.

[325] F. Mugele and J.-C. Baret. Electrowetting: from basics to applications. *J. Phys. Condens. Matter*, 17 (28):R705, 2005. doi: 10.1088/0953-8984/17/28/R01.

[326] F. Mugele, M. Duits, and D. Van den Ende. Electrowetting: a versatile tool for drop manipulation, generation, and characterization. *Adv. Colloid Interface Sci.*, 161(1):115–123, 2010. doi: 10.1016/j.cis.2009.11.002.

[327] V. Mukund and B. Hof. The critical point of the transition to turbulence in pipe flow. *J. Fluid Mech.*, 839:76–94, 2018. doi: 10.1017/jfm.2017.923.

[328] S. T. Munkejord, M. Hammer, and S. W. Løvseth. CO$_2$ transport: Data and models – a review. *Applied Energy*, 169:499–523, 2016. doi: 10.1016/j.apenergy.2016.01.100.

[329] R. Natalini. Recent mathematical results on hyperbolic relaxation problems. Preprint of IAC, CNR, 1998.

[330] C. Navier. Mémoire sur les lois du mouvement des fluides. *Mémoires de l'Académie Royale des Sciences de l'Institut de France*, 6(1823):389–440, 1823.

[331] W. Nernst. Zur kinetik der in lösung befindlichen körper. *Z. Phys. Chem.*, 2(1):613–637, 1888.

[332] W. Nernst. Die elektromotorische wirksamkeit der jonen. *Z. Phys. Chem.*, 4(1):129–181, 1889.

[333] A. Neuville, R. Toussaint, and J. Schmittbuhl. Hydrothermal coupling in a self-affine rough fracture. *Phys. Rev. E*, 82(3):036317, 2010. doi: 10.1103/PhysRevE.82.036317.

[334] A. Neuville, R. Toussaint, and J. Schmittbuhl. Hydraulic transmissivity and heat exchange efficiency of open fractures: a model based on lowpass filtered apertures. *Geophys. J. Int.*, 186(3):1064–1072, 2011. doi: 10.1111/j.1365-246X.2011.05126.x.

[335] A. Neuville, E. G. Flekkøy, and R. Toussaint. Influence of asperities on fluid and thermal flow in a fracture: A coupled lattice Boltzmann study. *J. Geophys. Res. Solid Earth*, 118(7):3394–3407, 2013. doi: 10.1002/jgrb.50256.

[336] C. Neuzil and J. V. Tracy. Flow through fractures. *Water Resour. Res.*, 17(1):191–199, 1981. doi: 10.1029/WR017i001p00191.

[337] C. P. Nielsen and H. Bruus. Concentration polarization, surface currents, and bulk advection in a microchannel. *Phys. Rev. E*, 90(4):043020, 2014. doi: 10.1103/PhysRevE.90.043020.

[338] C. P. Nielsen and H. Bruus. Sharp-interface model of electrodeposition and ramified growth. *Phys. Rev. E*, 92(4):042302, 2015. doi: 10.1103/PhysRevE.92.052310.

[339] J. Nikuradse. Strömungsgestze in rauhen rohren. In *Forschungsheft auf dem Gebiete des Ingenieurwesens*, volume 361. VDI-Verlag, 1933.

[340] R. H. Nochetto, A. J. Salgado, and S. W. Walker. A diffuse interface model for electrowetting with moving contact lines. *Math. Models Methods Appl. Sci.*, 24(01):67–111, 2014. doi: 10.1142/S0218202513500474.

[341] C. Noiriel. Resolving time-dependent evolution of pore-scale structure, permeability and reactivity using x-ray microtomography. *Rev. Mineral Geochem.*, 80:247–285, 2015. doi: 10.2138/rmg.2015.80.08.

[342] C. Noiriel, P. Gouze, and D. Bernard. Investigation of porosity and permeability effects from microstructure changes during limestone dissolution. *Geophys. Res. Lett.*, 31(24):L24603, 2004. doi: 10.1029/2004GL021572.

[343] C. Noiriel, D. Bernard, P. Gouze, and X. Thibault. Hydraulic properties and microgeometry evolution accompanying limestone dissolution by acidic water. *Oil & gas science and technology*, 60(1):177–192, 2005. doi: 10.2516/ogst:2005011.

[344] A. Obliger, M. Jardat, D. Coelho, S. Bekri, and B. Rotenberg. Pore network model of electrokinetic transport through charged porous media. *Phys. Rev. E*, 89(4):043013, 2014. doi: 10.1103/PhysRevE.89.043013.

[345] C. T. O'Konski and H. C. Thacher Jr. The distortion of aerosol droplets by an electric field. *J. Phys. Chem.*, 57(9):955–958, 1953. doi: 10.1021/j150510a024.

[346] A. P. Oron and B. Berkowitz. Flow in rock fractures: The local cubic law assumption reexamined. *Water Resour. Res.*, 34(11):2811–2825, 1998.

[347] S. Osher and J. A. Sethian. Fronts propagating with curvature-dependent speed: algorithms based on Hamilton–Jacobi formulations. *J. Comput. Phys.*, 79(1):12–49, 1988. doi: 10.1016/0021-9991(88)90002-2.

[348] Pacific Institute. Water Conflict Chronology. http://www.worldwater.org/chronology.html, 2018.

[349] C. C. Paige and M. A. Saunders. Solution of sparse indefinite systems of linear equations. *SIAM J. Numer. Anal.*, 12(4):617–629, 1975. doi: 10.1137/0712047.

[350] H. Pellat. Force agissant á la surface de séparation de deux diélectriques. *C. R. Hebd. Séances Acad. Sci.*, 119:675, 1894.

[351] H. Pellat. Mesure de la force agissant sur les diélectriques liquides non électrisés placés dans un champ élitrique. *C. R. Hebd. Séances Acad. Sci.*, 119:691, 1895.

[352] J. Pereira Nunes, M. Blunt, and B. Bijeljic. Pore-scale simulation of carbonate dissolution in micro-ct images. *J. Geophys. Res. Solid Earth*, 121:558–576, 2016. doi: 10.1002/2015JB012117.

[353] C. S. Peskin. The immersed boundary method. *Acta Numerica*, 11:479–517, 2002. doi: 10.1017/S0962492902000077.

[354] N. H. Pham, R. S. Voronov, N. R. Tummala, and D. V. Papavassiliou. Bulk stress distributions in the pore space of sphere-packed beds under darcy flow conditions. *Phys. Rev. E*, 89(3):033016, 2014. doi: 10.1103/PhysRevE.89.033016.

[355] M. Planck. Ueber die erregung von electricität und wärme in electrolyten. *Ann. Phys.*, 275(2):161–186, 1890. doi: 10.1002/andp.18902750202.

[356] M. Planck. Ueber die potentialdifferenz zwischen zwei verdünnten lösungen binärer electrolyte. *Ann. Phys.*, 276(8):561–576, 1890. doi: 10.1002/andp.18902760802.

[357] J. Plateau. Experimental and theoretical researches into the figures of equilibrium of a liquid mass without weight. *Philos. Mag.*, 38(257):445–455, 1869. doi: 10.1080/14786445708642346.

[358] F. Plouraboué, P. Kurowski, J.-P. Hulin, S. Roux, and J. Schmittbuhl. Aperture of rough cracks. *Phys. Rev. E*, 51(3):1675, 1995. doi: 10.1103/PhysRevE.51.1675.

[359] O. Plümper, A. Botan, C. Los, Y. Liu, A. Malthe-Sørenssen, and B. Jamtveit. Fluid-driven metamorphism of the continental crust governed by nanoscale fluid flow. *Nat. Geosci.*, 10(9):685, 2017. doi: 10.1038/ngeo3009.

[360] J. L. M. Poiseuille. Recherches expérimentales sur le mouvement des liquides dans les tubes de très-petits diamètre. *C. R. Acad. Sci.*, 12:112–15, 1841.

[361] M. Pollack, A. Shenderov, and R. Fair. Electrowetting-based actuation of droplets for integrated microfluidics. *Lab Chip*, 2(2):96–101, 2002. doi: 10.1039/b110474h.

[362] Y. Pomeau. Front motion, metastability and subcritical bifurcations in hydrodynamics. *Physica D*, 23 (1-3):3–11, 1986. doi: 10.1016/0167-2789(86)90104-1.

[363] Y. Pomeau. The long and winding road. *Nat. Phys.*, 12(3):198, 2016. doi: 10.1038/nphys3684.

[364] L. Ponson, H. Auradou, M. Pessel, V. Lazarus, and J.-P. Hulin. Failure mechanisms and surface roughness statistics of fractured Fontainebleau sandstone. *Phys. Rev. E*, 76(3):036108, 2007. doi: 10.1103/PhysRevE.76.036108.

[365] S. Popinet. Numerical models of surface tension. *Annu. Rev. Fluid Mech.*, 50(1):49–75, 2018. doi: 10.1146/annurev-fluid-122316-045034.

[366] S. R. Pride and F. Morgan. Electrokinetic dissipation induced by seismic waves. *Geophysics*, 56(7): 914–925, 1991. doi: 10.1190/1.1443125.

[367] R. F. Probstein. *Physicochemical hydrodynamics: an introduction.* John Wiley & Sons, 2005.

[368] A. Prosperetti and G. Tryggvason. *Computational methods for multiphase flow.* Cambridge University Press, 2009.

[369] J. Qian, H. Zhan, W. Zhao, and F. Sun. Experimental study of turbulent unconfined groundwater flow in a single fracture. *J. Hydrol.*, 311(1-4):134–142, 2005. doi: 10.1016/j.jhydrol.2005.01.013.

[370] J. Qian, H. Zhan, S. Luo, and W. Zhao. Experimental evidence of scale-dependent hydraulic conductivity for fully developed turbulent flow in a single fracture. *J. Hydrol.*, 339(3-4):206–215, 2007. doi: 10.1016/j.jhydrol.2007.03.015.

[371] T. Qian, X.-P. Wang, and P. Sheng. Molecular scale contact line hydrodynamics of immiscible flows. *Phys. Rev. E*, 68(1):016306, 2003. doi: 10.1103/PhysRevE.68.016306.

[372] T. Qian, X.-P. Wang, and P. Sheng. Power-law slip profile of the moving contact line in two-phase immiscible flows. *Phys. Rev. Lett.*, 93(9):094501, 2004. doi: 10.1103/PhysRevLett.93.094501.

[373] T. Qian, X.-P. Wang, and P. Sheng. A variational approach to moving contact line hydrodynamics. *J. Fluid Mech.*, 564:333–360, 2006. doi: 10.1017/S0022112006001935.

[374] D. Quéré. Wetting and roughness. *Annu. Rev. Mater. Res.*, 38:71–99, 2008. doi: 10.1146/annurev.matsci.38.060407.132434.

[375] G. Quincke. Ueber eine neue art elektrischer ströme. *Ann. Phys.*, 183(5):1–47, 1859. doi: 10.1002/andp.18591830502.

[376] L. Rayleigh. On the theory of surface forces. II. Compressible fluids. *Philos. Mag.*, 33(201):209–220, 1892. doi: 10.1080/14786449208621456.

[377] W. Ren and W. E. Boundary conditions for the moving contact line problem. *Phys. Fluids*, 19(2): 022101, 2007. doi: 10.1063/1.2646754.

[378] F. Reuss. Charge-induced flow. *Proceedings of the Imperial Society of Naturalists of Moscow, 1809*, 3: 327–344, 1809.

[379] A. Revil, H. Schwaeger, L. Cathles, and P. Manhardt. Streaming potential in porous media: 2. theory and application to geothermal systems. *J. Geophys. Res. Solid Earth*, 104(B9):20033–20048, 1999. doi: 10.1029/1999JB900090.

[380] O. Reynolds. An experimental investigation of the circumstances which determine whether the motion of water shall be direct or sinuous, and of the law of resistance in parallel channels. *Philos. Trans. R. Soc.*, 174:935–982, 1883. doi: 10.1098/rstl.1883.0029 2053-9223.

[381] O. Reynolds. On the theory of lubrication and its application to Mr. Beauchamp Tower's experiments, including an experimental determination of the viscosity of olive oil. *Philos. Trans. R. Soc.*, 177: 157–234, 1886. doi: 10.1098/rstl.1886.0005.

[382] A. RezaeiDoust, T. Puntervold, S. Strand, and T. Austad. Smart water as wettability modifier in carbonate and sandstone: A discussion of similarities/differences in the chemical mechanisms. *Energy Fuels*, 23(9):4479–4485, 2009. doi: 10.1021/ef900185q.

[383] C. L. Rice and R. Whitehead. Electrokinetic flow in a narrow cylindrical capillary. *J. Phys. Chem.*, 69 (11):4017–4024, 1965. doi: 10.1021/j100895a062.

[384] J. R. Rice and M. P. Cleary. Some basic stress diffusion solutions for fluid-saturated elastic porous media with compressible constituents. *Rev. Geophys.*, 14(2):227–241, 1976. doi: 10.1029/RG014i002p00227.

[385] S. Rojas and J. Koplik. Nonlinear flow in porous media. *Phys. Rev. E*, 58(4):4776, 1998. doi: 10.1103/PhysRevE.58.4776.

[386] S. Roux, J. Schmittbuhl, J.-P. Vilotte, and A. Hansen. Some physical properties of self-affine rough surfaces. *Europhys. Lett.*, 23(4):277, 1993. doi: 10.1209/0295-5075/23/4/007.

[387] Y. Saad. *Iterative methods for sparse linear systems*, volume 82. SIAM, 2003.

[388] Y. Saad and M. H. Schultz. Gmres: A generalized minimal residual algorithm for solving nonsymmetric linear systems. *SIAM J. Sci. and Stat. Comput.*, 7(3):856–869, 1986. doi: 10.1137/0907058.

[389] E. H. Saenger, F. Enzmann, Y. Keehm, and H. Steeb. Digital rock physics: Effect of fluid viscosity on effective elastic properties. *Journal of Applied Geophysics*, 74(4):236–241, 2011. doi: 10.1016/j.jappgeo.2011.06.001.

[390] M. Sahimi. Flow phenomena in rocks: from continuum models to fractals, percolation, cellular automata, and simulated annealing. *Rev. Mod. Phys.*, 65(4):1393, 1993. doi: 10.1103/RevModPhys.65.1393.

[391] M. Sahimi. *Applications of percolation theory*. CRC Press, 2014.

[392] H. Salwen, F. W. Cotton, and C. E. Grosch. Linear stability of Poiseuille flow in a circular pipe. *J. Fluid Mech.*, 98(2):273–284, 1980. doi: 10.1017/S0022112080000146.

[393] M. Sano and K. Tamai. A universal transition to turbulence in channel flow. *Nat. Phys.*, 12:249–254, 2016. doi: 10.1038/nphys3659.

[394] R. Saurel and R. Abgrall. A multiphase Godunov method for compressible multifluid and multiphase flows. *J. Comput. Phys.*, 150(2):425–467, 1999. doi: 10.1006/jcph.1999.6187.

[395] R. Saurel and C. Pantano. Diffuse-interface capturing methods for compressible two-phase flows. *Annu. Rev. Fluid Mech.*, 50(1), 2018. doi: 10.1146/annurev-fluid-122316-050109.

[396] D. A. Saville. Electrohydrodynamics: the Taylor–Melcher leaky dielectric model. *Annu. Rev. Fluid Mech.*, 29(1):27–64, 1997. doi: 10.1146/annurev.fluid.29.1.27.

[397] R. Scardovelli and S. Zaleski. Direct numerical simulation of free-surface and interfacial flow. *Annu. Rev. Fluid Mech.*, 31(1):567–603, 1999. doi: 10.1146/annurev.fluid.31.1.567.

[398] J. Schmittbuhl, F. Schmitt, and C. Scholz. Scaling invariance of crack surfaces. *J. Geophys. Res. Solid Earth*, 100(B4):5953–5973, 1995. doi: 10.1029/94JB02885.

[399] O. Schnitzer and E. Yariv. The Taylor–Melcher leaky dielectric model as a macroscale electrokinetic description. *J. Fluid Mech.*, 773:1–33, 2015. doi: 10.1017/jfm.2015.242.

[400] R. B. Schoch, J. Han, and P. Renaud. Transport phenomena in nanofluidics. *Rev. Mod. Phys.*, 80(3):839, 2008. doi: 10.1103/RevModPhys.80.839.

[401] J. A. Sethian and P. Smereka. Level set methods for fluid interfaces. *Annu. Rev. Fluid Mech.*, 35(1): 341–372, 2003. doi: 10.1146/annurev.fluid.35.101101.161105.

[402] S. Shapin. The experimental philosophy and its institutions. In *The Scientific Revolution*, chapter 3, pages 72–100. Wiley-Blackwell, 2008.

[403] J. Shen and X. Yang. A phase-field model and its numerical approximation for two-phase incompressible flows with different densities and viscosities. *SIAM J. Sci. Comput.*, 32(3):1159–1179, 2010. doi: 10.1137/09075860X.

[404] J. Shen and X. Yang. Decoupled, energy stable schemes for phase-field models of two-phase incompressible flows. *SIAM J. Numer. Anal.*, 53(1):279–296, 2015. doi: 10.1137/140971154.

[405] J. R. Shewchuk. Triangle: Engineering a 2D quality mesh generator and delaunay triangulator. In M. C. Lin and D. Manocha, editors, *Applied Computational Geometry: Towards Geometric Engineering*, volume 1148 of *Lecture Notes in Computer Science*, pages 203–222. Springer-Verlag, 1996.

[406] H.-Y. Shih, T.-L. Hsieh, and N. Goldenfeld. Ecological collapse and the emergence of travelling waves at the onset of shear turbulence. *Nat. Phys.*, 12:245–248, 2015. doi: 10.1038/nphys3548.

[407] I. A. Shiklomanov. Appraisal and assessment of world water resources. *Water International*, 25:11–32, 2000. doi: 10.1080/02508060008686794.

[408] H. Si. Tetgen, a delaunay-based quality tetrahedral mesh generator. *ACM Trans. Math. Softw.*, 41(2): 11:1–11:36, 2015. ISSN 0098-3500. doi: 10.1145/2629697.

[409] R. Sibson. Implications of fault-valve behaviour for rupture nucleation and recurrence. *Tectonophysics*, 211(1-4):283–293, 1992. doi: 10.1016/0040-1951(92)90065-E.

[410] M. Siena, M. Riva, J. Hyman, C. L. Winter, and A. Guadagnini. Relationship between pore size and velocity probability distributions in stochastically generated porous media. *Phys. Rev. E*, 89(1):013018, 2014. doi: 10.1103/PhysRevE.89.013018.

[411] A. Siria, M.-L. Bocquet, and L. Bocquet. New avenues for the large-scale harvesting of blue energy. *Nat. Rev. Chem.*, 1(11):0091, 2017. doi: 10.1038/s41570-017-0091.

[412] E. Skjetne, A. Hansen, and J. Gudmundsson. High-velocity flow in a rough fracture. *J. Fluid Mech.*, 383:1–28, 1999. doi: 10.1017/S0022112098002444.

[413] M. v. Smoluchowski. Contribution to the theory of electro-osmosis and related phenomena. *Bull. Int. Acad. Sci. Cracovie*, 3:184–199, 1903.

[414] M. v. Smoluchowski. Zur theorie der elektrischen kataphorese und der oberflächenleitung. *Phyz. Z.*, 6:529–531, 1905.

[415] J. H. Snoeijer and B. Andreotti. Moving contact lines: scales, regimes, and dynamical transitions. *Annu. Rev. Fluid Mech.*, 45:269–292, 2013. doi: 10.1146/annurev-fluid-011212-140734.

[416] A. Solbrå, A. W. Bergersen, J. van den Brink, A. Malthe-Sørenssen, G. T. Einevoll, and G. Halnes. A Kirchhoff-Nernst-Planck framework for modeling large scale extracellular electrodiffusion surrounding morphologically detailed neurons. *bioRxiv*, page 261107, 2018. doi: 10.1101/261107.

[417] R. Span and W. Wagner. A new equation of state for carbon dioxide covering the fluid region from the triple-point temperature to 1100 k at pressures up to 800 mpa. *J. Phys. Chem. Ref. Data*, 25(6): 1509–1596, 1996. doi: 10.1063/1.555991.

[418] T. M. Squires and S. R. Quake. Microfluidics: Fluid physics at the nanoliter scale. *Rev. Mod. Phys.*, 77 (3):977, 2005. doi: 10.1103/RevModPhys.77.977.

[419] V. Srinivasan, V. K. Pamula, and R. B. Fair. An integrated digital microfluidic lab-on-a-chip for clinical diagnostics on human physiological fluids. *Lab Chip*, 4(4):310–315, 2004. doi: 10.1039/b403341h.

[420] D. Stauffer and A. Aharony. *Introduction to percolation theory*. CRC Press, 1994.

[421] O. Stern. Zur theorie der elektrolytischen doppelschicht. *Berichte der Bunsengesellschaft für physikalische Chemie*, 30(21-22):508–516, 1924. doi: 10.1002/bbpc.192400182.

[422] W. H. Stockmayer. Theory of molecular size distribution and gel formation in branched-chain polymers. *J. Chem. Phys.*, 11(2):45–55, 1943. doi: 10.1063/1.1723803.

[423] G. G. Stokes. On the theories of the internal friction of fluids in motion, and of the equilibrium and motion of elastic solids. *Trans. Cambridge Philos. Soc.*, 8:287–319, 1845.

[424] A. Strickler. *Beiträge zur Frage der Geschwindigkeitsformel und der Rauhigkeitszahlen für Ströme, Kanäle und geschlossene Leitungen.* Mitteilungen des Amtes für Wasserwirtschaft, 1923.

[425] S. Succi. *The Lattice Boltzmann Equation: For Complex States of Flowing Matter.* Oxford University Press, 2018.

[426] Y. Sui, H. Ding, and P. D. M. Spelt. Numerical simulations of flows with moving contact lines. *Annu. Rev. Fluid Mech.*, 46:97–119, 2014. doi: 10.1146/annurev-fluid-010313-141338.

[427] M. Sussman and E. G. Puckett. A coupled level set and volume-of-fluid method for computing 3D and axisymmetric incompressible two-phase flows. *J. Comput. Phys.*, 162(2):301–337, 2000. doi: 10.1006/jcph.2000.6537.

[428] M. Sussman, P. Smereka, and S. Osher. A level set approach for computing solutions to incompressible two-phase flow. *J. Comput. Phys.*, 114(1):146–159, 1994. doi: 10.1006/jcph.1994.1155.

[429] S. P. Sutera and R. Skalak. The history of Poiseuille's law. *Annu. Rev. Fluid Mech.*, 25(1):1–20, 1993. doi: 10.1146/annurev.fl.25.010193.000245.

[430] H. L. Swinney and J. P. Gollub. *Hydrodynamic instabilities and the transition to turbulence.* Oxford University Press, 1981.

[431] K. A. Takeuchi, M. Kuroda, H. Chaté, and M. Sano. Directed percolation criticality in turbulent liquid crystals. *Phys. Rev. Lett.*, 99(23):234503, 2007. doi: 10.1103/PhysRevLett.99.234503.

[432] L. Talon, H. Auradou, and A. Hansen. Permeability estimates of self-affine fracture faults based on generalization of the bottleneck concept. *Water Resour. Res.*, 46(7):W07601, 2010. doi: 10.1029/2009WR008404.

[433] L. Talon, H. Auradou, and A. Hansen. Permeability of self-affine aperture fields. *Phys. Rev. E*, 82(4): 046108, 2010. doi: 10.1103/PhysRevE.82.046108.

[434] P. Talwani and S. Acree. Pore pressure diffusion and the mechanism of reservoir-induced seismicity. *Pure. Appl. Geophys.*, 122:947–965, 1984. doi: 10.1007/BF00876395.

[435] L. Tanner. The spreading of silicone oil drops on horizontal surfaces. *Journal of Physics D: Applied Physics*, 12(9):1473, 1979. doi: 10.1088/0022-3727/12/9/009.

[436] G. Taylor. Studies in electrohydrodynamics. I. The circulation produced in a drop by electrical field. *Proc. Royal Soc. A*, 291(1425):159–166, 1966. doi: 10.1098/rspa.1966.0086.

[437] K. E. Teigen and S. T. Munkejord. Sharp-interface simulations of drop deformation in electric fields. *IEEE T. Dielect. El. In.*, 16(2), 2009. doi: 10.1109/TDEI.2009.4815181.

[438] K. E. Teigen and S. T. Munkejord. Influence of surfactant on drop deformation in an electric field. *Phys. Fluids*, 22(11):112104, 2010. doi: 10.1063/1.3504271.

[439] K. E. Teigen, P. Song, J. Lowengrub, and A. Voigt. A diffuse-interface method for two-phase flows with soluble surfactants. *J. Comput. Phys.*, 230(2):375 – 393, 2011. ISSN 0021-9991. doi: 10.1016/j.jcp.2010.09.020.

[440] H. Tennekes, J. L. Lumley, J. Lumley, et al. *A first course in turbulence.* MIT press, 1972.

[441] The CGAL Project. *CGAL User and Reference Manual.* CGAL Editorial Board, 4.8 edition, 2016. URL http://doc.cgal.org/4.8/Manual/packages.html.

[442] R. Thompson. The seismic electric effect. *Geophysics*, 1(3):327–335, 1936. doi: 10.1190/1.1437119.

[443] G. Tomar, D. Gerlach, G. Biswas, N. Alleborn, A. Sharma, F. Durst, S. Welch, and A. Delgado. Two-phase electrohydrodynamic simulations using a volume-of-fluid approach. *J. Comput. Phys.*, 227(2): 1267 – 1285, 2007. doi: 10.1016/j.jcp.2007.09.003.

[444] L. Torvalds and J. Hamano. Git: Fast version control system. http://git-scm.com, 2005.

[445] S. Torza, R. Cox, and S. Mason. Electrohydrodynamic deformation and bursts of liquid drops. *Phil. Trans. R. Soc. Lond. A*, 269(1198):295–319, 1971. doi: 10.1098/rsta.1971.0032.

[446] D. J. Tritton. *Physical fluid dynamics.* Springer Science & Business Media, 2012.

[447] G. Tryggvason, R. Scardovelli, and S. Zaleski. *Direct numerical simulations of gas–liquid multiphase flows*. Cambridge University Press, 2011.

[448] V. Tzelepis, K. N. Moutsopoulos, J. N. Papaspyros, and V. A. Tsihrintzis. Experimental investigation of flow behavior in smooth and rough artificial fractures. *J. Hydrol.*, 521:108–118, 2015. doi: 10.1016/j.jhydrol.2014.11.054.

[449] S. O. Unverdi and G. Tryggvason. A front-tracking method for viscous, incompressible, multi-fluid flows. *J. Comput. Phys.*, 100(1):25–37, 1992. doi: 10.1016/0021-9991(92)90307-K.

[450] M. Vallet, B. Berge, and L. Vovelle. Electrowetting of water and aqueous solutions on poly (ethylene terephthalate) insulating films. *Polymer*, 37(12):2465–2470, 1996. doi: 10.1016/0032-3861(96)85360-2.

[451] R. Van der Sman and S. Van der Graaf. Diffuse interface model of surfactant adsorption onto flat and droplet interfaces. *Rheologica acta*, 46(1):3–11, 2006. doi: 10.1007/s00397-005-0081-z.

[452] H. A. Van der Vorst. Bi-CGSTAB: A fast and smoothly converging variant of Bi-CG for the solution of nonsymmetric linear systems. *SIAM J. Sci. and Stat. Comput.*, 13(2):631–644, 1992. doi: 10.1137/0913035.

[453] J. D. van der Waals. *Over de Continuiteit van den Gas-en Vloeistoftoestand*. PhD thesis, University of Leiden, 1873.

[454] J. D. van der Waals. The thermodynamic theory of capillarity under the hypothesis of a continuous variation of density. *J. Stat. Phys.*, 20(2):200–244, 1893. doi: 10.1007/BF01011514.

[455] O. Voinov. Hydrodynamics of wetting. *Fluid Dynamics*, 11(5):714–721, 1976. doi: 10.1007/BF01012963.

[456] A. G. Volkov, D. Deamer, D. Tanelian, and V. Markin. Electrical double layers at the oil/water interface. *Progress in surface science*, 53(1):1–134, 1996. doi: 10.1016/S0079-6816(97)82876-6.

[457] H. von Helmholtz. Ueber einige gesetze der vertheilung elektrischer ströme in körperlichen leitern mit anwendung auf die thierisch-elektrischen versuche. *Ann. Phys.*, 165(6):211–233, 1853.

[458] H. von Helmholtz. Studien über electrische grenzschichten. *Ann. Phys.*, 243(7):337–382, 1879.

[459] C. von Terzaghi. *Erdbaumechanik auf bodenphysikalischer Grundlage*. Deuticke, 1925.

[460] R. S. Voronov, S. B. VanGordon, V. I. Sikavitsas, and D. V. Papavassiliou. Distribution of flow-induced stresses in highly porous media. *Appl. Phys. Lett.*, 97(2):024101, 2010. doi: 10.1063/1.3462071.

[461] J. O. Waldeland and S. Evje. A multiphase model for exploring tumor cell migration driven by autologous chemotaxis. *Chem. Eng. Sci.*, 2018. doi: 10.1016/j.ces.2018.06.076.

[462] A. D. Waller. A demonstration on man of electromotive changes accompanying the heart's beat. *J. Physiol.*, 8(5):229–234, 1887. doi: 10.1113/jphysiol.1887.sp000257.

[463] M. Wang, Y.-F. Chen, G.-W. Ma, J.-Q. Zhou, and C.-B. Zhou. Influence of surface roughness on nonlinear flow behaviors in 3D self-affine rough fractures: Lattice Boltzmann simulations. *Adv. Water Resour.*, 96:373–388, 2016. doi: 10.1016/j.advwatres.2016.08.006.

[464] J. L. Weisbach. *Lehrbuch der Ingenieur-und Maschinen-Mechanik: Theoretische Mechanik*, volume 1. Druck und Verlag von Friedrich Vieweg und Sohn, 1845.

[465] S. Whitaker. Flow in porous media i: A theoretical derivation of Darcy's law. *Transp. Porous Media*, 1 (1):3–25, 1986. doi: 10.1007/BF01036523.

[466] S. Whitaker. The Forchheimer equation: a theoretical development. *Transp. Porous Media*, 25(1): 27–61, 1996. doi: 10.1007/BF00141261.

[467] K. Wojtacki, L. Lewandowska, P. Gouze, and A. Lipkowski. Numerical computations of rock dissolution and geomechanical effects for CO_2 geological storage. *Int. J. Numer. Anal. Methods Geomech.*, 39: 482–506, 2015. doi: 10.1002/nag.2316.

[468] R. Woltmann. *Beyträge zur hydraulischen Architektur*. Dritter Band, Johann Christian Dietrich, Göttingen, 1794.

[469] World Energy Council. World energy resources. Technical report, World Energy Council, 2016.

[470] I. Wygnanski and F. Champagne. On transition in a pipe. Part 1. The origin of puffs and slugs and the flow in a turbulent slug. *J. Fluid Mech.*, 59(2):281–335, 1973. doi: 10.1017/S0022112073001576.

[471] I. Wygnanski, M. Sokolov, and D. Friedman. On transition in a pipe. Part 2. The equilibrium puff. *J. Fluid Mech.*, 69(2):283–304, 1975. doi: 10.1017/S0022112075001449.

[472] X. Xiong, J. Tao, S. Chen, and L. Brandt. Turbulent bands in plane-Poiseuille flow at moderate Reynolds numbers. *Phys. Fluids*, 27(4):041702, 2015. doi: 10.1063/1.4917173.

[473] Z. Xu and P. Meakin. Phase-field modeling of solute precipitation and dissolution. *J. Chem. Phys.*, 129(1):014705, 2008. doi: 10.1063/1.2948949.

[474] Y. Yan and J. Koplik. Flow of power-law fluids in self-affine fracture channels. *Phys. Rev. E*, 77(3): 036315, 2008. doi: 10.1103/PhysRevE.77.036315.

[475] C. Yang and D. Li. A method of determining the thickness of liquid-liquid interfaces. *Colloids Surf. A*, 113(1-2):51–59, 1996. doi: 10.1016/0927-7757(96)03544-3.

[476] Q. Yang, B. Q. Li, and Y. Ding. 3D phase field modeling of electrohydrodynamic multiphase flows. *Int. J. Multiph. Flow*, 57:1–9, 2013. doi: 10.1016/j.ijmultiphaseflow.2013.06.006.

[477] Q. Yang, B. Q. Li, J. Shao, and Y. Ding. A phase field numerical study of 3D bubble rising in viscous fluids under an electric field. *Int. J. Heat Mass Transf.*, 78:820–829, 2014. doi: 10.1016/j.ijheatmasstransfer.2014.07.039.

[478] T. Young. An essay on the cohesion of fluids. *Philos. Trans. R. Soc.*, 95:65–87, 1805. doi: 10.1098/rstl.1805.0005.

[479] P. Yue, C. Zhou, and J. J. Feng. Spontaneous shrinkage of drops and mass conservation in phase-field simulations. *J. Comput. Phys.*, 223(1):1–9, 2007. doi: 10.1016/j.jcp.2006.11.020.

[480] A. Zein, M. Hantke, and G. Warnecke. Modeling phase transition for compressible two-phase flows applied to metastable liquids. *J. Comput. Phys.*, 229(8):2964–2998, 2010. doi: 10.1016/j.jcp.2009.12.026.

[481] J. Zhang and D. Y. Kwok. A 2D lattice Boltzmann study on electrohydrodynamic drop deformation with the leaky dielectric theory. *J. Comput. Phys.*, 206(1):150–161, 2005. doi: 10.1016/j.jcp.2004.11.032.

[482] X. Zhang, M. A. Knackstedt, and M. Sahimi. Fluid flow across mass fractals and self-affine surfaces. *Physica A*, 233(3-4):835–847, 1996. doi: 10.1016/S0378-4371(96)00203-8.

[483] E. K. Zholkovskij, J. H. Masliyah, and J. Czarnecki. An electrokinetic model of drop deformation in an electric field. *J. Fluid Mech.*, 472:1–27, 2002. doi: 10.1017/S0022112002001441.

[484] R. W. Zimmerman and I.-W. Yeo. Fluid flow in rock fractures: From the Navier–Stokes equations to the cubic law. In *Dynamics of fluids in fractured rock*, pages 213–224. American Geophysical Union, 2013.

[485] L. Zou. *Numerical modeling of fluid flow and solute transport in rock fractures*. PhD thesis, KTH Royal Institute of Technology, 2016.

[486] L. Zou, L. Jing, and V. Cvetkovic. Roughness decomposition and nonlinear fluid flow in a single rock fracture. *Int. J. Rock Mech. Min. Sci.*, 75:102–118, 2015. doi: 10.1016/j.ijrmms.2015.01.016.

[487] L. Zou, L. Jing, and V. Cvetkovic. Shear-enhanced nonlinear flow in rough-walled rock fractures. *Int. J. Rock Mech. Min. Sci.*, 97:33–45, 2017. doi: 10.1016/j.ijrmms.2017.06.001.

[488] P.-E. Øren, S. Bakke, and R. Held. Direct pore-scale computation of material and transport properties for north sea reservoir rocks. *Water Resour. Res.*, 43(12):W12S04, 2007. ISSN 1944-7973. doi: 10.1029/2006WR005754.

Statistical mechanics of puff-splitting in the transition to pipe turbulence

Hong-Yan Shih, Gaute Linga, Grégoire Lemoult, Mukund, Vasudevan, Björn Hof, Joachim Mathiesen, and Nigel Goldenfeld

Statistical mechanics of puff-splitting in the transition to pipe turbulence

Hong-Yan Shih[1], Gaute Linga[2], Gregoire Lemoult[3], Vasudevan
Mukund[3], Björn Hof[3], Joachim Mathiesen[2] and Nigel Goldenfeld[1]

[1]*Department of Physics, University of Illinois at Urbana-Champaign,*
Loomis Laboratory of Physics, 1110 West Green Street, Urbana, Illinois, 61801-3080
[2]*Niels Bohr Institute, University of Copenhagen, Denmark*
[3]*Institute of Science and Technology Austria, Am Campus 1, 3400 Klosterneuburg, Austria*

Very close to the laminar-turbulent transition in pipe flow, localized regions of turbulence known as puffs proliferate and interact, leading to spatio-temporal intermittency. We develop a one-dimensional stochastic model of puff dynamics, taking into account puff decay, propagation and splitting, as well as short-range interactions whereby a puff experiences lifetime suppression and velocity pushing by a sufficiently close upstream puff. The universality class for the resulting laminar-turbulence transition in pipe flow is 1+1-dimensional directed percolation, with puff-puff interactions irrelevant at the renormalization group fixed point. Continuum and discrete numerical simulations are in agreement with the theory, after taking into account finite-size and crossover effects.

Fully-developed turbulence remains one of the most challenging problems in physics [1], due to the strong non-linearities arising from advection and the lack of an appropriate small parameter that can be used to identify and control the observed universal scaling behavior [2]. The phase diagram for simple fluid flows is governed by the Reynolds number, $\mathrm{Re} \equiv UD/\nu$, where U is a characteristic velocity, which in pipe flow we will take to be the centerline flow speed, D is a length scale that we will take to be the pipe diameter, and ν is the kinematic viscosity. At low Re, below about 2000 in pipes, fluid flow is smooth, deterministic and predictable (i.e. laminar), but becomes irregular, stochastic and unpredictable (i.e. turbulent) at higher Re, resulting in fully-developed turbulence in the asymptotic limit of $\mathrm{Re} \to \infty$. An impressive body of recent work has explored the laminar-turbulent transition observed in pipe flow around $\mathrm{Re} \sim 2000$ with considerable experimental ingenuity [3, 4] and theoretical detail, from multiple perspectives that encompass dynamical systems theory and statistical mechanics (for recent reviews and perspectives, see (e.g.) [5–9]). A synthesis is emerging that suggests the existence of universal scaling phenomena associated with transitional phenomena too. In this case, the universality class appears to be directed percolation (DP), as supported by experiments on Couette flow [10] and perhaps channel flow [11], simulations of Waleffe flow [12], theoretical predictions of pipe flow [13], and anticipated by earlier studies [14–16].

Despite the clear evidence for a non-equilibrium statistical mechanical phase transition in bounded flows, the situation for pipe flow is not yet clear despite the precision of modern measurements. Near the transition, puffs decay and split in a way that is memoryless with a characteristic time that depends super-exponentially on Re [3, 4], not the power-law divergence that one might have expected. Such behavior can nonetheless be consistent with DP [13, 17], because the time for turbulence to decay can be identified with the length of the longest directed percolation path. It also can arise through a sep-arate connection with extreme value statistics [18, 19], because Reynolds number-dependent thresholds control the fate of puffs [20]. Finally, recent experimental work has documented strong interactions between puffs [21], raising the question of whether or not they cause DP to break down close to the critical point.

In this Letter, we propose a model for puff interactions that is abstracted from the experimental observations, and solve for the critical behavior using field theoretic arguments and numerical simulations. We find that the puff interactions give rise to strong nonlinearities, but these are irrelevant at the renormalization group (RG) fixed point governing the DP transition in all dimensions less than 4. The experimental situation is strongly limited by finite-size effects in pipe length and timescale, and we describe how these mask the underlying critical point behavior, leading to artifactual first-order transitions and anomalously low, non-universal effective order parameter exponents. These results show that in sufficiently long pipes, it would be possible to extract the universal critical exponents of the laminar-turbulent transition, and they would be consistent with DP also.

Phenomenology of puff interactions:- The question we address is the following. We start with a description of turbulent puffs in a pipe that is coarse-grained so that each puff is considered to be a single particle that can move on a line or a one-dimensional (1D) lattice. Later we will comment on the hydrodynamic basis for this assumption. The turbulent puffs can spontaneously relaminarize (i.e. "die"), diffuse and split (i.e. "birth"). A general configuration will be a gas of puffs that is very dilute near the laminar-turbulence transition, and becomes increasingly dense as the Reynolds number is increased. We wish to understand the functional form of this mean density field, which we will sometimes call the turbulent fraction. In addition to their intrinsic dynamics, puffs are being advected downstream by the mean flow, which we will take to be moving from left to right.

Systems of particles hopping predominantly in one direction along a line, with strong repulsive interactions, arise in many fields of physics, and are generally described by a class of models known as asymmetric exclusion processes (ASEP) [22, 23]. The variant of these models that is appropriate here as a minimal model is based upon the totally asymmetric exclusion process (TASEP), in which only unidirectional hopping is allowed. The question that is usually asked of ASEP models is how is the bulk dynamics of the particles affected by the boundary conditions? In these models, particles are injected at a given rate on the left and removed with a given rate on the right of the system. In our case we are primarily interested in the case of periodic boundary conditions. Particles are, however, not conserved in our case: they are born through splitting, and they die through decay. Thus the appropriate model for puffs combines TASEP with the additional birth and death processes of DP.

Let n_i be the occupation number of the site i in a 1D periodic lattice of N sites. Then the puff-splitting model (ignoring for now puff-puff interactions) is given by the following stochastic processes:

1. Puff at site i is removed with rate ω_d (*decay*)

2. Puff at site i moves to site $i+1$, if that site is empty, with rate p (*propagation*)

3. Puff at site i creates a puff at site $i+1$, if that site is empty, with rate w_s (*splitting*)

To implement this model, random asynchronous updating should be used, in which the three rate processes are carried out on randomly chosen particles in random order, with probabilities per unit time given by the coefficients p, ω_d and ω_s.

The mean field equation for this process is given by

$$\partial_t \langle n_i \rangle = -p\langle n_i(1 - n_{i+1}) \rangle + p\langle n_{i-1}(1 - n_i) \rangle \\ -\omega_d \langle n_i \rangle + \omega_s \langle n_{i-1}(1 - n_i) \rangle \quad (1)$$

The first term describes the process in which a puff hops away from site i onto the neighbouring downstream site $i + 1$, but only if the destination site is empty. This process happens with a rate p. If the puff does not hop, it is effectively moving backwards (i.e. upstream) compared to the mean flow of the puffs. The second process is similar but is a flow onto site i from the upstream site $i - 1$. Together these terms represent single puff hopping unless blocked by a downstream puff. The third term represents decay, and the forth term puff-splitting. Note that this term resembles the second half of the puff hopping process, but its effect is different because there is no term which effectively removes the puff at site i, as does the first term in eq. (1).

Living in one dimension, puff-puff interactions are very strong, and there are two additional microscopic interactions that need to be considered in addition to the fact the puffs cannot pass through one another: a puff that is upstream of another occupying its nearest-neighbour site can neither split nor hop to the right, until the downstream puff has itself hopped downstream or decayed. First, the lifetime of the puff that is downstream of its nearest-neighbour will have a drastically shortened lifetime (by perhaps 5 orders of magnitude) compared to a free puff. We will call this "suppression"; it arises from the way in which a puff distorts the mean velocity profile. Second, the puffs have a strong short-range repulsion, which we will call "pushing": a puff that is created by splitting will for a short distance experience a faster downstream velocity that has the effect of separating it quickly from its mother puff. If the daughter does not get pushed then it will have a high likelihood of decaying rapidly.

These interactions can be added to the simple puff-splitting model by two additional rules. *Suppression* can be modeled by assuming that the decay rate is much greater if a puff is immediately downstream of another puff, i.e. $\omega_d \to \tilde{\omega}$. *Pushing* can be modeled by introductin an increased hopping rate r if a puff is immediately downstream of another puff, i.e. $p \to r$. For now, we will not include these terms.

If we set $p = 0$, then this model describes purely splitting and decay. Since splitting followed by decay represents hopping (i.e. anisotropic diffusion), and there is a limit of one puff per site, this model includes the four basic processes of directed percolation (DP): diffusion, de-coagulation, coagulation and annihilation [24]. For ω_d large enough, the ultimate fate of the system is to be empty. As ω_d becomes smaller, there will be a continuous transition in the DP universality class to a state with persistent mean number of particles $\rho \equiv \langle n_i \rangle \sim (\omega_c - \omega_d)^\beta$, with $\beta = 0.276$ in 1D.

The question that we now address is how the additional terms in the puff-splitting model modify the critical behavior from DP. We will answer the question by writing down a stochastic hydrodynamic model for the puff-splitting model, and then analyze its critical behaviour using renormalization group arguments.

Stochastic hydrodynamics for puff-splitting model:- The discrete stochastic puff-splitting model can be expressed as a field theory using standard techniques that use the Doi formalism [25], followed by a Martin–Siggia–Rose [26–28] transformation to a coherent state path integral [29]. We will not use that method here, although we will need to use the result later. An alternative, shown in the Appendix, is to derive the stochastic equation by writing down the master equation, and then performing a Kramers-Moyal expansion to second order to derive the corresponding Fokker-Planck equation, and thence the

Langevin equation [30]. In this coarse-grained formulation that neglects higher order derivatives, the lattice becomes a continuum ($i \to x$). This amounts to writing $n_i \to \rho(x)$ and

$$n_{i+1} \approx \rho(x) + \partial_x \rho(x) + \frac{1}{2}\partial_x^2 \rho(x) \qquad (2)$$

and reading off the noise, to obtain

$$\partial_t \rho = -\omega_d \rho + \frac{1}{2}(p+\omega_s)\partial_x^2 \rho - (p+\omega_s)\partial_x \rho + \omega_s \rho(1-\rho)$$
$$+(2p+\omega_s)\rho\partial_x\rho - \frac{\omega_s}{2}\rho\partial_x^2\rho + \sqrt{\rho(1-\rho)}\eta \qquad (3)$$

where $\eta(x,t)$ is a white noise delta-correlated in space and time. The dynamics is controlled by multiplicative noise, which has the effect that the empty state is absorbing. This form of the noise arises because of the rule that there can only be one particle per site. If this were enforced by an explicit coagulation term of the form $2n_i \to n_i + \varnothing$, the equations would be the same but the minus sign in the noise term would be replaced by a plus sign.

Eq. (3) is similar to the Langevin equation for DP, but with the addition of three terms: the term proportional to $\partial_x \rho$ and the last two terms of second order in ρ. The linear term arises because the puff dynamics is diffusive (the second order term, linear in ρ) but in a frame moving with the net velocity of the puffs. This anisotropic diffusion can be removed by a Galilean transformation into the comoving frame. The second term is proportional to $\rho\partial_x\rho$ and has the functional form of the advective nonlinearity in Burgers equation. Such terms naturally arise in TASEP models, and loosely speaking lead to shocks that model the bunching up of particles, as occurs in traffic jams, transcription by ribosomes moving on mRNA etc. These shocks are regularized by the higher order derivative terms, including the third extra term and the linear diffusive term. We will refer to the terms $\rho\partial_x\rho$ and $\rho\partial_x^2\rho$ as the Burgers-like terms.

Universality class of the puff-splitting model:- The puff-splitting model without the Burgers-like terms is in the universality class of DP. We now examine whether or not the Burgers-like terms change the universality class, by calculating whether or not they are relevant or irrelevant in the renormalization group sense at the fixed point that controls DP. To do that, we will use the field theoretic RG, in which the critical dynamics of DP is generated by a Martin–Siggia–Rose action of the form [29]

$$A(\rho,\tilde\rho) = \int d^d x\, dt\, \big[\tilde\rho\left(\partial_t + D(r-\partial_x^2)\right)\rho$$
$$-u_3\tilde\rho(\rho - \tilde\rho)\rho + u_4\tilde\rho^2\rho^2 + O(\rho^5)\big] \qquad (4)$$

where $\tilde\rho$ is a so-called response field that arises during the representation of the problem as a field theory, u_3 and u_4

are coupling constants of cubic and quartic terms, D is an effective diffusion coefficient, and r is a control parameter that vanishes at the critical point (for an excellent review, see Ref. [29], pp. 173-174). The requirement that the action be dimensionless implies that the dimensions of the fields can be expressed in terms of the momentum cut-off μ as follows: $[x] = \mu^{-1}$, $[t] = \mu^{-2}$, $[\rho] = \mu^{d/2}$, $[D] = \mu^0$, $[r] = \mu^2$, $[u_3] = \mu^{2-d/2}$, $[u_4] = \mu^{2-d}$.

The lowest order nonlinearity beyond free field theory is the cubic term, whose scaling dimension is $2 - d/2$, implying that the critical behavior deviates from mean field theory for $d < 4$ (for an introduction to the renormalization group for DP, see Ref. [29], p. 404 et seq.). The cubic nonlinearity is the only contributor to the non-analytic scaling behavior below four dimensions, and the critical behavior can be calculated using (e.g. an expansion in $4 - \epsilon$ dimensions) (see (e.g.) [31]). The quartic coupling constant u_4 has scaling dimension $2 - d$, so as the momentum cut-off $\mu \to \infty$, the quartic coupling gets weaker and weaker, and is irrelevant in the RG sense at the four dimensional fixed point that controls the behavior for $d < 4$. Thus, even as low as $d = 1$, DP is controlled by the cubic nonlinearity only. We now apply the same reasoning to the Burgers-like terms in Eq. (3), but work directly with the stochastic differential equation rather than the field theoretic action.

The stochastic differential equation corresponding to the DP action of Eq. (4) is [29]:

$$\partial_t \rho = -D(r - \partial_x^2)\rho - u_3\rho^2 + \xi \qquad (5)$$
$$\langle \xi(x,t)\xi(x',t')\rangle = 2u_3\rho(x,t)\delta(x-x')\delta(t-t') \qquad (6)$$

Note that the dimension of all the terms in the equation is $\mu^{2+d/2}$. Thus, to see how the Burgers-like terms scale under renormalization, we calculate the coupling constant dimensions using the known scaling dimensions of space and the field ρ. Denoting the coupling constant of the Burgers term as λ_1, we equate

$$[\lambda_1 \rho\partial_x\rho] = \mu^{2+d/2} \qquad (7)$$

to obtain

$$[\lambda_1] = \mu^{1-d/2} \qquad (8)$$

At the fixed point in $d = 4$, this has negative scaling dimensions and flows to zero as $\mu \to \infty$. We conclude that this Burgers-like term is irrelevant for DP. Similarly, the coupling constant λ_2 for the Burgers-like term $\rho\partial_x^2\rho$ scales as $\mu^{-d/2}$ and thus is also irrelevant at the DP fixed point. These results are consistent with earlier studies briefly mentioned in Ref. ([32]) (p. 471 and 477).

Puff suppression and pushing:- The experiments suggest that puffs that are close and downstream of another puff, experience an additional rate of decay, $\tilde\omega$ and a higher velocity to the right. We can model suppression in the

stochastic hydrodynamic model by a term that in mean field theory follows:

$$\partial_t \langle n_i \rangle = -\tilde{\omega} \langle n_{i-1} n_i \rangle \tag{9}$$

and model pushing by an enhanced hopping at a rate r for nearest neighbour downstream puffs:

$$\partial_t \langle n_i \rangle = -r \langle n_i n_{i-1}(1 - n_{i+1}) \rangle + r \langle (1 - n_i) n_{i-1} n_{i-2} \rangle. \tag{10}$$

Going to the continuum stochastic hydrodynamical description, these terms will all be represented by high order operators of the form

$$I_{\alpha\beta\gamma} \equiv \lambda_{\alpha\beta\gamma} \rho^\alpha \left(\partial_x^\beta \rho \right)^\gamma \tag{11}$$

where the coupling constants $\lambda_{\alpha\beta\gamma}$ scale as $\mu^{y_{\alpha\beta\gamma}}$ with

$$y_{\alpha\beta\gamma} = 2(2 - \alpha - \gamma) - \beta\gamma. \tag{12}$$

For $\alpha, \beta, \gamma \geq 1$, $y_{\alpha\beta\gamma} < 0$, so the effect of puff suppression and pushing, at least at large scales is irrelevant and should not change the universality class of the transition from DP.

Numerical results on lattice model:- To verify these predictions, we have performed numerical simulations. The RG calculation reveals the asymptotic critical scaling, but in practice there might be slow crossovers to the true critical behavior, due to the finite length of a pipe and the finite time for sampling puff dynamics. These effects will be acute near any putative critical point, and so it is important to be able to predict how these effects will be manifested in experiments and simulations. In addition, the divergence of the relaxation time near the critical point means that simulations may be biased by long-lived transients, and these need to be taken into account also.

To rule out sensitive dependence on the numerical implementation, two different computer codes with different update rules and parameter sets were used to check the results. In the first, a minimal discrete model was used to check numerically the conclusions based on perturbative RG arguments given above. In the second, a continuum stochastic dynamics simulation was performed, with a greater level of realism regarding the interactions between the puffs, as determined experimentally. In both simulations, we observe the emergence of a jammed or crystalline phase above the turbulence transition due to the "traffic jams" experienced by puffs. As the transition is approached from higher Reynolds numbers, the crystalline phase effectively melts due to strong fluctuations through the appearance of interspersed disordered regions. Both simulations, when analysed properly, show that the asymptotic universality class is directed percolation, but we identify strong artifacts that complicate the direct observation in experiments of the asymptotic critical scaling.
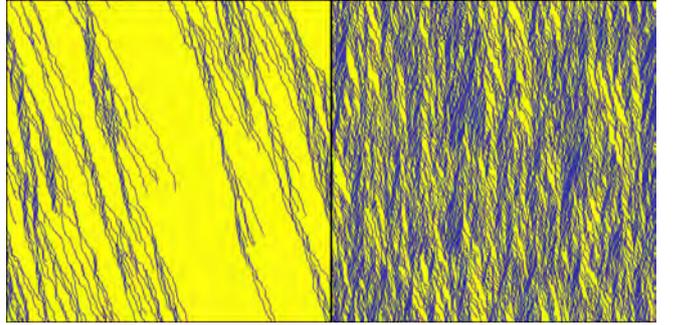

FIG. 1. Numerical simulations of the lattice model for systems respectively below (left panel) and above (right panel) the critical point. Clearly visible above the critical point are traffic jams of puffs, forming a crystalline phase, interspersed with regions of disordered puffs. As the transition is approached from above, the disordered eventually dominate, leading to the pure DP behavior at the critical point. In these simulations, $\omega_d = 0.01$, $\tilde{\omega} = 0.01$, $p = r = 0.5$, and $\omega_{push} = \omega_s$ with $\omega_s = 0.0175$ in the left panel and $\omega_s = 0.0375$ in the right panel.

We performed the numerical simulations on a periodic lattice of length L (see Fig. 1). In addition to the nearest-neighbor rules *propagation*, *decay* and *splitting* described above, additional rules are implemented modeling *suppression* and *pushing*. Specifically, in each time step all puffs on the lattice are submitted randomly to one of three actions, move, split and decay. After we have picked a given action, we execute it with a probability computed from predefined rates. The move shifts a puff on site i one lattice unit ahead at a rate p provided that the site $i + 1$ is vacant. A splitting event of a puff on site i introduces a new puff either at site $i + 1$ or site $i + 2$ with pre-defined rates ω_s and ω_{push}, respectively. The push is only possible if the sites $i + 1$ and $i + 2$ are vacant. Please note that we could instead have introduced the new puff on either of the sites $i - 1$ or $i - 2$ without changing quantitatively the dynamics. A puff on a site i decays with a rate ω_d if the site $i + 1$ is vacant. Otherwise it decays at a higher rate $\tilde{\omega}$. We then performed the simulations for different systems sizes and for a given number of time steps. We output the density of puffs on the lattice at regular time steps and check whether the system has collapsed into the absorbing state. We also take care to remove long-lived transients, and only take data once the transients have decayed. This required us to run as much as 10^7 time steps before equilibration, when close to the transition.

The results of our simulations are summarized in Fig. (2). The turbulent fraction ρ varies with the splitting rate $(\omega_s - \omega_c)^\beta$ with $0.27 < \beta < 0.285$, consistent with the expectation from DP. We have verified that the puff dynamics is in a range where there are strong pushing and "traffic jam" effects.
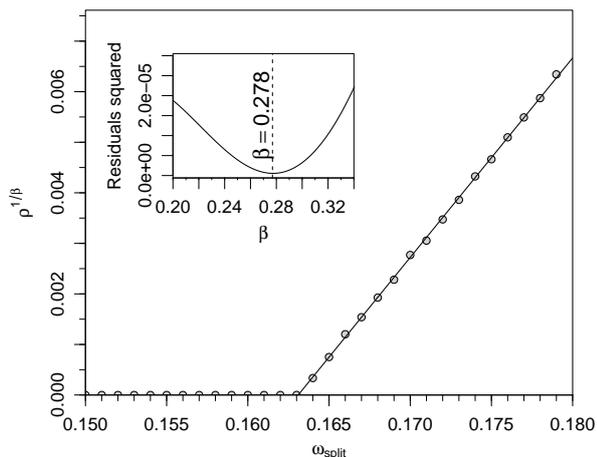
FIG. 2. Turbulent fraction ρ as a function of splitting rate, for a system size $L = 3200$ and averaged over 400 simulations and after a transient of $T = 10^7$ time steps. The vertical axis is the turbulent fraction $\rho^{1/\beta}$ where β has been estimated by a linear model whose residual is shown as function of β in the inset. The value of $\beta = 0.278$ used in the vertical axis varies slightly but has a sample variation in the range 0.270 to 0.285, which is consistent with the known value $\beta \approx 0.276$ for DP. In these simulations, $\omega_d = 0.04$, $\tilde{\omega} = 0.2$, $p = r = 0.5$, and $\omega_{push} = \omega_s$ as on the abscissa.

Numerical results on continuum model:- The discrete model of puff dynamics captures the basic puff interactions efficiently, allowing the universality class to be determined. Nevertheless, it is important to check that a molecular dynamics simulation of interacting puffs, using the measured effective potential between puffs, is in the universality class of the minimal models presented above, and so indeed exhibits the predicted DP scalings. We have checked this by solving the equations of motion. The experimental results indicate the excess velocity of a downstream neighbour puff depends exponentially on the separation, with a decay constant that is roughly twice the puff extent. Puffs extend about $20D$, so the interaction range is given by $\lambda \sim 40D$. The stochastic equations of motion of puffs are given by:

$$\frac{\mathrm{d}x_i}{\mathrm{d}t} = v(x_{i+1} - x_i) + \sqrt{D}\xi_i(t) \qquad (13)$$

where $v(\ell) = 1 - e^{-\ell/\lambda}$, $\omega_d(\ell) = \omega_d^0 [A + (1 - A)v(\ell)]$ and $\omega_s(\ell) = \omega_s^0 [A^{-1} + (1 - A^{-1})v(\ell)]$, and $\xi_i(t)$ is a Gaussian white noise, such that $\langle \xi_i(t)\xi_j(t') \rangle = \delta_{ij}\delta(t - t')$. Here A is a prefactor for the exponential amplification/reduction when a puff is close upstream. Note that these equations of motion have been formulated in a co-moving frame, in order to limit the number of input variables.

In our simulations, we have introduced a model Reynolds number R through setting $\omega_d^0 = \bar{\omega} - R$ and $\omega_s^0 = \bar{\omega} + R$. We have chosen the fixed model values $\bar{\omega} = 0.005$, $A = 50$, $\lambda = 0.1$, and $D = 0.001$ to mimic the experimental results in Ref. [21]. The initial state was chosen to be equidistant spacing with ℓ resulting from solving $\omega_d(\ell) = \omega_s(\ell)$ (i.e. the mean field solution). Eq. (13) was solved numerically using the Itô formalism and an explicit Euler scheme. Fig. 3 shows space-time plots over three realisations in a rather small ($L = 100$ system) for the initial time window $t \in [0, 10000]$; for R below, approximately on, and above the critical point. Below criticality (Fig. 3a), the turbulent fraction quickly decays and less of the domain is in a crystalline state, whereas above (Fig. 3c), the turbulent fraction stays higher and the puffs remain jammed. Fig. 4 shows the time-asymptotic turbulent fraction as a function of R, averaged over up to 10 realisations per R. Every R where at least one of the realisations died out has been omitted; hence we should be guaranteed to move towards the true curve from above. It is clear that increasing system size yields consistent results and the possibility stabilize at lower values of ρ. The critical point at $R = R_c$ was computed by plotting $\rho^{1/\beta}$ versus R and extrapolating a linear fit to the lowest 20% of the data points to intersect with the abscissa (see inset of Fig. 4). With the parameters above, our results give the value 3.455×10^{-5}. Now, plotting $t^\alpha \rho_t$ against $t|\epsilon|^\nu$, where $\epsilon = R - R_c$, should give two scalings below and above criticality. Shown in Fig. 5 are only data from the $L = 10000$ simulations, and indeed the results are consistent with DP, since, by using only the DP exponents and the computed R_c, the scaled data collapses onto two universal curves.

Finite-size effects and artifactual first-order transitions:- Directed percolation lifetimes diverge rapidly near the critical point, and failure to take this properly into account can generate misleading results. This is illustrated in Fig. 6. In particular these effects are related to the finite size in space L and the finite simulation time (number of time steps) T. Since the system exhibits critical slowing down $\rho_t \sim t^{-\alpha}$ at the critical point, the number of time steps required to reach a converged turbulent fraction ρ, diverges. Near the transition correlation lengths in space and time respectively diverge with critical exponents $\nu_\perp$ and $\nu_\parallel$ respectively. Thus, if the simulation domain does not scale in the same way as the transition is approached, finite size or finite time effects will arise. This can be quantified by the quantity

$$Q \equiv T/L^{\nu_\parallel/\nu_\perp}. \qquad (14)$$

If $Q = O(1)$ as the critical point is approached, the scaling is not contaminated by finite-size or finite-time effects. If $Q \ll 1$, the time of simulation is too short, and so some sample paths will survive even though they would in fact die out at longer times. This corresponds to the regime in Fig. (6) where T is the limiting factor, and ω_c is under-estimated. On the other hand, if

(a) $R = 0.00001$ (b) $R = 0.000035$ (c) $R = 0.00005$
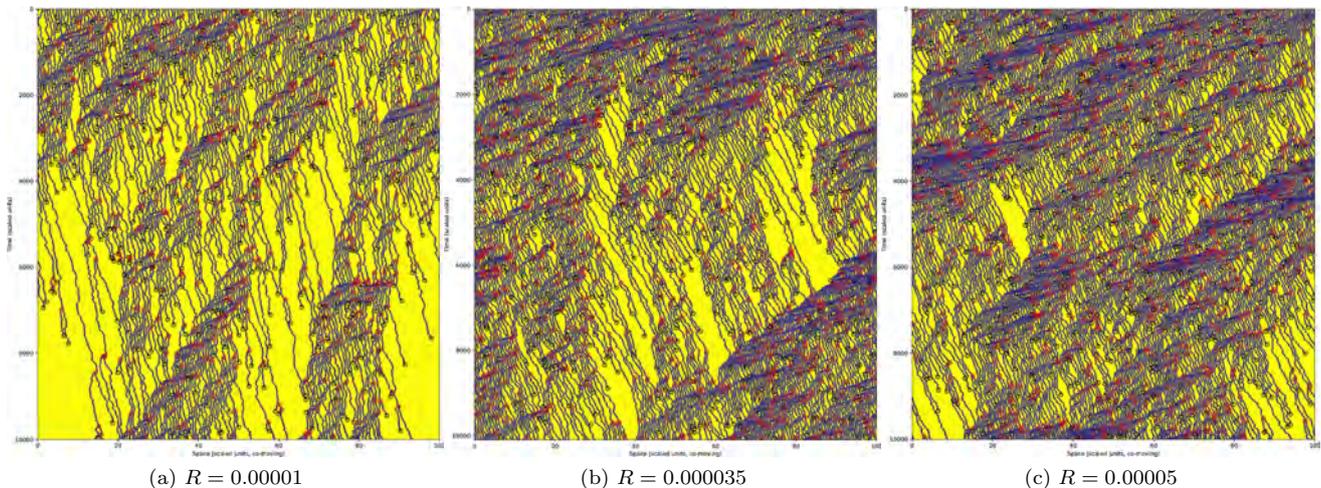
FIG. 3. Spacetime plots at (from left to right) increasing model Reynolds numbers R for the continuous numerical model. Panel (a) shows subcritical behaviour, while (b) and (c) are supercritical. The continuum model clearly exhibits the same phenomenology as the minimal discrete model, with puff traffic jams (crystalline phases) interspersed by disordered regions, whose extent grows as the critical point is approached from above.
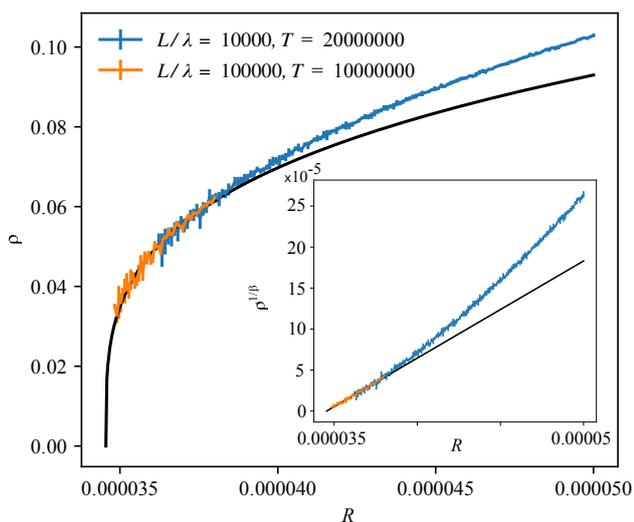
FIG. 4. Time-asymototic turbulent fraction ρ versus model Reynolds number R for the continous model. The solid black line is the DP asymptote (determined in the inset). Inset: $\rho^{1/\beta}$ versus R, to be consistent with DP the data should be linear close to the critical point. (Corrections to scaling are expected and clearly observed.)

FIG. 5. Data collapse for the continous model for the $L = 10000$ case shown in Fig. 4. The only parameter used was R_c, determined from the linear extrapolation shown in the inset of Fig. 4. The critical exponents are from DP.

$Q \gg 1$ as $\omega \to \omega_c$, L is not large enough for there to be enough trajectories to survive to T, and so some of the trajectories that should have survived to long times will have decayed due to stochastic effects, so that it appears that ρ vanishes at a higher ω than the correct ω_c. As a result, it will seem that ρ jumps discontinuously or rises very quickly from the over-estimated ω_c, implying the interpretation of a first-order transition, or a small

value of β (which would give rise to a steeper rise of the order parameter). Only if $Q = O(1)$ as the transition is approached will the correct scaling be found.

These scaling arguments lead to a surprising consequence. In the regime where $Q \gg 1$, running the simulations for too long a time will mean that the trajectories will ultimately die out, leading to the artifactual conclusion that the transition is first order, or has a value of β that is smaller than the DP value, and in fact, will not
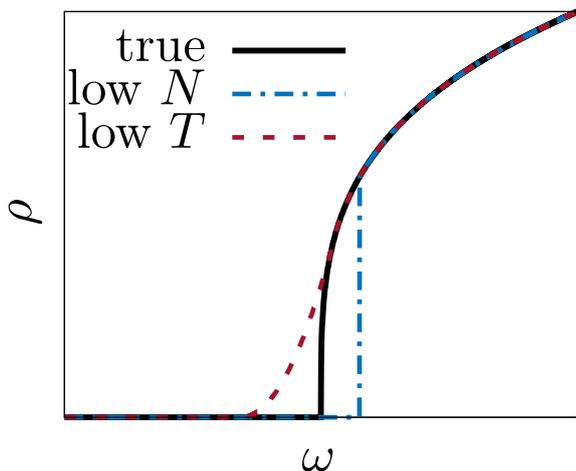
FIG. 6. Sketch of how finite size effects that give rise to error in the estimation of the critical exponent β close the critical point at $\omega = \omega_c$. If the system size L (called N in the figure but we will change that) is the limiting factor, fluctuations will kill turbulent states above ω_c, leading to an overestimation of ω_c and a lower perceived exponent β (or the perception of a discontinuous phase transition). If the simulation time T is the limiting factor, long-lived turbulent states do not have time to decay and this leads to an underestimation of ω_c, and a higher perceived β.

have a fixed value, but will appear to continually change as a function of the finite time T.

We have verified these scaling predictions in the discrete and continuous simulations. For example
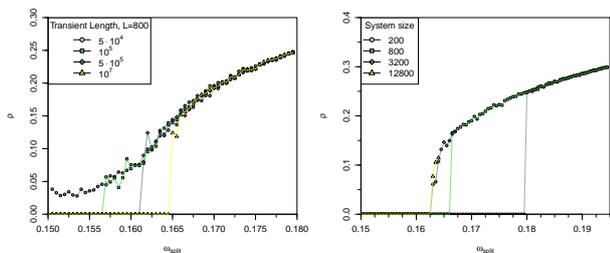
FIG. 7. Demonstration of finite size and time artifacts on the order parameter scaling of directed percolation. (a) System size $L = 800$, simulation time shown in legend. As the simulation time is increased, the transition becomes apparently first order. As the simulation time is decreased the transition does not occur until an anomalously small value of ω_s. (b) System size is varied between 200 and 12800 while simulation time is held constant at $T = 5 \cdot 10^7$. The transition becomes apparently first-order for small system sizes.

Effects of weak and strong pushing:- We can use the finite-size scaling to deduce how artifacts can arise in finite-size and time simulations as the strength of the pushing effect, denoted here as F, is increased. Physically, the

strength of pushing is determined by the magnitude of the puff interaction range λ, but this can also be a range of hopping parameter in the discrete model. The essential result of increasing F is that the puff interactions have an effective hard core size that is of order F. Thus in effect, the system size has been *reduced* by the factor F. This means that if we keep L and T fixed but simply vary F, the effective value of Q is replaced by $Q_F \equiv QF^{\nu_\parallel/\nu_\perp}$. Then for $Q_F \ll 1$, the transition will be rounded and the critical ω_s will be under-estimated. For $Q_F \gg 1$, the transition will appear to be discontinuous or have an unexpectedly small β. This artifactual result will be found in the strong pushing limit.

Discussion:- We conclude that RG theory and simulations indicate that even with strong puff-puff interactions of the suppression-pushing type, the universality class for the transition to pipe turbulence is consistent with directed percolation.

In the model considered here, the unit of turbulence is considered to be a single puff, and the model purely describes the interactions between puffs treated as space-filling particles. The dynamics of these puffs is modeled by rules that encapsulate the actual hydrodynamic interactions arising from the way in which one puff influences the mean velocity profile across the pipe. However, one can also ask what is the dynamics of turbulence in general, and in particular on scales smaller than a single puff? Do they also exhibit the characteristics of directed percolation, as originally implied by Pomeau [15]. This question is distinct from the model considered here, and can be addressed by attempting to derive the effective theory for turbulence from the Navier-Stokes equation, as was done in Ref. [13]. The result in this case was that the most singular contribution to the behavior near the onset of turbulence arose from the interplay between a collective large-scale zonal flow and small scale turbulent anisotropy. Remarkably, the ensuing Landau theory model turns out also to be in the universality class of directed percolation, at least asymptotically close to the transition. The point we wish to emphasise is that the occurrence of directed percolation in this case is very different from what happens in the puff-splitting model of the present paper. In fact, the puff-splitting model describes decay, merging and splitting of point particles and these dynamics are all that is needed in order for the directed percolation universality class to emerge.

[1] S. Pope, *Turbulent Flows* (Cambridge University Press, Cambridge, UK, 2000).

[2] U. Frisch, *Turbulence: the legacy of AN Kolmogorov* (Cambridge university press, 1995).

[3] B. Hof, A. de Lozar, D. J. Kuik, and J. Westerweel, Phys. Rev. Lett. **101**, 214501 (2008).

[4] K. Avila, D. Moxey, A. de Lozar, M. Avila, D. Barkley, and B. Hof, Science **333**, 192 (2011).

[5] B. Song and B. Hof, Journal of Statistical Mechanics: Theory and Experiment **2014**, P02001 (2014).

[6] P. Manneville, European Journal of Mechanics-B/Fluids **49**, 345 (2015).

[7] D. Barkley, Journal of Fluid Mechanics **803**, P1 (2016).

[8] Y. Pomeau, Nature Physics **12**, 198 (2016).

[9] N. Goldenfeld and H.-Y. Shih, Journal of Statistical Physics **167**, 575 (2017).

[10] G. Lemoult, L. Shi, K. Avila, S. V. Jalikop, M. Avila, and B. Hof, Nature Physics **12**, 254 (2016).

[11] M. Sano and K. Tamai, Nature Physics **12**, 249 (2016).

[12] M. Chantry, L. S. Tuckerman, and D. Barkley, Journal of Fluid Mechanics **824**, R1 (2017).

[13] H.-Y. Shih, T.-L. Hsieh, and N. Goldenfeld, Nature Physics **12**, 245 (2016).

[14] K. Kaneko, Progress of Theoretical Physics **72**, 480 (1984).

[15] Y. Pomeau, Physica **23D**, 3 (1986).

[16] H. Chate and P. Manneville, Physical Review Letters **58**, 112 (1987).

[17] M. Sipos and N. Goldenfeld, Physical Review E **84**, 035304 (2011).

[18] N. Goldenfeld, N. Guttenberg, and G. Gioia, Physical Review E **81**, 035304 (2010).

[19] H.-Y. Shih and N. Goldenfeld, "Extreme value statistics and finite-size scaling at the laminar-turbulent critical point in pipe flow," (2018), unpublished.

[20] A. P. Willis and R. R. Kerswell, Physical Review Letters **98**, 014501 (2007).

[21] V. Mukund and B. Hof, arXiv preprint arXiv:1709.06372 (2017).

[22] D. Helbing, Reviews of Modern Physics **73**, 1067 (2001).

[23] T. Chou, K. Mallick, and R. Zia, Reports on Progress in Physics **74**, 116601 (2011).

[24] H. Hinrichsen, Advances in Physics **49**, 815 (2000).

[25] M. Doi, Journal of Physics A: Mathematical and General **9**, 1465 (1976).

[26] P. Martin, E. Siggia, and H. Rose, Physical Review A **8**, 423 (1973).

[27] H.-K. Janssen, Zeitschrift für Physik B Condensed Matter **23**, 377 (1976).

[28] C. d. Dominicis, in *J. Phys.(Paris), Colloq* (1976) pp. C1–247.

[29] U. C. Täuber, *Critical dynamics: a field theory approach to equilibrium and non-equilibrium scaling behavior* (Cambridge University Press, 2014).

[30] C. Gardiner, Springer Series in Synergetics, Berlin: Springer,— c1994, 2nd ed. 1985. Corr. 3rd printing 1994 (1994).

[31] N. Goldenfeld, *Lectures On Phase Transitions And The Renormalization Group* (Addison-Wesley Reading, MA, 1992).

[32] M. Mobilia, I. T. Georgiev, and U. C. Täuber, Journal of Statistical Physics **128**, 447 (2007).

SUPPLEMENTARY MATERIAL: MASTER EQUATION FOR THE PUFF SPLITTING MODEL

In this Supplementary Material, we derive Eq. (3) of the main paper. The puff splitting model is based on the reactions of decay, hopping and splitting process in one dimension:

$$A_i \xrightarrow{\omega_\mathrm{d}} E_i, \tag{15}$$

$$A_i + E_{i+1} \xrightarrow{p} E_i + A_{i+1}, \tag{16}$$

$$A_i + E_{i+1} \xrightarrow{\omega_\mathrm{s}} A_i + A_{i+1}, \tag{17}$$

where A_i denotes a particle at site i, E_i represents the vacancy at site i, and $i = 1, 2, .., L$. We introduce the coarse-grained particle density centered at site i over a length scale of K lattice sites with a uniform kernel as n_i, specifically,

$$n_i = \frac{1}{K} \sum_{j=-K/2}^{K/2} N_{i+j}, \tag{18}$$

where $N_i = 0, 1$ is the particle number at each site i. We denote the state vector by $\mathbf{n} = (n_1, n_2, ..., n_L)^T$ and define the lattice density operator $\mathcal{E}_i^{\pm}$ as

$$\mathcal{E}_i^{\pm} f(n_i) = f(n_i \pm \Delta), \tag{19}$$

and the master equation can be represented as

$$\partial_t P(\mathbf{n}, t) = \frac{1}{\Delta} \sum_i \left[(\mathcal{E}_i - 1)\omega_d n_i + (\mathcal{E}_{i-1}\mathcal{E}_i^{-1} - 1)\omega_s n_{i-1}(1 - n_i) + (\mathcal{E}_{i-1}\mathcal{E}_i^{-1} - 1)p n_{i-1}(1 - n_i) \right] P(\mathbf{n}, t), \tag{20}$$

where $\Delta = 1/K$. By applying Kramers-Moyal expansion with truncation to the second order,

$$\mathcal{E}_i^{\pm} \approx 1 \pm \Delta \partial_{n_i} + \frac{1}{2}\Delta^2 \partial_{n_i}^2 + ..., \tag{21}$$

Eq. (20) can be rewritten into a Fokker-Planck equation:

$$\partial_t P(\mathbf{n}, t) = -\sum_i \frac{\partial(A_i P)}{\partial n_i} + \frac{1}{2}\Delta\sum_{i,j}\frac{\partial^2(B_{ij}P)}{\partial n_i \partial n_j}, \tag{22}$$

where

$$A_i = -\omega_d n_i - p n_i(1 - n_{i+1}) + (p + \omega_s)n_{i-1}(1 - n_i), \tag{23}$$

$$B_{ij} = [\omega_d n_i + \omega_s n_i(1 - n_{i+1}) + p n_i(1 - n_{i+1}) + p n_{i-1}(1 - n_i)]\,\delta_{ij} + 2p n_i(1 - n_j)\delta_{j,i+1}. \tag{24}$$

The corresponding Langevin equation in Ito's sense is

$$\partial_t \mathbf{n} = \mathbf{A}(\mathbf{n}) + \boldsymbol{\xi}(t), \tag{25}$$

$$\langle \xi_i(t)\xi_{i'}(t')\rangle = \Delta B_{ii'}\delta(t - t'). \tag{26}$$

In continuum limit in space, the density operator is defined as

$$\tilde{\mathcal{E}}_x^{\pm} f[\rho(y)] = f[\rho(y) \pm \Delta\delta(y - x)], \tag{27}$$

and Eq. (20) becomes

$$\begin{aligned}
\partial_t P(\rho, t) = \frac{1}{\Delta}\bigg\{ &\int (\tilde{\mathcal{E}}_x - 1)\omega_d\rho(x)P\,dx \\
&+ \iint \left(\tilde{\mathcal{E}}_y\tilde{\mathcal{E}}_x^{-1} - 1\right) p\rho(y)\left[1 - \rho(x)\right]\delta(x - y - \epsilon)P\,dxdy \\
&+ \iint \left(\tilde{\mathcal{E}}_x^{-1} - 1\right)\omega_s\rho(y)\left[1 - \rho(x)\right]\delta(x - y - \epsilon)P\,dxdy \bigg\},
\end{aligned} \tag{28}$$

where ϵ is the lattice spacing. The Kramers-Moyal expansion gives

$$\tilde{\mathcal{E}}_x^{\pm} \approx 1 \pm \Delta\frac{\delta}{\delta\rho(x)} + \frac{1}{2}\Delta^2\frac{\delta^2}{\delta\rho(x)^2} + ..., \tag{29}$$

and with truncation to the second order, Eq. (28) becomes

$$\begin{aligned}
\partial_t P(\rho, t) \approx &-\int \frac{\delta}{\delta\rho(x)}\left\{-\omega_d\rho(x - \epsilon) + (p + \omega_s)\rho(x - \epsilon)\left[1 - \rho(x)\right] - p\rho(x)\left[1 - \rho(x + \epsilon)\right]\right\}dx \\
&+ \Delta\int \frac{\delta^2}{\delta\rho(x)^2}\left\{\omega_d\rho(x) + (p + \omega_s)\rho(x - \epsilon)\left[1 - \rho(x)\right] + p\rho(x)\left[1 - \rho(x + \epsilon)\right]\right\}dx \\
&+ \Delta\iint \frac{\delta^2}{\delta\rho(x)\delta\rho(y)}\left\{-2p\rho(y)\left[1 - \rho(x)\right]\delta(x - y + \epsilon)\right\}dxdy.
\end{aligned} \tag{30}$$

By using

$$\rho(x \pm \epsilon) \approx \rho(x) \pm \epsilon\partial_x\rho(x) + \frac{1}{2}\epsilon^2\partial_x\rho(x) + ..., \tag{31}$$

Eq. (30) can be written into a Fokker-Planck equation:

$$\partial_t P(\rho, t) \approx -\int \frac{\delta}{\delta\rho(x)}\left[\mathcal{A}(\rho, x)P\right]dx + \frac{1}{2}\Delta\iint \frac{\delta^2}{\delta\rho(x)\delta\rho(y)}\left[\mathcal{B}(\rho, x, y)P\right]dxdy, \tag{32}$$

where

$$\begin{aligned}
\mathcal{A}(\rho, x) = &-\omega_d\rho(x) + \omega_s\rho(x)\left[1 - \rho(x)\right] + \frac{1}{2}\epsilon^2(p + \omega_s)\partial_x^2\rho(x) \\
&-\epsilon(p + \omega_s)\partial_x\rho(x) + \epsilon(2p + \omega_s)\rho(x)\partial_x\rho(x) - \frac{1}{2}\epsilon^2\omega_s\rho(x)\partial_x^2\rho(x),
\end{aligned} \tag{33}$$

$$\begin{aligned}
\mathcal{B}(\rho, x, y) = &\left\{\omega_d\rho(x) + (2p + \omega_s)\rho(x)\left[1 - \rho(x)\right] + \frac{1}{2}\epsilon^2(p + \omega_s)\partial_x^2\rho(x)\right. \\
&\left.-\epsilon(p + \omega_s)\partial_x\rho(x) + \epsilon\omega_s\rho(x)\partial_x\rho(x) - \frac{1}{2}\epsilon^2(2p + \omega_s)\rho(x)\partial_x^2\rho(x)\right\}\delta(x - y) \\
&-2p\left\{\rho(x)\left[1 - \rho(x)\right] + \left[1 - \rho(x)\right]\left[-\epsilon\partial_x\rho(x) + \frac{1}{2}\epsilon^2\partial_x^2\rho(x)\right]\right\}\delta(x - y + \epsilon).
\end{aligned} \tag{34}$$

The corresponding Langevin equation in Ito's sense is

$$\partial_t \rho(x) = \mathcal{A}(\rho, x) + \xi(x, t), \tag{35}$$

$$\langle \xi(x, t)\xi(y, t')\rangle = \Delta\mathcal{B}(\rho, x, y)\delta(t - t'). \tag{36}$$

By setting $\epsilon = 1$, near transition $\rho \ll 1$, one obtains

$$\partial_t \rho \approx -\omega_d \rho + \omega_s \rho\,(1 - \rho) + \frac{1}{2}(p + \omega_s)\partial_x^2 \rho - (p + \omega_s)\partial_x \rho$$

$$+ (2p + \omega_s)\rho\partial_x \rho - \frac{1}{2}\omega_s\rho\partial_x^2\rho + \sqrt{a\rho - b\rho^2}\,\eta, \tag{37}$$

where $\eta(x, t)$ is a Gaussian white noise and a and b are functions of ω_d, ω_s and p. The nonlinear term in the square root that multiplies the white noise η can be replaced by $\sqrt{\rho}$ near the transition where $\rho \to 0$. This equation is of the form of Eq. (3).

Self-similar distributions of fluid velocity and stress heterogeneity in a dissolving porous limestone

Gaute Linga, Joachim Mathiesen, and François Renard

RESEARCH ARTICLE

Key Points:
- The fluid-solid interaction problem is solved numerically in a porous limestone core sample at several stages of dissolution
- Probability density functions of fluid velocity and solid stress evolve self-similarly as porosity and flow rate is varied
- The unified distributions provide an additional explanation of the sensitivity of rocks to failure due to fluid flow and dissolution

Correspondence to:
G. Linga,
linga@nbi.dk

Self-similar distributions of fluid velocity and stress heterogeneity in a dissolving porous limestone

Gaute Linga[1] [iD]**, Joachim Mathiesen[1]** [iD]**, and François Renard[1,2,3]** [iD]

[1]Niels Bohr Institute, University of Copenhagen, Copenhagen, Denmark, [2]Physics of Geological Processes, Department of Geosciences, University of Oslo, Oslo, Norway, [3]ISTerre, Université Grenoble Alpes, Grenoble, France

Abstract In a porous rock, the spatial distribution of the pore space induces a strong heterogeneity in fluid flow rates and in the stress distribution in the rock mass. If the rock microstructure evolves through time, for example, by dissolution, fluid flow and stress will evolve accordingly. Here we consider a core sample of porous limestone that has undergone several steps of dissolution. Based on 3-D X-ray tomography scans, we calculate numerically the coupled system of fluid flow in the pore space and stress in the solid. We determine how the flow field affects the stress distribution both at the pore wall surface and in the bulk of the solid matrix. We show that during dissolution, the heterogeneous stress evolves in a self-similar manner as the porosity is increased. Conversely, the fluid velocity shows a stretched exponential distribution. The scalings of these common master distributions offer a unified description of the porosity evolution, pore flow, and the heterogeneity in stress for a rock with evolving microstructure. Moreover, the probability density functions of stress invariants (mechanical pressure or von Mises stress) display heavy tails toward large stresses. If these results can be extended to other kinds of rocks, they provide an additional explanation of the sensitivity to failure of porous rocks under slight changes of stress.

1. Introduction

Reactive fluid flow in porous rocks under stress is ubiquitous both in nature and in industrial applications. Porous flow controls rock weathering, diagenesis in the crust, karst formation, and large-scale fluid circulations at the origin of ore deposits [*Jamtveit and Hammer*, 2012; *Bjørlykke and Høeg*, 1997]. Fluid flow coupled to deformation of porous rocks control the degree to which earthquake-induced deformation can drive transient or permanent changes in crustal permeability [*Rice and Cleary*, 1976]. In fault zones, fluid may exert a pore pressure large enough to reduce the apparent strength along the slip surface, providing an explanation for the apparent low heat frictional force observed on the San Andreas Fault in California [*Byerlee*, 1990]. When coupled to rock transformations in fault zones, this mechanism was also proposed to explain how long-term variations of fluid pressure could control the seismic cycle [*Sibson*, 1992; *Gratier et al.*, 2003].

Industrial applications include enhanced oil recovery, carbon dioxide sequestration, hydraulic fracturing, and cement aging. Injection of CO_2 into geological formations, aquifers, or depleted petroleum reservoirs, poses a promising route to reduce greenhouse gas emissions in the framework of Carbon Capture and Storage [*IEA*, 2014]. Since such formations often contain carbonate minerals, they may react with the injected CO_2-rich fluid, resulting in changes of the pore space geometry that couples to deformation [*Rohmer et al.*, 2016]. This modifies both reactive surface area, porosity, permeability, and, finally, the ability of the rock to store carbon in minerals [*Noiriel et al.*, 2004, 2005].

Search for macroscopic properties, such as porosity or permeability, from local-scale description of microstructures, show that the presence of heterogeneities controls nonlinearities in the transport properties of a porous medium [*Bernabé and Revil*, 1995]. The recent development of the field of Digital Rock Physics now allows to calculate various mechanical and transport properties in rocks based on the full 3-D images of the samples measured by X-ray microtomography [*Arns et al.*, 2002; *Andrä et al.*, 2013; *Øren et al.*, 2007]. Fluid flow at the pore scale has been studied using 3-D porous media extracted by X-ray microtomography to characterize processes such as capillary trapping, CO_2 sequestration, multiphase flow, solute transport, time-dependent evolution of microstructures during fluid-rock interactions [*Blunt et al.*, 2013; *Noiriel*, 2015; *Bultreys et al.*, 2016; *Misztal et al.*, 2015], and numerical modeling methods are reviewed in [*Meakin and Tartakovsky*, 2009]. Elastic properties change during rock transformation (dissolution and precipitation) and depend on the initial

microstructure [*Wojtacki et al.*, 2015]. For example, if either micropores or macropores dissolve preferentially in a limestone rock, the resulting change of elastic parameters and seismic wave velocities would be different [*Arson and Vanorio*, 2015].

On the one hand, simulations of flow through porous solids have determined that there exists orders of magnitude variations in local fluid velocity, even at the millimeter scale [*Brown*, 1987; *Bijeljic et al.*, 2013; *De Anna et al.*, 2013; *Le Borgne et al.*, 2013], indicating that both local pressure gradients and channeling flow are important [*Brown*, 1987]. On the other hand, the study of coupled fluid flow and solid deformation is the basis of the theory of poroelasticity [*Rice and Cleary*, 1976; *Coussy*, 2004]. Here we study the coupling between stress and fluid flow in a porous rock that dissolves. The complexity of fluid flow and stress heterogeneity stems from randomness of the medium and the possible coupling between forces in the solid and forces exerted by the flowing fluid. The stress distribution in the solid phase, and in particular at the solid-fluid interface, is highly heterogeneous at the scale of grains and pores in the rock. Regions of high stress are prone to stress-enhanced dissolution and crack formation, while regions of low stress are prone to precipitation due to solute transport in the pore space. These processes, over time, alter the pore space geometry and constitute a feedback loop between flow and deformation.

We characterize numerically how heterogeneities in stress, fluid flow, and microstructures impact the hydromechanical behavior of a limestone rock that has undergone several steps of dissolution. We aim to answer the following questions:

1. How does single-phase fluid flow through the pore space of a rock sample under external load affect the stress distribution in it, and, in particular, what is the effect of a heterogeneous microstructure on the stress distribution?
2. How does rock dissolution modify the state of stress and yield strength in the solid?
3. How does dissolution in the rock modify single-phase fluid flow?

The main objectives are (1) to examine whether the stress distributions in the bulk of the solid and at the solid-fluid interface can be described by a common probability density function (PDF) and (2) to quantify the effects of dissolution, i.e., changes in the complex pore space, on the stress distribution, and flow properties. We address these objectives by computational means, using the finite element method to solve the coupled fluid-solid mechanics problem in three-dimensional digitized porous rocks. From our computations, we achieve the fluid velocity field and the stress field in both the fluid and in the solid. We further estimate the mechanical pressure and von Mises stress in the solid under various conditions of external and internal loading. We apply our method to a sample of limestone that has undergone successive steps of dissolution through the percolation of an acidic fluid. This sample was imaged in 3-D before percolation and at three successive steps of dissolution using synchrotron X-ray microtomography [*Noiriel et al.*, 2004, 2005].

The results of the present study can be of primary interest in domains where the heterogeneous and multiscale nature of rocks plays a key role, including, for example, oil and gas reservoir engineering, CO_2 geological sequestration, and fracture mechanics.

2. Model and Method

In this section, we present the numerical methods and the computational model used to calculate the state of stress in a porous solid with a percolating fluid. As we are interested in the instantaneous effects of steady fluid flow, we assume a timescale where the effect of chemical reactions is negligible and where the pore space geometry does not change — i.e., there is no evolution of the microstructure. In this regime, the computational problem involves a one-way coupling of normal stress from the fluid flow to the solid stress field.

2.1. Fluid Flow in the Pore Space

The Navier-Stokes equations, governing the incompressible fluid flow in the pores, are given by

$$\rho \left(\frac{\partial \mathbf{v}}{\partial t} + (\mathbf{v} \cdot \boldsymbol{\nabla}) \mathbf{v} \right) - \mu \boldsymbol{\nabla}^2 \mathbf{v} = -\boldsymbol{\nabla} P, \tag{1}$$

$$\boldsymbol{\nabla} \cdot \mathbf{v} = 0, \tag{2}$$

defined on a domain Ω_ℓ. Here $\mathbf{v}(\mathbf{x}, t)$ is the velocity field, P is the pressure of the fluid, ρ is the (constant) fluid density, and μ is the dynamic viscosity. Closure is obtained by supplying an initial condition $\mathbf{v}(\mathbf{x}, 0) = \mathbf{v}_0(\mathbf{x})$, and a set of boundary conditions:

$$\mathbf{v}(\mathbf{x}, t) = \mathbf{0} \quad \text{for} \quad \mathbf{x} \in \Gamma_{\text{wall}}, \tag{3}$$

$$P(\mathbf{x}, t) = P_{\text{in}} \quad \text{for} \quad \mathbf{x} \in \Gamma_{\text{in}}, \tag{4}$$

$$P(\mathbf{x}, t) = P_{\text{out}} \quad \text{for} \quad \mathbf{x} \in \Gamma_{\text{out}}. \tag{5}$$

Here $\Gamma = \Gamma_{\text{wall}} \cup \Gamma_{\text{in}} \cup \Gamma_{\text{out}}$ represents the entire boundary of Ω_ℓ, which we, for now, assume does not deform in time, while P_{in} and P_{out} are constant fluid pressures imposed at the inlet and outlet of the system, respectively.

For a porous rock we consider that the characteristic length scale ℓ_p of the pore space is small, such that the ratio between inertial and viscous forces is low, i.e., the Reynolds number $Re = \rho|\mathbf{v}|\ell_p/\mu \ll 1$. Thus, the advection part of equation (1), $\partial\mathbf{v}/\partial t + (\mathbf{v} \cdot \nabla)\mathbf{v}$, is assumed to be negligible. This assumption is verified, as in experiments by *Noiriel et al.* [2004] (see section 2.4), the speed $|\mathbf{v}|$ is in the range $1-4 \times 10^{-3}$ m s^{-1}, the typical pore size ℓ_p is in the range $1-3 \times 10^{-4}$ m, and the kinematic viscosity of water $\mu/\rho = 1 \times 10^{-5}$ m^2 s^{-1}, which gives a Reynolds number $Re < 0.1$.

In the limit of low Reynolds number, the Navier-Stokes equations (1) and (2) reduce to the Stokes equations, which are linear in velocity and pressure, and can therefore be solved using optimized linear solvers. The time dependence has now vanished, and we are seeking the steady flow field. By introducing the dimensionless variables $\tilde{\mathbf{x}}$, $\tilde{\mathbf{v}}$, and $\tilde{P}$, implicitly defined by

$$\mathbf{x} = L\tilde{\mathbf{x}}, \quad \mathbf{v} = \frac{L}{\mu}(P_{\text{in}} - P_{\text{out}})\tilde{\mathbf{v}}, \quad P = (P_{\text{in}} - P_{\text{out}})\tilde{P} + \frac{P_{\text{in}} + P_{\text{out}}}{2}, \tag{6}$$

where L is the system length; we obtain from equation (1) the well-known Stokes equation in nondimensional form,

$$\tilde{\nabla}^2\tilde{\mathbf{v}} = \tilde{\nabla}P, \tag{7}$$

$$\tilde{\nabla} \cdot \tilde{\mathbf{v}} = 0, \tag{8}$$

$$\tilde{\mathbf{v}}(\tilde{\mathbf{x}}) = \mathbf{0} \text{ for } \tilde{\mathbf{x}} \in \tilde{\Gamma}_{\text{wall}}, \tag{9}$$

$$\tilde{P}(\tilde{\mathbf{x}}) = \frac{1}{2} \text{ for } \tilde{\mathbf{x}} \in \tilde{\Gamma}_{\text{in}}, \tag{10}$$

$$\tilde{P}(\tilde{\mathbf{x}}) = -\frac{1}{2} \text{ for } \tilde{\mathbf{x}} \in \tilde{\Gamma}_{\text{out}}. \tag{11}$$

Here $\tilde{\nabla} = L\nabla$ is the scaled del operator, and $\tilde{\Gamma}$ (with the respective subscripts) is the scaled domain. Since these expressions are all independent of the constants ρ, μ, P_{in}, and P_{out}, all solutions to the Stokes equations are the same up to a scaling constant and a shift in pressure.

The stress tensor in Stokes flow in dimensional quantities is given by

$$\nabla = -P\mathbf{I} + \mu\left(\nabla\mathbf{v} + \nabla\mathbf{v}^\top\right), \tag{12}$$

which means that the dimensional strain tensor can be found from the nondimensional one,

$$\tilde{\nabla} = -\tilde{P}\mathbf{I} + \tilde{\nabla}\tilde{\mathbf{v}} + \tilde{\nabla}\tilde{\mathbf{v}}^\top, \tag{13}$$

by the transformation

$$\nabla = (P_{\text{in}} - P_{\text{out}})\tilde{\nabla} - \frac{P_{\text{in}} + P_{\text{out}}}{2}\mathbf{I}. \tag{14}$$

As a consequence, for a given pore space geometry, performing *one single* steady state simulation is sufficient to obtain the stress field for arbitrary inlet and outlet fluid pressures. Only the linear transformation described above is required to achieve the field resulting from the sought inlet/outlet conditions.

In the forthcoming, we use the following definitions:

$$P_0 = \frac{P_{in} + P_{out}}{2} \qquad \text{(base pressure)} \tag{15}$$

$$\Delta P = P_{in} - P_{out} \qquad \text{(pressure drop)} \tag{16}$$

to quantify the effect of fluid flow in the pore space.

2.2. Fluid-Solid Stress Coupling at the Pore Scale

At the boundary between fluid and solid, Γ_{wall}, the normal stress should be continuous if the solid-fluid interfacial tension is neglected:

$$[[\boldsymbol{\sigma}]] = \boldsymbol{\sigma} \cdot \mathbf{n}\big|_{\Gamma_{wall}^{(s)}} - \boldsymbol{\sigma} \cdot \mathbf{n}\big|_{\Gamma_{wall}^{(\ell)}} = \mathbf{0}, \tag{17}$$

where $\mathbf{n}$ is the unit normal at the interface, pointing into the solid. The superscripts (s) and (ℓ) denote evaluation at the solid and liquid sides of the interface, respectively. If we assume that we consider time scales in which the solid does not deform due to fluid flow (equations (7)–(11)), the no-slip boundary condition (9) on the fluid is valid, and hence, the viscous stress boundary condition on the solid is prescribed by the fluid. As mentioned above, this yields a one-way coupling from the fluid to the solid phase which encompasses computational simplification.

2.3. State of Stress in the Solid Phase

For small deformations, the solid phase is described by linear elasticity, such that stress, $\boldsymbol{\sigma}$, and strain, $\boldsymbol{\epsilon}$, are related via Hooke's law

$$\boldsymbol{\sigma} = \frac{E}{1+\nu}\left[\boldsymbol{\epsilon} + \frac{\nu}{1-2\nu}\mathbf{I}\mathrm{tr}(\boldsymbol{\epsilon})\right], \tag{18}$$

where E is Young's modulus and ν is Poisson's ratio. The strain tensor in the solid is given by

$$\boldsymbol{\epsilon} = \frac{1}{2}\left(\boldsymbol{\nabla}\mathbf{u} + \boldsymbol{\nabla}\mathbf{u}^{\top}\right), \tag{19}$$

where $\mathbf{u}(\mathbf{x})$ is the displacement field. By considering the static elastic field (i.e., time scales much larger than the time elastic waves take to propagate through the system), stress equilibrium in the rock is expressed by

$$\boldsymbol{\nabla} \cdot \boldsymbol{\sigma}[\mathbf{u}(\mathbf{x})] = \mathbf{0}, \tag{20}$$

where the right-hand side is equal to zero since we neglect body forces, such as gravity.

Closure of the equation system is obtained by supplying the following boundary conditions. Inside the rock, at the interface between fluid and solid interface, this boundary condition is given by equation (17). At the *outside* boundary of the solid, Γ_{ext}, i.e., the part of the boundary which is not in contact with the fluid, a prescribed normal traction (equivalent to a pressure force) is imposed:

$$\boldsymbol{\sigma} \cdot \mathbf{n} = -P_{ext}\mathbf{n}, \quad \text{for} \quad \mathbf{x} \in \Gamma_{ext} \setminus \Gamma_{bot}, \tag{21}$$

except at the bottom plane Γ_{bot}, where we apply a no-slip condition on the displacement field,

$$\mathbf{u}(\mathbf{x}) = \mathbf{0}, \quad \text{for} \quad \mathbf{x} \in \Gamma_{bot}, \tag{22}$$

in order to remove translational and rotational freedom and thereby achieve uniqueness of solution. Doing so, the force exerted by the fluid flowing in the pore space to the solid surfaces are integrated as a boundary condition and therefore coupled to the state of stress of the solid.

$\phi = 0.093$ $\phi = 0.110$ $\phi = 0.167$ $\phi = 0.201$

1 mm

(a)　　　**(b)**　　　**(c)**　　　**(d)**
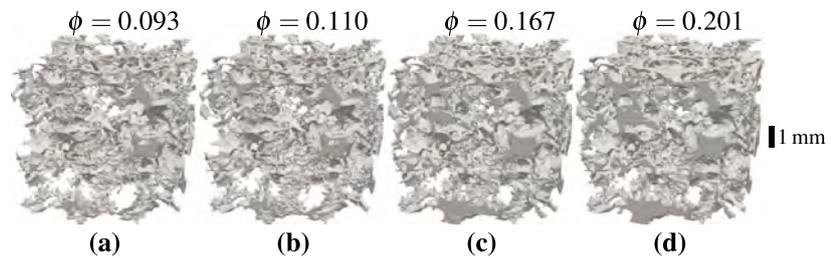
Figure 1. Fluid meshes of the limestone sample at different steps of dissolution. Subfigures show (a) initial geometry, and (b) one step, (c) two steps, and (d) three steps of dissolution. Fluid flow was from bottom to top during the experiments.

2.4. Geometry and Mesh of the Porous Samples

We consider a digital 3-D rock sample which was studied and described by *Noiriel et al.* [2004]. It is a crinoïdal limestone of middle Oxfordian age extracted from the Lérouville formation (Paris Basin). Acidic fluid was injected into this sample, leading to dissolution and porosity increase. The experiments were performed in the diffusion-controlled regime, at low injection rates to avoid dissolution fingering instabilities. The sample has undergone three steps of dissolution, and, between each dissolution step, it was scanned in 3-D, using X-ray microtomography at the European Synchrotron Radiation Facility, at a voxel resolution of 4.91 μm. The results are four digitized volumes: the initial sample before percolation and three volumes after the three stages of dissolution (Figure 1). The original 3-D digitized volumes were segmented to separate the pore space from the solid phase and resampled at 9.8 μm voxel size. The volumes used in the present study have dimensions of 340^3 voxels. The segmented images were prepared such that they constituted one connected cluster both for the solid and fluid phases; i.e., all disconnected "islands" were removed. The removed disconnected pores represented a fraction less than 0.05 of the total pore volume. The segmented volumes were then converted to a tetrahedral mesh for the fluid phase using ISO2MESH [*Fang and Boas*, 2009], a MATLAB interface to TETGEN [*Si*, 2015] for the surface mesh, and CGAL [*The CGAL Project*, 2016] for the volumetric mesh. The triangulated surface of this mesh is used as the inner surface of the solid mesh. This surface mesh was then embedded into a cubic surface mesh, which constituted the outer mesh (Figure 2). This cubic mesh was chosen to be slightly (about 2%) larger than the fluid mesh, such that the whole sample could be loaded uniformly, yielding the same total force on each side of the cube. A tetrahedral volume mesh was then generated between these surfaces. In this way, (1) the solid matrix can be loaded with a uniform normal stress at the outside boundary and (2) no-slip conditions can be appropriately applied for the fluid phase at the entire surface Γ, except inlet Γ_{in} and outlet Γ_{out}.

2.5. Computational Model

The rock we consider is a cubic, *sealed*, elastic porous sample which can be mechanically loaded along all axes, and saturated with a steadily flowing single-phase liquid. With this model, by varying the flow rate and the externally applied stress, one may obtain (1) the fluid velocity field in the pore space of the sample at
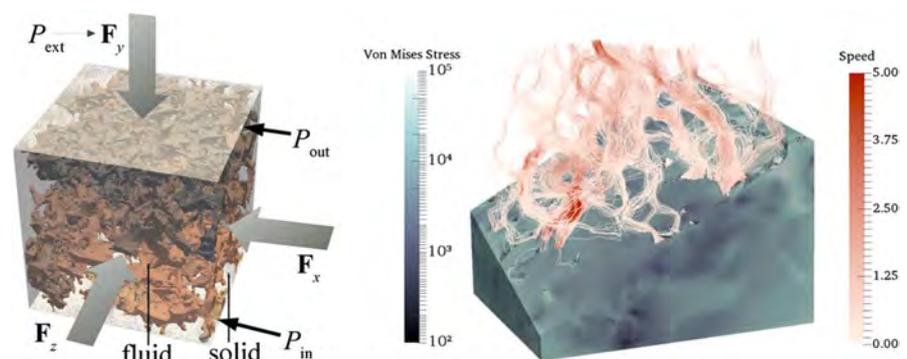
Figure 2. (left) Schematic setup of the model. (right) Simulated 3-D volume, after three dissolution steps, with fluid velocity streamlines and von Mises stress in the solid. The upper half has been clipped to display the fluid phase.

the different steps of dissolution, (2) the stress distribution in the solid space of the sample as a function of applied fluid pressure and external stress, and (3) the probability distributions of invariants of the stress tensor throughout the sample surface or volume.

2.6. Implementation

The coupled fluid-solid problem is solved numerically using the FENICS/DOLFIN framework [*Logg et al.*, 2012a, 2012b]. The FENICS project is a collection of software for automated solution of differential equations using the Finite Element Method (FEM), whereas DOLFIN is a C++/PYTHON library functioning as the main user interface to FENICS. It allows for efficient solution of differential equations requiring only a weak (variational) formulation of the problem to be specified.

2.6.1. Fluid Phase

The fluid equations (7) to (11) are solved using a continuous Galerkin method with first-order Lagrange (P_1) elements both for the velocity and pressure fields [*Langtangen et al.*, 2002]. Since this mixed-space formulation of the Stokes equations causes stability problems, as it violates the Babuska-Brezzi condition [*Brenner and Scott*, 2008], we use a pressure stabilization technique. This amounts to allowing a small grid-dependent compressibility which will smooth out the pressure field solution [*Langtangen et al.*, 2002], i.e.,

$$\boldsymbol{\nabla} \cdot \mathbf{v} = \delta h^2 \boldsymbol{\nabla}^2 P, \tag{23}$$

where h is the element size and δ is a heuristically chosen parameter. Here we have omitted the tildes used for scaled units for the sake of visual clarity. We verified that δ (= 0.04) was chosen small enough for the absolute difference in inlet/outlet flux to be well below 2%, such that the mass of fluid is almost conserved.

The weak formulation of the fluid equations can thus be stated as the following: Find $\mathbf{v} \in \mathcal{V}, P \in \mathcal{P}$ such that

$$\int_{\Omega_\ell} \left(\boldsymbol{\nabla}\mathbf{v} : \boldsymbol{\nabla}\mathbf{v}' - P\boldsymbol{\nabla} \cdot \mathbf{v}' + P'\boldsymbol{\nabla} \cdot \mathbf{v} + \delta h^2 \boldsymbol{\nabla}P \cdot \boldsymbol{\nabla}P' \right) \mathrm{d}V = -\int_{\Gamma_{\text{in}}} P_{\text{in}}\mathbf{n} \cdot \mathbf{v}'\mathrm{d}S - \int_{\Gamma_{\text{out}}} P_{\text{out}}\mathbf{n} \cdot \mathbf{v}'\mathrm{d}S \tag{24}$$

for all $\mathbf{v}' \in \mathcal{V}, P' \in \mathcal{P}$, and $\mathbf{v}(\mathbf{x}) = \mathbf{0}$ for $\mathbf{x} \in \Gamma_{\text{wall}}$. Here $\mathcal{V}$ and $\mathcal{P}$ are the function spaces for velocity and pressure, respectively.

2.6.2. Solid Phase

The elasticity problem is resolved similarly as the fluid phase using P_1 finite elements for the displacement field. The stress in the fluid is transferred to the boundary of the solid phase. The pressure field is given as nodal values, due to the use of first-order Lagrange elements, and can therefore be transferred directly to the solid mesh. However, the viscous stress is a derivative of the velocity field, and therefore exists as constant values on each element. Therefore, by stress reconstruction, the stress is interpolated on the boundary nodes, yielding an error of the order of the element size. To minimize this error, the mesh was refined near the fluid-solid boundaries. Additionally, the magnitude of the viscous stress is orders of magnitude smaller than that of the pressure, as shall be demonstrated in the next section, yielding an even smaller relative error in the boundary stress.

The weak problem formulation can be put as follows: Find $\mathbf{u}'$ in $\mathcal{V}$ such that

$$\int_{\Omega_s} \boldsymbol{\sigma}[\mathbf{u}] : \boldsymbol{\epsilon}[\mathbf{u}'] \, \mathrm{d}V = -\int_{\Gamma_{\text{ext}} \backslash \Gamma_{\text{bot}}} P_{\text{ext}}\mathbf{n} \cdot \mathbf{u}' \, \mathrm{d}S - \int_{\Gamma_{\text{wall}}} P\,\mathbf{n} \cdot \mathbf{u}' \, \mathrm{d}S + \int_{\Gamma_{\text{wall}}} \mathbf{u}' \cdot \boldsymbol{\sigma}_\ell^{\text{visc}} \cdot \mathbf{n} \, \mathrm{d}S, \tag{25}$$

for all $\mathbf{u}' \in \mathcal{V}$, and $\mathbf{u}(\mathbf{x}) = \mathbf{0}$ for $\mathbf{x} \in \Gamma_{\text{wall}}$.

2.7. Probability Density Functions

In the simulated samples, the *empirical* probability density functions (PDFs), $p(\psi)$ for any given scalar field (e.g., pressure, stress invariants, and fluid velocity components), ψ, can be calculated either on the surface or in the bulk (volume) of the sample. That is, $p(x)\,\mathrm{d}W$ gives the probability of finding the value x in an arbitrary infinitesimal volume or area $\mathrm{d}W$.

For the volumetric probability distribution functions, optimal representation is achieved by weighting each nodal value by the size of its surrounding volume, similar to its Voronoi cell. For a given node i, this weight can be expressed as

$$w_i = \frac{1}{4V} \sum_{j \in \mathcal{E}_i} V_j. \tag{26}$$

Here $\mathcal{E}_i$ is defined as the set of all mesh elements which contain node i, V_j is the volume of element j, and V is the total volume. Similarly, for the surface PDFs, the nodal weight is found by

$$w_i = \frac{1}{3A} \sum_{j \in \mathcal{F}_i} A_j \qquad (27)$$

where $\mathcal{F}_i$ is defined as the set of all mesh facets which have node i as a vertex, A_j is the area of facet j, and A is the total area. The PDF is then calculated by normalizing the weighted histogram of the given field. In order to minimize the effect of application of external loading, the nodes closest (within 2%) to the cubic bounding box are omitted.

3. Results

This section presents the results from the coupled fluid-solid simulations. In turn, we present the results from the fluid, and then the stress calculations in the solid due to fluid flow and porosity increase.

3.1. Main Assumptions

Our results are sensitive to a series of assumptions made, mainly related to the discretization of flow in the porous samples:

1. The segmentation process of solid and fluid does not unambiguously capture microporosity as some voxels could contain a fraction of solid and a fraction of porosity.
2. The removal of disconnected pores and the micropores smaller than the voxel size should contribute to stress heterogeneities. Note that the removed disconnected pores represented a fraction less than 0.05 of the total pore volume.
3. The meshing of the complex microstructure could be done in different ways. Note that we are here using unstructured meshes which better approximate the true microstructures than what would using, e.g., a Cartesian grid.
4. The elastic parameters of the solid phase are assumed to be constant throughout the sample.
5. The boundary conditions could have been chosen differently (e.g., strain controlled rather than stress controlled).
6. The sample has a finite size, limiting the range of length scales for the observed spatial correlations.

As such, perfect agreement in comparison to experiments should not be expected. However, the meshes corresponding to snapshots of the sample at different stages of dissolution are prepared in the same way, and therefore the *evolution* of the distributions should hold as long as we consider viscous flow and linear elastostatics. Moreover, the largest stress concentrations are expected to be found near the biggest pores, meaning that the discretization is justified, although, e.g., the "mesh porosity" is not the true porosity. Moreover, the fluid-solid solver was validated against cases where analytical expressions where available, e.g., for fluid flow in a cylindrical pipe and the stress field around a fluid-filled spherical pore. However, as the methods are rather standard and the framework is tested by the group of developers, we believe that the main sources of error lie in the points above, not in the solver itself.

3.2. Fluid Flow in the Pore Space

Here we present the results from pure fluid flow simulations. Due to the invariance under a linear transformation described in section 2.1, the results are given in scaled units. Similarly as in section 2.6.1, we have omitted the corresponding tildes for scaled units. Physical values are found by using equations (6) and (14).

In Figure 3, the simulated flow field is visualized by streamlines, i.e., integrated Lagrangian trajectories of the velocity field. As expected with increasing porosity, the flow through the sample increases. At low porosity, a few preferential flow paths are present. At higher porosities, more paths appear and cross-link with each other.

Flow through porous media is on the *macroscale* governed by Darcy's law,

$$\mathbf{q} = -\frac{k}{\mu} \boldsymbol{\nabla} P, \qquad (28)$$

where $\mathbf{q}$ is the flux (discharge per area) and k is the permeability. Here the flux is related to the mean velocity through the relation $\mathbf{q} = \phi \mathbf{v}$. Historically, much effort has been devoted to relating the permeability k to porosity ϕ, the most popular being the Kozeny-Carman relation commonly expressed as $k = C\phi^3/(1-\phi)^2$

$\phi = 0.093$ $\phi = 0.110$ $\phi = 0.167$ $\phi = 0.201$
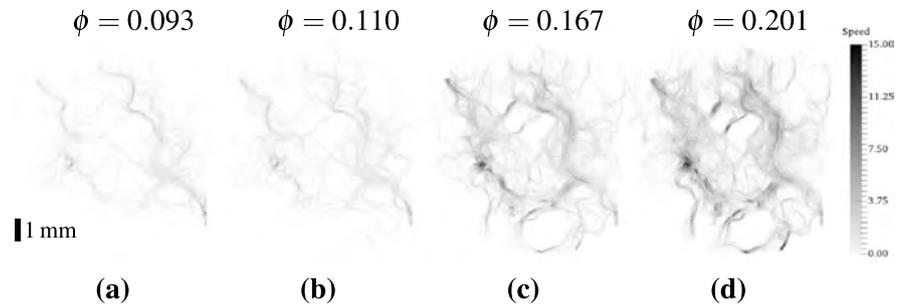
Figure 3. (a–d)Streamlines of simulated velocity field in the sample at different steps of dissolution. Figures 3a and 3b correspond to those in Figure 1.

[*Costa*, 2006; *Matyka et al.*, 2008], where *C* is a constant of dimension (length)^2 related to the geometry of the porous medium. The mean absolute velocity (speed) and the mean axial velocity (parallel to the pressure gradient) are plotted as functions of porosity, $\langle v_y \rangle (\phi)$, in Figure 4 (left), and display superlinear increase with porosity. The solid lines represent power law fittings to the data, which both yield exponents $\simeq 3$. Taking the pressure drop to be constant, the Kozeny-Carman relation predicts that the flux through any cross section of the sample $q = \mathbf{q} \cdot \hat{\mathbf{n}} = \phi \langle v_y \rangle$ of a porous media should depend on porosity as

$$q \propto \frac{\phi^3}{(1-\phi)^2}. \tag{29}$$

This means that the average velocity should scale as $\langle v \rangle \sim q/\phi \sim \phi^2/(1-\phi)^2$. The fittings shown in Figure 4 are thus not in quantitative agreement with Kozeny-Carman relations. However, this is not unexpected, as Kozeny-Carman relations, being derived for packed beds, are usually more applicable to configurations such as high-porosity sandstone, and less so for low-porosity limestone undergoing dissolution. This observation is consistent with the data presented in Figure 4 (right), where permeability *k* in physical units is plotted as a function of porosity ϕ, and the relationship $k \sim \phi^4$ grows faster than the prediction from the Kozeny-Carman relation. The behavior seen here is comparable to the data reported by *Ehrenberg et al.* [2006], although the magnitude is somewhat higher here, especially as dissolution progresses. The permeability calculated here, however, coincides well with the permeability reported in the original experiment [*Noiriel et al.*, 2004].

Figure 5 displays the measured probability distribution of fluid speed in the four volumes. The inset of Figure 5 shows the raw (nonnormalized) data, with a shift of the distribution toward higher speed as porosity is increased. The relevant features of the distributions are extracted by rescaling the speed, *v*, by the mean speed $\langle v \rangle$ in each sample (displayed in Figure 4), as shown in the main panel of Figure 5. The distributions collapse, apart from in the tail (possibly due to the finite size of the computational meshes). As the porosity increases, the distribution approaches a stretched exponential function for large *v*,

$$p(\hat{v}) \sim \exp\left(-\alpha \hat{v}^\beta\right) \tag{30}$$
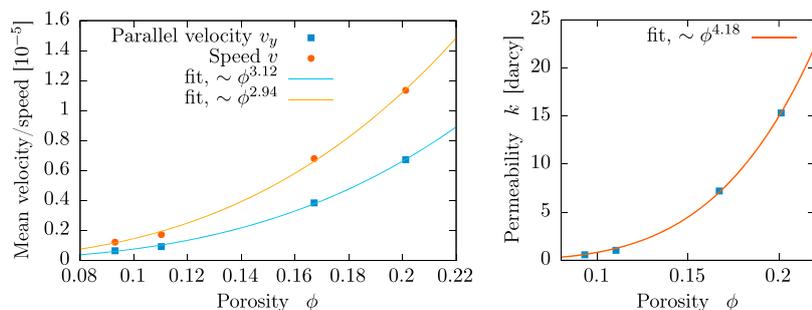
Figure 4. (left) Mean axial velocity/speed in the bulk of the fluid versus porosity in the sample, in scaled units. (right) Corresponding permeability in SI units.
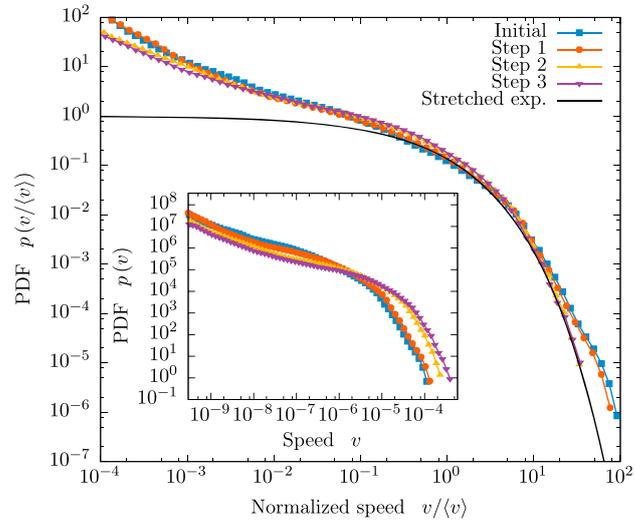
Figure 5. Probability density of the fluid velocity in the pore space at different steps of dissolution. The velocity distributions are collapsed upon rescaling by the average velocity. Inset: Nonnormalized distribution.

where $\hat{v} = v/\langle v \rangle$, the exponent $\beta \simeq 1/2$, and the scale parameter $\alpha \simeq 0.25$. This observation is consistent with established velocity statistics for disordered porous media [*Matyka et al.*, 2016], and the stretched exponential distribution can theoretically be inferred by considering the porous media as a collection of cylinders with exponentially distributed radii [*Holzner et al.*, 2015].

The fluid pressure distribution is shown in Figure 6 and displays a highly heterogeneous distribution between the inlet pressure $P_{\text{in}} = 1/2$ and the outlet pressure $P_{\text{out}} = -1/2$. The distribution is characterized by fluctuations (spikes) that are interpreted to be related to a heterogeneous distribution of dead-end pores. To quantify the heterogeneity in the pressure field arising from the flow, the deviation from a linear pressure profile (like what appears in hydrostatics with a constant gravitational force) can be calculated as

$$\Delta P_{\text{lin}}(\mathbf{x}) = P(\mathbf{x}) - P_{\text{lin}}(\mathbf{x}), \tag{31}$$

where $P_{\text{lin}}(\mathbf{x}) = 1/2 - y, y \in [0, 1]$ is the scaled coordinate along the direction of the imposed pressure drop, such that $y = 0$ corresponds to the inlet face, and conversely for $y = 1$. The resulting distribution is shown in the inset of Figure 6. The distribution is seen to be sharply peaked around $\Delta P_{\text{lin}} = 0$, due to the fixed pressure
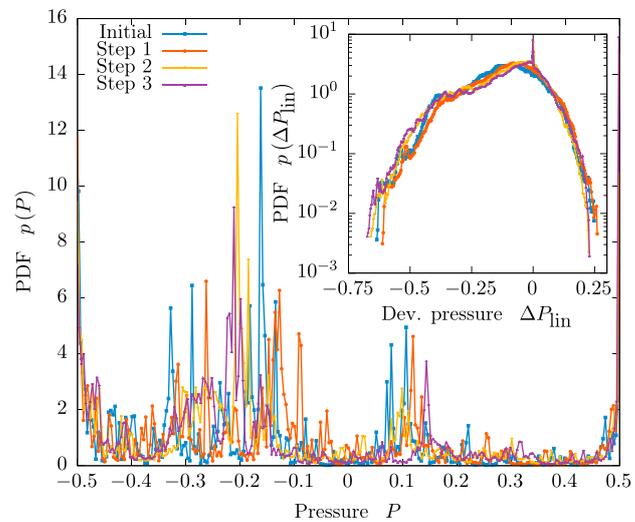
Figure 6. Fluid pressure statistics at the pore walls in the sample at different steps of dissolution.
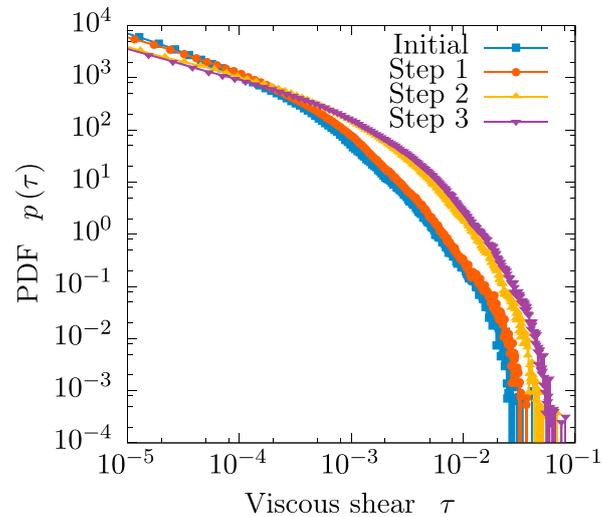
Figure 7. Fluid shear stress statistics at the pore walls in the sample at different steps of dissolution.

at inlet and outlet, but apart from this, slightly skewed toward negative values. This indicates a geometrical asymmetry in the sample: more dead-end pores stretch from the top (low pressure) to the bottom of the samples, than the other way around.

The fluid *pressure* exerts a *normal* traction $p\hat{\mathbf{n}}$ upon the solid matrix. The viscous flow field, on the other hand, contributes to a *tangential* traction. The *scaled* viscous stress tensor is given by

$$\boldsymbol{\sigma}_{\text{visc}} = \boldsymbol{\nabla}\mathbf{v} + \boldsymbol{\nabla}\mathbf{v}^{\top}, \qquad (32)$$

and to quantify this (while suppressing the influence of the boundary normal, which must be reconstructed on nodes, introducing an error of order element size), we report the distribution of τ, the largest absolute eigenvalue of $\boldsymbol{\sigma}_{\text{visc}}$, sampled over the surface nodes (as in *Voronov et al.* [2010]). The resulting distribution is shown in Figure 7. From the latter figure, it is clear that the viscous forces are, generally, at least $1-2$ orders of magnitude lower than the pressure drop, which again is lower than the base pressure P_0 and the external pressure P_{ext}. We emphasize that this observation is *independent* of the value of the viscosity μ, as the equations are linear, and therefore, only one unique solution for the stress field exists apart from a scaling (by ΔP) and a shift (by P_0).

3.3. Stress in the Porous Solid

In the following, the results from calculating the state of stress in the solid due to fluid flow and porosity increase are reported. In all cases, a Poisson's ratio $\nu = 0.3$, an external pressure $P_{\text{ext}} = 2.2 \times 10^7$ Pa, and a base pressure $P_0 = 1.0 \times 10^7$ Pa were used.

3.3.1. Measures of State of Stress in the Solid

In order to assess the impact of applied external stress on the porous sample, we consider frame-invariant quantities. Combinations of the first two invariants of the stress tensor will therefore be used (I_1 and I_2). First, the *mechanical pressure* is defined as

$$P_{\text{mech}} = -\frac{\text{tr}(\boldsymbol{\sigma})}{3}. \qquad (33)$$

Second, the *von Mises stress* [*von Mises*, 1913] is defined by

$$\sigma_{\text{vM}} = \sqrt{\frac{3}{2}\boldsymbol{\sigma}_{\text{dev}} : \boldsymbol{\sigma}_{\text{dev}}}, \qquad (34)$$

where the deviatoric stress tensor is defined by $\boldsymbol{\sigma}_{\text{dev}} = \boldsymbol{\sigma} + P_{\text{mech}}\mathbf{I}$. The von Mises stress is commonly used to predict yielding of materials under multiaxial loading. The tightly related von Mises *yield criterion* states
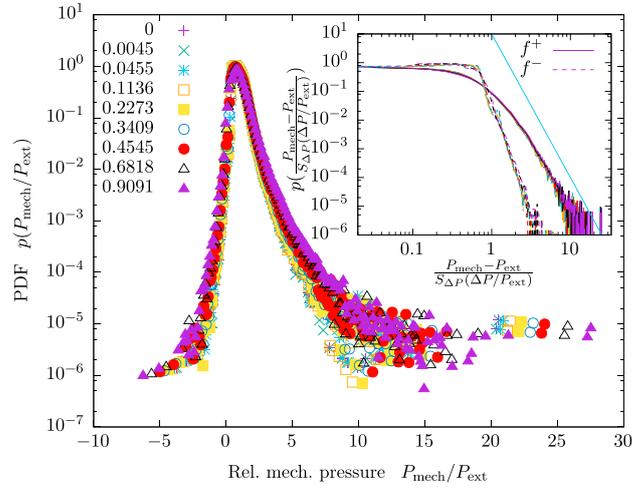
Figure 8. Probability density function of the mechanical pressure P_{mech} at the pore walls in the sample before dissolution, at various imposed fluid pressure drops ΔP. Here $P_{ext} = 2.2 \times 10^7$ Pa, $P_0 = 1.0 \times 10^7$ Pa. Inset: data collapse by rescaling. The straight line shows power law decay $p(x) \sim x^{-5}$ as a guide to the eye. Similar plots are also found for the various dissolution steps.

that a material starts to deform irreversibly when σ_{vM} reaches a certain critical threshold σ_{yield}. As such, it is a measure of how close to fracturing the material is when considering a brittle material such as a rock in the first kilometers of the Earth's crust. We note that we could as well have considered some of the common alternatives to the von Mises stress, such as the maximum principal stress (strain), i.e., the largest eigenvalue of the stress (strain) tensor, σ_1 (or $\sigma_1 - \nu(\sigma_2 + \sigma_3)$), and the results are largely similar.

3.3.2. Influence of Pressure Drop Over Fluid on Stress in the Solid

Figure 8 shows the probability distributions of P_{mech} in the sample before dissolution, normalized by the external pressure P_{ext}, obtained for various fluid pressure drops $\Delta P \in [0, P_{ext}]$. The distributions are peaked around $P_{mech}/P_{ext} = 1$, with a markedly heavy tail for large P_{mech}.

In the inset of Figure 8 the distributions are seen to collapse by the normalization

$$\hat{P} = \frac{P_{mech} - P_{ext}}{P_{ext} S_{\Delta P}\left(\frac{\Delta P}{P_{ext}}\right)}. \tag{35}$$

Here $S_{\Delta P}(\Delta P/P_{ext})$ is a scaling function described below.

For large $\hat{P}$, a power law behavior $p(\hat{P}) \sim \hat{P}^{-\gamma}$, where $\gamma \simeq 5$, can possibly be observed. The support is, however, only over 1 order of magnitude, and therefore, other distributions might also provide good fits, e.g., a stretched exponential distribution.

The probability distributions of the von Mises stress σ_{vM}, corresponding to Figure 8, are shown in Figure 9. The distributions of σ_{vM} display similar characteristics as the distributions for P_{mech}. Scaling by $S_{\Delta P}(\Delta P/P_{ext})$ yields the same data collapse as for $\hat{P}$, i.e., distributions of

$$\hat{\sigma}_{vM} = \frac{\sigma_{vM}}{P_{ext} S_{\Delta P}\left(\frac{\Delta P}{P_{ext}}\right)} \tag{36}$$

are independent of ΔP.

In Figure 10, the data points show the mean of the pore wall distribution of σ_{vM}/P_{ext}, plotted as a function of (normalized) pressure drop. A linear least squares fit is used to determine the scaling function:

$$S_{\Delta P}\left(\frac{\Delta P}{P_{ext}}\right) = 0.27 \frac{\Delta P}{P_{ext}} + 0.82. \tag{37}$$
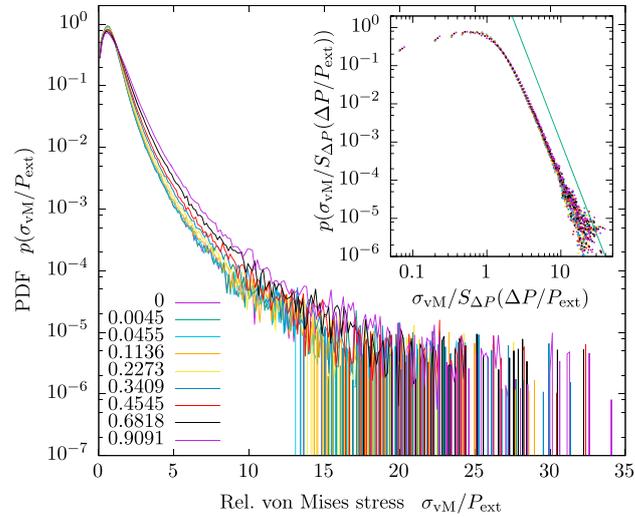
Figure 9. Probability density function of the von Mises stress σ_{vM} at the pore walls in the initial step of the sample, at various imposed pressure drops ΔP. P_{ext} and P_0 are the same as in Figure 8. Inset: data collapse by rescaling. A power law decay with exponent −5 is shown as a guide to the eye. Similar plots are also found for the various dissolution steps.

3.4. Influence of Dissolution and Increasing Porosity

The probability distributions of the mechanical pressure at the pore walls of the sample at different stages of dissolution are shown in Figure 11. Here the pressure values used were $P_{ext} = 2.2 \times 10^7$ Pa, $P_0 = 1.0 \times 10^7$ Pa, and $\Delta P = 0$. The peaks of the distributions are located at the same position, $P_{mech} = P_{ext}$, but the distributions become wider as the porosity is increased, indicating more stress concentration and more stress shadows with increasing dissolution.

To segregate the distributions of values above (+) and below (−) the peak at $P_{mech} = P_{ext}$, we define

$$f^{\pm} = \pm \frac{P_{mech} - P_{ext}}{P_{ext} S\left(\frac{\Delta P}{P_{ext}}\right) S_{\phi}(\phi)} \tag{38}$$

where the scaling function $S_{\phi}(\phi)$ is defined below (see equation (39)). As shown in the inset of Figure 11, the resulting distributions largely collapse: the distributions of f^+ are seen to fall onto the same curve, while f^- displays a slightly varying slope with dissolution step.
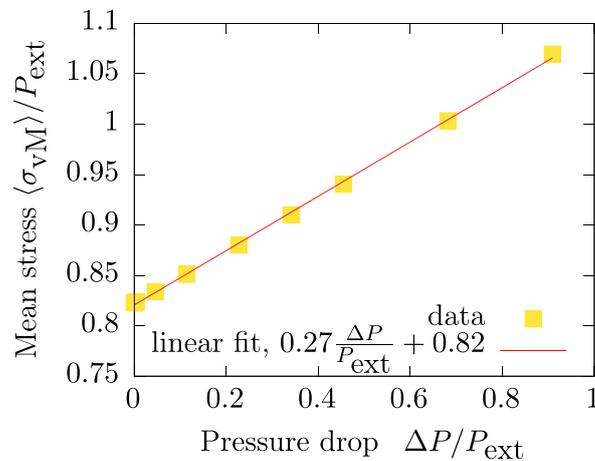
Figure 10. Mean von Mises stress as a function of the pressure drop ΔP inducing flow through the sample. The means are taken over the distributions in Figure 9.
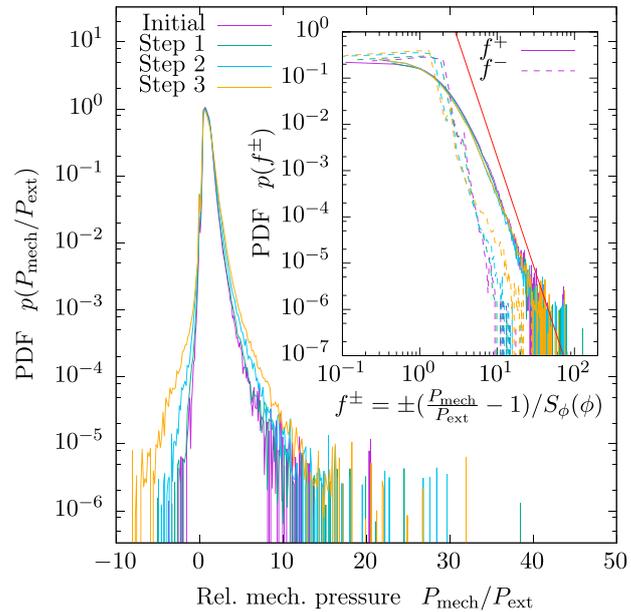
Figure 11. Probability density function of the mechanical pressure at the pore walls for all dissolution steps, at fixed $\Delta P = 0$. P_{ext} and P_0 are the same as in Figure 8. Inset: data collapse by rescaling. The line shows a power law with exponent -5 as a guide to the eye. Similar plots exist for other pressure drops.

The probability distribution of the (relative) von Mises stress is plotted for the pore walls in Figure 12 and for the solid bulk in Figure 13. The pore wall distributions display the same behavior and collapse by $S_\phi(\phi)$ as that of f^+ above. In comparison, the bulk distribution extends the suggested power law distribution, $p(\sigma_{vM}) \sim \sigma_{vM}^{-\gamma}$, $\gamma \simeq 5$, for large σ_{vM}.

The bulk averages of σ_{vM}, corresponding to the probability distributions shown in Figure 13, are plotted in Figure 14. The scaling function $S_\phi(\phi)$ is approximated as a fit to these points. We expect no deviatoric stress at $S_\phi(0) = 0$, and the simplest form satisfying this is

$$S_\phi(\phi) = C\phi^\beta. \tag{39}$$

Here the exponent $\beta \simeq 0.56$ yields the best fit of the experimental data using a least squares method. An even better fit would be achieved by using more complicated expressions with more fitting parameters, but for that
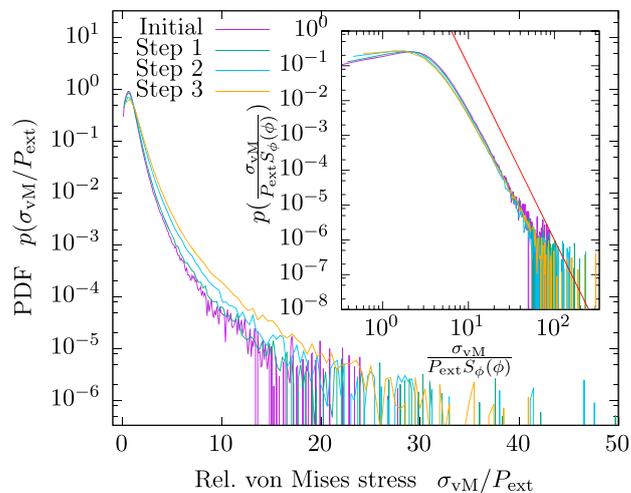
Figure 12. Probability density function of the von Mises stress at the pore walls for all samples, at fixed $\Delta P = 0$. P_{ext} and P_0 are the same as in Figure 8. Inset: data collapse by rescaling. Similar plots exist for other pressure drops.
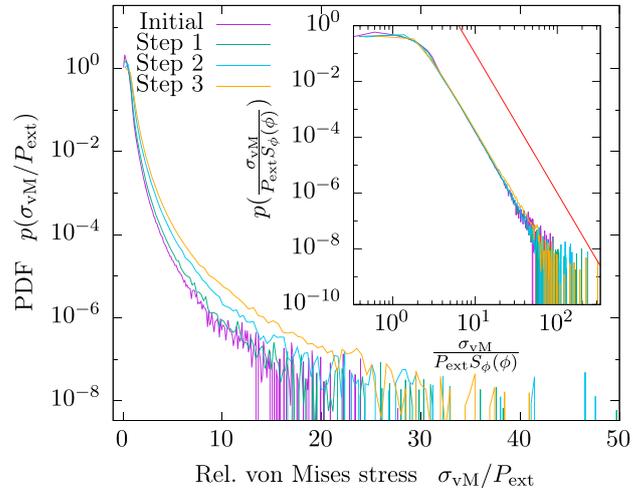
Figure 13. Probability density function of the von Mises stress in the bulk for all samples, at fixed $\Delta P = 0$. P_{ext} and P_0 are the same as in Figure 8. Inset: data collapse by rescaling, and a superimposed power law with exponent -5 as a guide to the eye. Similar plots exist for the other pressure drops.

to be justified one would also have required more than the four porosity levels available herein. Alternatively, exponential fits could be used, analogous to the compiled data of critical axial stress as a function of porosity in limestones summarized in *Croize et al.* [2013, section 3.1.3].

3.5. Common Probability Density Functions

As a consequence of the above analysis, all distributions considered will collapse onto the same master curves, by the scaling relationships

$$\hat{\tilde{P}} = \frac{P_{mech} - P_{ext}}{P_{ext} S_{\Delta P}\left(\frac{\Delta P}{P_{ext}}\right) S_\phi(\phi)}, \tag{40}$$

and

$$\tilde{\sigma}_{vM} = \frac{\sigma_{vM}}{P_{ext} S_{\Delta P}\left(\frac{\Delta P}{P_{ext}}\right) S_\phi(\phi)}, \tag{41}$$

where the scaling functions $S_{\Delta P}(\Delta P/P_{ext})$ and $S_\phi(\phi)$ are given by equations (39) and (37), respectively. This unified description of stress heterogeneities in the limestone sample studied here represents the main outcome of the present study.
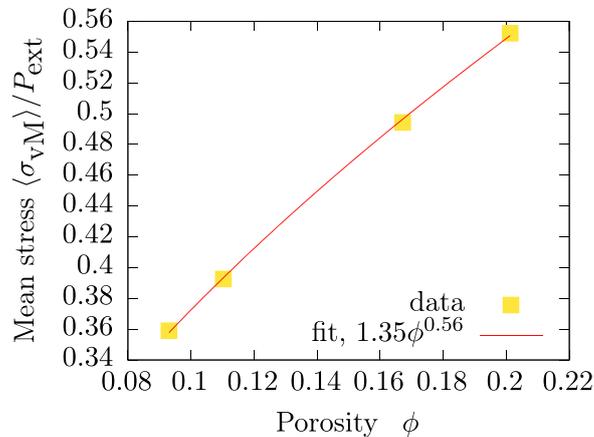
Figure 14. Bulk mean von Mises stress versus porosity. The data points correspond to the distributions in Figure 13.

4. Discussion

4.1. Complexity of Fluid Flow in a Porous Medium

Brown [1987] solved Reynolds equations in 2-D in a synthetic rough aperture fracture and showed that for low aperture, the roughness of the walls had a significant effect, leading to flow channeling. In a porous medium, the pore structure complexity generates a wide range of flow velocities, from the fast advective flows in the main channels, to the very slow diffusive flows in dead ends where the fluid is almost stagnant and rarely mix with that in the main channels [*Bijeljic et al.*, 2013]. The pore heterogeneities have a strong effect on the long-range spatial correlations of the flux. Numerical simulations show that the distributions of the kinetic energy and the velocity in the fluid follow power laws over at least 5 orders of magnitude [*Andrade et al.*, 1997; *Makse et al.*, 2000] and that the flow is correlated in space and time [*Le Borgne et al.*, 2008], leading to intermittency [*De Anna et al.*, 2013]. Increasing the complexity of pore geometry, from a simple bead-pack porous medium to natural rock samples with micropores and microfractures increases as well the range of velocities observed in the fluid. The velocity distribution is characterized by a main peak, controlled by the pressure drop imposed on the system, and a tail of slow velocities that increases with pore network complexity [*Bijeljic et al.*, 2013; *Jin et al.*, 2016]. Based on Lattice Boltzmann simulations, *Matyka et al.* [2016] proposed that the probability distribution function of fluid velocity, for velocities larger than the average fluid velocity, follows a "power exponential" law. This is in contrast with other studies which have proposed either a Gaussian or an exponential distribution [*Mansfield and Issa*, 1996; *Datta et al.*, 2013; *Bijeljic et al.*, 2013; *Lebon et al.*, 1996].

With regard to the speed distributions presented in section 3, a stretched exponential probability density function provides a good fit for large speeds. A shifted, stretched exponential (power exponential) distribution, as proposed by *Matyka et al.* [2016], would also be in agreement with our results, but this would require introducing another fitting parameter. Moreover, the evolving pore structure due to dissolution in our sample does not significantly alter the functional dependence of the probability density function of fluid velocities, when rescaled by the average velocity.

4.2. Coupling Fluid Flow and Deformation

The fluid flow in the porous medium exerts both shear and normal stress on the solid walls, as shown numerically for a rough fracture [*Lo and Koplik*, 2014]. Because of the complexity of the porous medium, additional complexity of the flow pattern exists and long-range correlations in the stress distribution at the solid interface emerge.

Flow-induced stresses have been modeled for several biological applications where porosity of the medium was quite high (above 80 %) and the solids were very soft. Under these conditions, numerical simulations indicate that the fluid viscous stress at the pore walls follows a gamma distribution [*Voronov et al.*, 2010]. Numerical models of fluid flow in highly deformable elastic porous media indicated that as the elastic solid deforms under flow, the relationship between pressure drop and flux becomes nonlinear and saturates for large-pressure gradients [*Hewitt et al.*, 2016]. Hysteresis due to the coupling between fluid and solid can emerge [*Guyer and Kim*, 2015]. *Pham et al.* [2014] calculated the stress exerted by a fluid around a spherical solid using Lattice Boltzmann simulations, and the existence of areas with stress concentration on the solid, and lognormal stress distribution was observed. However, in all these studies, the porosity was quite large and/or the solids were very soft and relevant for bioengineering applications. This renders comparison with solids that are stronger and with lower porosity, such as rocks, challenging.

In rocks, elastic deformations are quite small, usually below one percent, before irreversible strain occurs. Depending on stress and the mechanisms of irreversible deformation, such as closure and opening of microcracks or pore collapse, the relationship between porosity and permeability evolves, controlling the pore pressure gradient [*David et al.*, 1994]. Under loading, the microscale heterogeneities control both the initiation of microcracks and the overall strength of the material. Using a 2-D discrete element modeling approach applied to a granite rock, *Lan et al.* [2010] showed a difference between geometrical heterogeneities (i.e., difference of grain size), which control the nucleation of microfractures and initiation of damage, and strength heterogeneities at the grain contacts (i.e., elastic stiffness), which control the overall strength of the solid under uniaxial loading. In these simulations, the stresses inside the grains show a normal distribution for both the maximum and the minimum principal stresses, with an average value which corresponds to the external loading. Conversely, the normal stress at grain contacts shows a bimodal distribution. Some contacts are under tensile normal stress conditions and provide sites for the nucleation of extensional microfractures.

The evolution of elastic parameters and permeability during small elastic deformations of a Bentheim sandstone was experimentally measured and successfully modeled using X-ray microtomography images where unstructured meshes were built [*Jasinski et al.*, 2015]. The effect of fluid viscosity on the effective elastic properties of rocks and the attenuation of elastic waves was studied in *Saenger et al.* [2011] by solving the dynamic elastic equation in 3-D rock samples imaged with X-ray microtomography. Other researchers have simulated deformation of calcium carbonates with a back coupling to flow through dissolution [*Pereira Nunes et al.*, 2016] and precipitation [*Jiang and Tsuji*, 2014], although without accounting for the stress distribution in the solid matrix. In the present work, the fluid-solid coupling is only one way, and therefore, the effect of flow on changing pore space geometry cannot be assessed.

By considering probability density functions of bulk and pore wall properties, the results presented in section 3 show that for a steadily flowing fluid in the pore space of a limestone, the dominating force from the fluid stems from the base pressure in the solid, as the viscous force generated by the fluid is generally orders of magnitude lower. This implies that under such conditions, the viscous stress is of minor importance. Moreover, the stress distributions are controlled by the pressure drop ΔP in a simple manner. In particular, the position of the tail of the distributions of stress in the sample may ultimately depend on the maximum difference between external and internal pressure. This broad tail, with a power law decay with a quite strong exponent of -5, has the following consequence: a slight increase in fluid pressure or a small amount of dissolution will significantly increase the number of locations in the solid where the von Mises criteria (or another failure criteria) will be reached. A consequence of such behavior is the following. It is known that the injection or removal of fluid at depth can trigger induced seismicity [*Talwani and Acree*, 1984]. Recent field observations at the outcrop scale show that a small fluid injection can trigger microearthquakes at some distance from the injection point [*Guglielmi et al.*, 2015]. If they can be extended to other kinds of rocks, our results, with a heavy power law tail of stress heterogeneities, show that a small change in fluid pressure can drive a significant volume of the rock toward failure. The nature of microstructural heterogeneities and their relationships to fluid flow and stress would then provide an additional explanation of induced seismicity.

Whether the observed self-similarity persists if the porosity is increased beyond the range considered here, is an open question, and could be assessed, e.g., by using tomography data from experiments where more dissolution is performed. However, in the Earth's crust failure would occur before reaching a high porosity, which is what happens, for example, in karst with the formation of caves. Further, how the distribution changes if such failure occurs, i.e., the stress heterogeneity leads to fractures, is an interesting point in question. We expect the self-similar behavior will reach its end at latest when the first failure occurs, as the solid matrix will then reorganizes itself.

5. Conclusion

We have in this work computationally studied how an evolving microstructure influences fluid flow in the pore space of a rock, and how fluid flow influences the state of stress in the solid phase. We have considered a limestone which has been scanned at four stages of dissolution using X-ray microtomography.

Steady incompressible laminar fluid flow in the sample at each stage of dissolution was computed by solving Stokes' equations. By assuming negligible displacement of the fluid-solid boundary due to elastic deformation, the stress field from the fluid enters as a boundary condition on the solid, yielding a one-way numerical coupling. Both the fluid and the solid problems were solved numerically using the finite element method through the FEniCS/DOLFIN framework.

Our main finding is that as the rock is dissolved, and as the pressure drop driving the fluid flow is increased, the distribution of heterogeneous stress in the sample evolves in a self-similar manner. In particular, the probability distributions of the mechanical pressure and the von Mises stress can be collapsed onto the same curve by a normalization. The common master curves display a broad distribution, with a suggested power law tail for high stresses. The broad tail shows that the rock is very sensitive to small perturbations, and a slight fluid pressure increase locally would drive a significant number of local heterogeneities toward failure. We propose that this heavy tail can be used as a simple criterion for the integrity of porous rocks.

Whether the observed self-similar evolution is restricted to dissolution processes remains to be answered. For example, do other morphology-changing processes, such as fracturing or precipitation (lowering porosity) evolve similarly? A more fundamental question is related to identifying the link between pore geometry and

the velocity distribution/stress distribution. Future work will include a back coupling from solid deformation to fluid flow, yielding transient dynamics of fracture and/or precipitation-dissolution processes.

References

Andrä, H., et al. (2013), Digital rock physics benchmarks. Part II: Computing effective properties, *Comput. Geosci.*, *50*, 33–43, doi:10.1016/j.cageo.2012.09.008.

Andrade, J., M. Almeida, J. Mendes Filho, S. Havlin, B. Suki, and H. Stanley (1997), Fluid flow through porous media: The role of stagnant zones, *Phys. Rev. Lett.*, *79*(20), 3901–3904, doi:10.1103/PhysRevLett.79.3901.

Arns, C. H., M. A. Knackstedt, W. V. Pinczewski, and E. J. Garboczi (2002), Computation of linear elastic properties from microtomographic images: Methodology and agreement between theory and experiment, *Geophysics*, *67*(5), 1396–1405, doi:10.1190/1.1512785.

Arson, C., and T. Vanorio (2015), Chemomechanical evolution of pore space in carbonate microstructures upon dissolution: Linking pore geometry to bulk elasticity, *J. Geophys. Res. Solid Earth*, *120*, 6878–6894, doi:10.1002/2015JB012087.

Bernabé, Y., and A. Revil (1995), Pore-scale heterogeneity, energy dissipation and the transport properties of rocks, *Geophys. Res. Lett.*, *22*(12), 1529–1532, doi:10.1029/95GL01418.

Bijeljic, B., A. Raeini, P. Mostaghimi, and M. J. Blunt (2013), Predictions of non-Fickian solute transport in different classes of porous media using direct simulation on pore-scale images, *Phys. Rev. E*, *87*(1), 013011, doi:10.1103/PhysRevE.87.013011.

Bjørlykke, K., and K. Høeg (1997), Effects of burial diagenesis on stresses, compaction and fluid flow in sedimentary basins, *Mar. Pet. Geol.*, *14*, 267–276.

Blunt, M. J., B. Bijeljic, H. Dong, O. Gharbi, S. Iglauer, P. Mostaghimi, A. Paluszny, and C. Pentland (2013), Pore-scale imaging and modelling, *Adv. Water Resour.*, *51*, 197–216, doi:10.1016/j.advwatres.2012.03.003.

Brenner, S. C., and L. R. Scott (2008), *The Mathematical Theory of Finite Element Methods*, 3rd ed., Springer Science and Business Media, New York.

Brown, S. R. (1987), Fluid flow through rock joints: The effect of surface roughness, *J. Geophys. Res.*, *92*(B2), 1337–1347, doi:10.1029/JB092iB02p01337.

Bultreys, T., W. De Boever, and V. Cnudde (2016), Imaging and image-based fluid transport modeling at the pore scale in geological materials: A practical introduction to the current state-of-the-art, *Earth Sci. Rev.*, *155*, 93–128, doi:10.1016/j.earscirev.2016.02.001.

Byerlee, J. (1990), Friction, overpressure and fault normal compression, *Geophys. Res. Lett.*, *17*(12), 2109–2112, doi:10.1029/GL017i012p02109.

Costa, A. (2006), Permeability-porosity relationship: A reexamination of the Kozeny-Carman equation based on a fractal pore-space geometry assumption, *Geophys. Res. Lett.*, *33*, L02318, doi:10.1029/2005GL025134.

Coussy, O. (2004), *Poromechanics*, John Wiley, New York.

Croize, D., F. Renard, and J.-P. Gratier (2013), Compaction and porosity reduction in carbonates: A review of observations, theory, and experiments, *Adv. Geophys.*, *54*, 181–238, doi:10.1016/B978-0-12-380940-7.00003-2.

Datta, S. S., H. Chiang, T. S. Ramakrishnan, and D. A. Weitz (2013), Spatial fluctuations of fluid velocities in flow through a three-dimensional porous medium, *Phys. Rev. Lett.*, *111*, 064501, doi:10.1103/PhysRevLett.111.064501.

David, C., T.-F. Wong, W. Zhu, and J. Zhang (1994), Laboratory measurement of compaction-induced permeability change in porous rocks: Implications for the generation and maintenance of pore pressure excess in the crust, *Pure Appl. Geophys.*, *143*(1–3), 425–456, doi:10.1007/BF00874337.

De Anna, P., T. Le Borgne, M. Dentz, A. M. Tartakovsky, D. Bolster, and P. Davy (2013), Flow intermittency, dispersion, and correlated continuous time random walks in porous media, *Phys. Rev. Lett.*, *110*(18), 184502, doi:10.1103/PhysRevLett.110.184502.

Ehrenberg, S., G. Eberli, M. Keramati, and S. Moallemi (2006), Porosity-permeability relationships in interlayered limestone-dolostone reservoirs, *AAPG Bull.*, *90*(1), 91–114.

Fang, Q., and D. A. Boas (2009), Tetrahedral mesh generation from volumetric binary and grayscale images,paper presented at ISBI'09. IEEE International Symposium on Biomedical Imaging: From Nano to Macro, 2009, pp. 1142–1145, IEEE, doi:10.1109/ISBI.2009.5193259.

Gratier, J.-P., P. Favreau, and F. Renard (2003), Modeling fluid transfer along California faults when integrating pressure solution crack sealing and compaction processes, *J. Geophys. Res.*, *108*(B2), 2104, doi:10.1029/2001JB000380.

Guglielmi, Y., F. Cappa, J. P. Avouac, P. Henry, and D. Elsworth (2015), Seismicity triggered by fluid injection induced aseismic slip, *Science*, *348*, 1224–1226.

Guyer, R. A., and H. A. Kim (2015), Theoretical model for fluid-solid coupling in porous materials, *Phys. Rev. E*, *91*(4), 042406, doi:10.1103/PhysRevE.91.042406.

Hewitt, D. R., J. S. Nijjer, M. G. Worster, and J. A. Neufeld (2016), Flow-induced compaction of a deformable porous medium, *Phys. Rev. E*, *93*(2), 023116, doi:10.1103/PhysRevE.93.023116.

Holzner, M., V. L. Morales, M. Willmann, and M. Dentz (2015), Intermittent lagrangian velocities and accelerations in three-dimensional porous medium flow, *Phys. Rev. E*, *92*(1), 013015, doi:10.1103/PhysRevE.92.013015.

IEA (2014), Energy technology perspectives 2014, doi:10.1787/energy_tech-2014-en.

Jamtveit, B., and Ø. Hammer (2012), Sculpting of rocks by reactive fluids, *Geochem. Perspect.*, *1*, 341–477.

Jasinski, L., D. Sangaré, P. Adler, V. Mourzenko, J.-F. Thovert, N. Gland, and S. Békri (2015), Transport properties of a Bentheim sandstone under deformation, *Phys. Rev. E*, *91*(1), 013304, doi:10.1103/PhysRevE.91.013304.

Jiang, F., and T. Tsuji (2014), Changes in pore geometry and relative permeability caused by carbonate precipitation in porous media, *Phys. Rev. E*, *90*(5), 053306, doi:10.1103/PhysRevE.90.053306.

Jin, C., P. Langston, G. Pavlovskaya, M. Hall, and S. Rigby (2016), Statistics of highly heterogeneous flow fields confined to three-dimensional random porous media, *Phys. Rev. E*, *93*(1), 013122, doi:10.1103/PhysRevE.93.013122.

Lan, H., C. D. Martin, and B. Hu (2010), Effect of heterogeneity of brittle rock on micromechanical extensile behavior during compression loading, *J. Geophys. Res.*, *115*, B01202, doi:10.1029/2009JB006496.

Langtangen, H. P., K.-A. Mardal, and R. Winther (2002), Numerical methods for incompressible viscous flow, *Adv. Water Resour.*, *25*(8–12), 1125–1146, doi:10.1016/S0309-1708(02)00052-0.

Le Borgne, T., M. Dentz, and J. Carrera (2008), Lagrangian statistical model for transport in highly heterogeneous velocity fields, *Phys. Rev. Lett.*, *101*(9), 090601, doi:10.1103/PhysRevLett.101.090601.

Le Borgne, T., M. Dentz, and E. Villermaux (2013), Stretching, coalescence, and mixing in porous media, *Phys. Rev. Lett.*, *110*(20), 204501, doi:10.1103/PhysRevLett.110.204501.

Lebon, L., L. Oger, J. Leblond, J. Hulin, N. Martys, and L. Schwartz (1996), Pulsed gradient nmr measurements and numerical simulation of flow velocity distribution in sphere packings, *Phys.Fluids*, *8*(2), 293–301, doi:10.1063/1.869307.

Lo, T. S., and J. Koplik (2014), Channeling and stress during fluid and suspension flow in self-affine fractures, *Phys. Rev. E*, *89*(2), 023010, doi:10.1103/PhysRevE.89.023010.

Logg, A., K.-A. Mardal, and G. Wells (2012a), *Automated Solution of Differential Equations by the Finite Element Method: The FEniCS Book*, vol. 84, Springer Science and Business Media, New York.

Logg, A., G. N. Wells, and J. Hake (2012b), DOLFIN: A C++/Python finite element library, in *Automated Solution of Differential Equations by the Finite Element Method*, edited by A. Logg, K.-A. Mardal, and G. N. Wells, Springer, Berlin.

Makse, H. A., J. S. Andrade Jr., and H. E. Stanley (2000), Tracer dispersion in a percolation network with spatial correlations, *Phys. Rev. E*, *61*(1), 583, doi:10.1103/PhysRevE.61.583.

Mansfield, P., and B. Issa (1996), Fluid transport in porous rocks. I: EPI studies and a stochastic model of flow, *J. Magn. Reson., Ser. A*, *122*(2), 137–148, doi:10.1006/jmra.1996.0189.

Matyka, M., A. Khalili, and Z. Koza (2008), Tortuosity-porosity relation in porous media flow, *Phys. Rev. E*, *78*(2), 026306.

Matyka, M., J. Gołembiewski, and Z. Koza (2016), Power-exponential velocity distributions in disordered porous media, *Phys. Rev. E*, *93*, 013110, doi:10.1103/PhysRevE.93.013110.

Meakin, P., and A. M. Tartakovsky (2009), Modeling and simulation of pore-scale multiphase fluid flow and reactive transport in fractured and porous media, *Rev. Geophys.*, *47*, RG3002, doi:10.1029/2008RG000263.

Misztal, M. K., A. Hernandez-Garcia, R. Matin, H. O. Sørensen, and J. Mathiesen (2015), Detailed analysis of the lattice Boltzmann method on unstructured grids, *J. Comput. Phys.*, *297*, 316–339.

Noiriel, C. (2015), Resolving time-dependent evolution of pore-scale structure, permeability and reactivity using X-ray microtomography, *Rev. Mineral. Geochem.*, *80*, 247–285, doi:10.2138/rmg.2015.80.08.

Noiriel, C., P. Gouze, and D. Bernard (2004), Investigation of porosity and permeability effects from microstructure changes during limestone dissolution, *Geophys. Res. Lett.*, *31*, L24603, doi:10.1029/2004GL021572.

Noiriel, C., D. Bernard, P. Gouze, and X. Thibault (2005), Hydraulic properties and microgeometry evolution accompanying limestone dissolution by acidic water, *Oil Gas Sci. Technol.*, *60*(1), 177–192.

Øren, P.-E., S. Bakke, and R. Held (2007), Direct pore-scale computation of material and transport properties for north sea reservoir rocks, *Water Resour. Res.*, *43*, w12S04, doi:10.1029/2006WR005754.

Pereira Nunes, J., M. Blunt, and B. Bijeljic (2016), Pore-scale simulation of carbonate dissolution in micro-CT images, *J. Geophys. Res. Solid Earth*, *121*, 558–576, doi:10.1002/2015JB012117.

Pham, N. H., R. S. Voronov, N. R. Tummala, and D. V. Papavassiliou (2014), Bulk stress distributions in the pore space of sphere-packed beds under Darcy flow conditions, *Physical Review E*, *89*(3), 033016, doi:10.1103/PhysRevE.89.033016.

Rice, J. R., and M. P. Cleary (1976), Some basic stress diffusion solutions for fluid-saturated elastic porous media with compressible constituents, *Rev. Geophys.*, *14*(2), 227–241, doi:10.1029/RG014i002p00227.

Rohmer, J., A. Pluymakers, and F. Renard (2016), Mechano-chemical interactions in sedimentary rocks in the context of CO_2 storage: Weak acid, weak effects?, *Earth Sci. Rev.*, *157*, 86–110, doi:10.1016/j.earscirev.2016.03.009.

Saenger, E. H., F. Enzmann, Y. Keehm, and H. Steeb (2011), Digital rock physics: Effect of fluid viscosity on effective elastic properties, *J. Appl. Geophys.*, *74*(4), 236–241, doi:10.1016/j.jappgeo.2011.06.001.

Si, H. (2015), TetGen, a Delaunay-based quality tetrahedral mesh generator, *ACM Trans. Math. Softw.*, *41*(2), 11:1–11:36, doi:10.1145/2629697.

Sibson, R. (1992), Implications of fault-valve behaviour for rupture nucleation and recurrence, *Tectonophysics*, *211*(1–4), 283–293, doi:10.1016/0040-1951(92)90065-E.

Talwani, P., and S. Acree (1984), Pore pressure diffusion and the mechanism of reservoir-induced seismicity, *Pure Appl. Geophys.*, *122*, 947–965.

The CGAL Project (2016), *CGAL User and Reference Manual*, 4.9 ed., CGAL Editorial Board. [Available at http://doc.cgal.org/4.9/Manual/packages.html.]

von Mises, R. (1913), Mechanik der festen körper im plastisch-deformablen zustand. Nachrichten von der Gesellschaft der Wissenschaften zu Göttingen, Mathematisch-Physikalische Klasse, pp. 582–592.

Voronov, R. S., S. B. VanGordon, V. I. Sikavitsas, and D. V. Papavassiliou (2010), Distribution of flow-induced stresses in highly porous media, *Appl. Phys. Lett.*, *97*(2), 024101, doi:10.1063/1.3462071.

Wojtacki, K., L. Lewandowska, P. Gouze, and A. Lipkowski (2015), Numerical computations of rock dissolution and geomechanical effects for CO_2 geological storage, *Int. J. Numer. Anal. Methods Geomech.*, *39*, 482–506.

Transitional flow in self-affine rough fractures

Gaute Linga, Luiza Angheluta, and Joachim Mathiesen

In preparation (2018).

Transitional flow in self-affine rough channels

Gaute Linga,[1,][*] Luiza Angheluta,[2] and Joachim Mathiesen[1]

[1]*Niels Bohr Institute, University of Copenhagen,*

Blegdamsvej 17, DK-2100 Copenhagen, Denmark

[2]*Department of Physics, University of Oslo, P.O. Box 1048, Blindern, N-0316 Oslo, Norway*

Abstract

We present comprehensive direct numerical simulations of fluid flow in three-dimensional (3D) self-affine channels that are representative of fractures. We solve the time-dependent Navier–Stokes equations, from laminar flow, through transitional, to turbulent flow, focusing our investigation on the role of inertia and roughness on the macroscopic transport properties. In contrast to previous studies, we have access to the full, 3D time-dependent velocity field, and quantify the effect of unsteady and transitional flow on fracture permeability. We compute friction factors (geometric and Darcy fraction factor f_D) for flow spanning three orders of magnitude in velocity and one order of magnitude in roughness amplitude. The dependence of the friction factors on the Reynolds number Re can be approximated using a generalized Forchheimer law, which takes into account a finite transition region between a laminar asymptotic scaling, $f_\mathrm{D} \sim \mathrm{Re}^{-1}$ ($\mathrm{Re} \ll \mathrm{Re_c}$), and an inertial asymptote, $f_\mathrm{D} \sim$ constant ($\mathrm{Re} \gg \mathrm{Re_c}$). For each roughness amplitude, this leads to the identification of a critical Reynolds number $\mathrm{Re_c}$, where inertial effects arise, and a characteristic geometric friction factor. Based on the latter two quantities, the friction factor for all roughness amplitudes can be collapsed onto a single curve, where only the transition region is roughness dependent. To quantify the onset of unsteady flow, we compute the fluctuation-based Reynolds number $\mathrm{Re'}$, which beyond a certain *second* critical $\mathrm{Re}_{c,q}$, is shown to depend linearly on Re. For sufficiently high roughness, the linear dependence extends from $\mathrm{Re'} = 0$, suggesting that the turbulent transition changes character from sub- to supercritical as the roughness increases. We find that $\mathrm{Re}_{c,q}$ is comparable in magnitude to the $\mathrm{Re_c}$ for the departure from laminar friction, implying that transitional flow is an integral part of fracture flow, and must be accounted for in coarser simulations when Re and the roughness amplitude are sufficiently high.

---

[*] linga@nbi.dk

I. INTRODUCTION

The transport properties of fractured materials are industrially relevant for a range of reasons [1]. In aquifers and petroleum reservoirs, fractures are ubiquitous, and often the dominating part of the fluid transport in such media takes place in fracture networks [2–5]. Knowledge of the flow properties in the single fractures that together form the networks is hence necessary for safe and efficient operation downhole [6]. High velocity flow in such systems is of particular importance for geothermics, since turbulent mixing is known to increase heat conduction by several orders of magnitude. Further, hydraulic fractures may be driven by transitional flow [7]. Historically, much effort has been devoted to estimating the permeability (or conversely, flow resistance) of fractures [8, 9], e.g. by considering the properties of the aperture field [1, 10, 11]. For flows in pipes and channels, it was early on debated whether the departure at high flow rates from Darcy's law [12], which states that pressure loss is proportional to the discharge rate, was due to turbulence. However, careful studies have shown that this departure can be attributed to steady eddies; see e.g. [13, Sec. I].

On the other hand, flow in rough fractures is interesting from a turbulence perspective. The onset of turbulence in pipes and channel flow is a phenomenon that historically has received broad attention since the early experiments by Reynolds [14]. Only during the last decades, the phenomenon is beginning to be fully understood [15–19]. However, in the presence of roughness, much less is known. In the 1930's, Nikuradse undertook an extensive set of experiments on flow in pipes with a characteristic roughness length scale [20]. During recent years, this has been characterized as a non-equilibrium critical phenomenon by numerical and theoretical considerations [21–23]. The transition to turbulence in smooth-walled shear flows is believed to be subcritical, meaning that it is not driven by a linear instability, but requires a perturbance of a finite size to proliferate. In particular, experiments and simulations indicate that it belongs to the directed percolation (DP) universality class [24–27]. This expectedly holds for Hagen-Poiseuille (pipe) [15, 18, 28], Taylor–Couette (TCF) [29], plane Couette [30], and plane Poiseuille flow (PPF) [31].

It has been established experimentally that fractures in both geological and other materials are *self-affine* [32], i.e. the fracture surface $z = h(x, y)$ is statistically invariant under

the transformation

$$x \to \lambda x, \quad y \to \lambda y, \quad z \to \lambda^H z, \tag{1}$$

or $h(x, y) \sim \lambda^{-H} h(\lambda x, \lambda y)$ in a statistical sense [33, 34]. Here, H is the Hurst exponent, which is broadly considered to take the universal value $H = 0.8$ for fractures in three dimensions (3D). Note however, that there are exceptions, such as in sandstones ($H \simeq 0.6$) [35] and in glassy ceramics ($H \simeq 0.4$) [36, 37].

The early models for computing flow in fractures encompassed approximating fractures as two parallel plates, stated as the parallel plate (PPL) or cubic law, which gives the discharge rate $\mathbf{Q}$ as a function of the average pressure gradient $\boldsymbol{\nabla} p$ as

$$\mathbf{Q} = -\frac{d^3}{12\mu} \boldsymbol{\nabla} p, \quad \boldsymbol{\nabla} \cdot \mathbf{Q} = 0. \tag{2}$$

An improvement of the PPL amounts to letting d be a field that depends on the in-plane coordinates, which is termed the local cubic law (LCL) or the Reynolds equation (lubrication appriximation). An important research topic encompasses solving this equation for self-affine fractures, see e.g. [4, 38–40]

Beyond the lubrication approximation, Gutfraind and Hansen [41] and Zhang *et al.* [42] were probably the first to consider flow in self-affine geometries, albeit in two dimensions (2D). Drazer and Koplik [43, 44] considered the transport properties of 2D and 3D self-affine fractures. Brush and Thomson [45] evaluated the validity of the lubrication approximation by comparison to full 3D simulations. Lo and Koplik [46, 47] considered flow in self-affine fractures of both pure fluid and suspension flow in 3D self-affine fractures, and studied especially the flow channeling and fluid stress on the wall. Inertial effects have been studied both in fractures [48], in 2D porous media [49–52] and in 3D spherical packings [53–55] Notably, Skjetne *et al.* [48] simulated high-velocity time-independent flow in a self-affine 2D fracture joint in two dimensions. They found that the relationship between average forcing f and mean flow u_x was well described by a (weak inertia) cubic form [56, 57], $f \sim u_x + k u_x^3$ (k being an empirical constant) at low Reynolds numbers Re, and a Forchheimer law [58],

$$f = a u_x + b u_x^2, \tag{3}$$

at higher Re (a, b are empirical coefficients). The functional form (3) has provided good quantitative fits also in other rough geometries [52]. Zou *et al.* [59] studied unsteady flow in 2D fractures, and subsequently steady flow in 3D fractures [60]. Wang *et al.* [61] and Briggs

3

et al. [62] studied steady flow in self-affine fractures for somewhat lower Reynolds numbers. However, a proper assessment of the role of unsteady flow and the impact of velocity fluctuations on macroscopic transport properties seems to be lacking in the literature.

In the other end of the spectrum, an extensive body of research considers fully developed turbulence near rough walls (see [63] for a review). To our knowledge, however, there have been few works that have considered the transition to turbulence in fracture-like geometries. As such, addressing the universality class of the transition to turbulence, including resolving the associated large-scale spatiotemporal intermittency, would require domain sizes comparable to that considered by Chantry *et al.* [30]. In this direction, significant progress was made recently for rough-walled PPF [64] and TCF [65]. The present paper aims to show that it is possible, for significantly smaller domains, to address whether the transition to turbulence remains subcritical as a boundary roughness is imposed. In particular, we will find, by quantifying the velocity fluctuations, that the transition becomes supercritical given a sufficiently large roughness amplitude.

In this work, we consider high-velocity flow in three dimensional self-affine channels which realistically mimic real fracture geometries. The geometry is constructed to be a simple, albeit generic, description of a fracture: the same surface is shifted vertically to constitute both the upper and lower wall, and the channel is periodic in the x and y directions. This allows a Reynolds number based on the flux through any perpendicular cross section to be uniformly well-defined. Within this setup, we are primarily interested in the transport properties of the fracture when the flow within it goes from being stationary, in a time-independent steady-state (i.e. well within the laminar regime, which, as outlined above, is fairly well studied in the literature), to being in a steady state in a time-sampled statistical sense.

As already indicated, the main research questions underlying this investigation are:

- What is the impact of a generic roughness on the macroscopic flow properties (permeability, or conversely, friction factor) of a channel geometry?

- What is the effect of velocity fluctuations?

- How does the nature of the turbulent transition in a channel depend on roughness?

To characterize the effect of this transition, we first consider the geometrical properties of the fractures; i.e., we estimate in a classical way the permeability field of the fractures;

which gives a first estimate of the expected permeability of the fractures. Secondly, based on extensive direct numerical simulations (DNS) we measure the friction factor of the channels as a function of Reynolds number and roughness amplitude. We evaluate the prediction from the geometrical estimates, and are able to collapse the friction factors onto a single curve by a scaling argument. In particular, we find that a generalized Forchheimer law well captures the dependence of the friction factor on the Reynolds number. We also quantify the point where the flow becomes transitional by inspecting the temporal fluctuations in the velocity field.

The article is organized as follows. In Sec. II, we describe the fracture geometry and computational mesh used in the simulations. In Sec. III, we describe the problem set-up, the governing equations and the numerical methods, and in Sec. IV, we present our results. Finally, in Sec. V we discuss implications and limitations of our study, draw conclusions, and point to future work.

II. FRACTURE GEOMETRY AND MESH

In this section we describe the geometry of the rough channels, and the computational meshes used to represent them.

A. Self-affine channel

There is significant evidence for fracture surfaces being self-affine [32]. We therefore choose to study a system comprised of two identical, vertically shifted (along z), self-affine surfaces $z = h(x, y)$ and $z = h(x, y) + d$. Together they form a channel of constant height d, wherein an incompressible fluid is forced to flow along the x axis. This direction is henceforth called the streamwise direction, while the y direction is called the spanwise direction. In geoscience, this type of geometry is known as a fracture joint, resulting from mode I fracture, in contrast to a fault, where the surfaces woul be shifted both vertically and in the xy plane [48].

The self-affine profile is, as mentioned, described as a 2D surface in 3D space, which is statistically invariant under the transformation (1). Using a self-affine surface is also a simple and generic way of describing a rough surface profile where as few as possible length

5

scales are involved. In addition to the Hurst exponent H, there needs to be specified a lower cut-off (larger than the finite element size Δx), and a system size, L. However, this does not fully fix the vertical undulation of the surface. We therefore specify a root-mean-square height deviation, $A = L^{-1}\sqrt{\int_0^L \int_0^L h^2(x,y)\,\mathrm{d}x\,\mathrm{d}y}$, which we call *roughness amplitude*, which ultimately fixes the surface. Clearly, due to the self-affine nature of the surface, the latter scales with the finite system size as $A \sim L^H$. It is therefore evident that a proper study of the scaling properties of flow in self affine geometries would require to properly correct for finite-size effects, etc., which has been done in the lubrication approximation (see e.g. [4]), but is computationally costly for DNS in 3D. With this in mind, we will in the present work hold L fixed, leaving a scaling analysis for future work.

Our motivation for using a self-affine channel is twofold: (i) It is a simple way to introduce a random perturbation to an otherwise linearly stable flow, and (ii) it is a physically relevant system as it results from natural processes, such as brittle fractures [32, 66] and surface growth [34].

B. Computational meshes

Unstructured tetrahedral meshes are generated by first constructing a 256×256 (lattice units) self-affine surface with $H = 0.8$ using a Fourier filtering method [67]. There are several other ways of constructing such surfaces, but the Fourier method has the advantage that it results in a periodic surface, which will be of importance in imposing periodic boundary conditions on the flow field. To check that the surface is actually self-affine with the correct Hurst exponent, we compare the power spectrum of the surface height (measured along a line in the plane) with the theoretical one,

$$P(k_i) \sim k_i^{-1-2H}, \quad \text{for} \quad i \in \{x, y\}, \tag{4a}$$

$$P(k_r) \sim k_r^{-1-H}. \tag{4b}$$

Here, $\mathbf{k} = (k_x, k_y)$ is the wave vector in Fourier space and $k_r = |\mathbf{k}|$. The power spectrum of the self-affine surface is shown in Fig. 1, and is seen to yield a self-affine scaling, consistent with (4), over roughly two orders of magnitude.

After the self-affinity has been established, we interpolate the surface smoothly (using bicubic interpolation) between all the points of the lattice, in order to remove sharp edges in
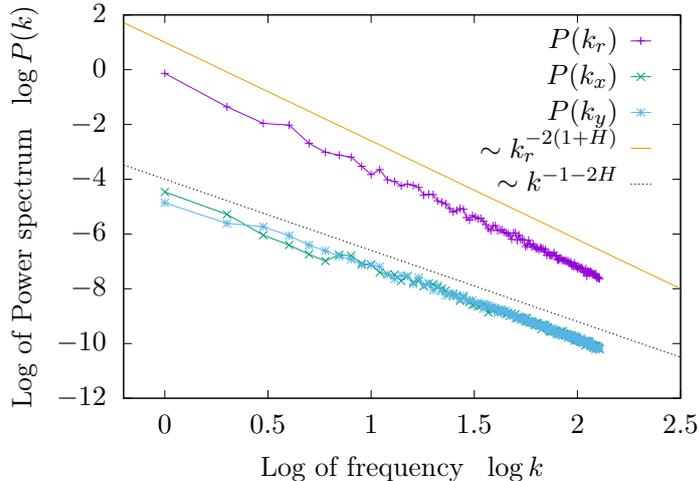
FIG. 1. Power spectrum of the self-affine surface used in this study, along x and y in Fourier space (k_x, k_y), and radially averaged, k_r. The solid lines show the theoretical power spectra of a surface with the Hurst exponent $H = 0.8$.

the mesh that could cause unsought numerical inaccuracies. Note that this implies that the roughness cut-off scale is somewhat larger than the mesh size. The resulting $512 \times 512\Delta x^2$ surface, which is ensured to be periodic, is scaled in the plane to 10×10 simulation units. The surface height is rescaled to yield a specified roughness amplitude A. The surface mesh is then copied and shifted a distance d vertically. At the corners making up the slab, nodes are added with a spacing Δx. The side faces nodes are then triangulated (with a typical length Δx) using the MESHPY [68] interface to TRIANGLE [69]. Finally, the interior of the slab is meshed using TETGEN [70]. The mesh is refined near the surface to represent the complex surface (but to resolve turbulent flow, a fine mesh in the bulk is also necessary).

To address the effects of inertia and roughness, we have in the simulations used one single initial self-affine surface, with the power spectrum shown in Fig. 1. The roughness amplitudes have been chosen to be $A = 0, 0.1d, 0.2d, 0.5d$, and $0.8d$, as compared to the channel width $d = 1$. More detailed mesh information is given in Appendix A, and the four meshes used in this study are visualized in Fig. 2.

7

(a) $A = 0$ (b) $A = 0.1$ (c) $A = 0.2$ (d) $A = 0.5$ (e) $A = 0.8$
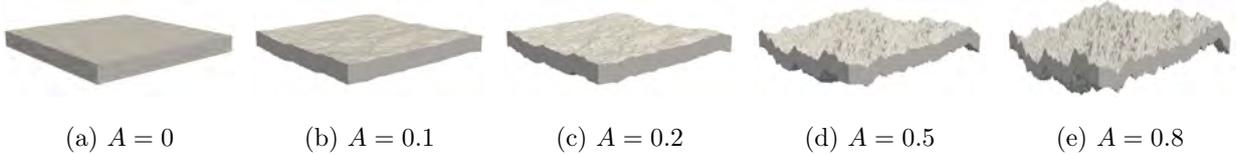
FIG. 2. The five meshes used in this study.

C. Brief discussion of length scales

For transitional flow, $\mathrm{Re} \sim 1000$, the Kolmogorov scale ℓ_K is comparable to the typical element size ℓ_{elem} (cf. Table II in Appendix A), which is generally smaller than the most dissipative eddies. As a comparison, extrapolation of the relationship $\ell_K \sim \mathrm{Re}^{-0.78}$ from the simulations by Mortensen and Valen-Sendstad [71] at a shear Reynolds number $\mathrm{Re}_\tau \simeq 180$ ($\mathrm{Re} \simeq 3000$), yields a comparable grid scale. Since their simulations were almost indistinguishable from the reference data by Moser *et al.* [72], we estimate that our simulation results, which are mostly concerned with $\mathrm{Re} \lesssim 2000$, should be sufficiently well-resolved. (However, rough meshes at $\mathrm{Re} \simeq 3000$ will be pushing the limits.) This is particularly true as the dominating source of error lies, in our case, in the particular realization of a self-affine surface. Finally, we verified *a posteriori* that mesh refinement gave no significant change in the macroscopic flow properties even for the highest roughness.

III. FLOW PROBLEM SETUP AND NUMERICAL METHOD

A. Governing equations and problem setup

As outlined above, the setup we consider is a flow in a rough channel. We consider the domain Ω to be periodic in the x and y directions, and constrained by the same, shifted, rough surface above and below in the z direction. The mean sampled over the xy plane of the lower surface is at $z = 0$, and the mean at the upper surface is at $z = d$.

Within the slab, we perform direct numerical simulation (DNS) of fluid flow. The incompressible flow is governed by the Navier–Stokes equations:

$$\partial_t \mathbf{u} + \mathbf{u} \cdot \boldsymbol{\nabla}\mathbf{u} - \nu\boldsymbol{\nabla}^2\mathbf{u} = -\boldsymbol{\nabla}p + \mathbf{f}, \quad \boldsymbol{\nabla} \cdot \mathbf{u} = 0. \tag{5}$$

Here $\mathbf{u}$ is the velocity field, ν is the kinematic viscosity, and p is the pressure. For convenience of notation, we have absorbed the constant density into the latter quantity.

8

The flow is driven by a constant, uniform body force $\mathbf{f}$, either to a laminar or a transitionally turbulent flow depending on the magnitude of $\mathbf{f}$. The force $\mathbf{f}$ is in the steady state (where the velocity is *at*, or temporally fluctuating around, a constant value) compensated by the friction between the flow field and the rough walls. At the same time it controls the injected energy per time, $\int_\Omega \mathbf{f} \cdot \mathbf{u} \, dV$ (V is volume), which is compensated by the (turbulent or laminar) dissipation rate, both at the walls and in the bulk. The present work is concerned with the transport properties of rough channels in this *statistical* steady state. The proper quantification of the transient dynamics of the transition process is left for future work.

In all simulations, no-slip conditions are applied at the boundaries, $\mathbf{u} = 0$ for $\mathbf{x} \in \partial\Omega$. In order not to trigger any spurious long-lived turbulent modes, we start all simulations from below, i.e. either at Re $= 0$ or from a steady laminar or a transitional state below the sought Re.

B. Numerical methods

The finite element method (FEM) for fluid flow simulations in *regular* geometries such as smooth pipes, ducts, and channels, is usually outperformed by spectral methods. However, when complex boundaries are present, the latter methods cannot be applied without loss of performance. Irregular geometries, such as in our case of rough cracks, are accurately represented by unstructured meshes, which leaves the FEM as a viable option.

In order to numerically resolve the Navier–Stokes equations (5), we use a customized version of the OASIS software [71], which is both fast and highly flexible. OASIS is built on top of the FEniCS/Dolfin framework [73, 74], which in turn interfaces to highly optimized linear solvers through the PETSc backend [75]. In fact, although most of the user interaction with OASIS/FEniCS is through the high-level Python interface, the runtime of the simulations are dominated by the backend PETSc Krylov solvers. This makes the runtime comparable to e.g. OpenFOAM [76].

To discretize the flow equations, we use a temporally second-order incremental pressure correction scheme (IPCS) [71]. The equations we solve, at time $t = n\Delta t$ (n is time step

number, Δt is the time step size), are

$$\frac{\mathbf{u}^* - \mathbf{u}^{n-1}}{\Delta t} + \hat{\mathbf{u}} \cdot \boldsymbol{\nabla}\tilde{\mathbf{u}} = \nu\boldsymbol{\nabla}^2\tilde{\mathbf{u}} - \boldsymbol{\nabla}p^* + \mathbf{f}, \tag{6a}$$

$$\boldsymbol{\nabla}^2\phi = -\frac{1}{\Delta t}\boldsymbol{\nabla}\cdot\mathbf{u}^*, \tag{6b}$$

$$\frac{\mathbf{u}^n - \mathbf{u}^*}{\Delta t} = -\boldsymbol{\nabla}\phi. \tag{6c}$$

Here, $\hat{\mathbf{u}} = (3\mathbf{u}^{n-1} - \mathbf{u}^{n-2})/2$ is an Adams–Bashforth projected advecting velocity, $\tilde{\mathbf{u}} = (\mathbf{u}^* + \mathbf{u}^{n-1})/2$ is the Crank–Nicholson interpolated advected velocity, and $\phi = p^{n-1/2} - p^*$ is an incremental pressure difference. In the above, velocity and pressure are solved in a segregated manner; Eq. (6a) is a velocity prediction step, Eq. (6b) is a pressure correction step, and Eq. (6c) is a velocity correction step. In this scheme, which is further documented in Ref. [71], Eqs. (6a) and (6b) are solved iteratively in an inner loop until a convergence criterion is reached, before in the end of a timestep (outer loop), Eq. (6c) is solved. For the spatial discretization, we use piecewise-linear Lagrange elements both for velocity and pressure (P_1–P_1), which yields second-order convergence in space.

IV. RESULTS

In this section, we report the results from our simulations of flow in rough channels. First we consider the geometrical properties of the fractures, and then we proceed to qualitatively inspecting the flow field and a typical simulation. We subsequently consider the macroscopic flow resistance, and finally the velocity fluctuations characterizing transitional flow.

A. Effective aperture field

It is well known in the literature that the *actual* fracture width is not limited by the vertical width (along the z coordinate), d, but rather by an *effective* channel width d_{eff}, which can be better approximated as the smallest distance between the channel walls measured perpendicularly to the local flow direction [48, 77]. Since this direction changes along the rough surface, it consitutes an *effective aperture field* in the xy plane. In our simulations, the vertical displacement is given by $d = 1$ everywhere, but the effective apperture depends sensitively and nontrivially on the roughness of the surfaces.

10

Now, we estimate the effective aperture field on purely geometrical grounds. The method we use is based on that by Mourzenko *et al.* [78], who suggested to fit the largest possible sphere at each point in the fracture to calculate the effective aperture. At a given in-plane coordinate (x, y), we locate a sphere of radius $R(z)$ centered at (x, y, z). Varying z, we seek a sphere of such a size that it barely touches the lower and upper channel walls, i.e. find the z for which the minimal distance to the above surface equals the minimum distance to the lower surface. This gives us an optimum $z = z_{\text{opt}}$ and a smallest effective channel width, $d_{\text{eff}} = 2R(z_{\text{opt}})$. Doing this for all $(x, y) \in [0, L] \times [0, L]$, we obtain the fields $z_{\text{opt}}(x, y)$ and $d_{\text{eff}}(x, y)$. The former can be related to the tortuosity of the flow field [79]. The latter, which is of primary interest here, is a geometric approximation to the effective aperture field.
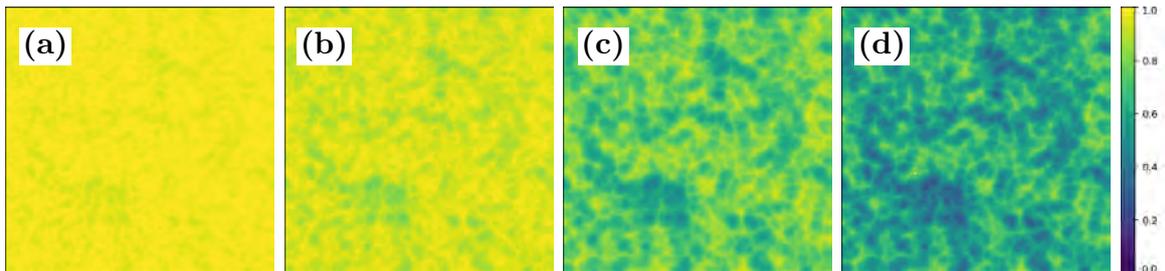
FIG. 3. Effective aperture field $d_{\text{eff}}(x, y)$ for increasing roughness amplitude A. Subfigures (a)–(d) correspond to (b)–(e) in Fig. 2.

The effective aperture fields $d_{\text{eff}}(x, y)$ are shown in Fig. 3 for increasing roughness. Here, it can be readily seen that the effective width depends strongly on the roughness amplitude, and for higher roughness, some areas are shielded by the most pronounced fracture tooths. In particular, it seems that an area with particularly low permeability emerges near the lower left corner, mimicking an obstacle.

It is also of interest to inspect the probability density functions of the effective aperture, sampled over the xy plane, which are shown in Fig. 4. We note that the distributions are slightly skewed, decrease as the roughness amplitudes increases, and seem to approach a normal distribution for the highest roughness. This is further seen in the inset, where we show the dependence of the mean effective aperture upon the roughness amplitude.

11
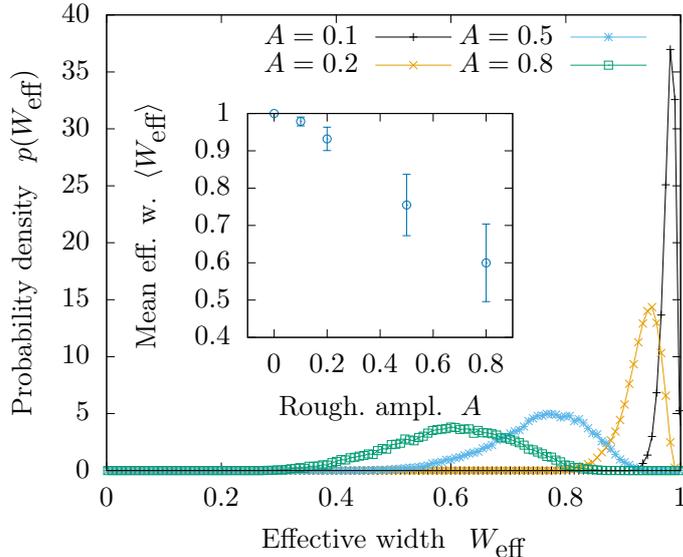
FIG. 4. Probability density of the effective aperture fields d_{eff} sampled over the plane (x, y). Inset: The mean of the distributions in the main panel, with the standard deviations plotted as bars.

B. Qualitative inspection of the velocity fields

We now turn to inspecting the velocity fields that arise in the self-affine channels as a body force (or average pressure gradient) $\mathbf{f}$ is imposed. Figure 5 (a) shows an instantaneous snapshot of the velocity field in the statistical steady state. Here, it can be seen that transient flow patterns are present, particularly at the streamwise periodic cross-sectional plane, show to the left in the figure.

To investigate the flow rate in time, we define a flux-based Reynolds number [80],

$$\text{Re} = \frac{Q_x}{L\nu} = \frac{\langle u_x \rangle \, d}{\nu} \tag{7}$$

where Q_x is the flux, i.e. volume per time, that passes through any (due to the incompressibility) cross section normal to the x-axis. Correspondingly, $\langle u_x \rangle$ is the mean velocity in the x direction. We can interpret Eq. (7) either in an instantaneous or a in statistical sense, depending on whether Q_x is a fluctuating quantity—which again will depend on the forcing f. In particular, for a given f, the *instantaneous Reynolds number* (for which we emphasize the time dependence by a subscript t) yields a unique value of Re in the following sense. Either, if the flow is unsteady, Re is found as the average over a sufficiently long time in the statistical steady state, i.e. $\text{Re} = \overline{\text{Re}_t}$; or if the flow is laminar and steady, the relation is

12
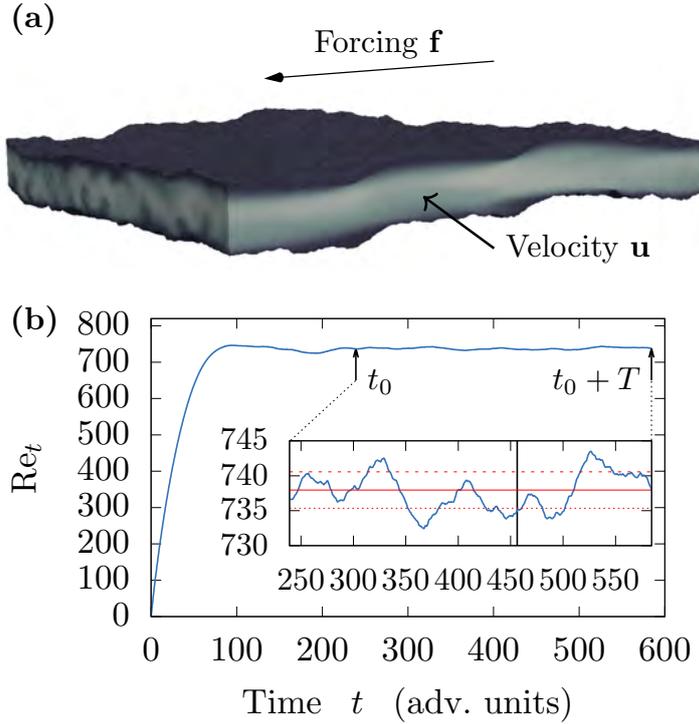
FIG. 5. A typical simulation in a self-affine channel with roughness amplitude $A = 0.2$, forcing $f = 1.5 \times 10^{-6}$ and viscosity $\nu = 9 \times 10^{-5}$. (a) A snapshot from the simulation after roughly 450 advective time units. The direction of forcing is shown, and the lighter color indicates higher speed. (b) Instantaneous Reynolds number Re_t (based on instantaneous flux) as a function of time. The time when a statistical steady state has been reached is indicated by t_0, and we indicate a sampling time T over which statistical quantities are estimated. Inset: Amplification of the Re_t signal during the sampling time, and the eventually estimated Re is indicated by a horizontal solid red line. The standard deviation (shown around Re as horizontal dashed red lines) shows that the error in the time signal is less than 0.4%. The snapshot in (a) is taken at the time indicated by a vertical black line.

$\mathrm{Re} = \lim_{t \to \infty} \mathrm{Re}_t$. The notion of the statistical steady state is exemplified in Fig. 5 (b). The latter shows the time evolution of Re_t, in the simulation shown in Fig. 5 (a), starting from a quiescent state at $\mathrm{Re}_t = 0$. After an initial transient of exponential relaxation toward a steady value, a noisy signal develops. Indicated in the figure is a sampling interval between $t = t_0$, where the statistical steady state has been reached, and $t = t_0 + T$. The inset of Fig. 5 (b) shows a close-up of the velocity signal in the sampling interval, displaying a fluc-

13
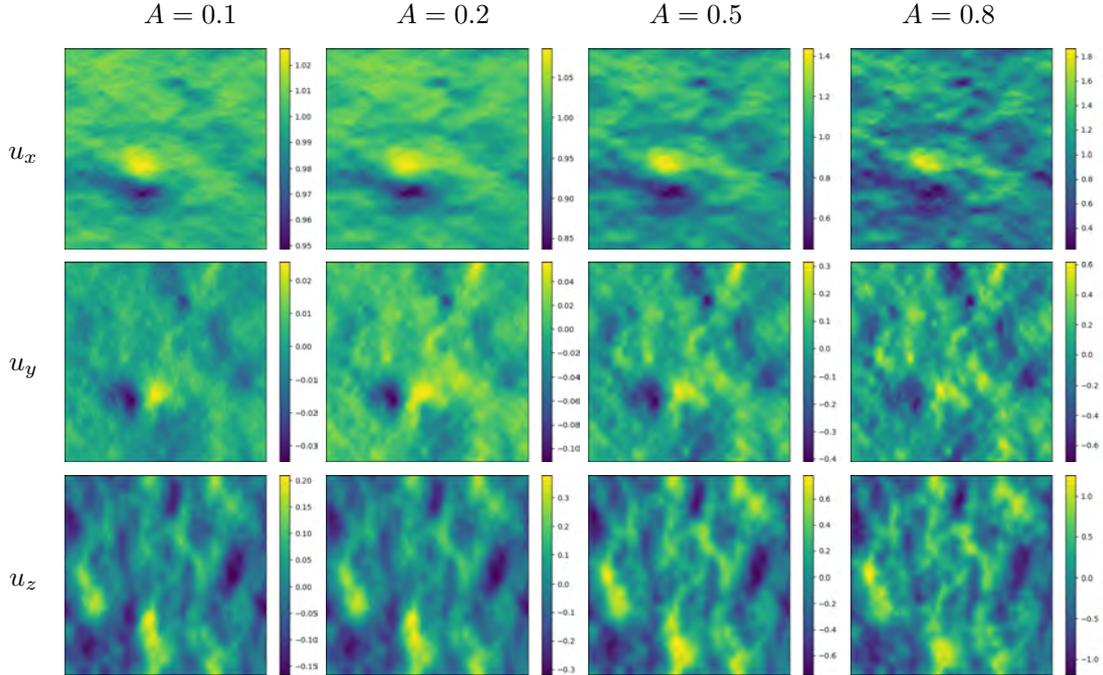
FIG. 6.   Depth-averaged velocity fields for low Re, i.e. laminar flow. The figure shows the three components of the velocity vector, for four values of roughness amplitude A. The velocity components are normalized by $\langle u_x \rangle$.

tuating signal. However, the standard deviation of this signal is less than 0.4% of Re, which is much less than the local fluctuations, meaning that $\lim_{t \to \infty} \mathrm{Re}_t \simeq \overline{\mathrm{Re}}$, and the steady and unsteady methods of computing Re are virtually equivalent.

Next, to qualitatively visualize the spatial distribution of local fluxes, we consider depth-averaged velocity fields, i.e. the velocity fields in the xy plane that result from averaging over $z \in [h, d + h]$. First, we present plots of the flow fields in the fully laminar, low inertia regime (Re ~ 1), shown in Fig. 6 for all velocity components normalized by $\langle u_x \rangle$. It is clear that similar features are present for all roughness amplitudes. In particular, one obstacle (the dark region in rows 1 and 2) leads to flow being directed around it. A bottleneck effect may result from this (see [10]), but this effect will be significantly smaller in 3D than in 2D fractures, since the flow is allowed to simply pass around the obstacle [48].

For the case of high inertia (Re ~ 1400), the velocity fields are well above the turbulent thresholds and thus strongly fluctuating in both time and space. In order to isolate the spatial fluctuations and visualize the mean transport channels, we therefore consider the *time-averaged velocity fields*, which are computed by averaging the flow field over time in

14
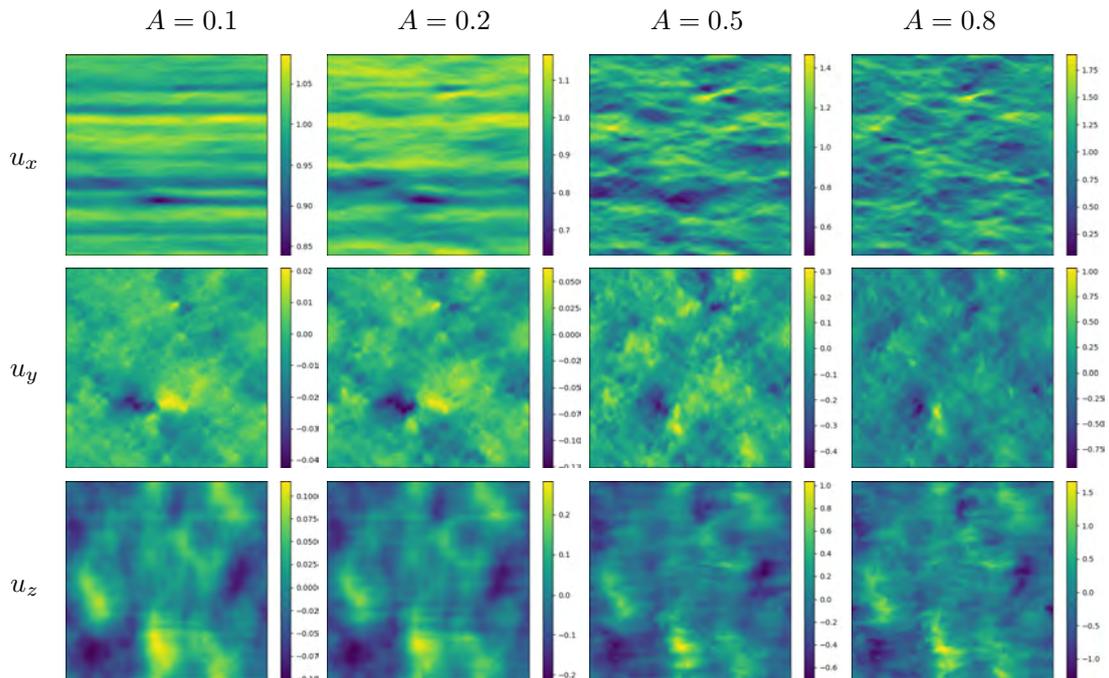
FIG. 7. The depth-and-time-averaged velocity field from high-Re simulations. Rows and columns correspond to Fig. 6.

the statistical steady state, i.e.,

$$\overline{\mathbf{u}}(\mathbf{x}) = \frac{1}{T} \int_{t_0}^{t_0+T} \mathbf{u}(\mathbf{x}, t) \, \mathrm{d}t, \tag{8}$$

where t_0 is some initial transient that ensures that the system is equilibrated, and T is the sampling time. We present in Fig. 7 corresponding plots to the above, and show the depth-averaged time-averaged velocity fields $\overline{\mathbf{u}}$ for varying roughness. From these plots, in particular by inspecting u_x (row 1), it is clear that at low roughness, preferential paths emerge that extend across the finite system. The slowest channel coincides with the obstacle noticed in the low Re regime (cf. Fig. 6). For higher roughness, this effect is less noticeable, in particular, the obstacle region cannot be seen for u_x (but it is possible to see it for u_y). This is possibly because the roughness amplitude is so high that there is now no continuous straight chord that connects the flow field "to itself" (through the periodic boundary condition).

15

C. Macroscopic flow properties

Now we proceed to inspecting the macroscopic properties of flow through self-affine chan-
nels. This amounts to relating the properties such as the flow rate, the imposed forcing,
and the roughness amplitude of the channel. Since $\mathbf{f} = f\hat{\mathbf{x}}$, we may define a dimensionless
geometrical friction coefficient (which can be seen as an inverse relative permeability):

$$C_f = \frac{fd^2}{12\nu \langle u_x \rangle}. \tag{9}$$

The reason for choosing this quantity is that, for Stokes flow (Re $\to$ 0), this C_f comes out
of the equations as a *purely geometric* quantity. Moreover, it takes the lowest value possible
(with no-slip condition on all fixed boundaries) in a plane channel. The only requirement
is the no-slip condition and a prescribed mean flow direction. The prefactor $1/12$ is chosen
such that $C_f = 1$ for laminar PPF.

Another commonly applied quantity e.g. for flow in pipes is the Darcy friction factor f_{D},
defined through the Darcy–Weisbach relation [81, 82]:

$$f_{\mathrm{D}} = \frac{fd}{\frac{1}{2} \langle u_x \rangle^2}. \tag{10}$$

Between these two quantities, we have the relation

$$C_f = \frac{f_{\mathrm{D}} \mathrm{Re}}{24}. \tag{11}$$

For the special case of laminar PPF, we thus have $f_{\mathrm{D}} = 24/\mathrm{Re}$.

In Fig. 8, we present a diagram of the statistical steady-state relationship between the
Reynolds number Re and the friction factor C_f for the various roughness amplitudes. It
is clear that for low Re, C_f attains a constant value dependent on the roughness A. At
higher Re, there seems to be a certain threshold where the scaling of C_f crosses over and
starts to grow, for higher Re, close to linearly. The point where the dependence departs
from the constant behaviour is where the inertial effects come into play. However, these
effects are not *necessarily* due to turbulence, and may come from growth of steady eddies
in the laminar regime. It is seen from Fig. 8 that the transition point appears at lower
Re for higher roughness amplitude A. For $A = 0$, owing to the subcritical nature of the
transition, unsteady flow does not occur by itself, since the flow is always linearly stable. In
particular, the flow needs a perturbation of a certain finite size for turbulence to proliferate
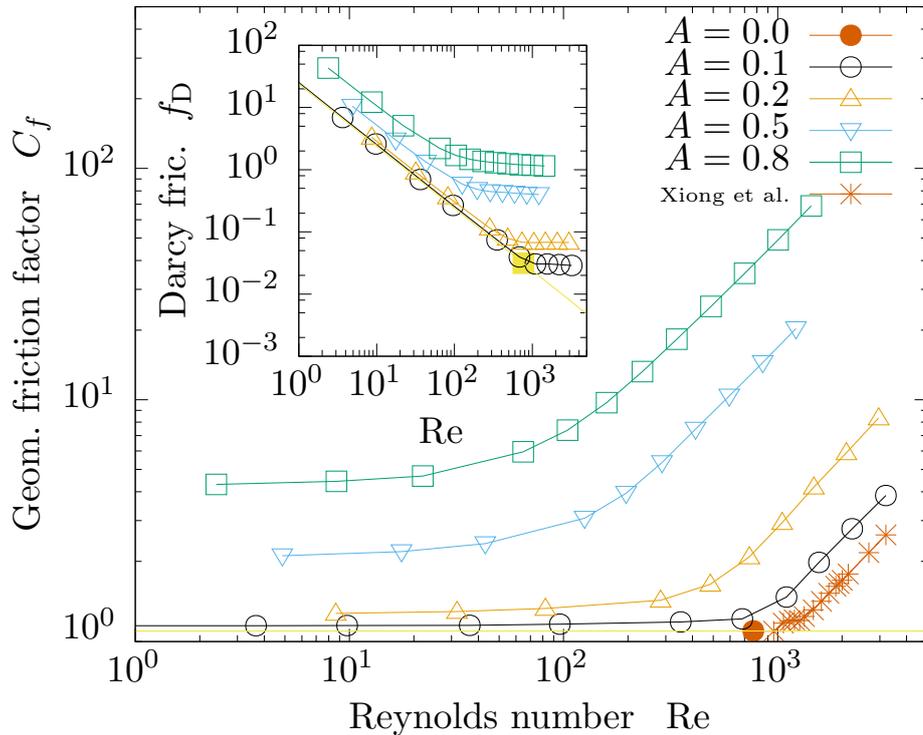
FIG. 8. Friction factor C_f plotted against Reynolds number Re for the five roughness amplitudes. The data for PPF marked with star symbols are taken from Xiong *et al.* [83]. Inset: Darcy friction factor f_D versus Re number for the same roughness amplitudes.

and spread [18, 26]. In Fig. 8, we therefore include the friction factor measurements of [83]. Their results are in good agreement with the current data, as the transition point is moved towards higher Re, and the same slope is evident for large Re. It should be noted that in the range roughly above Re = 1000, the latter authors observed and investigated large-scale turbulent patterns (bands and stripes), which are generally unattainable in our simulations due to domain size limitations. However, features of single turbulent bands were observed for the lowest roughness around Re = 1100.

The same data is plotted as a Moody diagram [84] in the inset of Fig. 8, showing the dependence of the Darcy friction factor f_D on Re. From the figure, we note that f_D seems either to almost saturate at a constant value, or to decay very weakly with Re. Whether this behaviour persists for higher Re remains an open question.

In order to quantify the point at which the inertial effects become apparent, the following

17

functional form provides a good fit to the entire range of data, at each roughness:

$$\frac{C_f}{C_{f,0}} = \left[1 + \left(\frac{\mathrm{Re}}{\mathrm{Re_c}}\right)^{\beta}\right]^{1/\beta}. \tag{12}$$

Here, $C_{f,0}$ is the *purely* geomeric friction factor, identified in the limit $\mathrm{Re} \to 0$, while $\mathrm{Re_c}$ is a critical Reynolds number where the inertial effects come into play. This function (the ℓ_β-norm of $(1, \mathrm{Re}/\mathrm{Re_c})$) has the feature that it interpolates between two scalings over the range in Re,

$$\frac{C_f}{C_{f,0}} = \begin{cases} 1 & \text{for} \quad \mathrm{Re} \ll \mathrm{Re_c}, \\[2mm] \frac{\mathrm{Re}}{\mathrm{Re_c}} & \text{for} \quad \mathrm{Re} \gg \mathrm{Re_c}. \end{cases} \tag{13}$$

The exponent β in Eq. (12) controls the width of the transition region between the two regimes; a high exponent indicates a narrow region (fast decay) and vice versa. Note also that when $\beta \to \infty$, $C_f/C_{f,0} = \max(1, \mathrm{Re}/\mathrm{Re_c})$. When $\beta = 1$, Eq. (12) is consistent with the Forchheimer law (3). Further, when $\beta = 2$, Eq. (12) attains a quadratic correction term for $\mathrm{Re}/\mathrm{Re_c} \ll 1$, which is consistent with the weak inertia law. Using Eq. (11), Eq. (12) can be written in terms of the Darcy friction factor as

$$\frac{f_\mathrm{D}}{f_{\mathrm{D},\infty}} = \left[\left(\frac{\mathrm{Re_c}}{\mathrm{Re}}\right)^{\beta} + 1\right]^{1/\beta}, \tag{14}$$

which attains the qualitatively correct asymptotes $f_\mathrm{D} \sim \mathrm{Re}^{-1}$ for $\mathrm{Re} \ll \mathrm{Re_c}$, and $f_\mathrm{D} \sim f_{\mathrm{D},\infty} = \mathrm{const.}$ for $\mathrm{Re} \gg \mathrm{Re_c}$, cf. [52, Eq. (5)]. The asymptote is then given by $f_{\mathrm{D},\infty} = 24C_{f,0}/\mathrm{Re_c}$.

It is thus clear that Eq. (12) (or equivalently, Eq. (14)) can be seen as a generalized Forchheimer equation. While Eq. (12) does not have a direct physical motivation, it describes the data well and provides an unbiased determination of $\mathrm{Re_c}$ for all roughness amplitudes A. $C_{f,0}$ can be read off directly from the simulation data in the $\mathrm{Re} \simeq 0$ limit, which means that β and $\mathrm{Re_c}$ can be considered as the only two fitting parameters in the expression, and are readily calculated using a nonlinear least squares method. In Fig. 9, we show the parameters computed from the data in Fig. 8 as a function of roughness A. Figure 9 (a) shows the purely geometric friction factor $C_{f,0}$ as a function of roughness amplitude A, computed by three methods. The first method is by direct numerical simulations, solving the Navier–Stokes (NS) equations. The data show that $C_{f,0}$ depends approximately quadratically on the roughness amplitude, increasing with roughly a factor 4 for the highest roughness. The
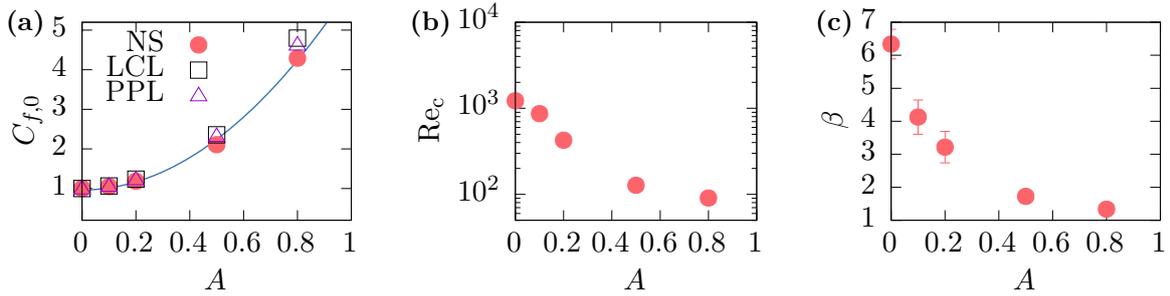
FIG. 9. Parameters based on the friction factor data in Fig. 8. The computed values at $A = 0$ are based on Ref. [83]. (a) The purely geometric friction factor computed from Navier–Stokes (NS) simulations, compared to that found by using the local cubic law (LCL) and the parallel plate law (PPL). A quadratic fit to the NS data is shown as a guide to the eye. (b) Critical Reynolds number $\mathrm{Re_c}$ where inertial effects arise, estimated by a least squares fit the generalized Forchheimer equation Eq. (12). (The error bars are smaller than the points.) (c) The exponent β which characterizes the transition region in Eq. (12), estimated the same fit as $\mathrm{Re_c}$ in (b).

second method applies the lubrication approximation and computes $C_{f,0}$ by the local cubic law (LCL), and the third approach consists in further assuming the confining boundaries to be flat, using the parallel plate law (PPL). The LCL method amounts to solving the Reynolds equation (2) using the effective aperture fields (see Fig. 3), effectively letting $d = d_{\mathrm{eff}}(x, y)$. The PPL method assumes the constant plate separation $d = \langle d_{\mathrm{eff}} \rangle$, which are shown in the inset of Fig. 4 (disregarding all fluctuations). Both the LCL and PPL predict the true friction factor fairly well, overestimating the friction loss by less than 10%. The overestimation may be due to the fact that a parabolic flow profile (which is the essence of the lubrication approximation) is not the least dissipative one when short-wavelength roughness is taken into account. We observe also that the PPL, which is a simplification of the LCL, performs better than the latter. A more thorough assessment of these predictions would require simulations in several realisations of self-affine surfaces at the same roughness amplitude A; see e.g. Ref. [45] for a study in this direction.

Figure 9 (b) shows the estimated critical Reynolds number $\mathrm{Re_c}$ as a function of roughness amplitude A. The estimated $\mathrm{Re_c}$ displays a decrasing trend with A, being reduced by more than an order of magnitude for the highest amplitudes. Combination of the quadratically increasing $C_{f,0}(A)$, in Fig. 9 (a), and the decaying $\mathrm{Re_c}(A)$, in Fig. 9 (b), precludes the

existence of a Strickler scaling [21, 85], i.e., $f_{D,\infty} \sim A^{1/3}$ [86]. However, the latter scaling is found in pipe flow with a Nikuradse-type roughness and furthermore at $\text{Re} \gtrsim 10^5$, and thus disagreement with our data is expected. Figure 9 (c) shows the estimated exponent β in Eq. (12). For low roughness amplitude A, the exponent is high, indicating a sharp transition between the two scaling regimes. For increasing A, β decreases monotonously, indicating broader transition regions, and approaches the standard Forchheimer value $\beta = 1$ for the highest roughness amplitudes considered.

A final test of the unified description of the data presented in Fig. 8 is to inspect how well they collapse when rescaled by the parameters $C_{f,0}$, Re_c (leaving now the additional fitting parameter β out of the picture). In Fig. 10, we plot for all simulated roughness amplitudes A, $C_f/C_{f,0}$ as a function of Re/Re_c. For all A, the data is seen to follow the
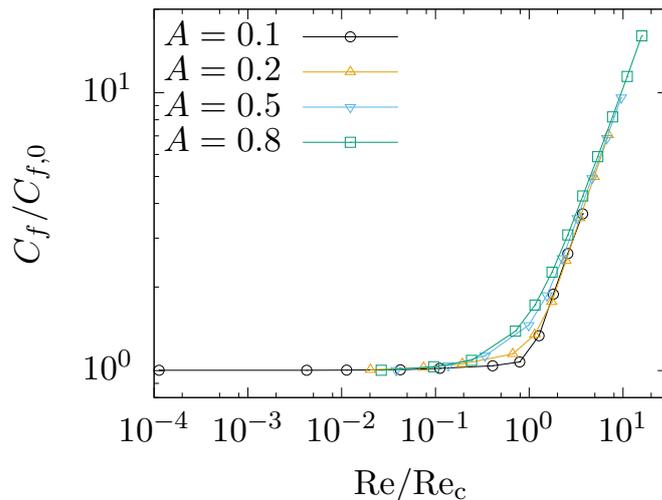
FIG. 10.   Data collapse of the scaled geometric friction factor, $C_f/C_{f,0}$, as a function of scaled Reynolds number Re/Re_c for all roughness amplitudes A considered in the present work. In particular, we show the data presented in Fig. 8, when C_f and Re are rescaled by the parameters $C_{f,0}$ and Re_c, respectively shown in Fig. 9 (a) and (b).

same asymptotic behaviour, differing only in the transition region (which in the least squares fit was captured by β). In particular, the transition region is seen to become wider as the roughness is increased, consistent with the quantitative observation of the behaviour of $\beta(A)$ in Fig. 9 (c).

D. Temporal fluctuations

We have until now characterized the onset of non-linear flow; however, to characterize the appearance of unsteady, transitional or turbulent flow, we need a method to estimate presence of such flows. Here, we separate between *steady* flow, which is always laminar, and unsteady flow, which can in principle both time-periodic laminar flow (where there is essentially no nonlinear transfer of energy across scales) or turbulent flow. However, we assume that for flow over a sufficiently large rough surface (with high enough amplitude to produce detaching vortices), a time-periodic signal from a single defect will not contribute noteworthy to the overall transport properties. Above this, there will be several (for an infinitely large domain, infinitely many) interacting 'defects' that produce vortices, and thus no time-periodic signal should be found. We therefore adopt the following heuristic notion of turbulence. By using Reynolds decomposition, the velocity field $\mathbf{u}(\mathbf{x}, t)$ can be decomposed into its *expectation value* $\overline{\mathbf{u}}(\mathbf{x})$ and the *velocity fluctuations* $\mathbf{u}'(\mathbf{x}, t)$:

$$\mathbf{u}(\mathbf{x}, t) = \overline{\mathbf{u}}(\mathbf{x}) + \mathbf{u}'(\mathbf{x}, t). \tag{15}$$

Now, an indicator function for turbulent intensity can be found by defining

$$q(\mathbf{x}, t) = |\mathbf{u}'(\mathbf{x}, t)|^2. \tag{16}$$

Since we are primarily interested in the global presence of transitional flow, we use the space-and-time averaged indicator function $\overline{\langle q \rangle}$, which should only depend on Re and A, where the error (or standard deviation) can be estimated based on the temporal fluctuations of $\langle q \rangle (t)$. This leads to the definition of a fluctuation-based Reynolds number [87],

$$\text{Re}' = \frac{\sqrt{\overline{\langle q \rangle}} d}{\nu}, \tag{17}$$

which has the property that it is approximately zero for steady or close to steady (laminar) flow, and positive for extended unsteady (transitional) flow.

In Fig. 11, we show the dependence of the fluctuation-based Reynolds number Re' on the flux-based Re for all simulated roughness amplitudes A. For sufficiently high Re, the data for all roughness amplitudes seemingly obey linear relationships. For the lowest amplitude, $A = 0.1$, the transition appears to be subcritical (as it is for $A = 0$). Around $\text{Re} \simeq 1100$, the error bars increase, indicating large temporal oscillations in the instantaneous turbulent intensity
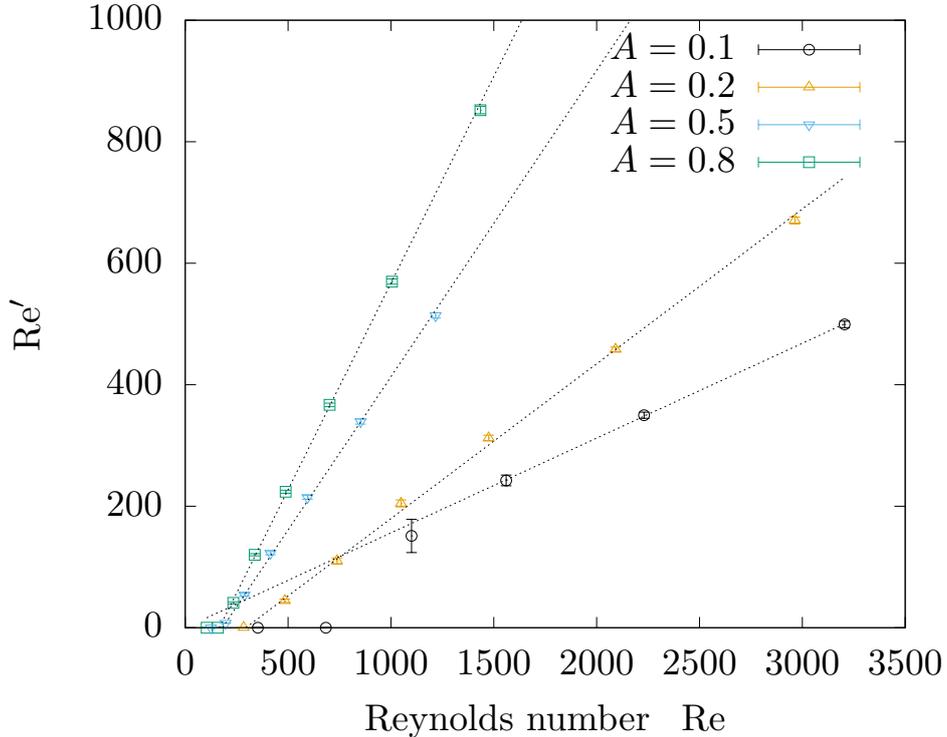
FIG. 11. The fluctuation-based Reynolds number Re' (indicator of turbulence) as a function of the flux-based Reynolds number Re, for all considered roughness amplitudes A.

$\langle q \rangle$. This indicates the presence of a metastable turbulent band which will eventually decay given sufficiently long time [31]. Furthermore, the linear trend found by fitting a linear slope to the data points for which $Re' \geq \delta$ ($\delta = 10^{-3}$ is a small numerical tolerance), does not extend down to $Re' = 0$. However, for $A \geq 0$ it does, meaning that unsteady flow is continuously produced by the boundary for $Re > Re_{c,q}$, where $Re_{c,q}$ is a *second* critical Reynolds number which quantifies the point where *transitional flow* sets in, in contrast to the point of nonlinear flow resistance quantified by Re_c. This suggests that the transition to turbulence changes from being subcritical to being supercritical at a roughness amplitude $A \in [0.1, 0.2]$.

Based on the adequacy of linear fits (as outlined above) to describe the $Re'(Re)$ data over roughly an order of magnitude, we propose the following relation:

$$Re' = \begin{cases} 0 & \text{for} \quad Re < Re_{c,q}, \\ k_q(Re - Re_{c,q}) & \text{for} \quad Re \geq Re_{c,q}, \end{cases} \tag{18}$$

22
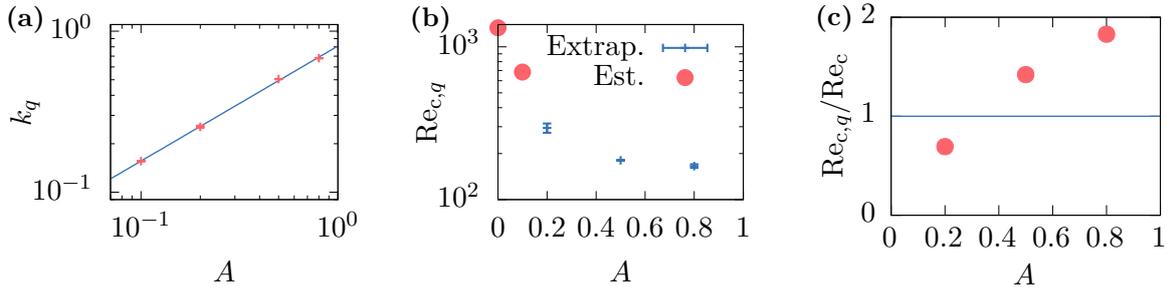
FIG. 12.   Parameters estimated from least squares linear fits to the data shown in Fig. 11. (a) The proportionality factor k_q shown in a double logscale plot. (b) The critical Reynolds number $\text{Re}_{c,q}$ where turbulence proliferates. The values for $A \geq 0.2$ (marked with blue error bars) are computed by linear extrapolation of the slopes to the $\text{Re}' = 0$ plane. The estimated values (marked as red dots) are computed as described in the main text. (c) The ratio between the turbulent critical Reynolds number $\text{Re}_{c,q}$ and the inertial critical Reynolds number Re_c.

which should hold for amplitudes $A \gtrsim 0.2$. In Eq. (18), both the proportionality factor k_q and the second critical Reynolds number $\text{Re}_{c,q}$ should depend on A.

In Fig. 12 we plot the parameters k_q and $\text{Re}_{c,q}$ resulting from linear fits of to the data shown in Fig. 11 (where $\text{Re}' \geq \delta$). In Fig. 12, we show the relationship between the proportionality factor k_q, which is well captured by a functional form $k_q = k_{q,0} A^\gamma$ ($k_{q,0} \simeq 0.8$, $\gamma \simeq 0.7$). However, neither the range in A nor the number of data points strictly suffice to justify this relation, but the functional form illustrates the general trend. Figure 12 (b) shows the relation between the critical Reynolds number $\text{Re}_{c,q}$ where transitonal flow sets in. By extrapolating the linear fits to the data in Fig. 11, we obtain three values of $\text{Re}_{c,q}$ (which are positive), which is not enough to get an idea of a trend. Thus, to give an idea of the trend, we augment the figure by two heuristically estimated values, based on simulations and the available literature. Here, the estimated values are, for $A = 0.1$, given by the highest value of Re where turbulence was not triggered in our simulations, and for $A = 0$, given by the point $\text{Re} \simeq 4/3 \times 1000$ (see [80] for the origin of the prefactor), where turbulence in PPF is more likely to spread than to decay [83].

The latter plot, Fig. 12 (b), calls for a comparison with Fig. 9 (b). In particular, we inspect now the relation between Re_c and $\text{Re}_{c,q}$, and since $\text{Re}_{c,q}$ could not be reliably computed, we consider only the highest roughness amplitudes, i.e., $A \geq 0.2$. As shown in Fig. 12 (c),

23

we find here that $\mathrm{Re}_{c,q}(A)$ and $\mathrm{Re}_c(A)$ are comparable, but that $\mathrm{Re}_{c,q}(A) > \mathrm{Re}_c(A)$ for sufficiently high roughness amplitude A. This implies that for the rough geometries, there is a window for $\mathrm{Re}_c < \mathrm{Re} < \mathrm{Re}_{c,q}$, where there are significant inertial effects, but no transitional or unsteady features are present. For low roughness amplitudes, $\mathrm{Re}_{c,q} < \mathrm{Re}_c$, and there is no such region; however, due to the finite transition region there may still be weak inertial features present below $\mathrm{Re}_{c,q}$. In the former regime, i.e. when $\mathrm{Re}_{c,q} > \mathrm{Re}_c$, standard (nonlinear) laminar correlations are expected to hold; whereas above, the transitonal and fluctuating flow patterns will have a significant effect on friction (which is already incorporated into the results herein), solute dispersion and heat transfer.

V. DISCUSSION

In this work, we have investigated flow in self-affine channels, representative of fracture joints, by extensive direct numerical simulations. The motivation for this study was twofold, in the sense that we sought to investigate the role of a generic, naturally occurring roughness both for the macroscopic transport properties, and the nature of the transition to turbulence in the presence of boundary roughness. A major advance compared to previous studies is that we pay particular attention to transitional flow, including the velocity fluctuations that are present during strong continuous forcing of such flows. In the following, we summarize and discuss our main findings, as well as the major limitations of our work.

In the geometries considered, the impact of a generic roughness on the macroscopic flow properties was found to be the following: (i) The purely geometric friction factor, $C_{f,0}$ corresponding to the $\mathrm{Re} \to 0$ limit of the geometric friction factor C_f, scales approximately quadratically with roughness amplitude A (root-mean-square height undulation of the rough surface). (ii) Secondly, the critical Reynolds number Re_c where inertial effects come into play decreases monotonously with A. (iii) The crossover region from the constant asymptote, $C_f \sim C_{f,0}$ for $\mathrm{Re} \ll \mathrm{Re}_c$, to the linear asymptote $C_f \sim \mathrm{Re}$ for $\mathrm{Re} \gg \mathrm{Re}_c$, can be described by a generalized Forchheimer equation (12). The velocity fluctuations associated with transitional flow turn out to have a pronounced effect, and in particular they appear at a second well-defined $\mathrm{Re}_{c,q}$, which has a qualitatively similar dependence on A as Re_c, and is larger than Re_c for sufficiently high A. Thus, there is then a region $\mathrm{Re} \in [\mathrm{Re}_c, \mathrm{Re}_{c,q}]$ where inertial effects are present but the flow remains laminar. This implies that turbulent

effects must be accounted for in simulations on larger scales already at such moderate Re. Finally, our simulations and subsequent analysis suggest the turbulent transition in a rough channel goes from being subcritical (at low A) to being supercritical at some $A_c \in [0.1, 0.2]$.

A major limitation of the present work is that we have, due to computational limitations, considered only a single realization of a self-affine surface, and varied only the amplitude of the undulation of that surface. In order to investigate the robustness and possible universal aspects of the present work, future research should not only consider ensemble averages of self-affine surfaces, but also of other types of roughness (e.g. Nikuradse-type roughness [20, 88]). Indeed, there is a possibility that our results are sensitive to e.g. the largest obstacle in the domain. A second limitation, related to this, is the question of scale. In our simulations, the domain size was fixed to $L = 10d$, while it is known that transport properties of self-affine channels scale nontrivially with the system size [4]. Future work should therefore critically reexamine whether the functional forms found here are valid regardless of L. Finally, to properly quantify the universality class of the transition, significantly larger domains are needed. As a comparison, the length scale of the domain considered by Chantry *et al.* [30] for Waleffe flow (model plane Couette flow), was roughly equivalent to $L \simeq 1280d$ (in our units). Such domain sizes are out of reach with the finite element method presented herein, and an alternative route might be to follow in the lines of Ishida *et al.* [64], who instead of resolving the complex boundary directly, used an effective body force to model boundary friction [89]. However, this type of roughness cannot produce vortices that are released into the bulk, and it is therefore doubtful whether the latter approach is valid when the roughness amplitude is sufficiently large. We hope to address some of these issues in the near future.

In conclusion, we believe that our results can be of interest both to the geophysical and to the turbulence communities, as we have provided new light on the role on transitional flow in the presence of a generic roughness found in many natural and industrial settings.

Appendix A: Detailed mesh information

The properties of the surface meshes used in this study are listed in Table I. As is seen from the table, the surface area increases with the roughness amplitude A, but this is independent of the self-affine property, as any undulated surface should scale as $S^2(A) - S^2(0) \sim A^2$. Here, S is the area of the self-affine part of the mesh with a given roughness scaling A, i.e. when the slab's faces are excluded. As a check, we verified that our meshes satisfy this. In principle, since $S \sim \Delta x^{-H}$, it is not expected to be finite for any nonzero roughness amplitude A. The surface that is *accessible* to the flow field will in any case be limited by the viscous boundary layer, which in the Reynolds number range we are considering is larger than this smallest scale.

TABLE I. Surface mesh information. The faces of the slabs are included.

A	Nodes	Facets	Total area	ℓ_{facet}
0.0	698,146	1,396,288	240.0000	0.01311
0.1	698,606	1,397,208	245.4747	0.01325
0.2	699,008	1,398,012	260.5035	0.01365
0.5	698,382	1,396,760	339.2817	0.01558
0.8	697,110	1,394,216	441.2603	0.01779

The properties of the full mesh are listed in Table II. The number of nodes and elements in the meshes are fairly constant, as the meshes were generated using identical procedures.

TABLE II. Full mesh information, including bulk and surface.

A	Nodes	Elements	Volume	ℓ_{elem}
0.0	3,696,368	21,526,314	100.0	0.0166
0.1	3,690,237	21,440,983	100.0	0.0167
0.2	3,672,117	21,302,242	100.0	0.0167
0.5	3,607,372	20,905,569	100.0	0.0168
0.8	3,518,454	20,382,889	100.0	0.0170

26

Appendix B: Probability density functions of the velocity field

Here, we consider the probability density functions (PDFs) of the velocity distributions for flow in the rough cracks. The probability distribution of velocity links the spatial velocity field to macroscopic properties such as permeability and tortuosity [90].

It is useful to compare our empirical PDFs with a case for which there is an analytical solution, namely Hele-Shaw flow along the x-direction. The velocity field is then given by

$$\mathbf{u}(z) = 6 \langle u_x \rangle \frac{z}{d} \left(1 - \frac{z}{d} \right) \hat{\mathbf{x}}. \tag{B1}$$

This gives, sampled uniformly over $z \in [0, d]$, the PDF

$$p\left(\hat{u}_x \right) = \begin{cases} \frac{1}{\sqrt{3(3 - 2\hat{u}_x)}} & \text{for} \quad \hat{u}_x \in [0, \frac{3}{2}], \\ 0 & \text{otherwise.} \end{cases} \tag{B2}$$

Here, we have defined the normalized velocity $\hat{u}_i = u_i / \langle u_x \rangle$ for $i \in \{x, y, z\}$. Note that this distribution diverges as $\sim (1 - u_x/u_{\max})^{-1/2}$ as $u_x \to u_{\max}^-$. The other components, $i = y, z$, have the PDF $p(\hat{u}_i) = \delta(\hat{u}_i)$, where $\delta(\cdot)$ is the Dirac delta distribution.

We obtain the velocity PDFs by sampling randomly 10^6 points over the entire volume, and creating a normalized histogram from the resulting values.

In Fig. 13, we show for low-inertia flow (Re ~ 1) the empirical velocity PDFs, for all five roughness amplitudes. In the main panel of Fig. 13, the distribution of the streamwise component is shown, and the left and right insets show, respectively, the spanwise and vertical components. Along with the empirical distribution, we show the theoretical distributions. We note first that the empirical distributions for $A = 0$ agree very well with the theoretical predictions, which serves as a validation of the method. Inspecting the main panel of Fig. 13, we notice a trend in how the PDF changes as the roughness amplitude is increased. The sharp peak *at* the maximum velocity which is present for $A = 0$ is gradually smoothed out as A increases, and another finite peak appears at $\hat{u}_x = 0$, and the distribution becomes bimodal. This can be attributed to the fact that when the roughness increases, more of the fluid is located within shielded areas, e.g. in "cavities" of the rough walls.

The spatial distributions of the spanwise component of the velocity fields are shown in the left inset of Fig. 13. Here, the distributions of $\hat{u}_y$ are sharply peaked around 0, fairly symmetric, and fall off superexponentially at higher values. The magnitude of the fluctuations in $\hat{u}_y$ increases with roughness, as seen from the increasing spread in values.
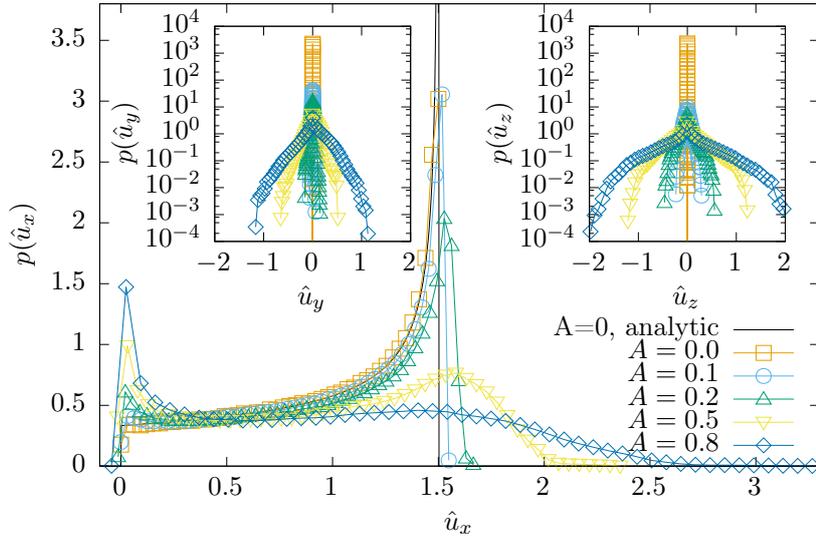
FIG. 13. Probability density functions of the velocity distributions at low Re, scaled by the mean axial velocity $\langle u_x \rangle$. Main panel: Velocity component in the streamwise direction, x. Inset, left: Velocity component in the spanwise direction, y. Inset, right: Velocity component in the vertical direction, z.

The same observation holds for the vertical velocity component $\hat{u}_z$, but the magnitude of the fluctuations are roughly twice the size of u_y, independently of the roughness.

We are now interested in how the PDF evolves as the inertia is increased. For demonstrational purposes, we hold the roughness fixed at $A = 0.8$. The data for $\hat{u}_x$ is presented in Fig. 14. The most notable feature here occurs for negative velocities. As the Reynolds number increases, a larger portion of the velocity field is negative. Since negative velocities, in the stationary frame, stems from backflow, this must be related to vortices forming in the wake of the roughness elements. This is furter justified by the fact that at the lowest Reynolds number, no backflow occurs, since vortices cannot exist at Re $\to 0$ (in the absence of singularities at the boundary, see e.g. [91]).

The height of the first peak seems to decrease with increasing Re. The location of the second peak does not seem to vary with Re in a monotonous manner. This is possibly due to the fact that $\langle u_x \rangle$, with which the fields are scaled, depends on the amount of fluid where $u_x < 0$.

In the left inset of Fig. 14, the distributions of the spanwise velocity component $\hat{u}_y$ are shown. The same trend is observed as for the distributions of negative $\hat{u}_x$; higher inertia

28
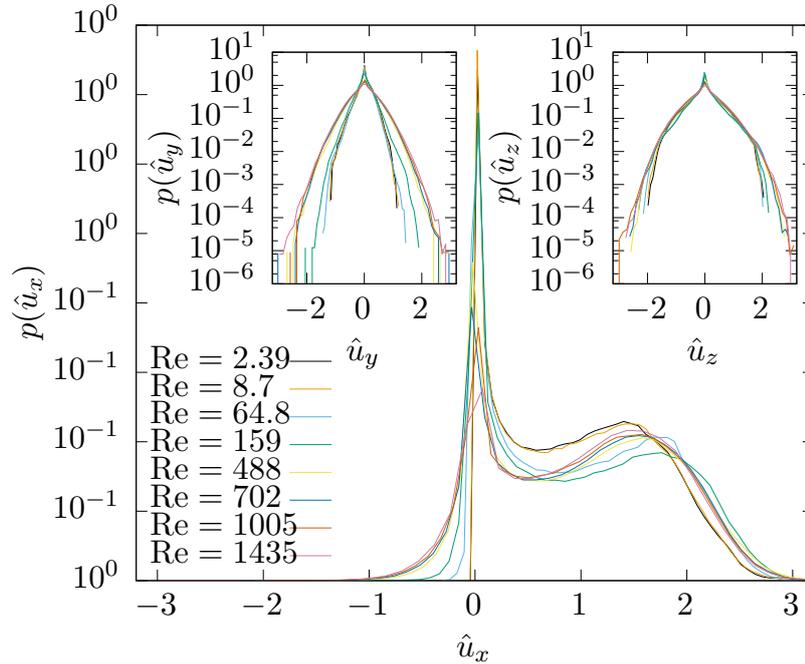
FIG. 14.   Probability density functions of velocity at a constant roughness amplitude $A = 0.8$. Main panel: velocity component along the streamwise direction, x. Left inset: velocity component in the spanwise direction, y. Right inset: velocity component in the vertical direction, z.

leads to higher spatial fluctuations (even relative to the mean flow). This effect is not present for the vertical component, shown in the right inset of Fig. 14. This indicates that the spatial fluctuations in this velocity component are imposed in essence by the vertical spatial fluctuations in the bounding surfaces.

Appendix C: Correlation functions

Here we present correlation functions in Fourier space, i.e. the power spectra of some of the involved fields.

It can be seen in Fig. 3 that a length scale typical of the shielding area emerges as the roughness amplitude is increased. This is quantified in Fig. 15, where the power spectrum of d_{eff} is plotted (along x and y). Here, cross-over from one exponent to another is seen to takes place. (For low roughness amplitudes, when no shielding takes place, one would expect that d_{eff} (and its scaling) is related to $\boldsymbol{\nabla} z$.)

In Fig. 16, we plot the power spectra of the depth-and-time averaged velocity components,
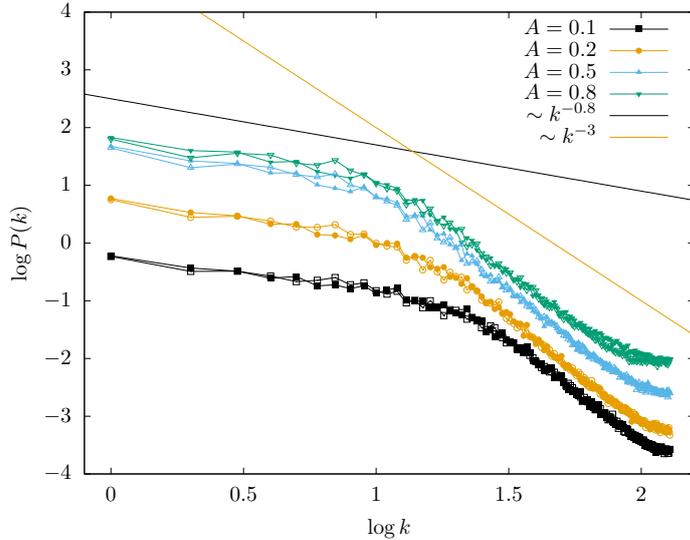
FIG. 15.   Power spectrum of the effective aperture fields d_{eff}. Closed symbols: along the x direction ($k = k_x$). Open symbols: along the y direction ($k = k_y$). The scalings in solid lines are meant as guides to the eye.

both for the low and the high Reynolds number cases. We first discuss the former. From the figure we see that at low roughness, the power spectra for u_x and u_y scale as the confining surfaces themselves, while at higher roughness, they scale as the effective aperture. We can interpret this in the sense that, as the roughness increases, the spatial fluctuations of the velocity field goes from being controlled by the surface undulations (of small amplitude), cf. Fig. 1, to being controlled by the effective aperture (i.e. angular effects), cf. Fig. 15. With regards to u_z, the situation is more involved. The latter is also the case for the high Re simulations.

[1] F. Plouraboué, P. Kurowski, J.-P. Hulin, S. Roux, and J. Schmittbuhl, Phys. Rev. E **51**, 1675 (1995).

[2] J. Bear, C.-F. Tsang, and G. De Marsily, *Flow and contaminant transport in fractured rock* (Academic Press, 1993).

[3] M. Sahimi, Rev. Mod. Phys. **65**, 1393 (1993).

[4] Y. Méheust and J. Schmittbuhl, Pure. Appl. Geophys. **160**, 1023 (2003).
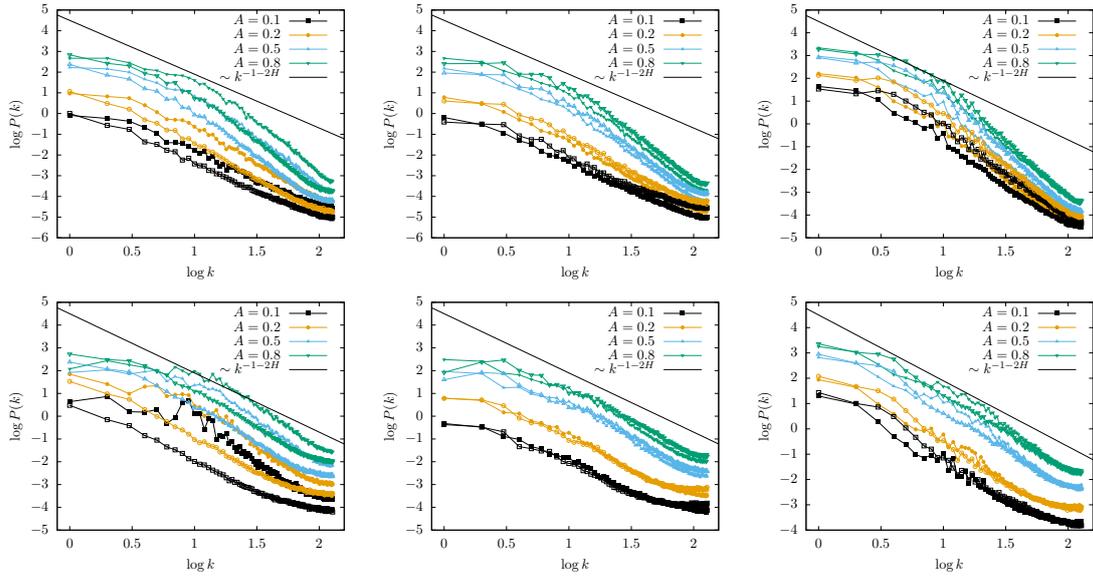
FIG. 16. Power spectrum along the x-direction (closed symbols) and along the y-direction of the three components of the depth-and-time averaged velocity field. Top row: low Re, corresponding to Fig. 6. Bottom row: high Re, corresponding to Fig. 7. Columns, left to right: u_x, u_y, u_z.

[5] I. Berre, F. Doster, and E. Keilegavlen, "Flow in fractured porous media: A review of conceptual models and discretization approaches," (2018), arXiv:1805.05701.

[6] R. W. Zimmerman and I.-W. Yeo, in *Dynamics of fluids in fractured rock* (American Geophysical Union, 2013) pp. 213–224.

[7] E. Dontsov, J. Fluid Mech. **797**, R2 (2016).

[8] V. Mourzenko, J.-F. Thovert, and P. Adler, Transp. Porous Media **45**, 89 (2001).

[9] G. O. Brown, in *Environmental and Water Resources History* (American Society of Civil Engineers, 2003) pp. 34–43.

[10] L. Talon, H. Auradou, and A. Hansen, Water Resour. Res. **46**, W07601 (2010).

[11] H. Auradou, G. Drazer, J.-P. Hulin, and J. Koplik, Water Resour. Res. **41**, W09423 (2005).

[12] H. Darcy, *Les fontaines publiques de la ville de Dijon* (Victor Dalmont, Paris, 1856).

[13] D. Lasseux, A. A. Abbasian Arani, and A. Ahmadi, Phys. Fluids **23**, 073103 (2011).

[14] O. Reynolds, Philos. Trans. R. Soc. **174**, 935 (1883).

[15] H.-Y. Shih, T.-L. Hsieh, and N. Goldenfeld, Nat. Phys. **12**, 245 (2015).

[16] K. Avila, D. Moxey, A. de Lozar, M. Avila, D. Barkley, and B. Hof, Science **333**, 192 (2011).

[17] D. Barkley, B. Song, V. Mukund, G. Lemoult, M. Avila, and B. Hof, Nature **526**, 550 (2015).

[18] D. Barkley, J. Fluid Mech. **803**, P1 (2016).

[19] V. Mukund and B. Hof, J. Fluid Mech. **839**, 76 (2018).

[20] J. Nikuradse, in *Forschungsheft auf dem Gebiete des Ingenieurwesens*, Vol. 361 (VDI-Verlag, 1933).

[21] N. Goldenfeld, Phys. Rev. Lett. **96**, 044503 (2006).

[22] N. Goldenfeld and H.-Y. Shih, J. Stat. Phys. **167**, 575 (2017).

[23] N. Guttenberg and N. Goldenfeld, Phys. Rev. E **79**, 065306 (2009).

[24] Y. Pomeau, Physica D **23**, 3 (1986).

[25] H. Hinrichsen, Adv. Phys. **49**, 815 (2000).

[26] P. Manneville, Eur. J. Mech. B Fluids **49**, 345 (2015).

[27] P. Manneville, Mechanical Engineering Reviews **3**, 15 (2016).

[28] G. Lemoult, H.-Y. Shih, G. Linga, J. Mathiesen, B. Hof, and N. Goldenfeld, "Statistical mechanics of puff-splitting in the transition to pipe turbulence," (2018), in preparation.

[29] G. Lemoult, L. Shi, K. Avila, S. V. Jalikop, M. Avila, and B. Hof, Nat. Phys. **12**, 254 (2016).

[30] M. Chantry, L. S. Tuckerman, and D. Barkley, J. Fluid Mech. **824**, R1 (2017).

[31] M. Sano and K. Tamai, Nat. Phys. **12**, 249 (2016).

[32] E. Bouchaud, J. Phys. Condens. Matter **9**, 4319 (1997).

[33] J. Feder, *Fractals* (Springer, 2013).

[34] A.-L. Barabási and H. E. Stanley, *Fractal concepts in surface growth* (Cambridge University Press, 1995).

[35] L. Ponson, H. Auradou, M. Pessel, V. Lazarus, and J.-P. Hulin, Phys. Rev. E **76**, 036108 (2007).

[36] D. Bonamy, L. Ponson, S. Prades, E. Bouchaud, and C. Guillot, Phys. Rev. Lett. **97**, 135504 (2006).

[37] A. Neuville, R. Toussaint, and J. Schmittbuhl, Phys. Rev. E **82**, 036317 (2010).

[38] S. R. Brown, J. Geophys. Res. Solid Earth **92**, 1337 (1987).

[39] Y. Méheust and J. Schmittbuhl, Geophys. Res. Lett. **27**, 2989 (2000).

[40] Y. Méheust and J. Schmittbuhl, J. Geophys. Res. Solid Earth **106**, 2089 (2001).

[41] R. Gutfraind and A. Hansen, Transp. Porous Media **18**, 131 (1995).

[42] X. Zhang, M. A. Knackstedt, and M. Sahimi, Physica A **233**, 835 (1996).

[43] G. Drazer and J. Koplik, Phys. Rev. E **62**, 8076 (2000).

[44] G. Drazer and J. Koplik, Phys. Rev. E **66**, 026303 (2002).

[45] D. J. Brush and N. R. Thomson, Water Resour. Res. **39**, SBH (2003).

[46] T. S. Lo and J. Koplik, Phys. Fluids **24**, 053303 (2012).

[47] T. S. Lo and J. Koplik, Phys. Rev. E **89**, 023010 (2014).

[48] E. Skjetne, A. Hansen, and J. Gudmundsson, J. Fluid Mech. **383**, 1 (1999).

[49] D. Edwards, M. Shapiro, P. Bar-Yoseph, and M. Shapira, Phys. Fluids A **2**, 45 (1990).

[50] J. Andrade Jr, M. Almeida, J. Mendes Filho, S. Havlin, B. Suki, and H. Stanley, Phys. Rev. Lett. **79**, 3901 (1997).

[51] S. Rojas and J. Koplik, Phys. Rev. E **58**, 4776 (1998).

[52] J. Andrade Jr, U. Costa, M. Almeida, H. Makse, and H. Stanley, Phys. Rev. Lett. **82**, 5249 (1999).

[53] R. J. Hill, D. L. Koch, and A. J. Ladd, J. Fluid Mech. **448**, 213 (2001).

[54] R. J. Hill, D. L. Koch, and A. J. Ladd, J. Fluid Mech. **448**, 243 (2001).

[55] M. Fourar, G. Radilla, R. Lenormand, and C. Moyne, Adv. Water Resour. **27**, 669 (2004).

[56] C. Mei and J.-L. Auriault, J. Fluid Mech. **222**, 647 (1991).

[57] D. Lo Jacono, F. Plouraboué, and A. Bergeon, Phys. Fluids **17**, 063602 (2005).

[58] P. H. Forchheimer, Zeitz. Ver. Duetch Ing. **45**, 1782 (1901).

[59] L. Zou, L. Jing, and V. Cvetkovic, Int. J. Rock Mech. Min. Sci. **75**, 102 (2015).

[60] L. Zou, L. Jing, and V. Cvetkovic, Int. J. Rock Mech. Min. Sci. **97**, 33 (2017).

[61] M. Wang, Y.-F. Chen, G.-W. Ma, J.-Q. Zhou, and C.-B. Zhou, Adv. Water Resour. **96**, 373 (2016).

[62] S. Briggs, B. W. Karney, and B. E. Sleep, J. Rock Mech. Geotechnical Eng. **9**, 105 (2017).

[63] J. Jiménez, Annu. Rev. Fluid Mech. **36**, 173 (2004).

[64] T. Ishida, G. Brethouwer, Y. Duguet, and T. Tsukahara, Phys. Rev. Fluids **2**, 073901 (2017).

[65] X. Zhu, R. A. Verschoof, D. Bakhuis, S. G. Huisman, R. Verzicco, C. Sun, and D. Lohse, Nat. Phys. **14**, 417 (2018).

[66] E. Bouchaud, G. Lapasset, and J. Planes, Europhys. Lett. **13**, 73 (1990).

[67] R. F. Voss, in *Fundamental algorithms for computer graphics* (Springer, 1985) pp. 805–835.

[68] A. Klöckner, "Meshpy," `https://mathema.tician.de/software/meshpy/` (2018).

[69] J. R. Shewchuk, in *Applied Computational Geometry: Towards Geometric Engineering*, Lecture Notes in Computer Science, Vol. 1148, edited by M. C. Lin and D. Manocha (Springer-

Verlag, 1996) pp. 203–222.

[70] H. Si, ACM Trans. Math. Softw. **41**, 11:1 (2015).

[71] M. Mortensen and K. Valen-Sendstad, Comput. Phys. Commun. **188**, 177 (2015).

[72] R. D. Moser, J. Kim, and N. N. Mansour, Phys. Fluids **11**, 943 (1999).

[73] A. Logg, K.-A. Mardal, and G. Wells, *Automated solution of differential equations by the finite element method: The FEniCS book*, Vol. 84 (Springer Science & Business Media, 2012).

[74] A. Logg, G. N. Wells, and J. Hake, in *Automated Solution of Differential Equations by the Finite Element Method* (Springer, 2012) pp. 173–225.

[75] S. Balay, S. Abhyankar, M. F. Adams, J. Brown, P. Brune, K. Buschelman, L. Dalcin, V. Eijkhout, W. D. Gropp, D. Kaushik, M. G. Knepley, D. A. May, L. C. McInnes, K. Rupp, B. F. Smith, S. Zampini, H. Zhang, and H. Zhang, "PETSc web page," `http://www.mcs.anl.gov/petsc` (2017).

[76] H. Jasak, A. Jemcov, Z. Tukovic, *et al.*, in *International workshop on coupled methods in numerical dynamics*, Vol. 1000 (IUC Dubrovnik, Croatia, 2007) pp. 1–20.

[77] B. Berkowitz, Adv. Water Resour. **25**, 861 (2002).

[78] V. V. Mourzenko, J.-F. Thovert, and P. M. Adler, J. Phys. II **5**, 465 (1995).

[79] A. Duda, Z. Koza, and M. Matyka, Phys. Rev. E **84**, 036319 (2011).

[80] It is perhaps more common to define the Reynolds number, Re, based on the channel half-width and the maximum velocity of the equivalent laminar PPF flow profile (see [31, 83]), $\mathrm{Re}_h = u_{\max}W/(2\nu)$. There is no simple relation between the maximum and mean velocity in rough boundary flows, which makes Eq. (7) a more practical definition. In unidirectional PPF (laminar or turbulent), $\mathrm{Re}_h = \frac{3}{4}\mathrm{Re}$.

[81] J. L. Weisbach, *Lehrbuch der Ingenieur-und Maschinen-Mechanik: Theoretische Mechanik*, Vol. 1 (Druck und Verlag von Friedrich Vieweg und Sohn, 1845).

[82] H. Darcy, *Recherches expérimentales relatives au mouvement de l'eau dans les tuyaux*, Vol. 1 (Mallet-Bachelier, 1857).

[83] X. Xiong, J. Tao, S. Chen, and L. Brandt, Phys. Fluids **27**, 041702 (2015).

[84] L. F. Moody, Trans. ASME **66**, 671 (1944).

[85] A. Strickler, *Beiträge zur Frage der Geschwindigkeitsformel und der Rauhigkeitszahlen für Ströme, Kanäle und geschlossene Leitungen* (Mitteilungen des Amtes für Wasserwirtschaft, 1923).

[86] In particular, the relation is better apprimated by an exponent higher than 2, which is seen by plotting $f_{D,\infty}$ versus A.

[87] Note that the definition (17) is similar to the common definition of the Reynolds number in homogeneous isotropic turbulence.

[88] M. Thakkar, A. Busse, and N. Sandham, J. Fluid Mech. **837** (2018), 10.1017/jfm.2017.873.

[89] A. Busse and N. D. Sandham, J. Fluid Mech. **712**, 169 (2012).

[90] M. Matyka, J. Gołembiewski, and Z. Koza, Phys. Rev. E **93**, 013110 (2016).

[91] H. K. Moffatt, Proc. Natl. Acad. Sci. **111**, 3663 (2014).

Electrohydrodynamic channeling effects in narrow fractures and pores

Asger Bolet, Gaute Linga, and Joachim Mathiesen

Physical Review E **97**, 043114 (2018)

Electrohydrodynamic channeling effects in narrow fractures and pores

Asger Bolet, Gaute Linga, and Joachim Mathiesen*

Niels Bohr Institute, University of Copenhagen, Blegdamsvej 17, DK-2400 Copenhagen, Denmark

In low-permeability rock, fluid and mineral transport occur in pores and fracture apertures at the scale of micrometers and below. At this scale, the presence of surface charge, and a resultant electrical double layer, may considerably alter transport properties. However, due to the inherent nonlinearity of the governing equations, numerical and theoretical studies of the coupling between electric double layers and flow have mostly been limited to two-dimensional or axisymmetric geometries. Here, we present comprehensive three-dimensional simulations of electrohydrodynamic flow in an idealized fracture geometry consisting of a sinusoidally undulated bottom surface and a flat top surface. We investigate the effects of varying the amplitude and the Debye length (relative to the fracture aperture) and quantify their impact on flow channeling. The results indicate that channeling can be significantly increased in the plane of flow. Local flow in the narrow regions can be slowed down by up to 5% compared to the same geometry without charge, for the highest amplitude considered. This indicates that electrohydrodynamics may have consequences for transport phenomena and surface growth in geophysical systems.

I. INTRODUCTION

Electric double layers (EDLs) play an important role in many chemical and physical processes, and are a controlling factor in many industrially applied microfluidic devices [1] and electrochemical cells [2]. Examples include nanofluidic devices for electrophoretic separation or the large-scale harvesting of energy by mixing fluids of different salinity ("blue energy") [3]. In biological systems, EDLs are important, e.g., for ion transport across membranes or for polymer aggregation [4–6]. In fluid-saturated low-permeability rock, the presence of an EDL can significantly alter the mineral transport and thereby inhibit or amplify transformation reactions, as demonstrated by field observations and nanopore molecular dynamics simulations [7]. Furthermore, EDLs alter the effective wetting properties of mineral surfaces (see, e.g., [8] for a study of reservoir sandstone), which could play an important role in enhanced oil recovery based on injection of low salinity fluids.

The transport of fluid and minerals in fluid-saturated porous rock often occurs in networks of narrow fractures or pores, many of which have (sub) micrometer-sized apertures. When the pore walls are charged, and the resulting EDL extends significantly into the pore fluid, it may change the bulk flow properties of single fractures and pores, and consequently of the whole network. Electrokinetic flow, however, is a highly nonlinear process, which is hard to quantitatively describe in even the most simple systems. In general, mean-field approximations are often used to model systems beyond the nanometer range [9,10]. From a number of simplifying assumptions, e.g., neglecting ion-ion correlations and non-Coulomb forces (so-called Gouy-Chapman theory), one obtains field equations, which can be used for basic theoretical considerations. Even then, only simple geometries permit analytical solutions, such

as cylindrical capillaries [11]. In equilibrium and when the electric field is weak, the linearized Poisson-Boltzmann equation can be applied:

$$\nabla^2 \varphi = \kappa^2 \varphi, \qquad (1)$$

where φ is the electric potential and κ^{-1} is the Debye length characterizing the extent of the EDL. However, when ion transport is coupled to fluid advection, the equilibrium assumption generally breaks down and other means must be pursued. Further, numerical simulations can be challenging, and have in general been limited to simple geometries such as finite-length symmetric channels, e.g., in studies of transient streaming potentials in single-phase flow [12,13] or in studies of electroconvection near permselective membranes [14,15].

Here, we consider electrokinetic flow in a model porous material or fracture by solving numerically the Stokes-Poisson-Nernst-Planck (SPNP) equations. In particular, we quantify how the permeability changes as the extent of the EDL compared to channel size is varied, and we also describe how the EDL can switch the channeling of the flow in our system from regions of small aperture to regions of larger aperture. The paper is organized as follows. In Sec. II, we present the model setup, the governing equations, and their dimensionless form; in Sec. III we present the simulation method and our numerical scheme; and in Sec. IV we present the results of the simulations, including validation, and effects of varying amplitude and relative Debye length. In Sec. V we discuss the technical aspects of our work and finally the conclusions and future directions follow in Sec. VI.

II. MODEL

A. Flow geometry and problem setup

We consider a model system consisting of an ionic solution near an undulated charged wall, as shown schematically in Fig. 1. Pressure-driven flow is imposed along the z direction.

---

*mathies@nbi.dk
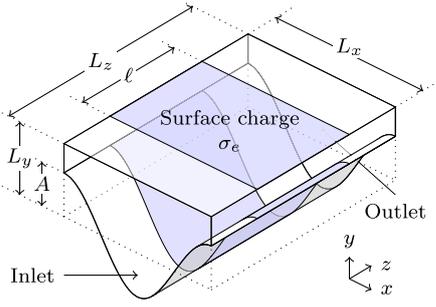
FIG. 1. Schematic setup of the model system. The inlet, charged-surface, and outlet areas (see text) are indicated. The x direction is periodic. Note that the dimensions are not to scale.

In the transverse direction, i.e., along the x axis, the system is considered to be periodic. In the y direction the domain is bounded by two surfaces, where the bottom surface is undulated and the top surface is flat. Along the flow direction, the domain is decomposed into three regions: an inlet region with no surface charge, a region of uniform surface charge, and an outlet region again with no surface charge. The inlet and outlet regions must be long enough in the flow direction so as to properly account for the decay of the EDL, as discussed in more detail in Sec. IV.

In our three-dimensional (3D) fluid slab (Fig. 1), the bottom surface is described by the function $y = h(x)$ and the top surface is located at $y = L_y$. In the plane perpendicular to y, our system is limited to a rectangle $(x,z) \in [0,L_x] \times [0,L_z]$. We seek to quantify how the EDL changes our flow when the translational symmetry is broken, which we here break in the x direction by a harmonic undulation,

$$h(x) = A \cos\left(\frac{2\pi x}{L_x}\right), \tag{2}$$

where A is the amplitude of the undulation.

B. Governing equations

The electrohydrodynamic problem is described by the SPNP equations, which couple three processes: fluid flow, electrostatics, and ion transport. The transport of ions is described by the Nernst-Planck equation. For ion i, the evolution of its number density, n_i, is given by

$$\frac{\partial n_i}{\partial t} = \nabla \cdot \left(-n_i \mathbf{u} + D_i \nabla n_i + \frac{D_i z_i q_e}{k_B T} n_i \nabla \varphi\right). \tag{3}$$

Here, $\mathbf{u}$ is the fluid velocity, D_i and z_i are, respectively, the diffusion constant and valency for ion i, q_e is the electron charge, k_B is Boltzmann's constant, T is the temperature, and φ is the electric potential.

In the limit of negligible inertia (i.e., Reynolds number Re $\ll 1$), assuming the fluid to be incompressible, fluid flow is governed by the Stokes equations:

$$\rho \frac{\partial \mathbf{u}}{\partial t} = -\nabla P + \mu \nabla^2 \mathbf{u} - \rho_e \nabla \varphi, \tag{4}$$

$$\nabla \cdot \mathbf{u} = 0. \tag{5}$$

Here, ρ is the density of the fluid, P is the pressure, μ is the dynamic viscosity, and the charge density ρ_e is given by

$$\rho_e = q_e \sum_{i=1}^{N} z_i n_i, \tag{6}$$

where N is the number of ion species in the fluid. Finally, the electrostatic problem is given by the Poisson equation:

$$\nabla^2 \varphi = -\frac{\rho_e}{\epsilon_r \epsilon_0}, \tag{7}$$

where ϵ_0 is the vacuum permittivity and ϵ_r is the relative permittivity. Together, Eqs. (3)–(7) constitute the time-dependent SPNP problem.

Boundary conditions

With regard to the velocity field, the Stokes equation is solved with a no-slip condition at the top and bottom walls of the undulated channel. In the z direction the flow is assumed to be periodic, such that the velocity field at the inlet matches that at the outlet. We drive the flow by introducing a body force along the z direction, which is equivalent to having an average pressure gradient, which we denote by $\partial P/\partial z$. In addition, we find that the resulting pressure at the inlet-outlet plane is approximately constant, and hence the solution is equivalent to having a constant-pressure boundary condition [16].

The Nernst-Planck equation is solved with a no-flux condition on the top and bottom channel walls, and at the inlet and outlet, we prescribe the number density n^∞ of the ions. Finally, for the Poisson equation, a surface charge boundary condition is specified:

$$\nabla \varphi \cdot \hat{\mathbf{n}} = \frac{\sigma_e(\mathbf{x})}{\epsilon_r \epsilon_0}, \tag{8}$$

where $\hat{\mathbf{n}}$ is the surface normal pointing out of the domain and σ_e is the surface charge. The prescribed surface charge is adjusted to keep a constant surface potential, through the Grahame equation for a symmetric monovalent solution [17]:

$$\sigma_e = \sqrt{8 k_B T n^\infty \epsilon_r \epsilon_0} \sinh\left(\frac{q_e \zeta}{2 k_B T}\right). \tag{9}$$

In deriving this equation, the ion-number density n^∞ is considered to be set infinitely far away from the charged wall, and ζ is the surface potential when also the electric potential is set to zero at infinity. Hence, the inlet is grounded, i.e., $\varphi = 0$, and at the outlet, a zero normal electric flux density is imposed, i.e., $\hat{\mathbf{n}} \cdot \nabla \varphi = 0$. As indicated above, all fields are taken to be periodic along the x direction.

C. Dimensionless form

For both numerical and analytical purposes, it is convenient to express the model in terms of dimensionless variables. We further limit ourselves to a system with a symmetric monovalent ion solution, where both ions have the same diffusion constant. Using the scaling reported in Table I [18], we obtain the following form of the Nernst-Planck equation (3):

$$\frac{\partial \tilde{n}_\pm}{\partial \tilde{t}} = \tilde{\nabla} \cdot (-\mathrm{Pe}\,\tilde{n}_\pm \tilde{\mathbf{u}} + \tilde{\nabla} \tilde{n}_\pm \pm \tilde{n}_\pm \tilde{\nabla} \tilde{\varphi}), \tag{10}$$

TABLE I. Physical variables, their symbols, and the normalization used in deriving dimensionless quantities, based on Ref. [18]. Note that n^∞ is chosen to be one of the ion-number densities at the inlet.

Variable	Symbol	Normalization
Ion-number density	n_i	n^∞
Electric potential	φ	$V_T = \frac{k_\mathrm{B} T}{z q_e}$
Length	x	R
Velocity	$\mathbf{u}$	$U_0 = \frac{\epsilon_0 \epsilon_r V_T^2}{\mu R}$
Time	t	$\frac{R^2}{D}$
Pressure	P	$\frac{\mu U_0}{R}$

where a tilde denotes that it is a dimensionless field, and the Péclet number is defined as $\mathrm{Pe} = R U_0 / D$. Here R is a typical length scale. The Stokes equations (4) and (5) become

$$\frac{1}{\mathrm{Sc}} \frac{\partial \tilde{\mathbf{u}}}{\partial \tilde{t}} = -\tilde{\boldsymbol{\nabla}} \tilde{P} + \tilde{\boldsymbol{\nabla}}^2 \tilde{\mathbf{u}} - \frac{R^2 \kappa^2}{2} \tilde{\rho}_e \tilde{\boldsymbol{\nabla}} \tilde{\varphi}, \qquad (11)$$

$$\tilde{\boldsymbol{\nabla}} \cdot \tilde{\mathbf{u}} = 0, \qquad (12)$$

where the Schmidt number is defined as $\mathrm{Sc} = \mu/(\rho D)$, the Debye length is defined as

$$\kappa^{-1} = \sqrt{\frac{k_\mathrm{B} T \epsilon_r \epsilon_0}{2 z^2 q_e^2 n^\infty}},$$

and the dimensionless form for the charge density is

$$\tilde{\rho}_e = \tilde{n}_+ - \tilde{n}_-. \qquad (13)$$

Finally, the Poisson equation (7) becomes

$$\tilde{\boldsymbol{\nabla}}^2 \tilde{\varphi} = -\frac{R^2 \kappa^2}{2} \tilde{\rho}_e. \qquad (14)$$

D. Time-independent form of the dimensionless equations

In this work, we are mainly interested in the steady-state behavior and the properties of electrohydrodynamic flow in narrow channels. We therefore seek the time-asymptotic solutions to the coupled equations (10), (11), (12), and (14). The time-independent set of equations is given by

$$\tilde{\boldsymbol{\nabla}} \cdot (-\mathrm{Pe}\, \tilde{n}_\pm \tilde{\mathbf{u}} + \tilde{\boldsymbol{\nabla}} \tilde{n}_\pm \pm \tilde{n}_\pm \tilde{\boldsymbol{\nabla}} \tilde{\varphi}) = 0, \qquad (15a)$$

$$-\tilde{\boldsymbol{\nabla}} \tilde{P} + \tilde{\boldsymbol{\nabla}}^2 \tilde{\mathbf{u}} - \frac{R^2 \kappa^2}{2} \tilde{\rho}_e \tilde{\boldsymbol{\nabla}} \tilde{\varphi} = 0, \quad \tilde{\boldsymbol{\nabla}} \cdot \tilde{\mathbf{u}} = 0, \quad (15b)$$

$$\tilde{\boldsymbol{\nabla}}^2 \tilde{\varphi} = -\frac{R^2 \kappa^2}{2} \tilde{\rho}_e. \qquad (15c)$$

III. SIMULATION METHOD

A. Numerical scheme

We solve the time-independent nonlinear equations (15) by a splitting scheme, where the flow equations (15b) are solved in one step, while the other equations, the nonlinear Poisson-Nernst-Planck (PNP) problem [Eqs. (15a) and (15c)], are solved in a second step using a Newton method. The final solution is achieved by iteratively alternating between the two steps using the algorithm outlined in Ref. [19]. The splitting

Algorithm 1. Hybrid solver for the SPNP system (adapted from Ref. [19]).

1. Solve Stokes equations (15b) to obtain $(\mathbf{u}, P)$.
2. Solve the linearized Poisson-Boltzmann equation (1) to get an initial guess for (φ, n_+, n_-).
3. Solve one Newton step [Eq. (A3)] in the PNP problem [Eqs. (15a) and (15c)] for $(\delta\varphi, \delta n_+, \delta n_-)$.
4. Update $(\varphi, n_+, n_-) \leftarrow (\varphi + \delta\varphi, n_+ + \delta n_+, n_- + \delta n_-)$.
5. Store $(\mathbf{u}_\mathrm{old}, P_\mathrm{old}) \leftarrow (\mathbf{u}, P)$.
6. Solve Stokes equations (15b) to get $(\mathbf{u}, P)$.
7. Find $(\delta\mathbf{u}, \delta P) \leftarrow (\mathbf{u}_\mathrm{old} - \mathbf{u}, P_\mathrm{old} - P)$.
8. Compute Error $:= \frac{1}{2}(\frac{\|(\delta\varphi, \delta n_+, \delta n_-)\|}{\|(\varphi, n_+, n_-)\|} + \frac{\|(\delta\mathbf{u}, \delta P)\|}{\|(\mathbf{u}, P)\|})$.
9. If Error $< \tau$, stop.
10. Else, go to step 3 for another iteration.

scheme results in a significant reduction in computational cost in comparison to monolithic solvers and further reduces the size of the system matrix. Finally, the scheme permits the use of specialized solvers for the two subproblems.

The proposed scheme is well suited for physical conditions where the electric field strength is relatively weak and the solute number density is low. However, for simulations where the field strength is high, it would be necessary to solve the *nonlinear* Poisson-Boltzmann equation in step 2 of Algorithm 1. This could give a sufficiently precise initial guess to achieve convergence in the subsequent PNP solution step. See, e.g., Refs. [20,21] for algorithms suitable for this purpose.

B. Implementation

Our numerical solvers are implemented in the open-source finite element framework FEniCS [22] through the Python interface to DOLFIN [23]. The Stokes equation is solved using an iterative finite element solver with a pressure-convection-diffusion preconditioner and Taylor-Hood elements, implemented in FENAPACK [24]. In Appendix A, we derive the Newton method to solve the PNP problem. The final method for solving the fully coupled problem is given in Algorithm 1. The Newton step Eq. (A3) is solved using the generalized minimal residual method with block Jacobi and incomplete LU preconditioning. To achieve convergence it is essential to provide a good initial guess. We establish an initial guess by solving the linearized Poisson-Boltzmann equation (1) with the same boundary conditions as the PNP problem. Note that the preconditioning of this system is done in an *ad hoc* manner and might be less robust when solving systems beyond the sizes considered here. More sophisticated preconditioners such as HYPRE EUCLID, which was used by [19] for similar purposes, were found not to be robust enough for strongly interacting EDLs.

C. Mesh generation

The mesh for the test case of a channel was generated by the built-in FEniCS function RectangleMesh for two dimensions (2D) and BoxMesh for three dimensions (3D), which produces a structured triangular or tetrahedral mesh. The mesh for the undulated channel was made by combining Triangle [25], via the Python package MESHPY [26], to produce the surface mesh, and TETGEN [27] for the volumetric mesh. The combination of

TABLE II. Numerical values of parameters used in the simulations, with physical units where applicable.

Quantity	Parameter	Value	Unit
Ref. concentration	n^∞	$[6.691 - 240.8] \times 10^{20}$	No./m^3
Zeta potential[a]	ζ	-51.34×10^{-3}	V
Channel aperture[b]	a	288×10^{-9}	m
Ref. length	R	96×10^{-9}	m
Temperature	T	298	K
Diffusivity	D	1.0×10^{-9}	m^2/s
Boltzmann const.	k_B	1.38×10^{-23}	J/K
Permittivity	$\epsilon_r \epsilon_0$	8.854×10^{-23}	C/V m
Dyn. viscosity	μ	1.003×10^{-3}	Pa s
Electron charge	q_e	1.602×10^{-19}	C
Valency	z	1	
Pressure gradient	$\frac{\partial P}{\partial z}$	1.0×10^{7}	Pa/m
Error tolerance	τ	1.0×10^{-5}	

[a]Prescribed.
[b]That is, channel half-height.

the two meshing tools allows us to produce a mesh that is periodic in both x and z directions. The grid resolution δx was varied within the interval $\delta x \in [0.2, 0.5]$.

IV. RESULTS

Using the model and methods described in the preceding sections, we performed simulations of electrohydrodynamic flow in channels in two and three dimensions, with and without undulations of the bottom surface. The physical parameters used in our simulations are given in Table II, although they enter through the dimensionless quantities given in Table I. Note that we assume a numerically moderate value of the zeta potential, which is in the relevant range for geological settings [28,29]. The computations were performed on an in-house computing cluster using up to 28 CPU cores @ 3.0 GHz and 512 GB RAM.

A. Electroviscous effects in a straight channel

We first validated our numerical methods against a theoretical expression for the flow in an infinitely long channel with noninteracting EDLs. In a straight channel (i.e., plane Poiseuille flow between charged plates), the flow is expected to be modified from the plane Poiseuille result by an effective *electric viscosity* μ_e, defined through

$$\langle u \rangle = \frac{a^2}{3\mu_e} \frac{\partial P}{\partial z}. \tag{16}$$

Here, $\langle u \rangle$ is the mean velocity of the fluid, and a is the channel half-height, henceforth denoted aperture. The aperture is in physical units given by $3R$ where R can be found in Table II. This expression is directly related to the permeability, K, defined through Darcy's law by $K = \langle u \rangle \mu / (\partial P / \partial z)$. Hence, we expect $K = \frac{1}{3} a^2 \mu / \mu_e$, and thus μ_e / μ can be seen as an inverse permeability (corrected for the scaling with a). In our simulations, with the parameters given in Table II, the permeability is in the absence of electroviscous effects given by $K \simeq 28$ mDa.

In Appendix B, assuming noninteracting EDLs, we derive the following theoretical estimate of the electric viscosity:

$$\mu_e = \mu \left[1 - \frac{6\beta}{\kappa^2 a^2 F_{cc}} f(\kappa a, \beta) \left(1 - \frac{1}{\kappa a} \tanh(\kappa a) \right) \right]^{-1}, \tag{17}$$

where $\beta = \epsilon_r \epsilon_0 \zeta^2 / (\mu D)$, and ζ is the surface potential, and we have used the expressions

$$F_{cc} = \int_0^1 2 \cosh \left(\frac{q_e \zeta}{k_B T} \frac{\cosh(\kappa a X)}{\cosh(\kappa a)} \right) dX, \tag{18}$$

$$f(\kappa a, \beta) = \frac{1 - \frac{1}{\kappa a} \tanh(\kappa a)}{1 + \frac{\beta}{F_{cc}} \left[\frac{1}{\kappa a} \tanh(\kappa a) - \operatorname{sech}^2(\kappa a) \right]}. \tag{19}$$

The integral in the expression for F_{cc} is computed numerically.

The expression for the streaming potential V_{str} is given by

$$V_{str} = \frac{2\zeta}{\mu D \kappa^2 F_{cc}} f(\kappa a, \beta) \Delta P. \tag{20}$$

In the limit of small Debye length compared to the channel width, i.e., $\kappa a \to \infty$, we have that $F_{cc} = 2$ and $f(\kappa, \beta) = 1$. Equation (20) then reduces to the classical mean-field Helmholtz-Smoluchowski equation $V_{str}/\Delta P = \epsilon_r \epsilon_0 \zeta / (\mu \sigma_f)$, where we have identified the conductivity $\sigma_f = 2Dz^2 q_e^2 n^\infty / k_B T$.

We compare our simulations to the analytical prediction of μ_e by integrating the total fluid flux $Q_z(\kappa a)$ through the channel for a range of values of the ratio of aperture to Debye length, κa. Note that we vary κa indirectly, by varying n^∞. Then, we use the following relation:

$$\frac{\mu_{e,h}}{\mu} = \frac{Q_z(0)}{Q_z(\kappa a)}. \tag{21}$$

As only half of the length of the channel in our numerical simulations is charged, we denote the resulting electroviscosity by $\mu_{e,h}$. In order to obtain a value for the electric viscosity that should correspond to the theoretical one, we scale it in the following way:

$$\frac{\mu_e}{\mu} = \frac{\frac{\mu_{e,h}}{\mu} - 1}{\frac{l}{L_z}} + 1. \tag{22}$$

The value in the denominator is the ratio of the length of the charged part of the channel, l, to total length, L_z, such that in our simulations we have that $l/L_z = 0.5$. As increased dissipation is expected mainly to take place in the charged part of the channel, we have here ignored inlet and outlet effects, and the accuracy of these expressions would therefore improve for longer domains. The streaming potential is measured by

$$\frac{V_{str}}{l} = \frac{\int_{\Gamma_{outlet}} \varphi \, ds}{l \int_{\Gamma_{outlet}} ds}, \tag{23}$$

where the integral is taken over the outlet boundary of the domain, Γ_{outlet}.

We tested our numerical simulations against the analytic results using both 2D and 3D versions of our code. In addition, we tested the influence of the numerical resolution on the results. In Fig. 2(a) we present plots of the measured electric
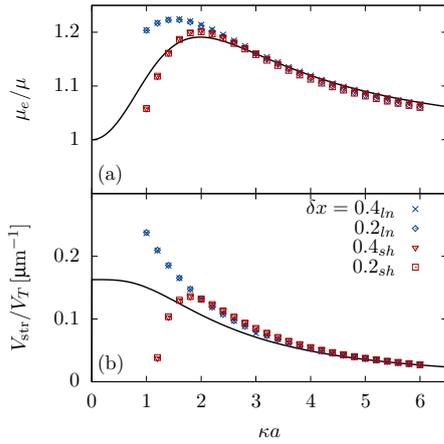
FIG. 2. Comparison of 2D simulations of two channel lengths to theoretical predictions. The blue points, where the resolution δx has a subscript ln correspond to simulations with channel length $160R$, and the red points, with a subscript sh, to simulations with channel length $40R$. Both channels have a width of $6R$. The solid lines denote the analytical results from Eqs. 17 (a) and 20 (b). In both cases the center half of the channel has a surface charge. (a) Plot of the electric viscosity as a function of κa. (b) The streaming potential in units of the thermal voltage.

viscosity and in 2(b) the streaming potential per length for 2D simulations, compared to the theoretical predictions of, respectively, Eqs. (17) and (20). For the theoretical curves, the ζ potential in Eq. (9) is not used directly. Instead we use an empirical value computed from our simulations, which here in physical units has the value $\zeta = -45.2$ mV. The quantities are plotted as a function of κa, i.e., the ratio of the channel aperture to the Debye length. We also investigate the effect of the domain length using two lengths, $L_x = 40R$ and $L_x = 160R$. With regard to the electric viscosity, shown in Fig. 2(a), it is clear that the value μ_e approaches the theoretical one for large values of κa but departs for small values of κa. This departure has different reasons for the two channel lengths. For the long channel, the departure arises because the linear Poisson-Boltzmann theory breaks down when we have strongly interacting EDLs, and for the short channel the departure is caused by surface charge which cannot be screened within the domain. The effect of strongly overlapping EDLs could be incorporated into the theoretical estimate by solving the nonlinear Poisson-Boltzmann equation numerically, or using the implicit solution found by Verwey and Overbeek [30, pp. 67] and extending the procedure in Appendix B.

In Fig. 2(b), we observe that the streaming potential V_{str} is in good agreement with the theory in the limit of large values of κa. The departure from the theoretical prediction for small values of κa appears for the same reasons as for the electric viscosity.

We further validated that our 2D steady-state solver gives the *physically* correct solution by comparing with the asymptotic solution to the full time-dependent equation system. For that purpose, we applied the independently developed time-dependent solver [31], implemented in the *Bernaise* framework [32], for flow through a circular packing with similar boundary conditions as considered in this paper. It was confirmed that the

time-dependent solver approached the steady-state solution in the large-time limit; in particular, the difference in streaming potential was less than 1% after a simulation time $T \simeq 10\tau_D$, where the Debye length based diffusive time scale is $\tau_D = \kappa^{-2}/D \simeq 5$ (see [31] or Supplemental Material [33]).

Figure 3 shows a comparison of our 3D simulations with 2D simulations in equivalent geometries, i.e., geometries translationally invariant in the transverse direction. In (a), we see that the curves for the electric viscosity coincide, meaning that the 3D simulations give comparable results to the 2D case. Likewise, we see in (b) that the streaming potentials of 2D and 3D compare well to each other. This gives a strong indication that the full 3D simulation constitutes a reliable approach.

An apparent discrepancy between the analytical and simulated results occurs when the Debye length becomes larger than the channel height. There are two reasons for this: (i) the overlapping double layers from top and bottom, and (ii) leakage of ions into the inlet and outlet zones, which leads to unphysical boundary conditions and a spurious negative streaming potential. The latter effect can be compensated by extending the inlet and outlet zones to be sufficiently long, such that to a good approximation, *both* $\tilde{n}_\pm = 1$ and $\hat{\mathbf{n}} \cdot \nabla \tilde{\varphi} = 0$ at both inlet and outlet [34].

FIG. 3. Comparison of 3D versus 2D channel flow simulations. The 2D channel is the short channel described in Fig. 2, and the 3D channel has the same size in the streamwise and vertical dimensions, while the additional horizontal dimension is periodic with length R. The analytical predictions shown as solid lines are the same as in Fig. 2. (a) Electric viscosity as a function of κa. (b) The streaming potential in units of thermal voltage as a function of κa.

B. Macroscopic effects due to an undulated surface

In order to quantify how the flow is affected by electroviscous effects in uneven channels, simulations were run in the geometry shown in Fig. 1 with an amplitude A varying from $0.5R$ to $3R$, and the other dimensions fixed to $L_x = 12R$, $L_y = 6R$, $L_z = 40R$, and $l = 20R$. From these simulations, we calculated μ_e and V_{str} as described in Sec. IV A, and the results are shown in Fig. 4. As shown in (a), the electric viscosity does not seem to be strongly affected, but it is worth noting that for increasing amplitude, a slight decrease is observed for small values of κa. The streaming potential, shown in (b), seems to be
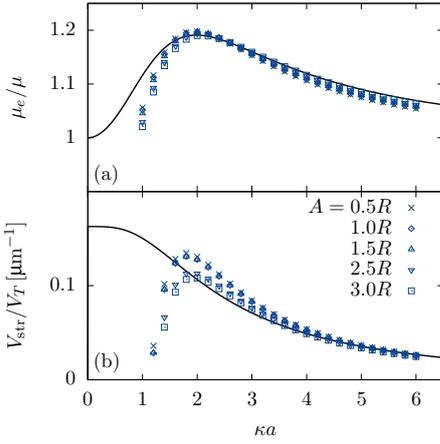
FIG. 4. Comparison of electric viscosity and streaming potential in 3D channels with varying undulation amplitude. The channels, shown schematically in Fig. 1, have dimensions given in the text, and A is given in the legend. The solid lines are theoretical predictions and the same as in Figs. 2 and 3. (a) The electric viscosity plotted as a function of κa. (b) The streaming potential in units of thermal voltage plotted as a function of κa.

more affected by the change of amplitude. This could be due to the overlap of double layers in the narrow regions, leading to a stronger nonlinear effect, but also more leaking to the boundary (i.e., a finite-size effect). However, these plots yield limited insight into the effect of any asymmetry induced by the undulation, as these quantities are averaged over the whole domain.

C. Quantification of flow channeling

In order to quantify the asymmetry induced by the electroviscous effect in the charged part of the channel, we define the following subdomains of Ω:

$$\Omega_{\text{tot}} = [0,12R] \times [-3R,6R] \times [15R,25R], \quad (24)$$

$$\Omega_y = [0,12R] \times [3R,6R] \times [15R,25R], \quad (25)$$

$$\Omega_x = [-3R,3R] \times [-3R,6R] \times [15R,25R]. \quad (26)$$

Here Ω_{tot} is a total cross-sectional subdomain of the channel, while Ω_x is the half of Ω_{tot} where the channel is narrowest along the x direction. Further, Ω_y is the top half (along the y direction) of Ω_{tot}.

Note that the domain of Ω_y has half the volume within the computational domain compared to that of Ω_{tot} for the undulated channel, as long as the amplitude is smaller or equal to $3R$. We then integrate the longitudinal component of the velocity field, u_z, in the subdomains and divide by the length in order to find the average flux through each subdomain:

$$Q_{z,i}(A,\kappa a) = \frac{1}{10R} \int_{\Omega_i} u_z \, dv, \quad (27)$$

where the index i refers to the subdomains defined in Eqs. (24)–(26).
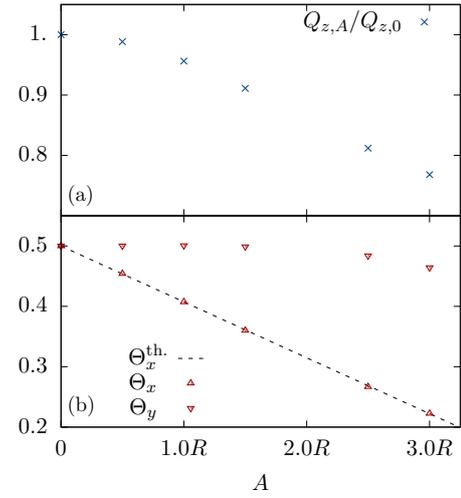
FIG. 5. Simulations in an undulated 3D channel without any electric effects included, i.e., $\kappa a = 0$. (a) Flow rate in undulated channels as a function of undulation amplitude A, relative to the flat channel $A = 0$. (b) The absolute asymmetry of the flow in the channel as a function of amplitude A. The linear dependence of Θ_x on A is in good agreement with the theoretical prediction Θ_x^{theor} derived in Appendix C.

Now, we define the absolute asymmetries Θ_x and Θ_y by

$$\Theta_i(A,\kappa a) = \frac{Q_{z,i}(A,\kappa a)}{Q_{z,\text{tot}}(A,\kappa a)}, \quad i \in \{x,y\}, \quad (28)$$

and finally the relative asymmetries θ_x and θ_y by

$$\theta_i(A,\kappa a) = \frac{\Theta_i(A,\kappa a)}{\Theta_i(A,0)}, \quad i \in \{x,y\}. \quad (29)$$

This quantity gives a measure of how the flow is re-distributed between regions of small and large aperture (θ_x) and between top and bottom (θ_y) due to a surface undulation, with amplitude A, and the effect of EDL, through κa.

It is interesting to first consider the isolated effect of an undulated geometry, i.e., flow without any electric effects, but with a variable amplitude on one of the sides. This is achieved by setting $\kappa a = 0$ in our simulations. In principle, this limiting case results in translational symmetry along the streamwise direction and thus reduces to a 2D Poisson problem (see Appendix C), but here we show results from full 3D simulations. In Fig. 5, both the relative flow rate, $Q(A,0)/Q(0,0)$, and the absolute asymmetries, $\Theta_i(A,0)$, are plotted as a function of amplitude A. In (a), we see that the total flow rate is significantly reduced. In (b), the absolute asymmetry along the vertical direction displays a rather weak dependence on the amplitude (it becomes pronounced only at $A = 2.5R$), while the absolute asymmetry along the x direction seems to depend linearly on the amplitude. This is also in agreement with the theoretical prediction based on a first-order expansion in the undulation amplitude A obtained in Appendix C.

The plots presented in Fig. 5(b), without electric effects, serve as a reference for the simulations with electrohydrodynamic effects, i.e., the relative asymmetries θ_i for $\kappa a > 0$. Plots of the relative asymmetries $\theta_x(A,\kappa a)$ and $\theta_y(A,\kappa a)$ are
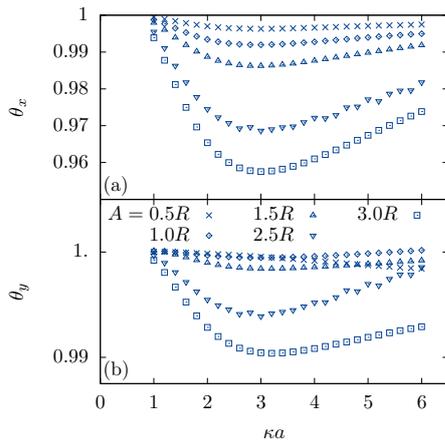
FIG. 6. Relative asymmetries are plotted as a function of κa. (a) The relative asymmetry in the plane of flow, θ_x. (b) The relative asymmetry normal to the plane of flow, θ_y.

FIG. 7. The flow field at $\kappa a = 3$ divided by the flow field for the flow without any electric effects, probed as described in the text. (a) to (d) show increasing amplitude.

shown in Fig. 6. Inspecting θ_x in Fig. 6(a), we see that there is an increased damping of the flow in the narrow part of the channel, which means that the electric effects amplify the channeling beyond what is caused by the amplitude alone [shown in Fig. 5(b)]. The effect in the vertical direction is weaker, as shown in Fig. 6(b), and only becomes visible when the amplitude is large enough to form a narrow region in the bottom of the channel. Even then, the effect is less than 1%. It should be noted that in our simulations only half of the channel is charged, and if a larger fraction of the wall was charged, the effect would presumably be stronger. An open question is whether this effect is linear in the length of the charged domain, as is the case with the electric viscosity [see Eq. (22)].

D. Local effects

In order to get a detailed understanding of the increased asymmetry and channeling of the flow in the undulated channel, we visualize the local ratio between the flow field with and without electric effects. To this end, we measured u_z in 40 cross sections evenly spaced in the interval $z \in [12.5R, 27.5R]$, which is inside the charged region of the channel. This was done for both the uncharged realization and the one corresponding to $\kappa a = 3.0$. The 40 cross sections were averaged in order to cancel out noise, and we denote the resulting z-averaged fields by $\langle u_z \rangle_z(\kappa a)$. However, near the walls there are still some artifacts present (see Fig. 7 below) due to a structured surface mesh and an amplification of errors as the reference solution was near 0 here—a consequence of the no-slip condition. In Fig. 7, we plot the ratio between the charged and noncharged flow fields, $\langle u_z \rangle_z(\kappa a)/\langle u_z \rangle_z(0)$. The panels in the figure show increasing amplitudes A for a fixed $\kappa a = 3$. In panels (a) and (b), we see that the main difference is in the boundary layer near the walls and there is only a minor increase in channeling. For sufficiently high amplitudes, shown in panels (c) and (d), it is clear that the flow is channeled to the region where the amplitude is largest. The local change in the flow rate is of the order of $10\% - 15\%$ in the narrow regions, particularly visible near the walls.
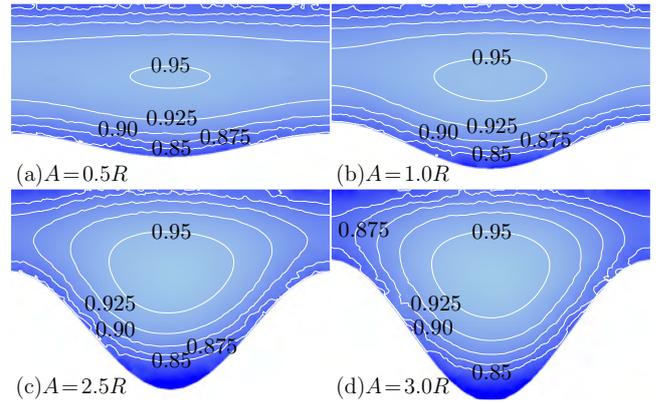
V. TECHNICAL DISCUSSION

In Figs. 2–4 and 6, we have plotted the physical quantities as a function of the ratio, κa, of the channel aperture and the Debye length. We note that there is a subtlety when varying κa, either through the Debye length κ^{-1} or by tuning the channel aperture a. This is due to the quadratic dependence on κ in Eq. (20). In this work, we have held a fixed while varying κ, indirectly by setting the reference concentration n^∞. There is also another effect at play when approaching low concentration in finite channels, namely, that the equilibrium approach of the Poisson-Boltzmann equation is less accurate as the advection term becomes more dominant in the Nernst-Planck equation. This effect could in part be responsible for the increase in the streaming potential, which was observed from Fig. 2 for the long tube. Mansouri *et al.* [12] avoided such complications by instead varying a when addressing the dependence of the streaming potential on κa for axially symmetric capillaries.

In this work, we have considered dilute solutions and moderate electric fields. When the ion concentrations approach that of, e.g., sea water, we would have to include the effect of dispersion forces near the charged walls, high-density corrections to the Nernst-lanck chemical potential, and account for other strongly coupled phenomena [35]. Simulations taking into account such size and correlation effects have, for example, been carried out in biological ion channels by Liu and Eisenberg [21]. In the context of strong electric fields, standard finite element methods have been shown to fail due to the violation of the Scharfetter-Gummel stability condition [20,21]. Methods employed, e.g., in simulating semiconductors [20], could be augmented with an advective term and thereby permit simulations of our system in the regimes of high ion-number densities and/or strong electric field.

As pointed out in Sec. IV, there is a quite pronounced effect of having a short inlet and outlet. This was, however, necessary in order to run full simulations in 3D since the PNP problem becomes increasingly hard to solve numerically when the system size increases—a hallmark of ill-preconditioned matrices for Krylov-subspace solvers. Therefore, in order to handle larger systems, we would have to either (i) rely on a direct solver implying a massive increase in the need for

computational resources, (ii) find a better preconditioner, or (iii) discard the Newton method approach in favor of other methods [21]. This could allow for a deeper investigation into the regime where the EDLs overlap and the linear Poisson-Boltzmann theory breaks down.

VI. CONCLUSION

Flow in highly irregular geometries with charged surfaces is commonplace in many geological and industrial settings. In some situations, even a moderate change of the local flow distribution can have an impact on the precipitation and chemical reactions [36]. We have in this paper considered the electrohydrodynamic effects on flow by numerically solving the Stokes-Poisson-Nernst-Planck equation in narrow undulated channels. The undulated channel geometry serves as a simplified model of microscale fractures, which often mediate the large-scale transport, e.g., in porous rock. By varying the amplitude of the channel undulation and the Debye length, we have analyzed the macroscopic flow changes in terms of the streaming potential and electric viscosity. Further, we have observed an enhanced channeling of the flow. In particular, we observe for the larger undulation amplitudes up to 5% flux reductions, relative to a system without surface charge. The local flow may vary as much as 10%. In comparison to pure hydrodynamic channeling, our results indicate that ridges may be even more prone to precipitation than valleys, leading to a positive feedback with enhanced channeling effects.

Our results offer insight into electrohydrodynamic flow in realistic pore and fracture geometries. Further studies would be of interest, primarily in larger and more complex samples, to get an even deeper understanding of electrohydrodynamic effects in geological settings. Further, it would be interesting to study the precipitation and/or dissolution dynamics in the presence of surface charge. Finally, electrohydrodynamics might be important in two-phase flow, where the local forces could alter the wetting properties and hence control the macroscopic fluid flow.

ACKNOWLEDGMENTS

APPENDIX A: NEWTON METHOD FOR THE NERNST-PLANCK-POISSON PROBLEM

The Nernst-Planck-Poisson problem takes the following nonlinear weak form:

$$
\begin{aligned}
0 = \int_\Omega & \psi \nabla^2 \varphi + \psi \frac{R^2 \kappa^2}{2}(n_+ - n_-) - c_+ \mathrm{Pe} \nabla \cdot (\mathbf{u} n_+) \\
& + c_+ \nabla^2 n_+ + c_+ \nabla \cdot (n_+ \nabla \varphi) - c_- \mathrm{Pe} \nabla \cdot (\mathbf{u} n_-) \\
& + c_- \nabla^2 n_- - c_- \nabla \cdot (n_- \nabla \varphi) dv,
\end{aligned} \tag{A1}
$$

where ψ is the test function for the electric potential and c_+, c_- are the test functions for the cation and anion number densities, respectively. We can develop a Newton method for solving the equation by viewing the weak form in Eq. (A1) as a functional called $F(\mathbf{U})$, where $\mathbf{U} = (\varphi, n_+, n_-)$, and then expanding around some $\mathbf{U}^0$. This gives

$$
0 = F(\mathbf{U}^0) + \int_\Omega \frac{\delta F(\mathbf{U})}{\delta \mathbf{U}} \delta \mathbf{U} \, dv \bigg|_{\mathbf{U}=\mathbf{U}^0} + O(\delta^2), \tag{A2}
$$

where $\delta \mathbf{U}$ is a variation away from $\mathbf{U}^0$. Now, performing this for Eq. (A1) and applying the appropriate boundary conditions gives the following linearized weak form:

$$
\begin{aligned}
0 = \int_\Omega & \left[-\nabla \psi \cdot \nabla \varphi^0 + \psi \frac{R^2 \kappa^2}{2}(n_+^0 - n_-^0) \right. \\
& + \frac{1}{\mathrm{Pe}} \nabla c_+ \cdot (\mathbf{u} n_+^0) - \nabla c_+ \cdot \nabla n_+^0 - \nabla c_+ \cdot (n_+^0 \nabla \varphi^0) \\
& \left. + \frac{1}{\mathrm{Pe}} \nabla c_- \cdot (\mathbf{u} n_-^0) - \nabla c_- \cdot \nabla n_-^0 + \nabla c_- \cdot (n_-^0 \nabla \varphi^0) \right] dv \\
& + \int_\Omega \left[-\nabla \psi \nabla \delta \varphi + \psi \frac{R^2 \kappa^2}{2}(\delta n_+ - \delta n_-) \right. \\
& + \frac{1}{\mathrm{Pe}} \nabla \cdot c_+ (\mathbf{u} \delta n_+) - \nabla c_+ \cdot \nabla \delta n_+ - \nabla \cdot c_+ (\delta n_+ \nabla \varphi^0) \\
& - \nabla \cdot c_+ (n_+^0 \nabla \delta \varphi) + \frac{1}{\mathrm{Pe}} \nabla c_- \cdot (\mathbf{u} \delta n_-) - \nabla c_- \cdot \nabla \delta n_- \\
& \left. + \nabla c_- \cdot (\delta n_- \nabla \varphi^0) + \nabla c_- \cdot (n_-^0 \nabla \delta \varphi) \right] dv \\
& + \int_\Gamma \psi \frac{R^2 \kappa^2}{2} \sigma_e ds.
\end{aligned} \tag{A3}
$$

This weak form can then be discretized and solved using the finite element method.

APPENDIX B: ANALYTICAL EXPRESSIONS FOR THE ELECTROVISCOUS EFFECT

Here we derive analytical expressions for flow in a channel, used as a comparison to our numerical simulations. The derivation closely follows the one found in [11,12], but is considered with channel flow instead of flow in a tube.

Consider the steady-state Nernst-Planck equation with a zero velocity field:

$$
\nabla \cdot (D_i n_i \nabla g_i) = 0, \tag{B1}
$$

where g_i is the chemical potential defined as

$$
g_i = \ln(n_i) + \frac{q_e z_i}{k_b T} \varphi. \tag{B2}
$$

Now if Eq. (B1) has to be satisfied, n_i must be given by

$$
n_i = n^\infty \exp\left(-\frac{q_e z_i}{k_b T} \varphi \right), \tag{B3}
$$

where n^∞ is the mean or inlet number density of the ions. Plugging Eq. (B3) for a symmetric monovalent solution into Eq. (7) yields the Poisson-Boltzmann equation

$$
\nabla^2 \varphi = \frac{2q_e n^\infty}{\epsilon_r \epsilon_0} \sinh\left(\frac{q_e z_i}{k_b T} \varphi \right). \tag{B4}
$$

Now expanding in φ around zero linearizes the Poisson-Boltzmann equation:

$$\nabla^2 \varphi = \kappa^2 \varphi. \tag{B5}$$

This can now be solved in a channel with walls at $x = \pm a$, under the following boundary conditions $\varphi|_{x=\pm a} = \zeta$, and that its transverse derivative is zero in the center of the channel, $\frac{\partial \varphi}{\partial x}|_{x=0} = 0$. This gives

$$\varphi(x) = \zeta \frac{\cosh(\kappa x)}{\cosh(\kappa a)}, \tag{B6}$$

and the charge density within the linear approximation becomes

$$\rho_e(x) = -\zeta \epsilon_r \epsilon_0 \kappa^2 \frac{\cosh(\kappa x)}{\cosh(\kappa a)}. \tag{B7}$$

Consider the Stokes equation in the same infinitely long channel with a pressure gradient and electric field along the z-direction:

$$\mu \frac{\partial^2 u_z}{\partial x^2} = -\frac{\partial P}{\partial z} - \rho_e E_z. \tag{B8}$$

Solving this with a no-slip condition at the walls and the charge density for Eq. (B7) yields

$$u_z(x) = \frac{\frac{\partial P}{\partial z}}{2\mu}(a^2 - x^2) - \frac{\epsilon_r \epsilon_0 \zeta E_z}{\mu}\left(1 - \frac{\cosh(\kappa x)}{\cosh(\kappa a)}\right). \tag{B9}$$

Now, to close the system, we assume that the charge-current flux along the z direction in the channel vanishes at steady state. The charge-current density is given as

$$J_{e(z)} = \rho_e(x)u_z(x) + \frac{2Dq_e^2}{k_B T} E_z n^\infty \cosh\left(\frac{q_e \varphi(x)}{k_B T}\right), \tag{B10}$$

and integrating it over the channel cross section gives the flux

$$\mathcal{L}\int_{-a}^{a} J_{e(z)} dx = -2\mathcal{L}a\frac{\partial P}{\partial z}\Omega\left[1 - \frac{1}{\kappa a}\tanh(\kappa a)\right]$$
$$+ \mathcal{L}a\Omega^2 E_z \mu \kappa^2\left[\frac{1}{\kappa a}\tanh(\kappa a) - \operatorname{sech}^2(\kappa a)\right]$$
$$- \frac{2\mathcal{L}aDq_e^2 n^\infty}{k_B T} E_z F_{cc}, \tag{B11}$$

where $\Omega = \frac{\epsilon_r \epsilon_0 \zeta}{\mu}$ and

$$F_{cc} = \int_0^1 2\cosh\left(\frac{q_e \zeta}{k_B T}\frac{\cosh(\kappa a X)}{\cosh(\kappa a)}\right)dX. \tag{B12}$$

Using the no-flux condition to get an expression of the ration of E_z and $\frac{\partial P}{\partial z}$ gives

$$\left.\frac{E_z}{\frac{\partial P}{\partial z}}\right|_{J_{e(z)}=0} = \frac{2\zeta}{\mu D \kappa^2 F_{cc}} f(\kappa a, \beta), \tag{B13}$$

where

$$f(\kappa a, \beta) = \frac{1 - \frac{1}{a\kappa}\tanh(\kappa a)}{1 + \frac{\beta}{F_{cc}}\left[\frac{1}{a\kappa}\tanh(\kappa a) - \operatorname{sech}^2(\kappa a)\right]}, \tag{B14}$$

$$\beta = \frac{\epsilon_r \epsilon_0 \zeta^2}{\mu D}. \tag{B15}$$

Integrating Eq. (B13) from one end of the channel to the other gives the Helmholtz-Smoluchowski equation

$$V_{str} = \frac{2\zeta}{\mu D \kappa^2 F_{cc}} f(\kappa a, \beta)\Delta P. \tag{B16}$$

To find the electroviscous effect, we use Eq. (B13) to eliminate E_z in Eq. (B9) and integrate to get the velocity flux Q_z along the z direction:

$$Q_z = \frac{2\mathcal{L}a\frac{\partial P}{\partial z}}{3\mu}\left[a^2 - \frac{6\beta}{\kappa^2 F_{cc}} f(\kappa a, \beta)\left(1 - \frac{1}{\kappa a}\tanh(\kappa a)\right)\right]. \tag{B17}$$

Now, the electric viscosity μ_e must be defined implicitly by

$$Q_z = \frac{2\mathcal{L}a^3\frac{\partial P}{\partial z}}{3\mu_e}; \tag{B18}$$

hence, from consistency, we have

$$\mu_e = \mu\left[1 - \frac{6\beta}{\kappa^2 a^2 F_{cc}} f(\kappa a, \beta)\left(1 - \frac{1}{\kappa a}\tanh(\kappa a)\right)\right]^{-1}. \tag{B19}$$

Note that μ_e also have the following functional definition

$$\frac{\mu_e}{\mu} = \frac{Q_{z,0}}{Q_{z,n_\infty}}, \tag{B20}$$

where the extra subscript on Q_z denotes the ion-number density.

APPENDIX C: FIRST-ORDER AMPLITUDE EXPANSION OF THE FLOW FIELD IN THE ABSENCE OF SURFACE CHARGE

Here we expand the flow field to the first order in a small surface undulation. We consider first the case where there is no surface charge. Hence, we consider a system and solution independent of the z coordinate; considering for simplicity the domain between $y = 0$ and $y = h(x)$. Without loss of generality, the domain has been inverted along y compared to the numerical simulations. The surface undulation function is given by $h(x) = H(1 + \epsilon \cos kx)$. We seek an expression which is first order in ϵ for the flow field ($\mathbf{u} = u_z \hat{\mathbf{z}}$). The equation to solve is the Poisson problem

$$\nabla^2 u_z = -f \tag{C1}$$

with the no-slip condition $u_z = 0$ on the top and bottom boundaries specified above. Following [37], we make the coordinate transformation

$$\eta = x, \tag{C2}$$

$$\zeta = \frac{y}{h(x)}, \tag{C3}$$

and in these coordinates, the domain is $\zeta \in [0,1]$. In the new coordinates, the Laplace operator is given by [37]

$$\nabla^2 = \frac{1}{h^2}\left(1 + \zeta^2 h_\eta^2\right)\partial_{\zeta\zeta} - 2\zeta\frac{h_\eta}{h}\partial_{\zeta\eta} + \partial_{\eta\eta}$$
$$+ \zeta\left[\left(2\frac{h_\eta}{h}\right)^2 - \frac{h_{\eta\eta}}{h}\right]\partial_\zeta, \tag{C4}$$

so to first order in ϵ, Eq. (C1) gives (letting $u_z = u^{(0)} + \epsilon u^{(1)}$)

$$
\begin{aligned}
H^2 \nabla^2 u_z = u^{(0)}_{\zeta\zeta} + \Lambda^2 u^{(0)}_{\beta\beta} &+ \epsilon\big[u^{(1)}_{\zeta\zeta} - 2\cos\beta u^{(0)}_{\zeta\zeta} \\
&+ 2\zeta\Lambda^2\sin\beta + \Lambda^2 u^{(1)}_{\beta\beta} + \Lambda^2\sin\beta\cos\beta u^{(0)}_{\zeta}\big] \\
&= -f, \quad (C5)
\end{aligned}
$$

where $\beta = k\eta$, and $\Lambda = kH$ characterizes the ratio between channel height and wavelength of the undulation. Solving this to zeroth and first order gives the solution

$$
u^{(0)} = \frac{f}{2}\zeta(1 - \zeta), \quad (C6)
$$

$$
u^{(1)} = \frac{f}{2}\left[(1 - 2\zeta)\zeta + \frac{\sinh\Lambda\zeta}{\sinh\Lambda}\right]\cos\beta \quad (C7)
$$

and, hence, the full expression in the original coordinates becomes

$$
u_z = \frac{f}{2}\left[\frac{y}{H}\left(1 - \frac{y}{H}\right) + \frac{\sinh\frac{\Lambda y}{H}}{\sinh\Lambda}\epsilon\cos kx\right], \quad (C8)
$$

to the first order in ϵ.

Integrating (C8) over y and subsequently over the narrowest region, $x \in [L_x/4, 3L_x/4]$ yields (note that the x axis is shifted

compared to the numerical simulations), according to the definition (27) of $Q_{z,x}(A,0)$,

$$
Q_{z,x}(A,0) = \frac{fHL_x}{2}\left[\frac{1}{12} - \frac{\epsilon}{\pi\Lambda}\left(1 - \frac{1}{\cosh\Lambda}\right)\right], \quad (C9)
$$

while the total flux is given by

$$
Q_{z,\text{tot}}(A,0) = \frac{fHL_x}{12}. \quad (C10)
$$

This yields, using Eq. (28), the absolute asymmetry

$$
\Theta_x(A,0) = \frac{1}{2} - \frac{6\epsilon}{\pi\Lambda}\left(1 - \frac{1}{\cosh\Lambda}\right). \quad (C11)
$$

Finally, identifying $H = L_y$, $A = L_y\epsilon$, and $\Lambda = 2\pi L_y/L_x$, we may write this in the somewhat more familiar form

$$
\Theta_x(A,0) = \frac{1}{2} - \frac{6AL_x}{2\pi^2 L_y^2}\left[1 - \frac{1}{\cosh\left(2\pi\frac{L_y}{L_x}\right)}\right]. \quad (C12)
$$

It is interesting to note that corrections to $Q_{z,t}(A,0)$ and $Q_{z,y}(A,0)$ are both of at least order $O(\epsilon^2)$, and hence the curves plotted against A should be flat at $A = 0$.

[1] H. A. Stone, A. D. Stroock, and A. Ajdari, Ann. Rev. Fluid Mech. **36**, 381 (2004).

[2] M. Van Soestbergen, P. Biesheuvel, and M. Bazant, Phys. Rev. E **81**, 021503 (2010).

[3] A. Siria, M.-L. Bocquet, and L. Bocquet, Nat. Rev. Chem. **1**, 0091 (2017).

[4] D. Chen, J. Lear, and B. Eisenberg, Biophys. J. **72**, 97 (1997).

[5] A. E. Cardenas, R. D. Coalson, and M. G. Kurnikova, Biophys. J. **79**, 80 (2000).

[6] B. Roux, T. Allen, S. Berneche, and W. Im, Q. Rev. Biophys. **37**, 15 (2004).

[7] O. Plümper, A. Botan, C. Los, Y. Liu, A. Malthe-Sørenssen, and B. Jamtveit, Nat. Geosci. **10**, 685 (2017).

[8] T. Hassenkam, C. S. Pedersen, K. Dalby, T. Austad, and S. L. S. Stipp, Colloids Surf. A **390**, 179 (2011).

[9] E.-A. Fiorentino, R. Toussaint, and L. Jouniaux, Geophys. J. Int. **205**, 648 (2016).

[10] E.-A. Fiorentino, R. Toussaint, and L. Jouniaux, Geophys. J. Int. **208**, 1139 (2016).

[11] C. L. Rice and R. Whitehead, J. Phys. Chem. **69**, 4017 (1965).

[12] A. Mansouri, C. Scheuerman, S. Bhattacharjee, D. Y. Kwok, and L. W. Kostiuk, J. Colloid Interface Sci. **292**, 567 (2005).

[13] A. Mansouri, S. Bhattacharjee, and L. W. Kostiuk, J. Phys. Chem. B **111**, 12834 (2007).

[14] E. Demekhin, V. Shelistov, and S. Polyanskikh, Phys. Rev. E **84**, 036318 (2011).

[15] C. L. Druzgalski, M. B. Andersen, and A. Mani, Phys. Fluids **25**, 110804 (2013).

[16] Our approach further prevents exceedingly long inflow and outflow transients in the coupled velocity-pressure subproblem, since the domain for the flow subproblem is closed.

[17] K. Graf, M. Kappl, and H.-J. Butt, *Physics and Chemistry of Interfaces* (Wiley, New York, 2006).

[18] C. P. Nielsen and H. Bruus, Phys. Rev. E **90**, 043020 (2014).

[19] G. Mitscha-Baude, A. Buttinger-Kreuzhuber, G. Tulzer, and C. Heitzinger, J. Comput. Phys. **338**, 452 (2017).

[20] R.-C. Chen and J.-L. Liu, J. Comput. Phys. **189**, 579 (2003).

[21] J.-L. Liu and B. Eisenberg, Phys. Rev. E **92**, 012711 (2015).

[22] A. Logg, K.-A. Mardal, and G. Wells, *Automated Solution of Differential Equations by the Finite Element Method: The FEniCS Book* (Springer Science & Business Media, Berlin, 2012), Vol. 84.

[23] A. Logg and G. N. Wells, ACM Trans. Math. Softw. **37**, 20:1 (2010).

[24] J. Blechta and M. Řehoř, "Fenapack", https://github.com/blechta/fenapack.

[25] J. R. Shewchuk, in *Applied Computational Geometry: Towards Geometric Engineering*, Lecture Notes in Computer Science Vol. 1148, edited by M. C. Lin and D. Manocha (Springer-Verlag, Berlin, 1996), pp. 203–222.

[26] MeshPy, https://documen.tician.de/meshpy/.

[27] H. Si, ACM Trans. Math. Softw. **41**, 11:1 (2015).

[28] A. Hiorth, L. Cathles, and M. Madland, Transp. Porous Media **85**, 1 (2010).

[29] E. Hilner, M. P. Andersson, T. Hassenkam, J. Matthiesen, P. Salino, and S. L. S. Stipp, Scie. Rep. **5**, 9933 (2015).

[30] E. J. W. Verwey and J. T. G. Overbeek, *Theory of the Stability of Lyophobic Colloids* (Elsevier, New York, 1948).

[31] G. Linga, A. Bolet, and J. Mathiesen (unpublished).

[32] G. Linga, A. Bolet, and J. Mathiesen (unpublished).

[33] See Supplemental Material at http://link.aps.org/supplemental/10.1103/PhysRevE.97.043114 for a comparison of time-dependent and steady-state solvers.

[34] Note that only the former is enforced at the inlet boundary, and both are enforced at the outlet boundary.

[35] M. Boström, D. R. M. Williams, and B. W. Ninham, Phys. Rev. Lett. **87**, 168103 (2001).

[36] C. I. Steefel, D. J. DePaolo, and P. C. Lichtner, Earth Planet. Sci. Lett. **240**, 539 (2005).

[37] S. Tsangaris and E. Leiter, J. Eng. Math. **18**, 89 (1984).

Transient electrohydrodynamic flow with concentration-dependent fluid properties: modelling and energy-stable numerical schemes

Gaute Linga, Asger Bolet, and Joachim Mathiesen

Transient electrohydrodynamic flow with concentration-dependent fluid properties: modelling and energy-stable numerical schemes

Gaute Linga*, Asger Bolet, Joachim Mathiesen

Niels Bohr Institute, University of Copenhagen, Blegdamsvej 17, DK-2100 Copenhagen, Denmark.

Abstract

Transport of electrolytic solutions under influence of electric fields occurs in phenomena ranging from biology to geophysics. Here, we present a continuum model for single-phase electrohydrodynamic flow, which can be derived from fundamental thermodynamic principles. This results in a generalized Navier–Stokes–Poisson–Nernst–Planck system, where fluid properties such as density and permittivity depend on the ion concentration fields. We propose strategies for constructing numerical schemes for this set of equations, where solving the electrochemical and the hydrodynamic subproblems are decoupled at each time step. We provide time discretizations of the model that suffice to satisfy the same energy dissipation law as the continuous model. In particular, we propose both linear and non-linear discretizations of the electrochemical subproblem, along with a projection scheme for the fluid flow. The efficiency of the approach is demonstrated by numerical simulations using several of the proposed schemes.

Keywords: electrokinetic flow, electrohydrodynamics, energy stable numerical schemes

1. Introduction

Electrokinetic or electrohydrodynamic flow concerns the coupled transport of charged species and fluid flow in the presence of electric fields. Such phenomena have gained increasing attention in recent years due to the rise of the fields of micro- [1] and nanofluidics [2]. Important technological applications include biomedical lab-on-a-chip devices [3], electrophoretic separation of macromolecules such as DNA and RNA [4], battery and fuel cell technology [5, 6], desalination of water [7], and the possibility of harvesting of energy due to salinity gradients ("blue energy") [8]. Further, electrokinetic effects can be important within geophysics [9, 10], as fluid flow through charged pores induces a *streaming potential* that counteracts the fluid motion and increases the apparent viscosity [11, 12, 13, 14]. In fluid-saturated porous rocks, large-scale transport can be mediated by electrochemical gradients [15].

Electrohydrodynamics is usually described by coupling incompressible fluid flow, governed by the Navier–Stokes equations, to solute transport, governed by the Nernst–Planck equations, and electrostatics, governed by a Poisson equation, thereby neglecting magnetic forces. This results in the strongly coupled Navier–Stokes–Poisson–Nernst–Planck (NSPNP) system of equations. Numerical approaches have often aimed for the steady-state solution to the governing equations [16, 14].

---

*Corresponding author.
Email address:* `linga@nbi.dk` (Gaute Linga)

To this end, commercial multi-physics software packages (e.g. Comsol) are available, and have long been successfully applied to simulate a variety microfluidic systems. With regard to the transient development of streaming potential, detailed simulations have often been limited to two-dimensional or axisymmetric geometries such as finite-length symmetric channels [17, 18]. In studies of electroconvection near permselective membranes [19], both finite element [20] and (pseudo-) spectral methods [21, 22, 23] have proven efficient. Recently, a spectral method was also applied in a study of the interaction between electrokinetics and turbulent drag [24]. In simulations of electrokinetic flow, the electrolyte solutions are usually assumed to be dilute enough for density, viscosity and permittivity to be independent of the local ion concentrations. The ion mobilities are usually taken to be proportional to the concentrations.

For the separate *subproblems* comprising the NSPNP problem, there exists many efficient numerical methods. For the Poisson–Nernst–Planck (PNP) problem, efficient approaches have been demonstrated for semi-conductors [25] and biological ion channels [26], where e.g. dispersion and size effects of ions can be included. For transient simulation of the Navier–Stokes equations, projection methods that date back to Chorin [27, 28] (see also Guermond, Minev, and Shen [29]), have imparted speedup compared to solving the monolithic problem, since it effectively decouples the computation of velocity and pressure (although at the cost of some reduced accuracy). For the full NSPNP problem, however, less is certain, but it seems clear that succesful numerical schemes should aim to decouple, at least, the fluid mechanical subproblem from the electrochemical subproblem, and thus take advantage of the progress made in numerically resolving each of these, although a direct combination does not necessarily yield a successful scheme.

In the field of diffuse-interface (or phase-field) methods for two-phase flow, recent years have seen progress in developing *energy-stable* numerical schemes. Such schemes are appealing because they share the common property with the physical models in the sense that they, in the absence of external driving forces, unconditionally dissipate energy. Hence, the schemes can be said to be thermodynamically consistent. Schemes that do not respect this energy law are prone to numerical errors and instabilities near singularities [30, 26], particularly applicable to flows involving sharp gradients such as both two-phase and electrohydrodynamic flow. Further, the energy laws permit to establish results on the convergence of numerical schemes. Schemes that require solving the fully coupled (nonlinear) problem implicitly can relatively easily be constructed to satisfy this property, while a splitting stategy introduces additional difficulty [31, 32]. Notably, Shen and Yang [26] presented linear, decoupled schemes for phase-field models with density contrast, relying in part on a projection method for the NS equations and a stabilization method for the phase-field equation.

The NSPNP system with two chemical species has been extensively studied by, e.g., Prohl and Schmuck [33, 34, 35, 36] who considered also the construction of an energy-stable scheme [35] with a coupling between the PNP and NS subproblems. Schemes for multi-ion electrohydrodynamics are also available [37]. An energy stable-splitting scheme for a thermodynamically consistent model for two-phase electrohydrodynamics [38] was presented and recently elaborated by Metzger [39, 40].

1.1. Contributions of this work

The objective of this paper is twofold. One is to obtain a generalized, thermodynamically consistent, model for electrohydrodynamics where the density, viscosity, mobilities, and permittivity depend on the ion concentrations. The second is to construct a *decoupled energy-stable* numerical scheme. To this end, we will consider a general, thermodynamically consistent model for single-phase flow including electric fields and transport of ions, i.e. a generalized NSPNP system. The subproblems of fluid flow and electrochemistry will be decoupled, where the key to energy-stability

lies in a forward-projected velocity that enters in the advection term in the solute transport equation, an idea which builds heavily on appraches used in two-phase flow models [31, 32, 26, 39]. For the electrochemical suproblem we propose discretization strategies that suffice to satisfy energy stability [35], one of which consititutes a linear scheme. For the fluid-mechanical part we consider two linear approaches, both a coupled strategy and a projection scheme for this subproblem. To the authors' knowledge, it is the first time an energy-stable projection scheme has been presented for electrohydrodynamic flow, in particular with concentration-dependent densities, viscosities and permittivities. Our schemes are shown to be numerically convergent by means of an electrohydrodynamic Taylor–Green vortex; to be numerically energy stable by a stress test of ions flowing in a closed container; a reaction cell to test the reliability of the reaction kinetics; and lastly applied to a geophysical setting, a porous media flow, to demonstrate the potential of the schemes in practical simulations.

1.2. Outline

The outline of the paper is as follows. In Sec. 2, we present a derivation of the model for electrohydrodynamic flow that we consider, and in Sec. 3, we investigate some properties of the resulting model. In Sec. 4 we present discretization strategies for the model, i.e. numerical schemes for the electrochemical and hydrodynamical subproblems. Further, in Sec. 5 we present numerical simulations using combinations of the numerical schemes presented, for the case of the conventional NSPNP model, and in Sec. 6 we conclude and provide a brief discussion.

1.3. Notation

Some remarks on notation is in place before we embark on the main part of the paper. We will denote an integral of a general quantity f over the domain Ω by

$$\int_\Omega f \, \mathrm{d}\Omega. \tag{1}$$

The L^2 inner product of the quantities a and b is denoted by (a, b). For example,

$$(f, g) = \int_\Omega f g \, \mathrm{d}\Omega \tag{2}$$

if f and g are scalars. The L^2 norm of a general quantity a is denoted by $\|a\|$. In particular,

$$\|f\|^2 = (f, f) = \int_\Omega |f|^2 \, \mathrm{d}\Omega. \tag{3}$$

A general time-discretized quantity a evaluated at the time step k is denoted by a^k. For the time discretization strategies in the forthcoming, we will make use of the backwards-differencing discrete differential operator. For the sake of simplicity, we adopt the following notation for a discrete time derivative:

$$\partial_\tau^- f^k = \frac{f^k - f^{k-1}}{\tau}, \tag{4}$$

where f is a general function (scalar or vector), and τ is a discrete time step.

2. A general model for single-phase electrohydrodynamics

Physically, single-phase electrohydrodynamic flow consists of the coupled system of fluid flow, ion transport and electrostatics. Such a continuum modelling approach is realistic down to the scale of a few nanometers. We will in the coming sections present a derivation, using variational principles, of a thermodynamically consistent and frame-invariant model of electrohydrodynamic flow, where the fluid properties are allowed to depend on the local concentrations of the chemical species. The main approximation underlying the model is that the volume of a fluid element does not change with increasing concentrations, only the weight, and hence the velocity field can be taken to be solenoidal. We will end up with the following partial differential equations, evolving in the spatial coordinate $\mathbf{x} \in \Omega \subset \mathbb{R}^d$, where Ω is the domain and d is the dimension, and in time t:

$$\rho \partial_t \mathbf{u} + (\mathbf{m} \cdot \boldsymbol{\nabla})\mathbf{u} - \boldsymbol{\nabla} \cdot (2\mu \mathbf{Du}) + \boldsymbol{\nabla} p = -\sum_i c_i \boldsymbol{\nabla} g_i, \tag{5}$$

$$\boldsymbol{\nabla} \cdot \mathbf{u} = 0, \tag{6}$$

$$\partial_t c_i + \mathbf{u} \cdot \boldsymbol{\nabla} c_i = \boldsymbol{\nabla} \cdot (K_i \boldsymbol{\nabla} g_i) + R_i \tag{7}$$

$$g_i = \sum_j \frac{\partial M_j}{\partial c_i} + z_i V - \frac{\partial \rho}{\partial c_i} \mathbf{a}_g \cdot \mathbf{x} - \frac{1}{2}|\boldsymbol{\nabla} V|^2 \frac{\partial \epsilon}{\partial c_i}, \tag{8}$$

$$\boldsymbol{\nabla} \cdot (\epsilon \boldsymbol{\nabla} V) = -\sum_i z_i c_i. \tag{9}$$

Here, the following quantites are involved.

ρ — fluid density,
$\mathbf{u}$ — velocity field,
$\mathbf{m}$ — advecting momentum (defined below),
μ — dynamic viscosity,
p — pressure,
c_i — concentration of ion species $i \in 1, \ldots, N$,
g_i — the chemical potential associated with species i,
K_i — the mobility of species i,
R_i — reaction source term for species i,
M_i — a specific energy related to having ion species i dissolved,
z_i — valency of species i,
$\mathbf{a}_g$ — the gravitational acceleration,
V — electric potential,
ϵ — electric permittivity.

In this general formulation, the fluid properties ρ, μ, K_i, M_i, and ϵ are allowed to depend on the set of concentrations $\{c_j\}_{j=1}^N$. In particular, we assume that the following linear equation of state holds for the density:

$$\rho(\{c_j\}) = \rho_0 + \sum_{j=1}^N \frac{\partial \rho}{\partial c_j} c_j. \tag{10}$$

Here, ρ_0 is the density of the "background" fluid, typically water, and the constant $\partial \rho / \partial c_i = \mathcal{M} w_i$, where $\mathcal{M}$ is a constant conversion factor and w_i is the number of nuclei in a given species j. Note

that in our formulation, we have reduced the number of parameters to a minimum, such that some prefactors have been absorbed into the relevant variables.

Eqs. (5) and (6) are the Navier–Stokes equations with variable density. Here, the advecting momentum $\mathbf{m} = \rho\mathbf{u} - \sum_i \frac{\partial\rho}{\partial c_i} K_i \boldsymbol{\nabla} g_i$, $\mathbf{m}$ differs from the canonical $\rho\mathbf{u}$ due to mass diffusion and migration through c_i. An unconventional forcing term on the right hand side (RHS) of (5), $-\sum_i c_i \boldsymbol{\nabla} g_i$ can by a redefinition of the pressure, and integration by parts, be written as the more conventional

$$\rho\mathbf{a}_g - \rho_e \boldsymbol{\nabla} V - \frac{1}{2}|\boldsymbol{\nabla} V|^2 \boldsymbol{\nabla}\epsilon, \tag{11}$$

which reveals the origin of the (conservative) driving forces in that may be present in the system. The terms represent, respectively, gravity, electric force, and a Helmholtz force due to permittivity gradients. However, the formulation of the RHS in (5) has e.g., numerical advantages, as g_i is constant at equilibrium, and therefore near equilibrium, the term $-\sum_i c_i \boldsymbol{\nabla} g_i$ will be less prone to catastrophic cancellation and pressure-buildup in the electric double layer [5]. Further, the symmetric gradient entering into the viscous term is defined by $\mathbf{Du} = \mathrm{sym}(\boldsymbol{\nabla}\mathbf{u}) = (\boldsymbol{\nabla}\mathbf{u} + \boldsymbol{\nabla}\mathbf{u}^T)/2$.

Eqs. (7) and (8) can be seen as a generalized Nernst–Planck equation. Typically in electro-hydrodynamics, the standard Nernst–Planck equation is used and the mobility that enters here is then given by $K_i = D_i c_i$, where D_i is the diffusion constant of species i. Further, M_j is then given by $M_j = c_j(\ln c_j - 1) + \beta_j c_j$, where is a constant that shall be elaborated on later.

Finally, (9) is the Poisson equation, or Gauss' law, with non-constant permittivity.

To close the system, we assign the following boundary conditions on the boundary $\partial\Omega$ of Ω:

$$\mathbf{u} = 0, \tag{12}$$

$$\mathbf{n} \cdot \epsilon\boldsymbol{\nabla} V = \sigma_e, \quad \text{or} \quad V = 0, \tag{13}$$

$$\mathbf{n} \cdot \boldsymbol{\nabla} g_i = 0. \tag{14}$$

Eq. (12) is the standard no-slip condition on the velocity field. Further, σ_e in Eq. (13) is the assigned surface charge of the boundary, and $\mathbf{n}$ is the unit normal vector pointing out of the domain. We consider a boundary that will either be charged or grounded. Eq. (14) represents a no-flux condition on the chemical species, i.e., impenetrable boundaries.

With regard to modelling the reaction terms R_i, we consider a sequence of reactions $m \in 1, \ldots, M$, where each reaction m can be written in the compact form

$$0 \rightleftharpoons \sum_m \nu_{m,i} \chi_i, \tag{15}$$

where $\nu_{m,i}$ is the *net* stoichiometric coefficent (products minus reactants) of ion i in reaction m, and χ_i is the chemical symbol of ion i. In Appendix A, we argue that we can model

$$R_i = \sum_m \nu_{m,i} \mathcal{R}_m \quad \text{with} \quad \mathcal{R}_m = -\mathcal{C}_m \cdot \sum_j \nu_{m,j} g_j, \tag{16}$$

where $\mathcal{C}_m \geq 0$ is a function of the involved variables. Such modelling of the reaction term was also considered by, e.g., Refs. [41, 39, 40]. Note that $\mathcal{C}_m$ can also be a function of the spatial coordinate $\mathbf{x}$, i.e., a reaction can be promoted or demoted in a certain region of the domain; effectively allowing to simulate, e.g., catalytic or other electrochemical systems.

2.1. Derivation of the model

We now present a derivation of a model for general electrohydrodynamic flow. The forthcoming analysis is similar to that considered by previous authors [38, 41]. We seek to formulate a model where the fluid properties are allowed to depend on the concentrations, which is both *frame-invariant* (Galilei invariant), thermodynamically consistent (dissipates free energy), and where the velocity field is solenoidal (divergence-free). The latter point limits the generality of the model, in the sense that we consider *quasi-incompressible* fluids; such that the local concentration fields only makes a fluid element heavier, but does not make it expand. This is a fair assumption for e.g. dissolving table salt in water under certain conditions. In general, however, liquids can both contract and expand with the addition of another component. Moreover, this behaviour can be non-monotonous.

The evolution of the concentration fields c_i can in general be written in the conservative form

$$\partial_t c_i + \boldsymbol{\nabla} \cdot (c_i \mathbf{u}) = -\boldsymbol{\nabla} \cdot \mathbf{J}_{c_i} + R_i, \tag{17}$$

where $\mathbf{J}_{c_i}$ is an undetermined diffusive flux, and R_i is a reaction source term. The left hand side is for convenience written in the convective form.

For the density field we assume the linear equation of state (10). With the quasi-incompressible assumption, the velocity field will still, as without any solutes, be solenoidal, i.e.,

$$\boldsymbol{\nabla} \cdot \mathbf{u} = 0. \tag{18}$$

Using (10), (18) and (17) we can derive the evolution of the density,

$$\partial_t \rho + \boldsymbol{\nabla} \cdot (\rho \mathbf{u}) = \sum_i \frac{\partial \rho}{\partial c_i} \left[\partial_t c_i + \boldsymbol{\nabla} \cdot (c_i \mathbf{u}) \right] \tag{19}$$

$$= \sum_i \frac{\partial \rho}{\partial c_i} \left[-\boldsymbol{\nabla} \cdot \mathbf{J}_{c_i} + R_i \right] \tag{20}$$

$$= -\boldsymbol{\nabla} \cdot \left(\sum_i \frac{\partial \rho}{\partial c_i} \mathbf{J}_{c_i} \right), \tag{21}$$

or

$$\partial_t \rho + \boldsymbol{\nabla} \cdot (\rho \mathbf{u}) = -\boldsymbol{\nabla} \cdot \mathbf{J}_\rho, \tag{22}$$

where we have used the condition that a reaction does not change the density, i.e., $\sum_i R_i \partial \rho / \partial c_i = 0$. This follows from the quasi-incompressible condition, and the fact that mass is conserved in a reaction (for all practical purposes, as the binding energy is, as far as these conservation laws are concerned, negligible compared to the rest energy of an atom or molecule). We have also implicitly defined the diffusive density flux,

$$\mathbf{J}_\rho = \sum_i \frac{\partial \rho}{\partial c_i} \mathbf{J}_{c_i}. \tag{23}$$

Eq. (22) suggests that the momentum is transported by the velocity

$$\mathbf{u}_{\mathrm{mom}} = \mathbf{u} + \rho^{-1} \mathbf{J}_\rho. \tag{24}$$

Following the discussion in Refs. [38, 41], the momentum should be transported by

$$\mathbf{m} = \rho \mathbf{u} + \mathbf{J}_\rho \tag{25}$$

6

in order for the model to be frame-invariant and not to introduce further nonlinearities. This gives the following evolution equation for the momentum:

$$\rho \partial_t \mathbf{u} + (\mathbf{m} \cdot \boldsymbol{\nabla})\mathbf{u} - \boldsymbol{\nabla} \cdot \mathbf{S} + \boldsymbol{\nabla} p = \mathbf{K}, \tag{26}$$

where $\mathbf{K}$ is a forcing term that will be determined by thermodynamic consistency, and $\mathbf{S}$ is a stress tensor to be decided.

The electric field can be found through Gauss' law:

$$\boldsymbol{\nabla} \cdot [\epsilon(\{c_i\})\mathbf{E}] = \rho_e, \tag{27}$$

where the total charge is

$$\rho_e = \sum_i z_i c_i. \tag{28}$$

In Eq. (27) we have taken the permittivity ϵ to be a function of the concentrations. This is motivated by, e.g, observations for aqueous NaCl solutions where it has been observed that permittivity can be significantly reduced due to multibody effects [42]. For simplicity we have dropped the weak dependence of permittivity on the electric fields [43] which for most purposes are insignificant [11]. Now, using (28) and (17) we can write,

$$\partial_t \rho_e + \boldsymbol{\nabla} \cdot (\rho_e \mathbf{u}) = -\sum_i \boldsymbol{\nabla} \cdot (z_i \mathbf{J}_{c_i}), = -\boldsymbol{\nabla} \cdot \mathbf{J}_e, \tag{29}$$

where we have used that $\sum_i z_i R_i = 0$ due to charge conservation in a reaction, and defined $\mathbf{J}_e = \sum_i z_i \mathbf{J}_{c_i}$. Using (27), we find

$$\partial_t \left[\epsilon(\{c_i\})\mathbf{E}\right] + \rho_e \mathbf{u} = -\mathbf{J}_e. \tag{30}$$

or

$$\epsilon \partial_t \mathbf{E} = -\rho_e \mathbf{u} - \mathbf{J}_e - \sum_i \mathbf{E} \frac{\partial \epsilon}{\partial c_i} \partial_t c_i. \tag{31}$$

We can now define the following general free energy density f:

$$f[\mathbf{u}, \{c_k\}, \mathbf{E}](\mathbf{x}, t) = \frac{1}{2}\rho(\{c_k\})\mathbf{u}^2 + \sum_i M_i(\{c_k\}) + \frac{1}{2}\epsilon(\{c_k\})\mathbf{E}^2 - \rho \mathbf{x} \cdot \mathbf{a}_g \tag{32}$$

and thus the total energy density

$$F = \int_\Omega f \, \mathrm{d}\Omega. \tag{33}$$

Now,

$$\frac{\mathrm{d}F}{\mathrm{d}t} = \int_\Omega \left[\mathbf{u} \cdot \rho \partial_t \mathbf{u} + \sum_i \frac{\partial f}{\partial c_i} \partial_t c_i + \mathbf{E} \cdot \epsilon \partial_t \mathbf{E}\right] \mathrm{d}\Omega \tag{34}$$

Further,

$$\frac{\partial f}{\partial c_i} = \left(\frac{\mathbf{u}^2}{2} - \mathbf{x} \cdot \mathbf{a}_g\right) \frac{\partial \rho}{\partial c_i} + \sum_k \frac{\partial M_k}{\partial c_i} + \frac{\mathbf{E}^2}{2} \frac{\partial \epsilon}{\partial c_i} \tag{35}$$

and hence

$$\frac{\mathrm{d}F}{\mathrm{d}t} = \int_{\Omega} \left[\mathbf{u} \cdot (-(\mathbf{m} \cdot \boldsymbol{\nabla})\mathbf{u} + \boldsymbol{\nabla} \cdot \mathbf{S} - \boldsymbol{\nabla}p + \mathbf{K}) + \sum_i \frac{\partial f}{\partial c_i} \partial_t c_i \right.$$

$$\left. - \mathbf{E} \cdot \left(\rho_e \mathbf{u} + \mathbf{J}_e + \sum_i \mathbf{E} \frac{\partial \epsilon}{\partial c_i} \partial_t c_i \right) \right] \mathrm{d}\Omega \quad (36)$$

Integrating in parts, using that all fluxes vanish at the boundary, we obtain

$$\frac{\mathrm{d}F}{\mathrm{d}t} = \int_{\Omega} \left[\sum_i (g_i - z_i V) \partial_t c_i + \mathbf{u} \cdot \mathbf{K} - \rho_e \mathbf{E} \cdot \mathbf{u} - \mathbf{E} \cdot \sum_i z_i \mathbf{J}_{c_i} \right] \mathrm{d}\Omega - \int_{\Omega} \mathbf{Du} : \mathbf{S} \mathrm{d}\Omega \quad (37)$$

where we have defined the chemical potential

$$g_i = \frac{\partial f}{\partial c_i} - \frac{1}{2} \mathbf{u}^2 \frac{\partial \rho}{\partial c_i} - \mathbf{E}^2 \frac{\partial \epsilon}{\partial c_i} + z_i V \quad (38)$$

$$= -\mathbf{x} \cdot \mathbf{a}_g \frac{\partial \rho}{\partial c_i} + \sum_k \frac{\partial M_k}{\partial c_i} - \frac{\mathbf{E}^2}{2} \frac{\partial \epsilon}{\partial c_i} + z_i V \quad (39)$$

Now,

$$\sum_i \int_{\Omega} (g_i - z_i V) \partial_t c_i \mathrm{d}\Omega = -\sum_i \int_{\Omega} (g_i - z_i V)(\boldsymbol{\nabla} \cdot (c_i \mathbf{u} + \mathbf{J}_{c_i}) - R_i) \, \mathrm{d}\Omega \quad (40)$$

$$= \sum_i \int_{\Omega} (\boldsymbol{\nabla} g_i + z_i \mathbf{E}) \cdot (c_i \mathbf{u} + \mathbf{J}_{c_i}) \, \mathrm{d}\Omega + \sum_i \int_{\Omega} g_i R_i \, \mathrm{d}\Omega \quad (41)$$

such that

$$\frac{\mathrm{d}F}{\mathrm{d}t} = \int_{\Omega} \mathbf{u} \cdot [\mathbf{K} + c_i \boldsymbol{\nabla} g_i] \, \mathrm{d}\Omega - \int_{\Omega} \mathbf{Du} : \mathbf{S} \mathrm{d}\Omega + \sum_i \int_{\Omega} \mathbf{J}_{c_i} \cdot \boldsymbol{\nabla} g_i \, \mathrm{d}\Omega + \sum_i \int_{\Omega} g_i R_i \, \mathrm{d}\Omega. \quad (42)$$

To choose the fluxes according to Onsager's variational principle (as in Refs. [38, 41]), we identify

$$\mathbf{J}_{c_i} = -K_i(\{c_k\}) \boldsymbol{\nabla} g_i, \quad (43)$$

where $K_i \geq 0$ are the mobilities. Further, the viscosity tensor can be modelled with the Newtonian form,

$$\mathbf{S} = 2\mu(\{c_k\}) \mathbf{Du}. \quad (44)$$

Note that the viscosity $\mu \geq 0$ can also depend on $\mathbf{Du}$ to model non-Newtonian fluids, but we shall not consider that here. Finally, to minimize the dissipation we choose the forcing term according to

$$\mathbf{K} = -\sum_i c_i \boldsymbol{\nabla} g_i. \quad (45)$$

The motivation for modelling the last term in (42) is given in Appendix A.

3. Properties of the model

In this section, we inspect some properties of the model presented in the preceding section.

3.1. Evolution of ion concentration

The first notable feature of the model is that the total ion concentration evolves only due to the reaction source term R_i:

$$\frac{\mathrm{d}}{\mathrm{d}t}\int_\Omega c_i\,\mathrm{d}\Omega = \int_\Omega \partial_t c_i\,\mathrm{d}\Omega = -\int_\Omega \boldsymbol{\nabla}\cdot\mathbf{J}_i\,\mathrm{d}\Omega + \int_\Omega R_i\,\mathrm{d}\Omega = \int_\Omega R_i\,\mathrm{d}\Omega, \tag{46}$$

where we identified the chemical flux as $\mathbf{J}_i = \mathbf{u}c_i - K_i\boldsymbol{\nabla}g_i$. When no reactions occur, the number of ions (integrated concentration) is conserved.

3.2. Mass conservation

The evolution of the density ρ can be expressed by using Eqs. (10) and (7):

$$\partial_t\rho = \sum_i \frac{\partial\rho}{\partial c_i}\partial_t c_i = \sum_i \frac{\partial\rho}{\partial c_i}(-\boldsymbol{\nabla}\cdot\mathbf{J}_i + R_i) = -\boldsymbol{\nabla}\cdot\mathbf{m}, \tag{47}$$

where we have, as in the previous section, used the condition that a reaction can not change the density, i.e., $\sum_i \frac{\partial\rho}{\partial c_i}R_i = 0$. Thus mass is conserved in the model:

$$\frac{\mathrm{d}}{\mathrm{d}t}\int_\Omega \rho\,\mathrm{d}\Omega = \int_\Omega \partial_t\rho\,\mathrm{d}\Omega = -\int_\Omega \boldsymbol{\nabla}\cdot\mathbf{m}\,\mathrm{d}\Omega = 0. \tag{48}$$

3.3. Free energy

Associated with the above system we have the free energy

$$F = \int_\Omega \left[\frac{1}{2}\rho|\mathbf{u}|^2 + \frac{1}{2}\epsilon|\boldsymbol{\nabla}V|^2 + \sum_i M_i - \rho\,\mathbf{a}_g\cdot\mathbf{x}\right]\mathrm{d}\Omega, \tag{49}$$

where the first term represents the kinetic energy, the second the electric field energy, the third term the chemical energy, and the last term the gravitational energy. We are now interested in an expression for the evolution of the free energy in time, i.e. $\mathrm{d}F/\mathrm{d}t$. We therefore decompose the free energy into:

$$F = F_\mathbf{u} + F_V + \sum_i F_{c_i} + F_g, \tag{50}$$

where

$$F_\mathbf{u} = \int_\Omega \frac{1}{2}\rho|\mathbf{u}|^2\,\mathrm{d}\Omega, \quad F_V = \int_\Omega \frac{1}{2}\epsilon|\boldsymbol{\nabla}V|^2\,\mathrm{d}\Omega, \tag{51}$$

$$F_{c_i} = \int_\Omega M_i\,\mathrm{d}\Omega, \quad \text{and} \quad F_g = -\int_\Omega \rho\,\mathbf{a}_g\cdot\mathbf{x}\,\mathrm{d}\Omega. \tag{52}$$

Now, we seek the temporal evolution of these quantities.

- The kinetic energy:

$$\frac{\mathrm{d}F_\mathbf{u}}{\mathrm{d}t} = \int_\Omega \partial_t \left[\frac{1}{2}\rho|\mathbf{u}|^2\right] \mathrm{d}\Omega \tag{53}$$

$$= (\mathbf{u}, \rho\partial_t\mathbf{u}) + \left(\frac{1}{2}|\mathbf{u}|^2, \partial_t\rho\right) \tag{54}$$

$$= (\mathbf{u}, \boldsymbol{\nabla}\cdot(2\mu\mathbf{Du}) + \boldsymbol{\nabla}p - \sum_i c_i\boldsymbol{\nabla}g_i) \tag{55}$$

$$= -\left\|\sqrt{2\mu}\mathbf{Du}\right\|^2 - (\mathbf{u}, \sum_i c_i\boldsymbol{\nabla}g_i) \tag{56}$$

$$= -\left\|\sqrt{2\mu}\mathbf{Du}\right\|^2 + \sum_i (g_i, \mathbf{u}\cdot\boldsymbol{\nabla}c_i) \tag{57}$$

$$= -\left\|\sqrt{2\mu}\mathbf{Du}\right\|^2 - \sum_i \left[(g_i, \partial_t c_i) + \left\|\sqrt{K_i}\boldsymbol{\nabla}g_i\right\|^2 - (g_i, R_i)\right], \tag{58}$$

where we have used the fact that K_i is non-negative.

- The electric field energy:

$$\frac{\mathrm{d}F_V}{\mathrm{d}t} = \frac{\mathrm{d}}{\mathrm{d}t}\int_\Omega \frac{1}{2}\epsilon|\boldsymbol{\nabla}V|^2\,\mathrm{d}\Omega \tag{59}$$

$$= (\boldsymbol{\nabla}V, \epsilon\partial_t\boldsymbol{\nabla}V) + \left(\frac{1}{2}|\boldsymbol{\nabla}V|^2, \partial_t\epsilon\right) \tag{60}$$

$$= (\boldsymbol{\nabla}V, \partial_t(\epsilon\boldsymbol{\nabla}V) - \boldsymbol{\nabla}V\partial_t\epsilon) + \left(\frac{1}{2}|\boldsymbol{\nabla}V|^2, \partial_t\epsilon\right) \tag{61}$$

$$= (\boldsymbol{\nabla}V, \partial_t(\epsilon\boldsymbol{\nabla}V)) - \left(\frac{1}{2}|\boldsymbol{\nabla}V|^2, \partial_t\epsilon\right) \tag{62}$$

$$= -(V, \partial_t\boldsymbol{\nabla}\cdot(\epsilon\boldsymbol{\nabla}V)) - \sum_i \left(\frac{1}{2}|\boldsymbol{\nabla}V|^2, \frac{\partial\epsilon}{\partial c_i}\partial_t c_i\right) \tag{63}$$

$$= \sum_i (z_i V - \frac{1}{2}|\boldsymbol{\nabla}V|^2\frac{\partial\epsilon}{\partial c_i}, \partial_t c_i) \tag{64}$$

- The chemical energy:

$$\frac{\mathrm{d}F_{c_i}}{\mathrm{d}t} = \int_\Omega \partial_t M_i\,\mathrm{d}\Omega = \sum_j \int_\Omega \frac{\partial M_i}{\partial c_j}\partial_t c_i\,\mathrm{d}\Omega \tag{65}$$

- The gravitational energy:

$$\frac{\mathrm{d}F_g}{\mathrm{d}t} = -\int_\Omega \partial_t\rho\,\mathbf{a}_g\cdot\mathbf{x}\,\mathrm{d}\Omega \tag{66}$$

$$= -\sum_i \left(\frac{\partial\rho}{\partial c_i}\mathbf{a}_g\cdot\mathbf{x}, \partial_t c_i\right) \tag{67}$$

10

Using eqs. (50), (58), (64) and (67) and the definition of g_i in Eq. (8) we obtain:

$$\frac{\mathrm{d}F}{\mathrm{d}t} = -\left\|\sqrt{2\mu}\mathbf{Du}\right\|^2 - \sum_i \left\|\sqrt{K_i}\boldsymbol{\nabla}g_i\right\|^2 + \sum_i (g_i, R_i). \tag{68}$$

Clearly, the two first terms on the right hand side of Eq. (68) are negative. Thus, what remains is to model the reaction terms R_i in such a way that the last term is also negative.

In particular, we obtain from Eq. (68) the free energy evolution

$$\frac{\mathrm{d}F}{\mathrm{d}t} = -\left\|\sqrt{2\mu}\mathbf{Du}\right\|^2 - \sum_i \left\|\sqrt{K_i}\boldsymbol{\nabla}g_i\right\|^2 - \sum_m \mathcal{C}_m \int_\Omega \left(\sum_i \nu_{m,i}g_i\right)^2 \mathrm{d}\Omega \leq 0. \tag{69}$$

Hence the free energy is decaying in time — i.e. the model is dissipative. This is an important property, as it guarantees that, in the absence of external driving forces, the system at all instances does not produce energy, i.e. it evolves towards a state of lower energy. Hence, a proper time discretization scheme should also have this property, in order to avoid spurious energy blow-up.

Note that we will not attempt to quantitatively model the reaction function $\mathcal{C}_m$ (apart from the example considered in Appendix A). This will in general require more detailed or phenomenological modelling of the particular chemical reaction m.

In the remainder of this article, we will for concreteness consider the chemical energy functions

$$M_i(\{c_k\}) = \alpha(c_i) + \beta_i c_i, \tag{70}$$

where β_i are constants. The role of β_i is to energetically penalize (or promote) the presence of a species c_i in comparison to ther species. Hence, the set of β_{ij} should fix a (chemical) equilibrium state of the system. Now, the derivative of M_i that enters into the model can be expressed by

$$\frac{\partial M_i}{\partial c_j} = \alpha'(c_j)\delta_{ij} + \beta_j \delta_{ij}, \tag{71}$$

where δ_{ij} is the Kronecker delta function. Note that since the β_i are constant, they will not affect the system through the chemical fluxes $\propto \boldsymbol{\nabla}g_i$, but will enter in the reaction term R_i.

Further, we will consider only permittivities which can be written in the form

$$\epsilon(\{c_k\}) = \epsilon_0 + \sum_k \epsilon_k(c_k), \tag{72}$$

where, in particular, no cross terms are present. Here, ϵ_0 is not the vacuum permittivity, but the permittivity of the background fluid. Note that on physical grounds $\epsilon > 0$ (in particular, the vacuum permittivity is an absolute lower bound) and hence ϵ_k should be always positive. This formulation is consistent, e.g., with the empirical relation found in simulations by Hess et al. [42] for a NaCl solution, where a relation $1/\epsilon(c) \propto 1 + kc$ (k is a constant) was reported.

4. Energy-stable time discretization

We will in the forthcoming consider schemes that are finite difference in time, and finite element in space. We present schemes to simulate the general model for single-phase electrohydrodynamics which was presented in the previous section. In this section, we will first present the schemes and

afterwards the appropriate variational form which is used in the finite element spatial discretization. To this end, for the velocity components we define the function space $\mathcal{V}$ as

$$\mathcal{V} = \{v \in H^1(\Omega) : v = 0 \text{ on } \partial\Omega\} \tag{73}$$

where $H^1(\Omega)$ is the Sobolev space containing functions f such that f^2 and $|\boldsymbol{\nabla} f|^2$ have finite integrals over Ω. For the remaining scalar fields we will use the spaces $\mathcal{X}$ which we define as simply $\mathcal{V}$ without the boundary restrictions.

4.1. Decoupled schemes

We will in this paper adopt a strategy known from simulating, e.g., two-phase flow. It is beneficial to split the problem in a hydrodynamical step and an electrochemical step, since it is in general harder both to effectively precondition and to solve the coupled system. On the other hand, there exists approaches for the effective solution of the subproblems PNP system (for the electrochemistry) and for the NS system (for the hydrodynamics). The decoupling strategy may also enable the construction of linear schemes, instead of non-linear, which are more easily solved.

The main advantages of the schemes presented here are that the computation of the electrochemical problem is decoupled from the hydrodynamic problem, while we are still able to guarantee the energy dissipation associated with the physical problem.

Hence, we shall now consider schemes which employ a divide-and-conquer strategy, with two subproblems to be solved *sequentially* at each time step k:

1. **Electrochemistry:** Using information from the previous time step $k-1$, i.e., $\{\mathbf{u}^{k-1}, p^{k-1}, c_1^{k-1}, \ldots, c_N^{k-1}, V^{k-1}\}$, obtain a numerical approximations of the primary electrochemical variables, i.e. $\{c_1^k, \ldots, c_N^k, V^k\}$ at the present time step k.
2. **Hydrodynamics:** Using the newly updated electrochemical variables $\{c_1^k, \ldots, c_N^k, V^k\}$ and hydrodynamic variables $\{\mathbf{u}^{k-1}, p^{k-1}\}$ from the previous time step $k-1$, obtain an approximation of the primary hydrodynamical variables, i.e. $\{\mathbf{u}^k, p^k\}$ at the present time step k.

4.2. Strategy for the electrochemistry step

Scheme. Suppose $\{\mathbf{u}^{k-1}, p^{k-1}, c_1^{k-1}, \ldots, c_N^{k-1}, V^{k-1}\}$ are given. Now, to obtain $\{c_1^k, \ldots, c_N^k, V^k\}$, solve

$$\partial_\tau^- c_i^k - \boldsymbol{\nabla} \cdot (\mathbf{u}^* \tilde{c}_i) - \boldsymbol{\nabla} \cdot \left(\tilde{K}_i \boldsymbol{\nabla} g_i^k \right) = \tilde{R}_i, \quad \text{for} \quad i \in [1, N], \tag{74a}$$

$$\boldsymbol{\nabla} \cdot \left(\epsilon^k \boldsymbol{\nabla} V^k \right) = \sum_i z_i c_i^k, \tag{74b}$$

where

$$g_i^k = \tilde{\alpha}' + \beta_i + z_i V^k - \frac{1}{2} |\boldsymbol{\nabla} V^k|^2 \tilde{\epsilon}_i' - \frac{\partial \rho}{\partial c_i} \mathbf{x} \cdot \mathbf{a}_g. \tag{74c}$$

Here, $\tilde{\alpha}'(c_i^k, c_i^{k-1})$ is a numerical approximation to $\alpha'(\xi^k)$, where $\min(c_i^k, c_i^{k-1}) \leq \xi^k \leq \max(c_i^k, c_i^{k-1})$. Further, $\tilde{K}_i(c_i^k, c_i^{k-1}) \geq 0$ approximates K_i, $\tilde{c}_i$ is an approximation to c_i, and $\tilde{R}_i$ is an approximation to R_i. Moreover,

$$\tilde{\epsilon}_i'(c_i^k, c_i^{k-1}) = \begin{cases} \frac{\epsilon_i(c_i^k) - \epsilon_i(c_i^{k-1})}{c_i^k - c_i^{k-1}} & \text{for} \quad c_i^k \neq c_i^{k-1}, \\ \frac{\partial \epsilon_i}{\partial c_i}(c_i^{k-1}), & \text{for} \quad c_i^k = c_i^{k-1}, \end{cases} \tag{75}$$

is an approximation to $\partial \epsilon_i / \partial c_i$. Recall also that $\partial \rho / \partial c_i$ is a constant.

The following boundary conditions are enforced on the boundary $\partial\Omega$

$$\mathbf{n} \cdot \boldsymbol{\nabla} g_i^k = 0, \tag{76a}$$

$$\mathbf{n} \cdot \epsilon^k \boldsymbol{\nabla} V^k = \sigma \quad \text{or} \quad V^k = 0. \tag{76b}$$

In eq. (74a) we have used the definition:

$$\mathbf{u}^* = \mathbf{u}^{k-1} - \frac{\tau}{\rho^{k-1}} \sum_i \tilde{c}_i \boldsymbol{\nabla} g_i^k, \tag{77}$$

which is a forward-projection of the velocity based on the chemical fluxes, and introduces a first-order error in τ. This projection is a key ingredient to obtaining Note that when the system approaches equilibrium, the second term, which is already close to equilibrium, vanishes.

Variational form. A variational form of eqs. (74a) to (74c) can be written as the following.
Find $(c_1^k, \ldots, c_N^k, g_1^k, \ldots g_N^k, V^k) \in \mathcal{X}^N \times \mathcal{X}^N \times \mathcal{X}$, such that for all $(b_1^k, \ldots, b_N^k, h_1^k, \ldots h_N^k, U^k) \in \mathcal{X}^N \times \mathcal{X}^N \times \mathcal{X}$, we have

$$\left(\partial_\tau^- c_i^k, b_i\right) - \left(\mathbf{u}^* \tilde{c}_i, \boldsymbol{\nabla} b_i\right) + \left(\tilde{K}_i \boldsymbol{\nabla} g_i^k, \boldsymbol{\nabla} b_i\right) = \left(\tilde{R}_i, b_i\right), \tag{78a}$$

$$\left(g_i^k, h\right) = \left(\tilde{\alpha}' + \beta_i + z_i V^k - \frac{1}{2}|\boldsymbol{\nabla} V^k|^2 \tilde{\epsilon}_i' - \frac{\partial\rho}{\partial c_i}\mathbf{x} \cdot \mathbf{a}_g, h\right) \tag{78b}$$

$$\left(\epsilon^k \boldsymbol{\nabla} V^k, \boldsymbol{\nabla} U\right) - \int_{\partial\Omega} \sigma U \, \mathrm{d}\Gamma = \sum_{i=1}^N \left(z_i c_i^k, U\right). \tag{78c}$$

4.2.1. Free energy evolution

Lemma 1. *For the electrochemical step, the following inequality holds:*

$$\partial_\tau^- F_{\mathrm{EC}}^k \leq \sum_i \left(\mathbf{u}^*, \tilde{c}_i \boldsymbol{\nabla} g_i^k\right) - \frac{1}{\tau} \sum_i \Delta F_{c_i}^k - \sum_i \left\|\sqrt{\tilde{K}_i} \boldsymbol{\nabla} g_i^k\right\|^2 + \left(\tilde{R}_i, g_i^k\right). \tag{79}$$

Here,

$$F_{\mathrm{EC}}^k = \sum_i F_{c_i}^k + F_V^k + F_g^k, \tag{80}$$

and

$$\Delta F_{c_i}^k = \tau \left(\tilde{\alpha}'(c_i^k, c_i^{k-1}) + \beta_i, \partial_\tau^- c_i^k\right) - F_{c_i}^k + F_{c_i}^{k-1}, \tag{81}$$

which represents an excess free energy introduced by the numerical approximation $\tilde{\alpha}'(c_i^k, c_i^{k-1})$ to $\alpha'(c)$.

Proof. By testing eq. (78a) with $b_i = g_i^k$, we get:

$$\left(\partial_\tau^- c_i^k, g_i^k\right) - \left(\mathbf{u}^* \tilde{c}_i, \boldsymbol{\nabla} g_i^k\right) = -\left\|\sqrt{\tilde{K}_i} \boldsymbol{\nabla} g_i^k\right\|^2 + \left(\tilde{R}_i, g_i^k\right), \tag{82}$$

and further, testing eq. (78b) with $h = \partial_\tau^- c_i^k$, we obtain:

$$\left(g_i^k, \partial_\tau^- c_i^k\right) = \frac{1}{\tau}\left(\tilde{\alpha}'(c_i^k, c_i^{k-1}) + \beta_i + z_i V^k - \frac{1}{2}|\boldsymbol{\nabla} V^k|^2 \tilde{\epsilon}'_i - \frac{\partial \rho}{\partial c_i}\mathbf{x}\cdot\mathbf{a}_g, c_i^k - c_i^{k-1}\right) \tag{83}$$

$$= \partial_\tau^- F_{c_i}^k + \frac{\Delta F_{c_i}^k}{\tau} + \left(z_i V^k, \partial_\tau^- c_i^k\right) - \left(\frac{1}{2}|\boldsymbol{\nabla} V^k|^2, \partial_\tau^- \epsilon_i^k\right) - \left(\frac{\partial \rho}{\partial c_i}\mathbf{x}\cdot\mathbf{a}_g, \partial_\tau^- c_i^k\right), \tag{84}$$

where we have introduced the splitting (81) and the shorthand definition of the discrete total chemical energy:

$$F_{c_i}^k = \int_\Omega \left[\alpha(c_i^k) + \beta_i c_i^k\right]\, \mathrm{d}\Omega. \tag{85}$$

By defining the shorthand discrete gravitational energy,

$$F_g^k = -\int_\Omega \rho^k\, \mathbf{x}\cdot\mathbf{a}_g\, \mathrm{d}\Omega, \tag{86}$$

where $\rho^k = \rho(\{c_i^k\})$, we find that the sum over the phases in the last term in Eq. (84) becomes

$$\sum_i \left(\frac{\partial \rho}{\partial c_i}\mathbf{x}\cdot\mathbf{a}_g, \partial_\tau^- c_i^k\right) = \left(\mathbf{x}\cdot\mathbf{a}_g, \partial_\tau^- \left[\rho_0 + \sum_i \frac{\partial \rho}{\partial c_i}c_i^k\right]\right) = \left(\mathbf{x}\cdot\mathbf{a}_g, \partial_\tau^- \rho^k\right) = -\partial_\tau^- F_g^k. \tag{87}$$

We also define the discrete electric energy by

$$F_V^k = \int_\Omega \frac{1}{2}\epsilon^k|\boldsymbol{\nabla} V^k|^2\, \mathrm{d}\Omega. \tag{88}$$

Now, testing eq. (78c) with $U = V^k$ yields:

$$\left(\epsilon^k\boldsymbol{\nabla} V^k, \boldsymbol{\nabla} V^k\right) - \int_{\partial\Omega} \sigma V^k\, \mathrm{d}\Gamma = \sum_i \left(z_i c_i^k, V^k\right). \tag{89}$$

Considering eq. (78c) with $k \to k-1$, and testing it with $U = V^k$, yields:

$$\left(\epsilon^{k-1}\boldsymbol{\nabla} V^{k-1}, \boldsymbol{\nabla} V^k\right) - \int_{\partial\Omega} \sigma V^k\, \mathrm{d}\Gamma = \sum_i \left(z_i c_i^{k-1}, V^k\right). \tag{90}$$

Subtracting eq. (90) from eq. (89) and dividing by τ gives

$$\sum_i z_i \left(\partial_\tau^- c_i^k, V^k\right) = \frac{1}{\tau}\left(\boldsymbol{\nabla} V^k, \epsilon^k\boldsymbol{\nabla} V^k - \epsilon^{k-1}\boldsymbol{\nabla} V^{k-1}\right) \tag{91}$$

$$= \left(\frac{\mathbf{E}^k + \mathbf{E}^{k-1}}{2\tau} + \frac{\mathbf{E}^k - \mathbf{E}^{k-1}}{2\tau}, \epsilon^k\left(\mathbf{E}^k - \mathbf{E}^{k-1}\right)\right) + \left(\mathbf{E}^k, \partial_\tau^- \epsilon^k \mathbf{E}^{k-1}\right) \tag{92}$$

$$= \frac{1}{2\tau}\left(\epsilon^k, |\mathbf{E}^k|^2 - |\mathbf{E}^{k-1}|^2\right) + \frac{1}{2\tau}\left\|\sqrt{\epsilon^k}\left(\mathbf{E}^k - \mathbf{E}^{k-1}\right)\right\|^2 + \left(\mathbf{E}^k, \partial_\tau^- \epsilon^k \mathbf{E}^{k-1}\right) \tag{93}$$

$$= \partial_\tau^- F_V^k + \frac{1}{2\tau}\left\|\sqrt{\epsilon^{k-1}}\left(\boldsymbol{\nabla} V^k - \boldsymbol{\nabla} V^{k-1}\right)\right\|^2 + \frac{1}{2}\left(\partial_\tau^- \epsilon^k, |\boldsymbol{\nabla} V^k|^2\right) \tag{94}$$

14

Now, combining eqs. (82), (84), (87) and (94), we obtain

$$\sum_i \partial_\tau^- F_{c_i}^k + \partial_\tau^- F_V^k + \partial_\tau^- F_g^k = -\frac{1}{\tau}\sum_i \Delta F_{c_i}^k + \sum_i \left(\mathbf{u}^*, \tilde{c}_i \boldsymbol{\nabla} g_i^k\right)$$

$$-\sum_i \left\|\sqrt{\tilde{K}_i}\boldsymbol{\nabla} g_i^k\right\|^2 - \frac{1}{2\tau}\left\|\sqrt{\epsilon^{k-1}}\left(\boldsymbol{\nabla} V^k - \boldsymbol{\nabla} V^{k-1}\right)\right\|^2 + \left(\tilde{R}_i, g_i^k\right). \quad (95)$$

which yields eq. (79) and thus completes the proof. $\qquad\square$

4.3. Strategies for the hydrodynamic step

For the hydrodynamic step, we can consider either the standard coupled approach, which is to solve the velocity and pressure simultaneously at each time step, or an approach which decouples the velocity and pressure at each step. We shall denote the former as Scheme I and the latter as Scheme II.

4.3.1. Scheme I: Coupled hydrodynamics
Scheme. The first scheme can be written in variational form as the following. Suppose that $\{\mathbf{u}^{k-1}, p^{k-1}, c_1^{k-1}, \ldots, c_N^{k-1}, c_1^k, \ldots, c_N^k, g_1^k, \ldots, g_N^k\}$ are given. Now, in order to obtain $\{\mathbf{u}^k, p^k\}$, we solve

$$\rho^{k-1}\partial_\tau^- \mathbf{u}^k + (\mathbf{m}^{k-1}\cdot\boldsymbol{\nabla})\mathbf{u}^k - \boldsymbol{\nabla}\cdot\left(2\mu^k \mathbf{D}\mathbf{u}^k\right) + \boldsymbol{\nabla} p^k$$

$$+ \frac{1}{2}\mathbf{u}^k\left(\partial_\tau^- \rho^k + \boldsymbol{\nabla}\cdot\mathbf{m}^{k-1}\right) = -\sum_i \tilde{c}_i \boldsymbol{\nabla} g_i^k, \quad (96a)$$

$$\boldsymbol{\nabla}\cdot\mathbf{u}^k = 0. \quad (96b)$$

Note that the last two terms on the left hand side of Eq. (97a) are an approximation to the mass conservation equation (47), i.e., $\partial_t \rho + \boldsymbol{\nabla}\cdot\mathbf{m} = 0$. The incorporation of these terms is a standard way of satisfying the discrete energy law at each time step. The equations (96a) and (96b) are solved in combinaton with the no-slip condition $\mathbf{u}^k = \mathbf{0}$.

Variational form. Find $(\mathbf{u}^k, p^k) \in \mathcal{V}^d \times \mathcal{X}$ such that for all $(\mathbf{v}, q) \in \mathcal{V}^d \times \mathcal{X}$,

$$\left(\rho^{k-1}\partial_\tau^- \mathbf{u}^k, \mathbf{v}\right) + \left((\mathbf{m}^{k-1}\cdot\boldsymbol{\nabla})\mathbf{u}^k, \mathbf{v}\right) + \left(2\mu^k \mathbf{D}\mathbf{u}^k, \mathbf{D}\mathbf{v}\right) - \left(p^k, \boldsymbol{\nabla}\cdot\mathbf{v}\right)$$

$$+ \frac{1}{2}\left(\mathbf{u}^k \partial_\tau^- \rho^k, \mathbf{v}\right) - \frac{1}{2}\left(\mathbf{m}^{k-1}, \boldsymbol{\nabla}(\mathbf{u}^k\cdot\mathbf{v})\right) = -\sum_i \left(\tilde{c}_i\boldsymbol{\nabla} g_i^k, \mathbf{v}\right), \quad (97a)$$

$$\left(q, \boldsymbol{\nabla}\cdot\mathbf{u}^k\right) = 0, \quad (97b)$$

with the Dirichlet boundary condition $\mathbf{u}^k = \mathbf{0}$.

4.3.2. Scheme II: Fractional-step hydrodynamics
Instead of solving for velocity and pressure in a coupled manner, we may use a projection method to decouple the velocity computation from the pressure. Such a scheme describing the somewhat similar equations of two-phase flow, was already proposed by, e.g., Shen and Yang [26].

15

Scheme. In the spirit of the latter reference, the scheme is given by the following. Suppose that $\{\mathbf{u}^{k-1}, p^{k-1}, c_1^{k-1}, \ldots, c_N^{k-1}, c_1^k, \ldots, c_N^k, g_1^k, \ldots, g_N^k\}$ are given.

- Tentative velocity step: To obtain the intermediate velocity $\tilde{\mathbf{u}}^k$, solve

$$\rho^{k-1}\frac{\tilde{\mathbf{u}}^k - \mathbf{u}^{k-1}}{\tau} + (\mathbf{m}^{k-1} \cdot \boldsymbol{\nabla})\tilde{\mathbf{u}}^k - \boldsymbol{\nabla} \cdot \left(2\mu^k \mathbf{D}\tilde{\mathbf{u}}^k\right) + \boldsymbol{\nabla} p^{k-1}$$
$$+ \frac{1}{2}\tilde{\mathbf{u}}^k \left(\partial_\tau^- \rho^k + \boldsymbol{\nabla} \cdot \mathbf{m}^{k-1}\right) = -\sum_i c_i^{k-1}\boldsymbol{\nabla} g_i^k, \quad (98)$$

  with $\tilde{\mathbf{u}}^k = \mathbf{0}$ on $\partial\Omega$.

- Pressure correction step: To obtain the corrected pressure p^k, solve

$$\boldsymbol{\nabla}^2(p^k - p^{k-1}) = \frac{\rho_0}{\tau}\boldsymbol{\nabla} \cdot \tilde{\mathbf{u}}^k, \quad (99)$$

  with the artificial Neumann condition $\mathbf{n} \cdot \boldsymbol{\nabla}(p^k - p^{k-1}) = 0$. Note that this introduces an $O(\tau)$ error at the boundary.

- Velocity correction step: To obtain the final velocity $\mathbf{u}^k$, solve

$$\rho^k\frac{\mathbf{u}^k - \tilde{\mathbf{u}}^k}{\tau} = -\boldsymbol{\nabla}\left(p^k - p^{k-1}\right), \quad (100)$$

  with the Dirichlet boundary condition on $\mathbf{u}^k = \mathbf{0}$, which supresses the error from the Neumann condition above.

Together with the analysis in the previous section, this constitutes a scheme which is decoupled between the three parts electrostatics, velocity and pressure. Therefore, it is significantly easier to solve than the fully coupled problem, and easier than solving for only velocity and pressure in a coupled manner.

Variational form.

- Tentative velocity step: Find $\tilde{\mathbf{u}}^k \in \mathcal{V}^d$ such that for all $\mathbf{v} \in \mathcal{V}^d$,

$$\left(\rho^{k-1}\frac{\tilde{\mathbf{u}}^k - \mathbf{u}^{k-1}}{\tau}, \mathbf{v}\right) + \left((\mathbf{m}^{k-1} \cdot \boldsymbol{\nabla})\tilde{\mathbf{u}}^k, \mathbf{v}\right) + \left(2\mu^k \mathbf{D}\tilde{\mathbf{u}}^k, \mathbf{Dv}\right) - \left(p^{k-1}, \boldsymbol{\nabla} \cdot \mathbf{v}\right)$$
$$+ \frac{1}{2}\left(\tilde{\mathbf{u}}^k \partial_\tau^- \rho^k, \mathbf{v}\right) - \frac{1}{2}\left(\mathbf{m}^{k-1}, \boldsymbol{\nabla}(\tilde{\mathbf{u}}^k \cdot \mathbf{v})\right) = -\sum_i \left(c_i^{k-1}\boldsymbol{\nabla} g_i^k, \mathbf{v}\right), \quad (101)$$

  with the Dirichlet boundary condition $\tilde{\mathbf{u}}^k = \mathbf{0}$ on $\partial\Omega$.

- Pressure correction step: Find $p^k \in \mathcal{X}$ such that for all $q \in \mathcal{X}$, we have

$$\left(\frac{1}{\rho_0}\boldsymbol{\nabla}(p^k - p^{k-1}), \boldsymbol{\nabla} q\right) = -\frac{1}{\tau}\left(\boldsymbol{\nabla} \cdot \tilde{\mathbf{u}}^k, q\right). \quad (102)$$

16

- Velocity correction step: Then, find $\mathbf{u}^k \in \mathcal{V}^d$ such that for all $\mathbf{v} \in \mathcal{V}^d$,

$$\left(\rho^k \frac{\mathbf{u}^k - \tilde{\mathbf{u}}^k}{\tau}, \mathbf{v}\right) = \left(p^k - p^{k-1}, \boldsymbol{\nabla} \cdot \mathbf{v}\right), \tag{103}$$

which we solve by explicitly imposing the Dirichlet boundary condition on $\mathbf{u}^k = \mathbf{0}$.

Note that using $\mathbf{v} = (\rho^k)^{-1} \boldsymbol{\nabla} q$ in eq. (103) yields, in combination with eq. (102)

$$\left(\boldsymbol{\nabla} \cdot \mathbf{u}^k, q\right) = \tau^2 \left(\left(\frac{1}{\rho^k} - \frac{1}{\rho_0}\right) \boldsymbol{\nabla}(\partial_\tau^- p^k), \boldsymbol{\nabla} q\right), \tag{104}$$

i.e., that the fractional-step scheme introduces a weak compressibility of order $O(\tau^2)$, which becomes increasingly small when $\rho^k \simeq \rho_0$. When the density does not vary with concentration, $\rho^k = \rho_0$ and the final velocity field $\mathbf{u}^k$ is divergence free.

Remark 1. *With a slight reformulation of the variational problem, we can simplify the computation of the velocity steps $\tilde{\mathbf{u}}^k$ and $\mathbf{u}^k$, by solving for each of the components successively, since in the decoupled approach none of the components $\tilde{u}_j^k$ and u_j^k, $j \in \{1, \ldots, d\}$ of $\tilde{\mathbf{u}}^k$ and $\mathbf{u}^k$, respectively, depend on the other components. This simplification is fairly commonplace [44]. We shall leave this technical detail for further work.*

4.3.3. Free energy evolution

Now we set out to show that a free energy inequality is satisfied for a discrete time update.

Lemma 2. *For the hydrodynamic step, the following inequality holds:*

$$\partial_\tau^- F_{\mathrm{NS}}^k \leq - \left\| \sqrt{2\mu^k} \mathbf{D}\mathbf{u}^k \right\|^2 - \sum_i \left(\tilde{c}_i \boldsymbol{\nabla} g_i^k, \mathbf{u}^*\right), \tag{105}$$

where

$$F_{\mathrm{NS}}^k = \begin{cases} F_{\mathbf{u}}^k & \text{for Scheme I,} \\ F_{\mathbf{u}}^k + \frac{\tau^2}{2} \left\| \frac{1}{\sqrt{\rho_0}} \boldsymbol{\nabla} p^k \right\|^2 & \text{for Scheme II.} \end{cases} \tag{106}$$

Here,

$$F_{\mathbf{u}}^k = \int_\Omega \frac{1}{2} \rho^k |\mathbf{u}^k|^2 \mathrm{d}\Omega. \tag{107}$$

Proof. We will first show that eq. (105) holds for Scheme I, and subsequently that it holds for Scheme II.

Scheme I. First, note that eq. (97a) can be written as

$$\left(\rho^{k-1} \frac{\mathbf{u}^k - \mathbf{u}^*}{\tau}, \mathbf{v}\right) + \left((\mathbf{m}^{k-1} \cdot \boldsymbol{\nabla})\mathbf{u}^k, \mathbf{v}\right) + \left(2\mu^k \mathbf{D}\mathbf{u}^k, \mathbf{D}\mathbf{v}\right) - \left(p^k, \boldsymbol{\nabla} \cdot \mathbf{v}\right)$$
$$+ \frac{1}{2}\left(\mathbf{u}^k \partial_\tau^- \rho^k, \mathbf{v}\right) + \frac{1}{2}\left(\mathbf{u}^k \boldsymbol{\nabla} \cdot \mathbf{m}^{k-1}, \mathbf{v}\right) = 0. \tag{108}$$

17

Testing this with $\mathbf{v} = \mathbf{u}^k$ yields:

$$\frac{1}{2\tau}\left\|\sqrt{\rho^k}\mathbf{u}^k\right\|^2 - \frac{1}{2\tau}\left\|\sqrt{\rho^{k-1}}\mathbf{u}^*\right\|^2 = -\left\|2\mu^k\mathbf{D}\mathbf{u}^k\right\|^2 - \frac{1}{2\tau}\left\|\sqrt{\rho^{k-1}}(\mathbf{u}^k - \mathbf{u}^*)\right\|^2, \qquad (109)$$

since

$$\left((\mathbf{m}^{k-1}\cdot\boldsymbol{\nabla})\mathbf{u}^k, \mathbf{u}^k\right) + \frac{1}{2}\left(\mathbf{u}^k\boldsymbol{\nabla}\cdot\mathbf{m}^{k-1}, \mathbf{u}^k\right) = 0. \qquad (110)$$

By considering eq. (77), and taking the inner product of it with $\rho^{k-1}\mathbf{u}^*$, we obtain

$$\frac{1}{2\tau}\left\|\sqrt{\rho^{k-1}}\mathbf{u}^*\right\|^2 - \frac{1}{2\tau}\left\|\sqrt{\rho^{k-1}}\mathbf{u}^{k-1}\right\|^2 = -\sum_i\left(\tilde{c}_i\boldsymbol{\nabla}g_i^k, \mathbf{u}^*\right) - \frac{1}{2\tau}\left\|\sqrt{\rho^{k-1}}(\mathbf{u}^* - \mathbf{u}^{k-1})\right\|^2. \qquad (111)$$

Summing eqs. (109) and (111) yields

$$\partial_\tau^- F_{\mathbf{u}}^k = -\left\|\sqrt{2\mu^k}\mathbf{D}\mathbf{u}^k\right\|^2 - \frac{1}{2\tau}\left\|\sqrt{\rho^{k-1}}(\mathbf{u}^k - \mathbf{u}^*)\right\|^2$$
$$- \sum_i\left(\tilde{c}_i\boldsymbol{\nabla}g_i^k, \mathbf{u}^*\right) - \frac{1}{2\tau}\left\|\sqrt{\rho^{k-1}}(\mathbf{u}^* - \mathbf{u}^{k-1})\right\|^2. \qquad (112)$$

Using eq. (106), this yields eq. (105).

Scheme II. The analysis for this scheme follows the same lines as in the above and closely resembles the lines of Shen and Yang [26].

Testing eq. (101) with $\tilde{\mathbf{u}}^k$ and using the definition of $\mathbf{u}^*$ yields

$$\frac{1}{2\tau}\left\|\sqrt{\rho^k}\tilde{\mathbf{u}}^k\right\|^2 - \frac{1}{2\tau}\left\|\sqrt{\rho^{k-1}}\mathbf{u}^*\right\|^2 + \frac{1}{2\tau}\left\|\sqrt{\rho^{k-1}}(\tilde{\mathbf{u}}^k - \mathbf{u}^*)\right\|^2 + \left\|2\mu^k\mathbf{D}\tilde{\mathbf{u}}^k\right\|^2 = \left(p^{k-1}, \boldsymbol{\nabla}\cdot\tilde{\mathbf{u}}^k\right). \qquad (113)$$

Testing eq. (102) with τp^k yields

$$\left(\boldsymbol{\nabla}\cdot\tilde{\mathbf{u}}^k, p^k\right) = -\tau\left(\frac{1}{\rho_0}\boldsymbol{\nabla}(p^k - p^{k-1}), \boldsymbol{\nabla}p^k\right) \qquad (114)$$

$$= -\frac{\tau}{2}\left\|\frac{1}{\sqrt{\rho_0}}\boldsymbol{\nabla}p^k\right\|^2 + \frac{\tau}{2}\left\|\frac{1}{\sqrt{\rho_0}}\boldsymbol{\nabla}p^{k-1}\right\|^2 - \frac{\tau}{2}\left\|\frac{1}{\sqrt{\rho_0}}\boldsymbol{\nabla}(p^k - p^{k-1})\right\|^2. \qquad (115)$$

Testing eq. (103) with $\tilde{\mathbf{u}}^k$, yields:

$$\frac{1}{2\tau}\left\|\sqrt{\rho^k}\mathbf{u}^k\right\|^2 - \frac{1}{2\tau}\left\|\sqrt{\rho^k}\tilde{\mathbf{u}}^k\right\|^2 - \frac{1}{2\tau}\left\|\sqrt{\rho^k}(\mathbf{u}^k - \tilde{\mathbf{u}}^k)\right\|^2 = \left(p^k - p^{k-1}, \boldsymbol{\nabla}\cdot\tilde{\mathbf{u}}^k\right). \qquad (116)$$

We also have that, from Eq. (100),

$$\left\|\sqrt{\rho^k}(\mathbf{u}^k - \tilde{\mathbf{u}}^k)\right\|^2 = \left\|\frac{1}{\sqrt{\rho^k}}\boldsymbol{\nabla}(p^k - p^{k-1})\right\|^2\tau^2. \qquad (117)$$

Combination of eqs. (111), (113) and (115) to (117) gives

$$\frac{1}{2\tau}\left\|\sqrt{\rho^k}\mathbf{u}^k\right\|^2 - \frac{1}{2\tau}\left\|\sqrt{\rho^{k-1}}\mathbf{u}^{k-1}\right\|^2 + \frac{\tau}{2}\left\|\frac{1}{\sqrt{\rho_0}}\boldsymbol{\nabla}p^k\right\|^2 - \frac{\tau}{2}\left\|\frac{1}{\sqrt{\rho_0}}\boldsymbol{\nabla}p^{k-1}\right\|^2$$
$$= -\frac{\tau}{2}\int_\Omega\left(\frac{1}{\rho_0} - \frac{1}{\rho^k}\right)|\boldsymbol{\nabla}(p^k - p^{k-1})|^2\,\mathrm{d}\Omega - \sum_i\left(\tilde{c}_i\boldsymbol{\nabla}g_i^k, \mathbf{u}^*\right) - \frac{1}{2\tau}\left\|\sqrt{\rho^{k-1}}(\mathbf{u}^* - \mathbf{u}^{k-1})\right\|^2$$
$$- \frac{1}{2\tau}\left\|\sqrt{\rho^{k-1}}(\tilde{\mathbf{u}}^k - \mathbf{u}^*)\right\|^2 - \left\|2\mu^k\mathbf{D}\tilde{\mathbf{u}}^k\right\|^2. \qquad (118)$$

18

The first term on the right hand side is positive, since $\rho_0 \leq \rho^k$. Now, Eq. (105) follows trivially by noting the definition (106). This concludes the proof. □

Remark 2. *Compared to Scheme I, the free energy in Scheme II has an extra $O(\tau^2)$ term related to pressure variations, cf. eq. (106). This is related to the weak numerical compressibility introduced by the splitting approach.*

4.4. Free energy evolution for the combined steps

Lemma 3. *For the schemes presented above, the following free energy inequality holds:*

$$\partial_\tau^- F^k \leq -\frac{1}{\tau} \sum_i \Delta F_{c_i}^k - \left\| \sqrt{2\mu^k} \mathbf{D} \mathbf{u}^k \right\|^2 - \sum_i \left\| \sqrt{\tilde{K}_i} \boldsymbol{\nabla} g_i^k \right\|^2 + \sum_i \left(\tilde{R}_i, g_i^k \right), \qquad (119)$$

where

$$F^k = F_{\mathrm{NS}}^k + F_{\mathrm{EC}}^k. \qquad (120)$$

Proof. This follows directly by summing eqs. (79) and (105). □

For any of the possible schemes considered above, if all $\Delta F_{c_i}^k \geq 0$, the scheme is energy stable, i.e.,

$$\partial_\tau^- F^k \leq 0, \qquad (121)$$

given the approriate boundary conditions and the fact that $\tilde{K}_i^k \geq 0$.

We will now consider approximations $\tilde{\alpha}'(c)$ of the chemical energy $\alpha(c)$ in order to satisfy the condition (121).

4.5. Approximating the chemical energy

In the previous section, several quantities were undefined. We now consider various numerical approximations of the chemical energy derivative $\tilde{\alpha}'$.

Nonlinear discretizations.

NL1 The first option is to use the non-linear approximation

$$\tilde{\alpha}'(c_i^k, c_i^{k-1}) = \frac{\alpha(c_i^k) - \alpha(c_i^{k-1})}{c_i^k - c_i^{k-1}}, \qquad (122)$$

which yields $\Delta F_{c_i}^k = 0$. This gives the least possible dissipation, while still leading to the correct inequality. On the downside, the expression (122) is ill-defined when $|c_i^k - c_i^{k-1}| \ll 1$, and in order not to focus on this issue we will not consider implementations of this approximation in the present paper.

NL2 A second option is to use the non-linear (unless $\alpha'(c) \sim c$) approximation

$$\tilde{\alpha}'(c_i^k, c_i^{k-1}) = \alpha'(c_i^k). \qquad (123)$$

Taylor expansion around c_i^k and the mean value theorem gives

$$F_{c_i}^k - F_{c_i}^{k-1} = \int_\Omega \left[\alpha'(c_i^k)(c_i^k - c_i^{k-1}) - \frac{\alpha''(\xi^k)}{2}(c_i^k - c_i^{k-1})^2 \right] \mathrm{d}\Omega \qquad (124)$$

where $\xi^k \in [\min(c_i^{k-1}, c_i^k), \max(c_i^{k-1}, c_i^k)]$. This gives

$$\Delta F_{c_i}^k = \tau \left(\tilde{\alpha}'(c_i^k, c_i^{k-1}), \partial_\tau^- c_i^k \right) - F_{c_i}^k + F_{c_i}^{k-1} \tag{125}$$

$$= \int_\Omega \frac{1}{2} \alpha''(\xi^k)(c_i^k - c_i^{k-1})^2 \, \mathrm{d}\Omega. \tag{126}$$

Typically, $\alpha''(c) > 0$, such as for a weak solution, where $\alpha(c) = c(\log c - 1)$. The latter leads to the common Nernst–Planck equation for the ion transport. For such a system, where $\alpha''(c) \geq 0$ everywhere, the inequality is satisfied. Note that if $\alpha''(c) < 0$ anywhere, a locally higher ion concentration would be favoured energetically, and effectively we could then have a negative mobility (which is mathematically ill-posed).

Linear discretizations.

L1 Another option is to use the linear approximation

$$\tilde{\alpha}'(c_i^k, c_i^{k-1}) = \alpha'(c_i^{k-1}) + \gamma \alpha''(c_i^{k-1})(c_i^k - c_i^{k-1}). \tag{127}$$

Taylor expansion around c_i^{k-1} and the mean value theorem gives

$$F_{c_i}^k - F_{c_i}^{k-1} = \int_\Omega \left[\alpha'(c_i^{k-1})(c_i^k - c_i^{k-1}) + \frac{\alpha''(c^{k-1})}{2}(c_i^k - c_i^{k-1})^2 + \frac{\alpha'''(\xi^k)}{3!}(c_i^k - c_i^{k-1})^3 \right] \mathrm{d}\Omega, \tag{128}$$

where $\xi^k \in [\min(c_i^{k-1}, c_i^k), \max(c_i^{k-1}, c_i^k)]$. This gives

$$\Delta F_{c_i}^k = \tau \left(\tilde{\alpha}'(c_i^k, c_i^{k-1}), \partial_\tau^- c_i^k \right) - F_{c_i}^k + F_{c_i}^{k-1} \tag{129}$$

$$= \int_\Omega \left[\left(\gamma - \frac{1}{2} \right) \alpha''(c_i^{k-1}) - \frac{\alpha'''(\xi^k)}{3!}(c_i^k - c_i^{k-1}) \right] (c_i^k - c_i^{k-1})^2 \, \mathrm{d}\Omega. \tag{130}$$

If $\gamma > 1/2$ the first term will be positive. For sufficiently small τ, it will dominate over the second term. However, we have *in general* no control over neither sign nor magnitude of the second term.

L2 To circumvent the latter problem, we may introduce a regularization of $\alpha(c)$, denoted by $\bar{\alpha}(c)$. Assuming $\alpha''(c)$ is always positive and monotonously non-increasing, we define

$$\bar{\alpha}''(c) = \alpha''(\max(c, c_\delta)), \tag{131}$$

where c_δ is a small cut-off concentration. Hence $0 \leq \bar{\alpha}''(c) \leq \bar{\alpha}''(c_\delta)$. We use the linear numerical approximation

$$\tilde{\alpha}' = \bar{\alpha}'(c_i^{k-1}) + \left[\gamma \bar{\alpha}''(c_i^{k-1}) + \frac{1}{2} \bar{\alpha}''(c_0) \right] (c_i^k - c_i^{k-1}), \tag{132}$$

where the second term inside the brackets is a stabilizing term of order τ, similar to what was used by Shen and Yang [26] for the case of two-phase flow. We expand around c_i^{k-1}:

$$F_{c_i}^k - F_{c_i}^{k-1} = \int_\Omega \left[\bar{\alpha}'(c_i^{k-1})(c_i^k - c_i^{k-1}) + \frac{\bar{\alpha}''(\xi^k)}{2}(c_i^k - c_i^{k-1})^2 \right] \mathrm{d}\Omega. \tag{133}$$

This gives

$$\Delta F_{c_i}^k = \int_\Omega \left[\gamma \bar{\alpha}''(c_i^{k-1}) + \frac{1}{2} \left(\bar{\alpha}''(c_0) - \bar{\alpha}''(\xi^k) \right) \right] (c_i^k - c_i^{k-1})^2 \, \mathrm{d}\Omega \tag{134}$$

$$\geq \gamma \int_\Omega \bar{\alpha}''(c_i^{k-1})(c_i^k - c_i^{k-1})^2 \, \mathrm{d}\Omega \geq 0, \tag{135}$$

where we have used that $\bar{\alpha}''(c_0) - \bar{\alpha}''(\xi^k) \geq 0$, and that $\gamma \geq 0$, and that $\bar{\alpha}''(c_0)$. Hence, we have derived a linear, and energy stable scheme, which approximates the equations of electrohydrodynamics, given some rather general assumptions on, and a regularization of, $\alpha(c)$. A similar regilarisation was considered recently by Metzger [40].

In order to ensure that the whole electrochemical step is linear, it is necessary to model $\tilde{K}_i$ and $\tilde{c}_i$ to depend on the previous time step. To this end, we will set

$$\tilde{K}_i = \tilde{K}_i(c_i^{k-1}), \quad \text{and} \quad \tilde{c}_i = c_i^{k-1}. \tag{136}$$

We have now considered general numerical schemes for electrohydrodynamics, and it is now necessary to give a brief summary and come with some concrete expressions.

Remark 3. *The regularization defined in eq. (131) can be applied also to the non-linear schemes to ensure that the energy is defined even if concentrations are numerically slightly negative, which might occur in simulations of highly depleted solutions, e.g. simulations of electrokinetic instabilities.*

4.6. Approximating the reaction term

It is in place to approximate the discrete reaction term $\tilde{R}_i$ which enters in (119). This term was modeled in the continuous model in (16) and discussed in Appendix A. Using (16), we can write the discrete version as

$$\tilde{R}_i = -\sum_m \tilde{\mathcal{C}}_m \sum_j \nu_{m,i} \nu_{m,j} g_j^k. \tag{137}$$

Here, the reaction functions $\tilde{\mathcal{C}}_m$ can be modelled as $\tilde{\mathcal{C}}_m = \mathcal{C}_m^k$, i.e. using values from the current step, for a non-linear scheme, or as $\tilde{\mathcal{C}}_m = \mathcal{C}_m^{k-1}$, i.e., using values from the previous step, for a linear scheme. In either case, we have that

$$\sum_i \left(\tilde{R}_i, g_i^k \right) = -\sum_m \left\| \sqrt{\tilde{\mathcal{C}}_m} \sum_i \nu_{m,i} g_i^k \right\|^2 \leq 0, \tag{138}$$

where the last equality holds given that $\tilde{\mathcal{C}}_m \geq 0$. For the remainder of this article, we shall for concreteness assume $\tilde{\mathcal{C}}_m = \mathcal{C}_m^{k-1}$.

4.7. Tentative summary

It is now appropriate to briefly summarize the major results so far.

Theorem 1. *Any decoupled scheme consisting of the combination of Scheme I or Scheme II (for the hydrodynamics), the chemical discretizations NL1, NL2 or L2, and the reaction term formulation (137), is energy stable.*

21

Proof. This follows from Lemma 3 and the results for $\Delta F_{c_i}^k$ in the definitions of the discretizations NL1, NL2, L2 above, along with the result (138) for the source term. □

Remark 4. *Because of the mentioned problem with the chemical discretization L1,* this approximation is not generally energy stable. *The discretization L1 can only be energy stable provided that* $\alpha'''(c) = 0$.

Remark 5. *When all $\Delta F_{c_i}^k \geq 0$, and the source term is modelled as* (137), *the free energy inequality eq.* (119) *becomes*

$$\partial_\tau^- F^k \leq - \left\| \sqrt{2\mu^k} \mathbf{D}\mathbf{u}^k \right\|^2 - \sum_i \left\| \sqrt{\tilde{K}_i} \boldsymbol{\nabla} g_i^k \right\|^2, \tag{139}$$

which bears striking similarity with its continuous counterpart, eq. (68). *In particular, it can be verified that the terms that differ between $\partial_\tau^- F^k$ and $\partial_t F$ are of order $O(\tau)$.*

4.8. Concretization and specification

The analysis thus far has considered quite general forms of the chemical energy α, that we have presented energy-stable approximations of, the mobility $\tilde{K}_i$, and the chemical concentration $\tilde{c}_i$. To be more specific, we therefore consider concrete forms of the undefined approximations that will be discretized and tested numerically.

4.8.1. Chemical energy function, mobility and permittivity assumptions

We consider the Nernst–Planck equation for solute transport. For the continuous equations, this imparts the following:

$$\alpha(c_i) = c_i(\ln c_i - 1), \quad \text{and} \quad K_i(c_i) = D_i c_i, \tag{140}$$

where D_i is the diffusion coefficient of ion species i. This corresponds to dilute ionic solutions. Since $\alpha'(c) = \ln c$ is undefined when $c \to 0$, we can regularize α below a small cut-off c_δ, as outlined above. Then, in the next time step, we assign $c_i^{k-1} \leftarrow \max(c_i^{k-1}, c_\delta)$. An examplary regularisation of the functional form $\alpha(c) = c(\ln c - 1)$ is shown in Fig. 1. The regularised functional forms are:
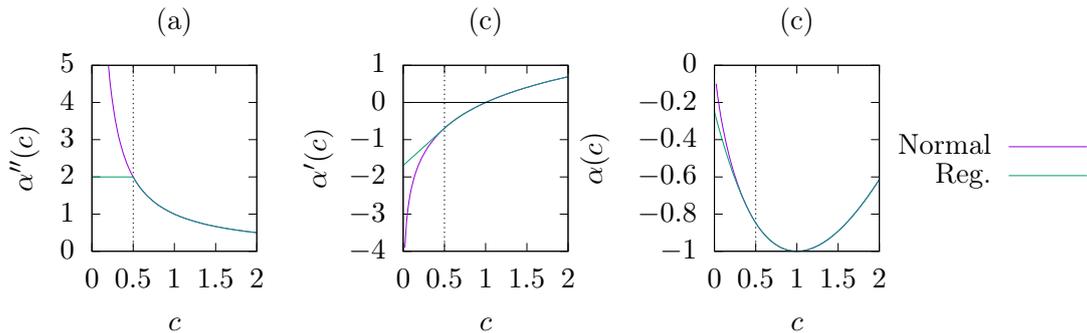
Figure 1: Regularisation of the chemical energy function $\alpha(c) = c(\ln c - 1)$, with the artificially high cutoff concentration $c_\delta = 0.5$ for visual clarity. The cutoff concentration is indicated by a dotted vertical line.

22

$$\bar{\alpha}''(c) = \frac{1}{\max(c, c_\delta)}, \tag{141}$$

$$\bar{\alpha}'(c) = \begin{cases} \ln c & \text{for} \quad c > c_\delta, \\ \ln c_\delta + \frac{c}{c_\delta} - 1 & \text{for} \quad c \leq c_\delta, \end{cases} \tag{142}$$

$$\bar{\alpha}(c) = \begin{cases} c(\ln c - 1) & \text{for} \quad c > c_\delta, \\ c(\ln c_\delta - 1) + \frac{c^2 - c_\delta^2}{2c_\delta} & \text{for} \quad c \leq c_\delta. \end{cases} \tag{143}$$

The same regularisation was assumed by Metzger [40].

Further, we will for simplicity assume in our simulations that the permittivity does not depend on the concentrations. Nevertheless, the schemes themselves support energy stability also in this case.

4.8.2. Schemes used in simulations

We define now the different schemes that will be used in simulations, and the associated approximations to (140) that will be used. In general, the approximations should be chosen to impart soluble equation systems, i.e., for which the finite element method yields spatial convergence.

We will in this work focus on the following discretizations:

NL2 Since the discretization NL2 is non-linear, it is necessary to use e.g. a Newton solver, where the matrices will be reassembled at each iteration, to solve this step. A weak coupling between the Nernst–Planck and Poisson equations can be obtained by

$$\tilde{K}_i = D_i c_i^{k-1} \quad \text{and} \quad \tilde{c}_i = c_i^{k-1}. \tag{144}$$

L2 The linear discretization in L2 imparts the following:

$$\tilde{K}_i = D_i \max(c_i^{k-1}, c_\delta) \quad \text{and} \quad \tilde{c}_i = c_i^{k-1}. \tag{145}$$

Without further ado, we might set $\gamma = 0$ to minimize the dissipation in this scheme.

Remark 6. *A stronger coupling between the Nernst–Planck and Poisson equations in the non-linear scheme NL2, could be obtained by letting $\tilde{K}_i = D_i c_i^k$ and $\tilde{c}_i = c_i^k$. In general, we cannot control the sign of $\tilde{K}_i$ here, since we solve for c_k. Hence, if c_k becomes (numerically) negative, we are not guaranteed to dissipate energy (but then the energy is not defined either). This issue could possibly be mitigated by a regularization.*

5. Numerical simulations

We have in the previous section shown how various discretization schemes satisfy a free energy inequality, which is also present in the models they are meant to approximate. In this section we proceed to show and compare the effectiveness of these schemes. The schemes have been implemented and simulations are carried out within the *Bernaise* framework, developed by the authors [45]. Bernaise is a flexible simulation environment for two-phase electrohydrodynamic flow, which is built on top of the Dolfin [46] interface to Python within the finite element framework Fenics [47]. As single-phase flow is a special case of two-phase flow, it works equally well for single-phase flow, which we consider in this paper. For all simulations we use triangular meshes and piecewise

quadratic (P2) finite elements for the velocity field, and piecewise linear (P1) elements for the remaining fields. We use meshes that resolve the spatial problem sufficiently well for the error to be dominated by the time discretization errors.

In the following, we consider simulations of a few interesting cases.

- First, to test the accuracy of the schemes, we consider the convergence towards an analytic solution.

- Second, to demonstrate the energy stability of the schemes, we consider an isolated, closed system of a concentration spreading in a charged cell. We display the various terms in the free energy and compare the various schemes evolving in time, with varying time step τ.

- Third, we consider a reaction cell to test the reaction part of the numerical schemes.

- Fourth, we show for a system the efficiency of the schemes to approach a steady state in an open complex geometry (porous medium) where energy is injected through a body force.

The schemes we consider are denoted by the following:

- **I-NL2:** Scheme I with the non-linear NL2 discretization.

- **I-L2:** Scheme I with the linear L2 discretization.

- **II-NL2:** Scheme II with the non-linear NL2 discretization.

- **II-L2:** Scheme II with the linear L2 discretization.

5.1. Accuracy test: Manufactured solution

Now we verify the accuracy of the schemes by inspecting whether the scheme converges to a manufactured analytical solution. Taylor–Green flow is one of a few cases for the Navier–Stokes equations where analytical solutions are available, and is therefore standard to use for validation purposes. To this end, we consider a two-dimensional Taylor–Green flow extended to account for electrohydrodynamics. The derivation of this manufactured solution is given in Appendix B. We consider flow of two counterions $i = \pm$, such that $z_\pm = \pm 1$, and assume constant density, viscosity, and permittivity, and neglect gravity.

We consider the double periodic domain $\mathbf{x} \in [0, 2\pi] \times [0, 2\pi]$, where the pressure p and the electric potential V is set to zero at $\mathbf{x} = (\pi/4, \pi/4)$ to fix the pressure and potential gauges, respectively. We obtain an analytical solution augmenting eq. (7) with the source term q on the right hand side, where

$$q(x, y) = \frac{Dc_0^2 C^2(t)}{2\epsilon} \left[\cos 2x + \cos 2y + 2 \cos 2x \cos 2y \right]. \tag{146}$$

The analytical solution to this Taylor–Green vortex is given by:

$$\mathbf{u} = U(t)(\hat{\mathbf{x}} \cos x \sin y - \hat{\mathbf{y}} \sin x \cos y), \tag{147}$$

$$p = -\frac{1}{4} \left(\rho_0 U^2(t) + \frac{c_0^2 C^2(t)}{\epsilon} \right) (\cos 2x + \cos 2y) - \frac{c_0^2 C^2(t)}{4\epsilon} \cos 2x \cos 2y \tag{148}$$

$$c_\pm = c_0(1 \pm \cos x \cos y \, C(t)) \tag{149}$$

$$V = -\frac{c_0}{\epsilon} \cos x \cos y \, C(t) \tag{150}$$

24

where

$$U(t) = \exp(-2\mu t/\rho_0), \tag{151}$$

$$C(t) = \chi \exp\left(-2D\left(1 + \frac{c_0}{\epsilon}\right)t\right). \tag{152}$$

A constraint ensuring that $c_\pm > 0$ is $0 \leq \chi < 1$. The parameters used in these simulations are $\rho = 3$, $\mu = 2$, $D = 2$, $c_0 = 1$, $\epsilon = 2$, and $\chi = 0.5$. Further, we stop the simulation after a final time $T = 0.25$, and measure the error norm respective to the analytical solution. In Fig. 2, we show
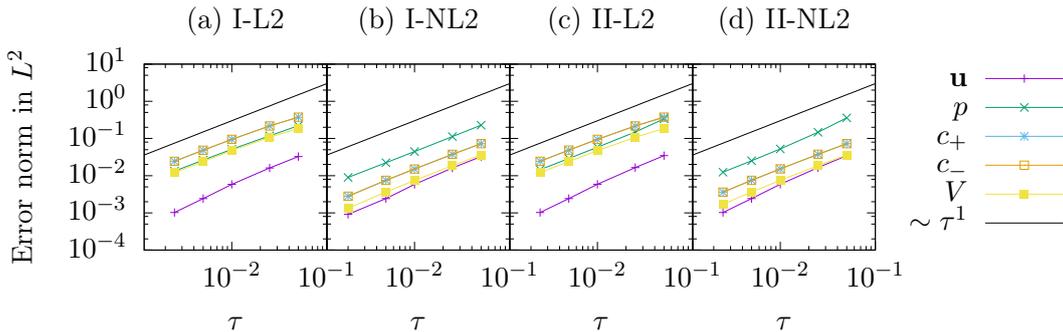
Figure 2: Temporal convergence of the schemes considered in the electrohydrodynamic Taylor–Green vortex case. The plots (a)–(d) show the L^2 error norm for the various schemes for all fields compared to the reference analytical solutions as a function of time step τ. The simulations are in good compliance with the theoretical first-order convergence prediction, indicated as a black solid slope (same in all plots).

convergence in the L^2 error norm for the four schemes considered. Schemes I and II are virtually indistingushable. The errors are about an order of magnitude smaller for the nonlinear NL2 scheme than for the linear L2 scheme, which not unexpected as the NL2 provided a better approximation of the derivative of α. Nonetheless, all schemes seem to be reliable in that they achieve the expected $O(\tau)$ convergence.

5.2. Stress test: Ion spreading in a charged reservoir

To numerically test the energy stability of the schemes in a complex and challenging setting, we construct a system setup where the individual contributions to the free energy from inertia, chemistry and electrostatics are of comparable magnitude during the simulation. The aim of this system is not to be physically realistic, but to reveal possible weaknesses of the schemes. We consider a fixed domain $\Omega = [0,1] \times [0,2]$, which could represent a microchannel. The geometry and initial state is sketched in Fig. 3.

On the lower boundary, we assume a uniform surface charge σ_e, and the upper boundary is assumed to be grounded, i.e. $V = 0$. The left and right boundary are assumed to be insulators. All four walls are subject to no-slip boundary conditions on the velocity, $\mathbf{u} = \mathbf{0}$. We consider an initial state where a Gaussian concentration profile of negatively charged species is placed above, and the same profile of positively charged species is placed below the center of the microchannel.

The electrochemical interaction between the upper and lower boundaries and the two species in the bulk leads to motion due to two mechanisms. The fluid regions with positive and negative charge are pulled (i) towards each other, and most prevalently, (ii) attracted towards opposite ends of the reservoir. This creates a flow in the system which eventually decays due to dissipation.

25
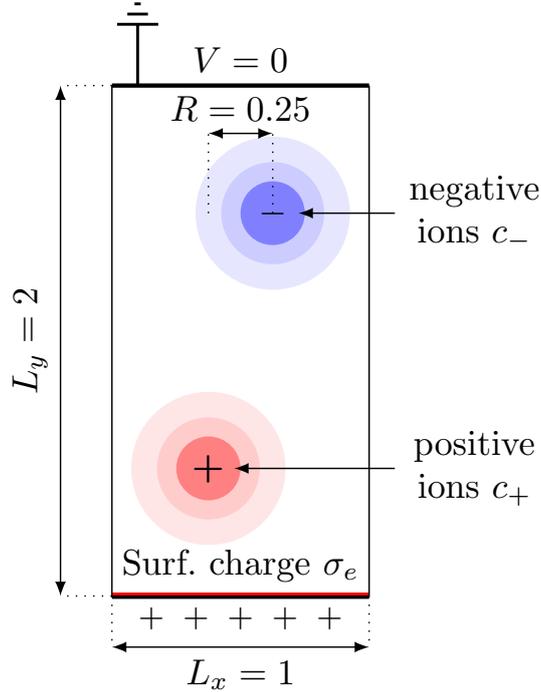
Figure 3: Schematic set-up of the initial state in the test case of ion spreading in a charged reservoir.

The simulation parameters are listed in Table 1. Note that we have assumed here a linear dependency of the viscosity upon the concentrations, i.e.,

$$\mu(c_\pm) = \mu_0 + \frac{\partial \mu}{\partial c_+}c_+ + \frac{\partial \mu}{\partial c_-}c_-, \tag{153}$$

where the constant coefficients $\partial \mu / \partial c_\pm$ are given in Table 1. Chosing $\partial \mu / \partial c_\pm \geq 0$ ensures that the viscosity is always positive. We have also assumed a dependency of the density upon the concentration, given through the parameters $\partial \rho / \partial c_\pm > 0$.

In Fig. 4 we show snapshots from a simulation of this system at several instances of time. The corresponding total free energy contributions, integrated over the domain, are shown in Fig. 5. Here, we have compared the two chemical discretization strategies L2 and NL2, and two time step sizes. From the latter figure, it is evident that the schemes approach the same equilibrium state regardless of the time step size τ and discretization. We observe that the increased dissipation due to a larger time step size results in lower fluid speed, which in turn leads to delayed equilibration. Moreover, as expected, the linear L2 scheme is more dissipative than the NL2 scheme and requires much a smaller time step to produce a reliable kinetic energy development, cf. Fig. 5. Nonetheless, the schemes always decrease the total free energy in every time step, as expected.

Table 1: Parameters used in the case of ion spreading in a reservoir.

Parameter	Symbol	Value
Base density	ρ_0	1.0
Base dynamic viscosity	μ_0	0.08
Diffusivity	D	0.01
Permittivity	ϵ	0.5
Surface charge	σ_e	1.0
Density per concentration	$\partial\rho/\partial c_\pm$	0.02
Dyn. viscosity per concentration	$\partial\mu/\partial c_\pm$	0.001
Solute mass	C_0	3.0
Initial spread of concentration (std. dev.)	R	0.25
Width of domain	L_x	1
Height of domain	L_y	2
Horizontal displacement of initial conc.	ℓ_x	0.125
Vertical displacement of initial conc.	ℓ_y	0.5
Total simulation time	T	10
Cut-off concentration (L2)	c_δ	0.1

5.3. Reaction cell

To verify the modelling and implementation of the reaction term, we now simulate a reaction cell test case. We consider the simple reaction

$$\text{A}^+ + \text{B}^- \rightleftharpoons \text{AB}. \tag{154}$$

We define $c_{\text{A}^+}, c_{\text{B}^-}$ and c_{AB} to be the associated concentrations. The associated stoichiometric coefficients are now $\nu_{\text{A}^+} = \nu_{\text{B}^-} = -1$ and $\nu_{\text{AB}} = 1$. We let the reference concentrations (at equilibrium) be defined by $c_{\text{A}^+}^0 = c_{\text{B}^-} \equiv c^0 = 3$ and $c_{\text{AB}} = 1$. We consider reaction kinetics as the example discussed in Appendix A, i.e.,

$$\mathcal{C} = \mathcal{C}_0 \frac{e^{g_{\text{AB}}} - e^{-g_{\text{A}^+} - g_{\text{B}^-}}}{g_{\text{AB}} - g_{\text{A}^+} - g_{\text{B}^-}}, \tag{155}$$
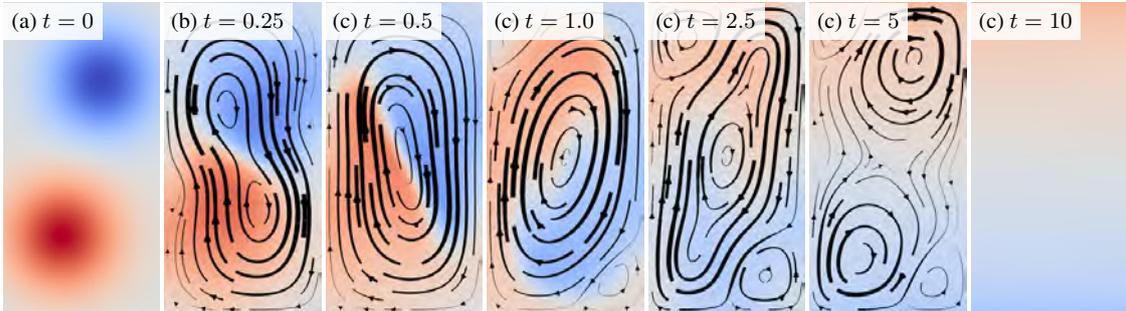
Figure 4: Snapshots in time of the ion spreading simulation case. The flow lines are normalized for each simulation and omitted in the first and last snapshots. The color indicates the net charge, red is positive, blue is negative, and gray is neutral. The related color scale is normalized for the entire simulation. For this simulation, Scheme II-NL2 with a time step $\tau = 0.005$ was used.

27
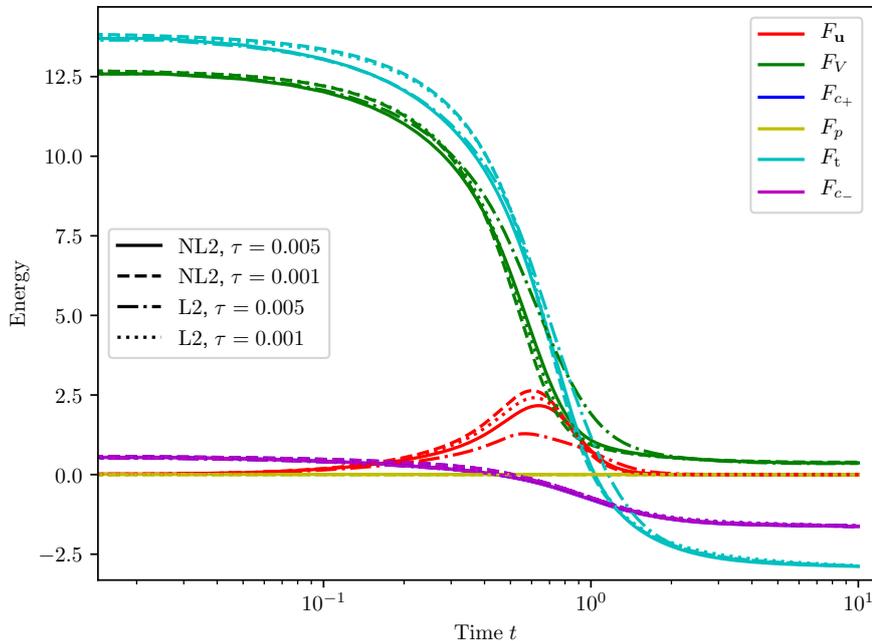
Figure 5: Free energy in time. All simulations are done using fractional step hydrodynamics, i.e., Scheme II.

which is a generalization of the law of mass action. Here, $\mathcal{C}_0$ is a constant coefficient. The same reaction kinetics was considered, e.g., by Campillo-Funollet et al. [41], Metzger [40]. Hence, in equilibrium, we should have

$$g_{AB} - g_{A^+} - g_{B^-} = 0, \quad \text{which gives} \quad \frac{c_{A^+} \cdot c_{B^-}}{c_{AB}} = \frac{\left(c^0\right)^2}{c_{AB}^0} = K_{sp}^{-1} = 9. \tag{156}$$

We consider a domain $\Omega = [-0.5, 0.5] \times [-0.5, 0.5]$, where we start out the simulation with a Gaussian distribution of neutral species AB centered at $(0,0)$ and with a standard deviation $R = 0.15$. At the bottom boundary we apply a surface charge σ_e, and the top boundary is grounded. At the left and right boundary we apply no-flux conditions, and all boundaries are subject to the no-slip condition on the velocity field. We take the initial average concentration of the chemical species AB in the domain to be $c_0 = 10$. The other ions are set to a (negligibly) low concentration $c_{A^+} = c_{B^-} = 10^{-4}$. Hence, in the absence of an applied electric field, the uniform equilibrium concentrations should be $c_{A^+} = c_{B^-} = 6$ and $c_{AB} = 4$.

The equilibrium state with an applied electric field is also possible to find quasi-analytically. The solution will thus only depend on the vertical coordinate y. We consider a domain $y \in [-\ell, \ell]$. At equilibrium, the electrochemical potentials must be constant:

$$g_i = \ln\left(\frac{c_i(y)}{c_i^0}\right) + z_i V(y) = \text{const.} \tag{157}$$

Without loss of generality, we take the electrostatic potential $V(y)$ to be antisymmetric about $y = 0$ (and thus omit the grounded boundary condition at the top). Thus, $V(0) = 0$. Further,

28

due to symmetry, the concentrations $c_{A^+}(0) = c_{B^-}(0) \equiv \bar{c}$ (const.) here. Therefore, the constant $g_i = \ln\left(\bar{c}/c_i^0\right)$ for $i \in \{A^+, B^-\}$, and

$$c_i(y) = \bar{c}e^{-z_i V(y)} \quad \text{for} \quad i \in \{A^+, B^-\}. \tag{158}$$

The neutral concentration will be uniform, i.e., $c_{AB} = K_{sp}\bar{c}^2$. This gives, in the Poisson equation,

$$\epsilon\frac{d^2 V}{dy^2} = -c_{A^+} + c_{B^-} = 2\bar{c}\sinh(V), \tag{159}$$

where we still need to determine the value of the unknown constant $\bar{c}$.

The average number of ions must be conserved. We started out with an average concentration c_0 of only AB which contains both A^+ and B^-. Conservation of both ions can, e.g., be written as:

$$c_{AB} + \frac{1}{2\ell}\int_{-\ell}^{\ell}\frac{c_{A^+} + c_{B^-}}{2}dy = c_0, \tag{160}$$

since we have already assumed that that the total number of ions of A^+ and B^- is equal. Inserting for c_{AB} and c_{A^+}, c_{B^-}, we get

$$K_{sp}\bar{c}^2 + \bar{c}\int_{-\ell}^{\ell}\cosh(V)\,dy = c_0. \tag{161}$$

The charged boundary condition can be written as

$$\frac{dV}{dy} = -\frac{\sigma_e}{\epsilon} \tag{162}$$

at both the upper and the lower boundary. We thus have to solve the nonlinear Poisson–Boltzmann equation (159) with the Neumann boundary conditions (162) coupled with the integral (161). This can be done numerically with standard ordinary differential equation solvers.

With the chosen parameters, we obtain $F_V = 1.5516$, $F_{c_{A^+}} = F_{c_{B^-}} = -0.6890$ and $F_{c_n} = 0.9927$. We choose also the dynamic parameters $D = 0.01$, $\mathcal{C}_0 = 10$, $\partial\rho/\partial c_{A^+} = \partial\rho/\partial c_{B^-} = 0.1$, $\partial\rho/\partial c_{AB} = 0.2$, $\partial\mu/\partial c_{A^+} = \partial\mu/\partial c_{B^-} = 0.02$, $\partial\mu/\partial c_{AB} = 0.04$, a time step $\tau = 0.01$ and a total simulation time $T = 10$. In Fig. 6 we demonstrate how the energy decays towards these values for the scheme II-NL2. As shown in the inset, the values are fairly close to the equilibrium values although we have not simulated many diffusive time scales. Therefore the (total) chemical energy is slightly above the equilibrium values. The other schemes yield similar results, but are omitted in the figure for visual clarity.

5.4. Application: Electrohydrodynamic flow in a charged porous medium

Finally, we test the applicability of the schemes in a case where energy is injected into the system. The overall discrete free energy inequality will then be broken. Energy stable schemes are nevertheless useful, since the dissipation guarantee in the bulk will still hold. The departure from global energy dissipation will be controlled by the flux through the inlet and the outlet of the system.

We consider flow in a two-dimensional domain $\Omega = \{(x, y) \in [-L_x/2, L_x/2] \times [-L_y/2, L_y/2]\}$, where L_x, L_y are domain size along the x, y directions, respectively, and $L_x > L_y$. The domain is taken to be periodic in the y-direction. Within the domain, there are $N = 8$ circular obstacles with
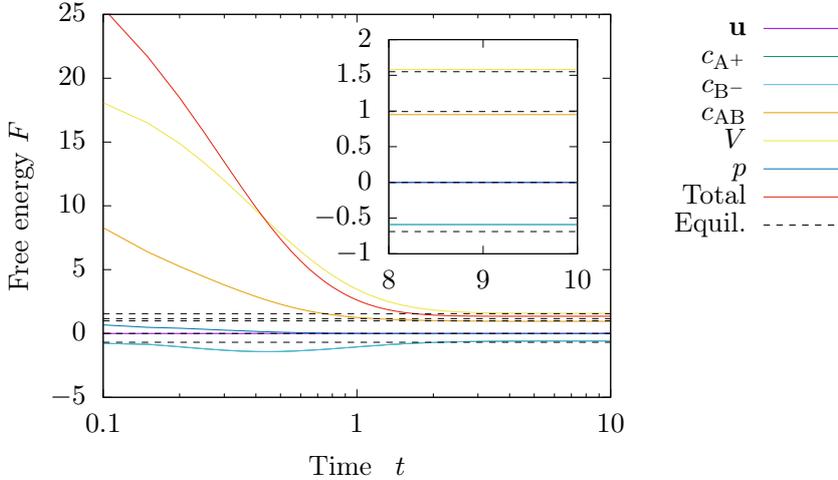
Figure 6: Free energy in time for the reaction cell simulation case. These simulations were carried out using Scheme II-NL2. The inset shows a close-up of the data (except the total energy, for clarity).

radius R placed randomly within the subdomain $[-L_y/2, L_y/2] \times [-L_y, L_y/2]$, but no closer to any other obstacle than R. We assume the no-slip boundary condition, $\mathbf{u} = \mathbf{0}$, on the obstacles, and $p = 0$ on left and right boundaries. The flow is driven by an average pressure gradient, implemented as a uniform body force $\mathbf{f}_b = f_b \hat{\mathbf{x}}$. Further, a constant concentration $c_+ = c_- = c_0$ is assumed at both inlet and outlet. The left side is grounded, $V = 0$, and on the right side we assume a no-flux condition on the electric field, $\hat{\mathbf{n}} \cdot \boldsymbol{\nabla} V = 0$. These boundary conditions are fairly standard in this kind of computation [17, 18, 14].

We will now compare the time-dependent solution using the schemes presented herein to the steady-state solution provided by the independently developed solver presented in a companion paper [14]. The simulations parameters are given in Table 2. A fine mesh size $h = 0.25$ was used to minimize errors from the spatial discretization. Based on the resulting maximum velocity $U \simeq 3 \cdot 10^{-1}$, the pore radius R, and the kinematic viscosity μ/ρ, we can estimate the Reynolds number to be $\mathrm{Re} = \rho U R/\mu \simeq 0.02$. Further, the Schmidt number can be estimated to $\mathrm{Sc} = \mu/(\rho D) \simeq 100$, and Péclet number $\mathrm{Pe} = U R/D = \mathrm{Re} \cdot \mathrm{Sc} \simeq 2$. We can also estimate the Debye length in these units to be $\lambda_D = \sqrt{\epsilon/(2c_0)} \simeq 1.5$, i.e., the dimensionless Debye length to pore size is $\lambda_D/R \simeq 0.5$.

The steady-state solver was run with the same settings as the time-dependent solver, only differing in the fact that the velocity field is periodic also in the x-direction (while the ionic system is finite in the x-direction), and that the inertial term is completely ignored ($\mathrm{Re} = 0$). Hence, this steady-state should represent a minimum of dissipation. The electric potential of the steady-state solver is presented in Fig. 7 and the velocity field is shown in Fig. 8.

In Fig. 9, we measure in time the potential at the right boundary, i.e. the streaming potential, as a function of time, obtained with the various time-dependent schemes. Also plotted is the reference streaming potential obtained with the steady-state solver. The total simulation time is $T = 50$. We may define a diffusive time scale τ_D based on the Debye length, $\tau_D = \lambda_D^2/D \simeq 5$; hence we have simulated here over about 10 of this diffusive time scale. This time scale may be present in the fast decay seen in the initial stages in Fig. 9. From Fig. 9, it is clear that the time step τ has a relatively strong effect on the resulting streaming potential. In particular, the $O(\tau)$ dissipative term that will

30

Table 2: Parameters used in the simulations presented here.

Parameter	Symbol	Value
Domain length along x	L_x	60
Domain length along y (periodic direction)	L_y	30
Number of obstacles	N	8
Obstacle radius	R	3.0
Concentration	c_0	1
Surface charge	σ_e	-5
Density	ρ	0.02
Dynamic viscosity	μ	4.5
Permittivity	ϵ	4.5
Diffusivity of ions	D	0.457
Average pressure gradient	f_b	0.09
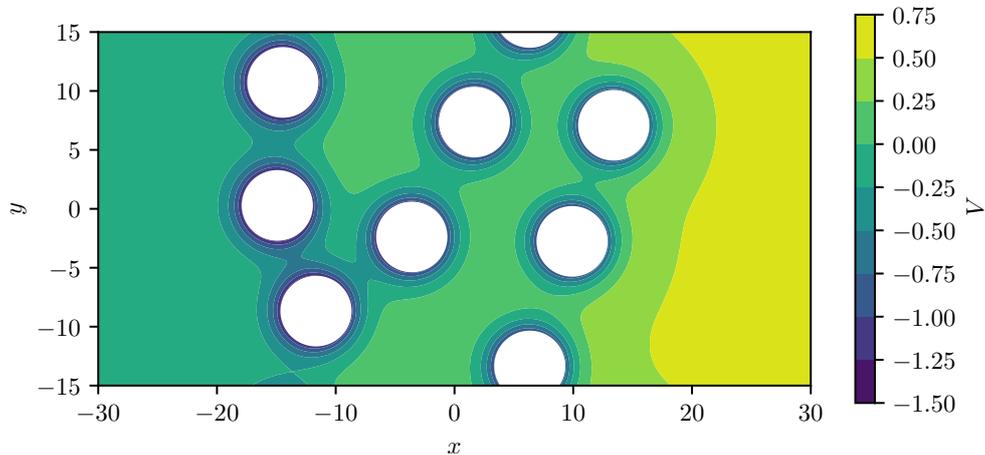
Figure 7: Steady state electric potential for the case of electrohydrodynamic flow in a porous medium.

be present in the steady state, due to the presence of $\mathbf{u}^*$ in the scheme, has consequences also for the streaming potential. Hence, good agreement is only found for relatively fine time steps. Finally, we conclude from this figure that the linear EC scheme L2 is less precise than the NL2 scheme, and hence NL2 may be required for this type of computation. For this particular problem, there does not seem to be a pronounced difference between the coupled and the splitting scheme.

6. Discussion and conclusion

The contribution of the work presented here is twofold. Firstly, we have presented a general model for single-phase electrohydrodynamic flows, where the fluid properties are allowed to depend on the concentrations of ions. Secondly, we have proposed discretization strategies for the resulting set of equations. The proposed schemes impart decoupled computation of electrochemistry and hydrodynamics, while still satisfying the same free energy inequality as the underlying model.

The results presented allow for the following discussion.
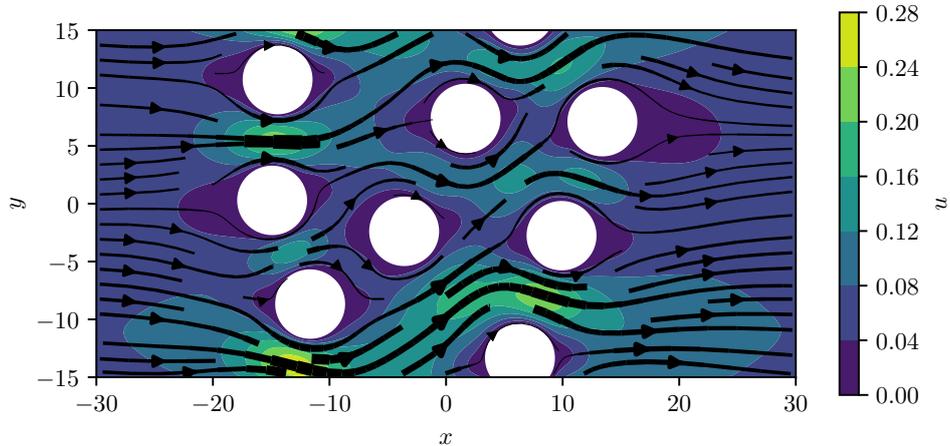
Figure 8: Steady-state velocity field for the case of electrohydrodynamic flow in a porous medium.

- The model presented in this work is fairly general, and provides a consistent way of including permittivity gradients, gravitational effects and vscosity dependence on salinity in simulations of electrohydrodynamics. This also imparts that the model can be used to study simplified systems, such as the effects of salinity gradients in the absence of electric fields. Further, the effects of non-constant density and permittivity can be included in studies of electrokinetic instabilities beyond the Boussinesq approximation.

- The limitations of the model are (i) that we have assumed quasi-incompressibility (solenoidal velocity field), and (ii) that we have assumed isothermal flow. The first assumption is commonplace even beyond the Boussinesq approximation, see e.g., [48, 49]. The second is standard in electrokinetics.

- Dependence on the electric field strength, in particular for the permittivity, has been ignored in the model, although studies indicate that it might be significant at high field strengths [11, 43]. It is in principle trivial to include this effect by letting ϵ be a function of $|\mathbf{E}|^2$ (as well as $\{c_i\}$) in (27).

- The decoupling strategy is highly efficient, in the sense that it permits the use of specialized numerical routines for the resulting subproblems. Hence, the schemes hould facilitate efficient simulations of electrohydrodynamic flows in arbitrary complex geometries.

- In particular, the fractional-step method (Scheme II) for the hydrodynamics leads to significant speed-up compared to the coupled hydrodynamics (Scheme I). Combined with the linear chemical discretization L2, which is based on a regularisation and a stabilization of the chemical potential, it yields a completely linear scheme that can be solved at each time step.

- Since the velocity field will typically have to be resolved with a higher spatial order than the pressure field (e.g., P2-P1 elements for the mixed problem) to deal with the Babuszka–Brezzi condition [50], the main computational cost may still be associated with computing the velocity field. In these cases, choosing a nonlinear chemical discretization (e.g., NL2) might be worthwhile, as it gives a more accurate solution while not contributing significantly to the computational runtime. The results shown in Sec. 5.4 underpin this observation.

32
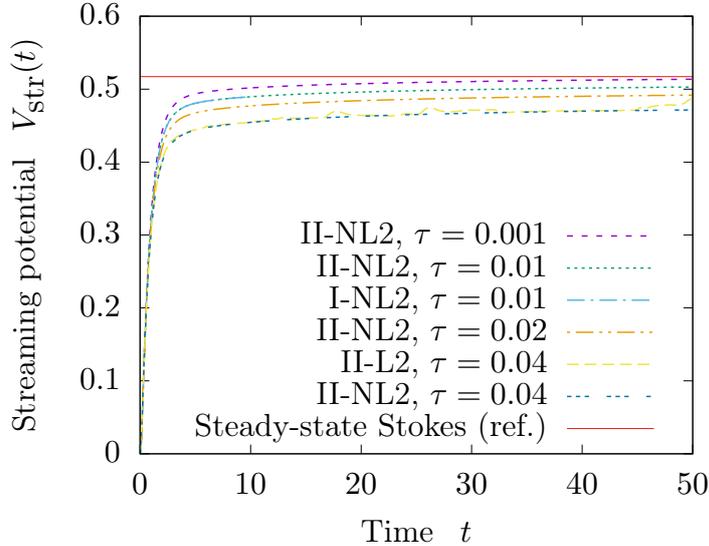
Figure 9: We show the time-development of the streaming potential, comparing the time-dependent solution $V(t)$ to the reference steady-state solution V_{ref} obtained by the method presented in [14]. The time-dependent solution relaxes exponentially to the steady-state solution.

- The decoupling between electrochemistry and hydrodynamics introduces a time step restriction (related to the Courant number), since the advective term in the chemical transport equation is integrated explicitly. Thus, fully implicit methods will possibly be more stable, allowing larger time steps, and may for certain applications be more efficient.

- The work presented here, in particular related to the numerical schemes, builds on many known results from the literature, e.g. [31, 32, 39, 26, 40]. A main novelty in the present work is to combine the results on chemical potential stabilization and fractional schemes known from phase-field simulations of two-phase flows [26] with electrochemical gradients [39, 40]. Further, these methods have been adapted to the case where fluid properties depend on concentrations rather than an order parameter (phase) field.

- Rigorously proving existence of solutions and convergence of the proposed numerical schemes is a challenge that has not been undertaken in the present work. Progress here could be made along the lines of related work, see e.g., Ref. [26, 40].

In future work, the model and scheme should be generalized to multiphase systems. In particular, this would impart a combination of the present work and the model by Campillo-Funollet et al. [41]. To simulate solid-liquid interaction, the geometry could be described by a phase field which could evolve due to chemical reactions at the interface, i.e., the function $\mathcal{C}$ could be nonzero only here. Then phase transformations from solute to could occur only at the phase field interface and proportionally (or another functional dependence) to the concentration of a given species. This could provide a refinement to other studies [51, 52].

A more challenging, but highly physically relevant, extension of the model would be to extend it to encompass non-isothermal flow and non-solenoidal velocity fields. This would require a derivation taking into account entropy production rather than free energy dissipation. Non-solenoidal velocity

33

fields would also require more sophisticated numerical schemes for reliable and efficient simulation.

Appendix A. Modelling the reaction terms

The reaction term R_i remains to be modelled, and the dissipation related to the reaction is given by (cf. (42))

$$\sum_i \int_\Omega g_i R_i \, d\Omega. \tag{A.1}$$

We consider a set of M possible reactions including all N chemical species, where we can write the reactions in the following way:

$$\nu_{1,1}\chi_1 + \ldots + \nu_{1,N}\chi_N \rightleftharpoons 0,$$

$$\vdots$$

$$\nu_{M,1}\chi_1 + \ldots + \nu_{M,N}\chi_N \rightleftharpoons 0,$$

where χ_i symbolizes the chemical species, and ν_i is the corresponding *net* stoichiometric coefficent. The latter is such that $\nu_i > 0$ for (net) products and $\nu_i < 0$ for (net) reactants. If the chemical species does not enter into the reaction, $\nu_i = 0$. More compactly, we can write

$$\sum_i \nu_{m,i}\chi_i \rightleftharpoons 0, \quad \forall m \in [1, M]. \tag{A.2}$$

Note that due to charge conservation in a reaction, $\sum_i z_i \nu_{m,i} = 0$ and due to mass conservation in a reaction, $\sum_i \nu_{m,i} \partial \rho / \partial c_i = 0$, for all reactions m. For each reaction m we have a reaction rate $\mathcal{R}_m$. The reaction source term that enters in the concentration equation of species i, can be written as

$$R_i = \sum_m \nu_{m,i} \mathcal{R}_m. \tag{A.3}$$

Now, what remains is to define $\mathcal{R}_m$ on physical grounds. We have from statistical mechanics that in equilibrium, the reaction (A.2) is given by

$$\sum_i \nu_{m,i} g_i^0 = 0, \tag{A.4}$$

where the superscript "0" indicates *local* equilibrium. This suggests that a form

$$\mathcal{R}_m = -\mathcal{C}_m \cdot \sum_i \nu_{m,i}(g_i - g_i^0) = -\mathcal{C}_m \cdot \sum_i \nu_{m,i} g_i, \tag{A.5}$$

where $\mathcal{C}_m \geq 0$, should drive the species towards equilibrium; in the sense that

- a term with $g_i > g_i^0$ should promote generation of more reactants ($\nu_{m,i} < 0$) and less products ($\nu_{m,i} > 0$),

- a term with $g_i < g_i^0$ should push towards less reactants and more products, and

- a term with $g_i = g_i^0$ should not contribute.

Inserting (A.3) and (A.5) into (A.1),

$$\sum_j \int_\Omega g_j R_j \, \mathrm{d}\Omega = -\sum_m \mathcal{C}_m \sum_i \sum_j \int_\Omega g_j \nu_{m,j} \nu_{m,i} g_i \, \mathrm{d}\Omega \tag{A.6}$$

$$= -\sum_m \mathcal{C}_m \int_\Omega \left(\sum_i \nu_{m,i} g_i \right)^2 \mathrm{d}\Omega \leq 0, \tag{A.7}$$

which is clearly dissipative.

Note that in general, no assumptions were made about $\mathcal{C}_m$ except that it should be nonnegative. For dilute systems described by the classical Nernst–Planck equations this is in general satisfied. Here, $g_i = \ln c_i - \ln c_i^0 + z_i V$, and in general, we can model by statistical rate theory:

$$\mathcal{R}_m = -k_{\mathrm{b},m} \prod_{\nu_{m,i}>0} c_i^{\nu_{m,i}} + k_{\mathrm{f},m} \prod_{\nu_{m,i}<0} c_i^{-\nu_{m,i}} \tag{A.8}$$

$$= \left[-k_{\mathrm{b},m} \prod_{\nu_{m,i}>0} (c_i^0)^{\nu_{m,i}} e^{\sum_{\nu_{m,i}>0} g_i \nu_{m,i}} + k_{\mathrm{f},m} \prod_{\nu_{m,i}<0} (c_i^0)^{-\nu_{m,i}} e^{-\sum_{\nu_{m,i}<0} g_i \nu_{m,i}} \right] e^{-\sum_{\nu_{m,i}>0} z_i \nu_{m,i} V}. \tag{A.9}$$

Here, $k_{\mathrm{f},m]}$ is the forward reaction rate and $k_{\mathrm{b},m}$ the backward rate. The references c_i^0 are defined through the equilibrium condition

$$0 = -k_{\mathrm{b},m} \prod_{\nu_{m,i}>0} (c_i^0)^{\nu_{m,i}} + k_{\mathrm{f},m} \prod_{\nu_{m,i}<0} (c_i^0)^{-\nu_{m,i}}, \tag{A.10}$$

which relates to the solubility product K_{sp} through the law of mass action,

$$K_{\mathrm{sp},m} = \frac{k_{\mathrm{f},m}}{k_{\mathrm{b},m}} = \frac{\prod_{\nu_{m,i}>0} (c_i^0)^{\nu_{m,i}}}{\prod_{\nu_{m,i}<0} (c_i^0)^{-\nu_{m,i}}}. \tag{A.11}$$

Inserting into the above,

$$\mathcal{R}_m = -k_{\mathrm{b},m} \prod_{\nu_{m,i}>0} (c_i^0)^{\nu_{m,i}} e^{-z_i \nu_{m,i} V} \left[e^{\sum_{\nu_{m,i}>0} g_i \nu_{m,i}} - e^{-\sum_{\nu_{m,i}<0} g_i \nu_{m,i}} \right] \tag{A.12}$$

$$= -k_{\mathrm{b},m} \prod_{\nu_{m,i}>0} (c_i^0)^{\nu_{m,i}} e^{-z_i \nu_{m,i} V} \frac{e^{\sum_{\nu_{m,i}>0} g_i \nu_{m,i}} - e^{-\sum_{\nu_{m,i}<0} g_i \nu_{m,i}}}{\sum_i g_i \nu_{m,i}} \sum_i g_i \nu_{m,i} \tag{A.13}$$

$$= -\mathcal{C}_m \sum_i g_i \nu_{m,i}. \tag{A.14}$$

Where we have identified

$$\mathcal{C}_m = k_{\mathrm{b},m} \prod_{\nu_{m,i}>0} (c_i^0)^{\nu_{m,i}} e^{-z_i \nu_{m,i} V} \frac{e^{\sum_{\nu_{m,i}>0} g_i \nu_{m,i}} - e^{-\sum_{\nu_{m,i}<0} g_i \nu_{m,i}}}{\sum_i g_i \nu_{m,i}} \tag{A.15}$$

Note that for any $x_1, x_2 \in \mathbb{R}$,

$$\zeta(x_1) - \zeta(x_2) = \zeta'(x)(x_1 - x_2), \tag{A.16}$$

for some $x \in [\min(x_1, x_2), \max(x_1, x_2)]$. Since $[\exp(x)]' \geq 0$ for all x, we have that $\mathcal{C}_m \geq 0$.

Appendix B. Derivation of manufactured solution

Here we derive the analytical solution used to show convergence. We will assume an incompressible flow where neither density nor permittivity depends on the ion concentrations.

A Taylor–Green vortex flow in the periodic domain $(x, y) \in \Omega = [0, 2\pi] \times [0, 2\pi]$, is given by

$$\mathbf{u} = U(t)(\hat{\mathbf{x}} \cos x \sin y - \hat{\mathbf{y}} \sin x \cos y), \tag{B.1}$$

$$c_\pm = c_0(1 \pm \cos x \cos y\, C(t)). \tag{B.2}$$

Solving the electrostatic problem yields

$$\rho_e = 2c_0 \cos x \cos y\, C(t) \tag{B.3}$$

$$V = \frac{c_0}{\epsilon} \cos x \cos y\, C(t) \tag{B.4}$$

which gives a residual of order $O(c_0/\epsilon)$. We assume the mobilities $K_\pm = Dc_\pm$, and the chemical energy function $\alpha(c) = c(\ln c - 1)$.

The divergence criterion is obtained by taking the divergence of the Navier–Stokes equations with constant density:

$$\rho_0(\boldsymbol{\nabla}\mathbf{u})^T : \boldsymbol{\nabla}\mathbf{u} + \boldsymbol{\nabla} \cdot (\rho_e \boldsymbol{\nabla} V) = -\boldsymbol{\nabla}^2\left(p + \sum_i c_i\right) = -\boldsymbol{\nabla}^2 p \tag{B.5}$$

Hence, inserting the manufactured solutions eqs. (B.1) and (B.2) yields

$$-\boldsymbol{\nabla}^2 p = -\rho_0 U^2(t)(\cos 2x + \cos 2y) - \frac{c_0^2 C^2(t)}{\epsilon}(\cos 2x + \cos 2y + 2\cos 2x \cos 2y) \tag{B.6}$$

$$= -\left(\rho_0 U^2(t) + \frac{c_0^2 C^2(t)}{\epsilon}\right)(\cos 2x + \cos 2y) - \frac{2c_0^2 C^2(t)}{\epsilon} \cos 2x \cos 2y \tag{B.7}$$

we find that the pressure is

$$p = -\frac{1}{4}\left(\rho_0 U^2(t) + \frac{c_0^2 C^2(t)}{\epsilon}\right)(\cos 2x + \cos 2y) - \frac{c_0^2 C^2(t)}{4\epsilon} \cos 2x \cos 2y \tag{B.8}$$

We have that

$$\rho_e \boldsymbol{\nabla} V = -\frac{c_0^2}{2\epsilon} C^2(t)\left[\hat{\mathbf{x}} \sin 2x(1 + \cos 2y) + \hat{\mathbf{y}}(1 + \cos 2x)\sin 2y\right] \tag{B.9}$$

and that

$$\boldsymbol{\nabla} p = \frac{1}{2}\left[\left(\rho_0 U^2(t) + \frac{c_0^2 C^2(t)}{\epsilon}(1 + \cos 2y)\right)\sin 2x\hat{\mathbf{x}} + \left(\rho_0 U^2(t) + \frac{c_0^2 C^2(t)}{\epsilon}(1 + \cos 2x)\right)\sin 2y\hat{\mathbf{y}}\right] \tag{B.10}$$

so that

$$\boldsymbol{\nabla} p + \rho_e \boldsymbol{\nabla} V = \frac{\rho_0 U^2(t)}{2}\left[\sin 2x\hat{\mathbf{x}} + \sin 2y\hat{\mathbf{y}}\right] \tag{B.11}$$

and since

$$\mathbf{u} \cdot \boldsymbol{\nabla}\mathbf{u} = \hat{\mathbf{x}}(u_x\partial_x u_x + u_y\partial_y u_x) + \hat{\mathbf{y}}(u_x\partial_x u_y + u_y\partial_y u_y) \tag{B.12}$$

$$= -\frac{U^2(t)}{2}\left[\hat{\mathbf{x}} \sin 2x + \hat{\mathbf{y}} \sin 2y\right]. \tag{B.13}$$

Hence, the Navier–Stokes equations give

$$\frac{U'(t)}{U(t)} = -\frac{2\mu}{\rho_0} \implies U(t) = \exp(-2\mu t/\rho_0). \tag{B.14}$$

Further, the ion transport equations must both be augmented by a carefully chosen source term q:

$$\partial_t c_\pm + \mathbf{u} \cdot \boldsymbol{\nabla} c_\pm - D\boldsymbol{\nabla} \cdot (\boldsymbol{\nabla} c_\pm + z_\pm c_\pm \boldsymbol{\nabla} V) = q(x, y), \tag{B.15}$$

where

$$q(x, y) = \frac{Dc_0^2 C^2(t)}{2\epsilon} \left[\cos 2x + \cos 2y + 2\cos 2x \cos 2y\right]. \tag{B.16}$$

This gives local charge conservation, but a local reaction changes the concentration of both ions.

Insertion gives us that

$$C(t) = \chi \exp\left(-2D\left(1 + \frac{c_0}{\epsilon}\right)t\right). \tag{B.17}$$

Hence the concentrations decay to the equilibrium concentrations. Note that $\chi < 1$ in order for the ion concentrations to stay positive.

[1] T. M. Squires, S. R. Quake, Microfluidics: Fluid physics at the nanoliter scale, Rev. Mod. Phys. 77 (3) (2005) 977, doi:10.1103/RevModPhys.77.977.

[2] R. B. Schoch, J. Han, P. Renaud, Transport phenomena in nanofluidics, Rev. Mod. Phys. 80 (3) (2008) 839, doi:10.1103/RevModPhys.80.839.

[3] J. Lee, C.-J. Kim, Surface-tension-driven microactuation based on continuous electrowetting, J. Microelectromech. Syst. 9 (2) (2000) 171–180, doi:10.1109/84.846697.

[4] S. Ghosal, Electrokinetic flow and dispersion in capillary electrophoresis, Annu. Rev. Fluid Mech. 38 (2006) 309–338.

[5] C. P. Nielsen, H. Bruus, Concentration polarization, surface currents, and bulk advection in a microchannel, Phys. Rev. E 90 (4) (2014) 043020, doi:10.1103/PhysRevE.90.043020.

[6] C. P. Nielsen, H. Bruus, Sharp-interface model of electrodeposition and ramified growth, Phys. Rev. E 92 (4) (2015) 042302, doi:10.1103/PhysRevE.92.052310.

[7] V. V. Nikonenko, A. V. Kovalenko, M. K. Urtenov, N. D. Pismenskaya, J. Han, P. Sistat, G. Pourcelly, Desalination at overlimiting currents: State-of-the-art and perspectives, Desalination 342 (2014) 85–106, doi:10.1016/j.desal.2014.01.008.

[8] A. Siria, M.-L. Bocquet, L. Bocquet, New avenues for the large-scale harvesting of blue energy, Nat. Rev. Chem. 1 (11) (2017) 0091, doi:10.1038/s41570-017-0091.

[9] A. Hiorth, L. Cathles, M. Madland, The impact of pore water chemistry on carbonate surface charge and oil wettability, Transp. Porous Media 85 (1) (2010) 1–21, doi:10.1007/s11242-010-9543-6.

[10] E. Hilner, M. P. Andersson, T. Hassenkam, J. Matthiesen, P. Salino, S. L. S. Stipp, The effect of ionic strength on oil adhesion in sandstone–the search for the low salinity mechanism, Scientific Reports 5 (2015) 9933, doi:10.1038/srep09933.

[11] S. R. Pride, F. Morgan, Electrokinetic dissipation induced by seismic waves, Geophysics 56 (7) (1991) 914–925, doi:10.1190/1.1443125.

[12] E.-A. Fiorentino, R. Toussaint, L. Jouniaux, Lattice Boltzmann modelling of streaming potentials: variations with salinity in monophasic conditions, Geophys. J. Int. 205 (1) (2016) 648–664, doi:10.1093/gji/ggw041.

[13] E.-A. Fiorentino, R. Toussaint, L. Jouniaux, Two-phase lattice Boltzmann modelling of streaming potentials: influence of the air-water interface on the electrokinetic coupling, Geophys. J. Int. 208 (2) (2016) 1139–1156, doi:10.1093/gji/ggw417.

[14] A. Bolet, G. Linga, J. Mathiesen, Electrohydrodynamic channeling effects in narrow fractures and pores, Phys. Rev. E 97 (2018) 043114, doi:10.1103/PhysRevE.97.043114.

[15] O. Plümper, A. Botan, C. Los, Y. Liu, A. Malthe-Sørenssen, B. Jamtveit, Fluid-driven metamorphism of the continental crust governed by nanoscale fluid flow, Nat. Geosci. 10 (9) (2017) 685, doi:10.1038/ngeo3009.

[16] G. Mitscha-Baude, A. Buttinger-Kreuzhuber, G. Tulzer, C. Heitzinger, Adaptive and iterative methods for simulations of nanopores with the PNP–Stokes equations, J. Comput. Phys. 338 (2017) 452–476, doi:10.1016/j.jcp.2017.02.072.

[17] A. Mansouri, C. Scheuerman, S. Bhattacharjee, D. Y. Kwok, L. W. Kostiuk, Transient streaming potential in a finite length microchannel, J. Colloid Interface Sci. 292 (2) (2005) 567–580, doi:10.1016/j.jcis.2005.05.094.

[18] A. Mansouri, S. Bhattacharjee, L. W. Kostiuk, Transient Electrokinetic Transport in a Finite Length Microchannel: Currents, Capacitance, and an Electrical Analogy, J. Phys. Chem. B 111 (44) (2007) 12834–12843, doi:10.1021/jp074386c.

[19] B. Zaltzman, I. Rubinstein, Electro-osmotic slip and electroconvective instability, J. Fluid Mech. 579 (2007) 173–226, doi:10.1017/S0022112007004880.

[20] V. S. Pham, Z. Li, K. M. Lim, J. K. White, J. Han, Direct numerical simulation of electroconvective instability and hysteretic current-voltage response of a permselective membrane, Phys. Rev. E 86 (4) (2012) 046310, doi:10.1103/PhysRevE.86.046310.

[21] E. Demekhin, V. Shelistov, S. Polyanskikh, Linear and nonlinear evolution and diffusion layer selection in electrokinetic instability, Phys. Rev. E 84 (3) (2011) 036318, doi:10.1103/PhysRevE.84.036318.

[22] C. L. Druzgalski, M. B. Andersen, A. Mani, Direct numerical simulation of electroconvective instability and hydrodynamic chaos near an ion-selective surface, Phys. Fluids 25 (11) (2013) 110804, doi:10.1063/1.4818995.

[23] C. Druzgalski, A. Mani, Statistical analysis of electroconvection near an ion-selective membrane in the highly chaotic regime, Phys. Rev. Fluids 1 (7) (2016) 073601, doi:10.1103/PhysRevFluids.1.073601.

[24] R. Ostilla-Mónico, et al., Controlling turbulent drag across electrolytes using electric fields, Faraday Discuss. 199 (2017) 159–173, doi:10.1039/c6fd00247a.

[25] R.-C. Chen, J.-L. Liu, An iterative method for adaptive finite element solutions of an energy transport model of semiconductor devices, J. Comput. Phys. 189 (2) (2003) 579–606, doi:10.1016/S0021-9991(03)00247-X.

[26] J. Shen, X. Yang, Decoupled, energy stable schemes for phase-field models of two-phase incompressible flows, SIAM J. Numer. Anal. 53 (1) (2015) 279–296, doi:10.1137/140971154.

[27] A. J. Chorin, A numerical method for solving incompressible viscous flow problems, J. Comput. Phys. 2 (1) (1967) 12–26, doi:10.1006/jcph.1997.5716.

[28] A. J. Chorin, Numerical solution of the Navier-Stokes equations, Math. Comput. 22 (104) (1968) 745–762, doi:10.1090/S0025-5718-1968-0242392-2.

[29] J.-L. Guermond, P. Minev, J. Shen, An overview of projection methods for incompressible flows, Comput. Methods Appl. Mech. Eng. 195 (44-47) (2006) 6011–6045, doi:10.1016/j.cma.2005.10.010.

[30] U. S. Fjordholm, S. Mishra, E. Tadmor, Well-balanced and energy stable schemes for the shallow water equations with discontinuous topography, J. Comput. Phys. 230 (14) (2011) 5587–5609, doi:10.1016/j.jcp.2011.03.042.

[31] S. Minjeaud, An unconditionally stable uncoupled scheme for a triphasic Cahn–Hilliard/Navier–Stokes model, Numer. Methods Partial Differ. Equ. 29 (2) (2013) 584–618, doi:10.1002/num.21721.

[32] F. Guillén-González, G. Tierra, Splitting Schemes for a Navier–Stokes–Cahn–Hilliard Model for Two Fluids with Different Densities, J. Comp. Math. 32 (6) (2014) 643–664, doi:10.4208/jcm.1405-m4410.

[33] A. Prohl, M. Schmuck, Convergent discretizations for the Nernst–Planck–Poisson system, Numerische Mathematik 111 (4) (2009) 591–630, doi:10.1007/s00211-008-0194-2.

[34] M. Schmuck, Analysis of the Navier–Stokes–Nernst–Planck–Poisson system, Math. Models Methods Appl. Sci. 19 (06) (2009) 993–1014, doi:10.1142/S0218202509003693.

[35] A. Prohl, M. Schmuck, Convergent finite element discretizations of the Navier-Stokes-Nernst-Planck-Poisson system, ESAIM: Math. Model Numer. Anal. 44 (3) (2010) 531–571, doi:10.1051/m2an/2010013.

[36] M. Schmuck, Modeling, analysis, and numerics in electrohydrodynamics, Ph.D. thesis, Eberhard-Karls-University Tubingen, 2008.

[37] G. Bauer, V. Gravemeier, W. A. Wall, A stabilized finite element method for the numerical simulation of multi-ion transport in electrochemical systems, Comput. Methods Appl. Mech. Eng. 223 (2012) 199–210, doi:10.1016/j.cma.2012.02.003.

[38] H. Abels, H. Garcke, G. Grün, Thermodynamically consistent, frame indifferent diffuse interface models for incompressible two-phase flows with different densities, Math. Models Methods Appl. Sci. 22 (03) (2012) 1150013, doi:10.1142/S0218202511500138.

[39] S. Metzger, On numerical schemes for phase-field models for electrowetting with electrolyte solutions, Proc.

Appl. Math. Mech. 15 (1) (2015) 715–718, doi:10.1002/pamm.201510346.

[40] S. Metzger, On stable, dissipation reducing splitting schemes for two-phase flow of electrolyte solutions, Numerical Algorithms (2018) 1–30doi:10.1007/s11075-018-0530-2.

[41] E. Campillo-Funollet, G. Grün, F. Klingbeil, On modeling and simulation of electrokinetic phenomena in two-phase flow with general mass densities, SIAM J. Appl. Math. 72 (6) (2012) 1899–1925, doi:10.1137/120861333.

[42] B. Hess, C. Holm, N. van der Vegt, Modeling multibody effects in ionic solutions with a concentration dependent dielectric permittivity, Phys. Rev. Lett. 96 (14) (2006) 147801, doi:10.1103/PhysRevLett.96.147801.

[43] F. Booth, The Dielectric Constant of Water and the Saturation Effect, Journal of Chemical Physics 19 (1951) 391–394, doi:10.1063/1.1748233.

[44] M. Mortensen, K. Valen-Sendstad, Oasis: A high-level/high-performance open source Navier–Stokes solver, Comput. Phys. Commun. 188 (2015) 177–188, doi:10.1016/j.cpc.2014.10.026.

[45] G. Linga, A. Bolet, J. Mathiesen, Bernaise: A flexible framework for simulating two-phase electrohydrodynamic flows in complex domains, submitted, available online at https://arxiv.org/abs/1805.11642, 2018.

[46] A. Logg, G. N. Wells, DOLFIN: Automated Finite Element Computing, ACM Trans. Math. Softw. 37 (2) (2010) 20:1–20:28, ISSN 0098-3500, doi:10.1145/1731022.1731030.

[47] A. Logg, K.-A. Mardal, G. Wells, Automated solution of differential equations by the finite element method: The FEniCS book, vol. 84, Springer Science & Business Media, 2012.

[48] K. Szewc, J. Pozorski, A. Taniere, Modeling of natural convection with smoothed particle hydrodynamics: non-Boussinesq formulation, Int. J. Heat Mass Transf. 54 (23-24) (2011) 4807–4816, doi:10.1016/j.ijheatmasstransfer.2011.06.034.

[49] J. Wu, J. Shen, X. Feng, Unconditionally stable Gauge–Uzawa finite element schemes for incompressible natural convection problems with variable density, J. Comput. Phys. 348 (2017) 776–789, doi:10.1016/j.jcp.2017.07.045.

[50] S. C. Brenner, L. R. Scott, The mathematical theory of finite element methods, vol. 15, Springer Science & Business Media, 2007.

[51] Z. Xu, P. Meakin, Phase-field modeling of solute precipitation and dissolution, J. Chem. Phys. 129 (1) (2008) 014705, doi:10.1063/1.2948949.

[52] C. Hawkins, L. Angheluta, B. Jamtveit, Hydrodynamic shadowing effect during precipitation of dendrites in channel flow, Phys. Rev. E 89 (2) (2014) 022402, doi:10.1103/PhysRevE.89.022402.

Bernaise: A flexible framework for simulating two-phase electrohydrodynamic flows in complex domains

Gaute Linga, Asger Bolet, and Joachim Mathiesen

Bernaise: A flexible framework for simulating two-phase electrohydrodynamic flows in complex domains

Gaute Linga,* Asger Bolet, and Joachim Mathiesen

Niels Bohr Institute, University of Copenhagen,

Blegdamsvej 17, DK-2100 Copenhagen, Denmark.

Abstract

Bernaise (Binary ElectRohydrodyNAmIc SolvEr) is a flexible high-level finite element solver of two-phase electrohydrodynamic flow in complex geometries. Two-phase flow with electrolytes is relevant across a broad range of systems and scales, from 'lab-on-a-chip' devices for medical diagnostics to enhanced oil recovery at the reservoir scale. For the strongly coupled multi-physics problem, we employ a recently developed thermodynamically consistent model which combines a generalized Nernst–Planck equation for ion transport, the Poisson equation for electrostatics, the Cahn–Hilliard equation for the phase field (describing the interface separating the phases), and the Navier–Stokes equations for fluid flow. As an efficient alternative to solving the coupled system of partial differential equations in a monolithic manner, we present a linear, decoupled numerical scheme which sequentially solves the three sets of equations. The scheme is validated by comparison to limiting cases where analytical solutions are available, benchmark cases, and by the method of manufactured solution. The solver operates on unstructured meshes and is therefore well suited to handle arbitrarily shaped domains and problem set-ups where, e.g., very different resolutions are required in different parts of the domain. *Bernaise* is implemented in Python via the FEniCS framework, which effectively utilizes MPI and domain decomposition, and should therefore be suitable for large-scale/high-performance computing. Further, new solvers and problem set-ups can be specified and added with ease to the *Bernaise* framework by experienced Python users.

---

* linga@nbi.dk

I. INTRODUCTION

Two-phase flow with electrolytes is encountered in many natural and industrial settings. Although Lippmann already in the 19th century [1, 2] made the observation that an applied electric field changes the wetting behaviour of electrolyte solutions, the phenomenon of electrowetting has remained elusive. Recent decades have seen an increased theoretical and experimental interest in understanding the basic mechanisms of electrokinetic or electrohydrodynamic flow [3, 4]. Progress in micro- and nanofluidics [5, 6] has enabled the use electrowetting to control small amounts of fluid with very high precision (see e.g. the comprehensive reviews by Mugele and coworkers [2, 7] and Nelson and Kim [8] and references therein). This yields potential applications in, e.g., "lab-on-chip" biomedical devices or microelectromechanical systems [9–11], membranes for harnessing blue energy [12], energy storage in fluid capacitors, and electronic displays [13–16].

It is known that electrohydrodynamic phenomena affects transport properties and energy dissipation in geological systems, as a fluid moving in a fluid-saturated porous medium sets up an electric field that counteracts the fluid motion [17–19]. Electrowetting may also be an important factor in enhanced oil recovery [20, 21]. Here, the injection of water of a particular salinity, or "smart water" [22], is known to increase the recovery of oil from reservoirs as compared to brine [23]. Further, transport in sub-micrometer scale pores in low-permeability rocks in the Earth's crust may be driven by gradients in the electrochemical potential [24], which may have consequences for, e.g., transport of methane-water mixtures in dense rocks.

Hence, a deepened understanding of electrowetting and two-phase electrohydrodynamics would be of both geological and technological importance. While wetting phenomena (or more generally, two-phase flow) on one hand, and electrohydrodynamics on the other, remain in themselves two mature and active areas of research which both encompass a remarkably rich set of phenomena, this article is concerned with the interface between these fields. For interested readers, there are several reviews available regarding wetting phenomena [25–27] and electrohydrodynamics [28–30]. Notably, the "leaky dielectric" model originally proposed by Taylor [31] (and revisited by Melcher and Taylor [28]) to describe drop deformation, is arguably the most popular description of electrohydrodynamics, but it does not describe ionic transport and considers all dielectrics to be weak conductors. In this work, we shall employ a model that does not make such simplifications. Recently, Schnitzer and Yariv

[32] showed rigorously that models of the latter type reduce to the Taylor–Melcher model in the double limit of small Debye length and strong electric fields. The simplified model may therefore have advantages in settings where those assumptions are justified, e.g., in simulations on larger scales; while the class of models considered here are more general and expected to be valid down to the smallest scale where the continuum hypothesis still holds.

Experimental and theoretical approaches [33–35] in two-phase electrohydrodynamic flows need to be supplemented with good numerical simulation tools. This is a challenging task, however: the two phases have different densities, viscosities and permittivities, the ions have different diffusivities and solubilites in the two phases, and moreover, the interface between the phases must be described in a consistent manner. Hence, much due to the complex physics involved, simulation of two-phase electrohydrodynamic phenomena with ionic transport is still in its infancy. It has been carried out with success e.g. in order to understand deformation of droplets due to electric fields [36–38], or for the purpose of controlling microfluidic devices (see e.g. [39]). Lu *et al.* [40] simulated and performed experiments on droplet dynamics in a Hele-Shaw cell. Notably, Walker *et al.* [41] simulated electrowetting with contact line pinning, and compared to experiments. In practical applications, such as in environmental remediation or oil recovery, the complex pore geometry is essential and it is therefore of interest to simulate and study electrowetting in such configurations. However, to our knowledge, there have been few numerical studies of these phenomena in the context of more complex geometries.

In this article, we introduce and describe *Bernaise* (Binary ElectRohydrodyNAmIc SolvEr), which is an open-source software/framework for simulating two-phase electrohydrodynamics. It is suitable for use in complex domains, operating on arbitrary unstructured meshes. The finite-element solver is written entirely in Python and built on top of the FEniCS framework [42], which (among other things) effectively uses the PETSc backend for scalability. FEniCS has in recent years found success in related applications, such as in high-performance simulation of turbulent flow [43], and for single-phase, steady-state electrohydrodynamic flow simulation in nanopores [44] and model fractures [45]. Since *Bernaise* was inspired by the *Oasis* solver for fluid flow [43], it is similar to the latter in both implementation and use.

In this work, we employ a phase-field model to propagate the interface between the two phases. Such *diffuse interface* models, as opposed to e.g. sharp interface models (see for

instance [46]), assume that the fluid-fluid interface has a finite size, and have the advantage that no explicit tracking of the interface is necessary. Hence, using a phase-field model has several advantages in our setting: it takes on a natural formulation using the finite element method; in sub-micrometer scale applications, the diffuse interface and finite interface thickness present in these models might correspond to the physical interface thickness (typically nanometer scale [47]); and the diffuse interface may resolve the moving contact line conundrum [27, 48]. Note that although *ab initio* and molecular dynamics simulation methods are in rapid growth due to the increase in computational power, and do not require explicit tracking of the interface or phenomenological boundary conditions, such methods are restricted to significantly smaller scales than continuum models are. Nevertheless, they serve as valuable tools for calibration of the continuum methods [48–51]. We note also that sharp-interface methods such as level-set [52, 53] and volume-of-fluid methods [38, 54, 55] are viable options for simulating electrohydrodynamics, but such methods shall not be considered here.

The use of phase field models to describe multiphase flow has a long history in fluid mechanics [56]. Notably, the "Model H" of Hohenberg and Halperin [57], for two incompressible fluids with matched densities and viscosities, is based on the coupled Navier–Stokes–Cahn–Hilliard system, and was introduced to describe phase transitions of binary fluids or single-phase fluid near the critical point. Lowengrub and Truskinovsky [58] later derived a thermodynamically consistent generalization of Model H where densities and viscosities were different in the two phases, however with the numerical difficulty that the velocity field was not divergence free. To circumvent this issue, Abels *et al.* [59] developed a thermodynamically consistent and frame invariant phase-field model for two-phase flow, where the velocity field was divergence free, allowing for the use of more efficient numerical methods. Lu *et al.* [40] proposed a phase-field model to describe electrohydrodynamics, but was restricted to flow in Hele-Shaw cells, using a Darcy equation to describe the flow between the parallel plates [60]. A phase-field approach to the leaky-dielectric model was presented by Lin *et al.* [61]. Using the Onsager variational principle, Campillo-Funollet *et al.* [62] augmented the model of Abels *et al.* [59] with electrodynamics, i.e. inclusion of ions, electric fields and forces. This can be seen as a more physically sound version of the model proposed by Eck *et al.* [63], which only contained a single "net charge" electrolyte species. A model for two-phase electrohydrodynamics was derived, with emphasis on contact line pinning, by

Nochetto *et al.* [64], but this does not appear to be frame-invariant, as the chemical potential depends quadratically on velocity [62]. In this work, we will therefore focus on the model by Campillo-Funollet *et al.* [62].

There is a vast literature on the discretization and simulations of immiscible two-phase flows including phase-field models (see e.g. [46, 56]), but here we focus on research which is immediately relevant concerning the discretization and implementation of the model by Campillo-Funollet *et al.* [62]. Grün and Klingbeil [65] discretized the model in Ref. [59] (without electrohydrodynamics) with a dual mesh formulation, using a finite volume method on the dual mesh for advection terms, and a finite element method for the rest. Based on the sharp-interface model benchmarks of Hysing *et al.* [66], Aland and Voigt [67] provided benchmarks of bubble dynamics comparing several formulations of phase-field models (without electrodynamics). Energy-stable numerical schemes for the same case were presented and analyzed in [68, 69]. Campillo-Funollet *et al.* [62] provided preliminary simulations of the two-phase electrohydrodynamics model in their paper, however with a simplified formulation of the chemical potential of the solutes. A scheme for the model in [62] which decouples the Navier–Stokes equations from the Cahn–Hilliard–Poisson–Nernst–Planck problem, was presented and demonstrated by Metzger [70, 71]. In the particular case of equal phasic permittivities, the Cahn–Hilliard problem could be decoupled from the Poisson–Nernst–Planck problem. Recently, a stable finite element approximation of two-phase EHD, with the simplifying assumptions of Stokes flow and no electrolytes, was proposed by Nürnberg and Tucker [72].

The main contributions of this article is to give a straightforward description of *Bernaise*, including the necessary background theory, an overview of the implementation, and a demonstration of its ease of use. Solving the coupled set of equations in a monolithic manner (as is done in Ref. [62] using their in-house ECONDROP software) is a computationally expensive task, and we therefore propose a new linear splitting scheme which sequentially solves the phase-field, chemical transport and the fluid flow *subproblems* at each time step. We demonstrate the validity of the approach and numerical convergence of the proposed scheme by comparing to limiting cases where analytical solutions are available, benchmark solutions, and using the method of manufactured solution. We demonstrate how the framework can be extended by supplying user-specified problems and solvers. We believe that due to its flexibility, scalability and open-source licensing, this framework has advantages over soft-

ware which to our knowledge may have *some* of the same functionality, such as EconDrop (in-house code of Grün and co-workers) and Comsol (proprietary). Compared to sharp-interface methods, the method employed in the current framework is automatically capable of handling topological changes and contact line motion, and the full three-dimensional (3D) capabilities allows to study more general phenomena than what can be achieved by axisymmetric formulations [38]. We expect *Bernaise* to be a valuable tool that may facilitate the development of microfluidic devices, as well as a deepened understanding of electrohydrodynamic phenomena in many natural or industrial settings.

The outline of this paper is as follows. In Sec. II, we introduce the sharp-interface equations describing two-phase electrohydrodynamics; then we present the thermodynamically consistent model of electrohydrodynamics by Campillo-Funollet *et al.* [62]. In Sec. III, we write down the variational form of the model, present the monolithic scheme, and present a linear splitting scheme for solving the full-fledged two-phase electrohydrodynamics. Sec. IV gives a brief presentation of *Bernaise*, and demonstrates its ease use through a minimal example. Further, we describe how *Bernaise* can be extended with user-specified problems and solvers. In Sec. V, we validate the approach as described in the preceding paragraph. Finally, in Sec. VI, we apply the framework to a geologically relevant setting where dynamic electrowetting effects enter, and present full 3D simulations of droplet coalescence and breakup. Finally, in Sec. VII we draw conclusions and point to future work.

We expect the reader to have a basic familiarity with the finite element method, the Python language, and the FEniCS package. Otherwise, we refer to the tutorial by Langtangen and Logg [73].

II. MODEL

The governing equations of two-phase electrohydrodynamics can be summarized as the coupled system of two-phase flow, chemical transport (diffusion and migration), and electrostatics [62]. We will now describe the sharp-interface equations that the phase-field model should reproduce, and subsequently the phase-field model for electrohydrodynamics. For the purpose of keeping the notation short, we consider a general electrokinetic scaling of the equations. The relations between the dimensionless quantities and their physical quantities are elaborated in Appendix A.

A. Sharp-interface equations

In the following, we present each equation of the physical (sharp-interface) model. With validity down to the nanometer scale, the fluid flow is described by the incompressible Navier–Stokes equations, augmented by some additional force terms due to electrochemistry:

$$\rho_i \left(\partial_t \mathbf{v} + (\mathbf{v} \cdot \boldsymbol{\nabla}) \mathbf{v} \right) - \mu_i \boldsymbol{\nabla}^2 \mathbf{v} + \boldsymbol{\nabla} p = - \sum_j c_j \boldsymbol{\nabla} g_{c_j}, \tag{1}$$

$$\boldsymbol{\nabla} \cdot \mathbf{v} = 0. \tag{2}$$

Here, ρ_i is the density of phase i, $\mathbf{v}$ is the velocity field, μ_i is the dynamic viscosity of phase i, $p(\mathbf{x}, t)$ is the pressure field [74], $c_j(\mathbf{x}, t)$ is the concentration of solute species j, and g_{c_j} is the associated electrochemical potential. The form of the right hand side of Eq. (1) is somewhat unconventional (and relies on a specific interpretation of the pressure), but has numerical advantages over other formulations as it avoids, e.g., pressure build-up in the electrical double layers [75].

The transport of the concentration field of species i is governed by the conservative (advection–diffusion–migration) equation:

$$\partial_t c_j + \mathbf{v} \cdot \boldsymbol{\nabla} c_j - \boldsymbol{\nabla} \cdot (K_{ij} c_j \boldsymbol{\nabla} g_{c_j}) = 0, \tag{3}$$

where K_{ij} is the diffusivity of species j in phase i. The electrochemical potential is in general given by

$$g_{c_j}(c_j, V) = \alpha'(c_j) + \beta_{ij} + z_j V, \tag{4}$$

where $\alpha'(c) = \partial \alpha / \partial c(c)$, and $\alpha(c)$ is a convex function describing the chemical free energy, β_{ij} is a parameter describing the solubility of species j in phase i, z_j is the charge if solute species j, and V is the electric potential. Eq. (3) can be seen as a generalized Nernst–Planck equation. With an appropriate choice of $\alpha(c)$, Eq. (3) reduces to the phenomenological Nernst–Planck equation, which has been established for the transport of charged species in dilute solutions under influence of an electric field. The latter amounts to a dilute solution, using the ideal gas approximation,

$$\alpha(c_j) \propto c_j (\ln c_j - 1). \tag{5}$$

With this choice of α, the solubility parameter β_{ij} can be interpreted as related to a reference

concentration $c_j^{\mathrm{ref},i}$, through the relation

$$\beta_{ij} = -\ln c_j^{\mathrm{ref},i}. \tag{6}$$

This gives a chemical energy $\mathcal{G}_j = \alpha(c_j) + \beta_{ij}c_j = c_j(\ln(c_j/c_j^{\mathrm{ref},i}) - 1)$ which has a minimum at $c_j = c_j^{\mathrm{ref},i}$ (see also [76]).

Since the dynamics of the electric field is much faster than that of charge transport, we can safely assume electrostatic conditions (i.e., neglect magnetic fields). This amounts to solving the Poisson problem (Gauss' law):

$$\boldsymbol{\nabla} \cdot (\varepsilon_i \boldsymbol{\nabla} V) = -\rho_e, \tag{7}$$

Here, ε_i is the electrical permittivity of phase i, and $\rho_e = \sum_j z_j c_j$ is the total charge density.

In the absence of advection, for the case of two symmetric charges, and under certain boundary conditions, Eqs. (3)–(7) lead to the simpler Poisson–Boltzmann equation (see Appendix B).

1. Fluid-fluid interface conditions

It is necessary to define jump conditions over the interface between the two fluids. We denote the jump in a physical quantity χ across the interface by $[\chi]_-^+$, and the unit vector $\hat{\mathbf{n}}_{\mathrm{int}}$ normal to the interface.

Firstly, due to incompressibility, the velocity field must be continuous:

$$[\mathbf{v}]_-^+ = 0. \tag{8}$$

The electrochemical potential must be continuous across the interface,

$$\left[g_{c_j}\right]_-^+ = 0. \tag{9}$$

Due to conservation of the electrolytes, the flux of ion species j *into* the interface must equal the flux *out of* the interface,

$$\left[K_{ij}c_j \boldsymbol{\nabla} g_{c_j}\right]_-^+ \cdot \hat{\mathbf{n}}_{\mathrm{int}} = 0, \tag{10}$$

and the normal flux of the electric displacement field $\mathbf{D} = -\epsilon_i \boldsymbol{\nabla} V$, and the electric potential, should be continuous (since by assumption, no free charge is located *betweeen* the fluids):

$$[\epsilon_i \boldsymbol{\nabla} V]_-^+ \cdot \hat{\mathbf{n}}_{\mathrm{int}} = 0, \quad [V]_-^+ = 0. \tag{11}$$

Finally, interfacial stress balance yields the condition

$$[p]_-^+ \, \hat{\mathbf{n}}_{\text{int}} - [2\mu_i \mathcal{D}\mathbf{v}]_-^+ \cdot \hat{\mathbf{n}}_{\text{int}} - \left[\varepsilon_i \mathbf{E} \otimes \mathbf{E} - \frac{1}{2}\varepsilon_i |\mathbf{E}|^2 \mathbf{I} \right]_-^+ \cdot \hat{\mathbf{n}}_{\text{int}} = \sigma\kappa\hat{\mathbf{n}}_{\text{int}}, \qquad (12)$$

where σ is the surface tension, κ is the curvature, and $\mathbf{E} = -\boldsymbol{\nabla}V$ is the electric field. Moreover, we have defined the shorthand symmetric (vector) gradient,

$$\mathcal{D}\mathbf{v} = \text{sym}\,(\boldsymbol{\nabla}\mathbf{v}) = \frac{1}{2}\left(\boldsymbol{\nabla}\mathbf{v} + \boldsymbol{\nabla}\mathbf{v}^T\right). \qquad (13)$$

Further, all gradient terms have been absorbed into the pressure. Note that Eq. (12) leads to a modified Young–Laplace law in equilibrium, which include Maxwell stresses.

2. Boundary conditions

There are a range of applicable boundary conditions for two-phase electrohydrodynamics. Here, we briefly discuss a few viable options. In the following, we let $\hat{\mathbf{n}}$ be a unit normal vector pointing out of the domain, and $\hat{\mathbf{t}}$ be a tangent vector to the boundary.

For the velocity, it is customary to use the no-slip condition $\mathbf{u} = \mathbf{0}$ at the solid boundary. Alternatively, the Navier slip condition, which is useful for modelling moving contact lines [50], could be used:

$$\hat{\mathbf{n}} \cdot \mathbf{v} = 0, \quad (\gamma\mathbf{v} - 2\mu\mathcal{D}\mathbf{v}\,\hat{\mathbf{n}}) \times \hat{\mathbf{n}} = \mathbf{0}, \qquad (14)$$

where γ is a slip parameter. The slip length μ/γ is typically of nanometer scale and dependent on the materials in question. However, since the implementation of such conditions may become slightly involved, we omit it in the following.

With regards to the electrolytes, it is natural to specify either a prescribed concentration at the boundary, $c_i = c_0$, or a no-flux condition out of the domain,

$$\hat{\mathbf{n}} \cdot \left(-\mathbf{u}c_j + K_{ij}c_j\boldsymbol{\nabla}g_{c_j} \right) = 0. \qquad (15)$$

For the electric potential, it is natural to prescribe either the Dirichlet condition $V = \bar{V}$, or a prescribed surface charge $\sigma_e(\mathbf{x})$,

$$\hat{\mathbf{n}} \cdot \boldsymbol{\nabla}V = \frac{\sigma_e}{\epsilon_i}. \qquad (16)$$

B. Phase-field formulation

In order to track the interface between the phases, we introduce an order parameter field ϕ which attains the values ± 1 respectively in the two phases, and interpolates between the two across a diffuse interface of thickness ϵ. In the sharp-interface limit $\epsilon \to 0$, the equations should reproduce the correct physics, and reduce to the model above, including the interface conditions. A thermodynamically consistent phase-field model which reduces to this formulation was proposed in Ref. [62]:

$$
\begin{aligned}
\partial_t(\rho(\phi)\mathbf{v}) + \boldsymbol{\nabla} \cdot (\rho(\phi)\mathbf{v} \otimes \mathbf{v}) - \boldsymbol{\nabla} \cdot [2\mu(\phi)\mathcal{D}\mathbf{v} + \mathbf{v} \otimes \rho'(\phi)M(\phi)\boldsymbol{\nabla}g_\phi] + \boldsymbol{\nabla}p \\
= -\phi\boldsymbol{\nabla}g_\phi - \sum_i c_i \boldsymbol{\nabla}g_{c_i},
\end{aligned}
\tag{17}
$$

$$
\boldsymbol{\nabla} \cdot \mathbf{v} = 0,
\tag{18}
$$

$$
\partial_t\phi + \mathbf{v} \cdot \boldsymbol{\nabla}\phi - \boldsymbol{\nabla} \cdot (M(\phi)\boldsymbol{\nabla}g_\phi) = 0,
\tag{19}
$$

$$
\partial_t c_j + \mathbf{v} \cdot \boldsymbol{\nabla}c_j - \boldsymbol{\nabla} \cdot (K_j(\phi)c_j\boldsymbol{\nabla}g_{c_j}) = 0,
\tag{20}
$$

$$
\boldsymbol{\nabla} \cdot (\varepsilon(\phi)\boldsymbol{\nabla}V) = -\rho_e.
\tag{21}
$$

Here, ϕ is the phase field, and it takes the value $\phi = -1$ in phase $i = 1$, and the value $\phi = 1$ in phase $i = 2$. Eq. (19) governs the conservative evolution of the phase field, wherein the diffusion term is controlled by the phase field mobility $M(\phi)$. Here, ρ, μ, ε, K_j depend on which phase they are in, and are considered slave variables of the phase field ϕ. Across the interface these quantities interpolate between the values in the two phases:

$$
\rho(\phi) = \frac{\rho_1 + \rho_2}{2} + \frac{\rho_1 - \rho_2}{2}\phi,
\tag{22}
$$

$$
\mu(\phi) = \frac{\mu_1 + \mu_2}{2} + \frac{\mu_1 - \mu_2}{2}\phi,
\tag{23}
$$

$$
\varepsilon(\phi) = \frac{\varepsilon_1 + \varepsilon_2}{2} + \frac{\varepsilon_1 - \varepsilon_2}{2}\phi,
\tag{24}
$$

$$
K_j(\phi) = \frac{K_{1,j} + K_{2,j}}{2} + \frac{K_{1,j} - K_{2,j}}{2}\phi.
\tag{25}
$$

These averages are all weighted arithmetically, although other options are available. For example, Tomar *et al.* [54] found that, in the case of a level-set method with smoothly interpolated phase properties, using a weighted harmonic mean gave more accurate computation of the electric field. However, López-Herrera *et al.* [55] found no indication that the harmonic mean was superior when free charges were present, and hence we adopt for simplicity

and computational performance the arithmetic mean, although it remains unsettled which mean would yield the most accurate result.

Further, the chemical potential of species c_j is given by

$$g_{c_j}(c_j, \phi) = \alpha'(c_j) + \beta_j(\phi) + z_j V, \tag{26}$$

where we, for dilute solutions, may model $\alpha(c) = c(\log c - 1)$ to obtain consistency with the standard Nernst–Planck equation. Further, we use a weighted arithmetic mean for the solubility parameters β_j:

$$\beta_j(\phi) = \frac{\beta_{1,j} + \beta_{2,j}}{2} + \frac{\beta_{1,j} - \beta_{2,j}}{2}\phi, \tag{27}$$

which, under the assumption of dilute solutions and with the interpretation (6), corresponds to a weighted geometric mean for the reference concentrations:

$$c_j^{\text{ref}}(\phi) = \left(c_j^{\text{ref},1}\right)^{\frac{1+\phi}{2}} \cdot \left(c_j^{\text{ref},2}\right)^{\frac{1-\phi}{2}}. \tag{28}$$

In analogy with g_{c_j} being the chemical potential of species c_j, we denote g_ϕ as the chemical potential of the phase field ϕ. It is given by:

$$g_\phi = \frac{\partial f}{\partial \phi} - \boldsymbol{\nabla} \cdot \frac{\partial f}{\partial \boldsymbol{\nabla}\phi} + \sum_j \beta_j'(\phi)c_j - \frac{1}{2}\varepsilon'(\phi)|\boldsymbol{\nabla}V|^2. \tag{29}$$

The free energy functional f of the phase field is defined by

$$f(\phi, \boldsymbol{\nabla}\phi) = \frac{3\sigma}{2\sqrt{2}}\left[\frac{\epsilon}{2}|\boldsymbol{\nabla}\phi|^2 + \epsilon^{-1}W(\phi)\right] = \tilde{\sigma}\left[\frac{\epsilon}{2}|\boldsymbol{\nabla}\phi|^2 + \epsilon^{-1}W(\phi)\right], \tag{30}$$

where where σ is the surface tension, ϵ is the interface thickness, and $W(\phi)$ is a double well potential. Here, we use $W(\phi) = (1 - \phi^2)^2/4$. We have also implicitly defined the scaled surface tension $\tilde{\sigma}$ for convenience of notation. With this free energy, we obtain

$$g_\phi = \tilde{\sigma}\epsilon^{-1}W'(\phi) - \tilde{\sigma}\epsilon\boldsymbol{\nabla}^2\phi + \sum_j \beta_j'(\phi)c_j - \frac{1}{2}\varepsilon'(\phi)|\boldsymbol{\nabla}V|^2. \tag{31}$$

We will assume this form throughout.

After some rewriting, exploiting Eq. (18) and the fact that $\rho'(\phi)$ is constant due to Eq. (22), Eq. (17) can be expressed as

$$\rho(\phi)\partial_t\mathbf{v} + \left((\rho(\phi)\mathbf{v} - \rho'(\phi)M(\phi)\boldsymbol{\nabla}g_\phi) \cdot \boldsymbol{\nabla}\right)\mathbf{v} - \boldsymbol{\nabla} \cdot [2\mu(\phi)\mathcal{D}\mathbf{v}] + \boldsymbol{\nabla}p$$
$$= -\phi\boldsymbol{\nabla}g_\phi - \sum_j c_j\boldsymbol{\nabla}g_{c_j}. \tag{32}$$

1. Phase field mobility

Given a proper definition of the phase-field mobility $M(\phi)$, the phase-field model should reduce to the sharp-interface model given in the previous section. As discussed at length in Ref. [62], the two following ways are viable options:

$$M(\phi) = \epsilon M_0, \tag{33a}$$

$$M(\phi) = M_0(1 - \phi^2)_+. \tag{33b}$$

Here M_0 is a constant, and $(\cdot)_+ = \max(\cdot, 0)$. Other formulations of M are possible; some of these will in the limit of vanishing interface width reduce to a sharp-interface model where the interface velocity does not equal the fluid velocity [59, 62].

2. Boundary conditions

Some of the interface conditions from the sharp-interface model carry over to the phase field model, but in addition, some new conditions must be specified for the phase field. Here we give a brief summary. We assume that the boundary of the domain Ω, $\partial\Omega$, can be divided into an inlet part $\partial\Omega_{\text{in}}$, an outlet part $\partial\Omega_{\text{out}}$, and a wall part $\partial\Omega_{\text{wall}}$. We shall primarily discuss the latter here.

For the velocity field, we assume the no-slip condition

$$\mathbf{v}(\mathbf{x}, t) = \mathbf{0} \quad \text{for} \quad \mathbf{x} \in \partial\Omega_{\text{wall}}. \tag{34}$$

Alternatively, a no-flux condition and a slip law could have been used; in particular, a generalized Navier boundary condition (GNBC) has been shown to hold yield a consistent description of the contact line motion [48, 49]. However, to limit the scope, the moving contact line paradox will in this work be overcome by interface diffusion.

With regards to the flow problem, the pressure gauge needs to be fixed. To this end, the pressure could be fixed somewhere on the boundary, or the pressure nullspace could be removed.

For the concentrations c_j, we may use a prescribed concentration, or the no-flux condition

$$\hat{\mathbf{n}} \cdot \left(K_j(\phi) c_j \boldsymbol{\nabla} g_{c_j} \right) = 0 \quad \text{on} \quad \partial\Omega_{\text{wall}}. \tag{35}$$

12

For the electric potential, we use either the Dirichlet condition $V = \bar{V}$ (which is reasonable at either inlet or outlet), or in the presence of charged (or neutral) boundaries, the condition

$$\hat{\mathbf{n}} \cdot \boldsymbol{\nabla} V = \frac{\sigma_e}{\varepsilon(\phi)} \quad \text{on} \quad \partial\Omega_{\text{wall}}, \tag{36}$$

similar to the sharp-interface condition. Note that $\sigma_e(\mathbf{x})$ is prescribed and can vary over the boundary.

We assume that the no-flux conditons hold on the phase field chemical potential,

$$\hat{\mathbf{n}} \cdot \boldsymbol{\nabla} g_\phi = 0 \quad \text{on} \quad \partial\Omega_{\text{wall}}. \tag{37}$$

For the phase field itself, a general dynamic wetting boundary condition can be expressed as [77]:

$$\epsilon\tau_w\partial_t\phi = -\tilde{\sigma}\epsilon\hat{\mathbf{n}} \cdot \boldsymbol{\nabla}\phi + \tilde{\sigma}\cos(\theta_e)f_w'(\phi), \tag{38}$$

where θ_e is the equilibrium contact angle, τ_w is a relaxation parameter, and $f_w(\phi) = (2 + 3\phi - \phi^3)/4$ interpolates smoothly between 0 (at $\phi = -1$) and 1 (at $\phi = 1$). In this work, we limit ourselves to studying fixed contact angles, i.e. considering Eq. (38) with $\tau_w = 0$. For a GNBC, the phase-field boundary condition (38) must be modelled consistently with the slip condition on the velocity [48].

III. DISCRETIZATION

For solving the equations of two-phase EHD, i.e. the model consisting of Eqs. (17)–(21), there are four operations that must be performed:

1. Propagate the phase field ϕ.

2. Propagate the chemical species concentrations c_i.

3. Update the electric potential V

4. Propagate the velocity $\mathbf{v}$ and pressure p.

The whole system of equations could in principle be solved simultaneously using implicit Euler discretization in time and e.g. Newton's method to solve the nonlinear system. However, in order to simulate larger systems faster, it is preferable to use a splitting scheme to solve for each field sequentially. One such splitting scheme was outlined in [70], based

13

on the energy-stable scheme without electrochemistry as developed by [68, 69]. However, that scheme did not take into account that the electric permittivities in the two fluids may differ, and when they do, the phase field and the electrochemistry computations become coupled through the electric field [71]. We will here discuss two strategies for solving the coupled problem of two-phase electrohydrodynamics. First, we present the fully monolithic, non-linear scheme, and secondly, we propose a new, fully practical linear operator splitting scheme. As we are not aware of any splitting schemes that are second-order accurate in time for the case of unmatched densities, we shall constrain our discussion to first-order in time schemes.

In the forthcoming, we will denote the inner product of any two scalar, vector, or tensor fields $\mathcal{A}, \mathcal{B}$ by $(\mathcal{A}, \mathcal{B})$. Further, we consider a discrete time step τ, and denote the (first-order) discrete time derivative by

$$\partial_\tau^- \mathcal{A}^k = \frac{\mathcal{A}^k - \mathcal{A}^{k-1}}{\tau}. \tag{39}$$

The equations are discretized on the domain $\Omega \subset \mathbb{R}^d$, $d = 2, 3$, with the no-slip boundary Γ. Since we do not consider explicitly in- and outlet boundary conditions in this work, we will omit this possible part of the domain for the sake of brevity.

We define the following finite element subspaces:

$$\mathbf{V}_h = (V_h)^d \quad \text{where} \quad V_h = \left\{ v \in H^1(\Omega) \right\} \quad \text{for velocity,} \tag{40}$$

$$P_h = \left\{ p \in L_0^2(\Omega) \right\} \quad \text{for pressure,} \tag{41}$$

$$\Phi_h = \left\{ \phi \in H^1(\Omega) \right\} \quad \text{for phase field,} \tag{42}$$

$$G_h = \left\{ g \in H^1(\Omega) \right\} \quad \text{for phase field chemical potential,} \tag{43}$$

$$C_h = \left\{ c \in H^1(\Omega) \right\} \quad \text{for concentrations,} \tag{44}$$

$$U_h = \left\{ V \in H^1(\Omega) \right\} \quad \text{for the electrostatic potential.} \tag{45}$$

A.   Monolithic scheme

Here we give the fully implicit scheme that follows from a naïve implicit Euler discretizion of the model (17)–(21), and supplemented by Eq. (31).

Assume that $(\mathbf{v}^{k-1}, p^{k-1}, \phi^{k-1}, g_\phi^{k-1}, c_1^{k-1}, \ldots, c_M^{k-1}, V^{k-1})$ is given. The scheme can then be summarized by the following. Find $(\mathbf{v}^k, p^k, \phi^k, g_\phi^k, c_1^k, \ldots, c_N^k, V^k) \in \mathbf{V}_h \times P_h \times \Phi_h \times G_h \times$

14

$(C_h)^N \times \mathcal{U}_h$ such that

$$\left(\rho^k \partial_\tau^- \mathbf{v}^k, \mathbf{u}\right) + \left(\left(\mathbf{m}^k \cdot \boldsymbol{\nabla}\right) \mathbf{v}^k, \mathbf{u}\right) + \left(2\mu^k \mathcal{D}\mathbf{v}^k, \mathcal{D}\mathbf{u}\right) - \left(p^k, \boldsymbol{\nabla} \cdot \mathbf{u}\right)$$
$$= -\left(\phi^k \boldsymbol{\nabla} g_\phi^k, \mathbf{u}\right) - \sum_j \left(c_j^k \boldsymbol{\nabla} g_{c_j}^k, \mathbf{u}\right), \quad (46a)$$

$$\left(\boldsymbol{\nabla} \cdot \mathbf{v}^k, q\right) = 0, \quad (46b)$$

$$\left(\partial_\tau^- \phi^k, \psi\right) - \left(\mathbf{v}^k \phi^k, \boldsymbol{\nabla}\psi\right) + \left(M^k \boldsymbol{\nabla} g_\phi^k, \boldsymbol{\nabla}\psi\right) = 0, \quad (46c)$$

$$\left(g_\phi^k, g_\psi\right) = \left(\tilde{\sigma}\epsilon^{-1} W'(\phi^k), g_\psi\right) - \tilde{\sigma}\cos(\theta_e) \int_\Gamma f_w'(\phi^k) g_\psi \, \mathrm{d}\Gamma + \left(\tilde{\sigma}\epsilon \boldsymbol{\nabla}\phi^k, \boldsymbol{\nabla} g_\psi\right)$$
$$+ \sum_j \left(\beta_j' c_j^k, g_\psi\right) - \left(\frac{1}{2}\varepsilon'|\boldsymbol{\nabla} V^k|^2, g_\psi\right), \quad (46d)$$

$$\left(\partial_\tau^- c_j^k, b_j\right) - \left(\mathbf{v}^k c_j^k, \boldsymbol{\nabla} b_j\right) + \left(K_j^k c_j^k \boldsymbol{\nabla} g_{c_j}^k, \boldsymbol{\nabla} b_j\right) = 0, \quad (46e)$$

$$\left(\varepsilon^k \boldsymbol{\nabla} V^k, \boldsymbol{\nabla} U\right) = \left(\rho_e^k, U\right) + \int_\Gamma \sigma_e U \, \mathrm{d}\Gamma, \quad (46f)$$

for all test functions $(\mathbf{u}, q, \psi, g_\psi, b_1, \ldots, b_N, U) \in \mathbf{V}_h \times P_h \times \Phi_h \times G_h \times (C_h)^N \times \mathcal{U}_h$. Here we have used

$$\mathbf{m}^k = \rho^k \mathbf{v}^k - \rho' M^k \boldsymbol{\nabla} g_\phi^k \quad (47)$$

and the shorthands

$$\rho^k = \rho(\phi^k), \quad \mu^k = \mu(\phi^k), \quad M^k = M(\phi^k), \quad \varepsilon^k = \varepsilon(\phi^k),$$
$$K_j^k = K_j(\phi^k), \quad \text{and} \quad \rho_e^k = \rho_e(\{c_j^k\}).$$

Note that Eqs. (46) constitute a fully coupled non-linear system and the equations must thus be solved simultaneously, preferably using a Newton method. This results in a large system matrix which must be assembled and solved iteratively, and for which there are in general no suitable preconditioners available. On the other hand, the scheme is fully implicit and hence expected to be fairly robust with regards to e.g. time step size. There are in general several options for constructing the linearized variational form to be used in a Newton scheme.

B. A linear splitting scheme

Now, we introduce a linear operator splitting scheme. This scheme splits between the processes of phase-field transport, chemical transport under an electric field, and hydrodynamic flow, such that the equations governing each of these processes are solved separately.

a. Phase field step   Find $(\phi^k, g_\phi^k) \in \Phi_h \times G_h$ such that

$$\left(\partial_\tau^- \phi^k, \psi\right) - \left(\mathbf{v}^{k-1}\phi^k, \boldsymbol{\nabla}\psi\right) + \left(M^{k-1}\boldsymbol{\nabla}g_\phi^k, \boldsymbol{\nabla}\psi\right) = 0 \tag{48a}$$

$$\begin{aligned}
\left(g_\phi^k, g_\psi\right) &= \tilde{\sigma}\epsilon^{-1}\left(\overline{W'}(\phi^k, \phi^{k-1}), g_\psi\right) + \tilde{\sigma}\epsilon\left(\boldsymbol{\nabla}\phi^k, \boldsymbol{\nabla}g_\psi\right) \\
&\quad - \tilde{\sigma}\cos(\theta_e)\int_\Gamma \overline{f'_w}(\phi^k, \phi^{k-1})\, g_\psi\, \mathrm{d}\Gamma + \sum_j \beta_j'\left(c_j^{k-1}, g_\psi\right) - \frac{1}{2}\varepsilon'\left(|\boldsymbol{\nabla}V^{k-1}|^2, g_\psi\right),
\end{aligned} \tag{48b}$$

for all test functions $(\psi, g_\psi) \in \Phi_h \times G_h$. Here, $\overline{W'}(\phi^k, \phi^{k-1})$ is a linearization of $W'(\phi^k)$ around ϕ^{k-1}:

$$\overline{W'}(\phi^k, \phi^{k-1}) = W'(\phi^{k-1}) + W''(\phi^{k-1})(\phi^k - \phi^{k-1}). \tag{49}$$

We have also used the discretization of Eq. 38

$$\tilde{\sigma}\epsilon\mathbf{n} \cdot \boldsymbol{\nabla}\phi^k = \tilde{\sigma}\cos(\theta_e)\overline{f'_w}(\phi^k, \phi^{k-1}), \tag{50}$$

where we have used the linearization

$$\overline{f'_w}(\phi^k, \phi^{k-1}) = f'_w(\phi^{k-1}) + f''_w(\phi^{k-1})(\phi^k - \phi^{k-1}). \tag{51}$$

b. Electrochemistry step   Find $(c_1, \dots, c_N, V) \in (C_h)^N \times U_h$ such that

$$\left(\partial_\tau^- c_j^k, b_j\right) - \left(\mathbf{v}^{k-1}c_j^k, \boldsymbol{\nabla}b_j\right) + \left(\bar{\mathbf{J}}_{c_j}^k, \boldsymbol{\nabla}b_i\right) = 0 \tag{52a}$$

$$\left(\varepsilon^k\boldsymbol{\nabla}V^k, \boldsymbol{\nabla}U\right) + \int_\Gamma \sigma_e U\, \mathrm{d}\Gamma + \left(\rho_e^k, U\right) = 0 \tag{52b}$$

for all test functions $(b_1, \dots, b_N, U) \in (C_h)^N \times U_h$. Here $\bar{\mathbf{J}}_{c_j}^k$ is a linear approximation of the diffusive chemical flux $\mathbf{J}_{c_j} = K_j(\phi)c_j\boldsymbol{\nabla}g_{c_j}$. For conciseness, we here constrain our analysis to ideal chemical solutions, i.e. we assume a common chemical energy function on the form $\alpha(c) = c(\ln c - 1)$. To this end, we approximate the flux by:

$$\bar{\mathbf{J}}_{c_j}^k = K_j^k(\boldsymbol{\nabla}c_i^k + c_i^k\beta_i'\boldsymbol{\nabla}\phi^k + z_i c_i^{k-1}\boldsymbol{\nabla}V^k). \tag{53}$$

c. Fluid flow step   Find $(\mathbf{v}^k, p^k) \in \mathbf{V}_h \times P_h$ such that

$$\begin{aligned}
\left(\rho^{k-1}\partial_\tau^- \mathbf{v}^k, \mathbf{u}\right) &+ \left((\bar{\mathbf{m}}^{k-1} \cdot \boldsymbol{\nabla})\mathbf{v}^k, \mathbf{u}\right) \\
&+ \frac{1}{2}\left(\mathbf{v}^k\partial_\tau^- \rho^k, \mathbf{u}\right) - \frac{1}{2}\left(\bar{\mathbf{m}}^{k-1}, \boldsymbol{\nabla}(\mathbf{v}^k \cdot \mathbf{u})\right) + \left(2\mu^k\mathcal{D}\mathbf{v}^k, \mathcal{D}\mathbf{u}\right) - \left(p^k, \boldsymbol{\nabla} \cdot \mathbf{u}\right) \\
&= -\left(\phi^k\boldsymbol{\nabla}g_\phi^k, \mathbf{u}\right) - \sum_j \left(c_j^k\boldsymbol{\nabla}g_{c_j}^k, \mathbf{u}\right) \tag{54a}
\end{aligned}$$

$$\left(q, \boldsymbol{\nabla} \cdot \mathbf{v}^k\right) = 0 \tag{54b}$$

for all test functions $(\mathbf{u}, q) \in \mathbf{V}_h \times P_h$. Here, we have used the following approximation of the advective momentum:

$$\bar{\mathbf{m}}^{k-1} = \rho^{k-1}\mathbf{v}^{k-1} - \rho' M^k \boldsymbol{\nabla} g_\phi^k. \tag{55}$$

Note that the terms in (54a) involving $\partial_\tau^- \rho^k + \boldsymbol{\nabla} \cdot \bar{\mathbf{m}}^{k-1}$, which is a discrete approximation of $\partial_t \rho + \boldsymbol{\nabla} \cdot \mathbf{m} = 0$, is included to satisfy a discrete energy dissipation law [78] (i.e., to improve stability). This step requires solving for the velocity and pressure in a coupled manner. This has the advantage that it yields accurate computation of the pressure, but the drawback that it is computationally challenging to precondition and solve, related to the Babuska–Brezzi (BB) condition (see e.g. [79]). Alternatively, it might be worthwhile to further split the fluid flow step into the following three substeps, at the cost of some lost accuracy [80].

- Tentative velocity step: Find $\tilde{\mathbf{v}}^k \in \mathbf{V}_h$ such that for all $\mathbf{u} \in \mathbf{V}_h$,

$$\left(\rho^{k-1}\frac{\tilde{\mathbf{v}}^k - \mathbf{v}^{k-1}}{\tau}, \mathbf{u}\right) + \left((\bar{\mathbf{m}}^{k-1} \cdot \boldsymbol{\nabla})\tilde{\mathbf{v}}^k, \mathbf{u}\right) + \left(2\mu^k \mathcal{D}\tilde{\mathbf{v}}^k, \mathcal{D}\mathbf{u}\right) - \left(p^{k-1}, \boldsymbol{\nabla} \cdot \mathbf{u}\right)$$
$$+ \frac{1}{2}\left(\tilde{\mathbf{v}}^k \partial_\tau^- \rho^k, \mathbf{u}\right) - \frac{1}{2}\left(\bar{\mathbf{m}}^{k-1}, \boldsymbol{\nabla}(\tilde{\mathbf{v}}^k \cdot \mathbf{u})\right) = -\left(\phi^k \boldsymbol{\nabla} g_\phi^k, \mathbf{u}\right) - \sum_i \left(c_i^{k-1} \boldsymbol{\nabla} g_i^k, \mathbf{u}\right), \tag{56a}$$

  with the Dirichlet boundary condition $\tilde{\mathbf{v}}^k = \mathbf{0}$ on Γ.

- Pressure correction step: Find $p^k \in P_h$ such that for all $q \in P_h$, we have

$$\left(\frac{1}{\rho_0}\boldsymbol{\nabla}(p^k - p^{k-1}), \boldsymbol{\nabla} q\right) = -\frac{1}{\tau}\left(\boldsymbol{\nabla} \cdot \tilde{\mathbf{v}}^k, q\right). \tag{56b}$$

- Velocity correction step: Then, find $\mathbf{v}^k \in \mathbf{V}_h$ such that for all $\mathbf{u} \in \mathbf{V}_h$,

$$\left(\rho^k \frac{\mathbf{v}^k - \tilde{\mathbf{v}}^k}{\tau}, \mathbf{u}\right) = \left(p^k - p^{k-1}, \boldsymbol{\nabla} \cdot \mathbf{u}\right), \tag{56c}$$

  which we solve by explicitly imposing the Dirichlet boundary condition $\mathbf{u}^k = \mathbf{0}$ on Γ.

Eqs. (56a), (56b), and (56c) should be solved sequentially, and constitutes a variant of a projection scheme, i.e., a fractional-step approach to the fluid flow equations [78, 80–83]. We will in this paper refer to the coupled solution of the fluid flow equations, unless stated

otherwise. Specifically, the fractional-step fluid flow scheme will only be demonstrated in the full 3D simulations in Sec. VI B.

The scheme presented above consists in sequentially solving three decoupled subproblems (or five decoupled subproblems for the fractional-step fluid flow alternative). The subproblems are all linear, and hence attainable for specialized linear solvers which could improve the efficiency. We note that the splitting introduces an error of order τ, i.e. the same as the scheme itself. Moreover, our scheme does not preserve the same energy dissipation law on the discrete level, that the original model does on the continuous level. We are currently not aware of any scheme for two-phase electrohydrodynamics with this property, apart from the fully implicit scheme presented in the previous section.

IV. BERNAISE

We have now introduced the governing equations and two strategies for solving them. Now, we will introduce the Bernaise package, and describe an implementation of a generic simulation problem and a generic solver in this framework. For a complete description of the software, we refer to the online Git repository [84]. The work presented herein refers to version 1.0 of *Bernaise*, which is compatible with version 2017.2.0 of FEniCS [42].

A. Python package

Bernaise is designed as a Python package, and the main structure of the package is shown in Fig. 1. The package contains two main submodules, `problems` and `solvers`. As suggested by the name, the `problems` submodule contains scripts where problem-specific geometries (or meshes), physical parameters, boundary conditions, initial states, etc., are specified. We will in Sec. IV B dive into the constituents of a problem script. The `solvers` submodule, on the other hand, contains scripts that are implementations of the numerical schemes required to solve the governing equations. Two notable examples that are implemented in *Bernaise* are the monolithic scheme (implemented as `basicnewton`) and the linear splitting scheme (implemented as `basic`). We shall in Sec. IV C describe the building blocks of such a solver. Further, a default solver compatible with a given problem is specified in the problem, but this setting can—along with most other settings specified in a problem—be overridden by

18

providing an additional keyword to the main script call (see below). Note that *not all* solvers are compatible with *all* problems, and vice versa.

```
BERNAISE
├─ sauce.py
├─ postprocess.py
├─ common
│  ├─ __init__.py
│  ├─ bcs.py
│  ├─ cmd.py
│  ├─ functions.py
│  ├─ io.py
│  └─ ...
├─ problems
│  ├─ __init__.py
│  ├─ charged_droplet.py
│  ├─ taylorgreen.py
│  ├─ snoevsen.py
│  ├─ charged_droplets_3D.py
│  └─ ...
├─ solvers
│  ├─ __init__.py
│  ├─ basic.py
│  ├─ basicnewton.py
│  ├─ fracstep.py
│  └─ ...
├─ utilities
│  └─ ...
└─ ...
```
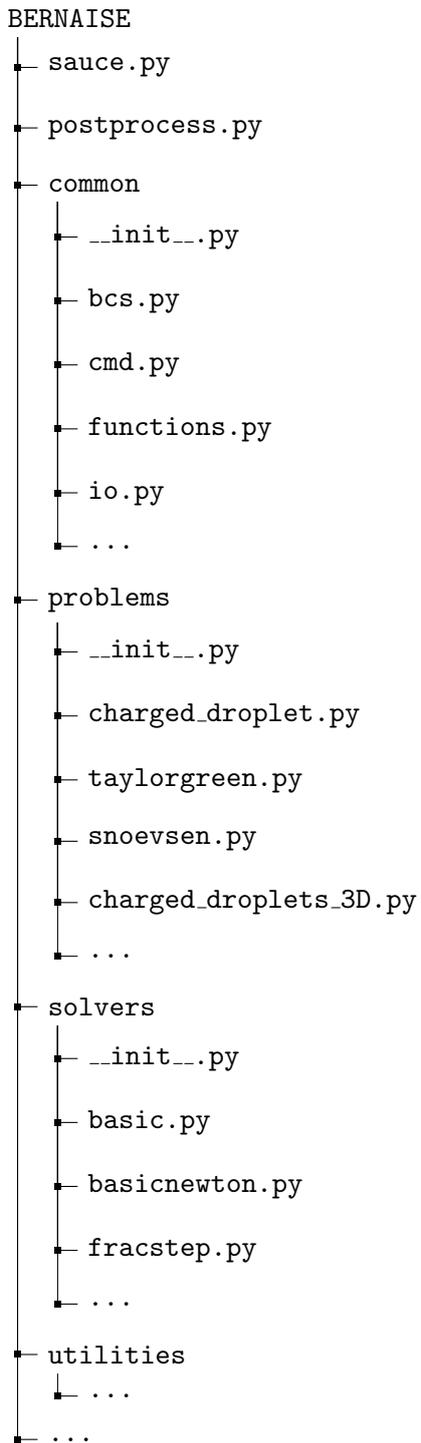
FIG. 1: Part of the directory structure of Bernaise.

A simulation is typically run from a terminal, pointing to the *Bernaise* directory, using

19

the command

```
>> python sauce.py problem=charged_droplet
```

where `charged_droplet` may be exchanged with another problem script of choice; albeit we will use `charged_droplet` as a pedagogical example in the forthcoming. The main script `sauce.py` fetches a `problem` and connects it with the `solver`. It sets up the finite element problem with all the given parameters, initializes the finite element fields with the specified initial state, and solves it with the specified boundary condition at each time step, until the specified (physical) simulation time `T` is exceeded. Any parameter in the problem can be overridden by specifying an additional keyword from the command line; for example, the simulation time can be set to 1000 by running the command:

```
>> python sauce.py problem=charged_droplet T=1000
```

After every given interval of steps, specified by the parameter `checkpoint_interval`, a checkpoint is stored, including all fields, and all problem parameters at the time of writing to file. The checkpoint can be loaded, and the simulation can be continued, by running the command:

```
>> python sauce.py problem=charged_droplet \
   restart_folder=results_charged_droplet/1/Checkpoint/
```

where the `restart_folder` points to an appropriate checkpoint folder. Here, the problem parameters stored within the checkpoint have precedence over the default parameters given in the `problem` script. Further, any parameters specified by command line keywords have precedence over the checkpoint parameters.

The role of the main module `sauce.py` is to allocate the required variables to run a simulation, to import routines from the specified problem and solver, to iterate the solver in time, and to output and store data at appropriate times. Hence, the main module works as a general interface to problems and solvers. This is enabled by overloading a series of functions, such that problem- and solver-specific functions are defined within the problem and solver, respectively. The structure of `sauce.py` is by choice similar to the `NSfracStep.py` script in the *Oasis* solver [43]; both in order to appeal to overlapping user bases, and to

keep the code readable and consistent with and similar to common FEniCS examples. However, an additional layer of abstraction in e.g. setting up functions and function spaces is necessary in order to handle a flexible number of subproblems and subspaces, depending on e.g. whether phase field, electrochemistry or flow is disabled, or whether we are running with a monolithic or operator splitting scheme. To keep the *Bernaise* code as readable and easily maintainable as possible, we have consciously avoided uneccessary abstraction. Only the boundary conditions (found in `common/bcs.py` are implemented as classes.

B.   The problems submodule

The basic user typically interacts with *Bernaise* by implementing a *problem* to be solved. This is accessible to *Bernaise* when put in the subfolder `problems`. The implementation consists in overloading a certain set of functions; all of which are listed in the `problems/__init__.py` file in the problems folder. The mandatory functions that must be overloaded for each problem are:

- `mesh`: defines the geometry. Equivalent to the `mesh` function in *Oasis* [43].

- `problem`: sets up all parameters to be overloaded, including defining solutes and types of finite elements. The default parameters are defined in the `problems/__init__.py` file.

- `initialize`: initializes all fields.

- `create_bcs`: sets all subdomains, and defines boundary conditions (including pointwise boundary condtions, such as pressure pinning). The boundary conditions are more thoroughly explained below.

Further, there are functions that *may* be overloaded.

- `constrained_domain`: set if the boundary is to be considered periodic.

- `pf_mobility`: phase field mobility function; cf. (33a) and (33b).

- `start_hook`: hook called before the temporal loop.

- `tstep_hook`: hook called at each time step in the loop.

- **end_hook**: hook called at the end of the program.

- **rhs_source**: explicit source terms to be added to the right hand side of given fields; used e.g. in the method of manufactured solution.

Note here the use of three *hooks* that are called during the course of a simulation. These are useful for outputting certain quantities during a simulation, e.g. the flux through a cross section, or total charge in the domain. The **start_hook** could also be used to call a steady-state solver to initialize the system closer to equilibrium, e.g. a solver that solves only the electrochemistry subproblem such that we do not have to resolve the very fast time scale of the initial charge equilibration.

In Listing 1, we show an implementation of the **problems** function, which sets the necessary parameters that are required for the **charged_droplet** case to run. Here, the **solutes** array (which defines the solutes), contains only one species, but it can in principle contain arbitrarily many.

```python
def problem():

    info_cyan("Charged droplet in an electric field.")


    # Define solutes
    # Format: name, valency, diffusivity in phase 1, diffusivity in phase 2,
    #         solubility energy in phase 1, solubility energy in phase 2
    solutes = [["c_p",  1, 1e-5, 1e-3, 4., 1.]]


    # Default parameters to be loaded unless starting from checkpoint.
    parameters = dict(
        solver="basic",                     # Solver to be used.
        folder="results_charged_droplet",  # Folder to store results in.
        dt=0.08,                            # Timestep
        t_0=0.,                             # Starting time
        T=8.,                               # Total simulation time
        grid_spacing=1./32,                 # Mesh size
        interface_thickness=0.03,           # Extent of diffuse interface
```

```
        solutes=solutes,                  # Array of solutes defined above

        Lx=2.,                            # Length of domain along x

        Ly=1.,                            # Length of domain along y

        rad_init=0.25,                    # Initial droplet radius

        V_left=10.,                       # Potential at left side

        V_right=0.,                       # Potential at right side

        surface_tension=5.,               # Surface tension

        concentration_init=10.,           # Initial (total) concentration

        pf_mobility_coeff=0.00002,        # Phase field mobility coeff. (M_0)

        density=[200., 100.],             # Density in phase 1, phase 2

        viscosity=[10., 1.],              # Viscosity in phase 1, phase 2

        permittivity=[1., 1.]             # Permittivity in phase 1, phase 2
    )
    return parameters
```

Listing 1: The `problems` function for the `charged_droplet` case.

In Listing 2, we show the code for the initialization stage. Here, `initial_pf` and `initial_c` are functions defined locally inside the `charged_droplet.py` problem script, that set the initial distributions of the phase field and the concentration field, respectively. Here, it should be noted how the (boolean) parameters `enable_PF`, `enable_EC` and `enable_NS` allow to switch on or off either the phase field, the electrochemistry or the hydrodynamics, respectively.

```
def initialize(Lx, Ly, rad_init, interface_thickness, solutes,
               concentration_init, restart_folder, field_to_subspace,
               enable_NS, enable_PF, enable_EC, **namespace):
    """ Create the initial state. """
    w_init_field = dict()
    if not restart_folder:
        x0, y0, rad0, c0 = Lx/4, Ly/2, rad_init, concentration_init
        # Initialize phase field
```

```
        if enable_PF:

            w_init_field["phi"] = initial_pf(
                x0, y0, rad0, interface_thickness,
                field_to_subspace["phi"].collapse())


        # Initialize electrochemistry
        if enable_EC:
            w_init_field[solutes[0][0]] = initial_c(
                x0, y0, rad0/3., c0, interface_thickness,
                field_to_subspace[solutes[0][0]].collapse())


    return w_init_field
```

Listing 2: The `initialize` function for the `charged_droplet` case.

C. The solvers submodule

Advanced users may develop solvers that can be placed in the `solvers` subdirectory. In the same way as with the `problems` submodule, a solver implementation constists of overloading a range of functions which are defined in `solvers/__init__.py`.

- `get_subproblems`: Returns a dictionary (`dict`) of the subproblems which the solver splits the problem into. This dictionary has points to the name of the fields and the elements (specified in problem) which the subspace is made up of.

- `setup`: Sets up the FEniCS solvers for each subproblem.

- `solve`: Defines the routines for solving the finite element problems, which are called at every time step.

- `update`: Defines the routines for assigning updated values to fields, which are called at the end of every time step.

The module `solvers/basicnewton.py` implements the monolithic scheme, while the module `solvers/basic.py` implements the segregated solver [85]. The problem is split up into the

24

subproblems corresponding to whether we have a monolothic or segragated solver in the function `get_subproblems`. Within the `setup` function, the variational forms are defined, and the solver routines are initialized. The latter are eventually called in the `solve` routine at every time step. Note that the element types are defined within the problem, and that the solvers in general can be applied for higher-order spatial accuracy without further ado. The task of `get_subproblems` is simply to link the subproblem to the element specification.

In Listing 3, we show how the `get_subproblems` function is implemented in the `basic` solver. As can be readily seen, the function formally splits the problem into the three subproblems `NS`, `PF`, and `EC`.

```python
def get_subproblems(solutes, enable_NS, enable_PF, enable_EC, **namespace):
    """ Returns dict of subproblems the solver splits the problem into. """
    subproblems = dict()
    if enable_NS:
        subproblems["NS"] = [dict(name="u", element="u"),
                             dict(name="p", element="p")]
    if enable_PF:
        subproblems["PF"] = [dict(name="phi", element="phi"),
                             dict(name="g", element="g")]
    if enable_EC:
        subproblems["EC"] = ([dict(name=solute[0], element="c")
                              for solute in solutes]
                             + [dict(name="V", element="V")])
    return subproblems
```

Listing 3: The `get_subproblems` subroutine of the `basic` solver.

The other functions (such as `setup`) are somewhat more involved, but can be found at the Git repository [84].

Note that the implementations of the solvers presented above are sought to be short and humanly readable, and therefore quite straightforwardly implemented. There are several ways to improve the efficiency (and hence scalability) of a solver, at the cost of lost intuitiveness [43].

D. Boundary conditions

Boundary conditions are among the few components of *Bernaise* which are implemented as classes. Physical boundary conditons may consist of a combination of Dirichlet and Neumann (or Robin) conditions, and the latter must be incorporated into the variational form. The boundary conditions are specified in the specific problem script, while the variational form is set up in the solver. To promote code reuse, keeping the physical boundary conditions accessible from the problems side, and simultaneously independent of the solver, the various boundary conditions are stored as classes in a separate module. The boundaries themselves should be set by the user within the `problem`. By importing various boundary condition classes from `common/bcs.py`, the boundary conditions can be inferred at user-specified boundaries.

Within the `bcs` module, the base class `GenericBC` is defined. The boolean member functions `is_dbc` and `is_nbc` specifies, respectively, whether the concrete boundary conditions impose a Dirichlet and Neumann condition, and both return false by default. The base class is inherited by various concrete boundary conditon classes, and by overloading these two member functions, the member functions `dbc` or `nbc` are respectively called at appropriate times in the code. There is a hierarchy of boundary conditions which inherit from each other. Some of the boundary conditions currently implemented in *Bernaise* are:

- `GenericBC`: Base class for all boundary conditions.

    - `Fixed`: Dirichlet condition, applicable for all fields.

        * `NoSlip`: The no-slip condition—a pure Dirichlet condition with the value **0**, applicable for velocity.

        * `Pressure`: Constant pressure boundary condition—adds a Neumann condition to the velocity, i.e. a boundary term in the variational form.

    - `Charged`: A charged boundary—a Neumann conditon intended for use with the electric potential V.

    - `Open`: An open boundary—a Neumann condition is applied.

We note that when a no-flux condition is to be applied, no specific boundary condition class needs to be supplied, since the boundary term in the variational form then disappears (in particular when considering conservative PDEs).

As an example, we show in Listing 4 the `create_bcs` function within the `charged_droplet` case. Here, the boundaries `Wall`, `Left`, etc., are defined in the standard Dolfin way as instances of a `SubDomain` class.

```python
def create_bcs(field_to_subspace, Lx, Ly, solutes, V_left, V_right,
               enable_NS, enable_PF, enable_EC,
               **namespace):
    """ The boundary conditions are defined in terms of field. """

    boundaries = dict(
        wall=[Wall(Lx)],
        left=[Left()],
        right=[Right(Lx)]
    )

    noslip = Fixed((0., 0.))

    bcs = dict()
    bcs_pointwise = dict()

    bcs["wall"] = dict()
    bcs["left"] = dict()
    bcs["right"] = dict()

    if enable_NS:
        bcs["wall"]["u"] = noslip
        bcs["left"]["u"] = noslip
        bcs["right"]["u"] = noslip
        bcs_pointwise["p"] = (0., "x[0] < DOLFIN_EPS && x[1] < DOLFIN_EPS")

    if enable_EC:
```

```
        bcs["left"]["V"] = Fixed(V_left)

        bcs["right"]["V"] = Fixed(V_right)


    return boundaries, bcs, bcs_pointwise
```

Listing 4: The `create_bcs` function within the `charged_droplet` case.

E.   Post-processing

An additional module provided in *Bernaise* is the post-processing module. It operates with methods analogously to how the main *Bernaise* script operates with problems. The base script `postprocess.py` pulls in the required method and analyses or operates on a specified folder. The methods are located in the folder `analysis_scripts/` and new methods can be implemented by users by adding scripts to this folder.

To exemplify its usage, we consider a method to analyse the temporal development of the energy. This is done by navigating to the root folder and calling

```
>> python postprocess.py method=energy_in_time folder=results_charged_droplet/1/
```

where we assume that the output of the simulation, we want to analyse, is found in the folder `results_charged_droplet/1/`. The analysis method `energy_in_time` above can, of course, be exchanged with another method of choice. A list of available methods can be produced by supplying the help argument from a terminal call:

```
>> python postprocess.py -h
```

Similar to the `problems` submodule, the methods are implemented by overloading a set of routines, where default routines are found in `analysis_scripts/__init__.py`. The routines required to implement an analysis method are the following:

- `description`: routine called when a question mark is added to the end of the method name during a call from the terminal, meant to obtain a description of the method without having to inspect the code.

- `method`: the routine that performs the desired analysis.

The implementation hinges on the `TimeSeries` class (located in `utilities/TimeSeries.py`), which efficiently imports the XDMF/HDF5 data files and the parameter files produced by a *Bernaise* simulation. Several plotting routines are implemented in `utilities/plot.py`, and these are extensively used in various analysis methods.

V. VALIDATION

With the aim of using *Bernaise* for quantitative purposes, it is essential to establish that the schemes presented in the above converges to the correct solution—in two senses:

- The numerical schemes should converge to the correct solution of the phase-field model.

- The solution of the phase-field model should converge to the correct sharp-interface equations [86].

Unless otherwise stated, we mean by convergence that the error in all fields χ should behave like,

$$\|\chi - \chi_e\|_h \sim C_h h^{k_h} + C_\tau \tau^{k_\tau} \tag{57}$$

where $\|\cdot\|_h$ is an L^2 norm, χ is the simulated field, χ_e is the exact solution, h is the mesh size, τ is the time step, k_h is the order of spatial convergence, k_τ is the order of temporal convergence ($k_\tau = 1$ in this work), and C_h and C_τ are constants.

In the following, we present convergence test in three cases. Firstly, in the limiting case of a stable bulk intrusion without electrochemistry, an analytical solution is available to test against. Secondly, using the method of manufactured solution, convergence of the full two-phase EHD problem to an augmented Taylor–Green vortex is shown. Thirdly, we show convergence towards a highly resolved reference solution for an electrically driven charged droplet.

We note that the aim of *Bernaise* is to solve coupled multi-physics problems, and while the solvers may contain subtle errors, they may be negligible for many applications, and dominant only in limiting cases. In addition to testing the whole, coupled multi-physics problem of two-phase EHD, a proper testing should also consider simplified settings where fewer physical mechanisms are involved simultaneously. A brief discussion of testing and such reduced models is given in Appendix C. In this section, we show the convergence of

the schemes in a few relevant cases, which we believe represent the efficacy of our approach. Tests of simplified-physics problems are found in the GitHub repository [84].

A. Stable bulk intrusion

A case where an analytic solution is available, is the stable intrusion of one fluid into another, in the absence of electrolytes and electric fields. A schematic view of the initial set-up is shown in Fig. 2. A constant velocity $\mathbf{v} = v_0 \hat{\mathbf{x}}$ is applied at both the left and right sides of the reservoir, and periodic boundary conditions are imposed at the perpendicular direction. We shall here consider the convergence to the solution of the phase-field equation, i.e. retaining a finite interface thickness ϵ. This effectively one-dimensional problem is implemented in `problems/intrusion_bulk.py`.
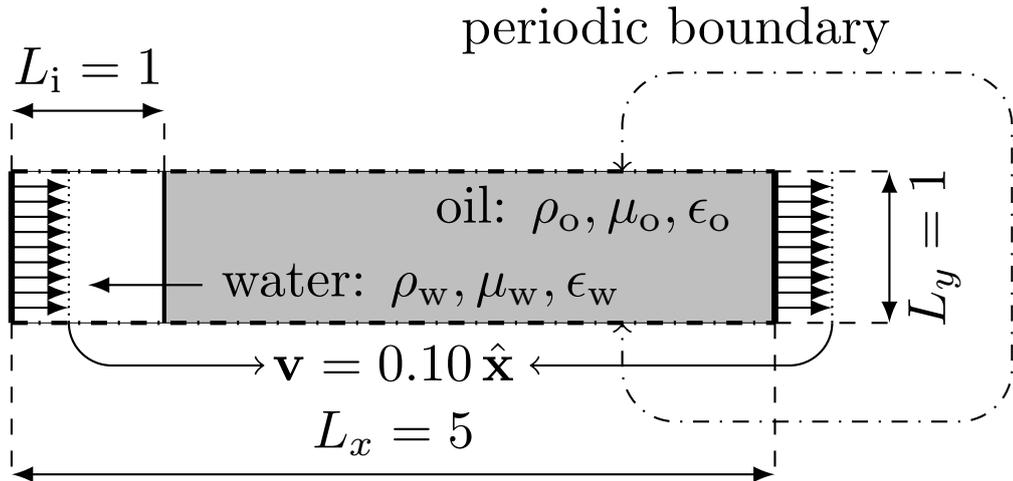
FIG. 2: Schematic set-up of the stable bulk flow intrusion test case. Here, the 'water' (subscript w) displaces the 'oil' (subscript o). At the left and right boundaries, a constant velocity is prescribed.

Due to the Galilean invariance, we expect the velocity field to be uniformly equal to the inlet and outlet velocities, i.e. $\mathbf{v}(\mathbf{x}, t) = v_0 \hat{\mathbf{x}}$. The exact analytical solution for the phase field is given by

$$\phi(\mathbf{x}, t) = \tanh\left(\frac{x - x_0 - v_0 t}{\sqrt{2}\epsilon}\right), \tag{58}$$

for which we shall consider the error norm. Note that the only parameters this analytical solution depends on are the initial position of the interface x_0, the injection velocity v_0, and the interface width ϵ. We consider the parameters $\rho_1 = \rho_2 = 1000$, $\mu_1 = 100$, $\mu_2 = 1$, $\sigma = 2.45$, $\epsilon = 0.03$, $M(\phi) = M_0 = 2 \cdot 10^{-5}$, $x_0 = 1$, $L_x = 5$, $L_y = 1$ and $v_0 = 0.1$.

Fig. 3 shows the convergence to the analytical solution with regards to temporal resolution. The order of convergence is consistent with the order of the scheme, indicating that the scheme is appreciable at least in the lack of electrostatic interactions.
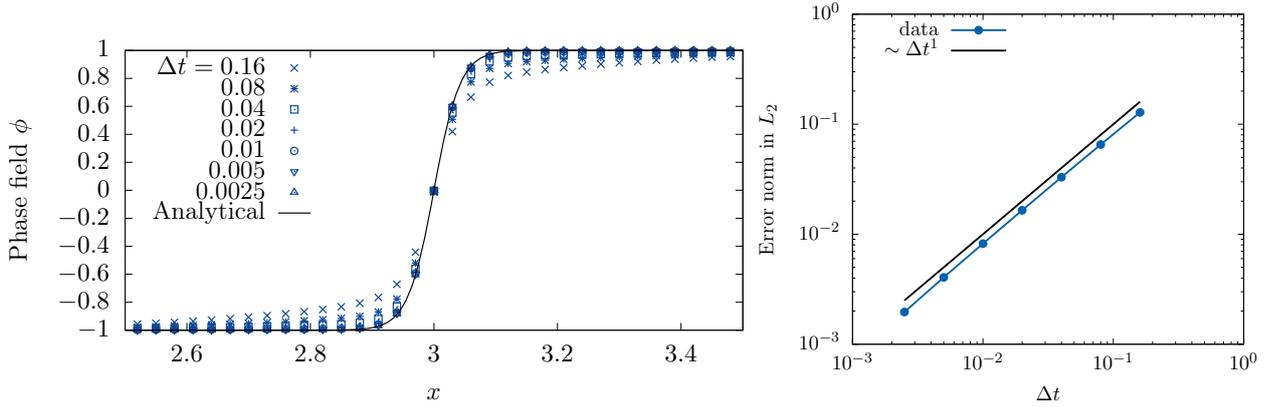
FIG. 3: Convergence in time for the case of stable intrusion. The mesh size is held fixed at $h = 0.0039$. Left: We show the phase field interpolated at equidistant points along the centerline for increasing temporal resolution. The solid black line is the analytical solution. Right: The integrated L^2 norm of the phase field plotted against time step. The solid black line shows the theoretical convergence order of the scheme ($\sim \tau$). As can be seen from the figure, it displays close to ideal scaling.

Fig. 4 shows the convergence of the phase field with regards to the spatial resolution. The scheme is seen to converge at the theoretical rate, $\sim h^2$.

B. Method of manufactured solution: a two-phase electrohydrodynamic Taylor–Green vortex

Having established convergence in the practically one-dimensional case, we now consider a slightly more involved setting where we use the method of manufactured solution to obtain a quasi-analytical test case.

The Taylor–Green vortex is a standard benchmark problem in computational fluid dy-
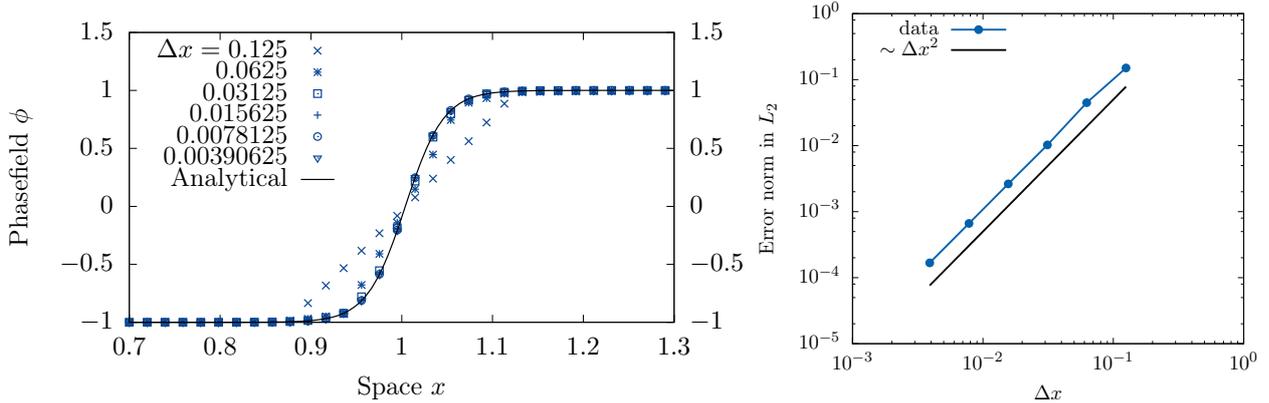
FIG. 4: Convergence in space for the case of stable intrusion. The time step is held fixed at $\tau = 0.0025$. Left: Phase field interpolated at equidistant points along the centerline for increasing spatial resolution. Right: The L^2 norm of the phase field is plotted against mesh resolution. The solid black line shows the theoretical convergence order ($\sim h^2$).

namics because it stands out as one of the few cases where exact analytical solutions to the Navier–Stokes equations are available. However, in the case of two-phase electrohydrodynamics, the Navier–Stokes equations couple to both the electrochemical and the phase field subproblems. In Ref. [76] the authors augmented the Taylor–Green vortex with electrohydrodynamics, and in this work we supplement the latter with a phase field and non-matching densities of the two phases.

We consider the full set of equations on the domain $\Omega = [0, 2\pi] \times [0, 2\pi]$, where all quantities may differ in the two phases. The two ionic species have opposite valency $\pm z$. The fields are given by

$$\mathbf{u} = U(t)(\hat{\mathbf{x}} \cos x \sin y - \hat{\mathbf{y}} \sin x \cos y), \tag{59a}$$

$$p = -\sum_{mn} \mathcal{P}_{mn}(t) \cos(2mx) \cos(2ny), \tag{59b}$$

$$\phi = \Phi(t) \cos x \cos y, \tag{59c}$$

$$c_\pm = c_0 (1 \pm \cos x \cos y\, C(t)), \tag{59d}$$

$$V = \frac{z c_0 C(t)}{\varepsilon} \cos x \cos y. \tag{59e}$$

32

Here, the time-dependent coefficients are given by

$$U(t) = U_0 \exp\left(-\frac{2\bar{\mu}}{\bar{\rho}}t\right), \tag{60}$$

$$C(t) = C_0 \exp\left(-2\bar{D}\left(1 + \frac{c_0}{\bar{\varepsilon}}\right)t\right), \tag{61}$$

$$\Phi(t) = \Phi_0 \exp\left(-2M\tilde{\sigma}\left(2\epsilon - \frac{1}{\epsilon}\right)t\right), \tag{62}$$

where U_0, C_0 and Φ_0 are scalars, and

$$\mathcal{P}_{mn} = \begin{cases} \mathcal{Q}_1(t) + \mathcal{Q}_2(t) & \text{for} \quad (m,n) \in \{(0,1),(1,0)\}, \\ \mathcal{Q}_2(t) & \text{for} \quad (m,n) \in \{(1,1)\}, \\ 0 & \text{otherwise}. \end{cases} \tag{63}$$

where

$$\mathcal{Q}_1 = \frac{1}{4}\rho U_0^2(t), \quad \text{and} \quad \mathcal{Q}_2 = \frac{z^2 c_0^2 C^2(t)}{4\epsilon}. \tag{64}$$

Further, a bar indicates the arithmetic average over the value in the two phases, i.e. $\bar{\chi} = (\chi_1 + \chi_2)/2$ for any quantity χ, and $\bar{D} = (\bar{D}_+ + \bar{D}_-)/2 = (D_{+,1} + D_{+,2} + D_{-,1} + D_{-,2})/4$ is the arithmetic average over all diffusivities. The time-dependent boundary conditions are set by prescribing the reference solutions at the boundary of Ω for all fields given in (59a)–(59e), except the pressure p, which is set (to the reference value) only at the corner point $(x,y) = (0,0)$. The method of manufactured solution now consists in augmenting the conservation equations (17), (19), (20) and (21) by appropriate source terms, such that the reference solution (59a)–(59e) solves the system exactly. These source terms were computed in Python using the *Sympy* package, and are rather involved algebraic expressions. The expressions are therefore omitted here, but can be found as a utility script in the *Bernaise* package. Note that in the special case of single-phase flow without electrodynamics, i.e. $\phi \equiv 1$ and $z = 0$, we retrieve the classic Taylor–Green flow (with a passive tracer concentration field), where all artificial source terms vanish.

We consider now the convergence towards the manufactured solution. We let the grid size $\Delta h \in [2\pi/256, 2\pi/16]$ and the time step $\tau \in [0.0001, 0.01]$, and evaluate the solution at the final time $T = 0.1$. The parameters for two phases used the simulation are given in Table I, while the non-phase specific parameters are given in Table II. Note that in order to test all parts of the implementation, all parameters are kept roughly in the same order of magnitude. When all the physical processes are included, the manufactured solution

33

TABLE I: Phasic parameters used in the Taylor–Green simulations.

Parameter	Symbol	Value in phase 1	Value in phase 2
Density	ρ	3	1
Viscosity	μ	3	5
Permittivity	ε	3	4
Cation diffusivity	D_+	3	1
Anion diffusivity	D_-	4	2
Cation solubility	β_+	2	-2
Anion solubility	β_-	1	-1

TABLE II: Non-phase-specific parameters used in the Taylor–Green simulations.

Parameter	Symbol	Value
Surface tension	σ	0.1
Interface thickness	ϵ	$1/\sqrt{2}$
Phase field mobility	M	1
Initial velocity	U_0	1
Initial concentration	c_0	1
Initial phase field	Φ_0	1
Initial conc. deviation	C_0	0.5

becomes an increasingly bad approximation and thus the resulting source terms become large. Thus, in order to avoid numerical instabilities, it was necessary to evaluate the error at a relatively short final time T. However, it should be enough to locate errors in most parts of the code.

We plot the L^2 errors of all the fields as a function of the grid size h in Fig. 5. In these simulations, we used a small time step $\tau = 0.0001$ to rule out the contribution of time discretization to the error, cf. Eq. (57). It is clear that the spatial convergence is close to ideal for all fields, indicating that the scheme approaches the correct solution. The pressure p displays slightly worse convergence and higher error norm than the other fields, which may

be due to the pointwise way of enforcing the pressure boundary condition (all other fields have Dirichlet conditions on the entire boundary).
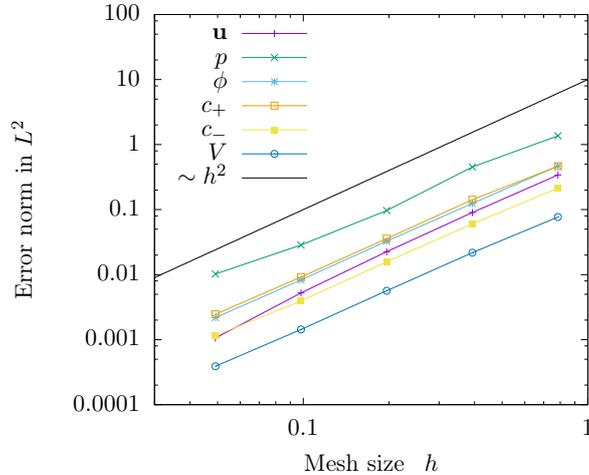
FIG. 5: Convergence in space for the two-phase electrohydrodynamic Taylor–Green manufactured solution. The solid black line shows the theoretical convergence rate based on the order of the finite elements chosen ($\sim h^2$). All fields display close to ideal convergence.

In Fig. 6, we plot the L^2 errors of the same fields as in Fig. 5, but as a function of the time step τ. In the simulations plotted here, we used a fine grid resolution with $h = 2\pi/256$ to rule out the contribution of spatial discretization to the error, cf. Eq. (57). Clearly, first order convergence is achieved for sufficient refinement, for all fields including the pressure.

C. Droplet motion driven by an electric field

We now consider a charged droplet moving due to an imposed electric field; a problem for which there is no analytical solution available. However, by comparing to a highly resolved numerical solution, convergence for the fully coupled two-phase electrohydrodynamic problem can be verified. This problem has already been partly presented in the above, and is implemented in `problems/charged_droplet.py`. A sketch showing the initial state is shown in Fig. 7. We consider an initially circular droplet, where a positive charge concentration is initiated as a Gaussian distribution, with variance δ_c^2, in the middle of the droplet. In this set-up, we consider only a single, positive species. The total amount of solute, i.e. integrated

35
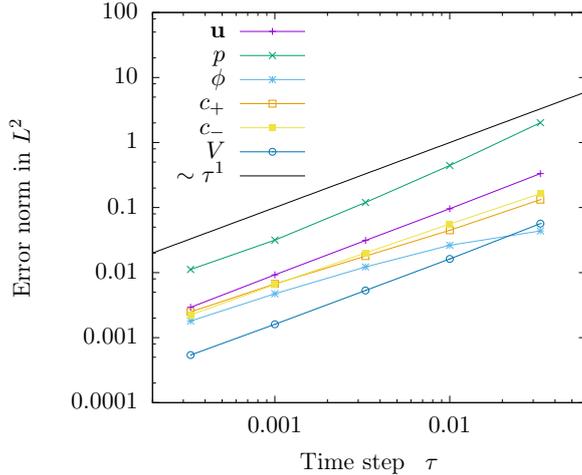
FIG. 6: Convergence in time for the two-phase electrohydrodynamic Taylor–Green manufactured solution. The solid black line shows the theoretical convergence rate of the scheme ($\sim \tau^1$). All fields display close to ideal convergence.

concentration, is $C_0 = \int_\Omega c_0 \, dA$. The left wall of the reservoir is kept at a positive potential, $V = \Delta V$, while the right wall is grounded, $V = 0$. The top and bottom walls are assumed to be perfectly insulating, i.e. a no-flux condition is applied on concentration fields and electric fields, and a no-slip condition is applied on the velocity. The fluid surrounding the droplet is neutral, and its parameters are chosen such that the solute is only very weakly soluble in the surrounding fluid, and the diffusivity here is very low here to prevent leakage. The droplet is accelerated by the electric field towards the right, before it is slowed down due to viscous effects upon approaching the wall.

With regards to reproducing the sharp-interface equations, we consider now the case of reducing the interface thickness $\epsilon \to 0$. To this end, we keep the ratio h/τ between mesh size and time step fixed, and further we keep the interface thickness ϵ proportional to h. The latter spans roughly 3-4 elements. Since the interface thickness ϵ changes, an important parameter in the phase-field model changes, which couples back to the equations, and thus the L$_2$ norm does not necessarily constitute a proper convergence measure. We therefore resort to using the *picture norm* or contour of the droplet as a measure, i.e. the zero-level set of the phase field $\phi = 0$. In particular, we will consider two observables: circumference and the center of mass (along x) of the droplet, as a function of resolution. A similar approach was taken for the case of phase-field models without electrodynamics by Aland and Voigt

36
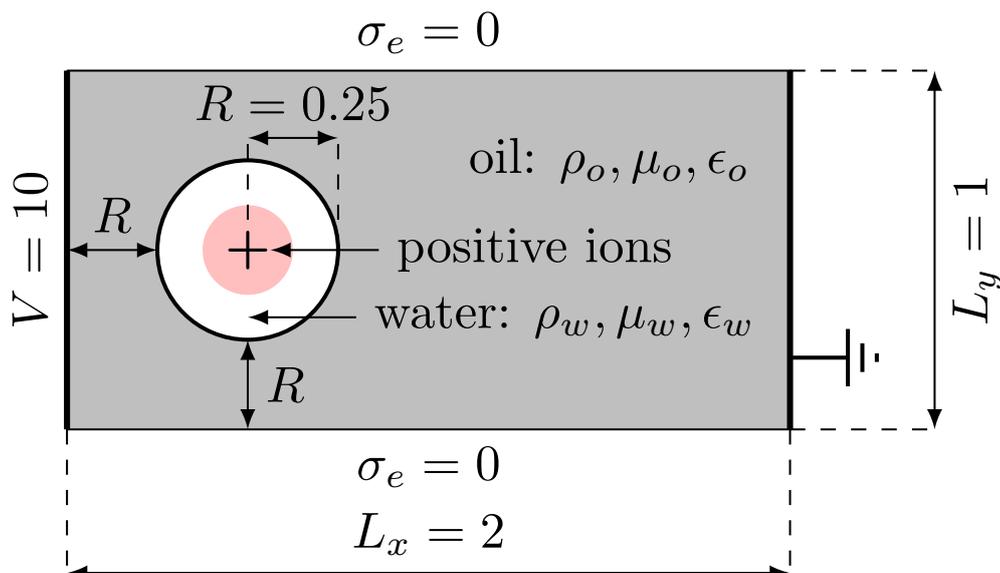
FIG. 7: Schematic set-up of the test case of droplet motion driven by an electric field. The 'water' droplet contains positive ions and is driven by the electric field set up between the high potential on the left wall and the grounded right wall.

[67] who compared their benchmarks to sharp interface results by Hysing *et al.* [66].

The resolutions used in our simulations are given in Table III. In order not to have to adjust the phase field mobility when refining, whilst still expecting to retrieve the sharp-interface model in the limit $\epsilon \to 0$, we choose the phase field mobility given by (33b). All parameters for the phasic quantities are given in Table IV, while the remaining parameters are given in Table V. From these parameters, using the unit scaling adopted in this paper, we find an approximate Debye length $\lambda_D = \sqrt{\varepsilon/(2z^2 c_R)} \simeq \sqrt{1/(2 \cdot 10)} \simeq 0.2$ (see Section B 2 in the Appendix for this expression), since we can approximate the order of magnitude of $c_R < C/(\pi R^2) = 10/(\pi \cdot 0.25^2)$ for a moderate screening.

In Fig. 8, we show the contour of the driven droplet at two time instances $t = 4$ and $t = 8$, and compare increasing resolution (simultaneously in space, time and interface thickness). Qualitatively inspecting the contours by eye, the droplet shapes seem to converge to a well defined shape with increasing resolution at both time instances. However, qualitive comparison is clearly not enough to assess the convergence. As in Refs. [66, 67], we define three observables:

TABLE III: Numerical parameters that vary with resolution in the charged droplet simulations: Mesh size h, time step τ, and interface thickness ϵ.

h	τ	ϵ
0.04	0.04	0.06
0.02	0.02	0.03
0.01	0.01	0.015
0.005	0.005	0.0075
0.0025	0.0025	0.00375

TABLE IV: Numerical parameters for the phases that are common for all charged droplet simulations.

Parameter	Symbol	Value, phase 1	Value, phase 2
Density	ρ	200.0	100.0
Permittivity	ε	1.0	1.0
Diffusivity	D	$1 \cdot 10^{-5} \ (\simeq 0)$	0.001
Solubility	β	4.0	1.0
Viscosity	μ	10.0	1.0

TABLE V: Numerical parameters not specific to phase for the charged droplet simulations.

Parameter	Symbol	Value
Potential difference	ΔV	10.0
Integrated concentration	C_0	10.0
Phase field mobility coeff.	M_0	$1.5 \cdot 10^{-5}$
Initial droplet radius	R	0.25
Initial conc. std. dev.	δ_c	0.0833
Surface tension	σ	5.0
Length in x-direction	L_x	2.0
Length in y-direction	L_y	1.0
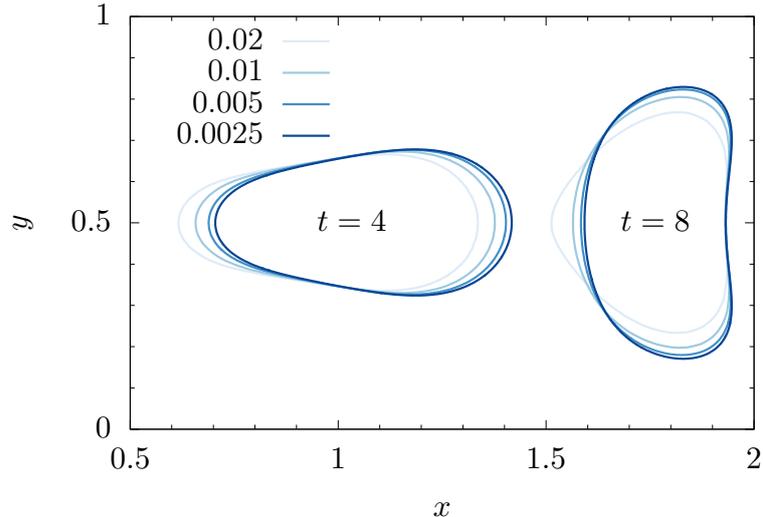
FIG. 8: Shape comparison of electrically driven charged droplet at two time instances. The effect of the four resolutions given in Table III is shown. The legend shown in the figure refers to both spatial (h) and temporal resolution (τ).

- Center of mass: We consider the center of mass of the dispersed phase (phase 2, i.e. $\phi < 0$),

$$x_{\mathrm{CM}} = \frac{\int_{\phi<0} x \, \mathrm{d}A}{\int_{\phi<0} \mathrm{d}A},$$

(65)

where we approximate the integral over the droplet (phase 2) by $\int_{\phi<0}(\cdot) \, \mathrm{d}A = \int_\Omega (1 - \phi)(\cdot)/2 \, \mathrm{d}A$.

- Drift velocity: Similarly as above, the velocity at which the droplet is driven is measured by

$$\mathcal{V} = \frac{\int_{\phi<0} \mathbf{u} \cdot \hat{\mathbf{x}} \, \mathrm{d}A}{\int_{\phi<0} \mathrm{d}A}.$$

(66)

- Circularity: Defined as the ratio of the circumference of the area-equivalent circle to the droplet circumference,

$$\mathcal{C} = \frac{2\sqrt{\pi \int_{\phi<0} \mathrm{d}A}}{\ell}.$$

(67)

.

The circumference ℓ and the integrals are computed by the post-processing method `geometry_in_time` which is built into *Bernaise*.

Fig. 9 shows the three quantities as a function of time for increasing resolution. (Here we have omitted the coarsest resolution $h = 0.04$ for visual clarity.) The curves seem to converge

39

towards well-defined trajectories with resolution. For a more quantitative comparison, we
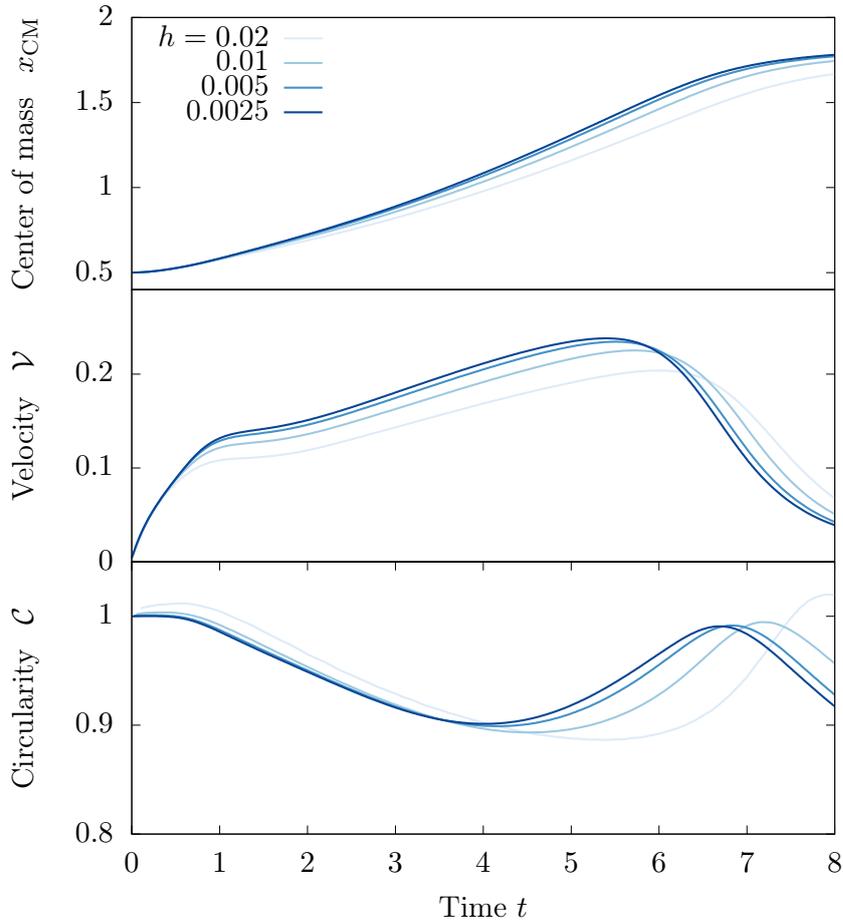
FIG. 9: Observable quantities as a function of time. Increasing resolutions (spatial and temporal) are compared.

define the time-integrated error norm,

$$\|e\|_p = \left(\frac{\int_0^T |q_{\mathrm{ref}}(t) - q(t)|^p \, \mathrm{d}t}{\int_0^T |q_{\mathrm{ref}}(t)|^p \, \mathrm{d}t} \right)^{1/p} \tag{68}$$

for a given quantity q. We can compute an empirical convergence rate of this norm,

$$k_{p,i} = \frac{\log \left(\|e\|_p (h_{i+1}) / \|e\|_p (h_i) \right)}{\log \left(h_{i+1}/h_i \right)} \tag{69}$$

for two successive resolutions ($h_{i+1} > h_i$). Here we shall consider the L^2 error norm in time, i.e. $p = 2$, and in practice we compute the integrals in time by cubic spline interpolation of

40

TABLE VI: Mesh size h, error norm $\|e\|_2$, and empirical convergence rate k_2 for increasing grid refinement, assuming the solution for the finest resolution to be exact.

h	$\|e\|_2$	k_2
Center of mass		
0.04	0.1798	
0.02	0.0955	0.9129
0.01	0.0410	1.2186
0.005	0.0126	1.7033
Drift velocity		
0.04	0.3427	
0.02	0.2067	0.7293
0.01	0.1032	1.0025
0.005	0.0341	1.5932
Circularity		
0.04	0.0891	
0.02	0.0423	1.0757
0.01	0.0205	1.0467
0.005	0.0060	1.7612

measurement points saved at every 5 time steps. There is no exact solution, or reference high-resolution sharp-interface solution available for this set-up. However, if we now assume that the finest resolution *is* the exact solution, and use this as the reference field in Eq. (68), we can compute error norms and convergence rates. These values are reported in Table VI. The computed convergence rates increase for all three observables and reach 1.6–1.7 with increasing resolution, indicating also quantitatively a convergence that is in agreement with the anticipated convergence rate. Considering Eq. (57), from the temporal discretization, we expect $k_2 \simeq 1$, and from the spatial $k_2 \simeq 2$. Depending on which term contributes most to the error, we will measure either of these rates. The values measured here indicate that both terms may be comparable in magnitude; however if we instead of using directly the finest solution as reference, extrapolated the trajectories further, we would presumptively

TABLE VII: Phasic parameters for the simulations of shear flow over a dead-end pore. The subscript $\pm$ indicates the value for both the positive and negative ions.

Parameter	Symbol	Value in phase 1	Value in phase 2
Viscosity	μ	1.0	1.0
Density	ρ	10.0	10.0
Permittivity	ϵ	1.0	1.0
Solution energy	$\beta_\pm$	4	1
Ion mobility	$D_\pm$	0.0001	0.01

have achieved lower convergence rates. This might indicate that the convergence error is eventually dominated by the temporal discretization, cf. Eq. (57).

VI. APPLICATIONS

A. Oil extrusion from a dead-end pore

Here, we present a demonstration of the method in a potential geophysical application. We consider a shear flow of one phase ("water") over a dead-end pore which is initially filled with a second phase ("oil"). The water phase contains initially a uniform concentration of positive and negative ions, $c_\pm|_{t=0} = c_0$, and the water–oil interface is modelled to be impermeable. The simulation of the dead-end pore is carried out to preliminarily assess the hypothesis that electrowetting could be responsible for the increased expelling of oil in low-salinity enhanced oil recovery. The problem set-up is schematically shown in Fig. 10. The phasic parameters used in the simulations are given in Table VII, and the remaining parameters are given in Table VIII. This problem is implemented in the file `problems/snoevsen.py`.

To investigate the effect of including electrostatic interactions, we show in Fig. 11 instantaneous snapshots of simulations with and without surface charge at different times. The left column, Figs. 11(a), 11(c), and 11(e), shows the results for vanishing surface charge, and the right column, Figs. 11(b), 11(d), and 11(f), shows the results for a surface charge of $\sigma_e = -10$.
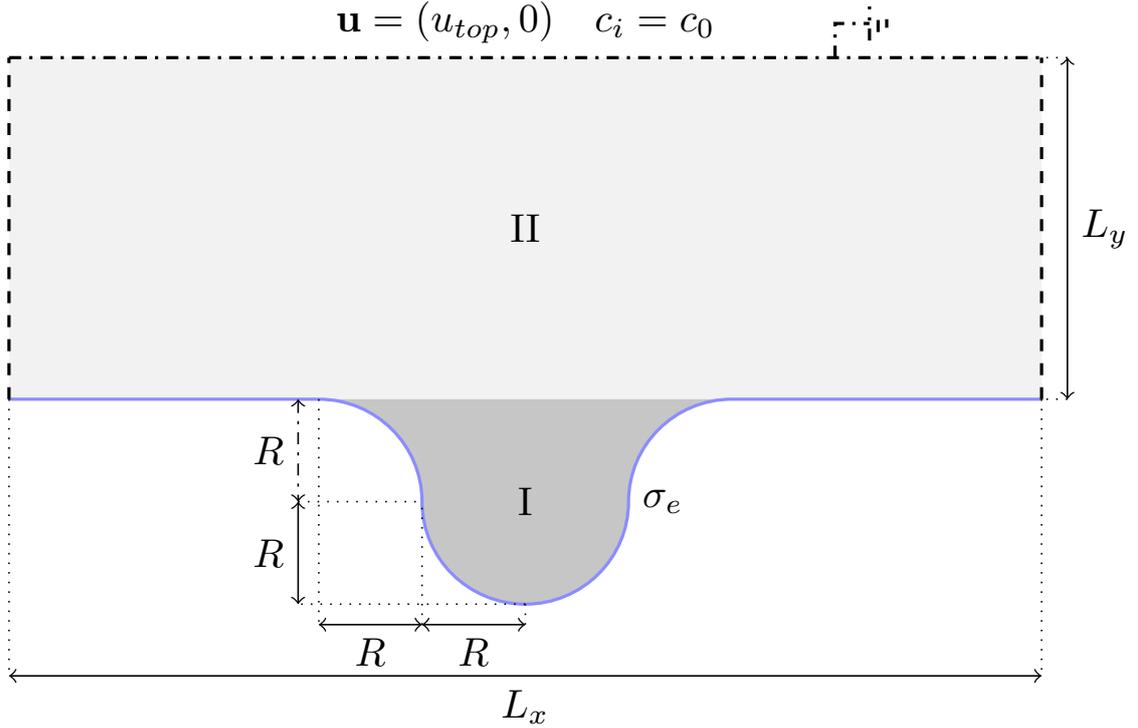
FIG. 10: A schematic depiction of the "dead-end pore" geometry, with the appropriate boundary conditions for the problem and specified initial conditions for the phase field. The geometry is specified by the two lengths L_x, L_y, and the radius R used to define the dead-end pore in the center of the channel by a circle and a circular smoothed inlet. The roman numerals indicate the phase, along with the tone of gray. The darker phase is the oil-like phase (I), and the lighter one is the water-like phase (II).

For the uncharged case, the frames that are shown are almost indistinguishable. In fact, the main difference is the numerical noise of the total charge, which is due to roundoff errors of machine precision. The initial dynamics of the oil plug interface, which is to equilibrate with the neutral contact angle and the shear flow, mainly happens before the first frame presented; compare Figs. 10 and 11(a).

A markedly different behavior is displayed in the right column, Figs. 11(b), 11(d), and 11(f), where a uniform surface charge density is enforced the walls at the simulation start, $t = 0$. Here, we see first that two tongues are intruding on both sides of the droplet, which push the droplet out into the center of the dead-end pore. The process is continued, as shown in the second frame, and finalized, as shown in the third frame, with the complete release of the droplet as the two tongues meet at the bottom of the dead-end pore, cutting

TABLE VIII: Simulation parameters for the simulations of shear flow over a dead-end pore.

Parameter	Symbol	Value
Length	L_x	3.0
Height	L_y	1.0
Total simulation time	T	20
Radius	R	0.3
Time step	τ	0.01
Resolution	h	$1/120$
Interface thickness	ε	0.02
Phase field mobility	M_0	$2.5 \cdot 10^{-6}$
Surface tension	σ	2.45
Surface charge	σ_e	$\{-10, 0\}$
Reference concentration	c_0	2
Shear velocity	u_{top}	0.2

the final contact point.

With these simulations, we have demonstrated the effects when a surface charge couples to hydrodynamics. This has lead to the observation that oil phase, on a larger scale than the Debye length, behaves like it is completely dewetting even when we locally enforce a neutral contact angle.

B. 3D simulations of droplet coalescence and breakup in an electric field

Finally, to demonstrate the ability of *Bernaise* to simulate 3D configurations, we present simulations of two oppositely charged droplets that coalesce. In order to achieve this efficiently, a fully iterative solver was implemented. The solver consists of a fractional step version of the `basic` solver, in the sense that within the fluid flow step, it splits between the velocity and pressure computations, as shown in Eqs. (56a), (56b), and (56c). The splitting introduces a weak compressibility which suffices to stabilize the problem [80] (with

44

respect to the BB condition) and thus we can use P_1 finite elements also for the velocity. The combination of fewer degrees of freedom and the applicability of iterative linear solvers imparts significant speed-up compared to coupled solvers, which is of paramount importance for 3D simulations. This yields advantages over solvers which rely on a mixed-element formulation of the hydrodynamic subproblem [71]. The detailed analysis of the fractional step solver will be published in a separate paper, but the implementation can be found in `solvers/fracstep.py`. For solving the linear systems iteratively, we use an algebraic multigrid (AMG) preconditioner and a generalized minimal residual (GMRES) linear solver for the electrochemical and the pressure correction step; Jacobi preconditioner (Jacobi) and a stabilized bi-conjugate gradient method (BiCGStab) for the velocity prediction, and Jacobi and GMRES for the velocity correction. For the phase field we use Jacobi and a conjugate gradient method.

To prevent leakage of ions out of the two coalescing droplets, a weighted geometric mean was used for the diffusivities:

$$K_j(\phi) = K_{j,1}^{\frac{1+\phi}{2}} \cdot K_{j,2}^{\frac{1-\phi}{2}}, \tag{70}$$

instead of the arithmetic mean (25) used in most of the article.

We consider a setup of two initially spherical droplets in a domain $\Omega = [0, L_x] \times [0, L_y] \times [0, L_z]$. The droplets are centered at $(L_x/2, L_y/2, (L_z \pm L_x)/2)$ and have a radius R. The lower droplet (along the z-axis) is initialized with a Gaussian concentration distribution of negative ions ($z_- = -1$), whereas the upper droplet is initialized with positive ions ($z_+ = 1$). The average concentration of the respective ion species within each droplet is c_0, such that the total charge in the system is zero, and the initial spread (standard deviation) of the Gaussian distribution is $R/3$. A potential V_0 is set on the top plane at $z = L_z$ and the bottom plane at $z = 0$ is taken to be grounded. We assume no-slip and no-flux conditions on all boundaries, except for the electrostatic potential V at the top and bottom planes, and the fluid is taken to be in a quiescent state at the initial time $t = 0$. The phasic parameters used in the simulations are given in Table IX, and the remaining parameters are given in Table X. The problem is implemented in the file `problems/charged_droplets_3D.py`.

Fig. 12 shows snapshots from the simulations at several instances of time. As seen from the figure, the droplets are set in motion towards each other by the electric field and collide with each other. Subsequently, the unified droplet is stretched, until it touches both electrodes. The middle part then breaks off, and as it is unstable, it further emits droplets

TABLE IX: Phasic parameters for the simulations of droplet coalescence and breakup in an electric field. The subscript $\pm$ indicates the value for both the positive and negative ions.

Parameter	Symbol	Value in phase 1	Value in phase 2
Viscosity	μ	1.0	0.5
Density	ρ	500.0	50.0
Permittivity	ϵ	1.0	2.0
Solution energy	$\beta_\pm$	2	0
Ion mobility	$D_\pm$	0.0001	0.1

TABLE X: Simulation parameters for the simulations of droplet coalescence and breakup in an electric field.

Parameter	Symbol	Value
Length along x	L_x	1.0
Length along y	L_y	1.0
Height	L_z	2.0
Total simulation time	T	20
Initial radius	R	0.2
Time step	τ	0.005
Resolution	h	1/64
Interface thickness	ε	0.01
Phase field mobility	M_0	$1 \cdot 10^{-5}$
Surface tension	σ	2.0
Initial avg. concentration	c_0	20.0

that are released to two two sides. Finally, two spherical caps form at each electrode, and a neutral drop is left in the middle, due to the initial symmetry. Similar behaviour has been observed in axisymmetric simulations (e.g. [87]).

We finally carry out a strong scaling test of the linear iterative solver on a single in-house

server with 80 dedicated cores. The results of average computational time per time step (averaged over 10 time steps) versus number of cores are shown in Fig. 13. We show here the amount of time spent per time step for all substeps in order to illuminate where most of the computational resources are spent. As can be seen, a significant portion of the computational time is spent on the electrochemical substep. Overall, the solver displays sublinear scaling with the number of cores, but the results are promising given that neither the solver nor the FEniCS install (a standard PPA install of FEniCS 2017.2.0 on Ubuntu 16.04 server) are fully optimized. Much could be gained by improving the two steps where solving a Poisson equation is involved; in particular it seems possible that more specifically tailored preconditioners than the straightforward AMG preconditioning could impart speedup. However, we stress that the division of labour between the steps is highly problem-dependent, and in particular, the electrochemical subproblem is susceptible to how far into the non-linear regime we are (see e.g., [45]).

VII. DISCUSSION AND CONCLUSION

We have in this work presented *Bernaise*, a flexible open-source framework for simulating two-phase electrohydrodynamics in complex geometries using a phase-field model. The solver is written in its entirety in Python, and is built on top of the FEniCS/DOLFIN framework [42, 88] for solving partial differential equations using the finite element method on unstructured meshes. FEniCS in turn interfaces to, e.g., scalable state-of-the art linear solvers through its PETSc backend [89]. We have proposed a linear operator-splitting scheme to solve the coupled non-linear equations of two-phase electrohydrodynamics. In contrast to solving the equations directly in a monolithic manner, the scheme sequentially solves the Cahn–Hilliard equation for the phase field describing the interface, the Poisson–Nernst–Planck equations for the electrochemistry (solute transport and electrostatics), and the Navier–Stokes equations for the hydrodynamics, at each time step. Implementation of new solvers and problems has been demonstrated through representative examples. Validation of the implementation was carried out by three means: (1) By comparison to analytic solutions in limiting cases where such are available, (2) by the method of manufactured solution through an augmented Taylor–Green vortex, and (3) through convergence to a highly resolved solution of a new two-phase electrohydrodynamics benchmark problem of

47

an electrically driven droplet. Finally, we have presented applications of the framework in non-trivial settings. Firstly, to test the applicability of the code in a complicated geometry, and to illuminate the effects of dynamic electrowetting, we simulated a shear flow of water containing an electrolyte over a dead-end pore initially filled with oil. This problem is relevant from a geophysical standpoint, and exemplifies the potential of the method to simulate the dynamics of the interaction between two-phase flow and electric double layers. Secondly, the ability of the framework to simulate three-dimensional configurations was demonstrated using a fully iterative version of the operator-splitting scheme, by simulating the coalescence and subsequent breakup of two oppositely charged droplets in an electric field. The parallel scalability of the latter solver was tested on in-house computing facilities. The results presented herein underpin our aim that *Bernaise* can become a valuable tool both within the micro- and nanofluidics community and within geophysical simulation.

There are several possible avenues for further development and use of *Bernaise*. With regards to computational effort, the linear operator-splitting scheme constitutes a major computational improvemnt over a corresponding monolithic scheme. For the resulting smaller and simpler subproblems, more specialized linear solvers and preconditioners can be used. However, the implementation of the schemes are still not fully optimized, as in many cases it is not strictly necessary to reassemble entire system matrices (multiple times) at every time step. Using ideas e.g. from Ref. [43] on how to effectively preassemble system matrices in FEniCS, one could achieve an implementation that is to a larger extent dominated by the backend linear solvers. However, as the phase field is updated at every time step, there may be less to gain in performance than what was the case in the latter reference.

With regard to solving the Navier–Stokes equations, the solvers considered herein either rely on a coupled solution of the (the `basic` and `basicnewton` solvers) or a fractional step approach that splits between the computations of velocity and pressure (the `fracstep` solver that was considered in Sec. VI B). Using direct linear solvers, the coupled solvers yield accurate prediction of the pressure and can be expected to be more robust. However, direct solvers have numerical disadvantages when it comes to scalability, and Krylov solvers require specifically tailored preconditioners to achieve robust convergence. An avenue for further research is to refine the `fracstep` solver and develop decoupled energy-stable schemes for this problem, which seems possible by building on literature on similar systems [68–71, 76, 78]. The implementation of such enhanced schemes in *Bernaise* is straighforward, as

48

demonstrated in this paper.

A clear enhancement of *Bernaise* would be adaptivity, both in time and space. Adaptivity in time should be implemented such that time step is variable and controlled by the globally largest propagation velocity (in any field), and a Courant number of choice. Adaptivity in space is presently only supported as a one-way operation. Adaptive mesh refinement is already used in the mesh initialization phase in many of the implemented problems. However, mesh coarsening has currently limited support in FEniCS and to the authors' knowledge there are no concrete plans of adding support for this. Hence, *Bernaise* lacks an adaptive mesh functionality, but this could be implemented in an *ad hoc* manner with some code restructuring.

In this article, we have not considered any *direct* dependence of the contact angle (i.e. the surface energies) on an applied electric field. However, the contact angle on scales below the Debye length is generally thought to be unaffected, albeit on scales larger than the insulator thickness, an apparent contact angle forms [90, 91]. Using the full two-phase electrohydrodynamic model presented herein, effective contact angle dependencies upon the zeta potential could be measured and used in simulations of more macroscopic models; i.e. models admissible on scales where the electrical double layers are not fully resolved. This would result in a modified contact angle energy that would be enforced as a boundary condition in a phase field model [92].

Physically, several extensions of the model could be included in the simulation framework. Surfactants may influence the dynamics of droplets and interfaces, and could be included as in e.g. the model by Teigen *et al.* [93]. The model in its current form further assumes that we are concerned with dilute solutions (i.e., ideal gas law for the concentration), and hence more complicated electrochemistry could to some extent be incorporated into the chemical free energy $\alpha(c)$.

Finally, the requirement of the electrical double layer to be well-resolved constitutes the main constraint for upscaling of the current method. Thus, for simulation of two-phase electrohydrodynamic flow on larger scales, if ionic transport need not be accounted for, it would only require minor modifications of the code to run the somewhat simpler Taylor–Melcher leaky dielectric model, e.g. in the formulation by Lin *et al.* [61], within the current framework.

Appendix A: Electrokinetic scaling of the equations

For completeness, we show here, as in a companion paper [91], how the dimensionless variable scaling assumed in this paper arises from the equations formulated in physical (e.g., SI) units. The scaling results in equations that are easier to work with, but that need to be scaled back to physical units in order to be e.g., compared to experiments.

For concreteness, we consider the standard Nernst–Planck equation (i.e., dilute solutions) for solute transport, which in physical units can be written as

$$\frac{\partial c_j}{\partial t} + \mathbf{u} \cdot \boldsymbol{\nabla} c_j = \boldsymbol{\nabla} \cdot \left(D_j \boldsymbol{\nabla} c_j - \frac{z_j q_e c_j}{k_{\mathrm{B}} T} \mathbf{E} \right), \tag{A1}$$

where k_{B} is Boltzmann's constant, T is the temperature, and q_e is the elementary charge. The Poisson equation is in physical units given by

$$\boldsymbol{\nabla} \cdot (\epsilon_0 \epsilon_{\mathrm{r}} \mathbf{E}) = \rho_e, \tag{A2}$$

where the net charge is given by $\rho_e = q_e \sum_j c_j$. The Navier–Stokes equations are given by the usual

$$\rho \left(\partial_t \mathbf{u} + \mathbf{u} \cdot \boldsymbol{\nabla} \mathbf{u} \right) - \mu \boldsymbol{\nabla}^2 \mathbf{u} + \boldsymbol{\nabla} p = -\rho_e \boldsymbol{\nabla} V, \tag{A3}$$

$$\boldsymbol{\nabla} \cdot \mathbf{u} = 0. \tag{A4}$$

Continuity of the normal stress across the interface between the phases can be formulated as

$$\left[2\mu \mathcal{D}\mathbf{u} - p'\mathbf{I} + \sigma\kappa\mathbf{I} + \epsilon_0 \epsilon_{\mathrm{r}} \mathbf{E} \otimes \mathbf{E} - \frac{1}{2}\epsilon_0 \epsilon_{\mathrm{r}} \mathbf{E}^2 \mathbf{I} \right] \cdot \hat{\mathbf{n}}_{\mathrm{int}} = \mathbf{0}, \tag{A5}$$

where p' is a pressure which has absorbed some extra gradient terms. We introduce now dimensionless versions of all physical variables, and indicate the dimensionless versions by a tilde. Further, all reference values are marked with an asterisk. Hence, we let $\tilde{t} = t/t^*$, $\tilde{\rho} = \rho/\rho^*$, $\tilde{\mathbf{u}} = \mathbf{u}/u^*$, $\tilde{p} = p/p^*$, $\tilde{\mu} = \mu/\mu^*$, $\tilde{c}_j = c_j/c^*$, $\tilde{V} = V/V^*$, $\tilde{D}_\pm = D_\pm/D^*$, $\tilde{\epsilon} = \epsilon_{\mathrm{r}}/\epsilon^*$,

and $\tilde{\sigma} = \sigma/\sigma^*$. All spatial dimensions are scaled by a reference linear size R^*, such that $\tilde{\mathbf{x}} = \mathbf{x}/R^*$. The electrostatic potential V is scaled by a thermal voltage,

$$V^* = V_T = \frac{k_{\mathrm{B}}T}{q_e}. \tag{A6}$$

The other reference values are given by [91]

$$t^* = \frac{R^*}{u^*}, \quad \rho^* = \frac{q_e c^* V_T}{(u^*)^2}, \quad D^* = u^* R^*, \quad p^* = q_e c^* V_T, \tag{A7}$$

$$\mu^* = \frac{q_e c^* V_T R^*}{u^*}, \quad \epsilon^* = \frac{q_e c^* (R^*)^2}{\epsilon_0 V_T}, \quad \sigma^* = q_e c^* V_T R^*. \tag{A8}$$

This constitutes an invertible set of relations between the physical and dimensionless variables. In particular, adopting the dimensionless variables and subsequently dropping the tildes, results in the set of equations (A1) to (A5) with $q_e = k_B T = 1$ and $\epsilon_0 \epsilon_{\mathrm{r}} \to \epsilon$. This is essentially the scaling adopted in this paper.

Appendix B: Poisson–Boltzmann equation for two phases

Here, we derive a generalized Poisson–Boltzmann equation for the case of two phases, valid in equilibrium. We are here considering the steady state of the sharp interface equations. Considering Eq. (3) with $\partial_t = 0$ and $\mathbf{v} = \mathbf{0}$, taking the inner product of it with g_{c_j}, and integrating over the domain Ω, we obtain

$$\int_\Omega K_{ij} c_j |\boldsymbol{\nabla} g_j|^2 \, \mathrm{d}\Omega = \int_{\partial\Gamma} K_{ij} c_j g_{c_j} \hat{\mathbf{n}} \cdot \boldsymbol{\nabla} g_{c_j} \, \mathrm{d}\Gamma = 0, \tag{B1}$$

where the last equality holds, since at equilibrium the fluxes must vanish at the boundary (and hence also in the bulk). Since c_j is positive, g_{c_j} may not vary. Hence, the electrochemical potential associated with electrolyte j must satisfy:

$$g_{c_j} = \alpha'(c_j) + \beta_{ij} + z_j V = C_j, \tag{B2}$$

where C_j is a constant. We assume that one of the two phases is connected to a reservoir far away, such that here $\beta_{ij} = \beta_R$, $c_j = c_R$ and $V = V_R$. Evaluating Eq. (B2) at the reservoir, we have

$$C_j = \alpha'(c_R) + \beta_R + z_j V_R. \tag{B3}$$

51

By defining $\chi(\cdot)$ as the inverse function of $\alpha'(\cdot)$, we may combine Eqs. (B2) and (B3) and invert with respect to c_j:

$$c_j = \chi\left(\alpha'(c_R) + \beta_R - \beta_{ij} - z_j(V - V_R)\right). \tag{B4}$$

Hence, by Eq. (7), we obtain a closed equation for V:

$$\boldsymbol{\nabla}^2 V = -\varepsilon_i^{-1} \sum_j z_j \chi\left(\alpha'(c_R) + \beta_R - \beta_{ij} - z_j(V - V_R)\right), \tag{B5}$$

with the above boundary conditions at the reservoir. The interface condition between the phases is $[V]_-^+ = 0$, i.e. continuity in V, and the boundary condition at the reservoir is $V = V_R$. Next, we consider some special cases of this equation.

1. Standard Poisson–Boltzmann

With two symmetric electrolytes, $j \in \{\pm\}$, $z_\pm = \pm z$, $\beta_{ij} = \beta_i$, $V_R = V$ and the ideal gas chemical potential, we have that $\alpha'(c) = \ln c$, $\chi(a) = e^a$, and we obtain from Eq. (B5):

$$\boldsymbol{\nabla}^2 V = \frac{2z c_R}{\varepsilon_i} e^{\beta_R - \beta_i} \sinh\left(zV\right) = \frac{\sinh\left(zV\right)}{\lambda_{D,i}^2 z}, \tag{B6}$$

where we have defined a phase-dependent Debye length $\lambda_{i,D} = \sqrt{\varepsilon_i e^{-\beta_R + \beta_i}/(2z^2 c_R)}$. Now, Eq. (B4) yields that the concentration is retrieved by

$$c_\pm = c_R e^{\beta_R - \beta_i \mp zV}. \tag{B7}$$

a. Linearized

When $|zV| \ll 1$, we may expand Eq. (B6) to the first order to obtain the linearized Poisson–Boltzmann equation:

$$\boldsymbol{\nabla}^2 V = \frac{V}{\lambda_{D,i}^2}. \tag{B8}$$

In principle, we can also expand Eq. (B7):

$$c_\pm = c_R e^{\beta_R - \beta_i} \left(1 \mp zV\right), \tag{B9}$$

so that the total charge density is given by

$$\rho_e = -2z^2 c_R e^{\beta_R - \beta_i} V. \tag{B10}$$

52

2. Net charge

Now we consider the single "net charge" model which was proposed in Ref. [63] and used in the simulations of Ref. [62]. (Note that these papers redefined the diffusivity to absorb the net charge, effectively $K_{ij}c_j \to K$; but this does not have consequences in the forthcoming.) Here, we have only one species $c_1 = \rho_e$ with charge z, and $\alpha'(c) = \lambda c$, such that $\chi(a) = \lambda^{-1}a$. We consider the reservoir to be neutrally charged. Further, $V_R = 0$, for simplicity. Eq. (B5) yields

$$\boldsymbol{\nabla}^2 V = \frac{z^2}{\varepsilon_i \lambda}\left(V - \frac{\beta_R - \beta_i}{z}\right), \tag{B11}$$

and Eq. (B4) becomes

$$\rho_e = z\lambda^{-1}\left(\beta_R - \beta_i - zV\right). \tag{B12}$$

Note that in the case of single-phase flow, Eq. (B11) becomes Eq. (B5) yields

$$\boldsymbol{\nabla}^2 V = \frac{z^2}{\varepsilon\lambda}V = \lambda_D^{-2}V, \tag{B13}$$

which is the linearized Poisson–Boltzmann equation (see Sec. B 1), where we have identified a Debye length $\lambda_D = \sqrt{\varepsilon\lambda}/z$. Eq. (B12) becomes:

$$\rho_e = -\lambda^{-1}z^2 V. \tag{B14}$$

Comparison to (B10) leads us to identify $2c_R = \lambda^{-1}$, which yields $\lambda_D = \sqrt{\varepsilon/(2z^2 c_R)}$ in compliance with the definition in Sec. B 1. Note that even though the equilibrium solution complies with the linearized, equilibrium Nernst–Planck equation, the dynamics, particularly with two phases, may differ significantly.

a. Simple case

It is interesting to investigate this equation for a single phase in a finite 1-D geometry, $x \in [0, L]$. We assume the boundary conditions $\mathrm{d}V/\mathrm{d}x|_{x=0} = -\sigma_e/\varepsilon$ and $V|_{x=L} = 0$. The solution is

$$V = -\frac{\sigma_e}{\varepsilon k}\left(\sinh kx - \tanh kL \cosh kx\right), \tag{B15}$$

where $k = z/\sqrt{\varepsilon\lambda}$. Thus,

$$\rho_e = \frac{z^2\sigma_e}{\varepsilon k\lambda}\left(\sinh kx - \tanh kL \cosh kx\right). \tag{B16}$$

Hence this form of the chemical potential yields an exact solution. Note however, that there is in principle no mechanism controlling the sign of ρ_e, which is natural given that it should here signify a net charge.

The total charge is

$$Q = \int_0^L \rho_e \, \mathrm{d}x = \frac{z^2 \sigma_e}{\varepsilon k \lambda} \int_0^L (\sinh kx - \tanh kL \cosh kx) \, \mathrm{d}x \tag{B17}$$

$$= \frac{z^2 \sigma_e}{\varepsilon k^2 \lambda} [\cosh kx - \tanh kL \sinh kx]_0^L \tag{B18}$$

$$= -\sigma_e \left[1 - \frac{1}{\cosh kL} \right], \tag{B19}$$

which approaches the (negative) applied surface charge in the limit of infinite domain, $L \to \infty$, as it should.

Appendix C: Some considerations on testing and applicability of the framework

To simplify the complexity of the problem, the scheme can be reduced to describe settings where fewer physical mechanisms are present simultaneously.

- The very simplest is *pure single-phase flow*, containing only point 4 from the list in Sec. III.

- Slightly more demanding is *single-phase flow with transport of a tracer dye* (in the absence of electric charges and fields), using points 2 and 4.

- More demanding, *pure two-phase flow* (with unmatched densities and viscosities), where only points 1 and 4 from the list above enter.

- In the absence of electric charges and external electric potential, two-phase flow with passive transport of a tracer dye can be modelled, i.e. using the points 1, 2 and 4.

- Time-dependent single-phase EHD can be modelled using points 2, 3 and 4.

- There is also a subtle case where all concentrations $c_i = 0$, but the electric field acts as a force on the interface of the two-phase flow only due to the jump in permittivity ε. This includes points 1, 3 and 4.

- Finally, the full-fledged two-phase EHD includes all the points in the list in Sec. III.

Rigorous testing the solver should therefore follow these steps of increasing complexity.

[1] G. Lippmann, *Relations entre les phénomènes électriques et capillaires*, Ph.D. thesis, Sorbonne (1875).

[2] F. Mugele and J.-C. Baret, J. Phys. Condens. Matter **17**, R705 (2005).

[3] W. Ristenpart, J. Bird, A. Belmonte, F. Dollar, and H. Stone, Nature **461**, 377 (2009).

[4] F. Mugele, Nature **461**, 356 (2009).

[5] T. M. Squires and S. R. Quake, Rev. Mod. Phys. **77**, 977 (2005).

[6] R. B. Schoch, J. Han, and P. Renaud, Rev. Mod. Phys. **80**, 839 (2008).

[7] F. Mugele, M. Duits, and D. Van den Ende, Adv. Colloid Interface Sci. **161**, 115 (2010).

[8] W. C. Nelson and C.-J. Kim, J. Adhes. Sci. Technol. **26**, 1747 (2012).

[9] M. Pollack, A. Shenderov, and R. Fair, Lab Chip **2**, 96 (2002).

[10] V. Srinivasan, V. K. Pamula, and R. B. Fair, Lab Chip **4**, 310 (2004).

[11] J. Lee and C.-J. Kim, J. Microelectromech. Syst. **9**, 171 (2000).

[12] A. Siria, M.-L. Bocquet, and L. Bocquet, Nat. Rev. Chem. **1**, 0091 (2017).

[13] G. Beni and S. Hackwood, Appl. Phys. Lett. **38**, 207 (1981).

[14] G. Beni and M. Tenan, J. Appl. Phys. **52**, 6011 (1981).

[15] G. Beni, S. Hackwood, and J. Jackel, Appl. Phys. Lett. **40**, 912 (1982).

[16] R. A. Hayes and B. J. Feenstra, Nature **425**, 383 (2003).

[17] S. R. Pride and F. Morgan, Geophysics **56**, 914 (1991).

[18] E.-A. Fiorentino, R. Toussaint, and L. Jouniaux, Geophys. J. Int. **205**, 648 (2016).

[19] E.-A. Fiorentino, R. Toussaint, and L. Jouniaux, Geophys. J. Int. **208**, 1139 (2016).

[20] T. Hassenkam, C. S. Pedersen, K. Dalby, T. Austad, and S. L. S. Stipp, Colloids Surf. A **390**, 179 (2011).

[21] E. Hilner, M. P. Andersson, T. Hassenkam, J. Matthiesen, P. Salino, and S. L. S. Stipp, Scientific Reports **5**, 9933 (2015).

[22] A. RezaeiDoust, T. Puntervold, S. Strand, and T. Austad, Energy Fuels **23**, 4479 (2009).

[23] N. Pedersen, T. Hassenkam, M. Ceccato, K. N. Dalby, K. Mogensen, and S. L. S. Stipp, Energy Fuels **30**, 3768 (2016).

[24] O. Plümper, A. Botan, C. Los, Y. Liu, A. Malthe-Sørenssen, and B. Jamtveit, Nat. Geosci.

10, 685 (2017).

[25] P.-G. De Gennes, Rev. Mod. Phys. **57**, 827 (1985).

[26] D. Bonn, J. Eggers, J. Indekeu, J. Meunier, and E. Rolley, Rev. Mod. Phys. **81**, 739 (2009).

[27] J. H. Snoeijer and B. Andreotti, Ann. Rev. Fluid Mech. **45**, 269 (2013).

[28] J. Melcher and G. Taylor, Ann. Rev. Fluid Mech. **1**, 111 (1969).

[29] D. A. Saville, Ann. Rev. Fluid Mech. **29**, 27 (1997).

[30] E. D. Fylladitakis, M. P. Theodoridis, and A. X. Moronis, IEEE Trans. Plasma Sci. **42**, 358 (2014).

[31] G. Taylor, Proceedings of the Royal Society of London. Series A. Mathematical and Physical Sciences **291**, 159 (1966).

[32] O. Schnitzer and E. Yariv, J. Fluid Mech. **773**, 1 (2015).

[33] E. K. Zholkovskij, J. H. Masliyah, and J. Czarnecki, J. Fluid Mech. **472**, 1 (2002).

[34] C. W. Monroe, L. I. Daikhin, M. Urbakh, and A. A. Kornyshev, Phys. Rev. Lett. **97**, 136102 (2006).

[35] C. W. Monroe, L. I. Daikhin, M. Urbakh, and A. A. Kornyshev, J. Phys. Condens. Matter **18**, 2837 (2006).

[36] Q. Yang, B. Q. Li, and Y. Ding, Int. J. Multiph. Flow **57**, 1 (2013).

[37] Q. Yang, B. Q. Li, J. Shao, and Y. Ding, Int. J. Heat Mass Transf. **78**, 820 (2014).

[38] J. Berry, M. Davidson, and D. J. Harvie, J. Comput. Phys. **251**, 209 (2013).

[39] J. Zeng, Int. J. Mol. Sci. **12**, 1633 (2011).

[40] H.-W. Lu, K. Glasner, A. Bertozzi, and C.-J. Kim, J. Fluid Mech. **590**, 411 (2007).

[41] S. W. Walker, B. Shapiro, and R. H. Nochetto, Phys. Fluids **21**, 102103 (2009).

[42] A. Logg, K.-A. Mardal, and G. Wells, *Automated solution of differential equations by the finite element method: The FEniCS book*, Vol. 84 (Springer Science & Business Media, 2012).

[43] M. Mortensen and K. Valen-Sendstad, Comput. Phys. Commun. **188**, 177 (2015).

[44] G. Mitscha-Baude, A. Buttinger-Kreuzhuber, G. Tulzer, and C. Heitzinger, J. Comput. Phys. **338**, 452 (2017).

[45] A. Bolet, G. Linga, and J. Mathiesen, Phys. Rev. E **97**, 043114 (2018).

[46] A. Prosperetti and G. Tryggvason, *Computational methods for multiphase flow* (Cambridge University Press, 2009).

[47] C. Yang and D. Li, Colloids Surf. A **113**, 51 (1996).

[48] T. Qian, X.-P. Wang, and P. Sheng, J. Fluid Mech. **564**, 333 (2006).

[49] T. Qian, X.-P. Wang, and P. Sheng, Phys. Rev. E **68**, 016306 (2003).

[50] Y. Sui, H. Ding, and P. D. M. Spelt, Ann. Rev. Fluid Mech. **46**, 97 (2014).

[51] Å. Ervik, M. O. Lysgaard, C. Herdes, G. Jiménez-Serratos, E. A. Müller, S. T. Munkejord, and B. Müller, J. Comput. Phys. **327**, 576 (2016).

[52] S. W. Walker and B. Shapiro, J. Microelectromech. Syst. **15**, 986 (2006).

[53] K. E. Teigen and S. T. Munkejord, Phys. Fluids **22**, 112104 (2010).

[54] G. Tomar, D. Gerlach, G. Biswas, N. Alleborn, A. Sharma, F. Durst, S. Welch, and A. Delgado, J. Comput. Phys. **227**, 1267 (2007).

[55] J. López-Herrera, S. Popinet, and M. Herrada, J. Comput. Phys. **230**, 1939 (2011).

[56] D. M. Anderson, G. B. McFadden, and A. A. Wheeler, Ann. Rev. Fluid Mech. **30**, 139 (1998).

[57] P. C. Hohenberg and B. I. Halperin, Rev. Mod. Phys. **49**, 435 (1977).

[58] J. Lowengrub and L. Truskinovsky, Proc. Royal Soc. A **454**, 2617 (1998).

[59] H. Abels, H. Garcke, and G. Grün, Math. Models Methods Appl. Sci. **22**, 1150013 (2012).

[60] Instead of the full Navier–Stokes equations, which would be necessary in the presence of boundaries in the two in-plane dimensions.

[61] Y. Lin, P. Skjetne, and A. Carlson, International Journal of Multiphase Flow **45**, 1 (2012).

[62] E. Campillo-Funollet, G. Grün, and F. Klingbeil, SIAM J. Appl. Math. **72**, 1899 (2012).

[63] C. Eck, M. Fontelos, G. Grün, F. Klingbeil, and O. Vantzos, Interfaces and free boundaries **11**, 259 (2009).

[64] R. H. Nochetto, A. J. Salgado, and S. W. Walker, Math. Models Methods Appl. Sci. **24**, 67 (2014).

[65] G. Grün and F. Klingbeil, J. Comput. Phys. **257**, 708 (2014).

[66] S.-R. Hysing, S. Turek, D. Kuzmin, N. Parolini, E. Burman, S. Ganesan, and L. Tobiska, Int. J. Numer. Methods Fluids **60**, 1259 (2009).

[67] S. Aland and A. Voigt, Int. J. Numer. Methods Fluids **69**, 747 (2012).

[68] F. Guillén-González and G. Tierra, J. Comp. Math. **32**, 643 (2014).

[69] G. Grün, F. Guillén-González, and S. Metzger, Commun. Comput. Phys. **19**, 1473 (2016).

[70] S. Metzger, Proc. Appl. Math. Mech. **15**, 715 (2015).

[71] S. Metzger, Numerical Algorithms , 1 (2018).

[72] R. Nürnberg and E. J. W. Tucker, Eur. J. Appl. Math. **28**, 470 (2017).

[73] H. P. Langtangen and A. Logg, *Solving PDEs in Python* (Springer, 2017).

[74] The interpretation of this pressure depends on the formulation of the force on the right hand side of Eq. (2).

[75] C. P. Nielsen and H. Bruus, Phys. Rev. E **90**, 043020 (2014).

[76] G. Linga, A. Bolet, and J. Mathiesen, "Transient electrohydrodynamic flow with concentration dependent fluid properties: modelling and energy-stable schemes," (2018), submitted.

[77] A. Carlson, G. Bellani, and G. Amberg, Phys. Rev. E **85**, 045302 (2012).

[78] J. Shen and X. Yang, SIAM J. Numer. Anal. **53**, 279 (2015).

[79] S. C. Brenner and L. R. Scott, *The mathematical theory of finite element methods*, Vol. 15 (Springer Science & Business Media, 2007).

[80] H. P. Langtangen, K.-A. Mardal, and R. Winther, Advances in Water Resources **25**, 1125 (2002).

[81] A. J. Chorin, J. Comput. Phys. **2**, 12 (1967).

[82] A. J. Chorin, Math. Comput. **22**, 745 (1968).

[83] J.-L. Guermond, P. Minev, and J. Shen, Comput. Methods Appl. Mech. Eng. **195**, 6011 (2006).

[84] G. Linga and A. Bolet, "Bernaise: Git repository," `https://www.github.com/gautelinga/ BERNAISE` (2018).

[85] The latter also contains an equilibrium solver for the quiescent electrochemistry problem, mainly to be used for initialization purposes.

[86] Obviously, when the physical interface thickness may be resolved by the phase field, the sharp-interface assumption might be less sensible than the diffuse. Hence, in such cases this point might be too crude.

[87] R. Pillai, J. Berry, D. Harvie, and M. Davidson, Physical Review E **92**, 013007 (2015).

[88] A. Logg and G. N. Wells, ACM Trans. Math. Softw. **37**, 20:1 (2010).

[89] S. Balay, S. Abhyankar, M. F. Adams, J. Brown, P. Brune, K. Buschelman, L. Dalcin, V. Eijkhout, W. D. Gropp, D. Kaushik, M. G. Knepley, D. A. May, L. C. McInnes, K. Rupp, B. F. Smith, S. Zampini, H. Zhang, and H. Zhang, "PETSc web page," `http://www.mcs.anl.gov/petsc` (2017).

[90] F. Mugele and J. Buehrle, J. Phys. Condens. Matter **19**, 375112 (2007).

[91] G. Linga, A. Bolet, and J. Mathiesen, "Controlling wetting with electrolytic solutions: phase-

field simulations of a droplet-conductor system," (2018), submitted.

[92] J.-J. Huang, H. Huang, and X. Wang, Int. J. Numer. Methods Fluids **77**, 123 (2015).

[93] K. E. Teigen, P. Song, J. Lowengrub, and A. Voigt, J. Comput. Phys. **230**, 375 (2011).

(a) $t = 3.0$, $\sigma_e = 0$

(b) $t = 3.0$, $\sigma_e = -10$

(c) $t = 6.0$, $\sigma_e = 0$

(d) $t = 6.0$, $\sigma_e = -10$

(e) $t = 9.0$, $\sigma_e = 0$

(f) $t = 9.0$, $\sigma_e = -10$
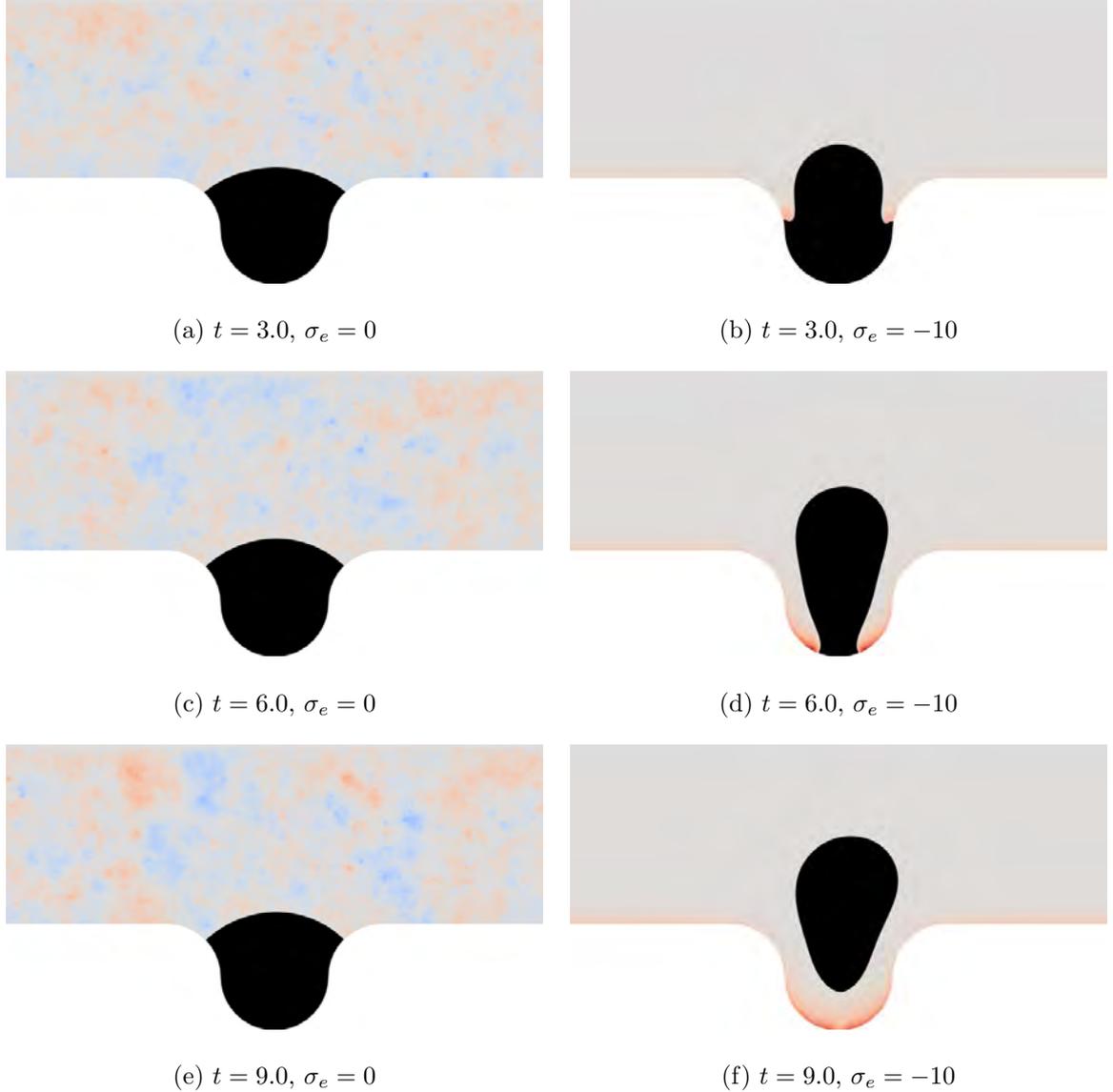
FIG. 11: Oil released from a dead-end pore. We show instantaneous snapshots from the simulations of the dead-end pore under a shear flow. The black phase is the oil phase, which does not contain solutes, and the other phase is the water phase, which contains monovalent positive and negative ions. The color in the lighter phase indicates the local net charge, red meaning positive charge, blue negative charge, and gray neutral charge. The color scale is relative to the maximum deviation from neutral charge for an entire simulation; therefore the neutral simulations display numerical noise (which is of the order of machine precision). In the left column the surface charge is zero, and in the right column, a uniform surface charge density $\sigma_e = -10$ is set. The rows show snapshots at different times t.

60

(a) $t = 0.0$ (b) $t = 0.25$ (c) $t = 0.5$ (d) $t = 0.75$ (e) $t = 1.0$ (f) $t = 1.25$ (g) $t = 1.5$

(h) $t = 1.75$ (i) $t = 2.0$ (j) $t = 2.25$ (k) $t = 2.5$ (l) $t = 2.75$ (m) $t = 3.0$ (n) $t = 4.0$
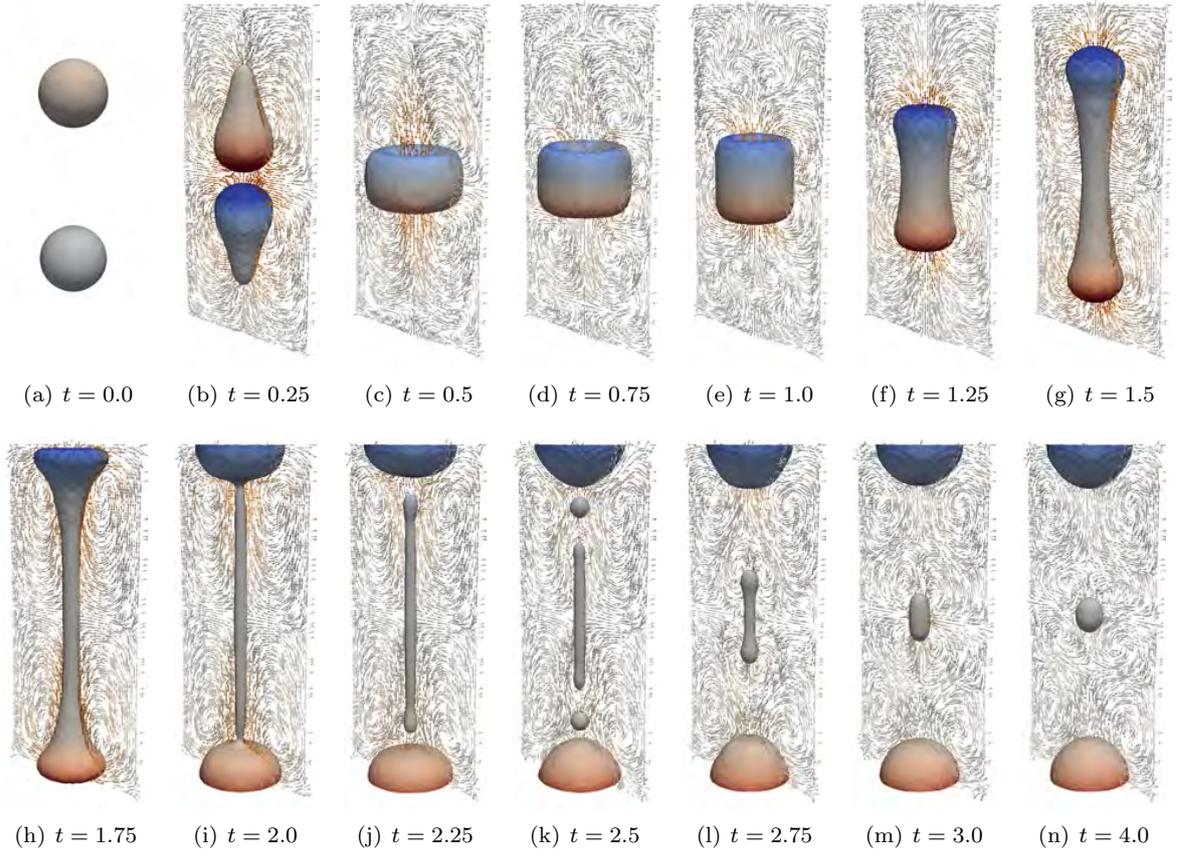
FIG. 12: Snapshots from the simulations of droplet coalescence and subsequent breakup in an electric field. The phase boundary shows the $\phi = 0$ isosurface of the phase field. The coloring indicates charge: red is positive and blue is negative. The color bar goes from -20 (deep blue) to 20 (deep red). The quivers show the velocity field in the $x = 0.5$ plane (color indicates intensity).
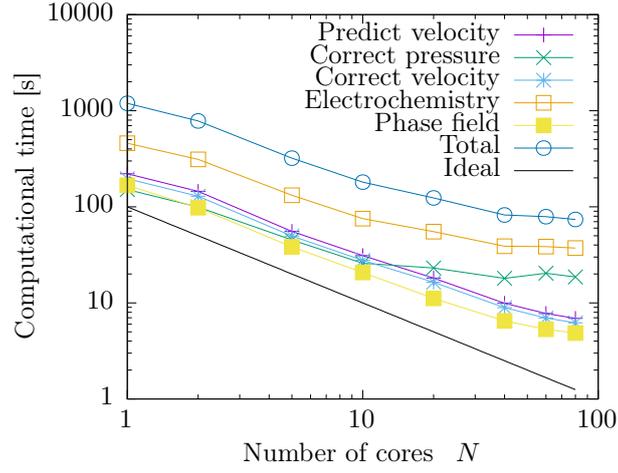
FIG. 13: Strong scaling test. We show computational time per timestep versus number of processor cores for the coalescence and breakup of droplets in 3D. The results are averaged over the 10 first timesteps for simulations with $128 \times 128 \times 256 = 4194304$ degrees of freedom, with a time step $\tau = 0.02$.

Controlling wetting with electrolytic solutions: Phase-field simulations of a droplet-conductor system

Gaute Linga, Asger Bolet, and Joachim Mathiesen

Controlling wetting with electrolytic solutions: Phase-field simulations of a droplet-conductor system

Gaute Linga,[*] Asger Bolet, and Joachim Mathiesen[†]

Niels Bohr Institute, University of Copenhagen, Blegdamsvej 17, DK-2100 Copenhagen, Denmark

The wetting properties of immiscible two-phase systems are crucial in applications ranging from laboratory-on-a-chip devices to field-scale oil recovery. It has long been known that effective wetting properties can be altered by the application of an electric field; a phenomenon coined as electrowetting. Here, we consider theoretically and numerically a single droplet sitting on an (insulated) conductor, i.e., within a capacitor. The droplet consists of a pure phase without solutes, while the surrounding fluid contains a symmetric monovalent electrolyte, and the interface between them is impermeable. Using nonlinear Poisson-Boltzmann theory, we present a theoretical prediction of the dependency of the apparent contact angle on the applied electric potential. We then present well-resolved dynamic simulations of electrowetting using a phase-field model, where the entire two-phase electrokinetic problem, including the electric double layers (EDLs), is resolved. The simulations show that, while the contact angle on scales smaller than the EDL is unaffected by the application of an electric field, an apparent contact angle forms on scales beyond the EDL. This contact angle relaxes in time towards a saturated apparent contact angle. The dependency of the contact angle upon applied electric potential is in good agreement with the theoretical prediction. The only phenomenological parameter in the prediction is shown to depend on the permeability ratio between the two phases. Based on the resulting unified description, we obtain an effective expression of the contact angle which can be used in more macroscopic numerical simulations, i.e. where the electrokinetic problem is not fully resolved.

I. INTRODUCTION

Precisely controlling the effective wetting properties of droplets in immiscible two-phase flows is desirable in many applications [1,2], from fabricating microfluidic devices [3–5] and electronic displays [6–9] to understanding the microscopic dynamics of enhanced oil recovery, which has field-scale consequences [10–14]. Lippmann already in the 19th century [15,16] laid the groundwork for the field of *electrowetting*, by making the observation that applying an electric field indeed *can* change the wetting behavior of conductive liquid-liquid systems. The dependence of the contact angle θ on the applied electric potential V_0 could be described by a quadratic law,

$$\cos\theta = \cos\theta_0 + \tfrac{1}{2}BV_0^2,\qquad(1)$$

where θ_0 is the contact angle in the absence of electrical fields, and B is a phenomenological parameter. Eq. (1) can also be inferred from Gibbs' adsorption isotherm [17,18].

Theoretical and experimental works have explained the basic mechanisms of electrowetting, particularly in the case of conducting liquids [16,19] separated from a conductor by a thin insulating layer. This concept of electrowetting-on-dielectric (EWOD) was pioneered by Berge [20,21], and such devices have an operating voltage of 10–20 V [22]. Careful experiments have shown that the contact angle described by Eq. (1) is a macroscopic effect, apparent only on scales

beyond the insulator thickness [23]. Two notable remaining open issues within electrowetting are (1) the dynamics of the contact line [24], and (2) the effect of electrolytes in either of the phases on the wetting properties [19]. The latter point was explored theoretically by Monroe *et al.* [17,25], who considered interfaces between two immiscible electrolytic solutions (ITIES), and obtained a transcendental expression for the contact angle of a droplet sitting on an isolated, grounded plate using an energy minimization approach. In contrast to conventional EWOD systems, the phases in ITIES systems contain ions which cannot pass over to the other phase (nor to the plate). The apparent contact angle in the case of conductive liquids can only become more acute with the application of a potential, while the latter work showed that contact angles in the presence of electrolytes (and in the absence of flow) could become both obtuse or acute depending on the concentrations, permittivities, and applied potential. Moreover, both theory and experiments [22] suggest that such electrolytic ITIES systems could operate on voltages in the range of 10–1000 mV, i.e., 1–2 orders of magnitude lower than conventional EWOD devices. This indicates that the energy consumption of such devices could be greatly reduced by incorporating such effects.

For conductive liquids with low net concentration of charge, the leaky-dielectric model is admissible. Originally, this model was proposed by Taylor [26] (and revisited by Melcher and Taylor [27]) to describe the distortion of drops in electric fields. Since advection and diffusion of charges is neglected in this model, the electric double layers (EDLs), characterized by the Debye length, are not resolved. As shown rigorously by Schnitzer and Yariv [28], it can be seen as a thin Debye layer

---

[*]linga@nbi.dk
[†]mathies@nbi.dk

limit of the full electro*kinetic* model [29,30]. However, when ionic effects are important and charges are not constrained to the liquid-liquid interface, the more detailed level of description (i.e., resolving the full electrokinetic model) is necessary. Several authors have considered the full model in the absence of boundaries (i.e., for droplets immersed in a liquid). Berry *et al.* [31] presented a sharp-interface combined level-set/volume-of-fluid method to simulate such systems, as an enhancement compared to the leaky-dielectric simulations by Tomar *et al.* [32] and the charge conservative model by López-Herrera *et al.* [33]. Eck *et al.* [24] provided the first direct simulation studies of dynamic electrowetting with electrolytes. The model used in the latter work belongs to the leaky-dielectric type, as the mobility does not depend on concentration. However, it contains a concentration regularization parameter which introduces a length scale, and effectively sets the thickness of the Debye layer. A similar model and a more detailed study were carried out by Nochetto *et al.* [34]. Other works have adopted a more macroscopic viewpoint and used the electrowetting contact angle as an input to model effective behavior on the microfluidic scale [35–37]. On the other hand, there are a number of assumptions underpinning the purely theoretical works of Monroe *et al.* [17]. As experiments remain sparse (albeit Frumkin undertook such studies already in the 1930s [22,38]), simulations would be of interest to test validity of, and extensions to, the theory. To the authors' knowledge, there has been no systematic numerical study of the direct dependency of the contact angle on applied electric potential for a fully resolved electrohydrodynamic model with partially soluble electrolytes.

In this work, we consider theoretically and numerically the effect of an applied potential on the wetting properties of an immiscible two-phase system consisting of a single droplet placed on an insulated electrode. The droplet phase is nonconducting, while the surrounding fluid contains an electrolyte, and all interfaces are taken to be impermeable. Such approximations are valid for many industrially and geologically relevant systems such as oil-in-water flows [31]. Using Poisson-Boltzmann theory and following the approach of Ref. [17], we develop a theoretical prediction for the apparent contact angle dependency on applied potential. In our simulations, we use the thermodynamically consistent and frame-invariant model for two-phase electrokinetic flow which was proposed by Campillo-Funollet *et al.* [39]. This phase-field model combines the Nernst-Planck equation for chemical transport, the Poisson equation for electrostatics, the Cahn-Hilliard equation for the description of the interface, and the Navier-Stokes equations for fluid flow. Using a recently introduced solver [40] for this model, we simulate electrowetting dynamically. We demonstrate explicitly that the contact angle is only apparent on scales beyond the Debye length, whereas the *microscopic* contact angle remains unaffected. Our main finding is that the apparent contact angle dependency is well described by the theoretical prediction, in particular when our only phenomenological quantity, the effective screening area, is modeled as a function solely of the ratio between the permittivities. This, microscopically viewed, *apparent* contact angle, can thus be turned into a *fixed* contact angle boundary condition which can be used for simulations on more macroscopic scales.
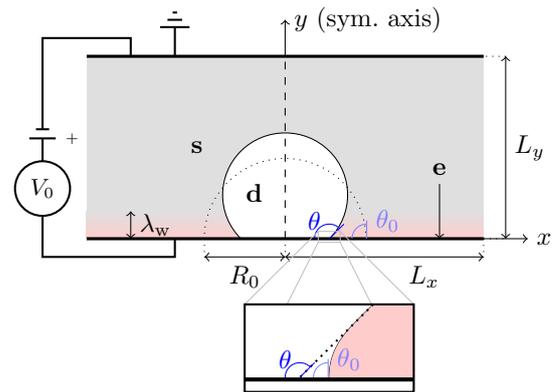
FIG. 1. Schematic setup of the numerical experiment. Here, **d** indicates the droplet phase, **s** indicates the surrounding phase, and **e** indicates the electrode. The figure shows the final state after the application of a potential difference V_0 between the two electrodes. Due to the dissolved electrolytes in phase **s**, an electric double layer, characterized by the Debye length $\lambda_\mathbf{s}$ is formed near the lower electrode, and an *apparent* contact angle θ is formed. Also indicated with a dotted line is the initial state of the droplet (where $V_0 = 0$), forming the contact angle θ_0. Note that the simulations considered herein exploit the indicated axial symmetry of the problem. A close-up view of the contact line shows how the contact angle θ_0 persists on small scales, whereas the apparent contact angle θ is only evident on sufficiently large scales.

II. MODEL SYSTEM

We consider a droplet (phase **d**), surrounded by another fluid (phase **s**), sitting on an electrode (phase **e**) in the presence of an electric field. A sketch of the system setup is shown in Fig. 1. Within the surrounding fluid, a binary salt is dissolved. We denote the concentrations of these ionic species by $c_\pm$. We consider symmetric ions, such that $z_\pm = \pm z$ are the valencies of the ions. The ions are not allowed to pass through the liquid-liquid interface (**ds**), and the droplet contains no ions. This setup is representative of most oil-in-water systems and most microfluidic applications.

The substrate is held at a constant electric potential $V = V_0$, while the system is grounded far from the droplet. We take the lower boundary, representing the electrode, to be impermeable for ions and the fluid phase, and hence assume a no-slip condition. This assumption, which implies zero conduction through the system, is the main distinction from most of the existing literature [16].

Conversely, the top boundary mimics a reservoir and thus assumes constant concentrations, i.e., $c_\pm = c_0$. Due to the impermeable boundary, an EDL is formed near the electrode, as quantified by the Debye length $\lambda_\mathbf{s}$ indicated in Fig. 1. It is well known that the local contact angle θ_0 is given by the interfacial energies between the three phases, while, on scales beyond $\lambda_\mathbf{s}$, an apparent contact line θ is formed. Using the presented setup, we shall in the forthcoming consider how this apparent contact angle depends on the applied potential V_0.

III. THEORY

Two-phase electrokinetic fluid dynamics is described by the coupled problem of solute transport, fluid flow, and

electrostatics. The Nernst-Planck equation governs the chemical transport,

$$\frac{\partial c_\pm}{\partial t} + \mathbf{u} \cdot \nabla c_\pm = \nabla \cdot \left(D_\pm \nabla c_\pm \mp \frac{z q_e c_\pm}{k_B T} \mathbf{E} \right), \qquad (2)$$

where t is the time, $\mathbf{u}$ is the fluid velocity, $\mathbf{E} = -\nabla V$ is the electric field, $D_\pm$ are the diffusivities of the "$\pm$" ions, k_B is Boltzmann's constant, T is the temperature, and q_e is the elementary charge. Electrostatic equilibrium is determined by the Poisson equation,

$$\nabla \cdot (\epsilon_0 \epsilon_r \mathbf{E}) = \rho_e, \qquad (3)$$

where ϵ_0 is the vacuum permittivity, ϵ_r is the relative permittivity, and the total charge is given by $\rho_e = q_e z(c_+ - c_-)$. The fluid flow is governed by the Navier-Stokes equations,

$$\rho(\partial_t \mathbf{u} + \mathbf{u} \cdot \nabla \mathbf{u}) - \mu \nabla^2 \mathbf{u} + \nabla p = -\rho_e \nabla V, \qquad (4)$$

$$\nabla \cdot \mathbf{u} = 0, \qquad (5)$$

where ρ is the density, μ is the dynamic viscosity, and p is the pressure. The equations are closed by boundary conditions and the continuity of the normal stress across the interface between the phases,

$$\left[2\mu \mathcal{D}\mathbf{u} - p'\mathbf{I} + \sigma_{ds}\kappa\mathbf{I} + \epsilon_0 \epsilon_r \mathbf{E} \otimes \mathbf{E} - \tfrac{1}{2}\epsilon_0 \epsilon_r \mathbf{E}^2 \mathbf{I} \right] \cdot \hat{\mathbf{n}} = \mathbf{0}. \qquad (6)$$

Here, the pressure p' has been redefined to absorb an osmotic contribution, $\mathcal{D}\mathbf{u} = (\nabla\mathbf{u} + \nabla\mathbf{u}^T)/2$ is the (symmetric) strain-rate tensor, σ_{ds} is the fluid-fluid surface tension, κ is the interface curvature, and $\hat{\mathbf{n}}$ is an interface normal.

A. Scaled variables

We employ a standard electrokinetic scaling to obtain dimensionless variables which are more practical to work with in the following. To this end, we introduce the dimensionless variables indicated by a tilde, such that $\tilde{t} = t/t^*$, $\tilde{\rho} = \rho/\rho^*$, $\tilde{\mathbf{u}} = \mathbf{u}/u^*$, $\tilde{p} = p/p^*$, $\tilde{\mu} = \mu/\mu^*$, $\tilde{c} = c/c^*$, $\tilde{V} = V/V^*$, $\tilde{D}_\pm = D_\pm/D^*$, $\tilde{\epsilon} = \epsilon_r/\epsilon^*$, and $\tilde{\sigma}_{ds} = \sigma_{ds}/\sigma_{ds}^*$. Here, all the quantities marked by an asterisk are reference values. Further, all length variables are scaled by a droplet reference linear size R^*, i.e., $\tilde{x} = x/R^*$. In particular, the electric potential V is scaled by the thermal voltage,

$$V^* = V_T = \frac{k_B T}{z q_e}. \qquad (7)$$

The remaining reference quantities are given by

$$t^* = \frac{R^*}{u^*}, \quad \rho^* = \frac{z q_e c^* V_T}{(u^*)^2}, \qquad (8)$$

$$D^* = u^* R^*, \quad p^* = z q_e c^* V_T, \quad \mu^* = \frac{z q_e c^* V_T R^*}{u^*}, \qquad (9)$$

$$\epsilon^* = \frac{z q_e c^* (R^*)^2}{\epsilon_0 V_T}, \quad \sigma_{ds}^* = z q_e c^* V_T R^*. \qquad (10)$$

Note that time $\tilde{t}$ is given in advective time units. Adopting the chosen scaling, and subsequently skipping the tildes, now results in a model consisting of the set of equations (2) to (6), but where $z q_e = k_B T = \epsilon_0 = 1$ and $\epsilon_r \to \epsilon$. For simplicity of notation we shall thus retain this normalization throughout the paper.

B. Equilibrium free energy

We are here interested in the time-asymptotic steady state of the droplet. Since there is an impermeable no-slip boundary at $y = 0$, and hence no charge transport through the system in the steady state, the steady state will be without fluid circulation. We can thus safely neglect the velocity field in seeking the time-asymptotic state.

We denote the phasic quantities of the concentrations by c_i, the (dynamic) viscosity by μ_i, the permittivities by ϵ_i, for phases $i \in \{\mathbf{d},\mathbf{s}\}$, and the interface energies by σ_j, for $j \in \{\mathbf{ds},\mathbf{de},\mathbf{es}\}$. The droplet and surrounding subvolumes are denoted by $\Omega_\mathbf{d}$ and $\Omega_\mathbf{s}$, respectively.

Following Monroe *et al.* [17], we write the Gibbs energy G of the system as

$$G = -\frac{1}{2} \sum_{i=\mathbf{d},\mathbf{s}} \int_{\Omega_j} \epsilon_j \mathbf{E}^2 \, d\Omega$$
$$+ \sum_{j=\pm} \int_{\Omega_\mathbf{s}} \left[(\ln c_j - 1)c_j + \frac{z_j}{z} c_j V \right] d\Omega + \sum_{i=\mathbf{d},\mathbf{s}} p \, \Omega_i$$
$$+ A_\mathbf{ds}\sigma_\mathbf{ds} + A_\mathbf{de}\sigma_\mathbf{de} + A_\mathbf{es}\sigma_\mathbf{es}. \qquad (11)$$

Here, $A_\mathbf{de}$ is the area between the droplet and the electrode, $A_\mathbf{ds}$ is the area between the droplet and the surroundings, and $A_\mathbf{es}$ is the area between the electrode and the surrounding fluid. Like $\Omega_\mathbf{s}$ and $A_\mathbf{es}$, this energy scales with the size of the domain, and we need to fix it by defining some reference. The reference state can be chosen as the state without a droplet, G_0. We denote the deviation from this reference by $\Delta G = G - G_0$.

In contrast to Monroe *et al.* [17], we consider here a droplet which does not contain electrolytes. Neglecting the energetic contribution of the electric field within the droplet and the charge distribution around the droplet, the deviation in Gibbs free energy from a reference state without a droplet can be written in the large-droplet approximation of nonlinear Poisson-Boltzmann theory [17] as

$$\frac{\Delta G}{\sigma_\mathbf{ds}} = A_\mathbf{de}\left[\frac{8\sqrt{2\epsilon_\mathbf{s}c_0}}{\sigma_\mathbf{ds}} \sinh^2\left(\frac{V_0}{4}\right) - \cos\theta_0 \right]$$
$$+ A_\mathbf{ds} + \frac{\Omega_\mathbf{d}}{\sigma_\mathbf{ds}}\Delta p. \qquad (12)$$

Here, Δp is the pressure difference across the interface, which here is to be considered as a Lagrange multiplier. Since Eq. (12) was derived without accounting for the energy within the droplet, this expression provides an upper bound for the energy. This can be realized by considering the contribution from the thin screening layer outside the droplet (interface **ds**) and the negative sign of the electric field inside the droplet.

C. A scaling ansatz

To somewhat simplify, we define the quantity

$$f_0 = \frac{8\sqrt{2\epsilon_\mathbf{s}c_0}}{\sigma_\mathbf{ds}}, \qquad (13)$$

which, along with the applied potential V_0, is predicted to be a control parameter of the system. To incorporate the effect of screening the electric field due to the droplet, we heuristically generalize Eq. (12). Since the electric flux into the droplet

is roughly proportional to the contact area $A_{\mathbf{de}}$, we postulate that the effect can effectively be incorporated by making the modification

$$\frac{\Delta G}{\sigma_{\mathbf{ds}}} = A_{\mathbf{de}}\left[f \sinh^2\left(\frac{V_0}{4}\right) - \cos\theta_0\right] + A_{\mathbf{ds}} + \frac{\Omega_{\mathbf{d}}}{\sigma_{\mathbf{ds}}}\Delta p, \tag{14}$$

where $f \to f_0$ in the limit of no electrical flux through the droplet (and hence no screening around). Note that, to be consistent with the "upper bound" observation made above, we must have $f \leqslant f_0$ for all sets of parameters. Further, making the ansatz that f/f_0 should depend only on quantities present in both phases, that *further* contribute to the energy in the equilibrium state [cf. Eq. (11)], we have

$$f = f_0 h\left(\frac{\epsilon_{\mathbf{d}}}{\epsilon_{\mathbf{s}}}\right), \tag{15}$$

where $h \leqslant 1$ is an unknown function.

D. Expression for the contact angle

When the surface tension $\sigma_{\mathbf{ds}}$ is sufficiently high, and considering a two-dimensional (2D) system, we may take the droplet to be a circular cap. We can write down expressions for the interfacial areas and the droplet volume in terms of circle radius r and angle θ:

$$A_{\mathbf{de}} = 2r\sin\theta, \quad A_{\mathbf{ds}} = 2r\theta,$$

$$\Omega_{\mathbf{d}} = r^2\left(\theta - \frac{1}{2}\sin 2\theta\right).$$

The latter yields

$$r = \frac{\sqrt{\Omega_{\mathbf{d}}}}{\sqrt{\theta - \frac{1}{2}\sin 2\theta}}. \tag{16}$$

Now, Eq. (14) can be written as

$$\frac{\Delta G}{\sigma_{\mathbf{ds}}} = 2\Omega_{\mathbf{d}}^{1/2}\frac{\xi\sin\theta + \theta}{\sqrt{\theta - \frac{1}{2}\sin 2\theta}} + \frac{\Omega_{\mathbf{d}}}{\sigma_{\mathbf{ds}}}\Delta p, \tag{17}$$

where

$$\xi = f \sinh^2\left(\frac{V_0}{4}\right) - \cos\theta_0. \tag{18}$$

We need to minimize ΔG with respect to the apparent contact angle θ; this amounts to finding the θ that minimizes

$$\chi(\theta) = \frac{\xi\sin\theta + \theta}{\sqrt{\theta - \frac{1}{2}\sin 2\theta}}, \tag{19}$$

i.e., solving

$$\chi'(\theta) = \frac{\xi\cos\theta + 1}{\sqrt{\theta - \frac{1}{2}\sin 2\theta}} - \frac{(\xi\sin\theta + \theta)(1 - \cos 2\theta)}{2\left(\theta - \frac{1}{2}\sin 2\theta\right)^{3/2}} = 0. \tag{20}$$

This gives

$$(\xi + \cos\theta)(\theta\cos\theta - \sin\theta) = 0. \tag{21}$$

The second factor on the left-hand side is nonzero for $\theta \in (0,\pi)$. Hence, the apparent contact angle is given by $\cos\theta = -\xi$ (which can also be verified to correspond to a minimum in χ). This can be written as

$$\cos\theta = \cos\theta_0 - f\sinh^2\left(\frac{V_0}{4}\right). \tag{22}$$

Thus we have a simple expression for what to expect from numerical simulations.

Notably, since we know from before that $f \leqslant f_0$, we thus have a prediction of a *lower bound* for the contact angle, namely

$$\cos\theta - \cos\theta_0 \geqslant -f_0 \sinh^2\left(\frac{V_0}{4}\right). \tag{23}$$

Furthermore, expression (22) is consistent with Lippmann's expression (1) in the limit of $V_0 \ll 1$. This leads us to the identification

$$B = -\frac{f}{8}, \tag{24}$$

and hence we have obtained a prediction of the phenomenological parameter B.

We shall check the validity of Eqs. (22) and (15) numerically in the forthcoming.

IV. PHASE-FIELD MODEL AND SIMULATIONS

For simulating the two-phase flow problem of dynamic electrowetting, we adopt a phase-field (or diffuse-interface) approach. The interface is described by the order parameter field ϕ which attains the values ± 1 respectively in the two phases, and interpolates between the two across the diffuse interface of thickness ζ. In the limit $\zeta \to 0$, the equations should reproduce the correct sharp-interface physics (see Ref. [40]). A thermodynamically consistent phase-field model fit for our purpose was formulated by Campillo-Funollet *et al.* [39], and is given by the following set of equations:

$$\partial_t(\rho(\phi)\mathbf{u}) + \boldsymbol{\nabla} \cdot (\rho(\phi)\mathbf{u} \otimes \mathbf{u})$$
$$- \boldsymbol{\nabla} \cdot [2\mu(\phi)\mathcal{D}\mathbf{u} + \mathbf{u} \otimes \rho'(\phi)M(\phi)\boldsymbol{\nabla}g_\phi] + \boldsymbol{\nabla}p$$
$$= -\phi\boldsymbol{\nabla}g_\phi - \sum_j c_j\boldsymbol{\nabla}g_{c_j}, \tag{25}$$

$$\boldsymbol{\nabla} \cdot \mathbf{u} = 0, \tag{26}$$

$$\partial_t\phi + \mathbf{u} \cdot \boldsymbol{\nabla}\phi - \boldsymbol{\nabla} \cdot (M(\phi)\boldsymbol{\nabla}g_\phi) = 0, \tag{27}$$

$$\partial_t c_j + \mathbf{u} \cdot \boldsymbol{\nabla}c_j - \boldsymbol{\nabla} \cdot (D_j(\phi)c_j\boldsymbol{\nabla}g_{c_j}) = 0, \tag{28}$$

$$\boldsymbol{\nabla} \cdot (\epsilon(\phi)\boldsymbol{\nabla}V) = -\rho_e. \tag{29}$$

Here, Eqs. (25) and (26) are the incompressible Navier-Stokes equations, the Nernst-Planck equation (28) governs solute transport, and the Poisson equation (29) determines electrostatic equilibrium. The phase field ϕ takes the value $\phi = -1$ in phase **s**, and the value $\phi = 1$ in phase **d**. The (conservative) temporal evolution of ϕ is governed by the Cahn-Hilliard equation (27), wherein the diffusion term is controlled by the phase-field mobility $M(\phi)$. Here, we use the

nonlinear phase-field mobility

$$M(\phi) = M_0(1 - \phi^2)_+, \qquad (30)$$

where M_0 is a constant and $(\cdot)_+ = \max(\cdot, 0)$.

The chemical potential of species $c_\pm$ is given by

$$g_{c_\pm}(c_\pm, \phi) = \ln(c_\pm) + \beta_\pm(\phi) \pm zV, \qquad (31)$$

where $\beta_\pm(\phi)$ is an energy penalty for dissolving ions $c_\pm$ in the phase given by ϕ. The chemical potential g_ϕ of the phase field ϕ is given by

$$g_\phi = \frac{3\sigma_{\mathbf{ds}}}{2\sqrt{2}}[\zeta^{-1}W'(\phi) - \zeta\nabla^2\phi]$$
$$+ \sum_j \beta_j'(\phi)c_j - \frac{1}{2}\epsilon'(\phi)|\nabla V|^2, \qquad (32)$$

where ϵ is the interface thickness and $W(\phi)$ is a double well potential. Here, we adopt the commonly used $W(\phi) = (1 - \phi^2)^2/4$.

The density field ρ, viscosity field μ, permittivity field ϵ, solubility energies $\beta_\pm$, and diffusivity fields $D_\pm$ all depend on the phase, i.e., ϕ. In this work, they are given by the following weighted arithmetic averages (WAA):

$$\rho(\phi) = \frac{\rho_{\mathbf{d}} + \rho_{\mathbf{s}}}{2} + \frac{\rho_{\mathbf{d}} - \rho_{\mathbf{s}}}{2}\phi, \qquad (33)$$

$$\mu(\phi) = \frac{\mu_{\mathbf{d}} + \mu_{\mathbf{s}}}{2} + \frac{\mu_{\mathbf{d}} - \mu_{\mathbf{s}}}{2}\phi, \qquad (34)$$

$$\epsilon(\phi) = \frac{\epsilon_{\mathbf{d}} + \epsilon_{\mathbf{s}}}{2} + \frac{\epsilon_{\mathbf{d}} - \epsilon_{\mathbf{s}}}{2}\phi, \qquad (35)$$

$$D_\pm(\phi) = \frac{D_{\pm,\mathbf{d}} + D_{\pm,\mathbf{s}}}{2} + \frac{D_{\pm,\mathbf{d}} - D_{\pm,\mathbf{s}}}{2}\phi, \qquad (36)$$

$$\beta_\pm(\phi) = \frac{\beta_{\pm,\mathbf{d}} + \beta_{\pm,\mathbf{s}}}{2} + \frac{\beta_{\pm,\mathbf{d}} - \beta_{\pm,\mathbf{s}}}{2}\phi. \qquad (37)$$

Tomar *et al.* [32] found, for a level-set electrohydrodynamics model with smoothed interfacial properties, that using a weighted harmonic average (WHA) for the permittivity yielded more precise results for the electric field than the WAA did. However, for a model including free charges, López-Herrera *et al.* [33] found no evidence that WHA was superior, and for simplicity we therefore use the WAA for all fields.

A. Boundary conditions

Most boundary conditions involved in the present work are of Dirichlet type. We set fixed electric potential at the top and bottom boundaries, and a no-slip condition on the velocity field at the bottom boundary, and fixed concentrations on the top boundary. Further, we assume a no-flux condition on the concentration fields at the bottom boundary. With regard to the phase field, a dynamic wetting boundary condition can be expressed as the following Robin condition [41]:

$$\zeta\tau_w\partial_t\phi = \sigma_{\mathbf{ds}}\left[-\frac{3\zeta}{2\sqrt{2}}\hat{\mathbf{n}}\cdot\nabla\phi + \cos(\theta_0)f_w'(\theta)\right], \qquad (38)$$

where θ_0 is the prescribed contact angle, τ_w is a relaxation parameter, and $f_w(\phi) = (2 + 3\phi - \phi^3)/4$ interpolates smoothly between 0 (at $\phi = -1$) and 1 (at $\phi = 1$). In order not to introduce an additional unknown timescale into the problem,
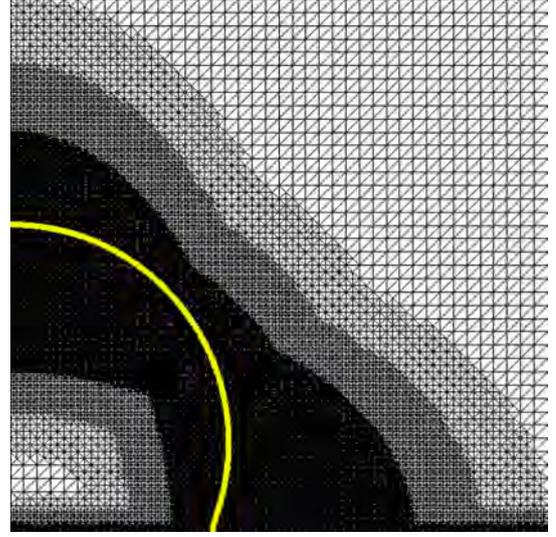
FIG. 2. Typical mesh used in simulations. The zero-level set of the phase field is shown as a solid yellow line.

we limit ourselves to considering Eq. (38) with $\tau_w = 0$. Electrowetting with emphasis on contact line pinning was previously studied numerically by Nochetto *et al.* [34], who used a generalized Navier boundary condition on the velocity field (cf. [42]). However, as contact-line modeling remains phenomenological, we shall leave it for further work.

B. Numerical implementation

We consider computationally the 2D domain $[0, L_x] \times [0, L_y]$, since, as indicated in Fig. 1, a mirror symmetry is present. Although alternatively an axially symmetric geometry could have been considered, we consider here the 2D case. In order to mimic a reflective boundary and without loss of generality, we use a free slip condition on the left-hand side and a no-flux condition on both electrolyte concentration and electric potential. The numerical benefits are that this avoids drift of the droplet (due to numerical noise or mesh asymmetries) and limits the computational domain to half the size.

The simulation is initiated with a (*half*) circular droplet cap of area $\pi R_0^2/4$ (in the *half* domain) that forms a contact angle of θ_0 with the surface, and a uniform concentration of both ions is set in the surrounding phase. At time $t = 0$, a potential V is set at the bottom electrode.

To solve the equations numerically we use the finite-element solver BERNAISE developed by the authors, and presented and validated in a separate work [40]. BERNAISE is written in Python and builds on the FEniCS/DOLFIN framework [43,44]. The solver operates on unstructured meshes and is therefore suitable when different parts of the domain require very different resolutions.

A typical mesh used in the simulations is shown in Fig. 2. The mesh is gradually refined near the electrode, to resolve the electrical double layer that arises here. Further, around the evolving interface, a fine mesh is required, both to resolve the diffuse interface associated with the phase field, and to resolve the Debye layer. In order to capture the motion

TABLE I. Physical parameters of a water-nitrobenzene system. The parameters related to solubility are typical of a monovalent electrolyte such as NaCl.

	Phase i		
Parameter	**d** (nitrobenzene)	**s** (water)	Unit
$\epsilon_{r,i}$	$\simeq 40$	$\simeq 80$	
c_i	0	0.1	M
	0	6×10^{25}	No./m^3
λ_i		$\simeq 3$	nm
$D_{\pm,i}$		$\simeq 1 \times 10^{-9}$	m^2/s
ρ_i	$\simeq 1.2$ g/mL	$\simeq 1.0 \times 10^{-3}$	kg/cm^3
μ_i/ρ_i	$\simeq 1.7 \times 10^{-6}$ m^2/s	$\simeq 10^{-6}$	m^2/s

of the interface without having to refine adaptively (which is both undesirable for parallelization, and has limited support in FEniCS), the mesh is refined beforehand over an extended area suitable for circle caps with both acute and obtuse contact angles.

We discretize the equations using finite elements in space, and finite difference in time. For the temporal integration of the equations, we use a first-order linearized operator-splitting scheme. The scheme is presented and validated in a companion paper [40], but is briefly outlined here. At each time step, we solve sequentially three subproblems. First, the phase-field equations (27) and (32) are solved in a coupled manner; then the electrochemical equations (28), with (31) inserted, and (29) are solved together; and finally the Navier-Stokes equations (25) and (26) are solved simultaneously. Each substep is semi-implicit, in that the equations are linearized around the variables at the previous time step. This yields an efficient, decoupled and fully linear scheme. More details on the scheme can be found in Ref. [40, Sec. III B], and the implementation is openly available.[1] With regard to spatial discretization, we use P$_2$ finite elements for the velocity field and P$_1$ elements for the scalar fields, which imparts second-order convergence in space. We use FEniCS' built-in direct linear solvers to achieve robust convergence.

C. Physical parameters

In Sec. III A, the governing equations were scaled, and since the simulations are carried out in these scaled variables, the results may correspond to a variety of parameter sets. However, it is interesting to consider concrete physical values in order to relate the numerical experiments to reality. We consider as an example the components of the ITIES setup considered by Monroe *et al.* [25], with a nitrobenzene droplet and water surroundings. The relevant phasic parameters are given in Table I. Additionally, the surface tension of the water-nitrobenzene interface is (in the order of magnitude) $\sigma_{\mathbf{ds}} \simeq 25 \times 10^{-3}$ kg/s^2 [45]. We are now in a position to

---

[1]See the GitHub repository https://github.com/gautelinga/BERNAISE. The numerical scheme is implemented in `solvers/basic.py`, and the simulation set-up is a customized version of `problems/electrowetting.py`.

estimate the expected control parameter f_0 defined in Eq. (13). Translating back to the dimensional quantities, we have the expression

$$f_0 = \frac{8 V_T^{3/2} \sqrt{2 z q_e c_0 \epsilon_0 \epsilon_{r,s}}}{\sigma_{\mathbf{ds}}}, \tag{39}$$

which gives a numerical (dimensionless) value of the order $f_0 \simeq 0.3$. By inspecting (23), we see that this value imparts significant deviations from the neutral angle even at moderate V_T. For example, complete dewetting is predicted at $V_0 \simeq 7 V_T$ (assuming the neutral contact angle $\theta_0 = \pi/2$ in the absence of electric field). For systems with lower surface tension and/or higher concentration, the effect should be stronger.

Inspired by the parameters for the water-nitrobenzene system, we make the simplifying assumptions $\rho_{\mathbf{d}} \simeq \rho_{\mathbf{s}}$, $\mu_{\mathbf{d}} \simeq \mu_{\mathbf{s}}$, and $D_- \simeq D_+$. On the other hand, we choose $\mu_{\mathbf{s}}/\rho_{\mathbf{s}} \sim D_{\pm}$ in order to reduce the computation required to equilibrate the charges in the system. This does not have consequences for the time-asymptotic solution [cf. Eq. (11)], and should only have minor consequences for the dynamics.

V. RESULTS

Here, we study numerically the dynamic relaxation to an apparent contact angle when an electric field is suddenly turned on. Simulation parameters, in scaled units, common for all simulations are set to $\rho_{\mathbf{d}} = \rho_{\mathbf{s}} = \mu_{\mathbf{d}} = \mu_{\mathbf{s}} = 10$, $M_0 = 2 \times 10^{-6}$, $D_{\pm,\mathbf{s}} = 1$, $D_{\pm,\mathbf{d}} = 0.001$, $\beta_{\pm,\mathbf{s}} = 0$, $\beta_{\pm,\mathbf{s}} = 4$. For specific sets of simulations, further parameters are given in Table II below. We use a time step $\tau = 0.25$ for all simulations, a minimum grid size $h_{\min} = 0.0125$ (unless otherwise stated), interface thickness $\zeta = 2 h_{\min}$, and a domain size $L_x = L_y = 2 R_0$.

A. Qualitative description

When the potential difference is applied at time $t = 0$, charge quickly flows towards the bottom electrode to screen the charge. Gradually, the contact line moves and an apparent contact angle forms. In Fig. 3, we visualize the relaxation to the apparent contact angle for one specific applied voltage. Inspecting the local contact angle, we see that the contact angle approaches the strictly enforced angle, here $\theta_0 = \pi/2$. This is further quantified in Fig. 4, where we compare the final state for

TABLE II. Parameters used in the simulations shown in Fig. 6, 7, and 9.

Sim.	R_0	c_0	$\epsilon_{\mathbf{s}}$	$\epsilon_{\mathbf{d}}$	$\lambda_{\mathbf{s}}$	$\sigma_{\mathbf{ds}}$	θ_0	$h_{\min} = \zeta/2$
A	1.0	10	0.1	0.2	0.071	5	$\pi/2$	0.0125
B	1.5	10	0.1	0.2	0.071	5	$\pi/2$	0.0125
C	4.0	10	0.1	0.2	0.071	5	$\pi/2$	0.0125
D	1.0	1	0.1	0.2	0.22	5	$\pi/2$	0.0125
E	1.0	1	0.1	0.2	0.22	5	$\pi/2$	0.025
F	1.5	10	0.1	2.0	0.071	5	$\pi/2$	0.0125
G	1.5	10	0.1	0.005	0.071	5	$\pi/2$	0.0125
H	1.5	10	0.9	0.2	0.21	5	$\pi/2$	0.0125
I	1.0	10	0.1	0.2	0.071	10	$\pi/2$	0.0125
J	1.0	10	0.1	0.2	0.071	5	$\pi/4$	0.0125

FIG. 3. Relaxation to the apparent contact angle when an electric field is suddenly applied. The electric potential difference is turned on to $V = 2.5$ at time $t = 0$. The red color in the surrounding fluid shows the net charge, and thus represents the EDL. (a) to (f) show increasing simulation time.

the same set-up, same parameters and applied potential, where only the droplet size is varied. As seen from the figure, the shape of the droplet is fairly robust to the size of the droplet, but is slightly distorted due to the presence of the three-phase contact region. However, as the Debye length becomes small compared to the droplet radius, the apparent contact angle persists.

B. Contact angle relaxation in time

We now seek to quantify the evolution of the apparent contact angle through time. We compute this angle by fitting a semicircle to the zero-level set of the phase field, for all points where $y \geqslant 0.1$ ($\sim R_0/10$ for most simulations). The intersection between this circle and the $y = 0$ plane determines the apparent contact angle θ. In Fig. 5, we plot the resulting contact angle in time for a range of potential drops.

C. Dependence of the contact angle on applied potential

In Fig. 6, we plot the contact angle as a function of applied potential, for a range of different parameter sets. The parameter
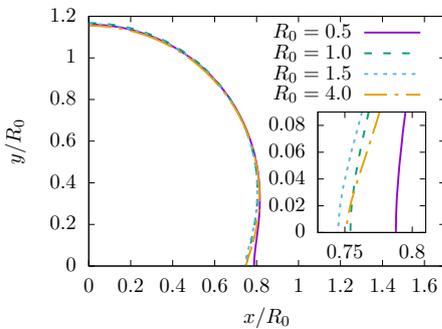
FIG. 4. Comparison of the droplet shape for different droplet size, when the Debye length and other parameters are kept constant. The Debye length is $\lambda_s = \sqrt{\epsilon_s/(2c_0)} \simeq 0.071$. The inset shows a close-up of the contact line.
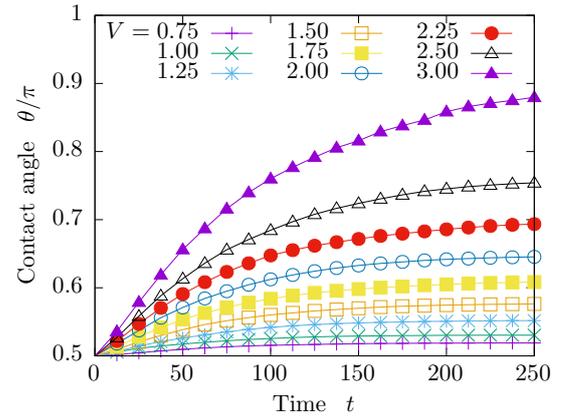
FIG. 5. Contact angle in time for a range of potential drops V_0. The lines between points are linearly interpolated for visual clarity.

sets corresponding to Fig. 6 are given in Table II. The functional form seems to be sensitively dependent on the parameters used.

The prediction of Eq. (22) suggests that plotting $\cos\theta - \cos\theta_0$ against the composite variable $(\sqrt{\epsilon_s c_0}/\sigma_{ds}) \sinh^2(V_0/4)$ should make the points fall on a straight line, provided that f is independent of V. In Fig. 7, we show for a range of different parameters the contact angle as a function of this composite variable. As predicted by Eq. (22), it is clear that the proposed functional form matches very well for the entire range until complete dewetting occurs. Indeed, we find that the points fall onto straight lines for a range of parameters. Further, the predicted inequality, (23), seems to be satisfied for all. From the figure, it is apparent that the slope of the curves depend mainly on the permittivities in the two phases.

To investigate the role of the permittivities in the two phases, we fit linear slopes to the data plotted in Fig. 7. In particular, we use $Y = \cos\theta - \cos\theta_0$ and $X = (\sqrt{\epsilon_s c_0}/\sigma_{ds}) \sinh^2(V_0/4)$, and find for each parameter set the slope k which minimizes the residual of the fit of $Y = kX$ to the (X, Y) data points. The resulting slopes k (which are all such that $-8\sqrt{2} \leqslant k \leqslant 0$) are plotted in Fig. 8 against the ratio between permittivities ϵ_d/ϵ_s for the respective parameter sets. Since we expect $f \leqslant f_0$, the y
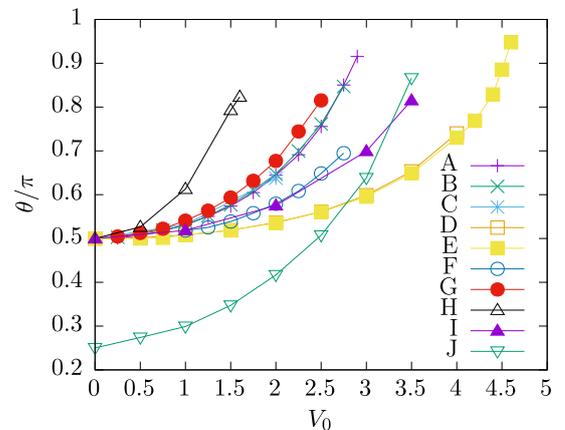
FIG. 6. We plot the apparent contact angle as a function of applied potential, for a range of parameters. The simulation sets A–J correspond to the parameter sets reported in Table II.
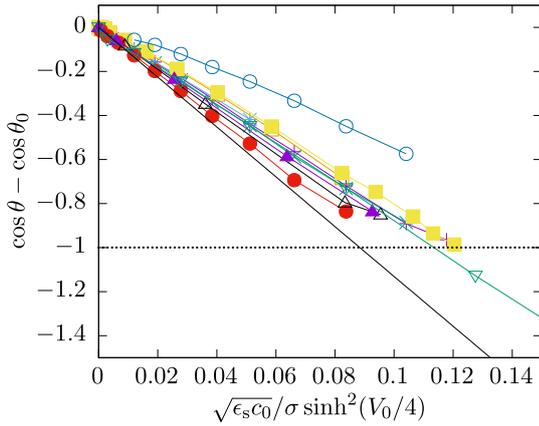
FIG. 7. We plot the quantities involved in Eq. (22) for a range of parameters.

axis has been shifted by the numerical prefactor in $f_0, 8\sqrt{2}$. We heuristically fit a function $B(\epsilon_d/\epsilon_s)^\alpha$ to these points using least squares, where B, α are (dimensionless) fitting parameters. The best fit gives $B \simeq 2.6$ and $\alpha = 0.28$ (with rather large residuals). Note that many functional forms would yield fairly equal results. Our motivation for using exactly this functional form was merely that it required the fewest possible parameters to provide a reasonable fit for the entire range. Nevertheless, using this scaling function, we are as expected able to collapse the data shown in Figs. 6 and 7. The resulting relationship is shown in Fig. 9. By inspection, moderate deviations from the exact relationship between the abscissa and ordinate quantities can be seen, indicating that improvement could be gained by explicitly taking into account the energy within and around the droplet in the free energy (12). This is, however, out of the scope of the current work.

Within the crude approximations made in deriving (22), however, the expression

$$\cos\theta = \cos\theta_0 - \frac{\sqrt{\epsilon_s c_0}}{\sigma_{ds}} \left[8\sqrt{2} - B\left(\frac{\epsilon_d}{\epsilon_s}\right)^\alpha \right] \sinh^2(V_0/4)$$

(40)
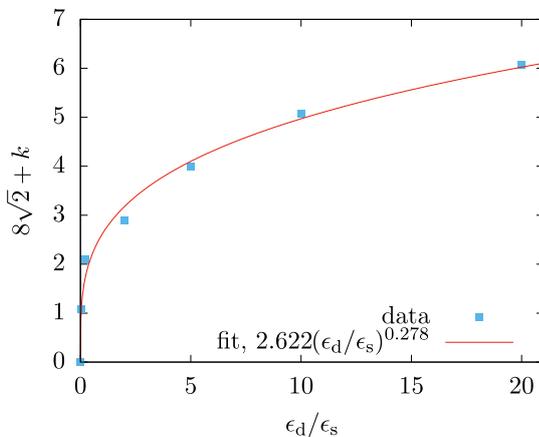
FIG. 8. Computed slopes from the data in Fig. 7 and several other sets of simulations, plotted against permittivity ratio ϵ_d/ϵ_s, shown along with a least squares fit.
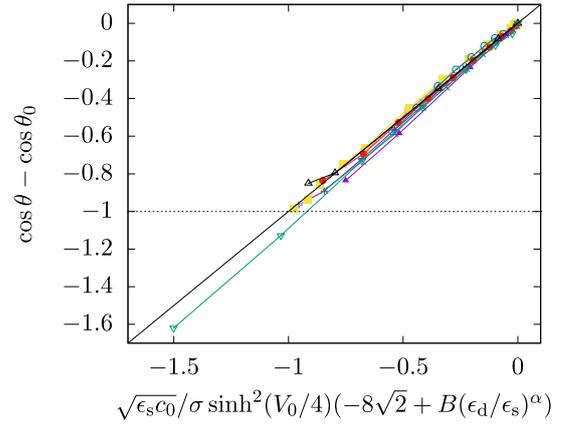
FIG. 9. Collapse of the contact angle data involved in Eq. (40), using the same data as presented in Figs. 6 and 7. The black solid line indicates an exact relationship between the ordinate and the abscissa.

well describes the apparent contact angle for the parameter range considered herein.

D. Relaxation times

As mentioned previously, it is out of the scope of this work to consider quantitative modeling of the contact line motion. However, it is in place to inspect the relaxation times associated with the final apparent contact angles presented in the previous subsection.

We estimate the relaxation times t_r by fitting an exponential function, $C + C' \exp(-t/t_r)$ to the contact angles as function of time t (cf. Fig. 5), where C, C', t_r are considered fitting parameters. In the main panel of Fig. 10, we show the relaxation times that correspond to the final contact angles shown in Fig. 6. The relaxation times are fairly constant for each parameter set. Deviations are noticeable when the applied voltage is low,
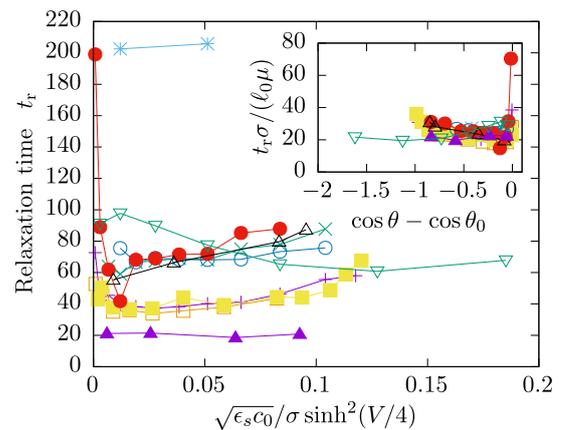
FIG. 10. The relaxation times for our simulations obtained by fitting exponential functions to the contact angle in time. The data correspond to what is shown in Fig. 6. Inset: Data collapse obtained by using a dimensionless relaxation time based on surface tension σ_{ds}, viscosity μ, and the initial wetting length scale ℓ_0. The outliers at low potential/contact angles are due to the poor fit of an exponential function to the data when the contact angle changes only slightly.
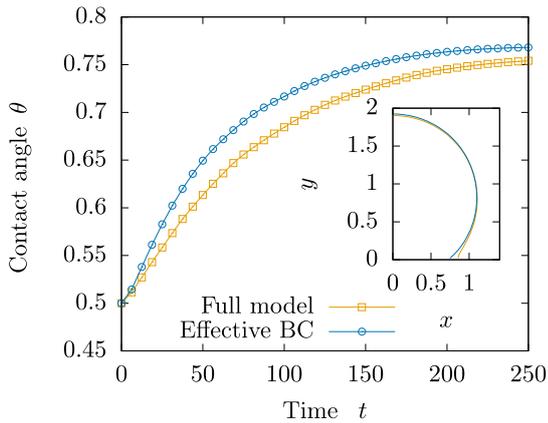
FIG. 11. Comparison of the evolution of the apparent contact angle as a function of time for the full model, including electrochemistry, and two-phase flow without direct resolution of the electrodynamics but instead using the boundary condition (42) and the relationship (40).

i.e., when the contact angle only changes very slightly and the exponential fit becomes unreliable. Further, at higher V_0, the apparent contact angle becomes very obtuse and thus θ becomes sensitive to the circular fit. The slight drift seen in the relaxation times should be attributed to that.

On dimensional grounds, we might expect, for flows dominated by viscous and capillary forces,

$$t_r \sim \frac{\ell_0 \mu}{\sigma_{ds}}, \tag{41}$$

where ℓ_0 is a typical length scale which we take to be the length of the wetted area in the initial state. This time scale is related to the capillary number $\mathrm{Ca} = \mu U_0 / \sigma_{ds}$, where $U_0 \sim \ell_0 / t_r$ is a characteristic velocity. The expectation is further admissible since have not introduced any (pinning) dissipation at the moving-contact line in our model. We check this by plotting the dimensionless quantity $t_r \sigma_{ds}/(\ell_0 \mu) \sim \mathrm{Ca}^{-1}$ against, e.g., the quantity $\cos\theta - \cos\theta_0$, and the resulting plot is shown in the inset of Fig. 10. The data points collapse fairly well, indicating that the time scale identified above *is* the relevant time scale in our simulations.

E. Comparison to effective modelling

As suggested by Eq. (40), it might be useful to avoid simulating dynamic electrowetting using the full model, and instead incorporate the result as a modified contact angle boundary condition. Recalling Eq. (38) (putting again $\tau_w = 0$), we may simply replace θ_0 by the expression for $\theta(V_0)$ given by Eq. (40). This yields the phase-field boundary condition

$$\frac{3\zeta}{2\sqrt{2}} \hat{\mathbf{n}} \cdot \boldsymbol{\nabla} \phi = \cos\left[\theta(V_0)\right] f'_w(\phi). \tag{42}$$

Now, we carry out a direct comparison between the full model and the effective model, where the whole electrokinetic problem is included only through the boundary condition. In Fig. 11 we show a direct comparison of the time evolution (for a simulation at $V_0 = 2.5$) between these two approaches. As can be seen from the figure, the *effective boundary condition (BC)*

approach leads to a faster relaxation to the final contact angle. The latter also slightly overshoots compared to the simulations using the full model, as can be seen from the inset of Fig. 11. Hence, the two approaches differ, but not necessarily significantly more than the variations seen within the simulations using the full model, as documented in Figs. 10 and 9. This indicates that the effective BC approach is admissible, but that further modeling might be necessary to quantitatively model the contact line motion.

VI. DISCUSSION

Compared to previous numerical studies of electrowetting [24,34,39], we have in this work used a model that accounts for different ions, and where the conductivity depends on the local ion concentrations instead of being held constant. We have studied systematically the effect of varying the applied potential, as well as other physical parameters. We confirm the results by Mugele and Buehrle [23] that the contact angle observed by Lippmann is a macroscopic *apparent* contact angle (also commented on by, e.g., [24]). For a conducting system, the key length scale is the insulator thickness d, and the apparent contact angle is only observed on scales beyond d. In our case, we consider an equipotential boundary, and therefore the length scale that controls the apparent contact angle is the Debye length λ_s in the surrounding fluid.

Monroe *et al.* [17] considered theoretically a setup where ions were dissolved in both phases, whereas we have considered the case where the droplet phase contained no ions. Hence, the analytical solution to the electrolyte system presented in Ref. [17] was not directly applicable in our case. Nonetheless, our numerical experiments have shown that a simplified and slightly heuristically generalized version of the prediction in Ref. [17] provides a good description of the contact angle as a function of the the applied potential, even for relatively large Debye lengths. From a theoretical point of view, a derivation explicitly taking into account, e.g., an electrostatic potential distribution along the droplet interface that minimizes the energy, could improve the suggested relation between contact angle and applied potential.

Clearly, many approximations underpin our results. First, for the Nernst-Planck equations to hold, we are limited to ideal (i.e., weak) ionic solutions. High concentrations would probably not be compatible with the assumption of impermeable interfaces. Furthermore, we have due to resolution requirements been limited to two-dimensional simulations. Future studies building on the present work should consider axisymmetric or fully three-dimensional geometries.

The assumption of a circular droplet geometry (away from the three-phase contact line) may fail when the surface tension, at least compared to the Maxwell stresses, becomes small. Hence, the results presented are only expected to hold for high surface tension. We emphasize that although the results presented herein [e.g., Eq. (40)] should clearly not be used outside their domain of validity, the work presented yields a recipe for extending the covered parameter space. Further, we demonstrated here that numerically resolving electrical double layers constitute an alternative route to obtaining very obtuse or acute contact angles in diffuse-interface simulations of two-phase flow with boundaries.

As mentioned previously, we have not attempted to model contact line friction quantitatively, since this remains in itself an important direction of research [41]. A next step could be to include the generalized Navier slip boundary condition [42,46], as was done by Nochetto *et al.* [34]. Finally, we have not considered any direct dependency between surface energies and the applied potential. In general, it would require more detailed modeling to reproduce all the electrochemical effects that are present in experimental settings.

VII. CONCLUSION

Controlling wetting properties of two-phase systems is desirable for a wide range of applications. We have in this paper considered how an applied electric field can control the wetting properties of an electrolytic two-phase system. To this end, the electrowetting setup of a droplet sitting on top of an isolated conductor, and where an electrolyte is dissolved in the surrounding phase, was numerically simulated. This was

achieved using a phase-field model for the full electrokinetic two-phase flow problem. We have confirmed observations of similar systems from the literature [23], i.e., that an *apparent* contact angle forms on scales beyond the Debye length, which characterizes the extent of the electric double layer. A main result of our work is summarized in our expression for the effective contact angle, Eq. (40), which was motivated by predictions from nonlinear Poisson-Boltzmann theory. For models operating on larger scales, the use of such an effective contact angle can greatly improve the computational efficiency.

[1] P.-G. De Gennes, Rev. Mod. Phys. **57**, 827 (1985).

[2] D. Bonn, J. Eggers, J. Indekeu, J. Meunier, and E. Rolley, Rev. Mod. Phys. **81**, 739 (2009).

[3] M. Pollack, A. Shenderov, and R. Fair, Lab Chip **2**, 96 (2002).

[4] V. Srinivasan, V. K. Pamula, and R. B. Fair, Lab Chip **4**, 310 (2004).

[5] J. Lee and C.-J. Kim, J. Microelectromech. Syst. **9**, 171 (2000).

[6] G. Beni and S. Hackwood, Appl. Phys. Lett. **38**, 207 (1981).

[7] G. Beni and M. Tenan, J. Appl. Phys. **52**, 6011 (1981).

[8] G. Beni, S. Hackwood, and J. Jackel, Appl. Phys. Lett. **40**, 912 (1982).

[9] R. A. Hayes and B. J. Feenstra, Nature (London) **425**, 383 (2003).

[10] T. Hassenkam, C. S. Pedersen, K. Dalby, T. Austad, and S. L. S. Stipp, Colloids Surf. A **390**, 179 (2011).

[11] E. Hilner, M. P. Andersson, T. Hassenkam, J. Matthiesen, P. Salino, and S. L. S. Stipp, Sci. Rep. **5**, 9933 (2015).

[12] A. RezaeiDoust, T. Puntervold, S. Strand, and T. Austad, Energy Fuels **23**, 4479 (2009).

[13] N. Pedersen, T. Hassenkam, M. Ceccato, K. N. Dalby, K. Mogensen, and S. L. S. Stipp, Energy Fuels **30**, 3768 (2016).

[14] A. Hiorth, L. Cathles, and M. Madland, Transp. Porous Media **85**, 1 (2010).

[15] G. Lippmann, Relations entre les phénomènes électriques et capillaires, Ph.D. thesis, Sorbonne, 1875.

[16] F. Mugele and J.-C. Baret, J. Phys. Condens. Matter **17**, R705 (2005).

[17] C. W. Monroe, L. I. Daikhin, M. Urbakh, and A. A. Kornyshev, Phys. Rev. Lett. **97**, 136102 (2006).

[18] V. G. Levich, *Physicochemical Hydrodynamics* (Prentice Hall, Englewood Cliffs, NJ, 1962).

[19] F. Mugele, Soft Matter **5**, 3377 (2009).

[20] B. Berge, C. R. Acad. Sci., Ser. 2: Mec. Phys. Sci. Terre **317**, 157 (1993).

[21] M. Vallet, B. Berge, and L. Vovelle, Polymer **37**, 2465 (1996).

[22] N. E. Cousens and A. R. Kucernak, Faraday Discuss. **199**, 63 (2017).

[23] F. Mugele and J. Buehrle, J. Phys. Condens. Matter **19**, 375112 (2007).

[24] C. Eck, M. Fontelos, G. Grün, F. Klingbeil, and O. Vantzos, Interfaces Free Boundaries **11**, 259 (2009).

[25] C. W. Monroe, L. I. Daikhin, M. Urbakh, and A. A. Kornyshev, J. Phys. Condens. Matter **18**, 2837 (2006).

[26] G. Taylor, Proc. R. Soc. London A **291**, 159 (1966).

[27] J. Melcher and G. Taylor, Ann. Rev. Fluid Mech. **1**, 111 (1969).

[28] O. Schnitzer and E. Yariv, J. Fluid Mech. **773**, 1 (2015).

[29] E. K. Zholkovskij, J. H. Masliyah, and J. Czarnecki, J. Fluid Mech. **472**, 1 (2002).

[30] D. A. Saville, Ann. Rev. Fluid Mech. **29**, 27 (1997).

[31] J. Berry, M. Davidson, and D. J. Harvie, J. Comput. Phys. **251**, 209 (2013).

[32] G. Tomar, D. Gerlach, G. Biswas, N. Alleborn, A. Sharma, F. Durst, S. Welch, and A. Delgado, J. Comput. Phys. **227**, 1267 (2007).

[33] J. López-Herrera, S. Popinet, and M. Herrada, J. Comput. Phys. **230**, 1939 (2011).

[34] R. H. Nochetto, A. J. Salgado, and S. W. Walker, Math. Models Methods Appl. Sci. **24**, 67 (2014).

[35] H.-W. Lu, K. Glasner, A. Bertozzi, and C.-J. Kim, J. Fluid Mech. **590**, 411 (2007).

[36] S. W. Walker and B. Shapiro, J. Microelectromech. Syst. **15**, 986 (2006).

[37] S. W. Walker, B. Shapiro, and R. H. Nochetto, Phys. Fluids **21**, 102103 (2009).

[38] A. Frumkin, B. Kabanow, and N. Nekrasow, Phys. Z. Sowjetunion **1**, 255 (1932).

[39] E. Campillo-Funollet, G. Grün, and F. Klingbeil, SIAM J. Appl. Math. **72**, 1899 (2012).

[40] G. Linga, A. Bolet, and J. Mathiesen, Bernaise: A flexible framework for simulating two-phase electrohydrodynamic flows in complex domains, arXiv:1805.11642.

[41] A. Carlson, G. Bellani, and G. Amberg, Phys. Rev. E **85**, 045302 (2012).

[42] T. Qian, X.-P. Wang, and P. Sheng, J. Fluid Mech. **564**, 333 (2006).

[43] A. Logg and G. N. Wells, ACM Trans. Math. Softw. **37**, 20 (2010).

[44] A. Logg, K.-A. Mardal, and G. Wells, *Automated Solution of Differential Equations by the Finite Element Method: The FEniCS Book*, Lecture Notes in Computational Science and Engineering Vol. 84 (Springer, Berlin, 2012).

[45] M. Dupeyrat and J. Michel, J. Colloid Interface Sci. **29**, 605 (1969).

[46] T. Qian, X.-P. Wang, and P. Sheng, Phys. Rev. E **68**, 016306 (2003).

A hierarchy of non-equilibrium two-phase flow models

Gaute Linga and Tore Flåtten

Submitted to *ESAIM: Proceedings & Surveys* (2018).

A HIERARCHY OF NON-EQUILIBRIUM TWO-PHASE FLOW MODELS

GAUTE LINGA[A,B,*] AND TORE FLÅTTEN[C]

ABSTRACT. We review a hierarchy of relaxation models for two-phase flow. The models are derived from the non-equilibrium Baer–Nunziato model, which is endowed with relaxation source terms to drive it towards equilibrium. The source terms cause transfer of volume, heat, mass and momentum due to differences between the phases in pressure, temperature, chemical potential and velocity, respectively. In the context of two-phase flow models, the *subcharacteristic condition* implies that the sound speed of an equilibrium system can never exceed that of the relaxation system. Here, previous work by Flåtten and Lund [*Math. Models Methods Appl. Sci.*, 21 (12), 2011, 2379–2407] and Lund [*SIAM J. Appl. Math.* 72, 2012, 1713–1741] is extended to encompass two-fluid models, i.e. models with separately governed velocities for the two phases. Each remaining model in the hierarchy is derived, and analytical expressions for the sound speeds are presented. Given only physically fundamental assumptions, the subcharacteristic condition is shown to be satisfied in the entire hierarchy, either in a weak or in a strong sense.

subject classification. 76T10, 35L60

key words. two-phase flow, relaxation systems, subcharacteristic condition

1. INTRODUCTION

The concurrent flow of two fluid phases occurs in a wide range of industrially relevant settings, including in nuclear reactors [10], petroleum production [1, 8], heat exchangers [51], cavitating flows [56], and within carbon capture, transport and storage (CCS) [9, 38, 46]. However, for most simulation purposes, resolving the full three-dimensional flow field may be too cumbersome, due to the complex interaction between the phases. In particular, this encompasses calculating the temporal evolution of the interface between the phases, and the transfer of mass, heat and momentum across it. Averaging methods (see e.g. Ishii and Hibiki [32] or Drew and Passman [16]) may therefore be applied to avoid direct computation of the interface. The resulting coarse-grained models may often be expressed as hyperbolic relaxation systems with source terms accounting for the interactions between the phases, driving them asymptotically towards equilibrium at a finite

rate. In a quasi-linear form, one-dimensional versions of such systems may be written as

$$\partial_t \mathbf{U} + \mathbf{A}(\mathbf{U})\partial_x \mathbf{U} = \frac{1}{\epsilon}\mathbf{Q}(\mathbf{U}), \tag{1}$$

wherein $\mathbf{U}(x,t) \in G \subseteq \mathbb{R}^N$ is the (smooth) vector of unknowns and $\mathbf{A}(\mathbf{U})$ is a matrix which we shall call the *Jacobian* of the system, in analogy to conservative systems.[1] Further, ϵ is a characteristic time associated with the relaxation process described by $\mathbf{Q}(\mathbf{U})$. For an extensive review of the existing literature on such systems, see e.g. Natalini [48], or, for a more concise summary, consider the first few sections of Solem et al. [58] and the references therein.

Two limits of the relaxation system (1) will be considered in this paper:

- The *non-stiff limit*, corresponding to the limit $\epsilon \to \infty$. In this case, we may write (1) as

$$\partial_t \mathbf{U} + \mathbf{A}(\mathbf{U})\partial_x \mathbf{U} = 0. \tag{2}$$

  We will refer to (2) as the *homogeneous system*.
- The formal *equilibrium limit*, which is characterized by $\mathbf{Q}(\mathbf{U}) \equiv 0$. This defines an equilibrium manifold [11] through $\mathcal{M} = \{\mathbf{U} \in G : \mathbf{Q}(\mathbf{U}) = 0\}$. We now assume that the reduced vector of variables $\mathbf{u}(x,t) \in \mathbb{R}^n$, where $n \leq N$, uniquely defines an equilibrium value $\mathbf{U} = \mathcal{E}(\mathbf{u}) \in \mathcal{M}$. We may then express (1) as

$$\partial_t \mathbf{u} + \mathbf{B}(\mathbf{u})\partial_x \mathbf{u} = 0, \quad \mathbf{U} = \mathcal{E}(\mathbf{u}), \tag{3}$$

  where $\mathbf{B}(\mathbf{u}) = \mathbf{P}(\mathbf{u})\mathbf{A}(\mathcal{E}(\mathbf{u}))\partial_\mathbf{u}\mathcal{E}(\mathbf{u})$ is the Jacobian of the reduced system. Herein, we have defined the operator $\mathbf{P}(\mathbf{u}) : \mathbb{R}^N \to \mathbb{R}^n$ through $\mathbf{P}(\mathbf{u})\partial_\mathbf{u}\mathcal{E}(\mathbf{u}) = \mathbf{I}_n$, i.e. the identity matrix. We will refer to (3) as the *equilibrium system*.

We expect solutions of (1) to approach solutions of (3) as $\epsilon \to 0$, i.e. in the *stiff limit*, where the relaxation towards equilibrium is assumed to be instantaneous.

1.1. **The subcharacteristic condition.** An essential concept which arises in the study of relaxation systems and their stability, is the so-called *subcharacteristic condition*. It was first introduced by Leray [36], subsequently independently found by Whitham [66], and later developed by Liu [39] for conservative 2×2 systems. For more general systems, Chen et al. [11] defined an entropy condition which they showed implies the subcharacteristic condition. Yong [68] proved that for $n = N-1$, the subcaracteristic condition is necessary for the linear stability of the equilibrium system. For strictly hyperbolic systems, Solem et al. [58] proved that it is also sufficient. Hence, for strictly hyperbolic relaxation systems where $n = N - 1$, *the subcharacteristic condition is equivalent to linear stability.*

For a general $N \times N$ relaxation system, such as (1), the condition may be formulated as follows.

Definition 1 (Subcharacteristic condition)**.** *Let the N eigenvalues of the matrix $\mathbf{A}$ of the homogeneous system* (2) *be given by Λ_i, sorted in ascending order as*

$$\Lambda_1 \leq \ldots \leq \Lambda_i \leq \Lambda_{i+1} \leq \ldots \leq \Lambda_N. \tag{4}$$

Similarly, let λ_j be the n eigenvalues of the matrix $\mathbf{B}$ of the equilibrium system (3)*. Herein, the homogeneous system* (2) *is applied to a local equilibrium state*

---

[1] In systems which can be written on the conservative form $\partial_t \mathbf{U} + \partial_x \mathbf{F}(\mathbf{U}) = 0$, we have that in the weak form (2), $\mathbf{A} = \partial_\mathbf{U}\mathbf{F}$ is the actual Jacobian of a flux $\mathbf{F}$.

$\mathbf{U} = \mathcal{E}(\mathbf{u})$, *such that* $\Lambda_i = \Lambda_i(\mathcal{E}(\mathbf{u}))$, *and* $\lambda_j = \lambda(\mathbf{u})$. *Now, the equilibrium system* (3) *is said to satisfy the* subcharacteristic condition *with respect to the homogeneous system* (2) *when (i) all* λ_j *are real, and (ii) if the* λ_j *are sorted in ascending order as*

$$\lambda_1 \leq \ldots \leq \lambda_j \leq \lambda_{j+1} \leq \ldots \leq \lambda_n, \tag{5}$$

then the eigenvalues of the equilibrium system are interlaced *with the eigenvalues of the homogeneous system, in the sense that* $\lambda_j \in [\Lambda_j, \Lambda_{j+N-n}]$.

The subcharacteristic condition has been shown to be an important trait of many physical models [5, 6, 21], since the eigenvalues then have a direct physical interpretation as the characteristic wave speeds of the system. In the context of relaxation models for two-phase flow, the fastest wave speeds are the speeds of pressure waves, which involve the *fluid-mechanical speeds of sound*. The subcharacteristic condition then implies in particular that *the sound speeds of an equilibrium model can never exceed that of the relaxation model it is derived from.* This is precisely the observation, well known in the fluid mechanics community, that the "frozen" speed of sound is higher than the equilibrium speed of sound [20, 26, 52].

1.2. **The model hierarchy.** In a general averaged two-phase flow model, the mixture will consist of two fluids which evolve independently. We assume *local thermodynamic equilibrium* in each phase, i.e. each of the phases may be described by an equation of state. Specifying two thermodynamic quantities then completely determines all thermodynamic properties of that phase. Herein lies also the assumption that the thermodynamic quantities are unaffected by the local velocity field. Each phase k may then be thought of as having separate pressures p_k, temperatures T_k, chemical potentials μ_k, and velocities v_k. Since the two-phase mixture will move towards phase equilibrium in each of the mentioned variables, we may model these interactions by employing *relaxation source terms* corresponding to the following *relaxation processes*:

$p -$ *volume transfer.* Relaxation towards mechanical equilibrium due to pressure differences between the phases, i.e. expansion or compression.

$T -$ *heat transfer.* Relaxation towards thermal equilibrium, due to temperature differences between the phases.

$\mu -$ *mass transfer.* Relaxation towards chemical equilibrium due to differences between the phases in chemical potential.[2]

$v -$ *momentum transfer.* Relaxation towards velocity equilibrium, due to velocity differences between the phases, i.e. interface friction.

The starting point of the forthcoming analysis will be the classical Baer–Nunziato (BN) model [3], which is a general formulation of a *two-fluid model*, in the sense that the phases are associated with separate velocity fields. The BN model is endowed with appropriate relaxation terms corresponding to each of these processes presented above. By considering the *homogeneous* and *equilibrium* limits of each relaxation process, i.e. assuming all combinations of zero or more of them to be instantaneous, we obtain a *hierarchy of models*, each with partial equilibrium in one or more of the aforementioned variables.

This hierarchy can be represented as a four-dimensional hypercube, as illustrated in Figure 1. Herein, each model is symbolized by a circle, and corresponds to a

---

[2]See also Remark 2.
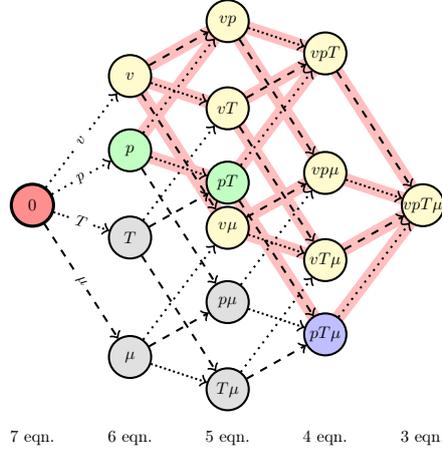
FIGURE 1. The 4-dimensional hypercube representing the model hierarchy. Parallel edges correspond to the same relaxation processes, and each vertex signifies a unique model in the hierarchy, assuming instantaneous relaxation in zero or more of the variables p (pressure), T (temperature), μ (chemical potential) and v (velocity). The leftmost, red circle denoted by "0" represents the Baer–Nunziato model [3]. The colored edges represent relaxation processes where a subcharacteristic condition has previously been explicitly established in the literature; models described in [20] and [40] are shown in yellow, whereas models described by [19] are shown in green. Subcharacteristic conditions were obtained in [44] for the model represented by the blue circle.

"corner" of the hypercube. Parallel edges, in turn, correspond to the same instantaneous relaxation assumption, in the direction of the arrow. The basic model, denoted by "0" and shown in red as the leftmost circle of Figure 1, is thus reducible to all models in the hierarchy. Many of the models in the hierarchy have already been derived, explicitly expressed and thoroughly analyzed, and in this respect, the current paper builds heavily on previous work [2, 7, 14, 23, 33, 35, 56, 57, 69].

The models shown in yellow circles in Figure 1 constitute the v-branch of the hierarchy, i.e. the *homogeneous flow* models, wherein the phase velocities are equal. Such models are subclass of the so-called drift-flux models, where the phasic velocities are related by an algebraic expression. Herein, the v-model was derived by [57], the vp-model is due to [33] (see also Refs. [2, 47]), and the vpT-model was studied e.g. by [21]. The $vpT\mu$-model is known as the *homogeneous equilibrium model* and has been studied by several authors, see e.g. Refs. [12, 18, 30, 31, 42, 60, 65]. Flåtten and Lund [20] collected results on the v-, vp-, vpT-, and $vpT\mu$-models, derived the $vp\mu$-model, and showed that the subcharacteristic condition was satisfied for all relaxation processes within this branch of the hierarchy. Lund [40] completed the v-hierarchy by deriving the vT-, $v\mu$- and $vT\mu$-models, and established the subcharacteristic condition in the remainder of the v-branch, given only physically fundamental assumptions.

With regards to the *two-fluid* models in the hierarchy, several of these models have been derived, employed in simulation [8, 10], and analyzed. Here, the p-model was analyzed e.g. in Refs. [13, 60], and the pT-model was studied e.g. in Refs. [19, 27].

An important issue with p-relaxed (one-pressure) two-fluid models is that they develop complex eigenvalues when the velocity difference between the phases exceeds a critical value, i.e. they become non-hyperbolic [15, 22, 44, 60, 64]. This may lead to the lack of stable mathematical and numerical solutions. Nevertheless, these models are extensively used for practical applications; and in numerical simulations they are often mitigated by specifying a regularizing interfacial pressure (see [10, 49, 61]). Further, estimates of fluid-mechanical sound speeds is of practical importance for the construction of efficient numerical schemes [27, 53]. For relations between two-fluid models, we find, as in Ref. [19], the need to state a weaker formulation of the subcharacteristic condition.

Definition 2 (Weak subcharacteristic condition)**.** *When the subcharacteristic condition of Definition 1 holds with the additonal equilibrium condition of equal phasic velocities, the* weak subcharacteristic condition *is said to be satisfied.*

The p- and pT-models were analyzed by Martínez Ferrer et al. [19], who showed that the subcharacteristic condition, in a weak or strong sense, is satisfied with respect to existing neighbouring models. Similarly, Morin and Flåtten [44] studied the $pT\mu$-model, and showed that subcharacteristic conditions were satisfied in relation to existing neighbouring models. The highlighted edges in Figure 1 summarize the relations between models where a subcharacteristic condition has already been shown to be satisfied.

1.3. **Contributions of this paper.** The objective of the current paper is to complete the study of the subcharacteristic condition in the full hierarchy of two-phase flow models, proving the remaining subcharacteristic conditions. In this respect, a generalization of the work by [20] and [40] is provided, extending the hierarchy to encompass also *two-fluid models*, i.e. models with separate momentum equations for the two phases. Herein, the inclusion of the two-fluid T-, μ-, $p\mu$- and $T\mu$-models represent original contributions. A similar hierarchical derivation of two-phase relaxation models was done in the thesis of Labois [35], who focused primarily on the stiffened gas equation-of-state. In our current work, expressions for the sound speeds of the models are provided, valid for general equations of state. Moreover, we show that the remaining 15 subcharactistic conditions are satisfied, i.e. that the subcharacteristic condition is everywhere respected in the hierarchy, either in a strong or in a weak sense. This is done by comparing the new expressions for the sound speeds to many known results from the literature, and by using techniques involving writing the difference of wave velocities as sums of squares (cf. [20, 40]). We present each of the models for which we prove at least one subcharacteristic condition.

1.4. **Outline.** The organization of the current paper is as follows. In Section 2 we present the basic model with all possible source terms, derive evolution equations for the primitive variables, and state a parameter set which suffices to satisfy the laws of thermodynamics. In Sections 3 to 8, we present in turn the v-, p-, T-, μ-, $p\mu$- and $T\mu$-models. For each model we give explicit analytic expressions for the sound speeds, and prove the remaining subcharacterisic conditions with respect to

related models. In Section 9 we show plots of the sound speeds in the different models, and briefly discuss physical and mathematical properties of models in the hierarchy. Finally, in Section 10, we draw conclusions and suggest possible future work.

2. BASIC MODEL

In this section, we present the basic BN model [3]. In this model, which is hyperbolic, the two phases have separate pressures, temperatures, chemical potentials and velocities. We state the model in a form reminiscent of that proposed by Saurel and Abgrall [54], but with all four possible relaxation source terms accounting for the interaction between the phases. From this, we determine the evolution equations of the primitive variables. Based on the evolution equations, we derive a parameter set which suffices for the model to satisfy fundamental physical laws.

2.1. **Governing equations.** In the following, we present the governing equations in the basic model, supplemented with physically appropriate relaxation terms. We let α_k denote volume fraction, v_k velocity, ρ_k density, p_k pressure, T_k temperature, μ_k chemical potential, e_k internal energy per mass, for each phase $k \in \{g, \ell\}$, where g denotes gas and ℓ denotes liquid.

2.1.1. *Volume advection.* We assume that apart from advection, the interface between the phases can only move due to pressure differences. This is commonly formulated as

$$\partial_t \alpha_g + v_i \partial_x \alpha_g = \mathscr{I}(p_g - p_\ell), \tag{6}$$

wherein v_i is an interface velocity and $\mathscr{I}$ is the pressure relaxation parameter. Hence, the volume fraction is advected with the velocity v_i. There are several discussions available on how to choose this interface velocity, see e.g. [14, 55]. In the following, we shall motivate it from a thermodynamic point of view, using the second law of thermodynamics.

The local volume transfer must occur so that the phase with the lowest pressure is compressed, and the phase with the highest pressure is expanded. This is enforced through $\mathscr{I} \geq 0$. Moreover, the volume fractions must satisfy $\alpha_g + \alpha_\ell = 1$, where $\alpha_k \in (0, 1)$, and hence only one evolution equation for the volume fractions is needed.

2.1.2. *Mass balance.* The evolution of the mass of each phase is contained in the balance equations

$$\partial_t \alpha_g \rho_g + \partial_x \alpha_g \rho_g v_g = \mathscr{K}(\mu_\ell - \mu_g), \tag{7}$$

$$\partial_t \alpha_\ell \rho_\ell + \partial_x \alpha_\ell \rho_\ell v_\ell = \mathscr{K}(\mu_g - \mu_\ell), \tag{8}$$

wherein $\mathscr{K}$ is the mass relaxation parameter, and the source terms on the right hand sides of (7) and (8) account for mass transfer between the phases [24, 25]. The mass transfer occurs from the phase with the highest chemical potential towards the phase with the lowest, which is ensured through the assumption $\mathscr{K} \geq 0$. We observe that *conservation of total mass* is contained by summing (7) and (8):

$$\partial_t \rho + \partial_x \left(\alpha_g \rho_g v_g + \alpha_\ell \rho_\ell v_\ell \right) = 0, \tag{9}$$

wherein we have defined the mixture density $\rho = \alpha_g \rho_g + \alpha_\ell \rho_\ell$.

2.1.3. *Momentum balance.* Similar balance laws apply for the momentum of each phase:

$$\partial_t\alpha_g\rho_g v_g + \partial_x(\alpha_g\rho_g v_g^2 + \alpha_g p_g) - p_i\partial_x\alpha_g = v_i\mathcal{K}(\mu_\ell - \mu_g) + \mathcal{M}(v_\ell - v_g), \quad (10)$$

$$\partial_t\alpha_\ell\rho_\ell v_\ell + \partial_x(\alpha_\ell\rho_\ell v_\ell^2 + \alpha_\ell p_\ell) - p_i\partial_x\alpha_\ell = v_i\mathcal{K}(\mu_g - \mu_\ell) + \mathcal{M}(v_g - v_\ell). \quad (11)$$

Herein, p_i is an interface pressure and $\mathcal{M}$ is the momentum relaxation parameter. Note that from the averaging procedure resulting in these models, the interface velocity v_i in (10) and (11) need not be the same as that in (6) (see e.g. Ref. [43]). However, we have chosen these to be equal to keep the notation to a minimum, as this will not influence the main conclusions of this paper. The source terms associated with v_i on the right hand sides of (10) and (11) represent the momentum of the condensating or vaporizing fluid, which is transferred to the other phase. The source terms associated with $\mathcal{M}$ represent interfacial friction, and are assumed to cause momentum transfer from the phase with highest velocity towards the one with lowest velocity, which is ensured by requiring $\mathcal{M} \geq 0$. We observe that *conservation of total momentum* is ensured by summing (10) and (11):

$$\partial_t\left(\alpha_g\rho_g v_g + \alpha_\ell\rho_\ell v_\ell\right) + \partial_x\left(\alpha_g\rho_g v_g^2 + \alpha_\ell\rho_\ell v_\ell^2 + \alpha_g p_g + \alpha_\ell p_\ell\right) = 0. \quad (12)$$

2.1.4. *Energy balance.* The balance laws for the energy of each phase may be stated as

$$\partial_t E_g + \partial_x\left(E_g v_g + \alpha_g v_g p_g\right) - p_i v_i \partial_x\alpha_g$$
$$= -p_i\mathcal{I}(p_g - p_\ell) + \left(\mu_i + \tfrac{1}{2}v_i^2\right)\mathcal{K}(\mu_\ell - \mu_g) + v_i\mathcal{M}(v_\ell - v_g) + \mathcal{H}(T_\ell - T_g), \quad (13)$$

$$\partial_t E_\ell + \partial_x\left(E_\ell v_\ell + \alpha_\ell v_\ell p_\ell\right) - p_i v_i \partial_x\alpha_\ell$$
$$= -p_i\mathcal{I}(p_\ell - p_g) + \left(\mu_i + \tfrac{1}{2}v_i^2\right)\mathcal{K}(\mu_g - \mu_\ell) + v_i\mathcal{M}(v_g - v_\ell) + \mathcal{H}(T_g - T_\ell). \quad (14)$$

Herein, μ_i is an interface chemical potential, $\mathcal{H}$ is the temperature relaxation parameter, and we have introduced the total phasic energy per volume $E_k = E_k^{\text{int}} + E_k^{\text{kin}}$, where the phasic internal and kinetic energies are given by, respectively,

$$E_k^{\text{int}} = \alpha_k\rho_k e_k, \quad (15)$$
$$E_k^{\text{kin}} = \tfrac{1}{2}\alpha_k\rho_k v_k^2. \quad (16)$$

On the right hand side of (13) and (14), the terms associated with $\mathcal{I}$ represent energy transfer due to expansion–compression work, the terms associated with $\mathcal{K}$ represent the energy which the condensating or vaporizing fluid brings into the other phase, the terms associated with $\mathcal{M}$ represent energy transfer due to frictious momentum transfer, and the terms associated with $\mathcal{H}$ represent pure heat flow. The latter should flow from the hotter to the colder phase, which is ensured through the assumption $\mathcal{H} \geq 0$. Moreover, we see that *total energy is conserved* by summing (13) and (14),

$$\partial_t E + \partial_x\left(E_g v_g + E_\ell v_\ell + \alpha_g v_g p_g + \alpha_\ell v_\ell p_\ell\right) = 0, \quad (17)$$

where we have introduced the mixed total energy per volume $E = E_g + E_\ell$. Note that the same observation on the interfacial velocity as pointed out in Section 2.1.3 applies to (13) and (14). The interface velocity is for simplicity of notation chosen to be the same v_i in (13) and (14) as in (6) and (10) and (11), but the choice does not have consequences for our main conclusions.

2.1.5. *Phase independent form.* With all possible relaxation terms, the BN model [3], as presented in (6) to (8), (10), (11), (13) and (14), can be stated compactly as

$$\partial_t \alpha_k + v_\mathrm{i} \partial_x \alpha_k = I_k, \tag{18}$$

$$\partial_t \alpha_k \rho_k + \partial_x \alpha_k \rho_k v_k = K_k, \tag{19}$$

$$\partial_t \alpha_k \rho_k v_k + \partial_x (\alpha_k \rho_k v_k^2 + \alpha_k p_k) - p_\mathrm{i} \partial_x \alpha_k = v_\mathrm{i} K_k + M_k, \tag{20}$$

$$\partial_t E_k + \partial_x \left(E_k v_k + \alpha_k v_k p_k \right) - p_\mathrm{i} v_\mathrm{i} \partial_x \alpha_k = -p_\mathrm{i} I_k + \left(\mu_\mathrm{i} + \tfrac{1}{2} v_\mathrm{i}^2 \right) K_k + v_\mathrm{i} M_k + H_k, \tag{21}$$

for each phase $k \in \{\mathrm{g}, \ell\}$. Herein, the shorthand forms of the relaxation source terms, I_k, K_k, H_k and M_k, have been defined such that $I_\mathrm{g} = -I_\ell = \mathscr{I}(p_\mathrm{g} - p_\ell)$, $K_\mathrm{g} = -K_\ell = \mathscr{K}(\mu_\ell - \mu_\mathrm{g})$, $H_\mathrm{g} = -H_\ell = \mathscr{H}(T_\ell - T_\mathrm{g})$, and $M_\mathrm{g} = -M_\ell = \mathscr{M}(v_\ell - v_\mathrm{g})$.

2.2. **Evolution of primitive variables.** In order to systematically derive other models in the hierarchy, and to derive a physically valid parameter set for the basic model, we now seek the evolution equations for *primitive variables*, such as phasic velocity v_k, density ρ_k, pressure p_k, temperature T_k, entropy s_k and chemical potential μ_k. To simplify the notation in the forthcoming, we introduce the phasic *material derivative*, defined by

$$\mathrm{D}_k \left(\cdot \right) \equiv \partial_t \left(\cdot \right) + v_k \partial_x \left(\cdot \right), \tag{22}$$

for each phase $k \in \{\mathrm{g}, \ell\}$.

In the forthcoming calculations, the following relation will prove useful. For an arbitrary quantity f, we have from (19) and (22) that

$$\alpha_k \rho_k \mathrm{D}_k f = \partial_t \alpha_k \rho_k f + \partial_x \alpha_k \rho_k v_k f - f K_k. \tag{23}$$

2.2.1. *Volume fraction.* For clarity we state the evolution equation for the volume fraction. Using (18), we have that

$$\mathrm{D}_k \alpha_k = I_k + (v_k - v_\mathrm{i}) \partial_x \alpha_k. \tag{24}$$

2.2.2. *Velocity.* We now seek the evolution equation for the phasic velocity. Using $f = v_k$ in (23), and (20), we obtain

$$\mathrm{D}_k v_k = (\alpha_k \rho_k)^{-1} \left((p_\mathrm{i} - p_k) \partial_x \alpha_k - \alpha_k \partial_x p_k + (v_\mathrm{i} - v_k) K_k + M_k \right). \tag{25}$$

2.2.3. *Density.* The density evolution equation is found by combining (19) and (24),

$$\mathrm{D}_k \rho_k = -\frac{\rho_k}{\alpha_k} (v_k - v_\mathrm{i}) \partial_x \alpha_k - \rho_k \partial_x v_k - \frac{\rho_k}{\alpha_k} I_k + \frac{1}{\alpha_k} K_k. \tag{26}$$

2.2.4. *Kinetic energy.* In order to obtain the evolution equation for the specific internal energy, we start by finding the evolution equations for the kinetic energy. Using $f = v_k^2/2$ in (23), and (16) and (25), we obtain

$$\partial_t E_k^{\mathrm{kin}} + \partial_x E_k^{\mathrm{kin}} v_k + \alpha_k v_k \partial_x p_k + v_k (p_k - p_\mathrm{i}) \partial_x \alpha_k = \left(v_\mathrm{i} v_k - \tfrac{1}{2} v_k^2 \right) K_k + v_k M_k. \tag{27}$$

2.2.5. *Internal energy.* We obtain the evolution equation for the internal energy by subtracting (27) from (21), expanding and collecting terms:

$$\partial_t E_k^{\text{int}} + \partial_x E_k^{\text{int}} v_k + \alpha_k p_k \partial_x v_k + p_\text{i}(v_k - v_\text{i})\partial_x \alpha_k = -p_\text{i} I_k + g_k K_k + (v_\text{i} - v_k)M_k + H_k, \tag{28}$$

where we have introduced a shorthand interface energy $g_k = \mu_\text{i} + \frac{1}{2}\left(v_\text{i} - v_k\right)^2$. Now, by using (15) and (28) and $f = e_k$ in (23), we obtain

$$\mathrm{D}_k e_k = \tfrac{1}{\alpha_k \rho_k}\left(-p_\text{i}(I_k + (v_k - v_\text{i})\partial_x \alpha_k) - \alpha_k p_k \partial_x v_k + (g_k - e_k)K_k + (v_\text{i} - v_k)M_k + H_k\right). \tag{29}$$

2.2.6. *Entropy.* The fundamental thermodynamic differential reads

$$\mathrm{d}e_k = T_k \mathrm{d}s_k + p_k \rho_k^{-2}\mathrm{d}\rho_k, \tag{30}$$

where s_k is the specific entropy of phase k. By writing (30) in terms of material derivatives, and inserting (26) and (29), we obtain the evolution equation for the phasic entropy as

$$\mathrm{D}_k s_k = (\alpha_k \rho_k T_k)^{-1}\big[(p_k - p_\text{i})\left(I_k + (v_k - v_\text{i})\partial_x \alpha_k\right) + (g_k - h_k)K_k + (v_\text{i} - v_k)M_k + H_k\big]. \tag{31}$$

Herein, the phasic specific enthalpy is defined as $h_k = e_k + p_k/\rho_k$. By using $f = s_k$ in (23) along with the identity $\mu_k = h_k - T_k s_k$, (31) may be written in the balance form

$$\partial_t S_k + \partial_x S_k v_k = T_k^{-1}\Big[(p_k - p_\text{i})\left(I_k + (v_k - v_\text{i})\partial_x \alpha_k\right) + (g_k - \mu_k)K_k + (v_\text{i} - v_k)M_k + H_k\Big] \tag{32}$$

where we have defined the phasic entropy per volume $S_k = \alpha_k \rho_k s_k$.

2.2.7. *Pressure.* The pressure differential in terms of the density and entropy differentials may be written as

$$\mathrm{d}p_k = c_k^2 \mathrm{d}\rho_k + \Gamma_k \rho_k T_k \mathrm{d}s_k, \tag{33}$$

where we have introduced the phasic *thermodynamic* speed of sound and the first Grüneisen coefficient, respectively defined by

$$c_k^2 = \left(\partial p_k / \partial \rho_k\right)_{s_k} \quad \text{and} \quad \Gamma_k = \rho_k^{-1}\left(\partial p_k / \partial e_k\right)_{\rho_k}. \tag{34}$$

By writing (33) in terms of the phasic material derivative, and inserting (26) and (29), we arrive at

$$\mathrm{D}_k p_k = \tfrac{\Gamma_k(p_k - p_\text{i}) - \rho_k c_k^2}{\alpha_k}\left(I_k + (v_k - v_\text{i})\partial_x \alpha_k\right)$$
$$- \rho_k c_k^2 \partial_x v_k + \tfrac{\Gamma_k(g_k - h_k) + c_k^2}{\alpha_k}K_k + \tfrac{\Gamma_k}{\alpha_k}(v_\text{i} - v_k)M_k + \tfrac{\Gamma_k}{\alpha_k}H_k. \tag{35}$$

2.2.8. *Temperature.* We now seek the equation governing the phasic temperature evolution. The temperature differential may in terms of the pressure and entropy differentials be written as

$$\mathrm{d}T_k = \Gamma_k T_k \rho_k^{-1} c_k^{-2}\mathrm{d}p_k + T_k C_{p,k}^{-1}\mathrm{d}s_k, \tag{36}$$

where the specific isobaric heat capacity is defined by $C_{p,k} = T_k\left(\partial s_k / \partial T_k\right)_{p_k}$. Now, writing (36) in terms of phasic material derivatives, and inserting (31) and (35),

we obtain

$$
\mathrm{D}_k T_k = \left[\frac{1 + \frac{\Gamma_k^2 C_{p,k} T_k}{c_k^2}}{\alpha_k \rho_k C_{p,k}} (p_k - p_\mathrm{i}) - \frac{\Gamma_k T_k}{\alpha_k} \right] (I_k + (v_k - v_\mathrm{i}) \partial_x \alpha_k) - \Gamma_k T_k \partial_x v_k
$$
$$
+ \left[\frac{\Gamma_k T_k}{\alpha_k \rho_k} + \frac{1 + \frac{\Gamma_k^2 C_{p,k} T_k}{c_k^2}}{\alpha_k \rho_k C_{p,k}} (g_k - h_k) \right] K_k + \frac{1 + \frac{\Gamma_k^2 C_{p,k} T_k}{c_k^2}}{\alpha_k \rho_k C_{p,k}} \left[(v_\mathrm{i} - v_k) M_k + H_k \right].
$$
$$(37)$$

2.2.9. *Chemical potential.* The natural differential of the phasic chemical potential reads

$$
\mathrm{d}\mu_k = \rho_k^{-1} \mathrm{d}p_k - s_k \mathrm{d}T_k. \tag{38}
$$

Therefore, writing (38) in terms of phasic material derivatives, and inserting (35) and (37), we obtain

$$
\mathrm{D}_k \mu_k = \frac{1}{\alpha_k} \left[\left(\Gamma_k - \frac{s_k}{C_{p,k}} - \frac{\Gamma_k^2 T_k s_k}{c_k^2} \right) \frac{(p_k - p_\mathrm{i})}{\rho_k} - c_k^2 + \Gamma_k T_k s_k \right] (I_k + (v_k - v_\mathrm{i}) \partial_x \alpha_k)
$$
$$
- \left(c_k^2 - \Gamma_k T_k s_k \right) \partial_x v_k + \frac{1}{\alpha_k \rho_k} \left[c_k^2 - \Gamma_k T_k s_k + \left(\Gamma_k - \frac{s_k}{C_{p,k}} - \frac{\Gamma_k^2 T_k s_k}{c_k^2} \right) (g_k - h_k) \right] K_k
$$
$$
+ \frac{1}{\alpha_k \rho_k} \left(\Gamma_k - \frac{s_k}{C_{p,k}} - \frac{\Gamma_k^2 T_k s_k}{c_k^2} \right) \left[(v_\mathrm{i} - v_k) M_k + H_k \right]. \quad (39)
$$

2.3. **Laws of thermodynamics.** For the model to correctly represent physical phenomena, it should be verified that it satisfies fundamental physical principles [20, 21]. We have already verified that it conserves mass, momentum and energy, respectively represented by (9), (12) and (17), where the latter is known as the first law of thermodynamics. We now consider the second law of thermodynamics, which states that the total entropy should be non-decreasing. The analysis in the following is reminiscent of that of various previous works [14, 20].

2.3.1. *Total entropy evolution.* The total entropy per volume is given by $S = S_\mathrm{g} + S_\ell$. The evolution equation for the total entropy is therefore found by summing (32) over $k \in \{\mathrm{g}, \ell\}$:

$$
\partial_t S + \partial_x (S_\mathrm{g} v_\mathrm{g} + S_\ell v_\ell) = \mathscr{S}_p + \mathscr{S}_\mu + \mathscr{S}_v + \mathscr{S}_T = \mathscr{S}, \tag{40}
$$

where we have defined the *entropy source terms*

$$
\mathscr{S}_p = \left(\frac{p_\mathrm{g} - p_\mathrm{i}}{T_\mathrm{g}} - \frac{p_\ell - p_\mathrm{i}}{T_\ell} \right) I_\mathrm{g} + \left[\frac{(p_\mathrm{g} - p_\mathrm{i})(v_\mathrm{g} - v_\mathrm{i})}{T_\mathrm{g}} - \frac{(p_\ell - p_\mathrm{i})(v_\ell - v_\mathrm{i})}{T_\ell} \right] \partial_x \alpha_\mathrm{g}, \tag{41}
$$

$$
\mathscr{S}_\mu = \left(\left(\mu_\mathrm{i} - \mu_\mathrm{g} + \tfrac{1}{2}(v_\mathrm{i} - v_\mathrm{g})^2 \right) T_\mathrm{g}^{-1} - \left(\mu_\mathrm{i} - \mu_\ell + \tfrac{1}{2}(v_\mathrm{i} - v_\ell)^2 \right) T_\ell^{-1} \right) K_\mathrm{g}, \tag{42}
$$

$$
\mathscr{S}_v = \left[(v_\mathrm{i} - v_\mathrm{g}) T_\mathrm{g}^{-1} - (v_\mathrm{i} - v_\ell) T_\ell^{-1} \right] M_\mathrm{g}, \tag{43}
$$

$$
\mathscr{S}_T = (T_\mathrm{g}^{-1} - T_\ell^{-1}) H_\mathrm{g}. \tag{44}
$$

2.3.2. *The second law of thermodynamics.* We define the *global entropy* as

$$
\Omega(t) = \int_{\mathscr{C}} S(x, t) \, \mathrm{d}x, \tag{45}
$$

where $\mathscr{C} \subseteq \mathbb{R}$ is some closed region.

Definition 3. *The* second law of thermodynamics *states that the global entropy is non-decreasing, i.e.,*

$$\frac{d\Omega}{dt} \geq 0 \quad \forall t, \tag{46}$$

in our context.

Proposition 1. *Sufficient conditions for the relaxation model given by (6) to (8), (10), (11), (13) and (14) to satisfy the second law of thermodynamics (Definition 3) are*

$$\mathscr{I}, \mathscr{K}, \mathscr{M}, \mathscr{H} \geq 0, \tag{47}$$

$$\min\{\mu_{\mathrm{g}}, \mu_{\ell}\} \leq \mu_{\mathrm{i}} \leq \max\{\mu_{\mathrm{g}}, \mu_{\ell}\}, \tag{48}$$

$$p_{\mathrm{i}} = \frac{\sqrt{T_{\ell}}p_{\mathrm{g}} + \sqrt{T_{\mathrm{g}}}p_{\ell}}{\sqrt{T_{\mathrm{g}}} + \sqrt{T_{\ell}}}, \tag{49}$$

$$v_{\mathrm{i}} = \frac{\sqrt{T_{\ell}}v_{\mathrm{g}} + \sqrt{T_{\mathrm{g}}}v_{\ell}}{\sqrt{T_{\mathrm{g}}} + \sqrt{T_{\ell}}}, \tag{50}$$

given only the physically fundamental assumption $T_k \geq 0$ for $k \in \{\mathrm{g}, \ell\}$.

Proof. By temporal differentiation of (45), in combination with (40) and (46), we obtain

$$\int_{\mathscr{C}} dx \, \mathscr{S}(x, t) \geq 0, \tag{51}$$

where we have assumed that the entropy flux of (40), $S_{\mathrm{g}}v_{\mathrm{g}} + S_{\ell}v_{\ell}$, vanishes at the boundary of $\mathscr{C}$. For (51) to be satisfied, clearly $\mathscr{S} \geq 0$ is a sufficient criterion, for which statement to hold the non-negativity of *all* the partial source terms $\mathscr{S}_p, \mathscr{S}_\mu, \mathscr{S}_T$ and $\mathscr{S}_v$ is in turn sufficient. We now show this for each of the terms under the conditions of (47) to (50).

Firstly, the conditions (49) and (50) inserted into (41) yields

$$\mathscr{S}_p = \mathscr{I}(p_{\mathrm{g}} - p_{\ell})^2 (T_{\mathrm{g}}T_{\ell})^{-1/2} \geq 0. \tag{52}$$

Now, (48) is equivalent to $\mu_{\mathrm{i}} = \beta_\mu \mu_{\mathrm{g}} + (1 - \beta_\mu)\mu_\ell$, with $\beta_\mu \in [0, 1]$. Hence, combination of (42) and (50) yields

$$\mathscr{S}_\mu = \mathscr{K}(\mu_\ell - \mu_{\mathrm{g}})^2 \left[(1 - \beta_\mu)T_{\mathrm{g}}^{-1} + \beta_\mu T_\ell^{-1}\right] \geq 0. \tag{53}$$

Next, (50) inserted into (43) yields

$$\mathscr{S}_v = \mathscr{M}(v_\ell - v_{\mathrm{g}})^2 (T_{\mathrm{g}}T_{\ell})^{-1/2} \geq 0. \tag{54}$$

Finally, (44) becomes

$$\mathscr{S}_T = \mathscr{H}(T_\ell - T_{\mathrm{g}})^2 (T_{\mathrm{g}}T_{\ell})^{-1} \geq 0, \tag{55}$$

and hence all the source terms are non-negative. $\qquad\square$

Remark 1. *The interface conditons (49) and (50) are sufficient, not necessary, and the square-root-of-temperature weighted average between the phasic values differs from choices in the literature, e.g. the initial choices by [3]. The reason for this particular weighting is that we enforced the interface velocities in (6), (10), (11), (13) and (14) to be equal. Allowing these to differ would enable other linear combinations of the phasic quantities, which could possibly be more suitable for numerical simulations [55]. These differences, however, do not have implications for the main conclusions of this paper.*

2.4. **Wave velocities.** We now consider the homogeneous limit of the BN model, where the source terms $\mathscr{I}, \mathscr{K}, \mathscr{M}, \mathscr{H} \to 0$. The resulting model has previously been extensively studied by several authors, see e.g. [54, 69]. The model has two fluid-mechanical sound speeds; one for each of the phases. The seven wave velocities are given by $\boldsymbol{\lambda}_0 = \{v_\mathrm{i}, v_\mathrm{g}, v_\ell, v_\mathrm{g} - c_\mathrm{g}, v_\mathrm{g} + c_\mathrm{g}, v_\ell - c_\ell, v_\ell + c_\ell\}$ [54].

In typical applications, the flow is subsonic, i.e. $|v_\mathrm{g} - v_\ell| \ll c_\mathrm{g}, c_\ell$ may be a valid approximation. Evaluated in the velocity equilibrium limit, taking $v \equiv v_\mathrm{g} = v_\ell$, the eigenvalues are, sorted in ascending order,

$$\boldsymbol{\lambda}_0^{(0)} = \{v - c_{0,+}, v - c_{0,-}, v, v, v, v + c_{0,-}, v + c_{0,+}\} \tag{56}$$

where we have defined $c_{0,+} = \max\{c_\mathrm{g}, c_\ell\}$ and $c_{0,-} = \min\{c_\mathrm{g}, c_\ell\}$ as the higher and lower sound speeds, respectively.

3. The v-model

We now study the model that arises upon imposing instantaneous equilibrium in velocity, i.e. letting the velocity relaxation parameter $\mathscr{M} \to \infty$, which we expect corresponds to

$$v_\mathrm{g} = v_\ell \equiv v. \tag{57}$$

Simultaneously, we require the term $M_\mathrm{g} = \mathscr{M}(v_\ell - v_\mathrm{g})$ to remain finite. By noting that for a general function f, the phasic material derivatives are equal for the two phases, i.e. $\mathrm{D}_k f = \partial_t f + v\partial_x f \equiv \mathrm{D}f$, then the system that results from evaluating (25) for the two phases $k \in \{\mathrm{g}, \ell\}$ can be solved to yield

$$M_\mathrm{g} = (Y_\mathrm{g} p_\ell + Y_\ell p_\mathrm{g} - p_\mathrm{i}) \, \partial_x \alpha_\mathrm{g} + \alpha_\mathrm{g} Y_\ell \partial_x p_\mathrm{g} - \alpha_\ell Y_\mathrm{g} \partial_x p_\ell, \tag{58}$$

where we have introduced the phasic mass fractions $Y_k = \alpha_k \rho_k / \rho$. The model that now results from inserting (57) and (58) into the basic model of Section 2, was analyzed by Flåtten and Lund [20, 40], as it constitutes the basic model of the v-branch of the hierarchy. The model is hyperbolic and has previously been studied by many authors [33, 50, 57].

3.1. **Wave velocities.** The wave velocities of the velocity equilibrium model, in the homogeneous limit where $\mathscr{I}, \mathscr{K}, \mathscr{H} \to 0$, are given by [20]

$$\boldsymbol{\lambda}_v = \{v - c_v, v, v, v, v + c_v\}. \tag{59}$$

Herein, the sound speed of this model is defined by

$$c_v^2 = Y_\mathrm{g} c_\mathrm{g}^2 + Y_\ell c_\ell^2. \tag{60}$$

Proposition 2. *The v-model satisfies the subcharacteristic condition with respect to the basic model, given only the physically fundamental conditions $\rho_k, c_k^2 > 0$, for $k \in \{\mathrm{g}, \ell\}$.*

Proof. We observe that $Y_\mathrm{g} + Y_\ell = 1$, and due to the given positivity conditions, we have that $Y_k \in (0, 1)$. Therefore, (60) implies that $\min\{c_\mathrm{g}, c_\ell\} \leq c_v \leq \max\{c_\mathrm{g}, c_\ell\}$. It then follows trivially that the wave velocities of the v-model are *interlaced* in the wave velocities (56) of the basic model evaluated in the velocity equilibrium state (57). Hence, the associated subcharacteristic condition of Definition 1 is satisfied. $\qquad\square$

4. The p-model

In this section, we consider the mechanical equilibrium model, which arises when we assume instantaneous mechanical equilibrium in the basic model of Section 2. We let the pressure relaxation parameter $\mathscr{I} \to \infty$, which we expect to correspond to $p_{\mathrm{g}} = p_\ell \equiv p$. Simultaneously, the product $I_{\mathrm{g}} = \mathscr{I}(p_{\mathrm{g}} - p_\ell)$ should remain finite. The mechanical equilibrium model is found by using (35) evaluated for each of the two phases. From this, we may find an expression for I_{g} without temporal derivatives, and insert it into the basic model of Section 2. The resulting model has been extensively studied previously [19, 54]. Like other one-pressure two-fluid models, the model is not hyperbolic.

4.1. **Wave velocities.** We consider now the homogeneous limit, where $\mathscr{K}, \mathscr{M}, \mathscr{H} \to 0$. The eigenvalues to the lowest order in the small parameter $\varepsilon = v_{\mathrm{g}} - v_\ell$, i.e. evaluated in the equilibrium state defined by (57), are given by [19]

$$\boldsymbol{\lambda}_p^{(0)} = \{v - c_p, v, v, v, v + c_p\}, \tag{61}$$

where the sound speed in the p-model is given by

$$c_p^2 = \left(\tfrac{\alpha_{\mathrm{g}}}{\rho_{\mathrm{g}}} + \tfrac{\alpha_\ell}{\rho_\ell} \right) \left(\tfrac{\alpha_{\mathrm{g}}}{\rho_{\mathrm{g}} c_{\mathrm{g}}^2} + \tfrac{\alpha_\ell}{\rho_\ell c_\ell^2} \right)^{-1}. \tag{62}$$

Proposition 3. *The p-model satisfies the weak subcharacteristic condition of Definition 2 with respect to the basic model of Section 2, subject only to the physically fundamental conditions $\rho_k, c_k^2 > 0$, for $k \in \{\mathrm{g}, \ell\}$, in the equilibrium state defined by (57).*

Proof. We see from (62) that c_p^2 is a convex combination

$$c_p^2 = \varphi_{\mathrm{g}} c_{\mathrm{g}}^2 + \varphi_\ell c_\ell^2, \qquad \text{where} \qquad \varphi_k = \left(\tfrac{\alpha_k}{\rho_k c_k^2} \right) \left(\tfrac{\alpha_{\mathrm{g}}}{\rho_{\mathrm{g}} c_{\mathrm{g}}^2} + \tfrac{\alpha_\ell}{\rho_\ell c_\ell^2} \right)^{-1}, \tag{63}$$

since $\varphi_{\mathrm{g}} + \varphi_\ell = 1$, and $\varphi_k \in (0,1)$, due to the given conditions. This implies that

$$\min\{c_{\mathrm{g}}, c_\ell\} \le c_p \le \max\{c_{\mathrm{g}}, c_\ell\}, \tag{64}$$

and hence the weak subcharacteristic condition is fullfilled with respect to the basic model, whose local eigenvalues evaluated in the same state are given by (56). $\square$

5. The T-model

In this section, we investigate the thermal-equilibrium model (T-model), which emerges from assuming instantaneous thermal equilibrium in the basic model of Section 2. To this end, we let $\mathscr{H} \to \infty$ herein, which we expect corresponds to

$$T_{\mathrm{g}} = T_\ell \equiv T, \tag{65}$$

in such a way that $H_{\mathrm{g}} = \mathscr{H}(T_\ell - T_{\mathrm{g}})$ remains finite. In the following we present the governing equations.

5.1. **Governing equations.** The full T-model may be stated as the basic model of Section 2, in which (13) and (14) are replaced by (17) and the thermal equilibrium condition (65).

In order to establish the impact of instantaneous thermal relaxation on the wave velocities, we need to express the model in a quasi-linear form, and thus obtain the velocities as the eigenvalues of the associated Jacobian. This is most easily done by exploiting the primitive variables, which is what we now turn to do.

Firstly, we have that the phasic pressure differential in terms of density and temperature may be written as

$$\mathrm{d}p_k = c_k^2 \zeta_k^{-1} \mathrm{d}\rho_k + \Gamma_k \rho_k C_{p,k} \zeta_k^{-1} \mathrm{d}T. \tag{66}$$

where we have introduced the ratio of specific heats $\zeta_k = 1 + \Gamma_k^2 C_{p,k} T / c_k^2$, and used (65). With (66), (25) becomes

$$\mathrm{D}_k v_k = \frac{\Delta_\mathrm{i} p_k}{m_k} \partial_x \alpha_k - \frac{c_k^2}{\rho_k \zeta_k} \partial_x \rho_k - \frac{\Gamma_k C_{p,k}}{\zeta_k} \partial_x T + \frac{\Delta_\mathrm{i} v_k}{m_k} K_k + \frac{1}{m_k} M_k, \tag{67}$$

where we have defined the phasic mass per volume $m_k = \alpha_k \rho_k$, the phasic interface pressure jump $\Delta_\mathrm{i} p_k = p_\mathrm{i} - p_k$, and the phasic interface velocity difference $\Delta_\mathrm{i} v_k = v_\mathrm{i} - v_k$. Furthermore, (37) becomes

$$\mathrm{D}_k T = -\left[\frac{\zeta_k \Delta_\mathrm{i} p_k}{\tilde{C}_{p,k}} + \frac{\Gamma_k T}{\alpha_k} \right] (I_k - \Delta_\mathrm{i} v_k \partial_x \alpha_k) - \Gamma_k T \partial_x v_k$$
$$+ \left[\frac{\Gamma_k T}{m_k} + \frac{\zeta_k}{\tilde{C}_{p,k}} (g_k - h_k) \right] K_k + \frac{\zeta_k}{\tilde{C}_{p,k}} \Delta_\mathrm{i} v_k M_k + \frac{\zeta_k}{\tilde{C}_{p,k}} H_k, \tag{68}$$

where we have introduced the extensive heat capacity at constant pressure $\tilde{C}_{p,k} = m_k C_{p,k}$. We now define the weighting factor $\theta_k = \tilde{C}_{p,k} \zeta_k^{-1} / (\tilde{C}_{p,\mathrm{g}} \zeta_\mathrm{g}^{-1} + \tilde{C}_{p,\ell} \zeta_\ell^{-1})$, for which clearly $\theta_\mathrm{g} + \theta_\ell = 1$ and $\theta_k \in (0,1)$. Multiplying (68) by θ_k, and summing over the phases yields

$$\partial_t T + (\theta_\mathrm{g} v_\mathrm{g} + \theta_\ell v_\ell) \partial_x T = -\left[\frac{\theta_\mathrm{g} \Gamma_\mathrm{g} T}{\alpha_\mathrm{g}} + \frac{\theta_\ell \Gamma_\ell T}{\alpha_\ell} \right] \frac{v_\mathrm{g} - v_\ell}{2} \partial_x \alpha_\mathrm{g} - \theta_\mathrm{g} \Gamma_\mathrm{g} T \partial_x v_\mathrm{g} - \theta_\ell \Gamma_\ell T \partial_x v_\ell$$
$$+ \left[\frac{p_\mathrm{g} - p_\ell}{\frac{\tilde{C}_{p,\mathrm{g}}}{\zeta_\mathrm{g}} + \frac{\tilde{C}_{p,\ell}}{\zeta_\ell}} - \frac{\theta_\mathrm{g} \Gamma_\mathrm{g} T}{\alpha_\mathrm{g}} + \frac{\theta_\ell \Gamma_\ell T}{\alpha_\ell} \right] I_\mathrm{g} + \left[\frac{h_\ell - h_\mathrm{g}}{\frac{\tilde{C}_{p,\mathrm{g}}}{\zeta_\mathrm{g}} + \frac{\tilde{C}_{p,\ell}}{\zeta_\ell}} + \frac{\theta_\mathrm{g} \Gamma_\mathrm{g} T}{m_\mathrm{g}} - \frac{\theta_\ell \Gamma_\ell T}{m_\ell} \right] K_\mathrm{g}$$
$$+ \frac{v_\ell - v_\mathrm{g}}{\frac{\tilde{C}_{p,\mathrm{g}}}{\zeta_\mathrm{g}} + \frac{\tilde{C}_{p,\ell}}{\zeta_\ell}} M_\mathrm{g}, \tag{69}$$

where have used the interface parameter definitions of (49) and (50) evaluated in thermal equilibrium (65) to simplify.

5.2. **Wave velocities.** We now seek the wave velocities, i.e. eigenvalues, in the homogeneous limit, where the relaxation source terms $\mathscr{I}, \mathscr{K}, \mathscr{M} \to 0$. From (24), it is then clear that α_g is a characteristic variable of the system, since the volume fraction is advected with the velocity v_i in the absence of relaxation source terms. By using (26), (67) and (69), the remaining, reduced system may now be expressed in the quasi-linear form $\partial_t \tilde{\mathbf{u}}_T + \tilde{\mathbf{A}}_T (\tilde{\mathbf{u}}_T) \partial_x \tilde{\mathbf{u}}_T = 0$, where $\tilde{\mathbf{u}}_T = [\rho_\mathrm{g}, \rho_\ell, v_\mathrm{g}, v_\ell, T]$, and the associated Jacobian is given by

$$\tilde{\mathbf{A}}_T = \begin{bmatrix} v_\mathrm{g} & 0 & \rho_\mathrm{g} & 0 & 0 \\ 0 & v_\ell & 0 & \rho_\ell & 0 \\ \frac{c_\mathrm{g}^2}{\rho_\mathrm{g} \zeta_\mathrm{g}} & 0 & v_\mathrm{g} & 0 & \frac{\Gamma_\mathrm{g} C_{p,\mathrm{g}}}{\zeta_\mathrm{g}} \\ 0 & \frac{c_\ell^2}{\rho_\ell \zeta_\ell} & 0 & v_\ell & \frac{\Gamma_\ell C_{p,\ell}}{\zeta_\ell} \\ 0 & 0 & \theta_\mathrm{g} \Gamma_\mathrm{g} T & \theta_\ell \Gamma_\ell T & \theta_\mathrm{g} v_\mathrm{g} + \theta_\ell v_\ell \end{bmatrix}, \tag{70}$$

from which we can find the remaining five eigenvalues. The characteristic polynomial of the latter is a fifth-degree polynomial, for which in general no closed-form

solution can be obtained. We now note that we may write $\tilde{\mathbf{A}}_T = \tilde{\mathbf{A}}_T^{(0)} + \varepsilon\tilde{\mathbf{A}}_T^{(1)}$, where $\varepsilon = v_\mathrm{g} - v_\ell$. The matrices are given by

$$\tilde{\mathbf{A}}_T^{(0)} = \begin{bmatrix} \bar{v} & 0 & \rho_\mathrm{g} & 0 & 0 \\ 0 & \bar{v} & 0 & \rho_\ell & 0 \\ \frac{c_\mathrm{g}^2}{\rho_\mathrm{g}\zeta_\mathrm{g}} & 0 & \bar{v} & 0 & \frac{\Gamma_\mathrm{g} C_{p,\mathrm{g}}}{\zeta_\mathrm{g}} \\ 0 & \frac{c_\ell^2}{\rho_\ell\zeta_\ell} & 0 & \bar{v} & \frac{\Gamma_\ell C_{p,\ell}}{\zeta_\ell} \\ 0 & 0 & \theta_\mathrm{g}\Gamma_\mathrm{g}T & \theta_\ell\Gamma_\ell T & \bar{v} \end{bmatrix}, \tag{71}$$

and $\tilde{\mathbf{A}}_T^{(1)} = \mathrm{diag}\,(\theta_\ell, -\theta_\mathrm{g}, \theta_\ell, -\theta_\mathrm{g}, 0)$, where we have taken $\bar{v} = \theta_\mathrm{g} v_\mathrm{g} + \theta_\ell v_\ell$. Hence, we approximate the eigenvalues by means of a perturbation expansion in the small parameter ε. To the lowest order in ε, $v_\mathrm{g} = v_\ell = \bar{v} = v$, and the eigenvalues of the T-model are given by

$$\boldsymbol{\lambda}_T^{(0)} = \{v - c_{T,+}, v - c_{T,-}, v, v, v + c_{T,-}, v + c_{T,+}\} \tag{72}$$

where the two distinct sound speeds of the model are given by

$$c_{T,\pm}^2 = \frac{\frac{c_\mathrm{g}^2 + c_\ell^2}{T}\left(\frac{1}{\tilde{C}_{p,\mathrm{g}}} + \frac{1}{\tilde{C}_{p,\ell}}\right) + \frac{\Gamma_\mathrm{g}^2 c_\ell^2}{m_\mathrm{g} c_\mathrm{g}^2} + \frac{\Gamma_\ell^2 c_\mathrm{g}^2}{m_\ell c_\ell^2}}{2\left[\frac{\Gamma_\mathrm{g}^2}{m_\mathrm{g} c_\mathrm{g}^2} + \frac{\Gamma_\ell^2}{m_\ell c_\ell^2} + \frac{1}{T}\left(\frac{1}{\tilde{C}_{p,\mathrm{g}}} + \frac{1}{\tilde{C}_{p,\ell}}\right)\right]}$$

$$\frac{\pm\sqrt{\left[\frac{c_\mathrm{g}^2 - c_\ell^2}{T}\left(\frac{1}{\tilde{C}_{p,\mathrm{g}}} + \frac{1}{\tilde{C}_{p,\ell}}\right) - \frac{\Gamma_\mathrm{g}^2 c_\ell^2}{m_\mathrm{g} c_\mathrm{g}^2} + \frac{\Gamma_\ell^2 c_\mathrm{g}^2}{m_\ell c_\ell^2}\right]^2 + 4\frac{\Gamma_\mathrm{g}^2\Gamma_\ell^2}{m_\mathrm{g} m_\ell}}}{2\left[\frac{\Gamma_\mathrm{g}^2}{m_\mathrm{g} c_\mathrm{g}^2} + \frac{\Gamma_\ell^2}{m_\ell c_\ell^2} + \frac{1}{T}\left(\frac{1}{\tilde{C}_{p,\mathrm{g}}} + \frac{1}{\tilde{C}_{p,\ell}}\right)\right]}. \tag{73}$$

Proposition 4. *The T-model satisfies the weak subcharacteristic condition with respect to the basic model of Section 2, subject only to the physically fundamental conditions $\rho_k, C_{p,k}, T > 0$, for $k \in \{\mathrm{g}, \ell\}$, in the equilibrium state defined by* (57).

Proof. We first show that the sound speeds are real. We note that on the given conditions, clearly $c_{T,\pm}^2 \in \mathbb{R}$, and moreover, $c_{T,+}^2 \geq 0$. The product of the sound speeds may be written as

$$c_{T,+}^{-2} c_{T,-}^{-2} = c_{0,+}^{-2} c_{0,-}^{-2} + \mathcal{Z}_T^0, \quad \text{where} \quad \mathcal{Z}_T^0 = \frac{T\left(\frac{\Gamma_\mathrm{g}^2}{m_\mathrm{g} c_\mathrm{g}^2} + \frac{\Gamma_\ell^2}{m_\ell c_\ell^2}\right)}{c_{0,+}^2 c_{0,-}^2\left(\frac{1}{\tilde{C}_{p,\mathrm{g}}} + \frac{1}{\tilde{C}_{p,\ell}}\right)}. \tag{74}$$

Based on the given conditions, it is clear that $\mathcal{Z}_T^0 \geq 0$ and therefore

$$0 \leq c_{T,+}^2 c_{T,-}^2 \leq c_{0,+}^2 c_{0,-}^2, \tag{75}$$

and hence also $c_{T,-}^2 \geq 0$, and thus $c_{T,\pm}$ are real, and by definition, positive. Now, using the definitions of $c_{0,\pm}$ and (73), it follows that

$$(c_{0,+}^2 - c_{T,+}^2)(c_{0,+}^2 - c_{T,-}^2)(c_{0,-}^2 - c_{T,+}^2)(c_{0,-}^2 - c_{T,-}^2) = -\mathcal{Q}_T^0, \tag{76}$$

where

$$\mathcal{Q}_T^0 = \left(c_\mathrm{g}^2 - c_\ell^2\right)^2 \frac{\Gamma_\mathrm{g}^2\Gamma_\ell^2}{m_\mathrm{g} m_\ell}\left[\frac{\Gamma_\mathrm{g}^2}{m_\mathrm{g} c_\mathrm{g}^2} + \frac{\Gamma_\ell^2}{m_\ell c_\ell^2} + \frac{1}{T}\left(\frac{1}{\tilde{C}_{p,\mathrm{g}}} + \frac{1}{\tilde{C}_{p,\ell}}\right)\right]^{-2}. \tag{77}$$

The given conditions ensure that $\mathcal{Q}_T^0 \geq 0$. The only ordering of sound speeds compatible with (75) and (76) is $0 \leq c_{T,-} \leq c_{0,-} \leq c_{T,+} \leq c_{0,+}$, and hence the subcharacteristic condition of Definition 1 is satisfied. $\square$

Proposition 5. *The vT-model of Lund* [40] *satisfies the subcharacteristic condition with respect to the T-model, given the physically fundamental assumptions* $\rho_k, C_{p,k}, T > 0$, *for* $k \in \{g, \ell\}$.

Proof. The sound speed of the vT-model is given by [40]

$$c_{vT}^2 = \frac{1}{\rho} \frac{m_g c_g^2 m_\ell c_\ell^2 \left(\frac{\Gamma_g}{m_g c_g^2} + \frac{\Gamma_\ell}{m_\ell c_\ell^2} \right)^2 + \frac{1}{T} \left(\frac{1}{\tilde{C}_{p,g}} + \frac{1}{\tilde{C}_{p,\ell}} \right) \left(m_g c_g^2 + m_\ell c_\ell^2 \right)}{\frac{\Gamma_g^2}{m_g c_g^2} + \frac{\Gamma_\ell^2}{m_\ell c_\ell^2} + \frac{1}{T} \left(\frac{1}{\tilde{C}_{p,g}} + \frac{1}{\tilde{C}_{p,\ell}} \right)}. \tag{78}$$

Now, using (73), we can write the product of the differences as

$$\left(c_{T,+}^2 - c_{vT}^2 \right) \left(c_{T,-}^2 - c_{vT}^2 \right) = -\mathcal{Q}_{vT}^T, \tag{79}$$

where

$$\mathcal{Q}_{vT}^T = Y_g Y_\ell \left[\frac{\frac{1}{T} \left(\frac{1}{\tilde{C}_{p,g}} + \frac{1}{\tilde{C}_{p,\ell}} \right) \left(c_g^2 - c_\ell^2 \right) - \frac{\Gamma_g^2 c_\ell^2}{m_g c_g^2} + \frac{\Gamma_\ell^2 c_g^2}{m_\ell c_\ell^2} + \left(\frac{1}{m_g} - \frac{1}{m_\ell} \right) \Gamma_g \Gamma_\ell}{\frac{\Gamma_g^2}{m_g c_g^2} + \frac{\Gamma_\ell^2}{m_\ell c_\ell^2} + \frac{1}{T} \left(\frac{1}{\tilde{C}_{p,g}} + \frac{1}{\tilde{C}_{p,\ell}} \right)} \right]^2. \tag{80}$$

With the given conditions, clearly $\mathcal{Q}_{vT}^T \geq 0$. Hence exactly one of the factors on the left hand side of (79) is negative, and combined with Proposition 4 we realize that $c_{T,-} \leq c_{vT} \leq c_{T,+}$, and hence the subcharacteristic condition is satisfied. $\square$

Proposition 6. *The pT-model satisfies the weak subcharacteristic condition with respect to the T-model, given the physically fundamental assumptions* $\rho_k, C_{p,k}, T > 0$ *for* $k \in \{g, \ell\}$ *in the equilibrium state defined by* (57).

Proof. The sound speed of the pT-model is given by [19]

$$c_{pT}^2 = \frac{\left(\frac{\alpha_g}{\rho_g} + \frac{\alpha_\ell}{\rho_\ell} \right) \left(\frac{1}{\tilde{C}_{p,g}} + \frac{1}{\tilde{C}_{p,\ell}} \right)}{\left(\frac{\alpha_g}{\rho_g c_g^2} + \frac{\alpha_\ell}{\rho_\ell c_\ell^2} \right) \left(\frac{1}{\tilde{C}_{p,g}} + \frac{1}{\tilde{C}_{p,\ell}} \right) + T \left(\frac{\Gamma_g}{\rho_g c_g^2} - \frac{\Gamma_\ell}{\rho_\ell c_\ell^2} \right)^2} \tag{81}$$

We may now write

$$\left(c_{T,+}^2 - c_{pT}^2 \right) \left(c_{T,-}^2 - c_{pT}^2 \right) = -\mathcal{Q}_{pT}^T, \tag{82}$$

where

$$\mathcal{Q}_{pT}^T = \frac{\alpha_g \alpha_\ell}{\rho_g c_g^2 \rho_\ell c_\ell^2 T} \left(\frac{1}{\tilde{C}_{p,g}} + \frac{1}{\tilde{C}_{p,\ell}} \right) \left[\frac{\Gamma_g^2}{m_g c_g^2} + \frac{\Gamma_\ell^2}{m_\ell c_\ell^2} + \frac{1}{T} \left(\frac{1}{\tilde{C}_{p,g}} + \frac{1}{\tilde{C}_{p,\ell}} \right) \right]^{-1}$$

$$\times \left[\frac{\left(\frac{1}{\tilde{C}_{p,g}} + \frac{1}{\tilde{C}_{p,\ell}} \right) \left(c_g^2 - c_\ell^2 \right) - T \left(\frac{\Gamma_g}{\rho_g c_g^2} - \frac{\Gamma_\ell}{\rho_\ell c_\ell^2} \right) \left(\frac{\Gamma_g c_\ell^2}{\alpha_g} + \frac{\Gamma_\ell c_g^2}{\alpha_\ell} \right)}{\left(\frac{\alpha_g}{\rho_g c_g^2} + \frac{\alpha_\ell}{\rho_\ell c_\ell^2} \right) \left(\frac{1}{\tilde{C}_{p,g}} + \frac{1}{\tilde{C}_{p,\ell}} \right) + T \left(\frac{\Gamma_g}{\rho_g c_g^2} - \frac{\Gamma_\ell}{\rho_\ell c_\ell^2} \right)^2} \right]^2. \tag{83}$$

Clearly $\mathcal{Q}_{pT}^T \geq 0$, on the given conditions. Hence exactly one factor on the left hand side of (82) is negative, yielding $c_{T,-} \leq c_{pT} \leq c_{T,+}$, and the weak subcharacteristic condition is satisfied. $\square$

6. The μ-model

We now proceed to investigate the chemical-equilibrium model (the μ-model), which arises when we assume instantaneous chemical equilibrium, i.e. let the chemical relaxation parameter $\mathscr{K} \to \infty$, which we expect corresponds to

$$\mu_{\mathrm{g}} = \mu_\ell \equiv \mu. \tag{84}$$

Simultaneously, we require the product $K_{\mathrm{g}} = \mathscr{K}(\mu_\ell - \mu_{\mathrm{g}})$ to remain finite, and in the forthcoming we seek to express this without any temporal derivatives.

Remark 2. *It should be noted that there does not seem to be a general agreement in the literature on how to properly model mass transfer (see e.g. [41, pp. 13]). Strictly enforcing (84) may sometimes lead to unphysical results [4]. The present choice (84) is primarily motivated by compliance with the v-subhierarchy compiled by [40], and evaluating the physical relevance of these models is out of the scope of the present work.*

The chemical potential evolution equation (39) may be written as

$$\mathrm{D}_k\mu = -\left[\psi_k\Delta_{\mathrm{i}}p_k + \xi_k\alpha_k^{-1}\right](I_k - \Delta_{\mathrm{i}}v_k\partial_x\alpha_k) - \xi_k\partial_x v_k + \chi_k K_k + \psi_k\Delta_{\mathrm{i}}v_k M_k + \psi_k H_k. \tag{85}$$

where we have used (84), and defined the shorthands

$$\xi_k = c_k^2 - \Gamma_k T_k s_k, \quad \psi_k = \frac{\Gamma_k\xi_k}{m_k c_k^2} - \frac{s_k}{\bar{C}_{p,k}}, \quad \chi_k = \frac{\xi_k^2}{m_k c_k^2} + \frac{T_k s_k^2}{\bar{C}_{p,k}} + \frac{1}{2}(\Delta_{\mathrm{i}}v_k)^2\psi_k. \tag{86}$$

By using (85) evaluated for each of the phases, and subtracting these expressions from each other, we obtain

$$K_{\mathrm{g}} = \kappa_\mu^{-1}\left(\xi_{\mathrm{g}}\partial_x v_{\mathrm{g}} - \xi_\ell\partial_x v_\ell - (\psi_{\mathrm{g}} + \psi_\ell)H_{\mathrm{g}}\right) - \mathscr{A}^\mu\partial_x\alpha_{\mathrm{g}} + (v_{\mathrm{g}} - v_\ell)\kappa_\mu^{-1}\partial_x\mu + \mathscr{K}_p^\mu I_{\mathrm{g}} - \mathscr{K}_v^\mu M_{\mathrm{g}} \tag{87}$$

where we have defined the shorthands

$$\kappa_\mu = \frac{T_{\mathrm{g}}s_{\mathrm{g}}^2}{\bar{C}_{p,\mathrm{g}}} + \frac{T_\ell s_\ell^2}{\bar{C}_{p,\ell}} + \frac{\xi_{\mathrm{g}}^2}{m_{\mathrm{g}}c_{\mathrm{g}}^2} + \frac{\xi_\ell^2}{m_\ell c_\ell^2} + \frac{1}{2}\left(\psi_{\mathrm{g}}(\Delta_{\mathrm{i}}v_{\mathrm{g}})^2 + \psi_\ell(\Delta_{\mathrm{i}}v_\ell)^2\right), \tag{88}$$

$$\mathscr{A}^\mu = \kappa_\mu^{-1}\left[\left(\psi_{\mathrm{g}}\Delta_{\mathrm{i}}p_{\mathrm{g}} + \frac{\xi_{\mathrm{g}}}{\alpha_{\mathrm{g}}}\right)\Delta_{\mathrm{i}}v_{\mathrm{g}} + \left(\psi_\ell\Delta_{\mathrm{i}}p_\ell + \frac{\xi_\ell}{\alpha_\ell}\right)\Delta_{\mathrm{i}}v_\ell\right], \tag{89}$$

$$\mathscr{K}_p^\mu = \kappa_\mu^{-1}\left[\psi_{\mathrm{g}}\Delta_{\mathrm{i}}p_{\mathrm{g}} + \psi_\ell\Delta_{\mathrm{i}}p_\ell + \frac{\xi_{\mathrm{g}}}{\alpha_{\mathrm{g}}} + \frac{\xi_\ell}{\alpha_\ell}\right], \quad \mathscr{K}_v^\mu = \kappa_\mu^{-1}\left(\psi_{\mathrm{g}}\Delta_{\mathrm{i}}v_{\mathrm{g}} + \psi_\ell\Delta_{\mathrm{i}}v_\ell\right). \tag{90}$$

6.1. **Governing equations.** By using the expression (87) to insert for K_{g} in the basic model of Section 2, the μ-model can now be summarized with the following set of equations:

- Volume advection: $\partial_t\alpha_{\mathrm{g}} + v_{\mathrm{i}}\partial_x\alpha_{\mathrm{g}} = I_{\mathrm{g}}$,
- Conservation of mass: $\partial_t\rho + \partial_x\left(\alpha_{\mathrm{g}}\rho_{\mathrm{g}}v_{\mathrm{g}} + \alpha_\ell\rho_\ell v_\ell\right) = 0$,
- Momentum balance:

$$\partial_t\alpha_{\mathrm{g}}\rho_{\mathrm{g}}v_{\mathrm{g}} + \partial_x(\alpha_{\mathrm{g}}\rho_{\mathrm{g}}v_{\mathrm{g}}^2 + \alpha_{\mathrm{g}}p_{\mathrm{g}}) - (p_{\mathrm{i}} - v_{\mathrm{i}}\mathscr{A}^\mu)\partial_x\alpha_{\mathrm{g}} - v_{\mathrm{i}}\xi_{\mathrm{g}}\kappa_\mu^{-1}\partial_x v_{\mathrm{g}} + v_{\mathrm{i}}\xi_\ell\kappa_\mu^{-1}\partial_x v_\ell$$
$$- v_{\mathrm{i}}(v_{\mathrm{g}} - v_\ell)\kappa_\mu^{-1}\partial_x\mu = v_{\mathrm{i}}\mathscr{K}_p^\mu I_{\mathrm{g}} + (1 - v_{\mathrm{i}}\mathscr{K}_v^\mu)M_{\mathrm{g}} - v_{\mathrm{i}}(\psi_{\mathrm{g}} + \psi_\ell)\kappa_\mu^{-1}H_{\mathrm{g}}, \tag{91}$$

- Energy balance:

$$\partial_t E_{\mathrm{g}} + \partial_x \left(E_{\mathrm{g}} v_{\mathrm{g}} + \alpha_{\mathrm{g}} v_{\mathrm{g}} p_{\mathrm{g}} \right) - \left[p_{\mathrm{i}} v_{\mathrm{i}} - \left(\mu + \tfrac{1}{2} v_{\mathrm{i}}^2 \right) \mathcal{A}^\mu \right] \partial_x \alpha_{\mathrm{g}}$$
$$- \left(\mu + \tfrac{1}{2} v_{\mathrm{i}}^2 \right) \kappa_\mu^{-1} \left[\xi_{\mathrm{g}} \partial_x v_{\mathrm{g}} - \xi_\ell \partial_x v_\ell + (v_{\mathrm{g}} - v_\ell) \partial_x \mu \right]$$
$$= \left[\left(\mu + \tfrac{1}{2} v_{\mathrm{i}}^2 \right) \mathcal{K}_p^\mu - p_{\mathrm{i}} \right] I_{\mathrm{g}} + \left[v_{\mathrm{i}} - \left(\mu + \tfrac{1}{2} v_{\mathrm{i}}^2 \right) \mathcal{K}_v^\mu \right] M_{\mathrm{g}} + \left[1 - \left(\mu + \tfrac{1}{2} v_{\mathrm{i}}^2 \right) (\psi_{\mathrm{g}} + \psi_\ell) \kappa_\mu^{-1} \right] H_{\mathrm{g}}, \quad (92)$$

Momentum and energy equations for the liquid phase are found by phase symmetry; interchanging indices g and ℓ.

6.2. **Evolution of primitive variables.** In order to write the system in a quasi-linear form, and thereby find the wave speeds of the μ-model, we use the evolution equations for the primitive variables. We therefore now seek the evolution of some of the primitive variables under the assumption of instantaneous chemical equilibrium.

We first define the weighting factor $\phi_k = \chi_k^{-1} / (\chi_{\mathrm{g}}^{-1} + \chi_\ell^{-1})$. Multiplying (85) by ϕ_k and summing over the phases, we get for the chemical potential

$$\partial_t \mu + (\phi_{\mathrm{g}} v_{\mathrm{g}} + \phi_\ell v_\ell) \partial_x \mu + G^\mu_{\alpha_{\mathrm{g}}} \partial_x \alpha_{\mathrm{g}} + \phi_{\mathrm{g}} \xi_{\mathrm{g}} \partial_x v_{\mathrm{g}} + \phi_\ell \xi_\ell \partial_x v_\ell$$
$$= \left[-\phi_{\mathrm{g}} (\psi_{\mathrm{g}} \Delta_{\mathrm{i}} p_{\mathrm{g}} + \xi_{\mathrm{g}} \alpha_{\mathrm{g}}^{-1}) + \phi_\ell (\psi_\ell \Delta_{\mathrm{i}} p_\ell + \xi_\ell \alpha_\ell^{-1}) \right] I_{\mathrm{g}}$$
$$+ (\phi_{\mathrm{g}} \psi_{\mathrm{g}} \Delta_{\mathrm{i}} v_{\mathrm{g}} - \phi_\ell \psi_\ell \Delta_{\mathrm{i}} v_\ell) M_{\mathrm{g}} + (\phi_{\mathrm{g}} \psi_{\mathrm{g}} - \phi_\ell \psi_\ell) H_{\mathrm{g}}, \quad (93)$$

where we have defined the shorthand coefficient

$$G^\mu_{\alpha_{\mathrm{g}}} = -\phi_{\mathrm{g}} \left(\psi_{\mathrm{g}} \Delta_{\mathrm{i}} p_{\mathrm{g}} + \xi_{\mathrm{g}} \alpha_{\mathrm{g}}^{-1} \right) \Delta_{\mathrm{i}} v_{\mathrm{g}} + \phi_\ell \left(\psi_\ell \Delta_{\mathrm{i}} p_\ell + \xi_\ell \alpha_\ell^{-1} \right) \Delta_{\mathrm{i}} v_\ell. \quad (94)$$

For the phasic velocity v_{g}, we find from (25) the evolution equation

$$\partial_t v_{\mathrm{g}} + \left[v_{\mathrm{g}} - \tfrac{\xi_{\mathrm{g}} \Delta_{\mathrm{i}} v_{\mathrm{g}}}{m_{\mathrm{g}} \kappa_\mu} \right] \partial_x v_{\mathrm{g}} + \tfrac{\xi_\ell \Delta_{\mathrm{i}} v_{\mathrm{g}}}{m_{\mathrm{g}} \kappa_\mu} \partial_x v_\ell + \tfrac{\Delta_{\mathrm{i}} v_{\mathrm{g}} \mathcal{A}^\mu - \Delta_{\mathrm{i}} p_{\mathrm{g}}}{m_{\mathrm{g}}} \partial_x \alpha_{\mathrm{g}} + \tfrac{1}{\rho_{\mathrm{g}}} \partial_x p_{\mathrm{g}} - \tfrac{\Delta_{\mathrm{i}} v_{\mathrm{g}} (v_{\mathrm{g}} - v_\ell)}{m_{\mathrm{g}} \kappa_\mu} \partial_x \mu$$
$$= \tfrac{\Delta_{\mathrm{i}} v_{\mathrm{g}}}{m_{\mathrm{g}}} \mathcal{K}_p^\mu I_{\mathrm{g}} + \tfrac{1}{m_{\mathrm{g}}} \left(1 - \Delta_{\mathrm{i}} v_{\mathrm{g}} \mathcal{K}_v^\mu \right) M_{\mathrm{g}} - \tfrac{\Delta_{\mathrm{i}} v_{\mathrm{g}}}{m_{\mathrm{g}}} \tfrac{\psi_{\mathrm{g}} + \psi_\ell}{\kappa_\mu} H_{\mathrm{g}}, \quad (95)$$

and v_ℓ is found by phase symmetry.

The phasic pressure evolution is found from (35). For the gas phase, it reads

$$\partial_t p_{\mathrm{g}} + v_{\mathrm{g}} \partial_x p_{\mathrm{g}} + P^\mu_{\mathrm{g}, \alpha_{\mathrm{g}}} \partial_x \alpha_{\mathrm{g}} + P^\mu_{\mathrm{g}, v_{\mathrm{g}}} \partial_x v_{\mathrm{g}} + P^\mu_{\mathrm{g}, v_\ell} \partial_x v_\ell + P^\mu_{\mathrm{g}, \mu} \partial_x \mu$$
$$= \alpha_{\mathrm{g}}^{-1} \left[-\left(\Gamma_{\mathrm{g}} \Delta_{\mathrm{i}} p_{\mathrm{g}} + \rho_{\mathrm{g}} c_{\mathrm{g}}^2 \right) + \left(\xi_{\mathrm{g}} + \tfrac{1}{2} \Gamma_{\mathrm{g}} (\Delta_{\mathrm{i}} v_{\mathrm{g}})^2 \right) \mathcal{K}_p^\mu \right] I_{\mathrm{g}}$$
$$+ \alpha_{\mathrm{g}}^{-1} \left[\Gamma_{\mathrm{g}} \Delta_{\mathrm{i}} v_{\mathrm{g}} - \left(\xi_{\mathrm{g}} + \tfrac{1}{2} \Gamma_{\mathrm{g}} (\Delta_{\mathrm{i}} v_{\mathrm{g}})^2 \right) \mathcal{K}_v^\mu \right] M_{\mathrm{g}}$$
$$+ \alpha_{\mathrm{g}}^{-1} \left[\Gamma_{\mathrm{g}} - \left(\xi_{\mathrm{g}} + \tfrac{1}{2} \Gamma_{\mathrm{g}} (\Delta_{\mathrm{i}} v_{\mathrm{g}})^2 \right) (\psi_{\mathrm{g}} + \psi_\ell) \kappa_\mu^{-1} \right] H_{\mathrm{g}}. \quad (96)$$

wherein we have defined the coefficients

$$P^\mu_{\mathrm{g}, \alpha_{\mathrm{g}}} = \alpha_{\mathrm{g}}^{-1} \left[\left(\xi_{\mathrm{g}} + \tfrac{1}{2} \Gamma_{\mathrm{g}} (\Delta_{\mathrm{i}} v_{\mathrm{g}})^2 \right) \mathcal{A}^\mu - \left(\Gamma_{\mathrm{g}} \Delta_{\mathrm{i}} p_{\mathrm{g}} + \rho_{\mathrm{g}} c_{\mathrm{g}}^2 \right) \Delta_{\mathrm{i}} v_{\mathrm{g}} \right], \quad (97)$$

$$P^\mu_{\mathrm{g}, v_{\mathrm{g}}} = \rho_{\mathrm{g}} c_{\mathrm{g}}^2 - \left(\xi_{\mathrm{g}} + \tfrac{1}{2} \Gamma_{\mathrm{g}} (\Delta_{\mathrm{i}} v_{\mathrm{g}})^2 \right) \xi_{\mathrm{g}} \alpha_{\mathrm{g}}^{-1} \kappa_\mu^{-1}, \quad (98)$$

$$P^\mu_{\mathrm{g}, v_\ell} = \left(\xi_{\mathrm{g}} + \tfrac{1}{2} \Gamma_{\mathrm{g}} (\Delta_{\mathrm{i}} v_{\mathrm{g}})^2 \right) \xi_\ell \alpha_{\mathrm{g}}^{-1} \kappa_\mu^{-1}, \quad (99)$$

$$P^\mu_{\mathrm{g}, \mu} = -\left(\xi_{\mathrm{g}} + \tfrac{1}{2} \Gamma_{\mathrm{g}} (\Delta_{\mathrm{i}} v_{\mathrm{g}})^2 \right) (v_{\mathrm{g}} - v_\ell) \alpha_{\mathrm{g}}^{-1} \kappa_\mu^{-1}. \quad (100)$$

The corresponding expressions related to the evolution of p_ℓ are found by phase symmetry.

6.3. **Wave velocities.** We now wish to derive the wave velocities of the μ-model in the homogeneous limit, where $\mathscr{I}, \mathscr{H}, \mathscr{M} \to 0$. In this limit, the volume fraction α_{g} is a characteristic variable with the associated eigenvalue v_{i}. The remaining, reduced model, i.e. (93), (95) and (96) for both phases, may then be expressed in the quasi-linear form $\partial_t \tilde{\mathbf{u}}_\mu + \tilde{\mathbf{A}}_\mu(\tilde{\mathbf{u}}_\mu)\partial_x \tilde{\mathbf{u}}_\mu = 0$, where the reduced vector of unknowns is $\tilde{\mathbf{u}}_\mu = [\mu, v_{\mathrm{g}}, v_\ell, p_{\mathrm{g}}, p_\ell]$, and the reduced Jacobian reads

$$
\tilde{\mathbf{A}}_\mu = \begin{bmatrix}
\phi_{\mathrm{g}} v_{\mathrm{g}} + \phi_\ell v_\ell & \phi_{\mathrm{g}} \xi_{\mathrm{g}} & \phi_\ell \xi_\ell & 0 & 0 \\
-\frac{\Delta_{\mathrm{i}} v_{\mathrm{g}}(v_{\mathrm{g}}-v_\ell)}{m_{\mathrm{g}} \kappa_\mu} & v_{\mathrm{g}} - \frac{\xi_{\mathrm{g}}\Delta_{\mathrm{i}} v_{\mathrm{g}}}{m_{\mathrm{g}} \kappa_\mu} & \frac{\xi_\ell \Delta_{\mathrm{i}} v_{\mathrm{g}}}{m_{\mathrm{g}} \kappa_\mu} & \rho_{\mathrm{g}}^{-1} & 0 \\
\frac{\Delta_{\mathrm{i}} v_\ell(v_{\mathrm{g}}-v_\ell)}{m_\ell \kappa_\mu} & \frac{\xi_{\mathrm{g}}\Delta_{\mathrm{i}} v_\ell}{m_\ell \kappa_\mu} & v_\ell - \frac{\xi_\ell \Delta_{\mathrm{i}} v_\ell}{m_\ell \kappa_\mu} & 0 & \rho_\ell^{-1} \\
P_{\mathrm{g},\mu}^\mu & P_{\mathrm{g},v_{\mathrm{g}}}^\mu & P_{\mathrm{g},v_\ell}^\mu & v_{\mathrm{g}} & 0 \\
P_{\ell,\mu}^\mu & P_{\ell,v_{\mathrm{g}}}^\mu & P_{\ell,v_\ell}^\mu & 0 & v_\ell
\end{bmatrix}. \tag{101}
$$

Again the eigenvalues λ are given the roots of a fifth degree polynomial, for which in general no closed-form solution exists. We therefore expand in the small parameter $\varepsilon = v_{\mathrm{g}} - v_\ell$, i.e. $\tilde{\mathbf{A}}_\mu = \tilde{\mathbf{A}}_\mu^{(0)} + \varepsilon \tilde{\mathbf{A}}_\mu^{(1)} + \ldots$, and $\lambda = \lambda^{(0)} + \varepsilon \lambda^{(1)} + \ldots$. Herein, the lowest-order system matrix reads, taking $\bar{v} = \phi_{\mathrm{g}} v_{\mathrm{g}} + \phi_\ell v_\ell$,

$$
\tilde{\mathbf{A}}_\mu^{(0)} = \begin{bmatrix}
\bar{v} & \phi_{\mathrm{g}} \xi_{\mathrm{g}} & \phi_\ell \xi_\ell & 0 & 0 \\
0 & \bar{v} & 0 & \rho_{\mathrm{g}}^{-1} & 0 \\
0 & 0 & \bar{v} & 0 & \rho_\ell^{-1} \\
0 & \rho_{\mathrm{g}} c_{\mathrm{g}}^2 - \xi_{\mathrm{g}}^2/(\alpha_{\mathrm{g}} \kappa_\mu^{(0)}) & \xi_{\mathrm{g}}\xi_\ell/(\alpha_{\mathrm{g}} \kappa_\mu^{(0)}) & \bar{v} & 0 \\
0 & \xi_{\mathrm{g}}\xi_\ell/(\alpha_\ell \kappa_\mu^{(0)}) & \rho_\ell c_\ell^2 - \xi_\ell^2/(\alpha_\ell \kappa_\mu^{(0)}) & 0 & \bar{v}
\end{bmatrix}, \tag{102}
$$

where we have used the lowest-order term of κ_μ, as defined in (88):

$$
\kappa_\mu^{(0)} = \frac{T_{\mathrm{g}} s_{\mathrm{g}}^2}{\bar{C}_{p,\mathrm{g}}} + \frac{T_\ell s_\ell^2}{\bar{C}_{p,\ell}} + \frac{\xi_{\mathrm{g}}^2}{m_{\mathrm{g}} c_{\mathrm{g}}^2} + \frac{\xi_\ell^2}{m_\ell c_\ell^2}. \tag{103}
$$

To the lowest order in ε, $v_{\mathrm{g}} = v_\ell = \bar{v} = v$, and thus the eigenvalue problem consists in finding the roots of $\det(\tilde{\mathbf{A}}_\mu^{(0)} - \lambda^{(0)}\mathbf{I}) = 0$. Hence, the full vector of eigenvalues is given by

$$
\boldsymbol{\lambda}_\mu^{(0)} = \{v - c_{\mu,+}, v - c_{\mu,-}, v, v, v + c_{\mu,-}, v + c_{\mu,+}\} \tag{104}
$$

where the two sound speeds in the μ-model are given by

$$
c_{\mu,\pm}^2 = \frac{\left(\frac{T_{\mathrm{g}} s_{\mathrm{g}}^2}{\bar{C}_{p,\mathrm{g}}} + \frac{T_\ell s_\ell^2}{\bar{C}_{p,\ell}}\right)(c_{\mathrm{g}}^2 + c_\ell^2) + \frac{\xi_\ell^2 c_{\mathrm{g}}^2}{m_\ell c_\ell^2} + \frac{\xi_{\mathrm{g}}^2 c_\ell^2}{m_{\mathrm{g}} c_{\mathrm{g}}^2}}{2\left[\frac{T_{\mathrm{g}} s_{\mathrm{g}}^2}{\bar{C}_{p,\mathrm{g}}} + \frac{T_\ell s_\ell^2}{\bar{C}_{p,\ell}} + \frac{\xi_{\mathrm{g}}^2}{m_{\mathrm{g}} c_{\mathrm{g}}^2} + \frac{\xi_\ell^2}{m_\ell c_\ell^2}\right]}
$$
$$
\pm \frac{\sqrt{\left[\left(\frac{T_{\mathrm{g}} s_{\mathrm{g}}^2}{\bar{C}_{p,\mathrm{g}}} + \frac{T_\ell s_\ell^2}{\bar{C}_{p,\ell}}\right)(c_{\mathrm{g}}^2 - c_\ell^2) + \frac{\xi_\ell^2 c_{\mathrm{g}}^2}{m_\ell c_\ell^2} - \frac{\xi_{\mathrm{g}}^2 c_\ell^2}{m_{\mathrm{g}} c_{\mathrm{g}}^2}\right]^2 + 4\frac{\xi_{\mathrm{g}}^2 \xi_\ell^2}{m_{\mathrm{g}} m_\ell}}}{2\left[\frac{T_{\mathrm{g}} s_{\mathrm{g}}^2}{\bar{C}_{p,\mathrm{g}}} + \frac{T_\ell s_\ell^2}{\bar{C}_{p,\ell}} + \frac{\xi_{\mathrm{g}}^2}{m_{\mathrm{g}} c_{\mathrm{g}}^2} + \frac{\xi_\ell^2}{m_\ell c_\ell^2}\right]} \tag{105}
$$

Proposition 7. *The μ-model satisfies the weak subcharacteristic condition with respect to the basic model of Section 2, given only the physically fundamental conditions $\rho_k, C_{p,k}, T_k > 0$ for $k \in \{\mathrm{g}, \ell\}$, in the equilibrium state defined by (57).*

Proof. We first note that $c_{\mu,\pm}^2 \in \mathbb{R}$ on the given conditions, and that $c_{\mu,+}^2 \geq 0$. The product of the sound speeds may be written as

$$c_{\mu,+}^{-2} c_{\mu,-}^{-2} = c_{0,+}^{-2} c_{0,-}^{-2} + \mathcal{Z}_\mu^0, \quad \text{where} \quad \mathcal{Z}_\mu^0 = c_{\mathrm{g}}^{-2} c_\ell^{-2} \frac{\frac{\xi_{\mathrm{g}}^2}{m_{\mathrm{g}} c_{\mathrm{g}}^2} + \frac{\xi_\ell^2}{m_\ell c_\ell^2}}{\frac{T_{\mathrm{g}} s_{\mathrm{g}}^2}{\bar{C}_{p,\mathrm{g}}} + \frac{T_\ell s_\ell^2}{\bar{C}_{p,\ell}}}. \tag{106}$$

Given the conditions we have that $\mathcal{Z}_\mu^0 \geq 0$, and hence

$$0 \leq c_{\mu,+}^2 c_{\mu,-}^2 \leq c_{0,+}^2 c_{0,-}^2. \tag{107}$$

Therefore also $c_{0,-}^2$ is positive, and thus we have that $c_{0,\pm}$ are real and, by choice, positive.

Now, the product of the differences of the sound speeds may be written as

$$(c_{0,+}^2 - c_{\mu,+}^2)(c_{0,+}^2 - c_{\mu,-}^2)(c_{0,-}^2 - c_{\mu,+}^2)(c_{0,-}^2 - c_{\mu,-}^2) = -\mathcal{Q}_\mu^0, \tag{108}$$

where

$$\mathcal{Q}_\mu^0 = \left(c_{\mathrm{g}}^2 - c_\ell^2\right)^2 \frac{\xi_{\mathrm{g}}^2 \xi_\ell^2}{m_{\mathrm{g}} m_\ell} \left[\frac{T_{\mathrm{g}} s_{\mathrm{g}}^2}{\bar{C}_{p,\mathrm{g}}} + \frac{T_\ell s_\ell^2}{\bar{C}_{p,\ell}} + \frac{\xi_{\mathrm{g}}^2}{m_{\mathrm{g}} c_{\mathrm{g}}^2} + \frac{\xi_\ell^2}{m_\ell c_\ell^2}\right]^{-2}. \tag{109}$$

Clearly, with the given conditions, $\mathcal{Q}_\mu^0 \geq 0$, and hence the only ordering of sound speeds compatible with (107) and (108) is $0 \leq c_{\mu,-} \leq c_{0,-} \leq c_{\mu,+} \leq c_{0,+}$, which means that the weak subcharacteristic condition is satisfied. $\qquad\square$

Proposition 8. *The $v\mu$-model satisfies the subcharacteristic condition with respect to the μ-model, subject only to the physically fundamental conditions $\rho_k, C_{p,k}, T_k > 0$, for $k \in \{\mathrm{g}, \ell\}$.*

Proof. The sound speed in the $v\mu$-model is given by [40]

$$c_{v\mu}^2 = \frac{1}{\rho} \frac{m_{\mathrm{g}} c_{\mathrm{g}}^2 m_\ell c_\ell^2 \left(\frac{\xi_{\mathrm{g}}}{m_{\mathrm{g}} c_{\mathrm{g}}^2} + \frac{\xi_\ell}{m_\ell c_\ell^2}\right)^2 + \left(\frac{T_{\mathrm{g}} s_{\mathrm{g}}^2}{\bar{C}_{p,\mathrm{g}}} + \frac{T_\ell s_\ell^2}{\bar{C}_{p,\ell}}\right)\left(m_{\mathrm{g}} c_{\mathrm{g}}^2 + m_\ell c_\ell^2\right)}{\frac{T_{\mathrm{g}} s_{\mathrm{g}}^2}{\bar{C}_{p,\mathrm{g}}} + \frac{T_\ell s_\ell^2}{\bar{C}_{p,\ell}} + \frac{\xi_{\mathrm{g}}^2}{m_{\mathrm{g}} c_{\mathrm{g}}^2} + \frac{\xi_\ell^2}{m_\ell c_\ell^2}}. \tag{110}$$

We now consider the product of the differences in the sound speeds of the two models, which may be written as

$$(c_{\mu,+}^2 - c_{v\mu}^2)(c_{\mu,-}^2 - c_{v\mu}^2) = -\mathcal{Q}_{v\mu}^\mu, \tag{111}$$

where

$$\mathcal{Q}_{v\mu}^\mu = Y_{\mathrm{g}} Y_\ell \left[\frac{\left(\frac{T_{\mathrm{g}} s_{\mathrm{g}}^2}{m_{\mathrm{g}} C_{p,\mathrm{g}}} + \frac{T_\ell s_\ell^2}{m_\ell C_{p,\ell}}\right)(c_{\mathrm{g}}^2 - c_\ell^2) - \frac{\xi_{\mathrm{g}}^2 c_\ell^2}{m_{\mathrm{g}} c_{\mathrm{g}}^2} + \frac{\xi_\ell c_{\mathrm{g}}^2}{m_\ell c_\ell^2} + \left(\frac{1}{m_{\mathrm{g}}} - \frac{1}{m_\ell}\right)\xi_{\mathrm{g}} \xi_\ell}{\frac{T_{\mathrm{g}} s_{\mathrm{g}}^2}{\bar{C}_{p,\mathrm{g}}} + \frac{T_\ell s_\ell^2}{\bar{C}_{p,\ell}} + \frac{\xi_{\mathrm{g}}^2}{m_{\mathrm{g}} c_{\mathrm{g}}^2} + \frac{\xi_\ell^2}{m_\ell c_\ell^2}}\right]^2. \tag{112}$$

Clearly $\mathcal{Q}_{v\mu}^\mu \geq 0$. Hence, exactly one of the factors on the left hand side of (111) must be negative, which gives $c_{\mu,-} \leq c_{v\mu} \leq c_{\mu,+}$, i.e. the subcharacteristic condition is satisfied. $\qquad\square$

7. The $p\mu$-model

We now consider the model which arises when we impose instantaneous mechanical-chemical equilibrium, i.e. we let the relaxation parameters $\mathscr{I}, \mathscr{K} \to \infty$, which we expect corresponds to

$$p_{\mathrm{g}} = p_\ell \equiv p \quad \text{and} \quad \mu_{\mathrm{g}} = \mu_\ell \equiv \mu. \tag{113}$$

Simultaneously, $I_{\mathrm{g}} = \mathscr{I}(p_{\mathrm{g}} - p_\ell)$ and $K_{\mathrm{g}} = \mathscr{K}(\mu_\ell - \mu_{\mathrm{g}})$ should remain finite. We now seek explicit expressions for these terms in order to find the governing equations of the model.

In the following analysis we use the parameter set stated in Section 2 and therefore let the interfacial pressure jump $\Delta_{\mathrm{i}} p = p_{\mathrm{i}} - p = 0$. From (35) and (85) we have

$$\mathrm{D}_k p = -\frac{\rho_k c_k^2}{\alpha_k}\left(\tilde{I}_k + \partial_x \alpha_k v_k\right) + \frac{\xi_k + \frac{1}{2}\Gamma_k(\Delta_{\mathrm{i}} v_k)^2}{\alpha_k} K_k + \frac{\Gamma_k}{\alpha_k}\Delta_{\mathrm{i}} v_k M_k + \frac{\Gamma_k}{\alpha_k} H_k, \tag{114}$$

$$\mathrm{D}_k \mu = -\frac{\xi_k}{\alpha_k}\left(\tilde{I}_k + \partial_x \alpha_k v_k\right) + \left[\frac{\xi_k^2}{m_k c_k^2} + \frac{T_k s_k^2}{\bar{C}_{p,k}} + \frac{1}{2}(\Delta_{\mathrm{i}} v_k)^2 \psi_k\right] K_k + \psi_k \Delta_{\mathrm{i}} v_k M_k + \psi_k H_k. \tag{115}$$

where we have defined $\tilde{I}_k = I_k - v_{\mathrm{i}}\partial_x \alpha_k = \partial_t \alpha_k$.

Eqs. (114) and (115) evaluated for each phase now constitute a 4×4 system which is straightforward to solve for the four unknowns $\partial p/\partial t$, $\partial \mu/\partial t$, $\tilde{I}_{\mathrm{g}}$, and K_{g}, in terms of spatial derivatives and the remaining source terms. The final expressions for the latter two are

$$\tilde{I}_{\mathrm{g}} = -\mathcal{P}_p^{p\mu}(v_{\mathrm{g}} - v_\ell)\partial_x p - \mathcal{G}_p^{p\mu}(v_{\mathrm{g}} - v_\ell)\partial_x \mu - \Phi_{\mathrm{g}}\partial_x \alpha_{\mathrm{g}} v_{\mathrm{g}} + \Phi_\ell \partial_x \alpha_\ell v_\ell + I_v^{p\mu} M_{\mathrm{g}} + I_T^{p\mu} H_{\mathrm{g}}, \tag{116}$$

$$K_{\mathrm{g}} = -\mathcal{P}_\mu^{p\mu}(v_{\mathrm{g}} - v_\ell)\partial_x p - \mathcal{G}_\mu^{p\mu}(v_{\mathrm{g}} - v_\ell)\partial_x \mu - \mathcal{V}_{\mu,\mathrm{g}}^{p\mu}\partial_x \bar{v} + \mathcal{K}_v^{p\mu} M_{\mathrm{g}} + \mathcal{K}_T^{p\mu} H_{\mathrm{g}}, \tag{117}$$

where the coefficients are given in Appendix A.

7.1. Governing equations.

Inserting the expressions (116) and (117) into the basic model of Section 2, we are now in a position to state the full model. The mechanical–chemical equilibrium model may thus be formulated as follows.

- Conservation of mass: $\partial_t \rho + \partial_x (m_{\mathrm{g}} v_{\mathrm{g}} + m_\ell v_\ell) = 0$,
- Momentum balance:

$$\partial_t m_{\mathrm{g}} v_{\mathrm{g}} + \partial_x m_{\mathrm{g}} v_{\mathrm{g}}^2 + \left(\alpha_{\mathrm{g}} + v_{\mathrm{i}}\mathcal{P}_\mu^{p\mu}(v_{\mathrm{g}} - v_\ell)\right)\partial_x p + v_{\mathrm{i}}\mathcal{G}_\mu^{p\mu}(v_{\mathrm{g}} - v_\ell)\partial_x \mu + v_{\mathrm{i}}\mathcal{V}_{\mu,\mathrm{g}}^{p\mu}\partial_x \bar{v}$$
$$= (1 + v_{\mathrm{i}}\mathcal{K}_v^{p\mu})M_{\mathrm{g}} + v_{\mathrm{i}}\mathcal{K}_T^{p\mu} H_{\mathrm{g}}, \tag{118}$$

- Energy balance:

$$\partial_t E_{\mathrm{g}} + \partial_x E_{\mathrm{g}} v_{\mathrm{g}} + \left[\alpha_{\mathrm{g}} v_{\mathrm{g}} + \left(\left(\mu + \tfrac{1}{2}v_{\mathrm{i}}^2\right)\mathcal{P}_\mu^{p\mu} - p\mathcal{P}_p^{p\mu}\right)(v_{\mathrm{g}} - v_\ell)\right]\partial_x p$$
$$+ \left[\left(\mu + \tfrac{1}{2}v_{\mathrm{i}}^2\right)\mathcal{G}_\mu^{p\mu} - p\mathcal{G}_p^{p\mu}\right](v_{\mathrm{g}} - v_\ell)\partial_x \mu + \left[\left(\mu + \tfrac{1}{2}v_{\mathrm{i}}^2\right)\mathcal{V}_{\mu,\mathrm{g}}^{p\mu} + p\Phi_\ell\right]\partial_x \bar{v}$$
$$= \left[v_{\mathrm{i}} + \left(\mu + \tfrac{1}{2}v_{\mathrm{i}}^2\right)\mathcal{K}_v^{p\mu} - pI_v^{p\mu}\right]M_{\mathrm{g}} + \left[1 + \left(\mu + \tfrac{1}{2}v_{\mathrm{i}}^2\right)\mathcal{K}_T^{p\mu} - pI_T^{p\mu}\right]H_{\mathrm{g}}. \tag{119}$$

The momentum and energy equations for the liquid phase are found by phase symmetry. Note that, like other p-relaxed models, the $p\mu$-model is expected to be non-hyperbolic for nonzero difference in the velocity unless a regularising interfacial pressure p_{i} is defined.

7.2. **Wave velocities.** We now wish to write the system in a quasilinear form, in order to find the wave speeds of the system, in the homogeneous limit where we let the relaxation terms $\mathscr{M}, \mathscr{H} \to 0$. To this end, we will express the model in the vector of unknowns $\mathbf{u}_{p\mu} = [p, \mu, \bar{v}, v_{\mathrm{g}}, v_\ell]$. We therefore seek the evolution equations for the elements of $\mathbf{u}_{p\mu}$.

For the volume evolution, we find, using (24) and (116), that

$$\partial_t \alpha_{\mathrm{g}} + \mathcal{P}_p^{p\mu}(v_{\mathrm{g}} - v_\ell)\partial_x p + \mathcal{G}_p^{p\mu}(v_{\mathrm{g}} - v_\ell)\partial_x \mu + \Phi_{\mathrm{g}}\partial_x \alpha_{\mathrm{g}} v_{\mathrm{g}} - \Phi_\ell \partial_x \alpha_\ell v_\ell = 0, \quad (120)$$

For the volume-averaged velocity $\bar{v}$ we find, using (25), (116), (117) and (120), that

$$\partial_t \bar{v} + (\alpha_{\mathrm{g}}\rho_{\mathrm{g}}^{-1} + \alpha_\ell \rho_\ell^{-1} + P_{\bar{v}}^{p\mu}\varepsilon^2)\partial_x p + G_{\bar{v}}^{p\mu}\varepsilon^2 \partial_x \mu + \alpha_{\mathrm{g}}\varepsilon\partial_x v_{\mathrm{g}}$$
$$- \alpha_\ell \varepsilon \partial_x v_\ell + \left(\Phi_{\mathrm{g}} v_{\mathrm{g}} + \Phi_\ell v_\ell - V_{\bar{v},\mathrm{g}}^{p\mu}\varepsilon\right)\partial_x \bar{v} = 0, \quad (121)$$

where we have defined the shorthand coefficients $P_{\bar{v}}^{p\mu}, G_{\bar{v}}^{p\mu}, V_{\bar{v},\mathrm{g}}^{p\mu}$ (for which expressions are given in Appendix A), used $\varepsilon = v_{\mathrm{g}} - v_\ell$, and inserted $\beta_{\mathrm{g}} = 1 - \beta_\ell = \sqrt{T_\ell}/(\sqrt{T_{\mathrm{g}}} + \sqrt{T_\ell})$. Now, for the pressure and chemical potentials, we get from (114) and (115) that

$$\partial_t p + \left(\Psi_{\mathrm{g}}^p v_{\mathrm{g}} + \Psi_\ell^p v_\ell\right)\partial_x p + G_p^{p\mu}\varepsilon\partial_x \mu + V_p^{p\mu}\partial_x \bar{v} = 0, \quad (122)$$

$$\partial_t \mu + P_\mu^{p\mu}\varepsilon\partial_x p + \left(\Psi_{\mathrm{g}}^\mu v_{\mathrm{g}} + \Psi_\ell^\mu v_\ell\right)\partial_x \mu + V_\mu^{p\mu}\partial_x \bar{v} = 0. \quad (123)$$

Again, the coefficients are given in Appendix A.

The homogeneous system in a quasilinear form thus reads $\partial_t \mathbf{u}_{p\mu} + \mathbf{A}_{p\mu}\left(\mathbf{u}_{p\mu}\right)\partial_x \mathbf{u}_{p\mu} = 0$, where the system Jacobian is given by

$$\mathbf{A}_{p\mu} = \begin{bmatrix} \Psi_{\mathrm{g}}^p v_{\mathrm{g}} + \Psi_\ell^p v_\ell & G_p^{p\mu}\varepsilon & V_p^{p\mu} & 0 & 0 \\ P_\mu^{p\mu}\varepsilon & \Psi_{\mathrm{g}}^\mu v_{\mathrm{g}} + \Psi_\ell^\mu v_\ell & V_\mu^{p\mu} & 0 & 0 \\ \frac{\alpha_{\mathrm{g}}}{\rho_{\mathrm{g}}} + \frac{\alpha_\ell}{\rho_\ell} + P_{\bar{v}}^{p\mu}\varepsilon^2 & G_{\bar{v}}^{p\mu}\varepsilon^2 & \Phi_{\mathrm{g}} v_{\mathrm{g}} + \Phi_\ell v_\ell - V_{\bar{v},\mathrm{g}}^{p\mu}\varepsilon & \alpha_{\mathrm{g}}\varepsilon & -\alpha_\ell\varepsilon \\ \frac{1}{\rho_{\mathrm{g}}} - \frac{\beta_\ell \mathcal{P}_\mu^{p\mu}}{m_{\mathrm{g}}}\varepsilon^2 & -\frac{\beta_\ell \mathcal{G}_\mu^{p\mu}}{m_{\mathrm{g}}}\varepsilon^2 & -\frac{\beta_\ell \mathcal{V}_{\mu,\mathrm{g}}^{p\mu}}{m_{\mathrm{g}}}\varepsilon & v_{\mathrm{g}} & 0 \\ \frac{1}{\rho_\ell} - \frac{\beta_{\mathrm{g}} \mathcal{P}_\mu^{p\mu}}{m_\ell}\varepsilon^2 & -\frac{\beta_{\mathrm{g}} \mathcal{G}_\mu^{p\mu}}{m_\ell}\varepsilon^2 & \frac{\beta_{\mathrm{g}} \mathcal{V}_{\mu,\mathrm{g}}^{p\mu}}{m_\ell}\varepsilon & 0 & v_\ell \end{bmatrix}. \quad (124)$$

Obtaining the associated eigenvalues exactly by analytic means is again unfeasible, as the problem consists in finding the roots of a fifth-degree polynomial. We therefore expand in ε: $\mathbf{A}_{p\mu} = \mathbf{A}_{p\mu}^{(0)} + \varepsilon\mathbf{A}_{p\mu}^{(1)} + \varepsilon^2\mathbf{A}_{p\mu}^{(2)} + \ldots$, where it is assumed that the matrices $\mathbf{A}_{p\mu}^{(i)}$ are independent of ε. To the lowest order, where $\varepsilon \to 0$, taking $v = v_{\mathrm{g}} = v_\ell$, we get the matrix

$$\mathbf{A}_{p\mu}^{(0)} = \begin{bmatrix} v & 0 & V_p^{p\mu,(0)} & 0 & 0 \\ 0 & v & V_\mu^{p\mu,(0)} & 0 & 0 \\ \frac{\alpha_{\mathrm{g}}}{\rho_{\mathrm{g}}} + \frac{\alpha_\ell}{\rho_\ell} & 0 & v & 0 & 0 \\ \frac{1}{\rho_{\mathrm{g}}} & 0 & 0 & v & 0 \\ \frac{1}{\rho_\ell} & 0 & 0 & 0 & v \end{bmatrix}, \quad (125)$$

where the superscript "(0)" on the coefficients signifies the zeroth-order expansion in ε, such that

$$V_p^{p\mu,(0)} = \frac{\frac{T_g s_g^2}{\bar{C}_{p,g}} + \frac{T_\ell s_\ell^2}{\bar{C}_{p,\ell}}}{\left(\frac{\alpha_g}{\rho_g c_g^2} + \frac{\alpha_\ell}{\rho_\ell c_\ell^2}\right)\left(\frac{T_g s_g^2}{\bar{C}_{p,g}} + \frac{T_\ell s_\ell^2}{\bar{C}_{p,\ell}}\right) + \left(\frac{\xi_g}{\rho_g c_g^2} - \frac{\xi_\ell}{\rho_\ell c_\ell^2}\right)^2}. \tag{126}$$

The eigenvalues in the $p\mu$-model are, to the lowest order in ε,

$$\boldsymbol{\lambda}_{p\mu}^{(0)} = \{v - c_{p\mu}, v, v, v, v + c_{p\mu}\}, \tag{127}$$

where we have identified the sound speed $c_{p\mu}$ of the model, given by

$$c_{p\mu}^2 = \frac{\left(\frac{\alpha_g}{\rho_g} + \frac{\alpha_\ell}{\rho_\ell}\right)\left(\frac{T_g s_g^2}{\bar{C}_{p,g}} + \frac{T_\ell s_\ell^2}{\bar{C}_{p,\ell}}\right)}{\left(\frac{\alpha_g}{\rho_g c_g^2} + \frac{\alpha_\ell}{\rho_\ell c_\ell^2}\right)\left(\frac{T_g s_g^2}{\bar{C}_{p,g}} + \frac{T_\ell s_\ell^2}{\bar{C}_{p,\ell}}\right) + \left(\frac{\xi_g}{\rho_g c_g^2} - \frac{\xi_\ell}{\rho_\ell c_\ell^2}\right)^2}. \tag{128}$$

Proposition 9. *The $p\mu$-model satisfies the weak subcharacteristic condition with respect to the p-model, given only the physically fundamental conditions $\rho_k, C_{p,k}, T_k > 0$, for $k \in \{g, \ell\}$, in the equilibrium state defined by* (57).

Proof. From (62) and (128), we observe that we may write

$$c_{p\mu}^{-2} = c_p^{-2} + \mathcal{Z}_{p\mu}^p, \quad \text{where} \quad \mathcal{Z}_{p\mu}^p = \frac{\left(\frac{\xi_g}{\rho_g c_g^2} - \frac{\xi_\ell}{\rho_\ell c_\ell^2}\right)^2}{\left(\frac{\alpha_g}{\rho_g} + \frac{\alpha_\ell}{\rho_\ell}\right)\left(\frac{T_g s_g^2}{\bar{C}_{p,g}} + \frac{T_\ell s_\ell^2}{\bar{C}_{p,\ell}}\right)}. \tag{129}$$

Due to the given physical conditions, $\mathcal{Z}_{p\mu}^p \geq 0$, and hence $0 \leq c_{p\mu} \leq c_p$, i.e. the weak subcharacteristic condition is satisfied. $\square$

Proposition 10. *The $p\mu$-model satisfies the weak subcharacteristic condition with respect to the μ-model, under the physically fundamental conditions $\rho_k, C_{p,k}, T_k > 0$, for $k \in \{g, \ell\}$, in the equilibrium state defined by* (57).

Proof. Using the expressions (105) and (128) for the sound speeds in the two models, we may write

$$(c_{\mu,+}^2 - c_{p\mu}^2)(c_{\mu,-}^2 - c_{p\mu}^2) = -\mathcal{Q}_{p\mu}^\mu, \tag{130}$$

where

$$\mathcal{Q}_{p\mu}^\mu = \frac{\frac{\alpha_g \alpha_\ell}{\rho_g c_g^2 \rho_\ell c_\ell^2}\left(\frac{T_g s_g^2}{\bar{C}_{p,g}} + \frac{T_\ell s_\ell^2}{\bar{C}_{p,\ell}}\right)\left[\left(\frac{T_g s_g^2}{\bar{C}_{p,g}} + \frac{T_\ell s_\ell^2}{\bar{C}_{p,\ell}}\right)\left(c_g^2 - c_\ell^2\right) - \left(\frac{\xi_g}{\rho_g c_g^2} - \frac{\xi_\ell}{\rho_\ell c_\ell^2}\right)\left(\frac{\xi_g c_\ell^2}{\alpha_g} + \frac{\xi_\ell c_g^2}{\alpha_\ell}\right)\right]^2}{\left[\frac{T_g s_g^2}{\bar{C}_{p,g}} + \frac{T_\ell s_\ell^2}{\bar{C}_{p,\ell}} + \frac{\xi_g^2}{m_g c_g^2} + \frac{\xi_\ell^2}{m_\ell c_\ell^2}\right]\left[\left(\frac{\alpha_g}{\rho_g c_g^2} + \frac{\alpha_\ell}{\rho_\ell c_\ell^2}\right)\left(\frac{T_g s_g^2}{\bar{C}_{p,g}} + \frac{T_\ell s_\ell^2}{\bar{C}_{p,\ell}}\right) + \left(\frac{\xi_g}{\rho_g c_g^2} - \frac{\xi_\ell}{\rho_\ell c_\ell^2}\right)^2\right]^2}. \tag{131}$$

Clearly, on the given conditions, $\mathcal{Q}_{p\mu}^\mu \geq 0$. Therefore, exactly one factor on the left hand side of (130) is negative, and hence $c_{\mu,-} \leq c_{p\mu} \leq c_{\mu,+}$, so the weak subcharacteristic condition is satisfied. $\square$

Proposition 11. *The $vp\mu$-model satisfies the subcharacteristic condition with respect to the $p\mu$-model, given the physically fundamental conditions $\rho_k, C_{p,k}, T_k > 0$.*

Proof. The sound speed in the $vp\mu$-model is given by [20, 40]

$$c_{vp\mu}^2 = \frac{1}{\rho} \frac{\frac{T_g s_g^2}{\tilde{C}_{p,g}} + \frac{T_\ell s_\ell^2}{\tilde{C}_{p,\ell}}}{\left(\frac{\alpha_g}{\rho_g c_g^2} + \frac{\alpha_\ell}{\rho_\ell c_\ell^2}\right)\left(\frac{T_g s_g^2}{\tilde{C}_{p,g}} + \frac{T_\ell s_\ell^2}{\tilde{C}_{p,\ell}}\right) + \left(\frac{\xi_g}{\rho_g c_g^2} - \frac{\xi_\ell}{\rho_\ell c_\ell^2}\right)^2}. \tag{132}$$

Now, we may write

$$c_{vp\mu}^{-2} = c_{p\mu}^{-2} + \mathcal{Z}_{vp\mu}^{p\mu}, \qquad \text{where} \qquad \mathcal{Z}_{vp\mu}^{p\mu} = \frac{\alpha_g \alpha_\ell}{\rho_g \rho_\ell}\left(\rho_\ell - \rho_g\right)^2 c_{p\mu}^{-2}, \tag{133}$$

which is clearly positive, due to the given conditions. Thus, $0 \le c_{vp\mu} \le c_{p\mu}$, i.e. the subcharacteristic condition is satisfied. $\qquad\square$

Remark 3. *By direct comparison of* (128) *and* (132), *we find the ratio*

$$\frac{c_{p\mu}}{c_{vp\mu}} = \sqrt{\rho\left(\frac{\alpha_g}{\rho_g} + \frac{\alpha_\ell}{\rho_\ell}\right)}. \tag{134}$$

This is exactly the same ratio as has been shown to hold for other models associated with v-relaxation in the p-branch of the hierarchy [19, 44]. *We can thus extend the relation*

$$\frac{c_p}{c_{vp}} = \frac{c_{pT}}{c_{vpT}} = \frac{c_{pT\mu}}{c_{vpT\mu}} = \frac{c_{p\mu}}{c_{vp\mu}}, \tag{135}$$

by the newly obtained ratio (134) *between the sound speeds of the vpμ- and pμ-models.*

Proposition 12. *The pTμ-model satisfies the weak subcharacteristic condition with respect to the pμ-model, given the physically fundamental conditions $\rho_k, C_{p,k}, T > 0$, in the equilibrium state defined by* (57).

Proof. In the equilibrium state defined by the $pT\mu$-model, we have $T_g = T_\ell \equiv T$. The sound velocity in the $pT\mu$-model is given in [44], and may be rewritten as

$$c_{pT\mu}^2 = \frac{\frac{\alpha_g}{\rho_g} + \frac{\alpha_\ell}{\rho_\ell}}{\frac{\alpha_g}{\rho_g c_g^2} + \frac{\alpha_\ell}{\rho_\ell c_\ell^2} + \tilde{C}_{p,g}T\left[\frac{1}{\Delta h}\left(\frac{1}{\rho_\ell} - \frac{1}{\rho_g}\right) + \frac{\Gamma_g}{\rho_g c_g^2}\right]^2 + \tilde{C}_{p,\ell}T\left[\frac{1}{\Delta h}\left(\frac{1}{\rho_g} - \frac{1}{\rho_\ell}\right) - \frac{\Gamma_\ell}{\rho_\ell c_\ell^2}\right]^2}, \tag{136}$$

where we have introduced the enthalpy difference $\Delta h = h_g - h_\ell$.

We may reorganize the last equality in (135) to yield

$$\frac{c_{p\mu}}{c_{pT\mu}} = \frac{c_{vp\mu}}{c_{vpT\mu}}. \tag{137}$$

Flåtten and Lund [20] showed that the subcharacteristic condition is satisfied between the models on the right hand side, i.e. that $0 \le c_{vpT\mu} \le c_{vp\mu}$. The same must hold for the models on the left hand side of (137), i.e. $0 \le c_{pT\mu} \le c_{p\mu}$, and hence the weak subcharacteristic condition is satisfied. In particular, we may write the sound speed as

$$c_{pT\mu}^{-2} = c_{p\mu}^{-2} + \mathcal{Z}_{pT\mu}^{p\mu}, \tag{138}$$

where

$$\mathcal{Z}_{pT\mu}^{p\mu} = \tilde{C}_{p,g}\tilde{C}_{p,\ell}T \frac{\left[\frac{1}{\Delta h}\left(\frac{1}{\rho_\ell} - \frac{1}{\rho_g}\right)\left(\frac{s_g}{\tilde{C}_{p,g}} + \frac{s_\ell}{\tilde{C}_{p,\ell}}\right) + \frac{\Gamma_g}{\rho_g c_g^2}\frac{s_\ell}{\tilde{C}_{p,\ell}} + \frac{\Gamma_\ell}{\rho_\ell c_\ell^2}\frac{s_g}{\tilde{C}_{p,g}}\right]^2}{\left(\frac{\alpha_g}{\rho_g} + \frac{\alpha_\ell}{\rho_\ell}\right)\left(\frac{s_g^2}{\tilde{C}_{p,g}} + \frac{s_\ell^2}{\tilde{C}_{p,\ell}}\right)}. \tag{139}$$

Clearly, $\mathcal{Z}_{pT\mu}^{p\mu} \geq 0$ based on the given conditions. $\qquad\qquad\square$

8. The $T\mu$-model

We now investigate the model which arises when we assume instantaneous thermal-chemical equilibrium, i.e. let the relaxation parameters $\mathcal{K}, \mathcal{H} \to \infty$, which expectedly corresponds to

$$T_{\mathrm{g}} = T_\ell \equiv T \quad \text{and} \quad \mu_{\mathrm{g}} = \mu_\ell \equiv \mu. \tag{140}$$

The products $H_{\mathrm{g}} = \mathcal{H}(T_\ell - T_{\mathrm{g}})$ and $K_{\mathrm{g}} = \mathcal{K}(\mu_\ell - \mu_{\mathrm{g}})$ remain finite, and may be expressed in terms of spatial derivatives and remaining source terms. In the forthcoming, we seek explicit expressions for these terms to insert into the basic model of Section 2.

The equilibrium conditions are contained in (68) and (85). These may be combined to yield

$$K_{\mathrm{g}} = -\mathcal{A}_\mu^{T\mu}\partial_x\alpha_{\mathrm{g}} - \mathcal{G}_\mu^{T\mu}\varepsilon\partial_x\mu - \mathcal{T}_\mu^{T\mu}\varepsilon\partial_x T - \mathcal{V}_{\mu,\mathrm{g}}^{T\mu}\partial_x\alpha_{\mathrm{g}}v_{\mathrm{g}} + \mathcal{V}_{\mu,\ell}^{T\mu}\partial_x\alpha_\ell v_\ell + \mathcal{K}_p^{T\mu}\tilde{I}_{\mathrm{g}} + \mathcal{K}_v^{T\mu}\varepsilon M_{\mathrm{g}} \tag{141}$$

where the coefficients are given in Appendix B.

8.1. **Governing equations.** We are now in a position to state the $T\mu$-model in its entirety, by inserting (141) into the basic model of Section 2. The model can be expressed by the following equation set:

- Volume advection: $\partial_t\alpha_{\mathrm{g}} + v_{\mathrm{i}}\partial_x\alpha_{\mathrm{g}} = I_{\mathrm{g}}$,
- Conservation of mass: $\partial_t\rho + \partial_x\left(\alpha_{\mathrm{g}}\rho_{\mathrm{g}}v_{\mathrm{g}} + \alpha_\ell\rho_\ell v_\ell\right) = 0$,
- Conservation of momentum:

$$\partial_t\alpha_{\mathrm{g}}\rho_{\mathrm{g}}v_{\mathrm{g}} + \partial_x(\alpha_{\mathrm{g}}\rho_{\mathrm{g}}v_{\mathrm{g}}^2 + \alpha_{\mathrm{g}}p_{\mathrm{g}})$$
$$+ v_{\mathrm{i}}\left[\mathcal{G}_\mu^{T\mu}(v_{\mathrm{g}} - v_\ell)\partial_x\mu + \mathcal{T}_\mu^{T\mu}(v_{\mathrm{g}} - v_\ell)\partial_x T + \mathcal{V}_{\mu,\mathrm{g}}^{T\mu}\partial_x\alpha_{\mathrm{g}}v_{\mathrm{g}} - \mathcal{V}_{\mu,\ell}^{T\mu}\partial_x\alpha_\ell v_\ell\right]$$
$$+ \left(v_{\mathrm{i}}^2\left(\mathcal{V}_{\mu,\mathrm{g}}^{T\mu} + \mathcal{V}_{\mu,\ell}^{T\mu}\right) - p_{\mathrm{i}}\right)\partial_x\alpha_{\mathrm{g}} = v_{\mathrm{i}}\mathcal{K}_p^{T\mu}I_{\mathrm{g}} + \left(1 + v_{\mathrm{i}}\mathcal{K}_v^{T\mu}(v_{\mathrm{g}} - v_\ell)\right)M_{\mathrm{g}}, \quad (142)$$

- Conservation of energy: $\partial_t E + \partial_x\left(E_{\mathrm{g}}v_{\mathrm{g}} + E_\ell v_\ell + \alpha_{\mathrm{g}}v_{\mathrm{g}}p_{\mathrm{g}} + \alpha_\ell v_\ell p_\ell\right) = 0$.

8.2. **Wave velocities.** We now seek the wave velocities of the model in the homogeneous limit, where $\mathcal{I}, \mathcal{M} \to 0$. As usual, we are interested in the zeroth-order expansion in $\varepsilon = v_{\mathrm{g}} - v_\ell$.[3] We may therefore directly evaluate the evolution equations in this limit, and take $v_{\mathrm{g}} = v_\ell = v$ if they are outside the differential operator.

After some tedious, but fairly straightforward algebra, we find that to the lowest order in ε, the wave velocities of the $T\mu$-model are given by

$$\boldsymbol{\lambda}_{T\mu}^{(0)} = \{v - c_{T\mu,+}, v - c_{T\mu,-}, v, v + c_{T\mu,-}, v + c_{T\mu,+}\}. \tag{143}$$

---

[3]Strictly speaking, exact eigenvalues may be found analytically in this model, since noting that α_{g} is a characteristic variable reduces the eigenvalue problem to finding the solutions of a fourth-degree polynomial, which is analytically tractable.

Herein, $c_{T\mu,\pm}$ are the sound speeds of this model, which may be expressed by

$$
\begin{aligned}
c_{T\mu,\pm}^2 = \tfrac{1}{2}\Bigg\{ & \frac{\Delta h^2 m_{\mathrm g} m_\ell \left(c_{\mathrm g}^2 + c_\ell^2\right)}{\tilde C_{p,\mathrm g}\tilde C_{p,\ell}T^2 c_{\mathrm g}^2 c_\ell^2} + \frac{m_\ell + m_{\mathrm g}\left(1+\frac{\Gamma_\ell}{c_\ell^2}\Delta h\right)^2}{\tilde C_{p,\mathrm g}T} + \frac{m_{\mathrm g} + m_\ell\left(1-\frac{\Gamma_{\mathrm g}}{c_{\mathrm g}^2}\Delta h\right)^2}{\tilde C_{p,\ell}T} \pm \\
& \left[\left(\frac{\Delta h^2 m_{\mathrm g} m_\ell\left(c_{\mathrm g}^2 - c_\ell^2\right)}{\tilde C_{p,\mathrm g}\tilde C_{p,\ell}T^2 c_{\mathrm g}^2 c_\ell^2} - \frac{m_\ell - m_{\mathrm g}\left(1+\frac{\Gamma_\ell}{c_\ell^2}\Delta h\right)^2}{\tilde C_{p,\mathrm g}T} + \frac{m_{\mathrm g} - m_\ell\left(1-\frac{\Gamma_{\mathrm g}}{c_{\mathrm g}^2}\Delta h\right)^2}{\tilde C_{p,\ell}T}\right)^2 + 4 m_{\mathrm g} m_\ell\left(\frac{1+\frac{\Gamma_\ell}{c_\ell^2}\Delta h}{\tilde C_{p,\mathrm g}T} + \frac{1-\frac{\Gamma_{\mathrm g}}{c_{\mathrm g}^2}\Delta h}{\tilde C_{p,\ell}T}\right)^2\right]^{\frac12}\Bigg\} \\
& \times \left[\frac{\Delta h^2 m_{\mathrm g} m_\ell}{\tilde C_{p,\mathrm g}\tilde C_{p,\ell}T^2 c_{\mathrm g}^2 c_\ell^2} + \frac{\frac{m_\ell}{c_\ell^2} + \frac{m_{\mathrm g}}{c_{\mathrm g}^2}\left(1+\frac{\Gamma_\ell}{c_\ell^2}\Delta h\right)^2}{\tilde C_{p,\mathrm g}T} + \frac{\frac{m_{\mathrm g}}{c_{\mathrm g}^2} + \frac{m_\ell}{c_\ell^2}\left(1-\frac{\Gamma_{\mathrm g}}{c_{\mathrm g}^2}\Delta h\right)^2}{\tilde C_{p,\ell}T} + \left(\frac{\Gamma_\ell}{c_\ell^2} - \frac{\Gamma_{\mathrm g}}{c_{\mathrm g}^2} - \frac{\Gamma_{\mathrm g}\Gamma_\ell}{c_{\mathrm g}^2 c_\ell^2}\Delta h\right)^2\right]^{-1}.
\end{aligned}
\tag{144}
$$

Proposition 13. *The $T\mu$-model satisfies the weak subcharacteristic condition with respect to the T-model, given the physically fundamental conditions $\rho_k, C_{p,k}, T > 0$, in the equilibrium state defined by (57).*

Proof. We may write

$$
\left(c_{T,+}^2 - c_{T\mu,+}^2\right)\left(c_{T,+}^2 - c_{T\mu,-}^2\right)\left(c_{T,-}^2 - c_{T\mu,+}^2\right)\left(c_{T,-}^2 - c_{T\mu,-}^2\right) = -\mathcal{Q}_{T\mu}^T, \tag{145}
$$

where

$$
\begin{aligned}
\mathcal{Q}_{T\mu}^T = m_{\mathrm g} m_\ell \Bigg[& \left(\frac{1}{\tilde C_{p,\ell}T} + \frac{1+\Gamma_\ell c_\ell^{-2}\Delta h}{\tilde C_{p,\mathrm g}T}\right)\left(\frac{1}{\tilde C_{p,\mathrm g}T} + \frac{1-\Gamma_{\mathrm g} c_{\mathrm g}^{-2}\Delta h}{\tilde C_{p,\ell}T} + \frac{\Gamma_\ell}{m_\ell}\left(\frac{\Gamma_\ell}{c_\ell^2} - \frac{\Gamma_{\mathrm g}}{c_{\mathrm g}^2} - \frac{\Gamma_{\mathrm g}\Gamma_\ell}{c_{\mathrm g}^2 c_\ell^2}\Delta h\right)\right)c_{\mathrm g}^2 \\
& - \left(\frac{1}{\tilde C_{p,\mathrm g}T} + \frac{1-\Gamma_{\mathrm g} c_{\mathrm g}^{-2}\Delta h}{\tilde C_{p,\ell}T}\right)\left(\frac{1}{\tilde C_{p,\ell}T} + \frac{1+\Gamma_\ell c_\ell^{-2}\Delta h}{\tilde C_{p,\mathrm g}T} - \frac{\Gamma_{\mathrm g}}{m_{\mathrm g}}\left(\frac{\Gamma_\ell}{c_\ell^2} - \frac{\Gamma_{\mathrm g}}{c_{\mathrm g}^2} - \frac{\Gamma_{\mathrm g}\Gamma_\ell}{c_{\mathrm g}^2 c_\ell^2}\Delta h\right)\right)c_\ell^2 \Bigg]^2 \\
& \times \Bigg[\left(\frac{\Delta h^2 m_{\mathrm g} m_\ell}{\tilde C_{p,\mathrm g}\tilde C_{p,\ell}T^2 c_{\mathrm g}^2 c_\ell^2} + \frac{1}{\tilde C_{p,\mathrm g}T}\left(\frac{m_\ell}{c_\ell^2} + \frac{m_{\mathrm g}}{c_{\mathrm g}^2}\left(1+\frac{\Gamma_\ell}{c_\ell^2}\Delta h\right)^2\right) + \frac{1}{\tilde C_{p,\ell}T}\left(\frac{m_{\mathrm g}}{c_{\mathrm g}^2} + \frac{m_\ell}{c_\ell^2}\left(1-\frac{\Gamma_{\mathrm g}}{c_{\mathrm g}^2}\Delta h\right)^2\right)\right. \\
& \left.+ \left(\frac{\Gamma_\ell}{c_\ell^2} - \frac{\Gamma_{\mathrm g}}{c_{\mathrm g}^2} - \frac{\Gamma_{\mathrm g}\Gamma_\ell}{c_{\mathrm g}^2 c_\ell^2}\Delta h\right)^2\right)\left(\frac{1}{\tilde C_{p,\mathrm g}T} + \frac{1}{\tilde C_{p,\ell}T} + \frac{\Gamma_\ell^2}{m_\ell c_\ell^2} + \frac{\Gamma_{\mathrm g}^2}{m_{\mathrm g} c_{\mathrm g}^2}\right)\Bigg]^{-2}. \tag{146}
\end{aligned}
$$

Moreover, we may write

$$
\left(c_{T,+}^2 + c_{T,-}^2\right) - \left(c_{T\mu,+}^2 + c_{T\mu,-}^2\right) = \mathscr{Z}_{T\mu}^T \tag{147}
$$

where

$$
\begin{aligned}
\mathscr{Z}_{T\mu}^T = \Bigg[& \left(\frac{1}{\tilde C_{p,\mathrm g}T} + \frac{1-\frac{\Gamma_{\mathrm g}}{c_{\mathrm g}^2}\Delta h}{\tilde C_{p,\ell}T} + \frac{\Gamma_\ell}{m_\ell}\left(\frac{\Gamma_\ell}{c_\ell^2} - \frac{\Gamma_{\mathrm g}}{c_{\mathrm g}^2} - \frac{\Gamma_{\mathrm g}\Gamma_\ell}{c_{\mathrm g}^2 c_\ell^2}\Delta h\right)\right)\frac{m_\ell c_{\mathrm g}^2}{c_\ell^2} \\
& + \left(\frac{1}{\tilde C_{p,\ell}T} + \frac{1+\frac{\Gamma_\ell}{c_\ell^2}\Delta h}{\tilde C_{p,\mathrm g}T} - \frac{\Gamma_{\mathrm g}}{m_{\mathrm g}}\left(\frac{\Gamma_\ell}{c_\ell^2} - \frac{\Gamma_{\mathrm g}}{c_{\mathrm g}^2} - \frac{\Gamma_{\mathrm g}\Gamma_\ell}{c_{\mathrm g}^2 c_\ell^2}\Delta h\right)\right)\frac{m_{\mathrm g} c_\ell^2}{c_{\mathrm g}^2}\Bigg] \\
& \times \Bigg[\left(\frac{\Delta h^2 m_{\mathrm g} m_\ell}{\tilde C_{p,\mathrm g}\tilde C_{p,\ell}T^2 c_{\mathrm g}^2 c_\ell^2} + \frac{\frac{m_\ell}{c_\ell^2} + \frac{m_{\mathrm g}}{c_{\mathrm g}^2}\left(1+\frac{\Gamma_\ell}{c_\ell^2}\Delta h\right)^2}{\tilde C_{p,\mathrm g}T} + \frac{\frac{m_{\mathrm g}}{c_{\mathrm g}^2} + \frac{m_\ell}{c_\ell^2}\left(1-\frac{\Gamma_{\mathrm g}}{c_{\mathrm g}^2}\Delta h\right)^2}{\tilde C_{p,\ell}T} + \left(\frac{\Gamma_\ell}{c_\ell^2} - \frac{\Gamma_{\mathrm g}}{c_{\mathrm g}^2} - \frac{\Gamma_{\mathrm g}\Gamma_\ell}{c_{\mathrm g}^2 c_\ell^2}\Delta h\right)^2\right) \\
& \times \left(\frac{1}{\tilde C_{p,\mathrm g}T} + \frac{1}{\tilde C_{p,\ell}T} + \frac{\Gamma_\ell^2}{m_\ell c_\ell^2} + \frac{\Gamma_{\mathrm g}^2}{m_{\mathrm g} c_{\mathrm g}^2}\right)\Bigg]^{-1}. \tag{148}
\end{aligned}
$$

Clearly, $\mathcal{Z}_{T\mu}^T \geq 0$ and $\mathcal{Q}_{T\mu}^T \geq 0$ on grounds of the given conditions. The only possible ordering of sound speeds is thus $0 \leq c_{T\mu,-} \leq c_{T,-} \leq c_{T\mu,+} \leq c_{T,+}$, i.e. the weak subcharacteristic condition is satisfied. $\qquad\square$

Proposition 14. *The $T\mu$-model satisfies the weak subcharacteristic condition with respect to the μ-model, given the physically fundamental conditions $\rho_k, C_{p,k}, T > 0$, in the equilibrium state defined by* (57).

Proof. We note that we may write

$$\left(c_{\mu,+}^2 - c_{T\mu,+}^2\right)\left(c_{\mu,+}^2 - c_{T\mu,-}^2\right)\left(c_{\mu,-}^2 - c_{T\mu,+}^2\right)\left(c_{\mu,-}^2 - c_{T\mu,-}^2\right) = -\mathcal{Q}_{T\mu}^\mu, \qquad (149)$$

where

$$
\mathcal{Q}_{T\mu}^\mu = m_{\mathrm{g}} m_\ell \left[\left(\frac{s_\ell}{\tilde{C}_{p,\ell}} + \frac{s_{\mathrm{g}}\left(1+\frac{\Gamma_\ell}{c_\ell^2}\Delta h\right)}{\tilde{C}_{p,\mathrm{g}}} \right)\left(\frac{s_{\mathrm{g}}}{\tilde{C}_{p,\mathrm{g}}} + \frac{s_\ell\left(1-\frac{\Gamma_{\mathrm{g}}}{c_{\mathrm{g}}^2}\Delta h\right)}{\tilde{C}_{p,\ell}} - \left(\frac{\Gamma_\ell}{c_\ell^2} - \frac{\Gamma_{\mathrm{g}}}{c_{\mathrm{g}}^2} - \frac{\Gamma_{\mathrm{g}}\Gamma_\ell}{c_{\mathrm{g}}^2 c_\ell^2}\Delta h\right)\frac{\xi_\ell}{m_\ell} \right) c_{\mathrm{g}}^2 \right.
$$
$$
\left. - \left(\frac{s_{\mathrm{g}}}{\tilde{C}_{p,\mathrm{g}}} + \frac{s_\ell\left(1-\frac{\Gamma_{\mathrm{g}}}{c_{\mathrm{g}}^2}\Delta h\right)}{\tilde{C}_{p,\ell}} \right)\left(\frac{s_\ell}{\tilde{C}_{p,\ell}} + \frac{s_{\mathrm{g}}\left(1+\frac{\Gamma_\ell}{c_\ell^2}\Delta h\right)}{\tilde{C}_{p,\mathrm{g}}} + \left(\frac{\Gamma_\ell}{c_\ell^2} - \frac{\Gamma_{\mathrm{g}}}{c_{\mathrm{g}}^2} - \frac{\Gamma_{\mathrm{g}}\Gamma_\ell}{c_{\mathrm{g}}^2 c_\ell^2}\Delta h\right)\frac{\xi_{\mathrm{g}}}{m_{\mathrm{g}}} \right) c_\ell^2 \right]^2
$$
$$
\times \left[\left(\frac{\Delta h^2 m_{\mathrm{g}} m_\ell}{\tilde{C}_{p,\mathrm{g}}\tilde{C}_{p,\ell}T^2 c_{\mathrm{g}}^2 c_\ell^2} + \frac{1}{\tilde{C}_{p,\mathrm{g}}T}\left(\frac{m_\ell}{c_\ell^2} + \frac{m_{\mathrm{g}}}{c_{\mathrm{g}}^2}\left(1+\frac{\Gamma_\ell}{c_\ell^2}\Delta h\right)^2 \right) + \frac{1}{\tilde{C}_{p,\ell}T}\left(\frac{m_{\mathrm{g}}}{c_{\mathrm{g}}^2} + \frac{m_\ell}{c_\ell^2}\left(1-\frac{\Gamma_{\mathrm{g}}}{c_{\mathrm{g}}^2}\Delta h\right)^2 \right) \right.\right.
$$
$$
\left.\left. + \left(\frac{\Gamma_\ell}{c_\ell^2} - \frac{\Gamma_{\mathrm{g}}}{c_{\mathrm{g}}^2} - \frac{\Gamma_{\mathrm{g}}\Gamma_\ell}{c_{\mathrm{g}}^2 c_\ell^2}\Delta h\right)^2 \right)\left(\frac{Ts_{\mathrm{g}}^2}{\tilde{C}_{p,\mathrm{g}}} + \frac{Ts_\ell^2}{\tilde{C}_{p,\ell}} + \frac{\xi_{\mathrm{g}}^2}{m_{\mathrm{g}}c_{\mathrm{g}}^2} + \frac{\xi_\ell^2}{m_\ell c_\ell^2} \right) \right]^{-2}. \qquad (150)
$$

Now, we may also write $\left(c_{\mu,+}^2 + c_{\mu,-}^2\right) - \left(c_{T\mu,+}^2 + c_{T\mu,-}^2\right) = \mathcal{Z}_{T\mu}^\mu$, where

$$
\mathcal{Z}_{T\mu}^\mu = \left\{ \left[\frac{s_{\mathrm{g}}}{\tilde{C}_{p,\mathrm{g}}} + \frac{s_\ell\left(1-\frac{\Gamma_{\mathrm{g}}}{c_{\mathrm{g}}^2}\Delta h\right)}{\tilde{C}_{p,\ell}} - \left(\frac{\Gamma_\ell}{c_\ell^2} - \frac{\Gamma_{\mathrm{g}}}{c_{\mathrm{g}}^2} - \frac{\Gamma_{\mathrm{g}}\Gamma_\ell}{c_{\mathrm{g}}^2 c_\ell^2}\Delta h\right)\frac{\xi_\ell}{m_\ell} \right]^2 \frac{m_\ell c_{\mathrm{g}}^2}{c_\ell^2} \right.
$$
$$
\left. + \left[\frac{s_\ell}{\tilde{C}_{p,\ell}} + \frac{s_{\mathrm{g}}\left(1+\frac{\Gamma_\ell}{c_\ell^2}\Delta h\right)}{\tilde{C}_{p,\mathrm{g}}} + \left(\frac{\Gamma_\ell}{c_\ell^2} - \frac{\Gamma_{\mathrm{g}}}{c_{\mathrm{g}}^2} - \frac{\Gamma_{\mathrm{g}}\Gamma_\ell}{c_{\mathrm{g}}^2 c_\ell^2}\Delta h\right)\frac{\xi_{\mathrm{g}}}{m_{\mathrm{g}}} \right]^2 \frac{m_{\mathrm{g}} c_\ell^2}{c_{\mathrm{g}}^2} \right\}
$$
$$
\times \left[\left(\frac{\Delta h^2 m_{\mathrm{g}} m_\ell}{\tilde{C}_{p,\mathrm{g}}\tilde{C}_{p,\ell}T^2 c_{\mathrm{g}}^2 c_\ell^2} + \frac{1}{\tilde{C}_{p,\mathrm{g}}T}\left(\frac{m_\ell}{c_\ell^2} + \frac{m_{\mathrm{g}}}{c_{\mathrm{g}}^2}\left(1+\frac{\Gamma_\ell}{c_\ell^2}\Delta h\right)^2 \right) \right.\right.
$$
$$
\left.\left. + \frac{1}{\tilde{C}_{p,\ell}T}\left(\frac{m_{\mathrm{g}}}{c_{\mathrm{g}}^2} + \frac{m_\ell}{c_\ell^2}\left(1-\frac{\Gamma_{\mathrm{g}}}{c_{\mathrm{g}}^2}\Delta h\right)^2 \right) + \left(\frac{\Gamma_\ell}{c_\ell^2} - \frac{\Gamma_{\mathrm{g}}}{c_{\mathrm{g}}^2} - \frac{\Gamma_{\mathrm{g}}\Gamma_\ell}{c_{\mathrm{g}}^2 c_\ell^2}\Delta h\right)^2 \right)\left(\frac{Ts_{\mathrm{g}}^2}{\tilde{C}_{p,\mathrm{g}}} + \frac{Ts_\ell^2}{\tilde{C}_{p,\ell}} + \frac{\xi_{\mathrm{g}}^2}{m_{\mathrm{g}}c_{\mathrm{g}}^2} + \frac{\xi_\ell^2}{m_\ell c_\ell^2} \right) \right]^{-1}.
$$
$$(151)$$

Clearly, $\mathcal{Q}_{T\mu}^\mu \geq 0$ and $\mathcal{Z}_{T\mu}^\mu \geq 0$ for the given conditions. The only possible ordering of the sound speeds is therefore $0 \leq c_{T\mu,-} \leq c_{\mu,-} \leq c_{T\mu,+} \leq c_{\mu,+}$, i.e. the eigenvalues of the relaxed model are interlaced between the eigenvalues of the parent model, and the weak subcharacteristic condition is satisfied. $\qquad\square$

Proposition 15. *The $vT\mu$-model satisfies the subcharacteristic condition with respect to the $T\mu$-model, given the physically fundamental conditions $\rho_k, C_{p,k}, T > 0$.*

Proof. The sound speed in the $vT\mu$-model is given by [40]

$$c_{vT\mu}^2 = \frac{\frac{\Delta h^2 m_g m_\ell c_v^2}{\tilde{C}_{p,g}\tilde{C}_{p,\ell}T^2 c_g^2 c_\ell^2 \rho} + \frac{\left(\rho + m_g \frac{\Gamma_\ell}{c_\ell^2}\Delta h\right)^2}{\tilde{C}_{p,g}T} + \frac{\left(\rho - m_\ell \frac{\Gamma_g}{c_g^2}\Delta h\right)^2}{\tilde{C}_{p,\ell}T}}{\frac{\Delta h^2 m_g m_\ell}{\tilde{C}_{p,g}\tilde{C}_{p,\ell}T^2 c_g^2 c_\ell^2} + \frac{\frac{m_\ell}{c_\ell^2} + \frac{m_g}{c_g^2}\left(1+\frac{\Gamma_\ell}{c_\ell^2}\Delta h\right)^2}{\tilde{C}_{p,g}T} + \frac{\frac{m_g}{c_g^2} + \frac{m_\ell}{c_\ell^2}\left(1-\frac{\Gamma_g}{c_g^2}\Delta h\right)^2}{\tilde{C}_{p,\ell}T} + \left(\frac{\Gamma_\ell}{c_\ell^2} - \frac{\Gamma_g}{c_g^2} - \frac{\Gamma_g\Gamma_\ell}{c_g^2 c_\ell^2}\Delta h\right)^2}$$

(152)

We may now write the product of the differences between the sound speeds as

$$\left(c_{T\mu,+}^2 - c_{vT\mu}^2\right)\left(c_{T\mu,-}^2 - c_{vT\mu}^2\right) = -\mathcal{Q}_{vT\mu}^{T\mu},$$

(153)

where

$$\mathcal{Q}_{vT\mu}^{T\mu} = Y_g Y_\ell \left[\frac{\frac{\Delta h^2 m_g m_\ell (c_g^2 - c_\ell^2)}{\tilde{C}_{p,g}\tilde{C}_{p,\ell}T^2 c_g^2 c_\ell^2} + \frac{\Gamma_\ell \Delta h}{\tilde{C}_{p,g}Tc_\ell^2}\left(m_\ell + m_g\left(1+\frac{\Gamma_\ell}{c_\ell^2}\Delta h\right)\right) + \frac{\Gamma_g \Delta h}{\tilde{C}_{p,\ell}Tc_g^2}\left(m_g + m_\ell\left(1-\frac{\Gamma_g}{c_g^2}\Delta h\right)\right)}{\frac{\Delta h^2 m_g m_\ell}{\tilde{C}_{p,g}\tilde{C}_{p,\ell}T^2 c_g^2 c_\ell^2} + \frac{\frac{m_\ell}{c_\ell^2} + \frac{m_g}{c_g^2}\left(1+\frac{\Gamma_\ell}{c_\ell^2}\Delta h\right)^2}{\tilde{C}_{p,g}T} + \frac{\frac{m_g}{c_g^2} + \frac{m_\ell}{c_\ell^2}\left(1-\frac{\Gamma_g}{c_g^2}\Delta h\right)^2}{\tilde{C}_{p,\ell}T} + \left(\frac{\Gamma_\ell}{c_\ell^2} - \frac{\Gamma_g}{c_g^2} - \frac{\Gamma_g\Gamma_\ell}{c_g^2 c_\ell^2}\Delta h\right)^2}\right]^2.$$

(154)

Due to the given conditions, it is clear that $\mathcal{Q}_{vT\mu}^{T\mu} \geq 0$, and thus exactly one of the factors on the left hand side of (153) is negative. Hence, the sound speeds must be ordered as $c_{T\mu,-} \leq c_{vT\mu} \leq c_{T\mu,+}$, i.e. the subcharacteristic condition is satisfied. $\square$

Proposition 16. *The $pT\mu$-model satisfies the weak subcharacteristic condition with respect to the $T\mu$-model, subject to the physically fundamental conditions $\rho_k, C_{p,k}, T > 0$, in the equilibrium state defined by* (57).

Proof. The sound speed in the $pT\mu$-model is stated in (136). We note that we may write

$$\left(c_{T\mu,+}^2 - c_{pT\mu}^2\right)\left(c_{T\mu,-}^2 - c_{pT\mu}^2\right) = -\mathcal{Q}_{pT\mu}^{T\mu},$$

(155)

where

$$\mathcal{Q}_{pT\mu}^{T\mu} = \frac{\tilde{C}_{p,g}\tilde{C}_{p,\ell}T^2}{\Delta h^2 \rho_g^2 \rho_\ell^2}$$

$$\times \left[\frac{\Delta h^2 m_g m_\ell}{\tilde{C}_{p,g}\tilde{C}_{p,\ell}T^2 c_g^2 c_\ell^2}(c_g^2 - c_\ell^2) + \frac{\rho_g \rho_\ell}{\tilde{C}_{p,\ell}T}\left(\frac{1}{\rho_\ell} - \frac{1-\frac{\Gamma_g}{c_g^2}\Delta h}{\rho_g}\right)\left(1 - \alpha_\ell \frac{\Gamma_g}{c_g^2}\Delta h\right) - \frac{\rho_g \rho_\ell}{\tilde{C}_{p,g}T}\left(\frac{1}{\rho_g} - \frac{1+\frac{\Gamma_\ell}{c_\ell^2}\Delta h}{\rho_\ell}\right)\left(1 + \alpha_g \frac{\Gamma_\ell}{c_\ell^2}\Delta h\right)\right]^2$$

$$\times \left[\frac{\Delta h^2 m_g m_\ell}{\tilde{C}_{p,g}\tilde{C}_{p,\ell}T^2 c_g^2 c_\ell^2} + \frac{\frac{m_\ell}{c_\ell^2} + \frac{m_g}{c_g^2}\left(1+\frac{\Gamma_\ell}{c_\ell^2}\Delta h\right)^2}{\tilde{C}_{p,g}T} + \frac{\frac{m_g}{c_g^2} + \frac{m_\ell}{c_\ell^2}\left(1-\frac{\Gamma_g}{c_g^2}\Delta h\right)^2}{\tilde{C}_{p,\ell}T} + \left(\frac{\Gamma_\ell}{c_\ell^2} - \frac{\Gamma_g}{c_g^2} - \frac{\Gamma_g\Gamma_\ell}{c_g^2 c_\ell^2}\Delta h\right)^2\right]^{-1}$$

$$\times \left[\frac{\alpha_g}{\rho_g c_g^2} + \frac{\alpha_\ell}{\rho_\ell c_\ell^2} + \frac{\tilde{C}_{p,g}T}{\Delta h^2}\left(\frac{1}{\rho_\ell} - \frac{1-\frac{\Gamma_g}{c_g^2}\Delta h}{\rho_g}\right)^2 + \frac{\tilde{C}_{p,\ell}T}{\Delta h^2}\left(\frac{1}{\rho_g} - \frac{1+\frac{\Gamma_\ell}{c_\ell^2}\Delta h}{\rho_\ell}\right)^2\right]^{-2}.$$

(156)

Due to the given conditions, it is clear that $\mathcal{Q}_{pT\mu}^{T\mu} \geq 0$. Hence, exactly one of the factors on the left hand side of (155) must be negative, and therefore $c_{T\mu,-} \leq c_{pT\mu} \leq c_{T\mu,+}$, i.e. the weak subcharacteristic condition is satisfied. $\square$

9. Comparison and discussion of models

In this section, we compare the models in the hierarchy. We first show plots for relevant cases, and then briefly discuss physical and numerical aspects of the different models.

9.1. **Comparison of sound speeds.** We now present plots of the sound speeds in all the models in the hierarchy, for different physically relevant conditions, in order to illustrate the effect of different equilibrium assumptions. Plots with the same physical parameters were presented by Lund [40] for the v-branch of the hierarchy, building on plots by [20]. [19] and [44] presented similar plots for the p-branch of the hierarchy. In the following, results for the complete hierarchy are shown.

The main panel of Figure 2 shows the fluid-mechanical sound speeds of all the models in the hierarchy for a water-steam mixture at atmospheric conditions. The thermophysical parameters are shown in Table 1. Apart from the fact that the subcharacteristic condition is always respected, we notice that there are mainly two equilibrium assumptions that affect the propagation speeds, namely those of p- and v-relaxation, respectively. First, imposing instantaneous equilibrium in pressure attracts the sound velocities to the lower bound of the parent models, which can be seen in the insets of Figure 2. Further imposing velocity equilibrium, the sound velocity is reduced by a factor (see Remark 3)

$$\sqrt{\rho\left(\frac{\alpha_{\mathrm{g}}}{\rho_{\mathrm{g}}} + \frac{\alpha_{\ell}}{\rho_{\ell}}\right)} \simeq \sqrt{\alpha_{\mathrm{g}}\alpha_{\ell}\frac{\rho_{\ell}}{\rho_{\mathrm{g}}}}. \tag{157}$$

The approximation made is valid when $\rho_{\mathrm{g}} \ll \rho_{\ell}$, which is the case here. Hence, these equilibrium assumptions seem to have severe impact on the wave velocities, in particular when the density difference between the phases is large.

TABLE 1. Parameters for a water-steam mixture at atmospheric pressure.

Quantity	Symbol	Unit	Gas	Liquid
Pressure	p	MPa	0.1	0.1
Temperature	T	K	372.76	372.76
Density	ρ	$\mathrm{kg\,m^{-3}}$	0.59031	958.64
Speed of sound	c	$\mathrm{m\,s^{-1}}$	472.05	1543.4
Heat capacity	C_p	$\mathrm{J\,kg^{-1}\,K^{-1}}$	2075.9	4216.1
Entropy	s	$\mathrm{m^2\,s^{-2}\,K^{-1}}$	7358.8	1302.6
Grüneisen coefficient	Γ	$(-)$	0.33699	0.4

In Figure 3, the sound speeds in the entire hierarchy are plotted for a CO_2 mixture at 50 bar, whose thermophysical properties are given in Table 2. By close inspection, it can be seen that the subcharacteristic condition is everywhere respected. In particular, the sound speeds of an equilibrium system are always interlaced between the sound speeds in the parent models. Again, the pressure relaxation has the most prominent effect on the sound speed, but also combining thermal and chemical equilibrium seems to have a strong effect.

9.2. **Discontinuous sound speeds.** All the models considered in the present paper are only strictly valid when the gas fraction $\alpha_{\mathrm{g}} \in (0, 1)$. One would expect the sound speeds of the models to be continuous at the phase boundary, i.e. at the
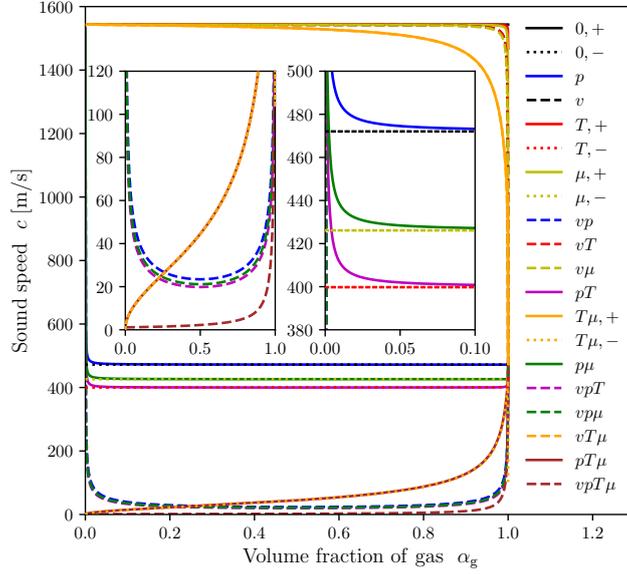
FIGURE 2. Sound velocities in a water-steam mixture at atmospheric conditions. The insets show close-ups of parts of the plots in the main panel.
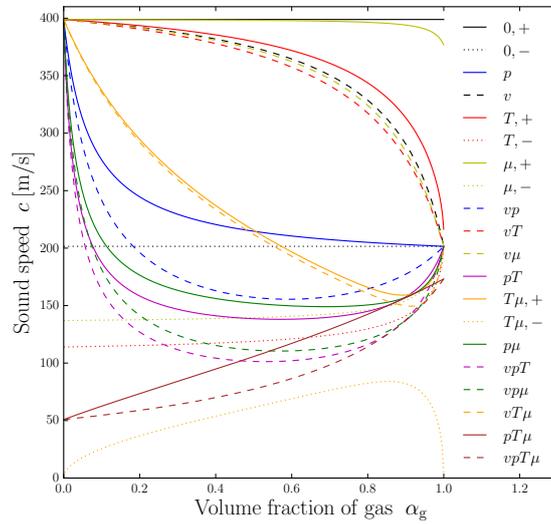

FIGURE 3. Sound speeds in a two-phase CO_2 mixture at 50 bar.

transition between single and two-phase flow, in the sense that the two-phase speed of sound should reduce to the single-phase speed of sound in the limit where one

phase disappears:

$$\lim_{\alpha_k \to 1} c_X \to c_k \qquad (158)$$

for a given model X in the hierarchy. However, some of the models have wave speeds that are discontinuous at the phase boundary. In particular, this concerns the $pT\mu$- and $vpT\mu$-models, whose sound speeds are discontinuous in both limits $\alpha_k \to 1$, which can be seen directly by evaluating the analytic expressions in these limits (see Refs. [40, 44]).

The T- and μ-models have "half-continuous" sound speeds, in the sense that for the "$\pm$" sound waves, only one of them is continuous in the limit $\alpha_k \to 1$. For the μ-model, taking $\alpha_\ell \to 1$ in (105) yields

$$\lim_{\alpha_\ell \to 1} c_{\mu,\pm}^2 = \frac{\frac{T_g s_g^2}{C_{p,g}}(c_g^2 + c_\ell^2) + \frac{\xi_g^2 c_\ell^2}{c_g^2} \pm \left| \frac{T_g s_g^2}{C_{p,g}}(c_g^2 - c_\ell^2) - \frac{\xi_g^2 c_\ell^2}{c_g^2} \right|}{2\left[\frac{T_g s_g^2}{C_{p,g}} + \frac{\xi_g^2}{c_g^2}\right]}, \qquad (159)$$

which is equivalent to

$$\lim_{\alpha_\ell \to 1} c_{\mu,+} = \max\left(\frac{c_g}{\sqrt{1 + \frac{\xi_g^2}{c_g^2}\frac{C_{p,g}}{T_g s_g^2}}}, c_\ell\right), \quad \text{and} \quad \lim_{\alpha_\ell \to 1} c_{\mu,-} = \min\left(\frac{c_g}{\sqrt{1 + \frac{\xi_g^2}{c_g^2}\frac{C_{p,g}}{T_g s_g^2}}}, c_\ell\right).$$
$$(160)$$

Clearly, only one of these approach the appropriate phasic value c_ℓ^2. The result limits for $\alpha_g \to 1$ are found by phase symmetry. Similarly, we find for the T-model, from (73), that

$$\lim_{\alpha_\ell \to 1} c_{T,+} = \min\left(\frac{c_g}{\sqrt{1 + \frac{\Gamma_g^2 C_{p,g} T}{c_g^2}}}, c_\ell\right), \quad \text{and} \quad \lim_{\alpha_\ell \to 1} c_{T,-} = \min\left(\frac{c_g}{\sqrt{1 + \frac{\Gamma_g^2 C_{p,g} T}{c_g^2}}}, c_\ell\right),$$
$$(161)$$

to which the same observation applies.

The remaining sound speeds are continuous at the phase boundary; for the $T\mu$-model in the sense that $\lim_{\alpha_k \to 1} c_{T\mu,+} = c_k$ and $\lim_{\alpha_k \to 1} c_{T\mu,-} = 0$, which can be deduced from the analytic expression (144).

TABLE 2. Parameters for a two-phase CO_2 mixture at 50 bar.

Quantity	Symbol	Unit	Gas	Liquid
Pressure	p	MPa	5.0	5.0
Temperature	T	K	287.43	287.43
Density	ρ	$kg\,m^{-3}$	156.71	827.21
Speed of sound	c	$m\,s^{-1}$	201.54	398.89
Heat capacity	C_p	$J\,kg^{-1}\,K^{-1}$	3138.0	3356.9
Entropy	s	$m^2\,s^{-2}\,K^{-1}$	1753.9	1128.8
Grüneisen coefficient	Γ	$(-)$	0.30949	0.63175

9.3. **Physical considerations.** It is commonly argued that pressure relaxation is a much faster process than the other relaxation processes [56, 69]. Temperature relaxation, or heat flow, is associated with diffusion, which is an intrinsically slow process. Chemical potential relaxation, i.e. mass transfer, is also slow compared to pressure relaxation. Zein et al. [69] provide interesting discussions on the topic and argue that temperature relaxation is faster than chemical relaxation. Generally, the magnitudes of the different relaxation times may be strongly problem-dependent. Such considerations may have implications, e.g., for the mass flow through a nozzle, which has been shown to be linked to the subcharacteristic condition [37].

Apart from this, effects not captured by the coarse-grained flow models may come into play, and which model is more accurate may depend heavily on the flow regime under consideration. The effects that arise from having independent phasic pressures may be of importance for the wave dynamics of the system, and thus models with different pressures may be sensible, even though the associated relaxation time is commonly thought to be comparatively short. With regards to evaluating the physical relevance of the models presented herein, experimental data on sound speeds in two-phase flow can be found for various systems [67, 34, 59, 62].

9.4. **Numerical considerations.** A well-known problem with p-relaxed (one–pressure) two-fluid models is that they develop complex eigenvalues when $v_{\mathrm{g}} \neq v_\ell$. This is commonly resolved e.g. by adding a regularising pressure which enforces hyperbolicity [10, 13, 17, 49, 63]. It is worth noting that the two-fluid models with independent phasic pressures, i.e. the T-, μ- and $T\mu$-models, are locally hyperbolic even for small perturbations away from velocity equilibrium, due to the following argument: *An eigenvalue of a matrix with real coefficients may only be complex if its complex conjugate is also an eigenvalue. Since the eigenvalues of the individual phasic pressure models are real and distinct when $\varepsilon = v_{\mathrm{g}} - v_\ell = 0$, they must remain so for sufficiently small ε, as the eigenvalues may only become complex in a continuous way.* In order to determine how large ε may be before hyperbolicity is lost, we must find the higher-order corrections in ε to the eigenvalues, which is beyond the scope of this work.

10. Conclusions and further work

In this paper, we have presented and completed a hierarchy of relaxation models for two-phase flow, which arises when we impose instantaneous equilibrium in different combinations of velocity, pressure, temperature and chemical potential. The starting point of the analysis has been the classic seven-equation Baer–Nunziato model [3] equipped with relaxation source terms. We have in the present work provided the T-, μ-, $p\mu$-, and $T\mu$-models, which represent original contributions to the hierarchy. Explicit expressions for the sound speeds of these models have been derived. Using the new expressions and results from the literature, we have shown analytically that the subcharacteristic condition is always satisfied in the hierarchy, given velocity equilibrium between the phases. To this end, we have contributed with 15 new subcharacteristic conditions, stated in propositions 2–16. Out of these, five have been shown in a strong sense, and ten hold in a weak sense, i.e. given equilibrium in velocity.

In further work, the hierarchy could be extended to multi-component or multi-phase flow, as already initiated by [28, 29, 45]. Moreover, the different models could be implemented and studied numerically for relevant cases (cf. [55]). Upon

comparison with experimental data, one may then unravel under which conditions the different models are admissible.

Appendix A. Coefficients in the $p\mu$-model

The coefficients in the $p\mu$-model are given by

$$\mathcal{P}_p^{p\mu} = \frac{\alpha_g \alpha_\ell \kappa_\mu}{\rho_g c_g^2 \rho_\ell c_\ell^2 \kappa_{p\mu}}, \quad \mathcal{G}_p^{p\mu} = \frac{1}{\kappa_{p\mu}}\left[\frac{\alpha_g}{\rho_g c_g^2} + \frac{\alpha_\ell}{\rho_\ell c_\ell^2} + \frac{\alpha_\ell \Gamma_g T_g + \alpha_g \Gamma_\ell T_\ell}{\rho_g c_g^2 \rho_\ell c_\ell^2} s^*\right],$$

$$\mathcal{P}_\mu^{p\mu} = \frac{\alpha_g \alpha_\ell}{\rho_g c_g^2 \rho_\ell c_\ell^2 \kappa_{p\mu}}\left(\frac{\xi_g}{\alpha_g} + \frac{\xi_\ell}{\alpha_\ell}\right), \quad \mathcal{G}_\mu^{p\mu} = -\frac{1}{\kappa_{p\mu}}\left(\frac{\alpha_g}{\rho_g c_g^2} + \frac{\alpha_\ell}{\rho_\ell c_\ell^2}\right), \quad \mathcal{V}_{\mu,g}^{p\mu} = -\frac{1}{\kappa_{p\mu}}\left(\frac{\xi_g}{\rho_g c_g^2} - \frac{\xi_\ell}{\rho_\ell c_\ell^2}\right),$$

$$\begin{aligned}
I_v^{p\mu} = \frac{\alpha_g \alpha_\ell}{\rho_g c_g^2 \rho_\ell c_\ell^2 \kappa_{p\mu}}\Bigg\{&\left(\frac{s_g}{\bar{C}_{p,g}}\left[\frac{\xi_g}{\alpha_g} + \frac{\xi_\ell}{\alpha_\ell}\right] + \frac{\Gamma_g}{\alpha_g}\left[\frac{T_g s_g^2}{\bar{C}_{p,g}} + \frac{T_\ell s_\ell^2}{\bar{C}_{p,\ell}}\right] - \frac{\Gamma_g \xi_\ell}{\alpha_g \alpha_\ell}\left[\frac{\xi_g}{\rho_g c_g^2} - \frac{\xi_\ell}{\rho_\ell c_\ell^2}\right]\right.\\
&\left. - \left[\frac{\Gamma_g \Gamma_\ell}{\alpha_g \alpha_\ell}\left(\frac{\xi_g}{\rho_g c_g^2} - \frac{\xi_\ell}{\rho_\ell c_\ell^2}\right) + \frac{\Gamma_g s_\ell}{\alpha_g \bar{C}_{p,\ell}} - \frac{\Gamma_\ell s_g}{\alpha_\ell \bar{C}_{p,g}}\right]T_\ell s^*\right)\Delta_i v_g\\
&+\left(\frac{s_\ell}{\bar{C}_{p,\ell}}\left[\frac{\xi_g}{\alpha_g} + \frac{\xi_\ell}{\alpha_\ell}\right] + \frac{\Gamma_\ell}{\alpha_\ell}\left[\frac{T_g s_g^2}{\bar{C}_{p,g}} + \frac{T_\ell s_\ell^2}{\bar{C}_{p,\ell}}\right] + \frac{\Gamma_\ell \xi_g}{\alpha_g \alpha_\ell}\left[\frac{\xi_g}{\rho_g c_g^2} - \frac{\xi_\ell}{\rho_\ell c_\ell^2}\right]\right.\\
&\left. + \left[\frac{\Gamma_g \Gamma_\ell}{\alpha_g \alpha_\ell}\left(\frac{\xi_g}{\rho_g c_g^2} - \frac{\xi_\ell}{\rho_\ell c_\ell^2}\right) + \frac{\Gamma_g s_\ell}{\alpha_g \bar{C}_{p,\ell}} - \frac{\Gamma_\ell s_g}{\alpha_\ell \bar{C}_{p,g}}\right]T_g s^*\right)\Delta_i v_\ell\Bigg\},
\end{aligned}$$

$$\begin{aligned}
I_T^{p\mu} = \frac{\alpha_g \alpha_\ell}{\rho_g c_g^2 \rho_\ell c_\ell^2 \kappa_{p\mu}}\Bigg\{&\left(\frac{s_g}{\bar{C}_{p,g}} + \frac{s_\ell}{\bar{C}_{p,\ell}}\right)\left[\frac{\xi_g}{\alpha_g} + \frac{\xi_\ell}{\alpha_\ell}\right] + \left(\frac{\Gamma_g}{\alpha_g} + \frac{\Gamma_\ell}{\alpha_\ell}\right)\left[\frac{T_g s_g^2}{\bar{C}_{p,g}} + \frac{T_\ell s_\ell^2}{\bar{C}_{p,\ell}}\right]\\
&- \frac{\Gamma_g \xi_\ell - \Gamma_\ell \xi_g}{\alpha_g \alpha_\ell}\left[\frac{\xi_g}{\rho_g c_g^2} - \frac{\xi_\ell}{\rho_\ell c_\ell^2}\right] - \left[\frac{\Gamma_g \Gamma_\ell}{\alpha_g \alpha_\ell}\left(\frac{\xi_g}{\rho_g c_g^2} - \frac{\xi_\ell}{\rho_\ell c_\ell^2}\right) + \frac{\Gamma_g s_\ell}{\alpha_g \bar{C}_{p,\ell}} - \frac{\Gamma_\ell s_g}{\alpha_\ell \bar{C}_{p,g}}\right](T_\ell - T_g)s^*\Bigg\},
\end{aligned}$$

$$\mathcal{K}_v^{p\mu} = \frac{1}{\kappa_{p\mu}}\left\{\left[\left(\frac{\alpha_g}{\rho_g c_g^2} + \frac{\alpha_\ell}{\rho_\ell c_\ell^2}\right)\frac{s_g}{\bar{C}_{p,g}} - \frac{\Gamma_g}{\rho_g c_g^2}\left(\frac{\xi_g}{\rho_g c_g^2} - \frac{\xi_\ell}{\rho_\ell c_\ell^2}\right)\right]\Delta_i v_g + \left[\left(\frac{\alpha_g}{\rho_g c_g^2} + \frac{\alpha_\ell}{\rho_\ell c_\ell^2}\right)\frac{s_\ell}{\bar{C}_{p,\ell}} + \frac{\Gamma_\ell}{\rho_\ell c_\ell^2}\left(\frac{\xi_g}{\rho_g c_g^2} - \frac{\xi_\ell}{\rho_\ell c_\ell^2}\right)\right]\Delta_i v_\ell\right\},$$

$$\mathcal{K}_T^{p\mu} = \frac{1}{\kappa_{p\mu}}\left\{\left(\frac{\alpha_g}{\rho_g c_g^2} + \frac{\alpha_\ell}{\rho_\ell c_\ell^2}\right)\left(\frac{s_g}{\bar{C}_{p,g}} + \frac{s_\ell}{\bar{C}_{p,\ell}}\right) - \left(\frac{\Gamma_g}{\rho_g c_g^2} - \frac{\Gamma_\ell}{\rho_\ell c_\ell^2}\right)\left(\frac{\xi_g}{\rho_g c_g^2} - \frac{\xi_\ell}{\rho_\ell c_\ell^2}\right)\right\},$$

$$\Phi_g = \frac{1}{\kappa_{p\mu}}\left\{\frac{\alpha_\ell}{\rho_\ell c_\ell^2}\left(\frac{T_g s_g^2}{\bar{C}_{p,g}} + \frac{T_\ell s_\ell^2}{\bar{C}_{p,\ell}}\right) - \frac{\xi_\ell}{\rho_\ell c_\ell^2}\left(\frac{\xi_g}{\rho_g c_g^2} - \frac{\xi_\ell}{\rho_\ell c_\ell^2}\right) - \left[\frac{\alpha_\ell}{\rho_\ell c_\ell^2}\left(\frac{T_g s_g}{\bar{C}_{p,g}} + \frac{T_\ell s_\ell}{\bar{C}_{p,\ell}}\right) + \left(\frac{\xi_g}{\rho_g c_g^2} - \frac{\xi_\ell}{\rho_\ell c_\ell^2}\right)\frac{\Gamma_\ell T_\ell}{\rho_\ell c_\ell^2}\right]s^*\right\}.$$

Herein, we have defined the shorthand denominator

$$\kappa_{p\mu} = \left(\frac{\alpha_{\mathrm{g}}}{\rho_{\mathrm{g}}c_{\mathrm{g}}^2} + \frac{\alpha_\ell}{\rho_\ell c_\ell^2}\right)\left(\frac{T_{\mathrm{g}}s_{\mathrm{g}}^2}{\tilde{C}_{p,\mathrm{g}}} + \frac{T_\ell s_\ell^2}{\tilde{C}_{p,\ell}}\right) + \left(\frac{\xi_{\mathrm{g}}}{\rho_{\mathrm{g}}c_{\mathrm{g}}^2} - \frac{\xi_\ell}{\rho_\ell c_\ell^2}\right)^2$$
$$- \left[\left(\frac{\alpha_{\mathrm{g}}}{\rho_{\mathrm{g}}c_{\mathrm{g}}^2} + \frac{\alpha_\ell}{\rho_\ell c_\ell^2}\right)\left(\frac{T_{\mathrm{g}}s_{\mathrm{g}}}{\tilde{C}_{p,\mathrm{g}}} + \frac{T_\ell s_\ell}{\tilde{C}_{p,\ell}}\right) - \left(\frac{\xi_{\mathrm{g}}}{\rho_{\mathrm{g}}c_{\mathrm{g}}^2} - \frac{\xi_\ell}{\rho_\ell c_\ell^2}\right)\left(\frac{\Gamma_{\mathrm{g}}T_{\mathrm{g}}}{\rho_{\mathrm{g}}c_{\mathrm{g}}^2} - \frac{\Gamma_\ell T_\ell}{\rho_\ell c_\ell^2}\right)\right] s^*$$

and an entropy contribution due to velocity differences

$$s^* = (v_{\mathrm{g}} - v_\ell)^2/[2(\sqrt{T_{\mathrm{g}}} + \sqrt{T_\ell})^2].$$

The coefficients related to the quasi-linear form are given by

$$P_{\bar{v}}^{p\mu} = \mathcal{P}_p^{p\mu} - \left(\frac{\beta_\ell}{\rho_{\mathrm{g}}} + \frac{\beta_{\mathrm{g}}}{\rho_\ell}\right)\mathcal{P}_\mu^{p\mu}, \quad G_{\bar{v}}^{p\mu} = \mathcal{G}_p^{p\mu} - \left(\frac{\beta_\ell}{\rho_{\mathrm{g}}} + \frac{\beta_{\mathrm{g}}}{\rho_\ell}\right)\mathcal{G}_\mu^{p\mu}, \quad V_{\bar{v},\mathrm{g}}^{p\mu} = \left(\frac{\beta_\ell}{\rho_{\mathrm{g}}} + \frac{\beta_{\mathrm{g}}}{\rho_\ell}\right)\mathcal{V}_{\mu,\mathrm{g}}^{p\mu},$$

$$\Psi_{\mathrm{g}}^p = \frac{1}{\kappa_{p\mu}}\left[\frac{\alpha_{\mathrm{g}}}{\rho_{\mathrm{g}}c_{\mathrm{g}}^2}\left(\frac{T_{\mathrm{g}}s_{\mathrm{g}}(s_{\mathrm{g}}-s^*)}{\tilde{C}_{p,\mathrm{g}}} + \frac{T_\ell s_\ell(s_\ell-s^*)}{\tilde{C}_{p,\ell}}\right) + \frac{\xi_{\mathrm{g}}}{\rho_{\mathrm{g}}c_{\mathrm{g}}^2}\left(\frac{\xi_{\mathrm{g}}+\Gamma_{\mathrm{g}}T_{\mathrm{g}}s^*}{\rho_{\mathrm{g}}c_{\mathrm{g}}^2} - \frac{\xi_\ell+\Gamma_\ell T_\ell s^*}{\rho_\ell c_\ell^2}\right)\right],$$

$$G_p^{p\mu} = \frac{1}{\kappa_{p\mu}}\left[\frac{\xi_{\mathrm{g}}+\Gamma_{\mathrm{g}}T_{\mathrm{g}}s^*}{\rho_{\mathrm{g}}c_{\mathrm{g}}^2} - \frac{\xi_\ell+\Gamma_\ell T_\ell s^*}{\rho_\ell c_\ell^2}\right], \quad V_p^{p\mu} = \frac{1}{\kappa_{p\mu}}\left[\frac{T_{\mathrm{g}}s_{\mathrm{g}}^2}{\tilde{C}_{p,\mathrm{g}}} + \frac{T_\ell s_\ell^2}{\tilde{C}_{p,\ell}} - \left(\frac{T_{\mathrm{g}}s_{\mathrm{g}}}{\tilde{C}_{p,\mathrm{g}}} + \frac{T_\ell s_\ell}{\tilde{C}_{p,\ell}}\right)s^*\right],$$

$$P_\mu^{p\mu} = \frac{\xi_{\mathrm{g}}\xi_\ell}{\rho_{\mathrm{g}}c_{\mathrm{g}}^2\rho_\ell c_\ell^2\kappa_{p\mu}}\left\{\frac{\xi_{\mathrm{g}}}{\rho_{\mathrm{g}}c_{\mathrm{g}}^2} - \frac{\xi_\ell}{\rho_\ell c_\ell^2} + \frac{\alpha_{\mathrm{g}}T_{\mathrm{g}}s_{\mathrm{g}}^2}{\xi_{\mathrm{g}}\tilde{C}_{p,\mathrm{g}}} - \frac{\alpha_\ell T_\ell s_\ell^2}{\xi_\ell\tilde{C}_{p,\ell}} - \left[\frac{\Gamma_\ell T_\ell}{\rho_\ell c_\ell^2} - \frac{\alpha_\ell T_\ell s_\ell}{\xi_\ell\tilde{C}_{p,\ell}} - \frac{\Gamma_{\mathrm{g}}T_{\mathrm{g}}}{\rho_{\mathrm{g}}c_{\mathrm{g}}^2} + \frac{\alpha_{\mathrm{g}}T_{\mathrm{g}}s_{\mathrm{g}}}{\xi_{\mathrm{g}}\tilde{C}_{p,\mathrm{g}}}\right]s^*\right\},$$

$$\Psi_{\mathrm{g}}^\mu = \frac{1}{\kappa_{p\mu}}\left[\left(\frac{\alpha_{\mathrm{g}}}{\rho_{\mathrm{g}}c_{\mathrm{g}}^2} + \frac{\alpha_\ell}{\rho_\ell c_\ell^2}\right)\frac{T_{\mathrm{g}}s_{\mathrm{g}}(s_{\mathrm{g}}-s^*)}{\tilde{C}_{p,\mathrm{g}}} - \frac{\xi_\ell}{\rho_\ell c_\ell^2}\left(\frac{\xi_{\mathrm{g}}+\Gamma_{\mathrm{g}}T_{\mathrm{g}}s^*}{\rho_{\mathrm{g}}c_{\mathrm{g}}^2} - \frac{\xi_\ell+\Gamma_\ell T_\ell s^*}{\rho_\ell c_\ell^2}\right)\right],$$

$$V_\mu^{p\mu} = \frac{1}{\kappa_{p\mu}}\left[\frac{\xi_\ell}{\rho_\ell c_\ell^2}\frac{T_{\mathrm{g}}s_{\mathrm{g}}(s_{\mathrm{g}}-s^*)}{\tilde{C}_{p,\mathrm{g}}} + \frac{\xi_{\mathrm{g}}}{\rho_{\mathrm{g}}c_{\mathrm{g}}^2}\frac{T_\ell s_\ell(s_\ell-s^*)}{\tilde{C}_{p,\ell}}\right].$$

APPENDIX B. COEFFICIENTS IN THE $T\mu$-MODEL

The coefficients in the $T\mu$-model are given by

$$\mathcal{A}_\mu^{T\mu} = \frac{(p_{\mathrm{g}}-p_\ell)(v_{\mathrm{g}}+v_\ell)}{2}A_{\mathrm{g}}^{T\mu}, \quad \mathcal{G}_\mu^{T\mu} = -\frac{m_{\mathrm{g}}m_\ell}{c_{\mathrm{g}}^2c_\ell^2 T\kappa_{T\mu}}\left[\frac{\zeta_{\mathrm{g}}}{\tilde{C}_{p,\mathrm{g}}} + \frac{\zeta_\ell}{\tilde{C}_{p,\ell}}\right],$$

$$\mathcal{T}_\mu^{T\mu} = \frac{m_{\mathrm{g}}m_\ell}{c_{\mathrm{g}}^2c_\ell^2 T\kappa_{T\mu}}\left[\frac{\Gamma_{\mathrm{g}}}{m_{\mathrm{g}}} + \frac{\Gamma_\ell}{m_\ell} - \frac{s_{\mathrm{g}}\zeta_{\mathrm{g}}}{\tilde{C}_{p,\mathrm{g}}} - \frac{s_\ell\zeta_\ell}{\tilde{C}_{p,\ell}}\right],$$

$$A_{\mathrm{g}}^{T\mu} = \frac{m_{\mathrm{g}}m_\ell}{c_{\mathrm{g}}^2c_\ell^2 T\kappa_{T\mu}}\left[\frac{\Gamma_\ell\zeta_{\mathrm{g}}}{m_\ell\tilde{C}_{p,\mathrm{g}}} - \frac{\Gamma_{\mathrm{g}}\zeta_\ell}{m_{\mathrm{g}}\tilde{C}_{p,\ell}} + \frac{\zeta_{\mathrm{g}}\zeta_\ell\Delta h}{\tilde{C}_{p,\mathrm{g}}\tilde{C}_{p,\ell}T}\right],$$

$$\mathcal{V}_{\mu,\mathrm{g}}^{T\mu} = \frac{m_{\mathrm{g}}m_\ell}{c_{\mathrm{g}}^2c_\ell^2 T\kappa_{T\mu}}\left[-\frac{c_{\mathrm{g}}^2}{\alpha_{\mathrm{g}}}\left(\frac{1}{\tilde{C}_{p,\mathrm{g}}} + \frac{1}{\tilde{C}_{p,\ell}}\right) + \frac{c_{\mathrm{g}}^2c_\ell^2}{\alpha_{\mathrm{g}}\alpha_\ell}\frac{\Gamma_\ell T}{\rho_\ell c_\ell^2}\left(\frac{\Gamma_{\mathrm{g}}}{c_{\mathrm{g}}^2} - \frac{\Gamma_\ell}{c_\ell^2}\right) + \frac{\Gamma_{\mathrm{g}}\Delta h}{\alpha_{\mathrm{g}}}\left(\frac{1}{\tilde{C}_{p,\ell}} + \frac{\Gamma_\ell^2 T}{m_\ell c_\ell^2}\right)\right],$$

$$\mathcal{V}_{\mu,\ell}^{T\mu} = \frac{m_{\mathrm{g}}m_\ell}{c_{\mathrm{g}}^2c_\ell^2 T\kappa_{T\mu}}\left[-\frac{c_\ell^2}{\alpha_\ell}\left(\frac{1}{\tilde{C}_{p,\mathrm{g}}} + \frac{1}{\tilde{C}_{p,\ell}}\right) - \frac{c_{\mathrm{g}}^2c_\ell^2}{\alpha_{\mathrm{g}}\alpha_\ell}\frac{\Gamma_{\mathrm{g}}T}{\rho_{\mathrm{g}}c_{\mathrm{g}}^2}\left(\frac{\Gamma_{\mathrm{g}}}{c_{\mathrm{g}}^2} - \frac{\Gamma_\ell}{c_\ell^2}\right) - \frac{\Gamma_\ell\Delta h}{\alpha_\ell}\left(\frac{1}{\tilde{C}_{p,\mathrm{g}}} + \frac{\Gamma_{\mathrm{g}}^2 T}{m_{\mathrm{g}}c_{\mathrm{g}}^2}\right)\right],$$

$$\mathcal{K}_p^{T\mu} = -(p_{\mathrm{g}}-p_\ell)A_{\mathrm{g}}^{T\mu} + \mathcal{V}_{\mu,\mathrm{g}}^{T\mu} + \mathcal{V}_{\mu,\ell}^{T\mu}, \quad \mathcal{K}_v^{T\mu} = -A_{\mathrm{g}}^{T\mu},$$

$$\kappa_{T\mu} = \frac{\Delta h^2 m_{\mathrm{g}}m_\ell}{\tilde{C}_{p,\mathrm{g}}\tilde{C}_{p,\ell}T^2 c_{\mathrm{g}}^2 c_\ell^2} + \frac{\frac{m_\ell}{c_\ell^2} + \frac{m_{\mathrm{g}}}{c_{\mathrm{g}}^2}\left(1+\frac{\Gamma_\ell}{c_\ell^2}\Delta h\right)^2}{\tilde{C}_{p,\mathrm{g}}T}$$
$$+ \frac{\frac{m_{\mathrm{g}}}{c_{\mathrm{g}}^2} + \frac{m_\ell}{c_\ell^2}\left(1-\frac{\Gamma_{\mathrm{g}}}{c_{\mathrm{g}}^2}\Delta h\right)^2}{\tilde{C}_{p,\ell}T} + \left(\frac{\Gamma_\ell}{c_\ell^2} - \frac{\Gamma_{\mathrm{g}}}{c_{\mathrm{g}}^2} - \frac{\Gamma_{\mathrm{g}}\Gamma_\ell}{c_{\mathrm{g}}^2 c_\ell^2}\Delta h\right)^2.$$

REFERENCES

[1] Ulf Jakob F Aarsnes, Tore Flåtten, and Ole Morten Aamo. Review of two-phase flow models for control and estimation. *Annu. Rev. Control*, 42:50–62, 2016.

[2] Grégoire Allaire, Sébastien Clerc, and Samuel Kokh. A five-equation model for the simulation of interfaces between compressible fluids. *J. Comput. Phys.*, 181(2):577–616, 2002.

[3] MR Baer and JW Nunziato. A two-phase mixture theory for the deflagration-to-detonation transition (ddt) in reactive granular materials. *Int. J. Multiphase Flow*, 12(6):861–889, 1986.

[4] Thomas Barberon and Philippe Helluy. Finite volume simulation of cavitating flows. *Comput. Fluids*, 34(7):832–858, 2005.

[5] Michaël Baudin, Christophe Berthon, Frédéric Coquel, Roland Masson, and Quang Huy Tran. A relaxation method for two-phase flow models with hydrodynamic closure law. *Numer. Math.*, 99(3):411–440, 2005.

[6] Michaël Baudin, Frédéric Coquel, and Quang-Huy Tran. A semi-implicit relaxation scheme for modeling two-phase flow in a pipeline. *SIAM J. Sci. Comput.*, 27(3):914–936, 2005.

[7] JB Bdzil, R Menikoff, SF Son, AK Kapila, and D Scott Stewart. Two-phase modeling of deflagration-to-detonation transition in granular materials: A critical examination of modeling issues. *Phys. Fluids*, 11(2):378–402, 1999.

[8] Kjell H Bendiksen, Dag Maines, Randi Moe, Sven Nuland, et al. The dynamic two-fluid model olga: Theory and application. *SPE Prod. Eng.*, 6(02):171–180, 1991.

[9] Torodd Berstad, Cato Dørum, Jana Poplsteinova Jakobsen, Steinar Kragset, Hailong Li, Halvor Lund, Alexandre Morin, Svend Tollak Munkejord, Mona Jacobsen Mølnvik, Håkon Ottar Nordhagen, et al. Co2 pipeline integrity: A new evaluation methodology. *Energy Procedia*, 4:3000–3007, 2011.

[10] Dominique Bestion. The physical closure laws in the cathare code. *Nuclear Engineering and Design*, 124(3):229–245, 1990.

[11] Gui-Qiang Chen, C David Levermore, and Tai-Ping Liu. Hyperbolic conservation laws with stiff relaxation terms and entropy. *Comm. Pure Appl. Math.*, 47(6):787–830, 1994.

[12] S Clerc. Numerical simulation of the homogeneous equilibrium model for two-phase flows. *J. Comput. Phys.*, 161(1):354–375, 2000.

[13] F Coquel, K El Amine, E Godlewski, B Perthame, and P Rascle. A numerical method using upwind schemes for the resolution of two-phase flows. *J. Comput. Phys.*, 136(2):272–288, 1997.

[14] Frédéric Coquel, Thierry Gallouët, Jean-Marc Hérard, and Nicolas Seguin. Closure laws for a two-fluid two-pressure model. *C. R. Acad. Sci. Paris*, 334(10):927–932, 2002.

[15] J Cortes, A Debussche, and I Toumi. A density perturbation method to study the eigenstructure of two-phase flow equation systems. *J. Comput. Phys.*, 147(2):463–484, 1998.

[16] Donald A Drew and Stephen L Passman. *Theory of multicomponent fluids*, volume 135. Springer-Verlag, 1999.

[17] Steinar Evje and Tore Flåtten. Hybrid flux-splitting schemes for a common two-fluid model. *J. Comput. Phys.*, 192(1):175–210, 2003.

[18] Gloria Faccanoni, Samuel Kokh, and Grégoire Allaire. Modelling and simulation of liquid-vapor phase transition in compressible flows based on thermodynamical equilibrium. *ESAIM: Math. Model. Numer. Anal.*, 46(5):1029–1054, 2012.

[19] Pedro José Martínez Ferrer, Tore Flåtten, and Svend Tollak Munkejord. On the effect of temperature and velocity relaxation in two-phase flow models. *ESAIM: Math. Model. Numer. Anal.*, 46(2):411–442, 2012.

[20] Tore Flåtten and Halvor Lund. Relaxation two-phase flow models and the subcharacteristic condition. *Math. Models Methods Appl. Sci.*, 21(12):2379–2407, 2011.

[21] Tore Flåtten, Alexandre Morin, and Svend Tollak Munkejord. Wave propagation in multicomponent flow models. *SIAM J. Appl. Math.*, 70(8):2861–2882, 2010.

[22] Thierry Gallouët, Philippe Helluy, Jean-Marc Hérard, and Julien Nussbaum. Hyperbolic relaxation models for granular flows. *ESAIM: Math. Model. Numer. Anal.*, 44(2):371–400, 2010.

[23] Thierry Gallouët, Jean-Marc Hérard, and Nicolas Seguin. Numerical modeling of two-phase flows using the two-fluid two-pressure approach. *Math. Models Methods Appl. Sci.*, 14(05):663–700, 2004.

[24] Sergey Gavrilyuk and Henri Gouin. A new form of governing equations of fluids arising from hamilton's principle. *International Journal of Engineering Science*, 37(12):1495–1520, 1999.

[25] Sergey Gavrilyuk and Richard Saurel. Mathematical and numerical modeling of two-phase compressible flows with micro-inertia. *J. Comput. Phys.*, 175(1):326–360, 2002.

[26] LG Gvozdeva and OA Predvoditeleva. Triple configurations of detonation waves in gases. *Combustion, Explosion and Shock Waves*, 5(4):309–316, 1969.

[27] M Hammer and A Morin. A method for simulating two-phase pipe flow with real equations of state. *Comput. Fluids*, 100:45–58, 2014.

[28] E Han, M Hantke, and S Müller. Efficient and robust relaxation procedures for multi-component mixtures including phase transition. *J. Comput. Phys.*, 338:217–239, 2017.

[29] M Hantke and S Müller. Analysis and simulation of a new multi-component two-phase flow model with phase transitions and chemical reactions. *Q. Appl. Math.*, 76:253–287, 2018.

[30] Philippe Helluy and Hélène Mathis. Pressure laws and fast legendre transform. *Math. Models Methods Appl. Sci.*, 21(04):745–775, 2011.

[31] Philippe Helluy and Nicolas Seguin. Relaxation models of phase transition flows. *ESAIM: Math. Model. Numer. Anal.*, 40(2):331–352, 2006.

[32] Mamoru Ishii and Takashi Hibiki. *Thermo-fluid dynamics of two-phase flow*. Springer-Verlag, 2011.

[33] AK Kapila, R Menikoff, JB Bdzil, SF Son, and D Scott Stewart. Two-phase modeling of deflagration-to-detonation transition in granular materials: Reduced equations. *Phys. Fluids*, 13(10):3002–3024, 2001.

[34] Susan Werner Kieffer. Sound speed in liquid-gas mixtures: Water-air and water-steam. *J. Geophys. Res.*, 82(20):2895–2904, 1977.

[35] Mathieu Labois. *Modélisation des déséquilibres mécaniques dans les écoulements diphasiques: Approches par relaxation et par modèle réduit*. PhD thesis, Université de Provence (Aix-Marseille I), 2008.

[36] Jean Leray. *Hyperbolic differential equations*. The Institute for Advanced Study, 1953.

[37] Gaute Linga, Peder Aursand, and Tore Flåtten. Two-phase nozzle flow and the subcharacteristic condition. *J. Math. Anal. Appl.*, 426(2):917–934, 2015.

[38] Gaute Linga and Halvor Lund. A two-fluid model for vertical flow applied to co2 injection wells. *Int. J. Greenh. Gas Con.*, 51:71–80, 2016.

[39] Tai-Ping Liu. Hyperbolic conservation laws with relaxation. *Commun. Math. Phys.*, 108(1):153–175, 1987.

[40] Halvor Lund. A hierarchy of relaxation models for two-phase flow. *SIAM J. Appl. Math.*, 72(6):1713–1741, 2012.

[41] Halvor Lund. *Relaxation models for two-phase flow with applications to CO$_2$ transport*. PhD thesis, Norges teknisk-naturvitenskapelige universitet, Fakultet for ingeniørvitenskap og teknologi, Institutt for energi-og prosessteknikk, 2013.

[42] Ralph Menikoff and Bradley J Plohr. The riemann problem for fluid flow of real materials. *Reviews of Modern Physics*, 61(1):75, 1989.

[43] Alexandre Morin. *Mathematical modelling and numerical simulation of two-phase multi-component flows of CO$_2$ mixtures in pipes*. PhD thesis, Norges teknisk-naturvitenskapelige universitet, Fakultet for ingeniørvitenskap og teknologi, Institutt for energi-og prosessteknikk, 2012.

[44] Alexandre Morin and Tore Flåtten. A two-fluid four-equation model with instantaneous thermodynamical equilibrium. *ESAIM: Math. Model. Numer. Anal.*, 50(4):1167–1192, 2016.

[45] Siegfried Müller, Maren Hantke, and Pascal Richter. Closure conditions for non-equilibrium multi-component models. *Continuum Mechanics and Thermodynamics*, 28(4):1157–1189, 2016.

[46] Svend Tollak Munkejord, Morten Hammer, and Sigurd W Løvseth. Co2 transport: Data and models–a review. *Appl. Energy*, 169:499–523, 2016.

[47] Angelo Murrone and Hervé Guillard. A five equation reduced model for compressible two phase flow problems. *J. Comput. Phys.*, 202(2):664–698, 2005.

[48] Roberto Natalini. Recent mathematical results on hyperbolic relaxation problems. In *Chapman & Hall/CRC Monogr. Surv. Pure Appl. Math.*, volume 99. Chapman & Hall/CRC, 1999.

[49] Michaël Ndjinga. Influence of interfacial pressure on the hyperbolicity of the two-fluid model. *C. R. Acad. Sci. Paris*, 344(6):407–412, 2007.

[50] Marica Pelanti and Keh-Ming Shyue. A mixture-energy-consistent six-equation two-phase numerical model for fluids with interfaces, cavitation and evaporation waves. *J. Comput. Phys.*, 259:331–357, 2014.

[51] J Pettersen, A Hafner, G Skaugen, and H Rekstad. Development of compact heat exchangers for CO$_2$ air-conditioning systems. *Int. J. Refrig.*, 21(3):180–193, 1998.

[52] DJ Picard and PR Bishnoi. Calculation of the thermodynamic sound velocity in two-phase multicomponent fluids. *Int. J. Multiphase Flow*, 13(3):295–308, 1987.

[53] Philip L Roe. Approximate riemann solvers, parameter vectors, and difference schemes. *J. Comput. Phys.*, 43(2):357–372, 1981.

[54] Richard Saurel and Rémi Abgrall. A multiphase Godunov method for compressible multifluid and multiphase flows. *J. Comput. Phys.*, 150(2):425–467, 1999.

[55] Richard Saurel and Carlos Pantano. Diffuse-interface capturing methods for compressible two-phase flows. *Annual Review of Fluid Mechanics*, 50(1), 2018.

[56] Richard Saurel, Fabien Petitpas, and Rémi Abgrall. Modelling phase transition in metastable liquids: application to cavitating and flashing flows. *J. Fluid Mech.*, 607:313–350, 2008.

[57] Richard Saurel, Fabien Petitpas, and Ray A Berry. Simple and efficient relaxation methods for interfaces separating compressible fluids, cavitating flows and shocks in multiphase mixtures. *J. Comput. Phys.*, 228(5):1678–1712, 2009.

[58] Susanne Solem, Peder Aursand, and Tore Flåtten. Wave dynamics of linear hyperbolic relaxation systems. *J. Hyperbol. Differ. Eq.*, 12(04):655–670, 2015.

[59] Herbert Städtke. *Gasdynamic aspects of two-phase flow: Hyperbolicity, wave propagation phenomena and related numerical methods.* John Wiley & Sons, 2006.

[60] H Bruce Stewart and Burton Wendroff. Two-phase flow: models and methods. *J. Comput. Phys.*, 56(3):363–409, 1984.

[61] JH Stuhmiller. The influence of interfacial pressure forces on the character of two-phase flow model equations. *Int. J. Multiphase Flow*, 3(6):551–560, 1977.

[62] S Tosse, Knut Vågsæther, and Dag Bjerketvedt. An experimental investigation of rapid boiling of CO_2. *Shock Waves*, 25(3):277–282, 2015.

[63] Imad Toumi and A Kumbaro. An approximate linearized riemann solver for a two-fluid model. *J. Comput. Phys.*, 124(2):286–300, 1996.

[64] Imad Toumi, Anela Kumbaro, and Henri Paillere. *Approximate Riemann solvers and flux vector splitting schemes for two-phase flow.* CEA Saclay, Direction de l'information scientifique et technique, 1999.

[65] Alexander Voss and Wolfgang Dahmen. *Exact Riemann solution for the Euler equations with nonconvex and nonsmooth equation of state.* PhD thesis, Fakultät für Mathematik, Informatik und Naturwissenschaften, 2005.

[66] Gerald Beresford Whitham. *Linear and nonlinear waves*, volume 42. John Wiley & Sons, 1974.

[67] Jinliang Xu and Tingkuan Chen. Acoustic wave prediction in flowing steam–water two-phase mixture. *Int. J. Heat Mass Tran.*, 43(7):1079–1088, 2000.

[68] Wen-An Yong. Basic aspects of hyperbolic relaxation systems. In *Advances in the Theory of Shock Waves*, pages 259–305. Springer, 2001.

[69] Ali Zein, Maren Hantke, and Gerald Warnecke. Modeling phase transition for compressible two-phase flows applied to metastable liquids. *J. Comput. Phys.*, 229(8):2964–2998, 2010.

A two-fluid model for vertical flow applied to CO$_2$ injection wells

Gaute Linga and Halvor Lund

A two-fluid model for vertical flow applied to CO_2 injection wells

Gaute Linga [a,b], Halvor Lund [a,*]

[a] SINTEF Energy Research, P.O. Box 4761 Sluppen, NO-7465 Trondheim, Norway
[b] Niels Bohr Institute, University of Copenhagen, Blegdamsvej 17, DK-2100 Copenhagen, Denmark

ABSTRACT

Flow of CO_2 in wells is associated with substantial variations in thermophysical properties downhole, due to the coupled transient processes involved: complex flow patterns, density changes, phase transitions, and heat transfer to and from surroundings. Large temperature variations can lead to thermal stresses and subsequent loss of well integrity, and it is therefore crucial to employ models that can predict this accurately. In this work, we present a model for vertical well flow that includes both two-phase flow and heat conduction. The flow is described by a two-fluid model, where mass transfer between the phases is modelled by relaxation source terms that drive the phases towards thermodynamic equilibrium. We suggest a new formulation of the mass transfer process that satisfies the second law of thermodynamics, and that is also continuous in the single-phase limit. This provides a more robust transition from two-phase to single-phase flow than the previous formulation. The model predicts which flow regimes are present downhole, and calculates friction and heat transfer depending on this. Moreover, the flow model is coupled with a heat conduction model for the layers that comprise the well, including tubing, packer fluid, casing, cement or drilling mud, and rock formation. This enables prediction of the temperature in the well fluid and in each layer of the well. The model is applied to sudden shut-in and blowout cases of a CO_2 injection well, where we employ the highly accurate Span–Wagner reference equation-of-state to describe the thermodynamics of CO_2. We predict pressure, temperature and flow regimes during these cases and discuss implications for well integrity.

1. Introduction

Carbon Capture and Storage (CCS) will play an important role on the path to a low-carbon society. In the two-degree scenario of the International Energy Agency (IEA), CCS is expected to reduce the global emissions of CO_2 by about seven gigatonnes per year in 2050 (IEA, 2014). The captured CO_2 can be transported to storage sites using both pipelines and ships. Several authors (Austegard et al., 2006; Kjärstad et al., 2014; Vermeulen, 2011; Roussanaly et al., 2014) have concluded that ship transport can be a cost-efficient solution for many offshore storage sites. Ship transport creates additional challenges when CO_2 is injected through a well into a reservoir. The transported CO_2 will typically be kept at a low temperature and pressure, close to the triple point (5.1 bar and $-56.6\,^\circ$C). Some heating will be required before the CO_2 is pumped into the well, in order to avoid damage to the well and the reservoirs due to low temperatures or high pressures. To predict the temperature and pressure conditions in a well, accurate and reliable models are required.

A significant body of research concerns the flow of CO_2 in reservoirs, and leakage through sealed wells (Nordbotten et al., 2005a,b; Nordbotten and Celia, 2011). The thermal effects of CO_2 flow in reservoirs have also been specifically considered (Goodarzi et al., 2010; André et al., 2007). However, models developed specifically for well flow of CO_2 seem to be scarce, especially for transient scenarios.

For wells without any downhole measuring equipment, steady state models can provide predictions for the pressure and temperature conditions in the well under steady conditions. Lindeberg (2011) proposed a simple model using Bernoulli's equation and a model for heat exchange with the surrounding rock, and used it to the predict temperature and pressure in the Sleipner CO_2 injection well. Pan et al. (2011) derived an analytic solution for steady-state flow of a CO_2–water mixture in a well using a drift-flux model. Similarly, Lu and Connell (2008) proposed a quasi-steady model to predict the bottomhole pressure and injection rate in a CO_2 injection well. Singhe et al. (2013) presented a simple quasi-steady analytical model for temperature effects in a gas injection well, and compared their model to results from the Ketzin injection well

* Corresponding author.
E-mail addresses: gaute.linga@nbi.ku.dk (G. Linga), halvor.lund@sintef.no (H. Lund).

(Henninges et al., 2011). Han et al. (2011) considered injection of relatively hot (supercritical) CO_2 at 35–45 °C, using a model based on that of Lu and Connell (2008). They focused on the effects of CO_2 injection on injectivity, due to cooling when water vaporizes in supercritical CO_2, and the following precipitation of salt. Precipitation of salt has been identified as one of the main causes of the pressure build-up experienced during CO_2 injection at Snøhvit (Hansen et al., 2013).

Transient models allow the prediction of conditions in wells that are subject to more transient operations such as blowout, shut-in and varying injection rates. Ruan et al. (2013) considered an axisymmetric two-dimensional model, accounting for the convection of water in the annulus in addition to that of the CO_2 in the tubing. They simulated injection using the Peng–Robinson cubic equation of state with a reservoir pressure of 27 MPa, which resulted in the CO_2 being in a single, dense phase during the injection scenario. Pan et al. (2009) implemented a drift-flux model in the TOUGH2 code with the ECO2N equation of state, and used it to simulate upwards flow of CO_2 and brine in a wellbore. Lu and Connell (2014) simulated CO_2 injection using the homogeneous equilibrium model and the Peng–Robinson cubic equation of state, coupled with a heat conduction model. The same authors have also presented a drift-flux model with phase slip (Lu and Connell, 2014).

Krogh et al. (2012) simulated offloading of CO_2 from ships and injection of liquid CO_2 using OLGA and HYSYS. They found that there is a high risk of hydrate formation and freezing in the formation and on the outside of the riser. Klinkby et al. (2011) also used OLGA to study transient variations in pressure, temperature and phase composition during injection of CO_2–brine mixtures into the proposed Vedsted pipeline, injection well, and reservoir. Li et al. (2015) focused on the well-head temperature during shut-in and start-up, also using OLGA. Azaroual et al. (2012) presented experiments and modelling of injection of supercritical CO_2 into saline aquifers. They focused on how e.g. precipitation of salt due to dryout in the near wellbore can lead to changes in injectivity. Three commercial simulators – PipeSIM, PROSPER and NEWSIM – were used and their results compared, which showed significant differences.

The available research on flow in vertical CO_2 wells is to a large extent based on either simplified steady-state models, or commercial simulators. The use of complex commercial simulators can make model validation difficult, since there is often little public data available about the details of the models.

1.1. Contributions of the current paper

In this paper, we aim to present a model that is suitable for vertical flow of CO_2, and to explain to a sufficient level of detail all parameters and sub-models used. The flow is described by a physically consistent two-fluid model, with the Span–Wagner reference equation-of-state (Span and Wagner, 1996) to describe the thermodynamics of CO_2. Friction and heat transfer in the flow are modelled specifically for each flow regime, such as bubbly, annular and mist flow. The flow model is coupled to a model for heat conduction through the various layers of the well, such as tubing, packer fluid, casing, cement and rock. Large temperature variations can be detrimental to well integrity and are therefore given special attention. The performance of the model is demonstrated by using it to simulate transient well operations, in particular critical incidents such as sudden shut-in and blowout.

1.2. Paper outline

In Section 2, we present the model including flow equations, heat conduction model and correlations employed for friction and fluid-to-wall heat transfer. Section 3 gives a brief description of the numerical methods used, with references to relevant literature, and Section 4 presents the simulation cases considered. In Section 5 we present results from simulations of sudden blowout and shut-in of a vertical CO_2 well, with emphasis on pressure and temperature conditions in the well. We also discuss the implications of the simulation results on well operations and well integrity. Finally, in Section 6, we summarize and draw conclusions.

2. Model

In this section, we present the model used in our simulations.

2.1. Flow model

In the present work, we consider pure CO_2 in at most two phases, i.e. liquid and gas. Since the vertical length scale of a well is several orders of magnitude larger than the radial scale, we consider a fluid flowing in one dimension. Modelling the flow in more than one dimension could require detailed resolution of the gas–liquid interface, as well as a much higher computational cost. For this reason, most models for well and pipeline flow are one-dimensional, with constitutive relations that implicitly account for higher-dimensional effects that cannot be explicitly captured in a one-dimensional model.

In order to allow for three-dimensional effects, such as phase separation, we employ a *two-fluid model*. This class of two-phase flow models is characterized by the property that the two phases are allowed to have individual velocities, i.e. each phase is governed by a separate momentum equation (Munkejord et al., 2009; Paillère et al., 2003; Stewart and Wendroff, 1984; Toumi, 1996). This is in contrast to the further simplified class of drift-flux models (Flåtten et al., 2010; Masella et al., 1998; Saurel et al., 2008; Zuber and Findlay, 1965), wherein the velocities of the two phases are related by a functional relation (a slip law).

Two-fluid models have been extensively studied in the literature, and are commonly used in numerous applications. A general seven-equation model for two-phase flow was derived by Baer and Nunziato (1986), and later revived by Saurel and Abgrall (1999), upon which many of later two-phase flow models have been based. To bring the phases towards equilibrium in velocity, pressure, temperature or specific Gibbs free energy at a finite rate, relaxation source terms are typically included in the equations of motion. This has been studied by a range of authors (Karlsen et al., 2004; Natalini, 1997; Pareschi and Russo, 2005; Pelanti and Shyue, 2014; Baudin et al., 2005). By assuming instantaneous equilibrium, i.e. infinitely stiff relaxation source terms, in zero or more of these variables, a hierarchy of models can be derived (Linga, 2015; Lund, 2012; Flåtten and Lund, 2011). For each imposed equilibrium condition, the number of partial differential equations (PDEs) in the model is reduced by one. Popular models in this context include e.g. a six-equation two-fluid model used in nuclear industry (Bestion, 1990; Tiselj et al., 2004), and a five-equation model used in simulation of pipeline transport of petroleum (Bendiksen et al., 1991).

For the purpose of our simulations, we assume that the time scale of the thermodynamic relaxation is much smaller than that of the flow, and hence we assume instantaneous equilibrium in pressure (p), temperature (T) and specific Gibbs free energy (μ). However, for practical reasons (which we shall discuss in Section 2.2), we choose to allow the specific Gibbs free energy to be out of equilibrium and model mass transfer using a relaxation process. The resulting five-equation two-fluid model (the pT-model, cf. Linga, 2015) was studied by Martínez Ferrer et al. (2012) and further by Morin and Flåtten (2015). Hammer and Morin (2014) combined the model with the Span–Wagner equation of state (Span and Wagner, 1996).

With source terms accounting for the interaction between phases and with the pipe wall, the model may be stated as the following set of PDEs, for time t and spatial coordinate x,

- Mass balance:

$$\partial_t(\alpha_g \rho_g) + \partial_x(\alpha_g \rho_g v_g) = \Psi, \tag{1}$$

$$\partial_t(\alpha_\ell \rho_\ell) + \partial_x(\alpha_\ell \rho_\ell v_\ell) = -\Psi, \tag{2}$$

- Momentum balance:

$$\partial_t(\alpha_g \rho_g v_g) + \partial_x(\alpha_g(\rho_g v_g^2 + p)) - p_i \partial_x \alpha_g$$
$$= v_i \Psi + f_i + \alpha_g \rho_g g_x - f_{\text{wall},g}, \tag{3}$$

$$\partial_t(\alpha_\ell \rho_\ell v_\ell) + \partial_x(\alpha_\ell(\rho_\ell v_\ell^2 + p)) + p_i \partial_x \alpha_g$$
$$= -v_i \Psi - f_i + \alpha_\ell \rho_\ell g_x - f_{\text{wall},\ell}, \tag{4}$$

- Energy conservation:

$$\partial_t E + \partial_x(E_g v_g + E_\ell v_\ell + \bar{v} p) = (\alpha_g \rho_g v_g + \alpha_\ell \rho_\ell v_\ell) g_x + Q. \tag{5}$$

Herein, we have used the volume fraction α_k, the density ρ_k, and the velocity v_k for each phase $k \in \{g, \ell\}$, where g denotes gas and ℓ denotes liquid. We have defined the total phasic energy by

$$E_k = \alpha_k \rho_k \left(e_k + \frac{1}{2}v_k^2\right), \tag{6}$$

where e_k is the specific internal energy. The common pressure is denoted by p, the mixed density and mixed total energy are respectively given by

$$\rho = \alpha_g \rho_g + \alpha_\ell \rho_\ell, \quad \text{and} \quad E = E_g + E_\ell, \tag{7}$$

and the volume-averaged velocity is given by

$$\bar{v} = \alpha_g v_g + \alpha_\ell v_\ell. \tag{8}$$

The regularizing interface pressure, which makes the model hyperbolic, is modelled as (Stuhmiller, 1977)

$$p_i = p - \delta \frac{\alpha_g \alpha_\ell \rho_g \rho_\ell}{\alpha_\ell \rho_g + \alpha_g \rho_\ell}(v_g - v_\ell)^2, \tag{9}$$

where $\delta \geq 1$, and in this work we choose $\delta = 1.2$. Further, f_i is an interfacial friction term, g_x is the gravitational acceleration along the x coordinate, $f_{\text{wall},k}$ represents the fluid–wall friction of phase k, and Q represents heat exchange with the surroundings. Finally, Ψ represents the mass transfer between the two phases, and v_i is the interfacial velocity. Expressions for these terms will be given in the following.

2.2. Mass transfer

The term Ψ, representing mass transfer between phases, can in general be expressed as $\Psi = \mathcal{K}(\mu_\ell - \mu_g)$, where $\mathcal{K}$ is associated with a characteristic *relaxation* time for the mass transfer. As $\mathcal{K} > 0$, the relaxation term drives the two phases asymptotically towards equilibrium in specific Gibbs free energy, i.e. mass is transferred from the phase with the highest Gibbs free energy to the phase with the lowest, until the values are equal. If the mass transfer is taken to be instantaneous (as advocated in the previous section), i.e. $\mathcal{K} \to \infty$ (zero relaxation time), the model is equivalent to the four-equation model with full thermodynamic equilibrium (Hammer and Morin, 2014), as described by Morin and Flåtten (2015). In particular, solutions of the relaxation model should approach solutions to the equilibrium model as $\mathcal{K} \to \infty$. For a recent survey of the underlying theory for general hyperbolic relaxation systems, consider Solem et al. (2015, Sec. 1) and the references therein.

Mass transfer also leads to transfer of momentum, represented by the term $v_i \Psi$ in Eqs. (3) and (4). As Morin and Flåtten (2015) point out, $v_i = (v_g + v_\ell)/2$ is the only interfacial velocity that satisfies the second law of thermodynamics (i.e. that the global entropy is nondecreasing), and that is also independent of the difference in specific Gibbs free energy $\mu_g - \mu_\ell$.

The relation between change in entropy and in kinetic energy, when transferring mass from one phase to the other, is found from the fundamental thermodynamic relation,

$$d(\rho e) = T\, dS + \mu\, d\rho = T\, dS, \tag{10}$$

where have utilized that the total mass is constant, $d\rho = 0$, and introduced the total volumetric entropy S and the mixture specific Gibbs free energy $\mu = e + (p - TS)/\rho$. The total energy $E = \rho e + E_{\text{kin}}$ is conserved,

$$dE = d(\rho e) + dE_{\text{kin}} = 0. \tag{11}$$

Combining Eqs. (10) and (11) yields

$$dS = -\frac{1}{T}\, dE_{\text{kin}}, \tag{12}$$

in other words the second law of thermodynamics, implied by the local relation $dS \geq 0$ (Morin and Flåtten, 2015; Flåtten and Lund, 2011; Lund, 2012; Linga, 2015), is satisfied as long as the kinetic energy is not increasing during the mass transfer process. Note that these relations only apply to the *local* mass transfer process, not the fluid flow model as a whole.

The interfacial velocity suggested by Morin and Flåtten (2015) conserves kinetic energy during the mass transfer relaxation process, and, in other words, no entropy is generated. However, this interfacial velocity presents problems if the mass transfer process brings us from a two-phase to a single-phase solution. In this case, kinetic energy cannot be conserved and entropy must be generated, as we will see next.

We will solve the equation system (1)–(5) using a fractional-step method, in which we

1. solve Eq. (1)–(5) system with $\Psi = 0$,
2. solve an ODE system for mass transfer given by

$$\frac{dM_g}{dt} = \Psi, \tag{13}$$

$$\frac{dM_\ell}{dt} = -\Psi, \tag{14}$$

$$\frac{d\Pi_g}{dt} = v_i \Psi, \tag{15}$$

$$\frac{d\Pi_\ell}{dt} = -v_i \Psi, \tag{16}$$

$$\frac{dE}{dt} = 0, \tag{17}$$

where we have introduced the shorthands $M_k \equiv \alpha_k \rho_k$ and $\Pi_k \equiv \alpha_k \rho_k v_k$ for mass and momentum of phase k, respectively. The mass transfer term is $\Psi = \mathcal{K}(\mu_\ell - \mu_g)$ where $\mathcal{K} \to \infty$, so the ODE system approaches thermodynamic equilibrium where $\mu_g = \mu_\ell$. We therefore rather solve a more straightforward discrete equation system.

Let M_k^* and Π_k^* denote the mass and momentum of phase k after the homogeneous step (step 1), and M_k and Π_k denote values after mass has been transferred (step 2). We need to conserve total mass, momentum and energy,

$$\sum_k M_k^* = \sum_k M_k \tag{18}$$

$$\sum_k \Pi_k^* = \sum_k \Pi_k \tag{19}$$

$$\sum_k M_k^* \left(e_k^* + \frac{1}{2}(v_k^*)^2 \right) = \sum_k M_k \left(e_k + \frac{1}{2}v_k^2 \right) \tag{20}$$

Through the equation of state we ensure thermodynamic equilibrium,

$$\mu_g(e_g, \rho_g) = \mu_\ell(e_\ell, \rho_\ell) \tag{21}$$

$$p_g(e_g, \rho_g) = p_\ell(e_\ell, \rho_\ell) \tag{22}$$

$$T_g(e_g, \rho_g) = T_\ell(e_\ell, \rho_\ell) \tag{23}$$

Together with $\sum_k \alpha_k = 1$, this gives us 7 equations and 8 unknowns ($\alpha_k, e_k, \rho_k, v_k$), which allows us to make a choice that determines the amount of entropy generated by the mass transfer, or in other words how much kinetic energy is lost.

However, if the equation of state predicts that the mass transfer will lead to a single-phase solution, we are forced to set $\alpha_V = v_V = 0$, where V is the vanishing phase. Interestingly, this uniquely determines the total kinetic energy after the mass transfer,

$$E_{\text{kin}} = \frac{1}{2}M_K v_K^2 = \frac{\left(\sum_k \Pi_k^* \right)^2}{2\sum_k M_k^*}, \tag{24}$$

where K is the phase that is kept. The change in kinetic energy is given by

$$\Delta E_{\text{kin}} = \frac{1}{2}\left[\frac{\left(\sum_k \Pi_k^* \right)^2}{\sum_k M_k^*} - \sum_k M_k^*(v_k^*)^2 \right] = -\frac{M_g^* M_\ell^*}{2\rho}(v_g^* - v_\ell^*)^2 \tag{25}$$

As we see, kinetic energy is lost, which corresponds to an increase in entropy as given by Eq. (12). With this insight, we therefore suggest a general expression for the kinetic energy lost,

$$\Delta E_{\text{kin}} = -\frac{1}{2}(M_g^*(\Delta v_g^*)^2 + M_\ell^*(\Delta v_\ell^*)^2) \cdot \left(\frac{|M_g - M_g^*|}{\rho - |M_g + M_g^* - \rho|} \right), \tag{26}$$

where $\Delta v_k^* \equiv v_k^* - \hat{v}^*$, and

$$\hat{v}^* = \frac{\Pi_g^* + \Pi_\ell^*}{\rho}, \tag{27}$$

is the centre-of-mass velocity. This expression (26) gives a smooth transition between cases where kinetic energy must be lost, and those where it can be conserved. For example, $\Delta E_{\text{kin}} = 0$ if the velocities are equal or if no mass is transferred, while eq. (25) is fulfilled if $M_g = 0$ or $M_\ell = 0$. We propose that this gives a numerically more robust transition from two-phase to single-phase flow than the previous formulation, which we experienced to give unphysical oscillations in the transition region.

2.3. Equation of state

The state-of-the-art reference equation-of-state (EOS) for CO_2 is that of Span and Wagner (1996), which gives the Helmholtz free energy in terms of phasic density and temperature, i.e. $a(\rho, T)$. It is formulated in terms of the non-dimensional Helmholtz free energy $\phi = a/RT$, where R is the specific gas constant, and is comprised of an ideal gas part, ϕ^0, and a residual part, ϕ^r,

$$\phi(\tau, \delta) = \phi^0(\tau, \delta) + \phi^r(\tau, \delta). \tag{28}$$

Here, $\tau = T_c/T$ is the non-dimensional inverse temperature, and $\delta = \rho/\rho_c$ is the non-dimensional density. ρ_c and T_c are the critical density and temperature, respectively. The expressions in the original paper (Span and Wagner, 1996) contain a total of 51 terms, including logarithms and exponentials, making it computationally demanding to solve compared to e.g. cubic equations of state.

However, due to their simplicity, cubic equations of state do not accurately describe the thermophysical properties of CO_2 on the vast range of densities and temperatures required for simulating CO_2 injection wells, in contrast to the Span–Wagner EOS. The energy–density equilibrium problem is solved using the approach of Hammer et al. (2013).

2.4. Flow regimes

The behaviour of two-phase flow can change dramatically depending on the amount of gas in the flow and the velocity of each phase. This behaviour can typically be divided into flow regimes, such as bubbly, stratified, slug, churn, annular and dispersed/mist flow.

Since experimental data and mathematical models for flow regimes in vertical CO_2 flow are rather scarce, we use the RELAP (Ransom et al., 1995) code to classify flow regimes. RELAP was developed for simulation of water–steam flow in cooling systems for nuclear reactors. Nevertheless, its expressions for flow regimes and friction are formulated so that the properties of any fluid can be used as input, which allows us to use them for CO_2 flow. We limit ourselves to bubbly, annular and mist flow, since these flow regimes are most relevant for the cases we look at. Slug flow is not expected to occur in vertical pipes of such large diameters as those we consider; in the RELAP code the maximum diameter where slug flow can occur is 8 cm.

2.5. Friction

The friction correlations we have employed are based on the RELAP code (Ransom et al., 1995). Since experimental data on CO_2 in large-diameter tubes are scarce, we assume that RELAP's correlations hold also for CO_2, as long as physical parameters for CO_2 are used as input.

2.6. Heat transfer

Heat transfer between the fluid and the pipe wall can depend significantly on which flow regime is present. For turbulent flow we use the correlation by Dittus and Boelter (1930). For subcooled and saturated boiling, we use the correlations by Chen (1966) and Forster and Zuber (1955).

2.7. Heat conduction

Heat conduction is modelled in the layers extending outwards from the well tubing. In a radial geometry this can be expressed as (Cannon, 1984)

$$\rho(r)c_p(r)\partial_t T(r, t) = \frac{1}{r}\partial_r(r\kappa(r)\partial_r T(r, t)), \tag{29}$$

where $\kappa(r)$, $\rho(r)$ and $c_p(r)$ are the thermal conductivity, density and specific heat capacity (at constant pressure) at radius r, respectively. Using this formulation, we neglect any heat conducted along the pipe (in the axial direction). Heat is nevertheless transported along the pipe by the fluid inside the well.

3. Numerical method

In this section, we present the numerical methods used in the simulations. We may write the equation system (1)–(5) as

$$\partial_t \mathbf{u} + \partial_x \mathbf{f}(\mathbf{u}) + \mathbf{B}(\mathbf{u})\partial_x \mathbf{w}(\mathbf{u}) = \mathbf{s}(\mathbf{u}). \tag{30}$$

In general terms, we can write Eq. (30) as

$$\partial_t \mathbf{u} = (\mathcal{A} + \mathcal{B})\mathbf{u}, \tag{31}$$

where $\mathcal{A}$ and $\mathcal{B}$ are the solution operators for the flow and source terms, respectively. If $\mathbf{u}^n$ is the solution at time t^n, then the solution $\mathbf{u}^{n+1}$ at time $t^{n+1} = t^n + \Delta t$ can be formally written as (LeVeque, 2002)

$$\mathbf{u}^{n+1} = e^{\Delta t(\mathcal{A}+\mathcal{B})}\mathbf{u}^n \tag{32}$$

Since the flow and source terms have somewhat different time scales, we treat them separately using a fractional-step approach. A fractional-step approach applies the solution operators in separate steps, as opposed to simultaneously. Strang splitting (Strang, 1968) is a second-order fractional-step method, as long as each step is of second order, and applies the operators in three steps,

$$\mathbf{u}^{n+1} = e^{\Delta t/2\mathcal{B}}e^{\Delta t\mathcal{A}}e^{\Delta t/2\mathcal{B}}\mathbf{u}^n \tag{33}$$

In other words, we first apply flux terms with time step $\Delta t/2$, then the source terms with time step Δt, and finally flux terms again. This splitting allows us to solve each substep in the most efficient way. In the following, we describe how each substep is solved.

3.1. Flow equations

The flow equations

$$\partial_t \mathbf{u} + \partial_x \mathbf{f}(\mathbf{u}) + \mathbf{B}(\mathbf{u})\partial_x \mathbf{w}(\mathbf{u}) = 0, \tag{34}$$

are solved with a finite-volume scheme. To achieve second spatial order, we use piecewise linear reconstruction based on the MUSCL approach, and use the FORCE flux to calculate the numerical fluxes. For more details, see Hammer and Morin (2014).

A main advantage of employing a finite-volume scheme is that conserved quantities are well conserved over shocks, not only for smooth solutions. However, such numerical schemes generally apply to the flux part ($\partial_x \mathbf{f}$) of Eq. (34), and the non-conservative part ($\mathbf{B}\partial_x \mathbf{w}$) must be integrated separately, e.g. as a source term. In our context, this affects only the numerical integration of the momentum Eqs. (3) and (4).

An important property that should be satisfied, is therefore that the *total* momentum should be conserved (up to the accuracy of the finite-volume scheme), according to its evolution equation, which is found by summing Eqs. (3) and (4):

$$\partial_t \Pi + \partial_x(\Pi_g v_g + \Pi_\ell v_\ell + p) = 0. \tag{35}$$

Here we disregard wall friction, gravity and heat transfer for the sake of the argument, and $\Pi \equiv \Pi_g + \Pi_\ell$ is the total momentum. In order to conserve the total momentum, summing the discretizations of Eqs. (3) and (4), the numerical scheme should therefore reduce to a pure flux formulation,

$$\partial_t \Pi_i = \frac{F_{i-1/2} - F_{i+1/2}}{\Delta x}. \tag{36}$$

In the model formulation of Hammer and Morin (2014), the momentum equations are discretized as

$$\partial_t \Pi_{g,i} = \frac{F_{g,i-1/2} - F_{g,i+1/2} + \alpha_g\,\Delta p_i}{\Delta x}, \tag{37}$$

$$\partial_t \Pi_{\ell,i} = \frac{F_{\ell,i-1/2} - F_{\ell,i+1/2} + \alpha_\ell\,\Delta p_i}{\Delta x}, \tag{38}$$

which yields the total momentum discretization

$$\partial_t \Pi_i = \frac{F_{\ell,i-1/2} - F_{\ell,i+1/2} + F_{g,i-1/2} - F_{g,i+1/2} + \Delta p_i}{\Delta x}. \tag{39}$$

The superfluous last term in Eq. (39), with respect to Eq. (36), shows that this formulation does not conserve total momentum properly. In the present model formulation, i.e. Eqs. (3) and (4), we have

$$\partial_t \Pi_{g,i} = \frac{F_{g,i-1/2} - F_{g,i+1/2} + p_i\,\Delta\alpha_{g,i}}{\Delta x}, \tag{40}$$

$$\partial_t \Pi_{\ell,i} = \frac{F_{\ell,i-1/2} - F_{\ell,i+1/2} + p_i\,\Delta\alpha_{\ell,i}}{\Delta x}, \tag{41}$$

which adds up to

$$\partial_t \Pi_i = \frac{F_{\ell,i-1/2} - F_{\ell,i+1/2} + F_{g,i-1/2} - F_{g,i+1/2}}{\Delta x}. \tag{42}$$

Identifying $F_{i\pm 1/2} = F_{g,i\pm 1/2} + F_{\ell,i\pm 1/2}$, this complies with Eq. (36). In other words, our model formulation ensures that whatever amount of momentum is added to one phase due to non-conservative terms, is subtracted from the other phase. Hence, the total momentum is conserved according to Eq. (35), up to the accuracy of the flux-based numerical scheme.

3.2. Source terms and closure relations

The source term ODEs

$$\frac{d\mathbf{u}}{dt} = \mathbf{s}(\mathbf{u}), \tag{43}$$

are solved using the Forward Euler method. Since we let the flow equations determine the global time step Δt, it might need to be reduced to ensure stability in the source terms ODE. In this case, more than one smaller time step Δt_s is performed that in total add up to Δt.

3.3. Heat equations

The heat equation (29) is solved using a finite volume scheme as described by Lund et al. (2015).

3.4. Reservoir boundary condition

The injection rate into a reservoir can be described by the *injectivity I*, which determines the injection rate resulting from a certain pressure difference between the well and the reservoir. This is implemented as a ghost cell with prescribed pressure $p = p_{\text{reservoir}} + (A\rho\hat{v})/I$ where $A\rho\hat{v}$ is the flow rate. The same procedure is used when fluid flows *out* of the reservoir, in which case the pressure in the well will be lower than the reservoir pressure. In other words we assume that the productivity and injectivity are equal.

4. Simulation cases

In the following, we describe the simulation cases including material parameters, initial and boundary conditions. In all cases, we use the same well geometry and material parameters. Key parameters are listed in Table 1. The parameters used are inspired by the conditions at the Sleipner CO_2 injection well (Lindeberg, 2011; Krogh et al., 2012), and hence the results are to some extent applicable to this well. However, in our case we consider a purely vertical well of length 1000 m, whereas the Sleipner well has significant horizontal deviation. In a real-world application, the reservoir injectivity/productivity will typically be time-dependent when the well starts to produce. However, since the effect of injectivity is not our main focus, we here assume a constant reservoir injectivity.

The heat conduction model assumes that the well is divided into five layers, whose properties are listed in Table 2. The layers are a 7 in. tubing, packer fluid, 9.5 in. casing, drilling mud (or cement for the lower 100 m), and a sandstone formation.

4.1. Sudden blowout

In this case, we consider an abrupt blowout scenario from a well. In the initial state, the well is closed at the top, and in contact with the reservoir at the bottom. The initial condition consists of a column of liquid in the lower part of the well, and gas in the upper

Table 1
Well and reservoir properties used in simulations.

Parameter	Value	Unit	Reference
Well depth	1000	m	Lindeberg (2011) and Krogh et al. (2012)
Ambient water temperature	5	°C	Krogh et al. (2012)
Geothermal gradient	41	°C/km	Lindeberg (2011)
Reservoir pressure	104	bar	Lindeberg (2011)
Injectivity/productivity	8.7×10^{-5}	kg/(s Pa)	Thu (2013)

Table 2
Material properties and dimensions for the layers surrounding the pipe.

Item	Radial segment [cm]	Axial segment [km]	Density [kg/m^3]	Thermal conductivity [W/(m K)]	Specific heat capacity [J/(kg K)]
Tubing (ST 52-3) (Albawi, 2013)	8.5–9.0	0–1	7850	40	500
Packer fluid (Halliburton, 2012)	9.0–11.1	0–1	1400	0.26	4000
Casing (ST 52-3) (Albawi, 2013)	11.1–12.2	0–1	7850	40	500
Drilling mud (Bjørkevoll, 2014)	12.2–15.5	0–0.9	1500	0.8	2500
Cement (Portland Class G) (Albawi, 2013)	12.2–15.5	0.9–1	1917	0.72	780
Sandstone (Castlegate) (Albawi, 2013)	15.5–500	0–1	2600	2.0	1000

part of the well. The pressure is assumed to be hydrostatic, extrapolated from the reservoir pressure in the bottom of the well. The temperature is assumed to be equal to the rock temperature until the boiling point is reached (at around 250 m depth), above which the temperature is set to be slightly above the boiling point, so that the fluid is in a gas state. The initial condition is illustrated in Fig. 1.

At $t = 0$, the well head is opened to atmospheric pressure, $p = 1.013$ bar. If the flow reaches sonic velocities, the flow is choked (see e.g. Linga et al., 2015) by imposing the choke pressure at the outlet, rather than the atmospheric pressure (Munkejord and Hammer, 2015). The lower end of the well is in contact with the reservoir, as described in Section 3.4, which causes CO_2 to flow from the reservoir into the well.

4.2. Sudden shut-in

In the shut-in case, we assume that there is a steady injection of CO_2 into the reservoir in the initial condition. The flow is set to 28.7 kg/s, similar to the flow in the Sleipner well (Thu, 2013). The bottom temperature is set to the reservoir temperature, and the pressure is set according to Section 3.4. The pressure in the rest of the well is set so that it balances the friction and gravity forces,

$$\partial_x p = f_{\text{grav}} - f_{\text{wall}}. \tag{44}$$
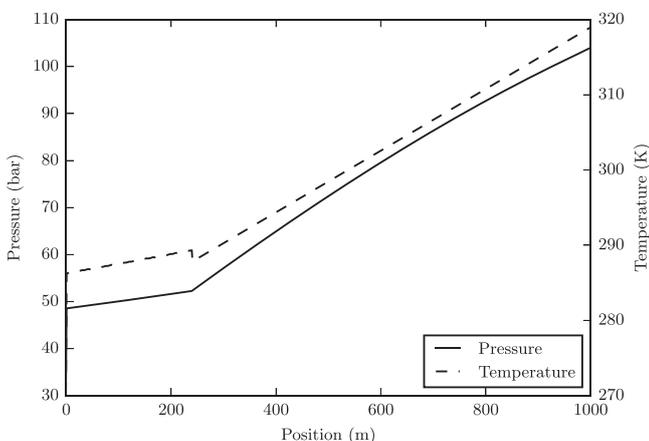
Fig. 1. Initial condition before blowout. There is liquid below $x \approx 250$ m, and gas above.
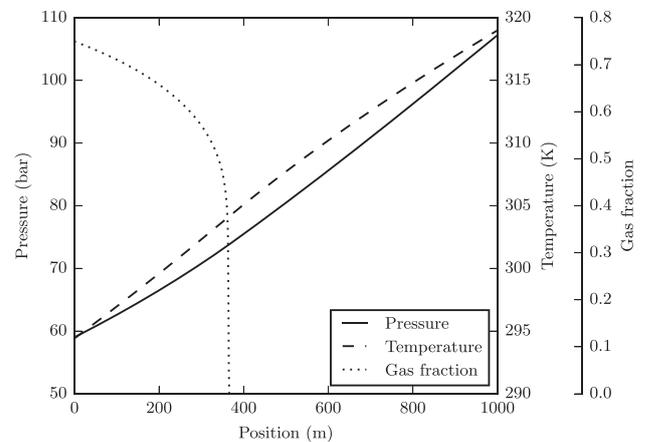

Fig. 2. Initial condition before shut-in.

The temperature is set by assuming the flow is isentropic, which leads to the initial condition depicted in Fig. 2. At $t = 0$, valves at both ends of the pipe are abruptly closed.

It turns out that the resulting initial well-head conditions are rather close to those present at Sleipner. The pressure and temperature at the Sleipner well-head are known to be 65 bar and 24 °C, whereas the gas fraction has been estimated to be around 0.85 (Thu, 2013).

5. Results and discussion

5.1. Blowout

The blowout case was simulated for 150 s, after which a somewhat steady flow out of the reservoir was reached. Fig. 3 shows the pressure at three locations in the pipe. The pressure at the outlet drops rapidly from 60 bar to approximately 10 bar in the first seconds, before it increases somewhat around $t = 7$ s. At this time, the speed of sound suddenly drops, since flow changes from pure gas to a two-phase mixture, as seen in Fig. 4. This causes the flow to be choked, resulting in a pressure jump. The pressure in the bottom part of the well drops slowly as the flow out of the reservoir increases, as specified in Section 3.4.

Fig. 4 shows the gas volume fraction for the well head and the middle of the well. A small amount of liquid occurs at the well head
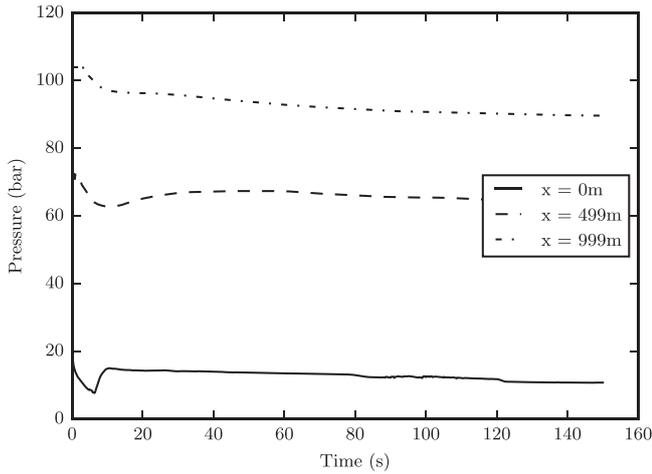
**Fig. 3.** Pressure during blowout for three pipe locations.

Fig. 4. Gas volume fraction during blowout at the well head and in the middle of the well.

in early phases of the blowout, which is likely to have been sucked up from the liquid column due to the rapid flow of gas. The middle of the well transitions gradually from pure liquid to almost pure gas over the course of the simulation, as the pressure slowly drops.
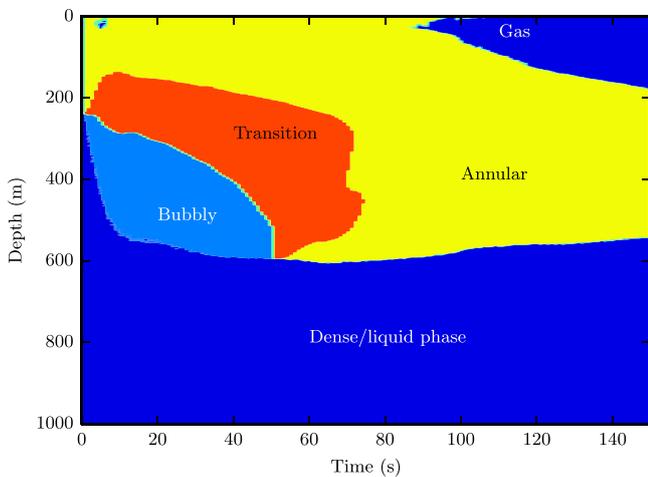

Fig. 5. Flow regimes during blowout.

Fig. 6. Temperature during blowout for three pipe locations.

Fig. 5 shows the flow regimes present in each part of the well. In the initial condition, the whole well is in a single-phase state (either pure liquid or pure gas). During the first 50–55 s, the upper part of the liquid column quickly boils and creates a zone of bubbly flow. When the velocity has increased sufficiently, most of the upper well has annular flow, with a liquid annulus and gas flowing in the middle. After around 100 s, the flow at the well head is purely gaseous.

During blowouts, very low temperatures can occur, which can be detrimental to well integrity and materials. Fig. 6 shows the temperature at three well locations. Since the flow in the bottom of the well comes directly from the reservoir, which has a temperature of 319 K, the lower part of the well does not experience any significant temperature drop. At the well head, however, temperatures as low as 225 K (or −48 °C) occur in the initial phase. The well head temperature rises somewhat when the flow is choked after around 7 s, and is thereafter steady at around 240 K (or −33 °C). This temperature is not necessarily low enough to cause damage to the steel pipe itself, but may be problematic due to mechanical stresses that arise due to thermal contraction.

It is important to note that our simulations do not predict any formation of dry ice in the well itself, although it might be formed just beyond the outlet at the well head. However, we assume that the temperature of the flow out of the reservoir is equal to the long-scale reservoir temperature. This is unlikely to hold on longer time scales, since some Joule–Thomson cooling will occur as the CO_2 fluid flows through the pores of the reservoirs and out into the well. The prediction of this phenomenon will require coupling the flow model to a reservoir model. Over time, the temperature of the flow from the reservoir will likely decrease, potentially damaging the well and allowing dry ice to form.

5.2. Shut-in

The shut-in case is simulated for around 40 s, which allows us to capture the most important features of the initial phase of a shut-in. Since valves are closed in both ends of the well, we can expect a pressure jump (water hammer) at the bottom valve, and a pressure decrease at the well head. As shown in Fig. 7, the bottom pressure increase is close to 10 bar. The pressure decrease at the well head is smaller, since there is two-phase flow in the upper part of the well, which makes the fluid more compressible. The fluid column, which is in motion initially, will be compressed at the bottom and decompressed at the top. This will cause pressure waves that propagate up and down the well, which are slowly damped by friction. These pressure oscillations are clearly seen in Fig. 7.
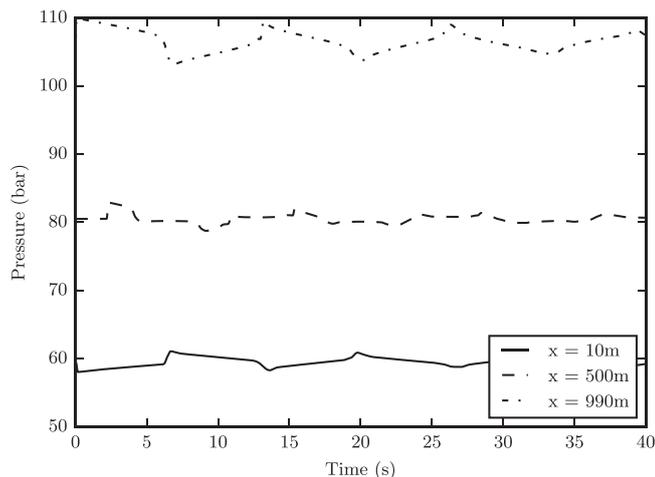
**Fig. 7.** Pressure during shut-in at three pipe locations.
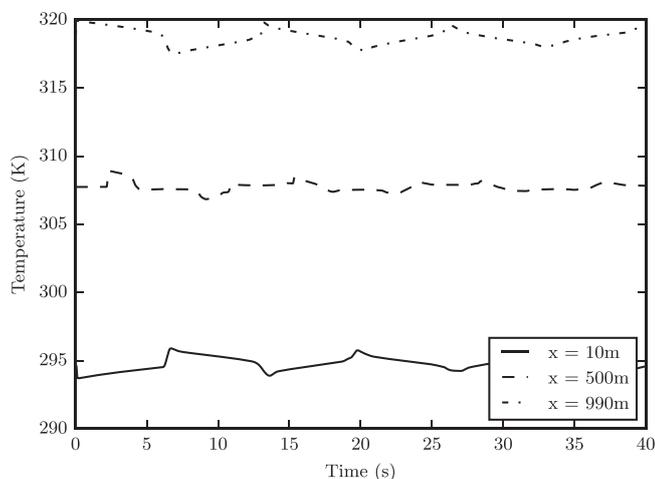
Fig. 8. Temperature during shut-in at three pipe locations.

Fig. 8 shows the temperature at three positions in the well. The temperature oscillations follow the pressure oscillations, since the fluid temperature is increased by compression.

Finally, Fig. 9 shows the flow regimes during the shut-in. The bottom of the well has a dense/liquid phase column which stretches up to a depth of around 370 m. At this depth, the liquid starts boiling, which leads to a layer of bubbly flow. Above this
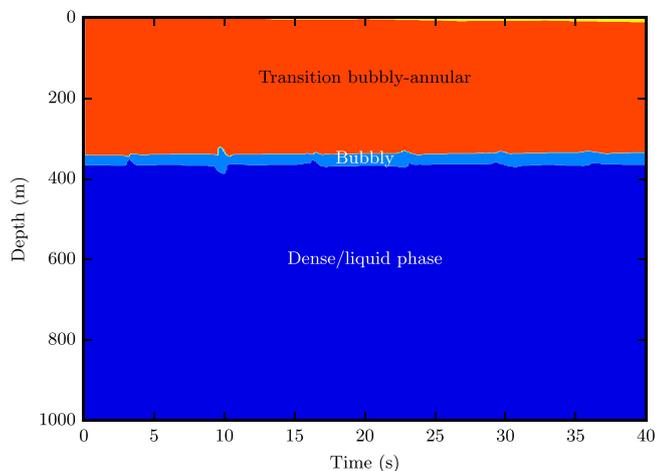
Fig. 9. Flow regimes during shut-in.

layer, the flow is predicted to be in a transition phase between bubbly flow and annular flow. These flow regimes are similar to what was observed by camera inspection in the Ketzin well during a shut-in (Henninges et al., 2011). In the upper part of the well, CO_2 was condensing and raining down on a layer of bubbly flow at around 300 m depth. The amount of bubbles decreased with depth until a stationary single-phase liquid column was reached. Although the geothermal conditions in our simulations are different than those at Ketzin, the results are qualitatively similar.

6. Conclusion

We have presented a two-fluid model for flow of CO_2 in a vertical injection well, coupled with a model for heat conduction in the layers that comprise the well. The flow model predicts what flow regime the flow is in, and calculates friction and heat transfer accordingly. It was derived with emphasis on making sure that the mass transfer was continuous in the single-phase limit. The thermodynamic closure of the flow was provided by the Span–Wagner reference equation-of-state for CO_2.

The model was applied to sudden blowout and shut-in cases. The well was chosen to mimic the Sleipner CO_2 injection well, with similar well depth, geothermal gradient, reservoir temperature and reservoir pressure. The predicted temperature in the blowout case was not low enough to lead to dry ice in the well itself. Dry ice may nevertheless form as the flow exits the well head, but this is outside the modelled domain. The assumption that flow out of the reservoir is at the reservoir temperature leads to steady temperature conditions in the lower parts of the well, but this assumption disregards any Joule–Thomson effect that may occur in the reservoir. We also predicted that annular flow is prevalent where the flow is in a two-phase state.

In the shut-in case, we predicted the water hammer effect resulting from simultaneously closing well-head and bottom-hole valves when there is a steady downwards flow. With a flow rate similar to that in the Sleipner well, the bottom-hole pressure jump was predicted to be around 10 bar. The pressure then oscillates in ≈ 13 s cycles as the fluid is compressed and decompressed. The fluid is found to be in a single-phase state up to around 370 m depth, above which the liquid starts to boil.

6.1. Further work

In further work, the model could be used to predict other transient operations of a well, such as shut-in on longer time scales, blowout with Joule–Thomson cooling in the reservoir, or intermittent injection from ships with resulting temperature variations. More realistic blowout and shut-in scenarios could also include valves that do not close or open suddenly, but are opened/closed over a certain time. The effect of a non-constant (time-dependent) injectivity, rather than a constant one used here, should also be considered. Moreover, horizontally deviating wells may behave differently due to e.g. different flow regimes, and could be worth looking into.

When it comes to applying the model for longer time scales (such as injection over several days/years), different numerical schemes are probably necessary to keep the computational cost at an acceptable level. For intermediate time scales, a semi-implicit scheme which solves pressure waves implicitly, could be used (see e.g. Chalons et al., 2011; Evje and Flåtten, 2005). For even longer time scales, the flow may be considered to be in a steady state, hence one can solve the steady-state ($\partial(\cdot)/\partial t = 0$) version of Eqs. (1)–(5) using an ODE solver.

Currently, there is little available high resolution experimental data for CO_2 wells. If such data become available, a proper model

validation could be performed to uncover potential modelling inaccuracies.

Acknowledgements

Appendix A. Nomenclature

Symbol	Description	Dimension	SI unit
A	Tubing cross-sectional area	L^2	m^2
a_k	Phase specific Heltmoltz free energy	L^2T^{-2}	m^2/s^2
c_p	Specific heat capacity at constant pressure	$L^2T^{-2}\Theta^{-1}$	m^2/(s^2 K)
E	Total energy density	$ML^{-1}T^{-2}$	kg/(m s^2)
e_k	Phase specific internal energy	L^2T^{-2}	m^2/s^2
E_k	Phase total energy density	$ML^{-1}T^{-2}$	kg/(m s^2)
E_{kin}	Kinetic energy density	$ML^{-1}T^{-2}$	kg/(m s^2)
f_i	Interface friction density	$ML^{-2}T^{-2}$	kg/(m^2 s^2)
$f_{\text{wall},k}$	Phase wall friction density	$ML^{-2}T^{-2}$	kg/(m^2 s^2)
g_x	Gravity on well axis	LT^{-2}	m/s^2
I	Reservoir injectivity	LT	ms
$\mathcal{K}$	Mass transfer rate constant	L^2T^{-3}	m^2/s^3
M_k	Phase mass per total volume	ML^{-3}	kg/m^3
p	Pressure	$ML^{-1}T^{-2}$	kg/(m s^2)
p_i	Interface pressure	$ML^{-1}T^{-2}$	kg/(m s^2)
Q	Heat transfer	$ML^{-1}T^{-3}$	kg/(m s^3)
r	Radius from tubing centre	L	m
R	Specific gas constant	$L^2T^{-2}\Theta^{-1}$	m^2/(s^2 K)
S	Volumetric entropy	$ML^{-1}T^{-2}\Theta^{-1}$	kg/(m s^2 K)
t	Time	T	s
v_k	Phase velocity	LT^{-1}	m/s
v_i	Interface velocity	LT^{-1}	m/s
$\hat{v}$	Centre-of-mass velocity	LT^{-1}	m/s
$\bar{v}$	Volume-averaged velocity	LT^{-1}	m/s
x	Distance along well	L	m
α_k	Phase volume fraction	–	–
δ	Regularizing pressure factor	–	–
κ	Thermal conductivity	$MLT^{-1}\Theta^{-1}$	kg m/(s K)
μ_k	Phase specific Gibbs free energy	L^2T^{-2}	m^2/s^2
Π_k	Phase momentum per total volume	$ML^{-2}T^{-1}$	kg/(m^2 s)
ρ	Mixture mass density	ML^{-3}	kg/m^3
ρ_k	Phase mass density	ML^{-3}	kg/m^3
Ψ	Mass density transfer rate	$ML^{-3}T^{-1}$	kg/(m^3 s)

References

Albawi, A., 2013. Influence of Thermal Cycling on Cement Sheath Integrity. Norwegian University of Science and Technology, Faculty of Engineering Science and Technology, Department of Petroleum Engineering and Applied Geophysics (Master's thesis).

André, L., Audigane, P., Azaroual, M., Menjoz, A., 2007. Numerical modeling of fluid–rock chemical interactions at the supercritical CO$_2$–liquid interface during CO$_2$ injection into a carbonate reservoir, the Dogger aquifer (Paris basin, France). Geologic Carbon Sequestration and Methane Hydrates Research from the TOUGH Symposium 2006. Energy Convers. Manag. 48 (6), 1782–1797, http://dx.doi.org/10.1016/j.enconman.2007.01.006, ISSN 0196-8904.

Austegard, A., Solbraa, E., De Koeijer, G., Mølnvik, M.J., 2006. Thermodynamic models for calculating mutual solubilities in H$_2$O–CO$_2$–CH$_4$ mixtures. Chem.

Eng. Res. Des. 84 (September (A9)), 781–794, http://dx.doi.org/10.1205/cherd05023.

Azaroual, M., Andre, L., Peysson, Y., Pironon, J., Broseta, D., Dedecker, F., Egermann, P., Desroches, J., Hy-Billiot, J., 2012. Behavior of the CO$_2$ injection well and the near wellbore during carbon dioxide injection in saline aquifers. In: Proceedings, TOUGH Symposium.

Baer, M., Nunziato, J., 1986. A two-phase mixture theory for the deflagration-to-detonation transition (DDT) in reactive granular materials. Int. J. Multiph. Flow 12 (6), 861–889.

Baudin, M., Berthon, C., Coquel, F., Masson, R., Tran, Q.H., 2005. A relaxation method for two-phase flow models with hydrodynamic closure law. Numer. Math. 99 (January (3)), 411–440.

Bendiksen, K.H., Malnes, D., Moe, R., Nuland, S., 1991. The dynamic two-fluid model OLGA: theory and application. SPE Prod. Eng. 6 (May (2)), 171–180, http://dx.doi.org/10.2118/19451-PA.

Bestion, D., 1990 Dec. The physical closure laws in the CATHARE code. Nucl. Eng. Des. 124 (3), 229–245, http://dx.doi.org/10.1016/0029-5493(90)90294-8.

Bjørkevoll, K.S., 2014. (SINTEF Petroleum) Personal communication.

Cannon, J.R., 1984. The One-Dimensional Heat Equation. Encyclopedia of Mathematics and Its Applications. Cambridge University Press, ISBN 9780521302432.

Chalons, C., Coquel, F., Kokh, S., Spillane, N., 2011. Large time-step numerical scheme for the seven-equation model of compressible two-phase flows. In: Fort, J., Furst, J., Halama, J., Herbin, R., Hubert, F. (Eds.), Finite Volumes for Complex Applications VI: Problems & Perspectives, Vols. 1 and 2, volume 4 of Springer Proceedings in Mathematics. CMLA ENS Cachan; IFP Energies Nouvelles; IRSN; LATP Univ Aix Marseille I; MOMAS Grp; Univ Paris XIII; Univ Paris Est Marne Vallee; Univ Pierre & Marie Curie, pp. 225–233, http://dx.doi.org/10.1007/978-3-642-20671-9_24, ISBN 978-3-642-20671-9. 6th International Symposium on Finite Volumes for Complex Applications, Prague, Czech Republic, June 06–10, 2011.

Chen, J.C., 1966. Correlation for boiling heat transfer to saturated fluids in convective flow. Ind. Eng. Chem. Process Des. Dev. 5 (3), 322–329, http://dx.doi.org/10.1021/i260019a023.

Dittus, F.W., Boelter, L.M.K., 1930. Heat transfer in automobile radiators of the tubular type. Univ. Calif. Publ. Eng. 2, 443–461.

Evje, S., Flåtten, T., 2005. Weakly implicit numerical schemes for a two-fluid model. SIAM J. Sci. Comput. 26 (5), 1449–1484.

Flåtten, T., Lund, H., 2011. Relaxation two-phase flow models and the subcharacteristic condition. Math. Models Methods Appl. Sci. 21 (December (12)), 2379–2407, http://dx.doi.org/10.1142/S0218202511005775.

Flåtten, T., Morin, A., Munkejord, S.T., 2010. Wave propagation in multicomponent flow models. SIAM J. Appl. Math. 70 (September (8)), 2861–2882, http://dx.doi.org/10.1137/090777700.

Forster, H.K., Zuber, N., 1955. Dynamics of vapor bubbles and boiling heat transfer. AIChE J. 1 (4), 531–535, http://dx.doi.org/10.1002/aic.690010425, ISSN 1547-5905.

Goodarzi, S., Settari, A., Zoback, M.D., Keith, D., et al.,2010. Thermal aspects of geomechanics and induced fracturing in CO$_2$ injection with application to CO$_2$ sequestration in Ohio River Valley. In: SPE International Conference on CO$_2$ Capture, Storage, and Utilization. Society of Petroleum Engineers.

Halliburton, 2012. N-SOLATE® High Performance Insulating Packer Fluids. http://www.halliburton.com/public/bar/contents/Data_Sheets/web/Sales_Data_Sheets/H05923.pdf (online; accessed 29.09.14).

Hammer, M., Morin, A., 2014. A method for simulating two-phase pipe flow with real equations of state. Comput. Fluids 100, 45–58, http://dx.doi.org/10.1016/j.compfluid.2014.04.030, ISSN 0045-7930.

Hammer, M., Ervik, Å., Munkejord, S.T., 2013. Method using a density-energy state function with a reference equation of state for fluid-dynamics simulation of vapor–liquid–solid carbon dioxide. Ind. Eng. Chem. Res. 52 (29), 9965–9978.

Han, W., Kim, K.-Y., Lu, M., McPherson, B., Lu, C., Lee, S.-Y., 2011. Injectivity changes and associated temperature disequilibrium: numerical study. 10th International Conference on Greenhouse Gas Control Technologies. Energy Procedia 4, 4552–4558, http://dx.doi.org/10.1016/j.egypro.2011.02.413, ISSN 1876-6102.

Hansen, O., Gilding, D., Nazarian, B., Osdal, B., Ringrose, P., Kristoffersen, J.-B., Eiken, O., Hansen, H., 2013. Snøhvit: the history of injecting and storing 1 Mt CO$_2$ in the fluvial Tubåen fm. GHGT-11. Energy Procedia 37, 3565–3573, http://dx.doi.org/10.1016/j.egypro.2013.06.249, ISSN 1876-6102.

Henninges, J., Liebscher, A., Bannach, A., Brandt, W., Hurter, S., Köhler, S., Möller, F., 2011. *P–T–ρ* and two-phase fluid conditions with inverted density profile in observation wells at the CO$_2$ storage site at Ketzin (Germany). 10th International Conference on Greenhouse Gas Control Technologies. Energy Procedia 4, 6085–6090, http://dx.doi.org/10.1016/j.egypro.2011.02.614, ISSN 1876-6102.

IEA, 2014. Energy Technology Perspectives., http://dx.doi.org/10.1787/energy_tech-2014-en, ISBN 978-92-64-20801-8.

Karlsen, K., Klingenberg, C., Risebro, N., 2004. A relaxation scheme for conservation laws with a discontinuous coefficient. Math. Comput. 73 (247), 1235–1259.

Kjärstad, J., Skagestad, R., Eldrup, N.H., Johnsson, F., 2014. Transport of CO$_2$ in the nordic region. 12th International Conference on Greenhouse Gas Control Technologies, GHGT-12. Energy Procedia 63, 2683–2690, http://dx.doi.org/10.1016/j.egypro.2014.11.290, ISSN 1876-6102.

Klinkby, L., Nielsen, C.M., Krogh, E., Smith, I.E., Palm, B., Bernstone, C., 2011. Simulating rapidly fluctuating CO$_2$ flow into the Vedsted CO$_2$ pipeline, injection well and reservoir. 10th International Conference on Greenhouse Gas

Control Technologies. Energy Procedia 4, 4291–4298, http://dx.doi.org/10.1016/j.egypro.2011.02.379, ISSN 1876-6102.

Krogh, E., Nilsen, R., Henningsen, R., 2012. Liquefied CO_2 injection modelling. The 6th Trondheim Conference on CO_2 Capture, Transport and Storage. Energy Procedia 23, 527–555, http://dx.doi.org/10.1016/j.egypro.2012.06.022, ISSN 1876-6102.

LeVeque, R.J., 2002. Finite Volume Methods for Hyperbolic Problems. Cambridge University Press, Cambridge, UK, ISBN 0-521-00924-3.

Li, X., Xu, R., Wei, L., Jiang, P., 2015. Modeling of wellbore dynamics of a CO_2 injector during transient well shut-in and start-up operations. Int. J. Greenh. Gas Control 42, 602–614, http://dx.doi.org/10.1016/j.ijggc.2015.09.016, ISSN 1750-5836.

Lindeberg, E., 2011. Modelling pressure and temperature profile in a CO_2 injection well. 10th International Conference on Greenhouse Gas Control Technologies. Energy Procedia 4, 3935–3941, http://dx.doi.org/10.1016/j.egypro.2011.02.332, ISSN 1876-6102.

Linga, G., Aursand, P., Flåtten, T., 2015. Two-phase nozzle flow and the subcharacteristic condition. J. Math. Anal. Appl. 426 (2), 917–934.

Linga, G., 2015. A Hierarchy of Non-equilibrium Two-Phase Flow Models (submitted for publication). Available online at http://folk.ntnu.no/gautelin/pub/twofluid.pdf.

Lu, M., Connell, L.D., 2008. Non-isothermal flow of carbon dioxide in injection wells during geological storage. Int. J. Greenh. Gas Control 2 (2), 248–258, http://dx.doi.org/10.1016/S1750-5836(07)00114-4, ISSN 1750-5836.

Lu, M., Connell, L.D., 2014. Transient, thermal wellbore flow of multispecies carbon dioxide mixtures with phase transition during geological storage. Int. J. Multiph. Flow 63, 82–92, http://dx.doi.org/10.1016/j.ijmultiphaseflow.2014.04.002.

Lu, M., Connell, L.D., 2014. The transient behaviour of CO_2 flow with phase transition in injection wells during geological storage – application to a case study. J. Pet. Sci. Eng. 124, 7–18, http://dx.doi.org/10.1016/j.petrol.2014.09.024.

Lund, H., Torsæter, M., Munkejord, S.T., 2015 Apr. Study of thermal variations in wells during CO_2 injection. In: SPE Bergen One Day Seminar, Bergen, Norway. Society of Petroleum Engineers, http://dx.doi.org/10.2118/173864-MS, Paper SPE-173864-MS.

Lund, H., 2012. A hierarchy of relaxation models for two-phase flow. SIAM J. Appl. Math. 72 (December (6)), 1713–1741, http://dx.doi.org/10.1137/12086368X.

Martínez Ferrer, P.J., Flåtten, T., Munkejord, S.T., 2012. On the effect of temperature and velocity relaxation in two-phase flow models. ESAIM: Math. Model. Numer. Anal. 46 (March (2)), 411–442, http://dx.doi.org/10.1051/m2an/2011039.

Masella, J.M., Tran, Q.H., Ferre, D., Pauchon, C., 1998. Transient simulation of two-phase flows in pipes. Int. J. Multiph. Flow 24 (August (5)), 739–755.

Morin, A., Flåtten, T., 2015. A two-fluid four-equation model with instantaneous thermodynamical equilibrium. ESAIM: M2AN, http://dx.doi.org/10.1051/m2an/2015074 (in press).

Munkejord, S.T., Hammer, M., 2015. Depressurization of CO_2-rich mixtures in pipes: two-phase flow modelling and comparison with experiments. Int. J. Greenh. Gas Control 37 (June), 398–411, http://dx.doi.org/10.1016/j.ijggc.2015.03.029.

Munkejord, S.T., Evje, S., Flåtten, T., 2009. A MUSTA scheme for a nonconservative two-fluid model. SIAM J. Sci. Comput. 31 (June (4)), 2587–2622, http://dx.doi.org/10.1137/080719273.

Natalini, R., 1997. Recent results on hyperbolic relaxation problems. Analysis of systems of conservation laws. In: Chapman & Hall/CRC Monographs and Surveys in Pure and Applied Mathematics., pp. 128–198.

Nordbotten, J.M., Celia, M.A., 2011. Geological Storage of CO_2: Modeling Approaches for Large-Scale Simulation. John Wiley & Sons.

Nordbotten, J.M., Celia, M.A., Bachu, S., 2005a. Injection and storage of CO_2 in deep saline aquifers: analytical solution for CO_2 plume evolution during injection. Trans. Porous Media 58 (3), 339–360.

Nordbotten, J.M., Celia, M.A., Bachu, S., Dahle, H.K., 2005b. Semianalytical solution for CO_2 leakage through an abandoned well. Environ. Sci. Technol. 39 (2), 602–611.

Paillère, H., Corre, C., García Cascales, J.R., 2003. On the extension of the AUSM+ scheme to compressible two-fluid models. Comput. Fluids 32 (July (6)), 891–916, http://dx.doi.org/10.1016/S0045-7930(02)00021-X.

Pan, L., Oldenburg, C.M., Wu, Y.-S., Pruess, K., 2009. Wellbore flow model for carbon dioxide and brine. Proceedings of the 9th International Conference on Greenhouse Gas Control Technologies (GHGT-9), Washington, DC, USA, 16–20 November 2008. Energy Procedia 1 (1), 71–78, http://dx.doi.org/10.1016/j.egypro.2009.01.012, ISSN 1876-6102.

Pan, L., Webb, S.W., Oldenburg, C.M., 2011. Analytical solution for two-phase flow in a wellbore using the drift-flux model. Adv. Water Resour. 34 (12), 1656–1665, http://dx.doi.org/10.1016/j.advwatres.2011.08.009, ISSN 0309-1708.

Pareschi, L., Russo, G., 2005. Implicit-explicit Runge–Kutta schemes and applications to hyperbolic systems with relaxation. J. Sci. Comput. 25, 129–155.

Pelanti, M., Shyue, K.-M., 2014. A mixture-energy-consistent six-equation two-phase numerical model for fluids with interfaces, cavitation and evaporation waves. J. Comput. Phys. 259, 331–357.

Ransom, V.H., et al., 1995. RELAP5/MOD3 Code Manual, NUREG/CR-5535. Idaho National Engineering Laboratory, ID.

Roussanaly, S., Brunsvold, A.L., Hognes, E.S., 2014. Benchmarking of CO_2 transport technologies: Part II – Offshore pipeline and shipping to an offshore site. Int. J. Greenh. Gas Control 28, 283–299.

Ruan, B., Xu, R., Wei, L., Ouyang, X., Luo, F., Jiang, P., 2013. Flow and thermal modeling of CO_2 in injection well during geological sequestration. Int. J. Greenh. Gas Control 19, 271–280.

Saurel, R., Abgrall, R., 1999. A multiphase Godunov method for compressible multifluid and multiphase flow. J. Comput. Phys. 150 (April (2)), 425–467.

Saurel, R., Petitpas, F., Abgrall, R., 2008. Modelling phase transition in metastable liquids: application to cavitating and flashing flows. J. Fluid Mech. 607 (July), 313–350, http://dx.doi.org/10.1017/S0022112008002061.

Singhe, A., Ursin, J., Henninges, J., Pusch, G., Ganzer, L., 2013. Modeling of temperature effects in CO_2 injection wells. GHGT-11. Energy Procedia 37, 3927–3935, http://dx.doi.org/10.1016/j.egypro.2013.06.291, ISSN 1876-6102.

Solem, S., Aursand, P., Flåtten, T., 2015. Wave dynamics of linear hyperbolic relaxation systems. J. Hyperbol. Differ. Equ. 12 (4), 655–670, http://dx.doi.org/10.1142/S0219891615500186.

Span, R., Wagner, W., 1996. A new equation of state for carbon dioxide covering the fluid region from the triple-point temperature to 1100 K at pressures up to 800 MPa. J. Phys. Chem. Ref. Data 25 (6), 1509–1596.

Stewart, H.B., Wendroff, B., 1984. Two-phase flow: models and methods. J. Comput. Phys. 56 (3), 363–409.

Strang, G., 1968. On the construction and comparison of difference schemes. SIAM J. Numer. Anal. 5 (3), 506–517.

Stuhmiller, J.H., 1977. The influence of interfacial pressure forces on the character of two-phase flow model equations. Int. J. Multiph. Flow 3 (December (6)), 551–560, http://dx.doi.org/10.1016/0301-9322(77)90029-5.

Thu, E.S., 2013. Modeling of Transient CO_2 Flow in Pipelines and Wells. Norwegian University of Science and Technology (Master's thesis).

Tiselj, I., Cerne, G., Horvat, A., Gale, J., Parzer, I., Giot, M., Seynhaeve, J., Kucienska, B., Lemonnier, H., 2004. WAHA3 Code Manual. JSI Report IJS-DP-8841. Jozef Stefan Institute, Ljubljana, Slovenia.

Toumi, I., 1996. An upwind numerical method for two-fluid two-phase flow models. Nucl. Sci. Eng. 123 (2), 147–168.

Vermeulen, T.N., June 2011. Knowledge Sharing Report – CO_2 Liquid Logistics Shipping Concept (LLSC): Overall Supply Chain Optimization. Technical Report. Global CCS Institute, Anthony Veder, Vopak.

Zuber, N., Findlay, J.A., 1965. Average volumetric concentration in two-phase flow systems. J. Heat Transf.: Trans. ASME 87 (November), 453–468.